Aerothermal Optimisation of Novel Cooling Schemes for High Pressure Components using Combined Theoretical, Numerical and Experimental Techniques



Benjamin W.M. Kirollos

Kellogg College

University of Oxford

A thesis submitted for the degree of

Doctor of Philosophy

Michaelmas 2015

Abstract

The continuing maturation of metal laser-sintering technology has presented the opportunity to de-risk the engine design process by experimentally down-selecting high pressure nozzle guide vane (HPNGV) cooling designs using laboratory tests of laser-sintered—instead of cast—parts to assess thermal performance. Such tests are very promising as a reliable predictor of the thermal-paint-engine-test, which is used during certification to validate cooling system designs. In this thesis, conventionally cast and laser-sintered parts are compared in back-to-back experimental tests at engine-representative conditions over a range of coolant mass flow rates. Tests were performed in the University of Oxford Annular Sector Heat Transfer Facility. The aerothermal performance of the cast and laser-sintered parts is shown to be very similar, demonstrating the utility of laser-sintered parts for preliminary engine thermal assessments.

It can be shown that in most situations counter-current heat exchanger arrangements outperform co-current arrangements. This concept, though familiar in the heat exchanger community, has not yet been applied to hot-section gas turbine cooling. In this thesis, the performance benefit of novel *reverse-pass* cooling systems—that is, systems in which the internal coolant flows substantially in the opposite direction to the mainstream flow—is demonstrated numerically and experimentally in film-cooled HPNGVs.

It is shown numerically that reverse-pass cooling systems always act to flatten lateral wall temperature variation and to reduce peak metal temperature by maximising internal convective cooling at the point of minimum film cooling effectiveness. Reverse-pass cooling systems therefore require less coolant than other internal flow arrangements to maintain acceptable metal temperatures. The benefits of reverse-pass cooling can be fully realised in systems with long, undisturbed surface length, such as the suction-side (SS) of a HPNGV, afterburner liners, HPNGV platforms, and combustor liners.

Three engine-scale HPNGVs with SS reverse-pass cooling systems were subsequently designed using bespoke numerical conjugate heat transfer and aerodynamic models to satisfy engine-realistic aerothermal and manufacturing constraints. The reverse-pass HPNGVs were metal laser-sintered and tested in back-to-back experiments with conventionally cooled HPNGVs in the Annular Sector Heat Transfer Facility. The reverse-pass HPNGVs are shown to reduce peak engine metal temperature by 30 K and reduce mean SS engine metal temperature by 60 K compared to conventionally cooled HPNGVs with the same cooling mass flow.

A physically-based infra-red thermography procedure was implemented which takes into account the transmittance of the external optics, the surface emissivity of the object, the black-body temperature-radiometric characteristics of the camera, and the time-varying surrounding radiance. Failure to account for surrounding radiance is shown to result in an absolute error in overall cooling effectiveness of 0.05.

A new experimental facility—the Coolant Capacity Rig—was developed in order to measure row-by-row, compartmental and total coolant capacity of HPNGVs to a precision of 0.03%, over a large range of pressure ratios and mass flows using a differential mass flow measurement technique, bypass system, and calibrated mass flow orifice. A novel method for estimating internal loss coefficients from the coolant capacity measurements has been devised which, uniquely, does not require internal pressure measurement.

To Mum and Dad

Acknowledgements

I would like to thank my supervisor Thomas Povey for his help and guidance, and for always fighting my corner. Working with Tom has been a privilege and a pleasure.

I am indebted to *Team Blowdown*—Ben Hall, Chris Hambidge, Matt Collins, Dominic Harris—for their expertise, time, and comradeship. They truly made the experiments possible. Many thanks also go to Salvador Luque Martinez, who patiently taught me the ways of the Sector, and upon whose work this thesis is built; and to Paul Beard, who helped run the Sector in the early days.

At Rolls-Royce I have had the privilege of working with Anton Rawlinson and Simon Gallimore—both very gifted engineers. I am grateful to the technicians and staff at Osney for all their support: Trevor Godfrey, Craig Parsons, Duncan Blake, Gerald Walker, Leo Verling, Paul Cox, Bill Godfrey, Hal Surtell, Kathryn Scott, Debbie Andrews and Laura Hook. To my other Osney lab-mates who shared the highs and lows—thanks for being there, and good luck for the future.

And most of all, my sincerest gratitude goes to Mum, Dad, Joe and Priyanka. I couldn't have done this without your love and support.

This project was jointly funded by the MoD and Rolls-Royce plc under the ENTAPS programme. University/college fees and stipend were funded by the EPSRC. An additional annual scholarship was awarded by Kellogg College, Oxford.

Contents

Abstract ..... **i**

Acknowledgements ..... **v**

Contents ..... **vii**

Nomenclature ..... **xiii**

1. Introduction **1**

1.1 Research Outcomes 2

1.2 Thesis Outline 2

2. Literature Review **5**

2.1 Justification for Increasing Turbine Entry Temperature 5

2.2 External Aerodynamics and Heat Transfer 6

2.3 General Cooling Design Strategy 8

2.4 Film Cooling 9

2.4.1 Important Parameters Affecting Film Cooling 10

2.4.2 Film Cooling Superposition 11

2.4.3 Aerodynamic Penalty of Film Cooling 11

2.4.4 Hole Shaping 12

2.5 Internal Cooling Technology 13

2.5.1 Pedestals and Pin-fins 14

2.5.2 Turbulator Ribs 14

2.5.3 Impingement Cooling 15

2.5.4 Serpentine Passages and Reverse-Pass Systems 15

2.6 Combined Cooling Technology 16

2.6.1 Transpiration Cooling 16

2.6.2 Dendritic, Lattice and Matric Cooling 17

2.6.3 Other Combined Cooling Systems 17

2.7 Experimental Methods 18

2.7.1 Linear Cascades, Annular Facilities and Annular Sector Facilities 18

2.7.2 Heat Transfer Measurements 19

2.8 Manufacture Methods for Testing 21

2.9 Conclusions 21

3. Reverse-Pass Concept Study 23
3.1 Long Plate Cooling Systems 24
3.2 Numerical Methods 26
3.3 Long Plate (Periodic) Temperature Distributions 28
3.4 Effect of Wall Thickness and Conductivity 30
3.5 Effect of Adiabatic Film Cooling Effectiveness Distribution 31
3.6 Long Plate Cooling Systems with Uniformly Distributed Inlet 32
3.7 Application of a Reverse-Pass System to the Suction Side of a HPNGV 34
3.8 Application of a Reverse-Pass System to the Pressure Side of a HPNGV 38
3.9 Conclusions 40

4. Design and Manufacture of Reverse-Pass High Pressure Nozzle Guide Vanes 43
4.1 Reverse-Pass Topology 43
4.2 Aerothermal Optimisation 47
4.3 Aerodynamic Modelling 48
4.3.1 Corrected Aerodynamic Boundary Conditions 49
4.3.2 Pedestal Bank Total Pressure Loss Correlation 51
4.3.3 Chevron Rib Total Pressure Loss Correlation 52
4.3.4 Smooth Duct Total Pressure Loss Estimation 53
4.3.5 Impingement and Pipe Fitting Total Pressure Loss Estimation 53
4.3.6 S4 and S5 Preliminary Area Estimation and TE Mass Flow Rate Estimation 54
4.4 Thermal Modelling 55
4.4.1 Thermal Boundary Conditions 55
4.4.2 Pedestal Bank Internal HTC Correlation 56
4.4.3 Smooth Duct and Chevron Rib Internal HTC Correlation 57
4.4.4 Coolant and Wall Temperature Prediction 57
4.5 Final Results of Aerothermal Modelling 60
4.6 Final Specification 68
4.7 Manufacture 72
4.7.1 Design Visualisation 72
4.7.2 Material Selection 74
4.7.3 Laser-Sintered Parts and Impingement/Baffle Plates 74
4.7.4 Platform Manufacture and Vane Pair Assembly 77
4.8 Proposed Improvements 79
4.9 Conclusions 80

5. Annular Sector Heat Transfer Facility 81
5.1 Purpose of Annular Sector Heat Transfer Facility 81
5.2 Overview of Sector Facility and Operating Conditions 82
5.3 Non-Dimensional Groups 90

5.3.1 Non-Dimensional Coolant Mass Flow Rate 90
5.3.2 Ratio of External to Internal Heat Transfer Coefficient 93
5.3.3 Adiabatic Film Cooling Effectiveness 94
5.3.4 Biot Number 96
5.3.5 Accuracy of Sector Overall Cooling Effectiveness Prediction 93
5.4 Summary of Sector Updates since Luque Martinez (2011) 97
5.5 Heater Mesh 100
5.6 Regulator 102
5.7 Sector Mass Flow Variation and Measurement 104
5.8 In-Situ Leak Test 110
5.9 Proposed Improvements to Ease Reconfiguration and Operation 113
5.10 Conclusions 115

6. Infra-Red Thermography 117
6.1 Introduction 117
6.2 Infra-Red Hardware and Data Acquisition Software 118
6.3 Surface Thermocouples 119
6.4 Selection of High Emissivity Paint 120
6.5 Infra-Red Thermography Theory Overview 122
6.6 Black-Body Calibration Theory 124
6.7 In-Situ Black-Body Calibration 125
6.8 Grey-Body vs Black Body Predictions 128
6.9 Grey-Body Calibration Theory 129
6.10 Grey-Body Calibration Assumptions 132
6.11 Determining $\tau\varepsilon$ 133
6.12 Run to run $q^*(t)$ 136
6.13 Pixel location for $q^*(t)$ evaluation 139
6.14 Proposed Improvements 143
6.15 Conclusions 144

7. Cooling Effectiveness Measurements 145
7.1 Overall Cooling Effectiveness and Mainstream Recovery Ratio 145
7.2 $\theta - c$ Regression 146
7.3 Justification for Overall Cooling Effectiveness vs $\dot{m}_c\sqrt{T_{0c}}/\dot{m}_m\sqrt{T_{0m}}$ 149
7.4 Image Registration 150
7.5 Mainstream Recovery Ratio c: Results 151
7.6 Mainstream Recovery Ratio c: Discussion 154
7.7 Overall Cooling Effectiveness θ: Results and Discussion 155
7.7.1 Discussion of Figure 7.8 158
7.7.2 Discussion of Figure 7.9 158

7.7.3 Discussion of Figure 7.10 162
7.7.4 Discussion of Figure 7.11 162
7.7.5 Discussion of Figure 7.12-7.14 166
7.7.6 Discussion of Figure 7.15-7.18 172
7.8 Proposed Improvements to Methodology 173
7.9 Conclusions 173

8. Raw Coolant Capacity Measurements 177
8.1 Introduction 177
8.2 Capacity Theory 178
8.3 Coolant Capacity Rig 180
8.4 Mass Flow Measurement 185
8.5 Calibration of CCR Orifice 187
8.6 Differential Mass Flow Measurement and Bypass Flow 191
8.7 Experimental Procedure – Practical Details 195
8.8 Best-Fit Curves 196
8.9 Raw Coolant Capacity Results 198
8.10 Interaction Testing 202
8.11 Proposed Improvements 206
8.12 Conclusions 207

9. Effective Row Area, Loss Coefficients, and Engine Coolant Capacity Prediction 209
9.1 Introduction 209
9.2 Network Flow Models 210
9.3 Population and Use of Network Flow Models 214
9.4 Baseline Cast and Baseline Laser-Sintered Network Flow Model 216
9.4.1 Calculating Baseline Loss Coefficients and Effective Row Areas 216
9.4.2 Calculating Baseline Row Capacities at Scaled Conditions 219
9.5 RP 1D Network Flow Model 220
9.6 RP 1D+ Network Flow Model 222
9.6.1 RP 1D+ S4 Ingestion 224
9.7 RP 3D Network Flow Model 225
9.7.1 Calculating RP 3D Loss Coefficients and Effective Row Areas 225
9.7.2 Calculating RP 3D Row Capacities at Scaled Conditions 229
9.8 Results: Effective Row Area and Loss Coefficients 230
9.9 Loss Model Predictions at CCR Conditions 233
9.10 Coolant Capacity Prediction and Validation at Sector Conditions 237
9.11 Coolant Capacity Prediction at Engine Conditions 242
9.12 Proposed Improvements 243
9.13 Conclusions 243

10. Conclusions 245
10.1 Laboratory Thermal Assessment of Laser-Sintered HPNGVs 245
10.2 Reverse-Pass Cooling Systems 245
10.3 Coolant Capacity and Loss Measurements 246
10.7 Future Study 246

11. References 249

Nomenclature

Abbreviations

1D, 2D, 3D	One-dimensional, two-dimensional, three-dimensional
ADC	Ambient drift compensation
AR	Anti-reflective
BR	Blowing ratio, BR = $(\rho u)_c/(\rho u)_m$
CAD	Computer aided design
CCD	Charge-coupled device
CCR	Coolant Capacity Rig
CFD	Computational fluid dynamics
CMP	Compartments
DR	Density ratio, DR = ρ_c/ρ_m
DMLS	Direct metal laser sintering
EDM	Electro-discharge machining
EFE	Environmentally friendly engine
eng.	Engine
FDM	Fused deposition modelling
FOV	Field of view
FPA	Focal plane array
HPNGV	High pressure nozzle guide vane
HT	Heat transfer
HTC	Heat transfer coefficient
IR	Infra-red
LE	Leading-edge
LEC	Leading-edge compartment
LP	Low pressure
M1	Design modified post laser-sintering
MR	Momentum flux ratio, MR = $(\rho u^2)_c/(\rho u^2)_m$
P1-P5	Film cooling row 1 to 5 on the pressure-side
PR	Pressure ratio
PRV	Pressure relief valve
PS	Pressure side
RIDN	Rear inner discharge nozzle
RODN	Rear outer discharge nozzle
ROI	Region of interest
RP	Reverse-pass
RPC	Reverse-pass compartment
RP 1D	1D reverse-pass design (known as RP1DA1 in all legacy files and documents)
RP 1D+	Modified 1D reverse-pass design (known as RP1DB2 in all legacy files and documents)
RP 2DA	2D reverse-pass design A (known as RP2DA in all legacy files and documents)
RP 2DB	2D reverse-pass design B (known as RP2DB in all legacy files and documents)
RP 3D	3D reverse-pass design (known as RP3D2 in all legacy files and documents)
RP S	Snail reverse-pass design (known as RPS in all legacy files and documents)
RR	Rolls-Royce
Sector	Annular Sector Heat Transfer Facility
SFC	Specific fuel consumption
SLA	Stereolithography
SLS	Selective laser sintering
S1-S5	Film cooling row 1 to 5 on the suction-side

S.D.	Surface distance
SS	Suction side
T500	Rolls-Royce Trent 500
TC	Thermocouple
TEC	Trailing-edge compartment
TET	Turbine entry temperature
TLC	Thermochromic liquid crystals
TE	Trailing-edge
TR	Temperature ratio T_3/T_1
TRL	Technology readiness level
UV	Ultra-violet

Lower-case

a	Heater mesh wire aperture [m]
a, b	Black-body calibration coefficients, $\sigma {T_{bb}}^4(\boldsymbol{x}) = aR(\boldsymbol{x}) + b$ [W·m^{-2}·Sr^{-1}·bit^{-1}]; mainstream recovery ratio regression constants, $c_i = a\left(p_{0c,i}/p_{0m,i}\right) + b$.
b_1, b_2, b_3, b_4	Constants for polynomial best-fit to capacity characteristic, $\Gamma^2 = \sum_{i=1}^{4} b_i \left(p_{0c}/p_{\text{atm}} - 1\right)^i$ [kg^2·s^{-2}·K·Pa^{-2}]
c	Mainstream recovery ratio, $c = T_r/T_{0m}$
c_p, $c_{p,c}$, $c_{p,m}$	Specific heat capacity, coolant, mainstream [J·kg^{-1}·K^{-1}]
d	Hydraulic diameter of internal coolant channel, $d = 4A/P$ [m]; heater mesh wire diameter [m].
f, f_0	Friction factor, friction factor of passage without HT augmentation geometry
h, h_1, h_2, $\bar{h}_2$	Heat transfer coefficient, external, internal, area-averaged internal [W·m^{-2}·K^{-1}]
h^*	Ratio of external to internal heat transfer coefficient, $h^* = h_1/h_2$
i, j	Indices
i	Row
j	Compartment
k_1, k_2	Constants for pressure calibration, $p = (V/k_1) + k_2$ [V·Pa^{-1}, Pa]
k, k_c, k_m, k_w	Thermal conductivity of air, coolant, mainstream, wall [W·m^{-1}·K^{-1}]
$\dot{m}$, $\dot{m}_c$, $\dot{m}_m$	Mass flow rate, coolant, mainstream [kg·s^{-1}]
$\dot{m}_{air}$	Air mass flow rate through engine core [kg·s^{-1}]
$\dot{m}_d$	Mass flow rate of external layer of gas [kg·s^{-1}], per unit depth [kg·s^{-1}·m^{-1}]
$\dot{m}_e$	Entrained mass flow rate [kg·s^{-1}], per unit depth [kg·s^{-1}·m^{-1}]
$\dot{m}_{TE}$	TE slot coolant mass flow rate [kg·s^{-1}], per unit depth [kg·s^{-1}·m^{-1}]
m^*	Non-dimensional coolant mass flow rate, $m^* = \left(\dot{m}_c c_{p,c}\right)/(h_1 A_{m^*})$
$\dot{m}_i^r$, $\dot{m}_j^c$	Mass flow rate through row i/compartment j [kg·s^{-1}·m^{-1}]
n_1, n_2, n_3, n_4	Scaling constants
p_0, p_{0u}	Total pressure, upstream total pressure [Pa]
p, p_d	Static pressure, downstream static pressure [Pa]
p_c, p_m	Static coolant/mainstream pressure [Pa]
p_{0c}, p_{0m}	Total coolant/mainstream pressure [Pa]
$p_{0u,j}^c$, $p_{0d,j}^c$	Upstream/downstream total pressure of loss element in compartment j [Pa]
$p_{0,j}^c\big\vert_H$, $p_{0,j}^c\big\vert_{i,L}$	Total pressure in compartment j during high-differential run H/low-differential run where row i is blocked [Pa]
$p_{d,i}^r$, $p_{\text{ext},i}^r$	Downstream/exhaust static pressure of row i [Pa]
p_{atm}	Atmospheric pressure [Pa]
$p_{ext,i}$	Pressure at exit of film cooling row [Pa]
p^*	Pressure ratio offset for capacity best-fit
q	Heat flux [W·m^{-2}]
q_{cam}	Radiance incident on IR camera, $q_{\text{cam}} = \sigma T_{bb}^4 = q_w' + q_R'' + q_{\text{opt}}$ [W·m^{-2}·Sr^{-1}]

q_{opt}	Radiance incident on IR camera due to the temperature of the optics, $q_{\text{opt}} = \sigma(1-\tau)T_{\text{opt}}^4$ [W·m^{-2}·Sr^{-1}]
q_w	Radiance from object of interest before optics, $q_w = \sigma\varepsilon T_w^4$ [W·m^{-2}·Sr^{-1}]
q'_w	Radiance incident on IR camera due to the temperature of object, $q'_w = \sigma\tau\varepsilon T_w^4$ [W·m^{-2}·Sr^{-1}]
q_R	Radiance from surroundings before reflection from vane of interest, $q_R = \sigma T_R^4$ [W·m^{-2}·Sr^{-1}]
q'_R	Radiance from surroundings after reflection from vane of interest and before optics, $q'_R = \sigma(1-\varepsilon)T_R^4$ [W·m^{-2}·Sr^{-1}]
q''_R	Radiance incident on IR camera due to the temperature of surroundings, $q''_R = \sigma\tau(1-\varepsilon)T_R^4$ [W·m^{-2}·Sr^{-1}]
q^*	Surrounding radiance $q^* = \left(q''_R + q_{\text{opt}}\right)/(1-\tau\varepsilon)$ [W·m^{-2}·Sr^{-1}]
q^*_{iso}	Surrounding radiance at isothermal conditions, $q^*_{\text{iso}}(t) = \sigma T_w^4$ [W·m^{-2}·Sr^{-1}]
r	Mainstream recovery factor
r_p	Overall pressure ratio across compressor and combustor, $r_p = p_3/p_1$
s	Span of the vane [m]
s_e	Equivalent slot width [m]
t	Time [s]
t_w	Wall thickness [m]
u_c, u_m	Coolant speed, mainstream speed [m·s^{-1}]
v	Speed [m·s^{-1}]
v_j^C	Speed within compartment j [m·s^{-1}]
v_{max}	Maximum speed within pedestal bank [m·s^{-1}]
w	Span-wise channel width [m]
x	Distance along wall [m]
$\boldsymbol{x}$	Location on vane [m]
x_i	Coolant ejection location of i^{th} module [m]
x'	Axial distance relative to the domain inlet in design [m]
x_{Nu_c}, x_{Nu_m}	Characteristic length for coolant/mainstream Nusselt number [m]
y	Coordinate normal to wall [m]

Upper-case

A	Adiabatic film cooling effectiveness decay rate, area [m^2]
A'	Increase in internal area due to pedestals, heater mesh cross-sectional area per unit width [m]
A_i^r, A_j^c	Flow area of row i/compartment j [m^2]
A_{m^*}	Surface area of the vane [m^2]
$A_{\dot{m}_c}$, $A_{\dot{m}_m}$	Coolant/mainstream area for momentum flux ratio measurement [m^2]
A^*	Constant for capacity best-fit [m^2]
Bi	Biot number, $\text{Bi} = (h_1 t_w)/k_w$
C_D	Discharge coefficient
D	Diameter [m]
G	Gaussian weighting function
H	Pedestal height [m]
I	Current [A]
K_j^c	Dimensionless loss coefficient within compartment j
$K_j^{c\prime}$	Dimensional loss coefficient within a compartment [J$^{0.5}$·kg$^{-0.5}$·K$^{-0.5}$·m^{-1}]
K_L	Dimensionless loss coefficient
L	Streamwise length of internal coolant channel [m]
M, M_m	Mach number, mainstream
N	Number of rows of pedestals/ribs, number of experimental runs

Nu	Nusselt number, Nu$= hx/k$
Nu_d, Nu_D	Nusselt number based on channel hydraulic diameter, pedestal diameter
Nu_c,Nu_m	Coolant/mainstream Nusselt number
P	Perimeter of internal coolant channel [m], power [W]
Pr	Prandtl number, Pr $= c_p\mu/k$
Pr_c, Pr_m	Prandtl number of coolant, mainstream
$Q_{adv,d}$	Advection heat flow within external layer of gas per unit depth [W·m^{-1}]
$Q_{adv,m}$	Advection heat flow between mainstream/existing films and external layer of gas per unit depth [W·m^{-1}]
$Q_{adv,c}$	Advection heat flow within coolant per unit depth [W·m^{-1}]
Q_{cond}	Conduction heat flow within wall per unit depth [W·m^{-1}]
$Q_{conv,d}$	Convection heat flow between external flow and wall per unit depth [W·m^{-1}]
$Q_{conv,c}$	Convection heat flow between internal flow and wall per unit depth [W·m^{-1}]
R	Specific gas constant of air [J·kg^{-1}·K^{-1}], raw IR camera pixel count [bit]
R_{mesh}, $R_{cabling}$	Electrical resistance of heater mesh/cabling [Ω]
Ra, $\widetilde{\mathrm{Ra}}_1$, $\widetilde{\mathrm{Ra}}_2$	Surface roughness [m], normalised external/internal surface roughness
Re_x	Reynolds number, $\mathrm{Re}_x = \rho V x/\mu$
Re_d, Re_D	Reynolds number based on channel hydraulic diameter, pedestal diameter
Re_c, Re_m	Coolant/mainstream Reynolds number
S	Streamwise pedestal spacing [m]
T_{0m}	Mainstream total temperature [K]
$T_{0m}{}'$	Temperature of fluid entrained into external heat transfer driving layer [K]
T_1	Core temperature at compressor inlet [K]
T_3	Core temperature at turbine inlet (TET) [K]
T_{aw}, T_{ad}	Adiabatic external wall temperature [K]
T_{bb}	Black-body temperature [K]
T_c, T_m	Static coolant/mainstream temperature [K]
T_{0c}, T_{0m}	Total coolant/mainstream temperature [K]
T_{atm}	Atmospheric temperature [K]
T_{amb}	Ambient temperature [K]
T_{opt}	Optics temperature [K]
T_{ce}	Coolant exit temperature [K]
T_d	External heat transfer driving/reference temperature [K]
T_{lim}	Limiting metal temperature [K]
T_r	Mainstream recovery temperature [K]
T_w, T_{w1}, T_{w2}	Wall temperature, external, internal [K]
T_R	Effective temperature of surroundings [K]
Tu	Turbulent intensity, Tu $= 100u'/\bar{u}$
U	Overall heat transfer coefficient, $U = ([1/h_1] + [1/h_2] + [t_w/k_w])^{-1}$ [W·m^{-2}·K^{-1}]
V	Voltage generated by Drake [V], volume [m^3]
$\boldsymbol{V}$	Vandermonde matrix
V_{mesh}	Voltage across heater mesh [V]
V_{atm}	Voltage from pressure transducer at atmospheric pressure [V]
$\boldsymbol{W_i}$	N×N diagonal weighting matrix around run i
$\dot{W}_{net}$	Net power output [W]
$\boldsymbol{X}$	2×N matrix of observations in weighted linear regression
$\boldsymbol{y}$	Column vector of N ones.

Greek

α	IR absorptivity
$\boldsymbol{\beta}_i$	Coefficients found from least squares minimisation, $\boldsymbol{\beta}_i = [c_i \quad \theta_i]^T$

γ	Ratio of specific heats, $\gamma = c_p/c_v$
Γ	Capacity, $\Gamma = \dot{m}\sqrt{T_0}/p_0$
Γ_c, Γ_m	Capacity of coolant, mainstream [kg·s^{-1}·K$^{0.5}$·Pa^{-1}]
Γ_i^r, Γ_j^c	Raw coolant capacity of row i/compartment j [kg·s^{-1}·K$^{0.5}$·Pa^{-1}]
$\Gamma_{i,L}$, $\Gamma_{i,H}$	Coolant capacity measured from CCR; low-differential run where row i is covered/high-differential run associated with low-differential run [kg·s^{-1}·K$^{0.5}$·Pa^{-1}]
$\tilde{\Gamma}_i^r$	Coolant capacity of row i when all rows are blowing [kg·s^{-1}·K$^{0.5}$·Pa^{-1}]
$\delta\dot{m}_e$	Entrainment mass flow rate into external layer of gas per unit depth [kg·s^{-1}·m^{-1}]
δx	Surface distance element [m]
Δp_0	Total pressure loss [Pa]
ΔT	Change in mainstream temperature [K]
ε	Cooling efficiency, $\varepsilon = (T_{ce} - T_{0c})/(T_{w1} - T_{0c})$; IR surface emissivity.
μ_c, μ_m, $\mu_{m,w}$	Dynamic viscosity of coolant, mainstream, mainstream at external wall temperature [Pa·s]
μ	Summation index
ρ_c, ρ_m	Density of coolant, mainstream [kg·m^{-3}]
σ	Stefan-Boltzmann constant [J·m^{-2}·s^{-1}·K^{-4}], Gaussian standard deviation
τ	IR transmittance
η	Adiabatic film cooling effectiveness, $\eta = (T_{0m} - T_{aw})/(T_{0m} - T_{ce})$
$\eta_{aw,i}$	Adiabatic film cooling effectiveness of i^{th} film cooling row in isolation
η_c	Compressor isentropic efficiency
η_{cycle}	Joule cycle efficiency
η_t	Turbine isentropic efficiency
θ	Overall cooling effectiveness, $\theta = (T_r - T_{w1})/(T_{0m} - T_{0c})$; viewing angle.
ϕ	Alternative overall cooling effectiveness definition, $\phi = (T_r - T_{w1})/(T_r - T_{0c})$
ζ	Specific capacity, $\zeta = \dot{m}\sqrt{T_0}/(p_0 A)$ [kg·s^{-1}·K$^{0.5}$·Pa^{-1}·m^{-2}]

1. Introduction

The jet engine has transformed human history. War, peace, politics, economics, health, migration, innovation—almost every aspect of modern life has been affected. The jet engine has given more people than ever the opportunity to reach any populated point on the planet in less than 48 hours.

There is significant research effort to make aircraft more powerful and efficient. Consequently, temperatures in the jet engine are being pushed higher, with the result that a modern high pressure nozzle guide vane (HPNGV) must survive in working gas temperatures well above its melting point. The HPNGV is actively cooled using increasingly complex systems that aim to maintain acceptable vane metal temperatures using the minimum amount of cooling flow.

Recent patents of turbine vane/blade cooling system concepts suggest that there is increasing interest in internal cooling designs resembling high-efficiency compact heat exchangers. There has been no discussion in the gas-turbine literature, however, of how optimisation methodology from the heat exchanger community can be brought to bear on the gas turbine hot-section cooling problem. It can be shown that in most situations counter-current heat exchanger arrangements (hot and cold streams flowing in opposite directions) outperform co-current arrangements. This concept, though familiar in the heat exchanger community, has not yet been examined in the context of cooling hot-section gas turbine components. This has inspired the study and development of novel *reverse-pass cooling systems for HPNGVs* reported in this thesis.

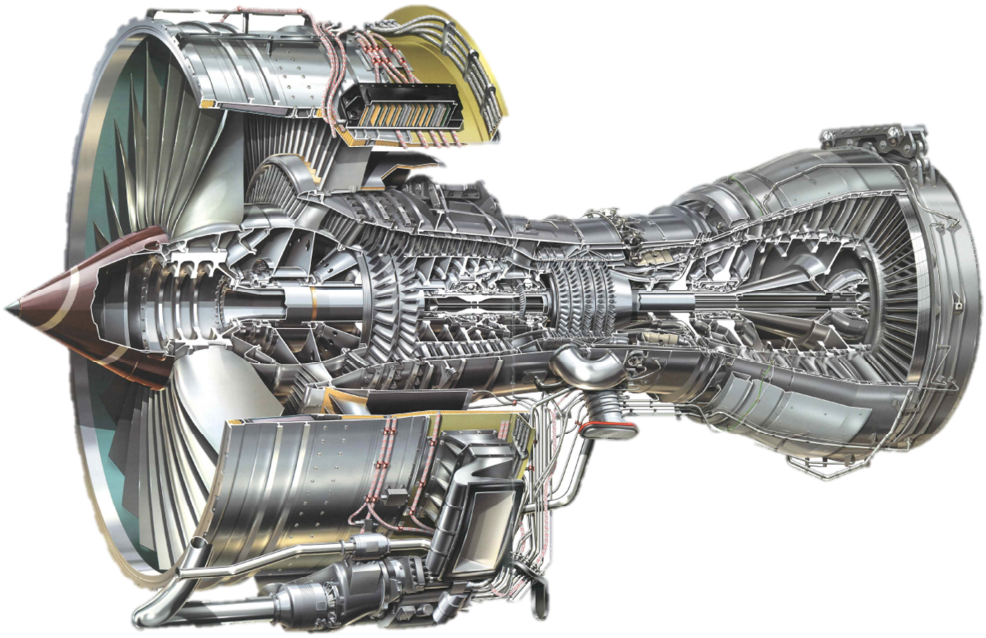


Figure 1.1. Diagram of the Rolls-Royce Trent 500, Crook and Horlor (2005)

The thermal performance of cooling systems for HPNGVs is typically assessed at engine conditions using a thermal-paint-test engine as part of the engine certification process. Such tests are generally restricted to final qualification of cooling systems before production. Promising cooling systems with some element of design risk (lower technology readiness level, TRL) would not normally be tested in engine products, extending the time required for new technology to enter service engines. This motivates the second focus of this thesis, which is the use of engine-scale laser-sintered parts in high TRL aerothermal laboratory experiments to accelerate the rate at which technology is transitioned from research into engine products.

1.1 Research Outcomes

In this thesis, the feasibility of using laser-sintered HPNGVs to assess the aerothermal performance of the equivalent cast HPNGV at laboratory conditions at a standard required to influence engine development programmes is demonstrated. A novel, physically based infra-red processing method was developed to account for time-varying surrounding radiance. A facility was designed, manufactured and utilised to measure HPNGV row-by-row coolant capacity and internal loss coefficients. A regression technique was implemented which estimates the overall cooling effectiveness and mainstream recovery ratio as a function of coolant-to-mainstream pressure ratio from a series of experimental tests.

The concept of reverse-pass cooling was explored and developed using bespoke 2D and 3D numerical models. Engine-scale laser-sintered reverse-pass HPNGVs were subsequently designed, manufactured and tested in back-to-back experiments with conventionally cooled HPNGVs in the Annular Sector Heat Transfer Facility. The key benefits of reverse-pass cooling (namely, greater temperature uniformity and reduced maximum metal temperature) are demonstrated both numerically and experimentally.

1.2 Thesis Outline

In *Chapter 2*, the relevant literature on HPNGV heat transfer, cooling technology and experimental methods for assessing thermal performance is reviewed. Further reference to the relevant literature is included in the appropriate chapter.

In *Chapter 3*, the concept of reverse-pass cooling hot-section engine components is examined using a bespoke 2D numerical conjugate heat transfer model. It is shown that reverse-pass cooling reduces peak temperature and significantly reduces lateral surface temperature variation.

In *Chapter 4*, the conclusions from the 2D numerical study are used to design engine-scale, three-dimensional HPNGVs with suction-side reverse-pass cooling systems which satisfy engine-realistic aerothermal and manufacturing constraints. Three reverse-pass-cooled HPNGVs were developed and

optimised using a bespoke 3D numerical conjugate heat transfer and aerodynamic model. The manufacture and assembly of the HPNGVs using direct metal laser sintering (DMLS) is reported.

In *Chapter 5*, the Annular Sector Heat Transfer Facility (Sector Facility) at the University of Oxford, which is used to replicate thermal-paint test conditions in the laboratory, is reviewed. Modifications to the facility since the work of Luque Martinez (2011) are reported.

In *Chapter 6*, the infra-red (IR) thermography techniques used to measure the temperature of the HPNGVs in the Sector Facility are described. A novel, physically based IR processing method is discussed which measures and compensates for time-varying surrounding radiation. Updates to the IR hardware and software in the Sector Facility are reported.

In *Chapter 7*, the overall cooling effectiveness of the baseline and reverse-pass HPNGVs measured in the Sector Facility is reported. Results are shown over a range of coolant-to-mainstream mass flow and pressure ratios. A new regression method for measuring both overall cooling effectiveness and mainstream recovery temperature from a series of experiments is detailed.

In *Chapter 8*, the new experimental facility (Coolant Capacity Rig) and method developed to measure the row-by-row coolant mass flow distribution are described. The raw experimental results are also presented in this chapter.

In *Chapter 9*, the raw results from Chapter 8 are processed in order to estimate the effective area of each row of cooling holes, the internal loss, and the coolant mass flow distribution at engine conditions.

In *Chapter 10*, the key findings and contributions of this thesis are summarised.

This thesis is the result of more than 500 tests in the Sector Facility, 1000 tests in the Coolant Capacity Rig/Flow Testing Facility, and over 2 TB worth of experimental data.

2. Literature Review

In this chapter, a background is given to HPNGV heat transfer, cooling technology, and experimental methods for assessing thermal performance. Further reference to the relevant literature is included in the appropriate chapter.

2.1 Justification for Increasing Turbine Entry Temperature

In an ideal gas turbine cycle (Joule/Brayton cycle) with non-isentropic compressor and turbine, the net non-dimensional power output ($\dot{W}_{net}/\dot{m}_{air}c_pT_1$) is a function of the overall pressure ratio across the compressor and combustor ($r_p = p_3/p_1$), the overall temperature ratio across the compressor and combustor (T_3/T_1), the compressor inlet temperature T_1, and the isentropic efficiencies of the compressor (η_c) and turbine (η_t):

$$\frac{\dot{W}_{net}}{\dot{m}_{air}c_pT_1} = \eta_t \frac{T_3}{T_1}\left(1 - r_p^{\frac{1-\gamma}{\gamma}}\right) + \frac{1}{\eta_c}\left(1 - r_p^{\frac{\gamma-1}{\gamma}}\right), \tag{2.1}$$

where $\dot{m}_{air}$ is the mass flow rate of air, c_p is the specific heat capacity of air, and γ is the ratio of specific heats.

The cycle efficiency (η_{cycle}) of an ideal gas turbine cycle with non-isentropic compressor/turbine is

$$\eta_{cycle} = \frac{\eta_t \frac{T_3}{T_1}\left(1 - r_p^{\frac{1-\gamma}{\gamma}}\right) + \frac{1}{\eta_c}\left(1 - r_p^{\frac{\gamma-1}{\gamma}}\right)}{\frac{T_3}{T_1} - 1 + \frac{1}{\eta_c}\left(1 - r_p^{\frac{\gamma-1}{\gamma}}\right)}. \tag{2.2}$$

Operating cost is reduced by maximising non-dimensional power output and cycle efficiency. An engine with greater non-dimensional power output requires less core flow to generate the power required for steady flight. Consequently, the core can be smaller, reducing engine weight and complexity. For a given nacelle size (core + bypass), reduced core flow affords greater bypass flow, which decreases specific fuel consumption (Cumpsty, 2003). Greater cycle efficiency reduces the specific fuel consumption of the engine (Saravanamuttoo et al., 2001) so that less fuel is required for a given journey, decreasing aircraft weight and raw fuel cost.

The cycle efficiency and non-dimensional power output of a gas turbine are plotted as a function of temperature ratio (T_3/T_1) and pressure ratio (r_p) in Fig. 2.1 for a ratio of specific heats of 1.3 and isentropic compressor/turbine efficiency of 0.9. It can be seen that cycle efficiency and non-dimensional power output increase with pressure ratio and temperature ratio (in the range

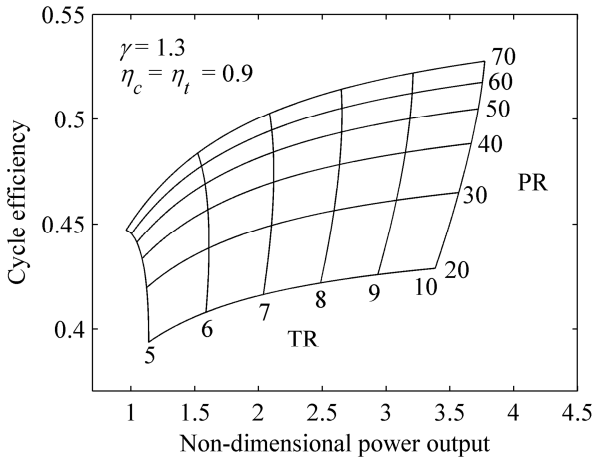


Figure 2.1. Joule cycle efficiency vs non-dimensional power output as a function of pressure ratio (PR) and temperature ratio (TR), non-isentropic compressor and turbine.

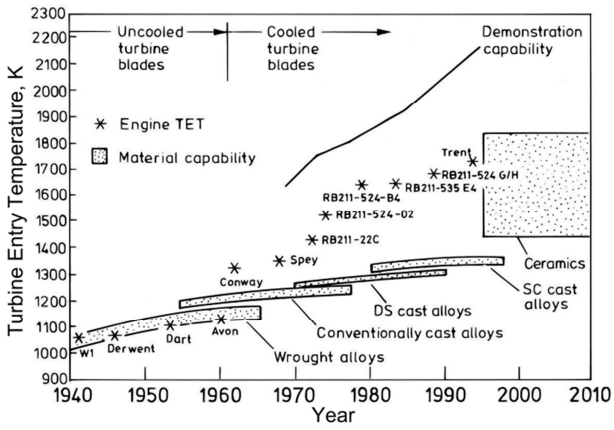


Figure 2.2. TET for Rolls-Royce engines since 1940, from Cumpsty (2003).

investigated). High turbine entry temperature (TET) and pressure are therefore targeted in order to reduce operating cost.

Current civil jet engines operate with a temperature ratio (T_3/T_1) ~6-7 and a pressure ratio of (p_3/p_1) ~50. TET is mainly restricted by: (i) the stoichiometric combustion temperature limit; (ii) the maximum allowable metal temperature of the high-pressure nozzle guide vane set by life requirements (Mazur et al., 2005); (iii) and the cycle efficiency penalty imposed by large turbine cooling flows (Horlock et al., 2001). The pressure ratio is a trade-off between performance, weight, cost, stability and life (Crook and Horlor, 2005).

Advances in materials and cooling technology have afforded greater TET at a given cooling flow while maintaining acceptable HPNGV metal temperatures (Fig. 2.2). Horlock et al. (2001) performed a cycle analysis which accounted for cooling flow and real gas effects, which demonstrated that cycle efficiency is maximised at an intermediate value of TET below the stoichiometric combustion limit, and high-pressure turbine cooling flow decreases cycle efficiency by approximately 0.5%. They argue that increasing cycle efficiency by reducing cooling flow is now more economical than increasing TET—i.e., we should target more efficient cooling systems. However, the advantages of increasing non-dimensional power output at greater TET were not considered.

2.2 External Aerodynamics and Heat Transfer

The core air flow through a HPNGV passage is unsteady, transonic and highly turbulent, with non-uniform inlet and outlet conditions. The flow is bounded by endwalls and vanes, which generate high amounts of vorticity. Vorticity and flow turning induces secondary flows, defined by Persico et al. (2009) as the component of velocity perpendicular to the inviscid flow direction.

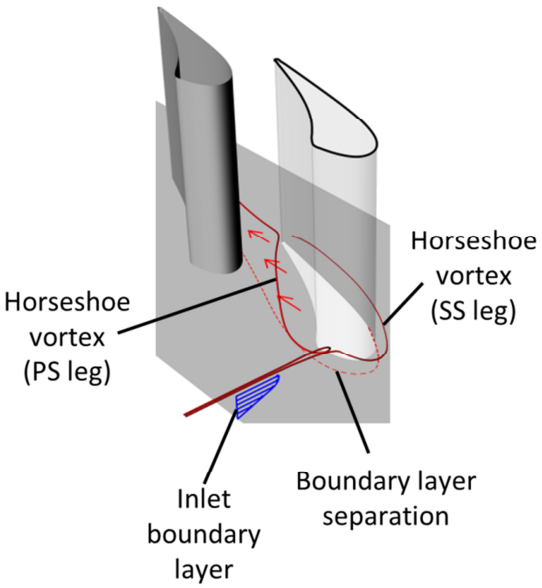


Figure 2.3. Secondary flows in a turbine passage (Thomas, 2014).

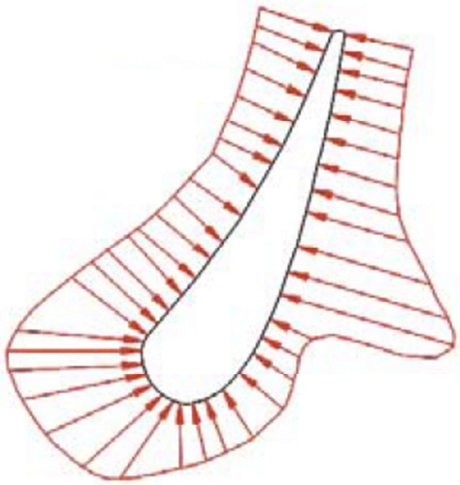


Figure 2.4. Typical turbine vane external heat transfer distribution (Han and Wright, 2006).

Much research has focused on understanding secondary flow structures, since they are responsible for 30-50% of the total aerodynamic loss in the high pressure turbine stage (Sharma and Butler, 1987) and directly impact wall heat transfer.

A modern view of secondary flow structures in a linear cascade is shown in Fig. 2.3. The stagnation of the inlet boundary layer at the leading-edge induces a horseshoe vortex around the pressure and suction side of the aerofoil. The relatively low-velocity boundary layer fluid is then over-turned compared to the mainstream flow, resulting in secondary flow. Recent studies such as Thomas (2014) have suggested that the classical view, which has been derived mainly from experiments in linear cascades (e.g., Herzig et al., 1954 and Langston, 1980), may overstate the extent and importance of secondary flows. The inlet contraction to most HPNGVs generates large streamwise acceleration which acts to reduce the thickness of the boundary layer, reducing the severity of secondary flows.

The addition of a radial pressure gradient in highly swirling, annular flows has also been studied, e.g., Sieverding et al. (1984) and Povey et al. (2007). It was found that secondary flows near the hub are suppressed whilst those at the casing are enhanced due to the interaction of the radial pressure gradient and the low momentum fluid in the endwall boundary layers.

Other significant flow features found in the HPNGV passage include shocks, separations, TE wake and cavity flows, which increase entropy and decrease total pressure. The aerodynamics of the coolant internal to the vane is simpler, due to lower Mach numbers and temperatures, resulting in an approximately incompressible internal flow field.

External heat transfer is partly dictated by the state of the boundary layer and is fundamentally governed by the Fourier conduction equation next to the wall:

$$q = k \left. \frac{\partial T}{\partial y} \right|_{y=0}, \tag{2.3}$$

where y is the co-ordinate normal to the wall, T is the fluid temperature, k is the thermal conductivity evaluated either at the wall temperature or across the near wall flow, and q is heat flux. The temperature gradient depends primarily on the velocity profile within the boundary layer and the driving temperature difference across the layer. This forms the basis of Newton's law of cooling, in which a *heat transfer coefficient* (h) is used to quantify the velocity profile which is to first order independent of temperature (Jones, 1991):

$$q = h(T_r - T_w), \tag{2.4}$$

where T_r is the mainstream recovery temperature, T_w is the wall temperature and $T_r - T_w$ is the driving temperature difference used to define the heat transfer coefficient.

For a given flow regime, a thicker boundary layer and lower driving temperature difference reduces $\partial T/\partial y|_{y=0}$ and hence reduces heat transfer. Turbulent boundary layers have a higher $\partial T/\partial y|_{y=0}$ at the wall than a laminar boundary layer of the same thickness. Stagnation regions, and regions where shocks have caused boundary layer separation and subsequent reattachment, experience the highest heat transfer rates because of thinner boundary layers. Many empirical relations exist which relate heat transfer (via the Nusselt number) to Reynolds number and Prandtl number (e.g., Kays et al., 2004). The typical heat transfer distribution around a turbine vane is shown in Fig. 2.4. The jump in heat transfer around the SS shoulder is due to laminar-turbulent boundary layer transition.

2.3 General Cooling Design Strategy

Without coolant to remove heat, the HPNGV would operate at the local recovery temperature of the mainstream gas. To maintain acceptable metal temperature, HPNGVs are cooled using combined internal and external (film) cooling systems. These are discussed separately.

An example of an HPNGV cooling system is shown in Fig. 2.5. Approximately 10% of the core air flow at the compressor exit is extracted for use as coolant for the HPNGV. The compressor exit air is relatively cool (~1000 K) in comparison to the core air flow from the combustor (~2000 K). The metal temperature is reduced by minimising the external (hot-side) heat transfer coefficient and maximising the internal (cold-side) heat transfer coefficient. Film cooling reduces heat flux to the vane by reducing the external driving temperature difference. Thermal barrier coatings on the external surface of the vane increase the wall thermal resistance but allow a large temperature drop in a layer

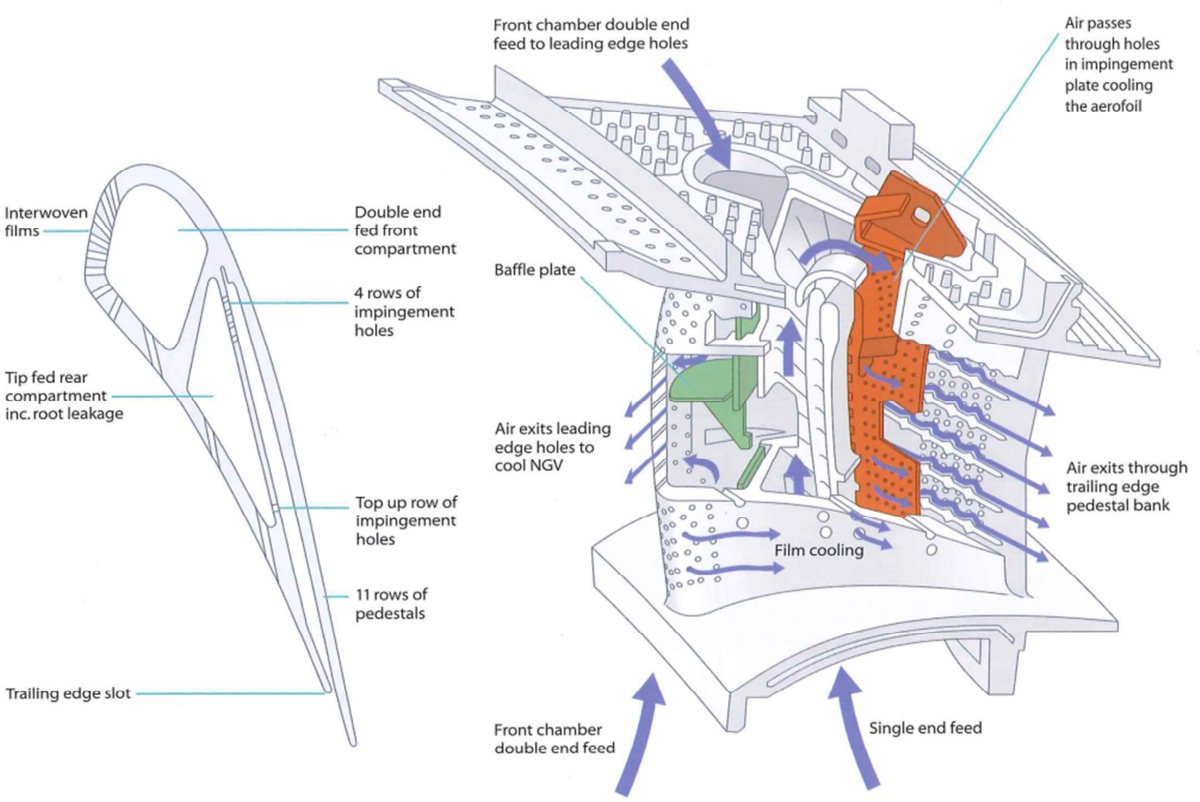


Figure 2.5. Example of cooled high pressure nozzle guide vane, from Crook and Horlor (2005).

of higher temperature capability (but lower mechanical capability). Internal convective cooling systems are designed to extract heat from the wall as effectively and efficiently as possible.

The optimum cooling strategy (e.g., the balance between mass flow rate, cooling effectiveness, film effectiveness and cooling efficiency) was investigated during the DPhil term of the author and is published in two papers (Kirollos and Povey, 2015b, 2015c). This work is not included in this thesis due to space limitations.

2.4 Film Cooling

Film cooling is essential to obtain current levels of TET. Relatively cool air from the compressor is discharged through small holes or slots in the external surface of the vane to create a film barrier between the hot mainstream gas and the HPNGV. An exhaustive pre-2003 literature survey and data compilation of film cooling correlations has been compiled by Gilboy and Gan (2003). A further review of film cooling literature can be found in Bogard (2006) and Han et al. (2000). Attempts have been made to correlate data across a wide range of operating conditions e.g. Baldauf et al. (2002).

Under certain mass flux, momentum flux and hole diameter-to-chord ratios typical of modern HPNGV designs, each film cooling jet may give rise to a pair of counter-rotating kidney vortices. Downstream of the hole, turbulent mixing dissipates the kidney vortices generating a uniform layer of coolant. The jet may attach or detach from the surface, depending mainly on the coolant-to-

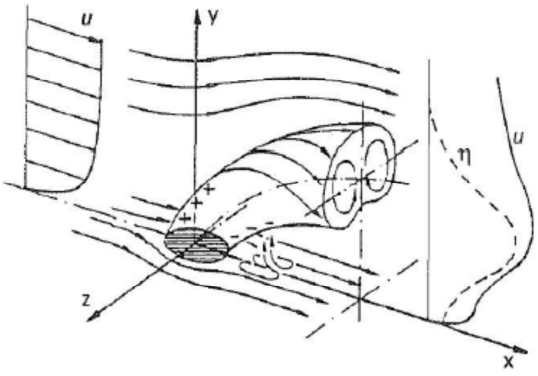


Figure 2.6. Injected jet flow structure with counter rotating kidney vortices (Haas et al., 1991).

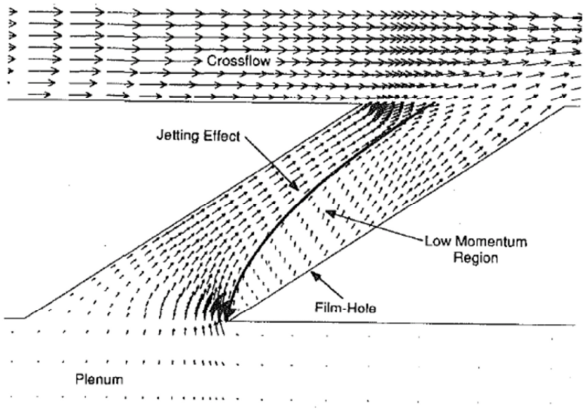


Figure 2.7. Velocity vector plot within film cooling hole (Leylek and Zerkle, 1993).

mainstream momentum flux ratio. A roll-up horseshoe vortex may be present at the leading edge of the jet, created as the mainstream funnels around the ejected fluid. The horseshoe and kidney vortices affect the rate of mainstream entrainment into the cooling layer, altering the effectiveness of the film. The vortical structures and velocity vector field created by a film cooling hole are shown in Figs. 2.6 and 2.7.

2.4.1 Important Parameters Affecting Film Cooling

Film cooling performance is typically quantified using the adiabatic film cooling effectiveness η, defined as

$$\eta = \frac{T_{0m} - T_{aw}}{T_{0m} - T_{ce}}, \tag{2.5}$$

where T_{0m} is the mainstream total temperature, T_{ce} is the coolant exit temperature (i.e., the temperature of the coolant at the point it is ejected into the mainstream), and T_{aw} is the adiabatic wall temperature. For high speed flows, the mainstream recovery temperature T_r is used instead of the mainstream total temperature. Physically, the film cooling effectiveness measures the reduction in the driving temperature for external heat transfer due to the introduction of the film.

The parameters that have a significant effect on film cooling performance are coolant-to-mainstream mass flux ratio BR $= (\rho u)_c/(\rho u)_m$, coolant-to-mainstream momentum flux ratio MR $= (\rho u^2)_c/(\rho u^2)_m$, mainstream turbulence, shape of the hole, injection and compound angle of the hole, surface curvature and surface roughness (Bogard, 2006). The energy flux ratio and thermal conductivity ratio also influence heat pick-up and storage.

Momentum flux ratio is governed by the coolant and mainstream total and static pressures, and is the main factor in determining the dynamics of the coolant jet on exit. High MR may cause jet

detachment, leading to low film effectiveness immediately downstream of the hole. The jet may or may not reattach downstream (Thole et al., 1992). In general, low MR leads to better jet attachment. The advantage of low MR must be balanced against the risk of hot gas ingestion which requires higher momentum flux ratio. Blowing ratio is fundamentally a measure of coolant mass flow rate. Greater BR for a given hole area results in a lower mixed out temperature downstream and therefore increased effectiveness, e.g., Baldauf et al., 2002. Studies have also looked at the effect of density ratio DR $= \rho_c/\rho_m$ (e.g. Sinha et al., 1991).

Convex surfaces create a positive gradient towards the wall causing low momentum film cooling flow to be overturned. The result is better film cooling attachment on convex surfaces than concave surfaces (Schwarz et al., 1990). The effect of surface roughness on film cooling performance is more complex, depending strongly on the mass flux ratio. In simple terms, at higher mass flux ratios film effectiveness improves with increasing surface roughness. At lower mass flux ratios, film effectiveness worsens with increasing surface roughness (e.g. Goldstein et al., 1985 and Guo et al., 2000).

Similarly, the effect of mainstream turbulence on film cooling effectiveness depends on the momentum flux ratio. At high momentum flux ratios, increased turbulence tends to improve film effectiveness, whilst as lower momentum flux ratios mainstream turbulence tends to worsen film effectiveness (Bons et al., 1996). It is thought that high levels of turbulence mitigate jet separation.

2.4.2 Film Cooling Superposition

In general, correlations are available for the film decay rate of single rows of cooling holes. However, most real applications use several rows in series. The interaction between multiple rows and their additive effect is the subject of many studies, such as Sinha et al. (1991), LeGrives & Nicolas (1977) and Zhu et al. (2008). The superposition model of Sellers (1963) is the industry standard method to predict the additive cooling effect of multiple rows from single row correlations.

A novel film cooling superposition model was developed alongside the work reported here and is published in Kirollos and Povey (2015a). This work is relatively removed from the core work of this thesis and is therefore omitted.

2.4.3 Aerodynamic Penalty of Film Cooling

Film cooling disrupts the mainstream flow and can lead to aerodynamic loss and reduced engine efficiency. Film cooling typically accounts for 20% of the total aerodynamic losses in a HPNGV (Friedrichs et al., 1997). These losses are generated when the coolant jet penetrates and mixes with the main flow with a resultant loss in total pressure. The effect can be demonstrated with a momentum-based control volume analysis. The form and magnitude of the loss depends on the difference in momentum between the coolant and mainstream, hole geometry and interaction with other jets.

Injection into high Mach number regions incurs greater aerodynamic loss and consequently film cooling injection is usually limited to the showerhead region and pressure-side. Harstel (1972) and Kollen & Koschel (1985) propose mixing models that predict the losses associated with film cooling injection.

2.4.4 Hole Shaping

Many studies have investigated the performance of novel hole geometries. Most current designs utilise cylindrical holes due to their relative ease of manufacture. A common variant is the 2-in-1 or 3-in-1 cooling hole, in which two or three cylindrical holes with slightly varying axes are merged into a single *bat-wing* shaped hole. Generally, holes are designed with injection angles as close to tangential as possible to reduce aerodynamic losses, with holes tightly packed to increase external coolant coverage. Both of these conditions are limited by the structural integrity of the vane.

A review of fan shaped hole technology pre-2005 is given in Bunker (2005). Some examples of the types of hole investigated are shown in Fig. 2.8. Fan shaped holes have been shown to increase film cooling effectiveness and reduce the dependence on turbulence and mass flux ratio (Goldstein et al., 1974). They show much better attachment and lift-off characteristics than cylindrical holes. However, fan shaped holes can lead to greater aerodynamic mixing loss than cylindrical holes due to a lower coolant momentum flux at exit.

The converging-slot-hole, or console, is a promising development on the fan shaped hole (Sargison et al., 2005), shown in Fig. 2.9. The flow accelerates towards exit which increases the coolant-to-mainstream momentum flux ratio. In some cases, console cooling has been shown to improve aerodynamic performance compared to an uncooled vane by reenergising the boundary layer. Consoles improve film cooling effectiveness and increase coolant coverage compared to cylindrical holes at all momentum fluxes ratios (Liu et al., 2010).

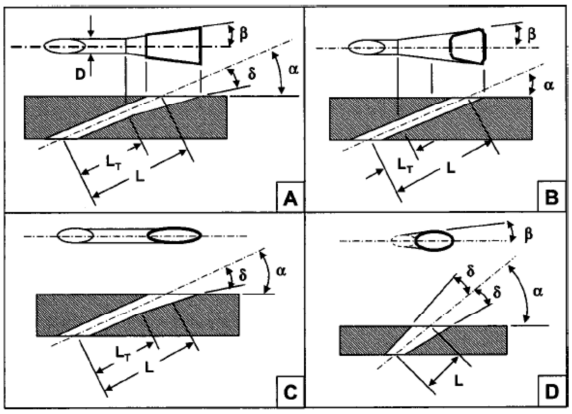


Figure 2.8. Four shaped film holes (Bunker, 2005).

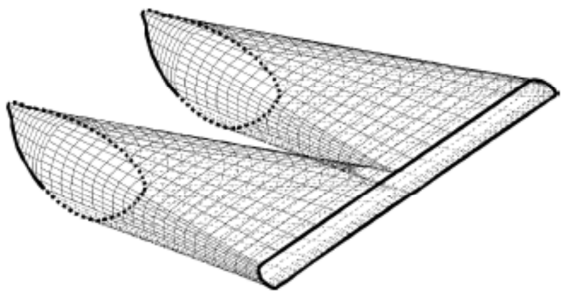


Figure 2.9. Two converging slot-holes (consoles) from Sargison et al., (2005).

A variety of hole shapes have been devised with the intention of reducing the strength of the kidney vortices. Two such designs are arrow shaped cooling holes (Okita & Nishihura, 2007) and cooling holes angled towards each other (Kusterer et al., 2006). Elliptical holes have also shown benefits (Colban et al., 2006).

Slots are typically considered the most effective method of film cooling. In comparison to a row of holes, slots provide better surface coverage and generate lower vorticity. This minimises the formation of the roll-up horseshoe and kidney vortices and reduces mainstream entrainment (e.g. Wilfert & Fottner, 1996 and Ganzert et al., 2000). However, slots significantly reduce the structural integrity of the vane.

2.5 Internal Cooling Technology

Internal convective cooling systems reduce HPNGV metal temperature by drawing heat through the metal into the coolant. The performance of internal cooling systems is typically quantified using overall cooling effectiveness θ and cooling efficiency ε. Overall cooling effectiveness θ is defined as:

$$\theta \equiv \frac{T_r - T_{w1}}{T_{0m} - T_{0c}}, \tag{2.6}$$

where T_{w1} is the external (hot-side) wall temperature, T_{0m} is the mainstream total temperature, T_{0c} is the coolant total temperature at entry to the vane, and T_r is the mainstream recovery temperature. The overall cooling effectiveness is a non-dimensional measure of external wall temperature. Hot-section components are typically designed to operate above a certain overall cooling effectiveness which is set by life requirements. Cooling efficiency ε is defined as:

$$\varepsilon = \frac{T_{ce} - T_{0c}}{T_{w1} - T_{0c}}, \tag{2.7}$$

where T_{ce} is the coolant exit temperature, i.e., the temperature of the coolant at exit from the internal cooling system. The cooling efficiency is a measure of the actual coolant heat pick-up to the theoretical maximum heat pick-up.

Overall cooling effectiveness and cooling efficiency are improved by increasing the internal HTC and wetted surface area. Increasing coolant mass flow enhances cooling effectiveness but reduces cooling efficiency, while longer passages increase cooling efficiency but decrease cooling effectiveness. The design of an internal cooling system is consequently a balance between cooling effectiveness, cooling efficiency, mass flow rate, allowable pressure drop and film effectiveness—though, generally speaking, convective cooling systems with high internal HTC and low pressure drop are desirable.

The internal HTC in a HPNGV can be augmented using pedestals, pin-fins, turbulator ribs and impingement cooling. These are reviewed in the following sections. All rely on the principle of

increasing internal HTC by disrupting the boundary layer and promoting mixing. Serpentine passages, utilised to increase cooling efficiency, are also reviewed.

2.5.1 Pedestals and Pin-fins

Pin-fins and pedestals are typically arrays of small cylinders that project out from a surface; either across the entire width of the cooling channel (commonly referred to as pedestal) or across part of the cooling channel (commonly referred to as pin-fin). By enhancing mixing in the internal flow, pedestals/pin-fins increase the internal heat transfer coefficient. The Nusselt number and friction factor of passages with pedestals depends upon Reynolds number and pedestal spacing (e.g., Metzger et al., 1982 and Van Fossen, 1982). The influence of the shape and the arrangement of the pedestals has also been studied, e.g., Chyu (1990), Chyu et al., (1998), Metzger et al., (1986) and Chyu et al., (1992).

The performance of pin-fins depends on the clearance/height ratio. For small clearances, pin-fins have the same characteristics as pedestals (Arora and Abdel-Messeh, 1989). As the clearance becomes larger, the mainstream avoids the high-resistance flow through the structures and any heat transfer benefit reduces. The heat transfer augmentation of pin-fins with a large clearance is typically estimated from the increase of wetted surface area only (Rawlinson, 2001).

2.5.2 Turbulator Ribs

Turbulators (sometimes known as vortex generators) are similar to pin-fins in that they are structures that project part way across the passage (Fig. 2.10). In contrast to pin-fins, however, the spacing and height of the turbulators is chosen such that the boundary layer trips and reattaches by the next turbulator. Heat transfer is augmented by impingement at the LE of the turbulator, reattachment of the boundary layer, vorticity generated by the turbulator, and increased wetted surface area. In the case of pin-fins, reattachment does not take place and the flow stagnates between pin-fins.

Turbulators typically span 10-15% of the hydraulic diameter d of the passage (where the hydraulic diameter $d = (4\times\text{flow area})/\text{perimeter}$) and have a spacing-to-height ratio of 5 to 15 (Han and Wright, 2006). Turbulators vary considerably in shape. In industry, the most common form of turbulators are continuous, parallel ribs angled at 45° and 60° to the flow (Fig. 2.11). Delta shaped ribs, V-shaped ribs, broken ribs and dimples have also been investigated. The performance of a rib is usually reported as a friction factor increase f/f_0 and heat transfer augmentation factor Nu/Nu_0, referenced to duct flow at a certain Reynolds number. In general, Nu/Nu_0 increases with f/f_0, and thus the selection of a turbulator design is a compromise between pressure drop and HTC rise. The effect of geometry such as spacing, height, angle and aspect ratio (Park et al., 1992) has been successfully correlated using the non-dimensional momentum roughness function and thermal roughness function (Cunha, 2006).

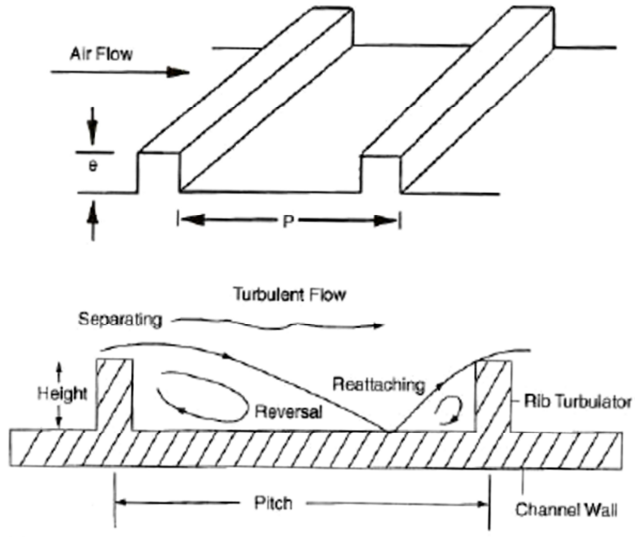


Figure 2.10. Flow separation and reattachment around turbulator ribs (Han & Dutta, 1995).

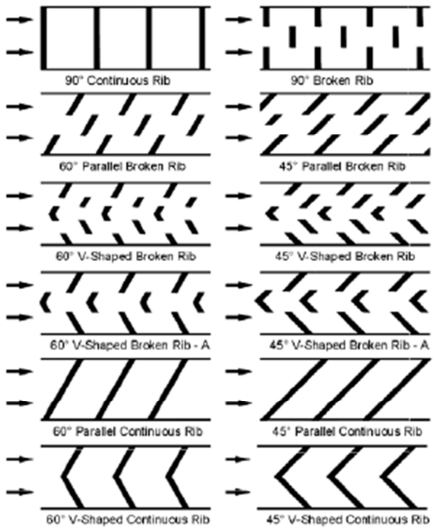


Figure 2.11. Turbulator ribs for heat transfer augmentation (Han & Zhang, 1992).

2.5.3 Impingement Cooling

The greatest internal heat transfer coefficient is arguably generated by impinging coolant directly on to the target wall. The stagnation and subsequent spreading of the flow creates high velocity gradients at the wall and high HTC. The complexity of the structure required for impingement cooling and its relatively high-loss nature currently limits its use to certain areas within the turbine vane. Advances in manufacturing methods are set to expand its application. Combined cooling technologies that incorporate impingement are of increasing interest (discussed later).

The separation distance between wall and distributor plate (typically a perforated plate) is key to the performance of an impingement system. As a rule of thumb, an optimum separation distance for heat transfer of approximately 2-3 hole diameters is often quoted (Brevet et al., 2002 and Jambunatha et al., 1992). The effect of spacing between impinging jets has also been researched and the ideal found to be approximately 4-5 hole diameters (Brevet et al., 2002), depending on the flow and geometric conditions. Nusselt numbers have been correlated for a wide range of Reynolds numbers, jet spacing and separation distances (Florschuetz et al., 1981 and Kercher and Tabakoff, 1970). Literature on non-standard impingement of individual jets or slot type jets is investigated by Martin (1977).

2.5.4 Serpentine Passages and Reverse-Pass Systems

Serpentine passage is used here to refer to *guided* internal coolant channels, i.e., channels that follow a path for a purpose. Serpentine passages benefit from increased heat pick-up per unit coolant mass flow rate, augmented heat transfer at bends (Liou et al., 2000), and the ability to tune local internal cooling to the needs of the vane (Kirollos and Povey, 2015c). The length of a serpentine passage is limited by the allowable pressure drop and allowable coolant temperature increase. Serpentine

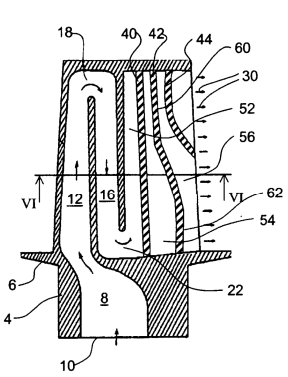


Figure 2.12. Patent by Kopmels (2009).

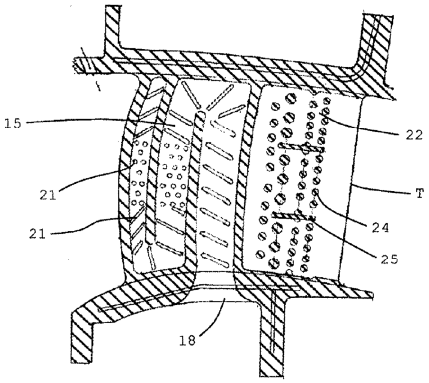


Figure 2.13. Patent by Tibbott (2010).

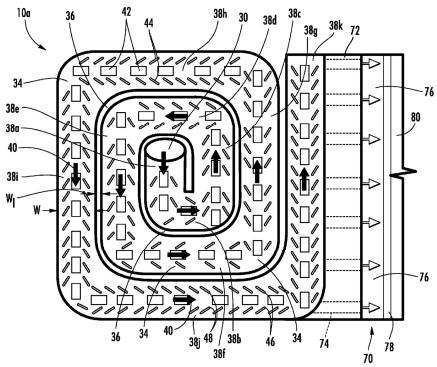


Figure 2.14. Patent by Liang (2010).

passages are predominantly found inside turbine blades and are orientated in the radial direction for ease of manufacture, e.g., Fig. 2.12. An extensive patent survey indicates that there is significant interest in radial serpentine passages for current and future vane cooling designs, e.g., Fig. 2.13.

Non-radial serpentine passages seem less common. This is a particular system of interest in the present study because it has theoretical advantages over all other systems and seems not to have been previously studied. Specifically, no patents or open literature were found in which internal flow is directed axially in the opposite direction to the mainstream like a counter-current heat exchanger—referred to in this thesis as *reverse-pass* systems. The exception to this is the snail-shaped serpentine passage such as shown in Fig. 2.14 that incorporates reverse-pass as a by-product.

2.6 Combined Cooling Technology

Cooling systems that aim to simultaneously increase internal heat transfer and enhance the effectiveness of the film are referred to here as *combined cooling technology*.

2.6.1 Transpiration Cooling

Transpiration cooling—where coolant passes through a porous wall material—is considered one of the most promising combined cooling technologies. Large wetted surface area increases cooling efficiency, and low exit velocity and uniform coverage increases film effectiveness (e.g., Horlock et al., 2001 and Eckert & Livingood, 1953). No material and manufacturing technique are currently available which achieve transpiration at the necessary temperatures and flow rates while being suitably resistant to blockage. Effusion cooling is an attempt to replicate the characteristics of transpiration cooling by using micro-holes (e.g., Battisti et al., 2006). The diameter and density of the holes can be locally tuned to optimise the film cooling performance to the local mainstream conditions.

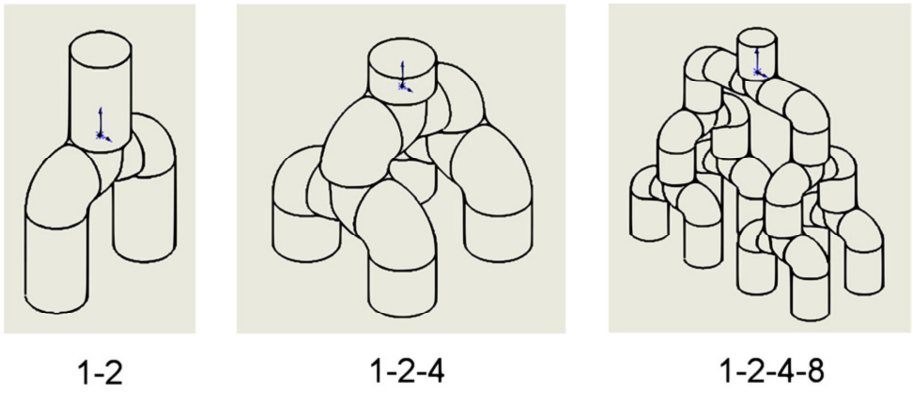


Figure 2.15. Schematic of three dendritic cooling structures (Luque et al., 2014).

2.6.2 Dendritic, Lattice and Matrix Cooling

Dendritic cooling technology developed by Batstone (2011) consists of a system of cooling *dendrites* that are contained within the wall to be cooled. Each dendrite enters the wall from the cold-side as one channel, splits within the wall, and then exits the wall as two or more channels, shown in Fig. 2.15. The convective heat transfer within the wall is increased due to impingement on the internal splits, the promotion of secondary flows and a large wetted surface. The pressure loss through each dendrite can be tuned locally to achieve the optimum momentum flux ratio and mass flux ratio for film cooling.

The operating principle of lattice and matrix cooling is similar to dendritic cooling. Cylindrical film cooling passages intersect at an angle, either fully (lattice) or partially (matrix). Convective efficiency and film cooling effectiveness are increased compared to non-intersecting cylindrical holes (Fletcher, 1997 and Nowlin, 2009). Compared to dendritic cooling, lattice and matrix cooling are easier to implement with current manufacturing technologies, and do not require thicker walls or more film cooling rows.

2.6.3 Other Combined Cooling Systems

There are many patents and papers describing combined cooling systems in which coolant impinges on an internal surface and is subsequently ejected as a cooling film. Figure 2.16 shows an example by Gillespie (1996) applied to the LE wall. An increasing number of patents describe ‘micro-circuit’ cooling arrangements (e.g., Figs. 2.17 and 2.18). These are designed to maximise cooling efficiency by increasing the pathlength within the system. A design by Immarigeon and Hassan (2006) is shown in Fig. 2.19 which includes a bank of pedestals and a flared hole. The use of these combined cooling systems is typically limited by structural integrity and maximum available pressure drop.

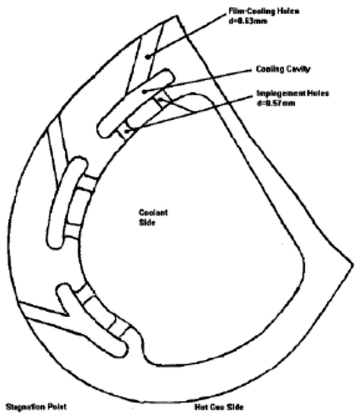


Figure 2.16. Impingement-showerhead (Gillespie, 1996).

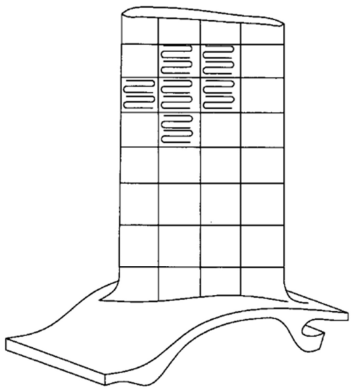


Figure 2.17. Micro-circuit patent by Liang (2009).

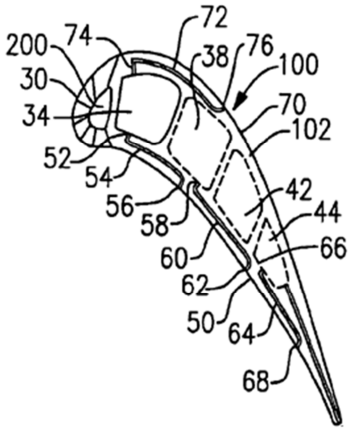


Figure 2.18. Micro-circuit patent by Devore et al. (2010).

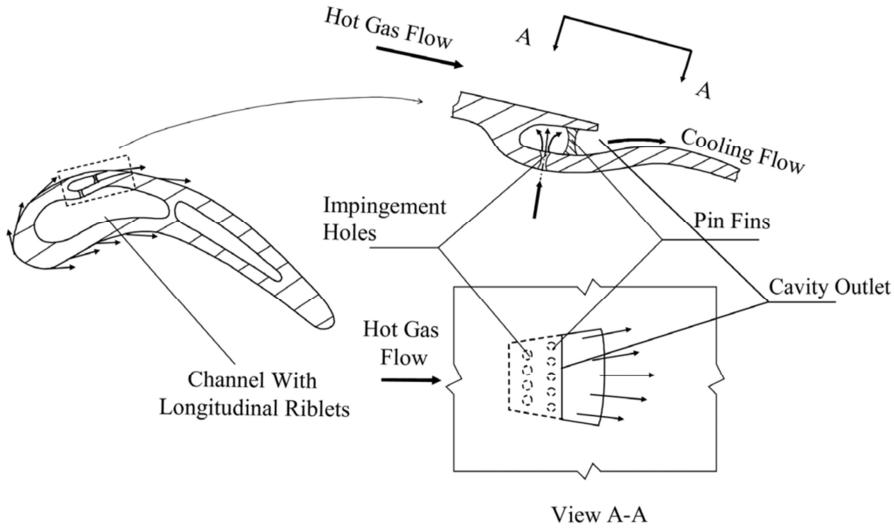


Figure 2.19. Impingement/film-cooling scheme (Immarigeon and Hassan, 2006).

2.7 Experimental Methods

Despite the continuing development of computational fluid dynamics (CFD), it is still difficult to accurately predict the heat transfer to gas turbine component surfaces using numerical methods. Experiments remain necessary for validation of predictions and designs, especially in situations that contain phenomena which are highly sensitive to numerical method, such as turbulent transport, transition, separation, shocks and surface roughness.

2.7.1 Linear Cascades, Annular Facilities and Annular Sector Facilities

Most turbine research is undertaken in linear cascades—an annular sector linearised to form a rectangular test section. Linear cascades are relatively simple, inexpensive and ideally suited to low-TRL research. The disadvantage of linear cascades is that real engine hardware cannot be used and engine-representative radial pressure gradients are not replicated. The latter have a large effect on

secondary flow development. Periodicity in linear cascades is usually achieved using tailboards and boundary layer suction.

Fully annular test facilities replicate engine conditions better than linear cascades and are typically used for high-TRL research. Real engine hardware can be tested in annular facilities with engine-representative radial pressure gradients, periodicity and secondary flow features. However, the design and operational costs of annular facilities is an order of magnitude greater than a linear cascade. Access for instrumentation is also more difficult.

A compromise is reached with annular sector test facilities, in which only a sector of the annulus—typically one-eighth—is investigated. Annular sector facilities generate radial pressure gradients, accommodate real engine hardware and cost less than a fully annular facility. Annular sector facilities have been widely used since the 1960s, with facilities at the NASA Lewis Research Centre (Bettner, 1968), Hot Section Facility (Calvert et al., 1970) and ABB STAL Sweden (Rådeklint and Hjalmarsson, 1998). More recently, aero-elastic measurements have been made on LP turbine blades at KTH (Vogt, 2005) and overall cooling effectiveness measurements at the UTRC, USA (Fujimoto et al., 2009) and the University of Oxford Annular Sector Heat Transfer Facility (Luque et al., 2009, 2011, 2013).

The main disadvantage of annular sector facilities compared to fully annular facilities is their lack of inherent periodicity. Wiers and Fransson (1998, 2000) showed that the periodicity of annular sector facilities is maximised when the mainstream flow exhausts into a large plenum immediately downstream of the test section. However, this can cause hub flow separation and so most annular sector facilities use tailboards. The feasibility of using downstream contoured sidewalls and deswirl vanes to generate periodic boundary conditions and engine-representative radial pressure gradients, secondary flow features and coolant redistribution has been demonstrated by Luque Martinez (2011) and Povey et al. (2007).

The heat transfer experiments in this thesis were carried out in the University of Oxford Annular Sector Heat Transfer Facility.

2.7.2 Heat Transfer Measurements

Thermocouples, thin-film gauges and hot-film gauges can be used to measure temperature at discrete locations. Thermocouples are used to infer temperature from the change in induced voltage across the junction of two dissimilar metals—known as the Seebeck or thermoelectric effect. Thin-film gauges are used to infer temperature from the change in material resistance, i.e., the change in voltage across the gauge for a constant current. Hot-film gauges are used to estimate heat flux by measuring the current needed to keep a gauge at constant temperature (Childs, 2001).

Full-coverage surface temperature is typically measured using liquid crystal thermography, infra-red thermography (IR) or thermal paint. A comparison of these full-coverage methods is given in Wright et al. (2005). Pressure sensitive paint uses the mass transfer analogy to infer *adiabatic* temperature in situations where two different temperature streams mix, e.g., film cooling.

The colour of thermal paint depends on the maximum temperature to which it is exposed, and, to a lesser extent, temperature history (e.g., Neely and Tracy, 2006). Colour change can occur at high temperatures (> 1300 K), making thermal paint ideal for the final qualification of cooling systems before production (Glezer, 2003). Several types of thermal paint with various colour-temperature ranges are often used simultaneously on different parts to reduce uncertainty. However, such tests are generally restricted to final qualification of cooling systems before production due to their cost and complexity.

Thermochromic liquid crystals (TLC) reversibly change colour with temperature (Ireland and Jones, 2000). A monotonic relationship between hue and temperature allows temperature to be recorded to a high degree of accuracy. TLCs are painted on to the test surface and can be considered thermally thin and aerodynamically smooth. The colour play (or temperature range) of current TLC technologies can be narrowband (~1°C) or wideband (~20°C). Technologies exist for colour play bands anywhere between -30°C and 115°C. Because colour play occurs within the visible spectrum, CCD cameras can be used, making liquid crystal thermography a relatively cheap method of full-coverage temperature measurement.

The calibration of liquid crystals is sensitive to age, exposure to UV light, temperature saturation (Anderson and Baughn, 2004), TLC thickness (Wiberg and Lior, 2004), pressure and lighting conditions. Most of these can be addressed with in-situ calibration and careful control of the operating conditions (Sabatino et al., 2000).

Infra-red (IR) thermography is used in the experiments reported in this thesis. IR thermography is discussed in detail in Chapter 5.

The mass transfer analogy allows heat transfer to be approximated from similarity between the energy and momentum equations. Pressure sensitive paints use oxygen-quenched photoluminescence, i.e., the colour of the surface depends on the local partial pressure of oxygen. Thus, by using a combination of gases, the adiabatic wall temperature can be inferred from the colour of the surface.

Local heat transfer coefficients can be inferred from the surface and gas temperature history and the wall properties using conduction models (e.g., Schultz and Jones, 1973). The most appropriate temperature measurement technique for HTC prediction depends on the aerodynamic frequency and the response-time of the measurement method.

2.8 Manufacture Methods for Testing

HPNGVs are often commercially investment-cast from a single crystal nickel alloy. This process is used to create large volumes of consistent, structurally and thermally resistant vanes. Casting is expensive for low volumes, and therefore the HPNGVs tested in this thesis are manufactured using direct metal laser sintering (DMLS). Metal powder is fused together using a focussed laser beam. Parts are built additively in layers typically 20 μm thick. A variety of materials can be used in the DMLS process, including Inconel, stainless steel, maraging steel, cobalt chrome, titanium Ti6AlV4 and Nimonic. Although DMLS components are not yet capable of withstanding engine temperature and pressures, their mechanical and thermal properties are enough to withstand conditions found in the Annular Sector Heat Transfer Facility.

Luque et al. (2013) incorporated a laser-sintered dendritic leading-edge into a cast HPNGV and assessed the thermal performance of the insert in the Annular Sector Heat Transfer Facility. Snyder et al. (2015) and Stimpson et al. (2015) performed fundamental studies of roughness and heat transfer characteristics of laser-sintered components. However, an assessment of the thermal performance of an entire laser-sintered high-pressure nozzle guide vane has not, to the author's knowledge, been attempted.

2.9 Conclusions

The concept of counter-current heat exchangers has not been examined in the context of cooling hot-section gas turbine components. Laser-sintering is becoming an increasingly mature technology but the feasibility of using an entire laser-sintered HPNGV to assess the thermal performance of the equivalent cast HPNGV has not been studied.

This thesis departs from the work in the literature by improving the performance of HPNGV cooling systems using counter-current heat exchanger theory. The performance of these *reverse-pass* systems is investigated using numerical conjugate heat transfer models. Novelly, prototype HPNGVs are manufactured in their entirety at engine-scale using metal laser-sintering and are tested at engine-representative conditions to measure cooling system performance.

3. Reverse-Pass Concept Study

Cooling systems for hot-section gas turbine components (e.g. turbine vanes/blades, combustor liners, afterburners) can be thought of as heat exchangers insofar as there is heat transfer between a 'hot' and a 'cold' fluid through a conductive wall. When thought of in this way, engine hot-section cooling designers would aim to increase internal coolant residence time and cold-side heat transfer coefficient, thereby increasing internal heat transfer between the two streams. In almost every practical system this would improve overall cooling performance. The aim of cooling systems is to keep metal temperatures below a specified limit, and here the analogy breaks down: the aim being to minimise the external heat transfer coefficient, rather than maximise it, as in a conventional heat exchanger.

It can be shown that in most situations counter-current heat exchanger arrangements (hot and cold streams flowing in opposite directions) outperform the co-current arrangements because the mean driving temperature difference is larger, e.g., Eastop and McConkey (1986). However, this simple concept has not yet been examined in the context of cooling hot-section gas turbine components—the closest literature being that of Hale et al. (2000), who discuss the non-conjugate effect of plenum flow direction on adiabatic film cooling effectiveness. There are numerous operational systems that would benefit from considering the cooling system in this way.

Most modern hot-section gas turbine components require film cooling in order to maintain metal temperatures below acceptable working limits. Film cooling is a source of additional coupling between the external and internal flows, complicating the direct analogy with heat exchangers. The purpose of this chapter is to numerically estimate the benefits of reverse-pass cooling (the combination of counter-current flow *and* film cooling) for typical film cooled hot-section components.

In this chapter, the thermal performance of reverse-pass arrangements is assessed using bespoke 2D numerical conjugate heat transfer models, and compared to baseline forward-pass and adiabatic arrangements. It is shown that for a modularised reverse-pass arrangement implemented in a flat plate, significantly less coolant is required to maintain metal temperatures below a specified limit than for the corresponding forward-pass system. The geometry is applicable to combustor liners and afterburners. Characteristically, reverse-pass systems have the benefit of reducing lateral temperature gradients in the wall. This is beneficial when thermal stresses are considered to be a life-limiting factor in design.

The concept is demonstrated by modelling the pressure and suction surfaces of a typical nozzle guide vane with both internal and film cooling. For the same cooling mass flow rate, the reverse-pass

system is shown to reduce the peak temperature on the suction side and reduce lateral temperature gradients on both suction and pressure sides.

The purpose here is to demonstrate numerically that by introducing concepts familiar in the heat exchanger community, engine hot-section cooling efficiency can be improved whilst respecting conventional manufacturing constraints.

The work in this chapter has been published in Kirollos and Povey (2014).

3.1 Long Plate Cooling Systems

The impact of the flow direction of internal coolant on wall temperature is now assessed for film cooled long plates (e.g. combustor liners, afterburners).

Three internal long plate cooling systems are considered (Fig. 3.1): (a) a forward-pass system in which the internal coolant flows in the same direction as the mainstream before being ejected as film cooling; (b) a reverse-pass system in which the internal coolant flows in the opposite direction to the mainstream before being ejected as film cooling; (c) an adiabatic system which relies solely upon film cooling. In each case, the long plate is fed by repeating coolant modules, such that all temperature distributions achieve periodicity after an initial starting length but before the mainstream temperature gradient becomes significant. The periodicity of each system is the length of one module. The periodic temperature distributions are identical to those of an infinitely long plate.

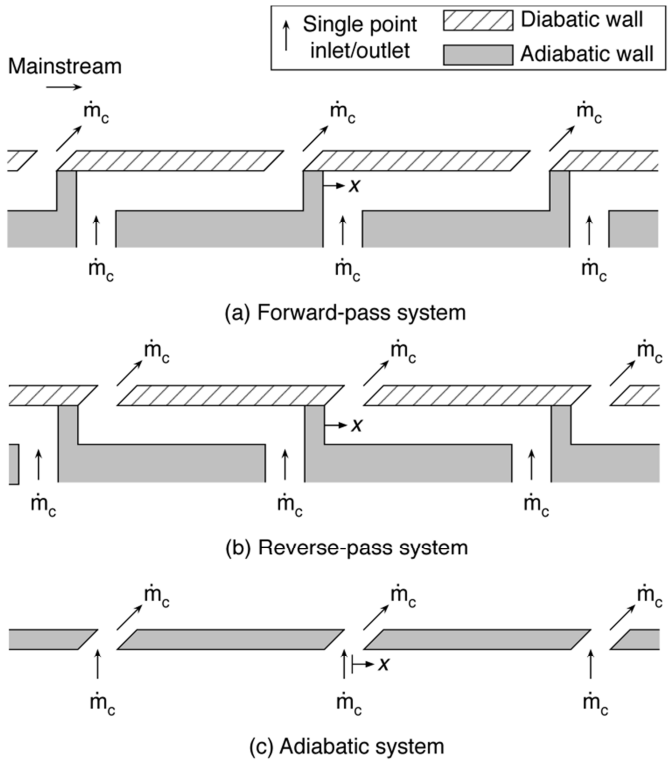


Figure 3.1. Long plate (periodic) forward-pass, reverse-pass and adiabatic cooling systems.

The boundary conditions for the model are listed in Table 3.1 and equation (3.1) and are chosen to be engine-representative. The coolant mass flow rate through each module, the mainstream and coolant temperatures, and the adiabatic film cooling effectiveness distribution functions, are set to be the same for all three systems in order to isolate the effect of internal flow-direction on cooling efficiency. Conceptually, the internal heat transfer coefficient/pressure drop can be controlled by a combination of heat transfer augmentation methods and the cross-sectional area of the passage. Similarly, the film decay rate and other governing non-dimensional groups can be matched between tests by modifying the cooling hole geometry.

$$\eta_{aw,i}(x) = \begin{cases} 0, & x < x_i \\ 0.25e^{-25(x-x_i)}, & x \geq x_i. \end{cases} \tag{3.1}$$

The design objective is that the wall temperature must nowhere exceed a limiting temperature (a metal effectiveness of 0.5). The module length of each system is increased or decreased such that the peak wall temperature is equal to the target limiting temperature. An effective system would require fewer modules to cool the same surface length (longer module with fixed coolant mass flow rate) than an ineffective system (shorter module with same fixed coolant mass flow rate).

A system performance measure, the percentage coolant saving, is defined as:

$$\%\ \text{Coolant saving}/100 \ = \ 1 \ - \frac{\text{adiabatic module length}}{\text{module length}} \tag{3.2}$$

where the performance measure uses the adiabatic system as the baseline. The energy equations are solved numerically for each system to calculate the fluid/wall temperatures.

Table 3.1. Boundary conditions for numerical model, based on data in Rawlinson (2001).

Boundary condition	**Symbol**	**Value**	**Units**
Mainstream total temperature	T_{0m}	2000	K
Inlet coolant total temperature	$T_{0c(in)}$	1000	K
External heat transfer coefficient	h_1	10000	W/m^{2}K
Internal heat transfer coefficient	h_2	10000	W/m^{2}K
Wall conductivity	k_w	30	W/mK
Wall thickness	t_w	0.001	m
Coolant mass flow per module per unit depth	$\dot{m}_c$	0.25	kg/s/unit depth
Specific heat capacity of air	c_p	1000	J/kgK
Limiting temperature	T_{lim}	1500	K

3.2 Numerical Methods

A bespoke numerical solver was written in MATLAB for these investigations. The solution domain is discretised as in Fig. 3.2. The energy equation for steady, non-dissipative, incompressible flow is solved in 2D using finite volume methods. Heat flow is broken down into: advection caused by mass flow; conduction within the wall; convection between solid and fluid (both sides of the wall). The net heat flow into each cell is set to zero, and iterative methods used to calculate the steady state temperature field for both solid and fluid in a conjugate manner.

To initialize the solver, mass flow rates between cells are set. In the internal duct the mass flow is set to $\dot{m}_c$ from a cell with an inlet source term. The external layer of gas is modelled as having a mass flux which is the sum of the latest film entering the layer and the entrained gas from the pre-existing films – this is illustrated in Fig. 3.2. The entrained mass flow rate between the pre-existing films and the external layer of gas is calculated from the adiabatic film cooling effectiveness using Kirollos and Povey (2015a), such that:

$$\delta\dot{m}_{e(k,i)} = -\frac{\dot{m}_{c(k)}\delta\eta_{aw(k,i)}}{\left(\eta_{aw(k,i)}\right)^2}, \tag{3.3}$$

where $\delta\dot{m}_{e(k,i)}$ is the entrained mass flow rate into the external layer of gas at cell i along the plate and k is the index of the most recently injected film. The mass flow rate of the external gas layer $\dot{m}_{d(i)}$ follows:

$$\dot{m}_{d(i)} = \dot{m}_{d(i-1)} + \delta\dot{m}_{e(k,i)}\,. \tag{3.4}$$

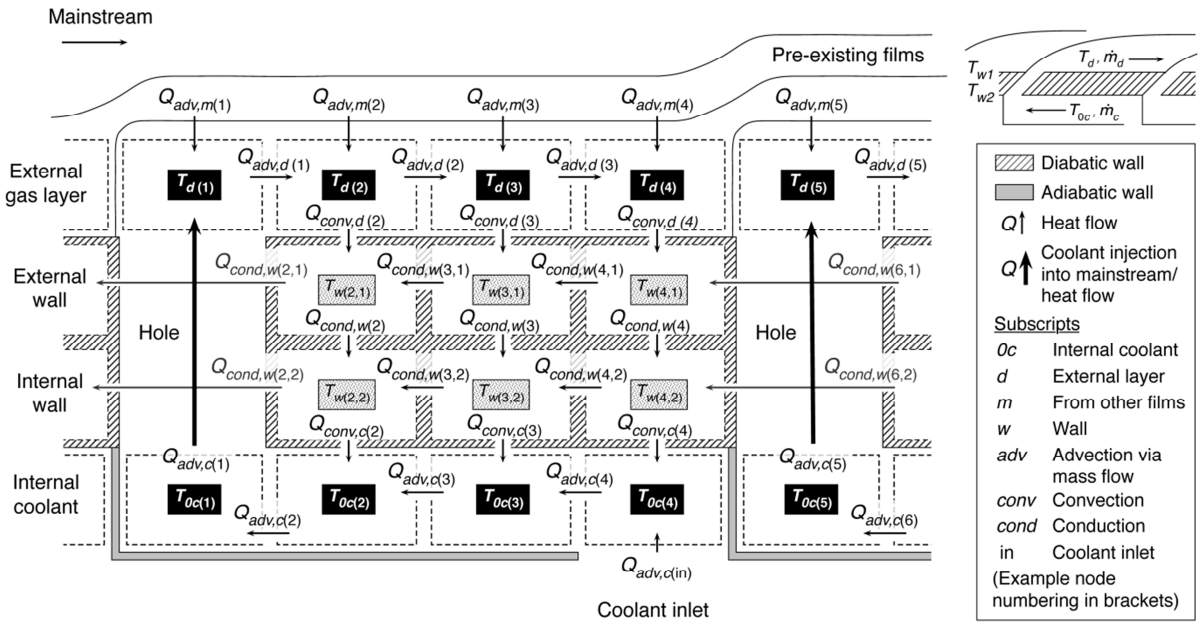


Figure 3.2. Discretisation for numerical solution with temperatures and heat flows.

Using this method, the external gas temperature is the relevant temperature for heat transfer, and this temperature is the only parameter that enters the conjugate model.

The advection heat flow term between cells within the external layer of gas is given by (referring to Fig. 3.2):

$$Q_{adv,d(i)} = \dot{m}_{d(i)} c_p \left(\frac{T_{d(i)} + T_{d(i+1)}}{2} \right), \tag{3.5}$$

where $\dot{m}_{d(i)}$ is calculated at the cell boundary and $T_{d(i)}$ is the temperature at the cell centre. The temperature at the cell boundary is calculated by averaging adjacent cell-centre temperatures. The advection into the external layer of gas from the previous films is calculated in a similar manner:

$$Q_{adv,m(i)} = \delta \dot{m}_{e(k,i)} c_p T_{0m(i)}{}', \tag{3.6}$$

where $T_{0m(i)}{}'$ is the temperature of the entrained fluid. This temperature is a function of the preceding films and the mainstream temperature, and is computed using the energy-based method of Kirollos and Povey (2015a). The internal advection terms are calculated in the same way:

$$Q_{adv,c(in)} = \dot{m}_c c_p T_{0c(in)} ; \tag{3.7}$$

$$Q_{adv,c(i)} = \dot{m}_c c_p \left(\frac{T_{0c(i)} + T_{0c(i-1)}}{2} \right). \tag{3.8}$$

The wall is modelled with 2 cell layers, each cell of size $\delta x \times t_{wall}/2$ (where δx is the length of cell i). The conduction between neighbouring cells is calculated using Fourier's law:

$$Q_{cond,w(i)} = \frac{k_{wall} \delta x}{t_{wall}/2} \left(T_{w(i,1)} - T_{w(i,2)} \right), \tag{3.9}$$

$$Q_{cond,w(i,j)} = \frac{k_{wall} (t_{wall}/2)}{\delta x} \left(T_{w(i,j)} - T_{w(i-1,j)} \right). \tag{3.10}$$

The external and internal wall temperatures $T_{w1(i)}$ and $T_{w2(i)}$ are calculated by extrapolating the cell-centred wall temperatures:

$$T_{w1(i)} = T_{w(i,1)} + \frac{T_{w(i,1)} - T_{w(i,2)}}{2}, \tag{3.11}$$

$$T_{w2(i)} = T_{w(i,2)} - \frac{T_{w(i,1)} - T_{w(i,2)}}{2}. \tag{3.12}$$

External convection is calculated with $T_{d(i)}$ as the driving/reference temperature – equation (3.13).

Whilst $T_{d(i)}$ is similar to the adiabatic wall temperature in that it accounts for film cooling effects, $T_{d(i)}$ also takes the upstream heat transfer history into account; i.e. $T_{d(i)}$ differs from the adiabatic wall temperature due to heat transferred through the conducting wall between the internal and external flow. This is analogous to the concept of adiabatic and non-adiabatic heat transfer coefficients described in Gomes and Neihuis (2013). Internal convection is calculated using the local bulk temperature $T_{0c(i)}$ as the reference temperature – equation (3.14).

$$Q_{conv,d(i)} = h_1 \delta x \left(T_{d(i)} - T_{w1(i)}\right). \tag{3.13}$$

$$Q_{conv,c(i)} = h_2 \delta x \left(T_{w2(i)} - T_{0c(i)}\right). \tag{3.14}$$

The sum of heat flows into and out of each cell is calculated, and the updated cell-centred temperature calculated until convergence was achieved. A mesh independence study was performed, the solution being independent for $\delta x < 0.2$ mm. The number of modules simulated in each case is sufficient to achieve periodic temperature distributions.

3.3 Long Plate (Periodic) Temperature Distributions

The periodic external driving temperature, internal coolant temperature and internal/external wall temperature distributions for the adiabatic, forward-pass and reverse-pass systems are shown in Figs. 3.3-3.5.

In the adiabatic case, h_2 is set to zero. Thus no heat is transferred to the coolant before ejection, and the temperature of the internal coolant remains at the coolant inlet temperature. The external layer gas temperature T_d rises as the film mixes with the mainstream, until the limiting temperature is reached (the design constraint on the problem). When a fresh film is injected T_d drops. The wall temperatures T_{w1} and T_{w2} are equal and closely follow T_d but there is rounding of the saw-tooth profile due to lateral conduction in the wall. The adiabatic system has a module length of 26.3 mm. This reference length is used to describe performance improvements for non-adiabatic systems according to equation (3.2).

For the forward-pass and reverse-pass diabatic systems, the module length is greater: a measure that the cooling system has greater effectiveness due to the internal cooling benefit. In the case of the forward-pass system (Fig. 3.4), the module length can increase to 33.7 mm for the same wall temperature limit. This represents a 22.1% cooling saving compared to the adiabatic case.

For the reverse-pass system (Fig. 3.5), the module length can be increased to 37.0 mm for the same wall temperature limit. This represents a 29.1% cooling saving compared to the adiabatic case. The coolant ejection temperature is 40 K higher in the reverse-pass case than the forward-pass case, due to

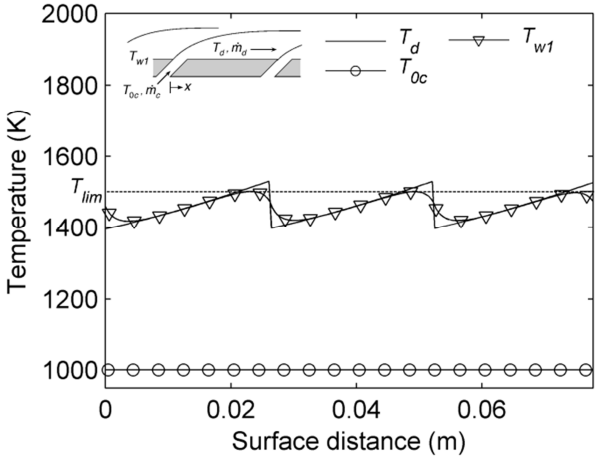


Figure 3.3. Temperature distributions of a long plate adiabatic cooling system. $T_{w1} = T_{w2}$.

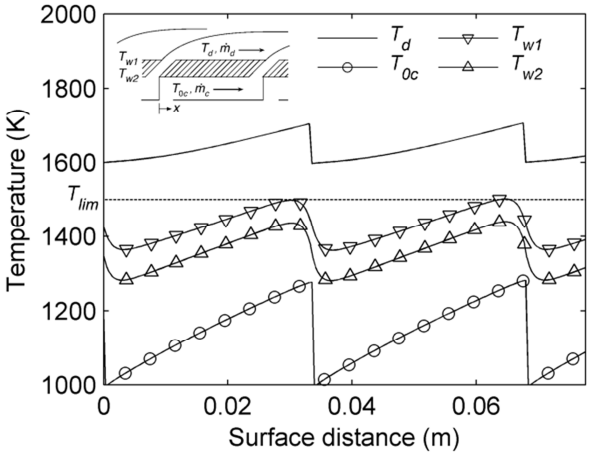


Figure 3.4. Temperature distributions of a long plate forward-pass system with point inlets.

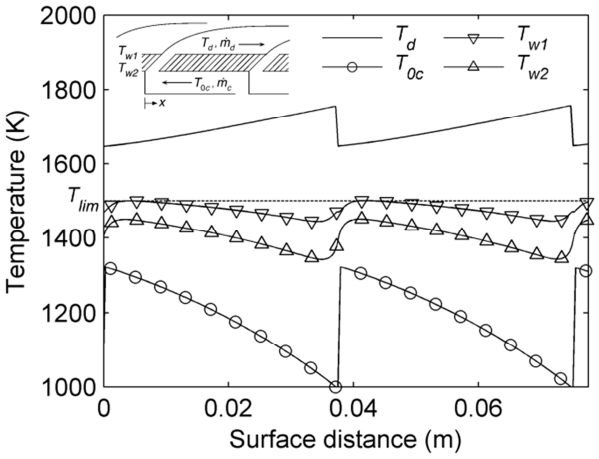


Figure 3.5. Temperature distributions of a long plate reverse-pass system with point inlets.

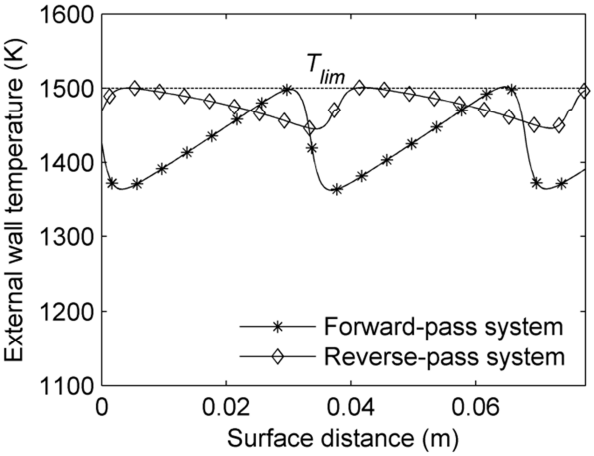


Figure 3.6. External wall temperature distributions of long plate forward-pass system and reverse-pass systems with point inlets.

greater heat pick-up in the reverse-pass system (counter-current heat exchanger analogy). The mean temperature difference between the internal wall and the internal coolant $\bar{T}_{w2} - \bar{T}_{0c}$ is greater in the reverse-pass system (220 K) than the forward-pass system (210 K). The mean temperature drop across the wall $\bar{T}_{w1} - \bar{T}_{w2}$ is also greater in the reverse-pass system (75 K) than the forward-pass system (70 K). Lateral non-uniformity of wall temperatures is significantly reduced in the reverse-pass system (158 K range) compared to the forward-pass system (219 K range), illustrating the benefits in parts with thermal stress limits.

The external wall temperature distributions of the reverse-pass and forward-pass systems are directly compared in Fig. 3.6 (data from Fig. 3.4 and Fig. 3.5). Uncharacteristically for internal/film cooled systems, the surface temperature of the reverse-pass system decreases with surface distance. This can be explained by first considering a reverse-pass system without film cooling. In this system, the wall temperature decreases with surface direction, followed by a positive jump in temperature as the new

reverse-pass module is inserted to the right. The peak temperature of the system is at the jump point, where the coolant is hottest. The wall temperature decreases again with surface distance, as it becomes progressively cooler towards the inlet of the reverse-pass module. And so on, periodically.

This 'sawtooth' sequence of decreasing wall temperatures followed by positive discontinuities is in the opposite direction to the sawtooth wave generated by the film alone (the adiabatic system of Fig. 3.3). When the two effects are additive, the direction of the sawtooth depends on the relative magnitude of the two opposing effects. For the boundary conditions given in Table 3.1, the effect of the internal convective cooling is greater than the external film cooling, and temperatures decrease with surface distance. Conceptually at least, a perfectly balanced system exists in which the two effects exactly cancel resulting in a flat temperature distribution.

Importantly, in a forward-pass system the internal and film cooling effects act to enhance temperature non-uniformities leading to large lateral differences in wall temperature. In the reverse-pass system, the wall temperature distribution is always flatter because the non-uniformities caused by internal and film cooling heat pick-up partially cancel.

3.4 Effect of Wall Thickness and Conductivity

As the conductivity of the wall approaches zero or the wall thickness tends to infinity, all diabatic systems (reverse-pass, forward-pass) start to look adiabatic. In the limit, there is no performance benefit associated with a particular diabatic system. In order to assess the effect of wall thickness and conductivity on the comparative performance of forward and reverse-pass cooling systems, the numerical model was run with varying wall thickness (0.5 to 3 mm) and two wall conductivities (10 W/mK and 30 W/mK), representing the likely range of engine-representative components. All other boundary conditions were unchanged from Table 3.1 and equation (3.1). As in the forgoing analysis, the measure of performance was the periodic module length required to maintain the surface below the limiting temperature. The percentage coolant saving was calculated for each test case. Results are given in Fig. 3.7.

As expected, the diabatic systems perform best when the wall conductivity is highest and the wall thickness is lowest. However, for a wall thickness of 3 mm the coolant saving is still significant, being at worst 11% (the case of k_w= 10 W/mK for a forward-pass system). For any given wall conductivity and wall thickness (within the range tested), the reverse-pass system always requires less coolant than a forward-pass system. For k_w = 30 W/mK, the reverse-pass system consistently requires 8% less coolant than a forward-pass system (for $0.5 < t_w < 3$ mm). For k_w= 10 W/mK, a reverse-pass system requires 3-10% less coolant than a forward-pass system, dependent on the wall thickness. (The percentage difference in coolant required between a forward-pass and reverse-pass system is a function of the *ratio* between lines in Fig. 3.7, and not the difference).

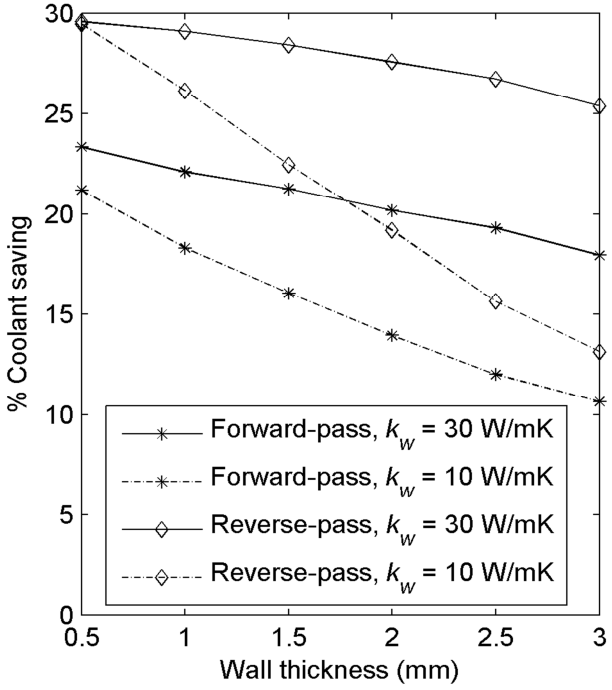


Figure 3.7. Effect of wall thickness and wall conductivity on percentage coolant saving for both long plate forward-pass and reverse-pass systems with point inlets.

As the wall becomes thicker (3 mm) with lower conductivity (k_w= 10 W/mK) all diabatic systems have smaller performance improvements over the adiabatic system, and the differences between particular diabatic designs decrease – as can be derived from the trends in Fig. 3.7.

3.5 Effect of Adiabatic Film Cooling Effectiveness Distribution

The effect of adiabatic film cooling effectiveness distribution on the performance of forward and reverse-pass cooling systems is now considered.

In systems with very high adiabatic film cooling effectiveness, cooling is dominated by the film, with little contribution from the internal cooling system. Conversely, in systems with low adiabatic film cooling effectiveness, the internal cooling system becomes dominant. The impact of this effect on the performance of forward-pass, reverse-pass and adiabatic systems is now quantified by comparing the predicted metal effectiveness for a number of film decay rates.

The adiabatic film cooling effectiveness $\eta_{aw,i}$ distributions used for this study were defined by:

$$\eta_{aw,i}(x) = \begin{cases} 0, & x < x_i \\ 0.25e^{-A(x-x_i)}, & x \geq x_i, \end{cases} \tag{3.15}$$

where i is the row number, x is surface distance, x_i is the x location of row i, and A is the film decay rate. Adiabatic film effectiveness is defined in equation (2.5) and measures the reduction in the driving temperature for external heat transfer due to film. An exponential decay function provides a

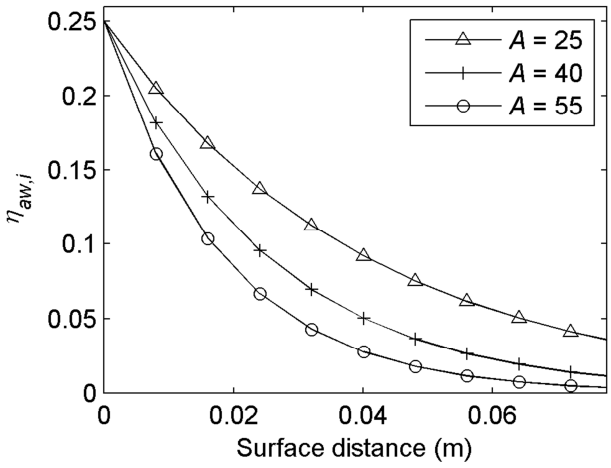


Figure 3.8. Adiabatic film cooling effectiveness distributions.

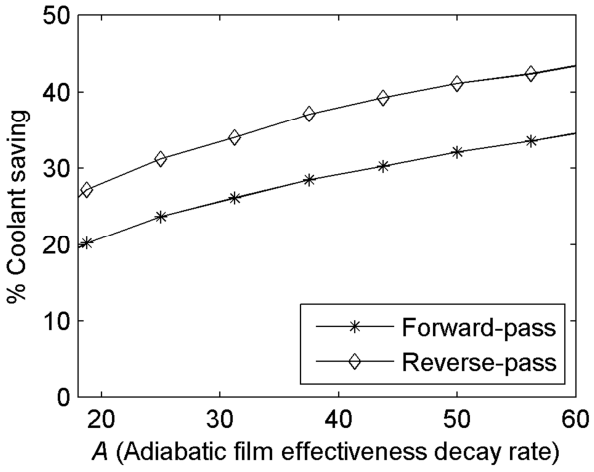


Figure 3.9. Effect of adiabatic film cooling effectiveness decay rate on percentage coolant saving for both forward-pass and reverse-pass long plate systems with point inlets.

reasonable approximation of real film effectiveness decay and is commonly used in preliminary film cooling design (e.g., Kingston et al., 2011). Film decay is due to the entrainment of hot mainstream gas into the film via mixing—approximated using equation (3.3). Decay rates between $18.75 < A < 60$ were tested—a physically realisable range which is approximately centred around a standard HPNGV decay rate of $A = 25$ (e.g., Rawlinson, 2001). Distributions for $A = 25$, 40 and 50 are shown in Fig. 3.8. All other boundary conditions were unchanged from Table 3.1.

For values in the range $18.75 < A < 60$, the percentage cooling saving for forward and reverse-pass systems over the adiabatic case are presented in Fig. 3.9. In this range, the diabatic cooling systems require 20 – 43% less coolant than an adiabatic system. The reverse-pass system consistently requires less coolant than the forward-pass system. As the decay rate increases and internal convective cooling becomes more important, the reverse-pass system increasingly outperforms the forward-pass system: at a decay rate of 18.75, the reverse-pass system requires 9% less coolant than the forward-pass system; at a higher decay rate of 60 the reverse-pass system requires 14% less coolant.

3.6 Long Plate Cooling Systems with Uniformly Distributed Inlet

Many hot-section internal cooling systems can be approximately represented by the schemes in Fig. 3.10. These schemes differ from those in Fig. 3.1 in that they have a distributed coolant inlet as opposed to a point inlet. Both a HPNGV leading edge compartment, and a SS impingement circuit could be thought of as being approximated by these scheme. In this section we assess the impact of distributed inlet flow (as opposed to point inlet flow) on the performance of forward-pass and reverse-pass systems.

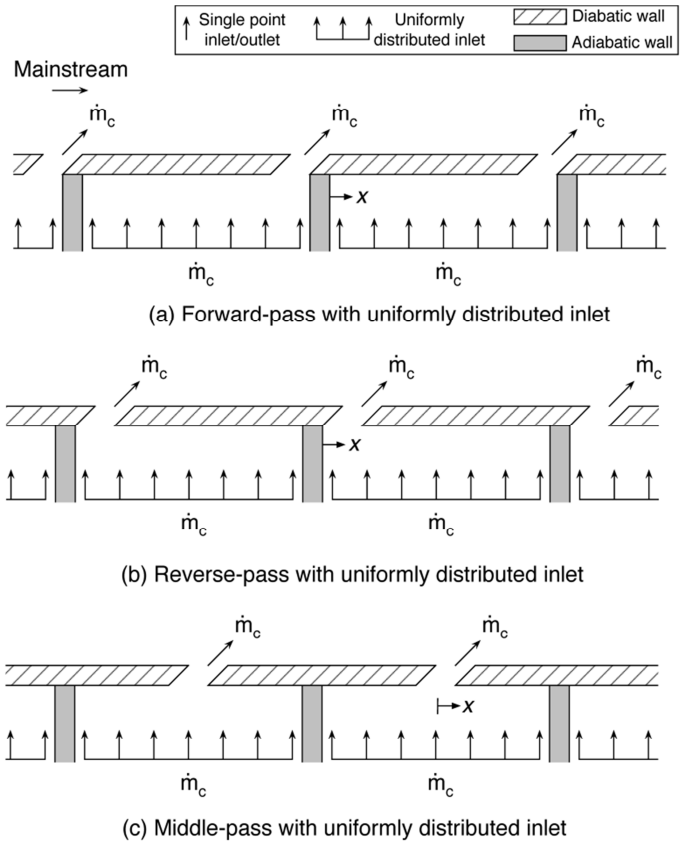


Figure 3.10. Periodic cooling systems with uniformly distributed inlets.

The foregoing analysis was repeated with three new geometries: (a) forward-pass system with uniformly distributed inlet; (b) reverse-pass system with uniformly distributed inlet; (c) symmetrically fed system (i.e. the outlet is in the middle of the plenum) with uniformly distributed inlet. The new geometries have the same total mass flow rate into and out of each plenum as the previous point-inlet tests. The boundary conditions are unchanged from the previous analysis—Table 3.1 and equation (3.1). Again, the periodic module length is adjusted so that the peak temperature is matched to the limiting temperature.

The temperature distributions for the forward-pass, reverse-pass and symmetrically fed distributed inlet systems are shown in Figs. 3.11, 3.12 and 3.13, respectively. The wall temperature distributions are similar for all three systems. Likewise, the coolant temperature distributions are similar, with little variation with surface distance (due to dilution with fresh coolant as the plenum mass flow rate accumulates). It is clear that the difference between forward and reverse-pass systems is negligible when distributed inlets are considered.

Figure 3.14 summarises the coolant saving for the five cooling systems tested thus far. All distributed inlet systems require 25.8% less than an adiabatic system. The forward-pass system with point inlet requires 22.1% less coolant, and a reverse-pass system requires 29.1% less. The distributed inlet

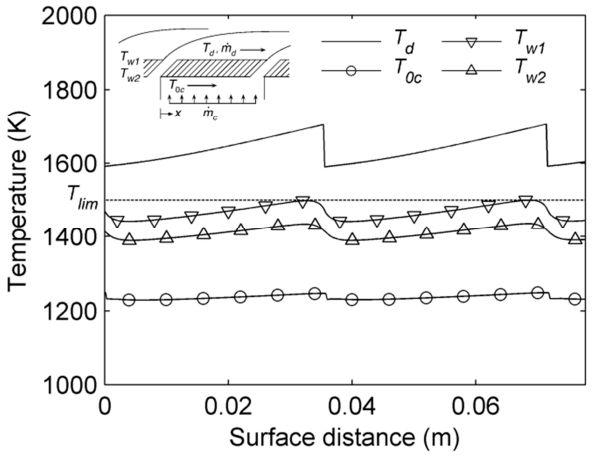


Figure 3.11. Temperature distributions of a periodic forward-pass cooling system with uniformly distributed inlet.

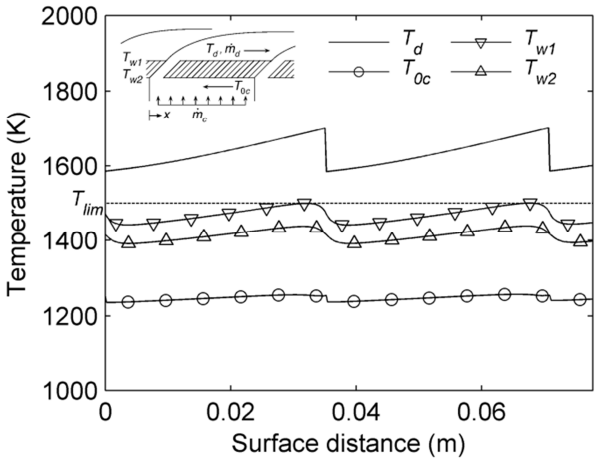


Figure 3.12. Temperature distributions of a periodic reverse-pass system with distributed inlet.

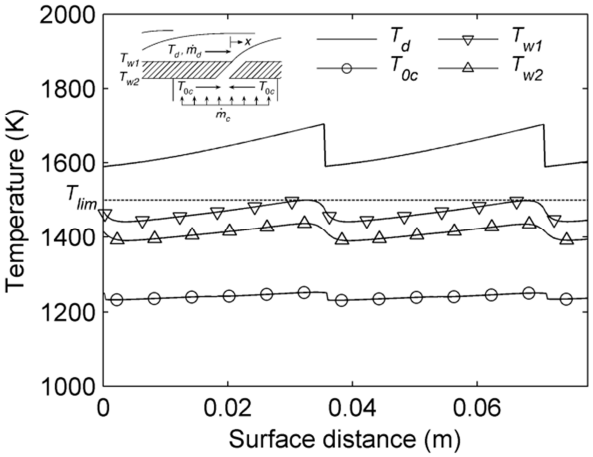


Figure 3.13. Temperature distributions of a periodic middle pass system with distributed inlet.

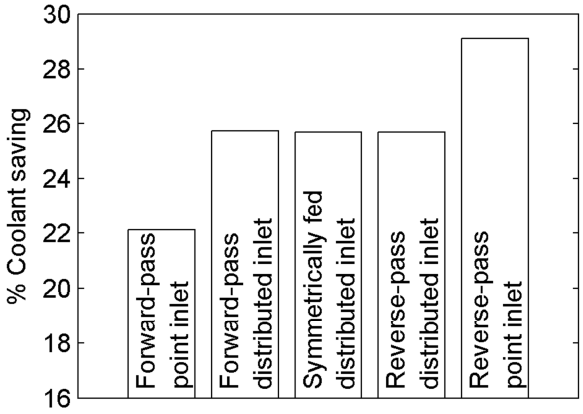


Figure 3.14. Percentage coolant saving of forward-pass and reverse-pass systems with point inlets and distributed inlets.

systems all have approximately the same performance, equal to the average of a forward-pass system with point inlet and a reverse-pass system with point inlet. The conclusion is that the benefit of a reverse-pass system is maximised when a point inlet is used.

3.7 Application of a Reverse-Pass System to the Suction Side of a HPNGV

The application of reverse-pass cooling to the suction side (SS) of a typical HPNGV is now considered. A typical HPNGV cooling system is shown schematically in Fig. 3.15a (modified from Crook and Horlor, 2005). There are two coolant compartments: the front compartment feeding the showerhead rows and the rear compartment feeding the impingement plate and trailing edge. The flow to both compartments can be thought of as being uniformly distributed. A cut-line to separate the PS and SS cooling systems is shown in Fig. 3.15a.

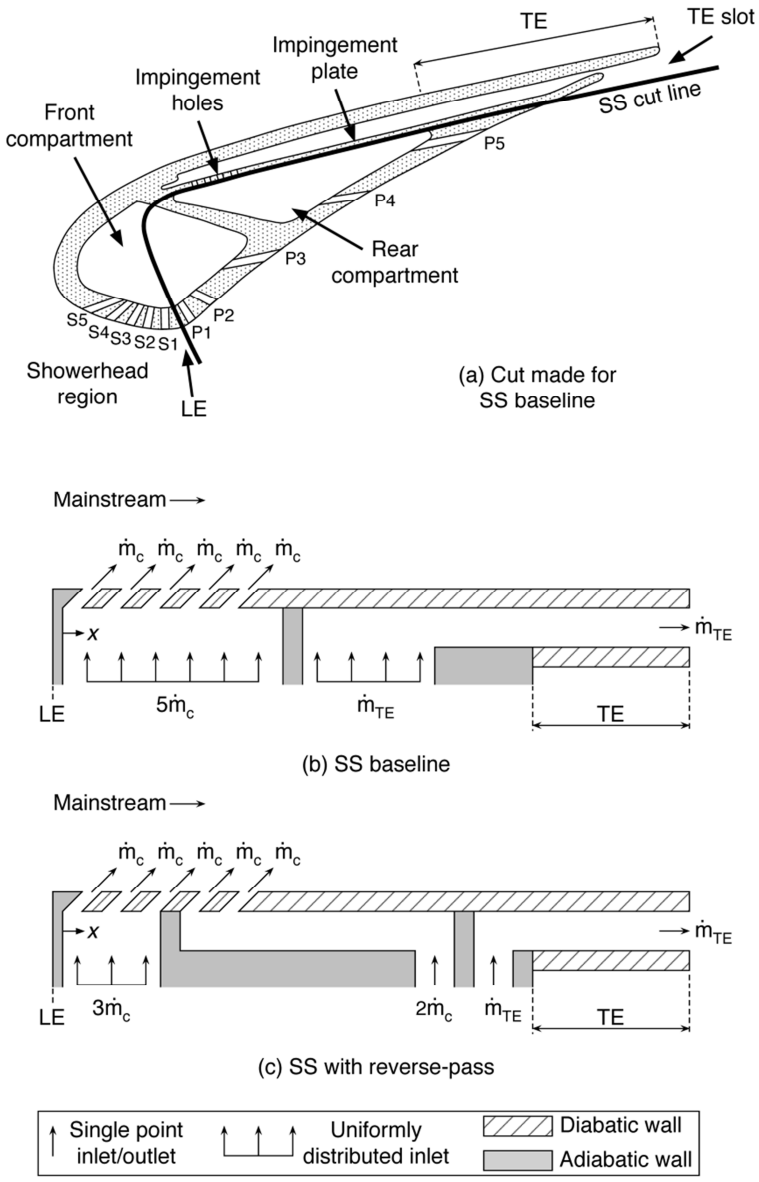


Figure 3.15. 2D representation of a baseline HPNGV SS and incorporation of a reverse-pass system. (a) modified from Crook and Horlor (2005).

The 2D numerical model representation of the SS cooling system is shown in Fig. 3.15b: the baseline system for this study. There are two distributed inlets: the first inlet feeds 5 rows of holes; the second inlet feeds the trailing edge slot. The corresponding reverse-pass system is shown in Fig. 3.15c. The constraints leading to this design are now described.

In the reverse-pass scheme (Fig. 3.15c), pressure loss between the coolant inlet and exit points will be higher than for a typical vane leading compartment (Fig. 3.15b). The system has been modelled using typical duct loss correlations and using the external aerodynamic field. The analysis demonstrated that to maintain the same coolant mass flow rates through the film rows, only the last two rows of the showerhead region (S4 and S5 in Fig. 3.15a) would have sufficient pressure margin to support a reverse-pass system. Rows S1 – S3 are already close to a critical pressure margin for typical cooling

system designs. This analysis informed the design of the reverse-pass scheme in Fig. 3.15c, in which S4 and S5 are the outlets of a reverse-pass channel, and S1-S3 have a conventional uniformly distributed inlet.

To maximise the benefit of the reverse-pass system, it should cover the greatest stream-wise length. The trailing edge (TE) design is heavily constrained however, and the length marked TE in Fig. 3.15a has been preserved in the reverse-pass design of Fig. 3.15c. The length TE represents the pedestal bank of a typical vane, beyond which it becomes less feasible to implement reverse-pass flow. A summary of inlet and outlet locations for both schemes is given in Tables 3.2 and **3.3**.

The boundary conditions for this study were unchanged from those in Table 3.1 and equation (3.1). The trailing edge mass flow rate per unit depth $\dot{m}_{TE}$ was set to 0.8 kg/s/unit depth. An adiabatic boundary condition was applied to the wall at the leading edge (LE), and a constant heat flux boundary condition was applied to the end of the TE – such that the heat flux at the final node n equals the heat flux at node $n-1$. The TE region was modelled as having two diabatic walls (double the convective heat transfer) to account for the additional heat transfer to the pressure side wall in this region (a first order approximation).

Table 3.2. Coolant outlet locations for SS and PS HPNGV study from Rawlinson (2001).

Suction side		Pressure side	
Outlet	Distance from LE (mm)	Outlet	Distance from LE (mm)
Outlet 1 (S1)	0	Outlet 1 (P1)	0
Outlet 2 (S2)	2	Outlet 2 (P2)	3
Outlet 3 (S3)	4	Outlet 3 (P3)	10
Outlet 4 (S4)	6	Outlet 4 (P4)	22
Outlet 5 (S5)	8	Outlet 5 (P5)	34
Total surface length (SS TE slot)	84	Total surface length (PS TE slot)	60

Table 3.3. Coolant inlet locations on the SS of the HPNGV. Baseline data from Rawlinson (2001).
Hyphenated numbers refer to uniformly distributed inlet. x^+ means that the coolant inlet in question is on the downstream side of the coolant module boundary at x.

Baseline		Reverse-pass system	
Inlet	Distance from LE (mm)	Inlet	Distance from LE (mm)
Inlet 1 (SS-baseline)	0-20	Inlet 1 (SS-RP)	0-6
Inlet 2 (SS-baseline)	20^+-30	Inlet 2 (SS-RP)	58
		Inlet 3 (SS-RP)	58^+

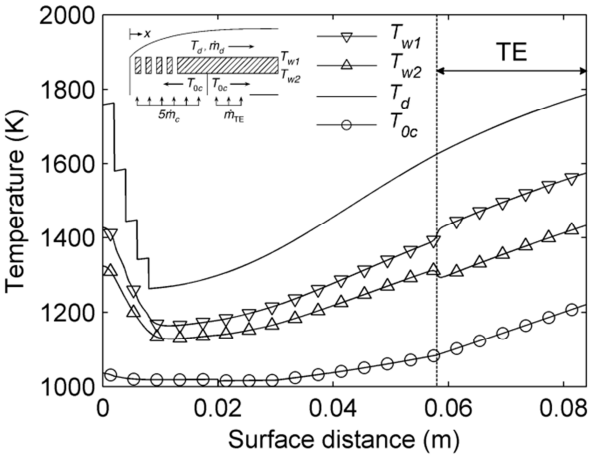


Figure 3.16. SS baseline temperature distributions.

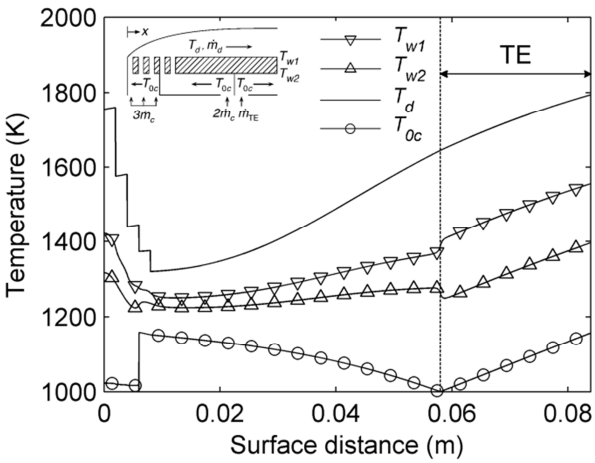


Figure 3.17. SS reverse-pass temperature distributions.

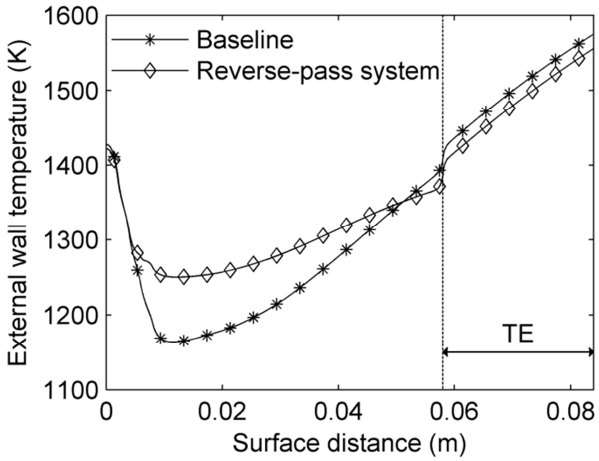


Figure 3.18. SS baseline and reverse-pass external wall temperature distributions.

To perform a back-to-back comparison of the performance of the two schemes, the coolant mass flow rates and coolant outlet locations for the baseline and reverse-pass geometries were kept the same, and the resulting temperature distributions compared. The 2D numerical solution procedure has been described. Temperature distributions of the baseline and reverse-pass suction side HPNGV designs are given in Figs. 3.16 and 3.17, respectively. The external wall temperature distributions of the two designs are compared directly in Fig. 3.18.

The average wall temperature is higher for the reverse pass system than the baseline system (Fig. 3.18). The life limiting regions (highest temperature) are cooler for the reverse-pass system, however, and lateral temperature distributions are reduced. We now quantify these changes.

In the TE region of the vane the reverse-pass system reduces wall temperatures fairly uniformly by 20K, including at the life limiting TE extremity, where temperatures are highest. The temperature decrease is due to fresh cooling air being injected at the inlet to the TE region (Fig. 3.15c). In contrast,

in the baseline design, the flow into the TE region has been warmed by passing first through the impingement system (Fig. 3.15b).

In the showerhead region there is little difference between the reverse-pass and baseline systems. The conclusion is that a reverse-pass system on the suction side of a HPNGV can be used to flatten temperature distributions and reduce peak temperatures. Temperatures on the early-to-mid suction side (where they are generally lowest) are increased by implementing a scheme of this sort.

3.8 Application of a Reverse-Pass System to the Pressure Side of a HPNGV

The application of reverse-pass cooling to the pressure side (PS) of a typical HPNGV is now considered. The HPNGV cooling system is shown schematically in Fig. 3.19a, with a cut line to represent the PS system which is now modelled.

The 2D numerical model representation of the PS cooling system is shown in Fig. 3.19b: the baseline system for this study. There are two distributed inlets: the first feeds the showerhead rows P1–P3 and the second feeds the PS rows P4 and P5. A third feed supplies the TE with fresh coolant. The corresponding reverse-pass system is shown in Fig. 3.19c. The constraints leading to this design are now described.

When the pressure loss model (duct flow correlations) and external aerodynamic field of the vane are considered, the only PS rows with sufficient pressure margin to implement reverse-pass cooling are rows P3 and P4. In the reverse-pass scheme (Fig. 3.19c) they each have an independent feed. There is insufficient space in a practicable vane to feed row P5 from an independent plenum, so it is fed from the same plenum as P4. P1 and P2 are fed conventionally.

Coolant outlet locations and mass flow rates are constrained to be the same for the baseline and reverse-pass cases studied (summary in Tables 3.2 and 3.4). All boundary conditions are given in Table 3.1 and equation (3.1). The TE mass flow rate was set to $\dot{m}_{TE}$ = 0.8 kg/s/unit depth. The TE region was modelled as having two diabatic walls (double the convective heat transfer) to account for the additional heat transfer to the SS wall in this region (a first order approximation).

Table 3.4. Coolant inlet locations on the PS of the HPNGV. Baseline data from Rawlinson (2001).
Hyphenated numbers refer to uniformly distributed inlet. x^+ means that the coolant inlet in question is on the downstream side of the coolant module boundary at x.

Baseline		Reverse-pass system	
Inlet	Distance from LE (mm)	Inlet	Distance from LE (mm)
Inlet 1 (PS-baseline)	0-22	Inlet 1 (PS-RP)	0-10
Inlet 2 (PS-baseline)	22^+-34	Inlet 2 (PS-RP)	22
Inlet 3 (PS-baseline)	34^+	Inlet 3 (PS-RP)	34
		Inlet 4 (PS-RP)	34^+

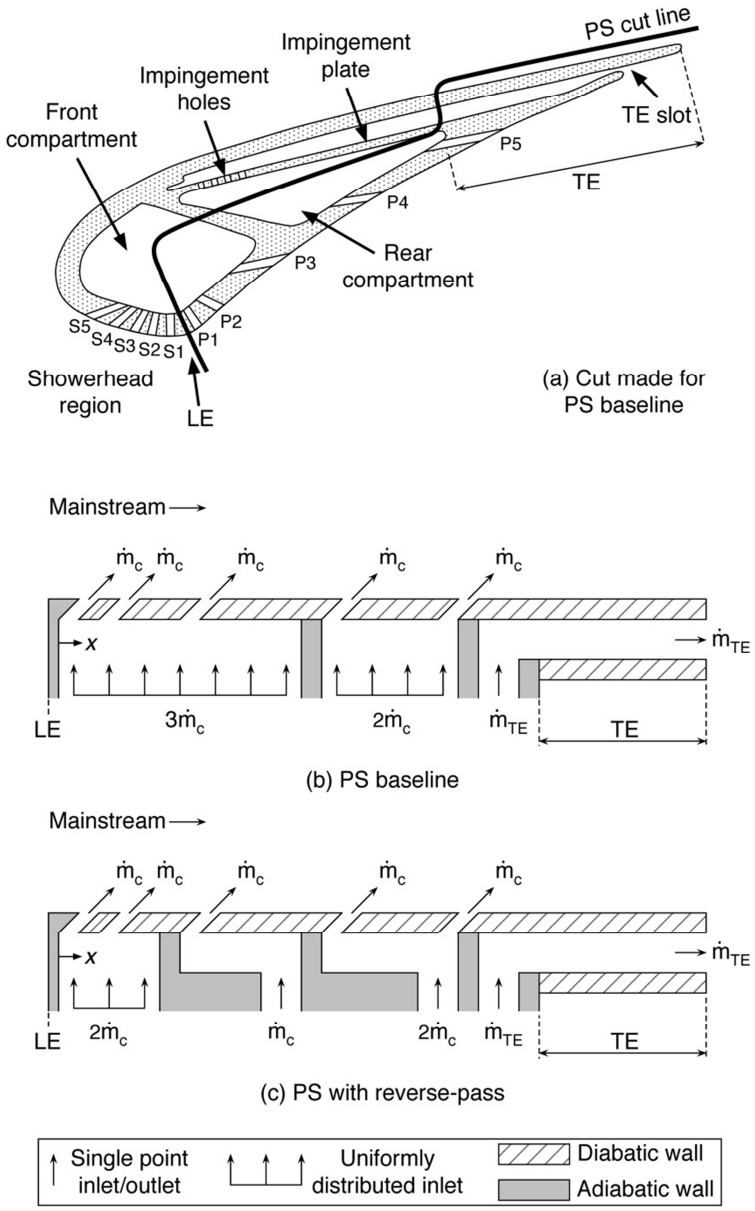


Figure 3.19. 2D representation of a baseline HPNGV PS and incorporation of a reverse-pass system. (a) modified from Crook and Horlor (2005).

Temperature distributions of the baseline and reverse-pass pressure side HPNGV designs are given in Figs. 3.20 and 3.21, respectively. The external wall temperature distributions of the two designs are compared directly in Fig. 3.22.

Comparing the temperature distributions in Fig. 3.22, the effect of moving from the baseline PS scheme to the reverse-pass scheme is to locally flatten the external wall temperature lateral distribution and reduce the LE temperature (by 15 K). Temperatures in the TE region are unchanged – here the model of the TE slot flow geometry is unaltered from the baseline case. The conclusion is that a realisable PS reverse-pass system is less effective at laterally flattening temperature distributions and reducing peak temperatures than on the SS of a typical HPNGV. The explanation

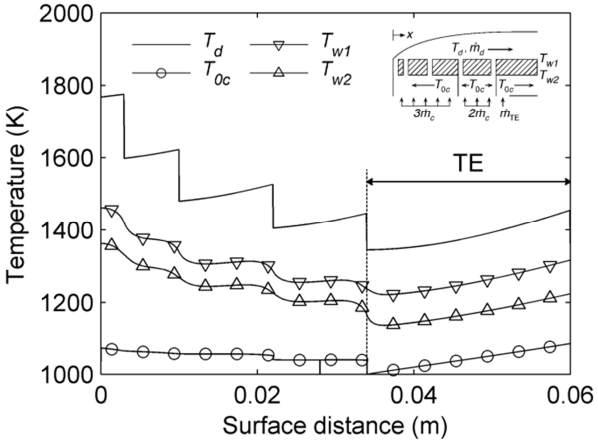


Figure 3.20. PS baseline temperature distributions.

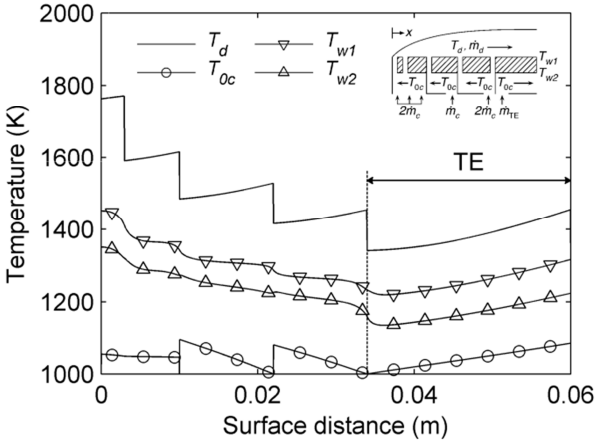


Figure 3.21. PS reverse-pass temperature distributions.

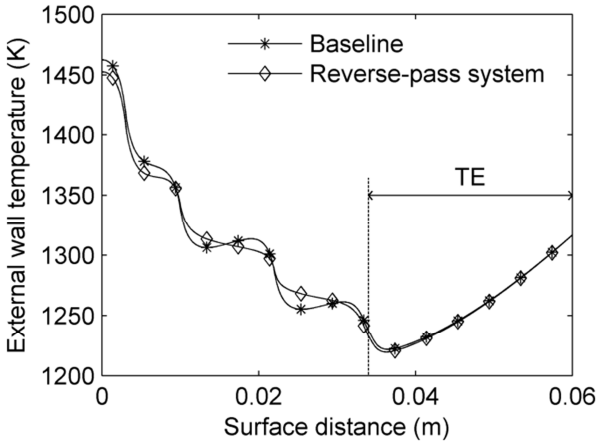


Figure 3.22. PS baseline and reverse-pass external wall temperature distributions.

lies in the fact that the system cannot be lengthened to the extent that the beneficial characteristics can be usefully realised. That is, the reverse-pass modules are too short (in practicable systems) for a useful amount of heat pick-up to occur.

3.9 Conclusions

In this chapter, the application of reverse-pass cooling to hot-section engine components has been examined, introducing concepts familiar in the heat exchanger community in the context of co-current and counter-current heat exchanger arrangements. The analysis has been conducted using a bespoke 2D numerical conjugate heat transfer model, which has allowed comparison of forward-pass and reverse-pass systems operating with the same boundary conditions. The design constraints and boundary conditions were chosen to be relevant to HPNGV or afterburner cooling system design.

Two performance metrics have been used to assess the benefits of these systems: 1) for long plates, the percentage reduction in cooling required to maintain the plate temperature below a limiting

temperature has been calculated; 2) for HPNGV cooling systems constrained to have the same coolant mass flow rate, the reduction in lateral temperature variation and reduction in peak temperature have been calculated.

The quantitative conclusions are as follows:

1) *Long plates with engine-realisable geometric and aero-thermal properties:*
   a) Diabatic cooling systems require 10-30% less coolant than equivalent adiabatic cooling systems. This benchmarks the importance of combined internal/external schemes.
   b) Reverse-pass systems require 3-10% less coolant than equivalent conventional diabatic cooling systems. This is in accord with the performance gains offered by counter-current heat exchangers (over co-current) justifying the design analogy.
   c) Reverse-pass systems act to flatten lateral wall temperature distributions. A temperature range reduction of 60% can be achieved compared to equivalent conventional diabatic cooling systems. This is achieved by maximising internal convective cooling at the point when the film is least effective.

2) *HPNGVs with engine-realisable geometric and aero-thermal properties*
   a) A reverse-pass cooling system can reduce temperatures in the TE region by 20 K, compared to a conventional design. This is due to the TE slot being fed with cooler air, introduced closer to the TE.
   b) A reverse-pass system can flatten SS lateral wall temperature distributions by approximately 110 K (from 444 K to 329 K for the systems tested), compared to a conventional design
   c) A reverse-pass system can reduce PS leading edge region temperatures by 15 K compared to conventional systems.

In certain applications, it has been demonstrated that engine hot-section component cooling performance can be improved using reverse-pass systems whilst respecting conventional manufacturing constraints. The performance improvements are a lowering of peak temperatures and a significant reduction in lateral component surface temperature variation. The benefits of reverse-pass cooling can be fully realised in systems where there is long undisturbed surface length, such as the SS of HPNGVs, afterburner liners, and combustor liners. In many such applications there is little penalty associated with implementing schemes of this sort, so serious consideration by designers is advocated.

4. Design and Manufacture of Reverse-Pass High Pressure Nozzle Guide Vanes

In this chapter, the design of engine-scale, three-dimensional high pressure nozzle guide vanes with suction-side reverse-pass cooling systems which satisfy engine-realistic aerothermal and manufacturing constraints is detailed. Three reverse-pass-cooled HPNGVs were developed and optimised using a bespoke numerical conjugate heat transfer and aerodynamic model. The model was developed to quickly predict pressures and temperatures and allowed for rapid design optimisation. Also reported in this chapter are the manufacture of the HPNGVs, impingement/baffle plates and visualisation aids, finishing, modification of cast platforms (EDM), and the assembly into a vane pair for testing.

4.1 Reverse-Pass Topology

The numerical concept study in the previous chapter demonstrated that reverse-pass systems are most beneficial when applied to long, undisturbed surfaces, such as the suction-side of an HPNGV. It was shown that the temperature uniformity benefit of a reverse-pass system increases with length (as demonstrated by the ineffectiveness of the shorter PS reverse-pass system as compared to the longer SS reverse-pass system, Figs. 3.18 and 3.22), and that the peak SS metal temperature at the trailing-edge is reduced by minimising the TE system length to minimise internal coolant temperature. For every millimetre reduction in TE system length, the maximum metal temperature at the TE extremity is reduced by ~1 K.

These observations suggest a general optimised SS reverse-pass arrangement of the form in Fig. 4.1, compared to a typical design in Fig. 4.2. Both the length of the reverse-pass system is maximised—improving metal temperature uniformity—and the length of the TE system is minimised—reducing peak SS metal temperature. The TE design is heavily constrained, with the TE system length in Fig. 4.1 representing the minimum below which it becomes less feasible to implement reverse-pass.

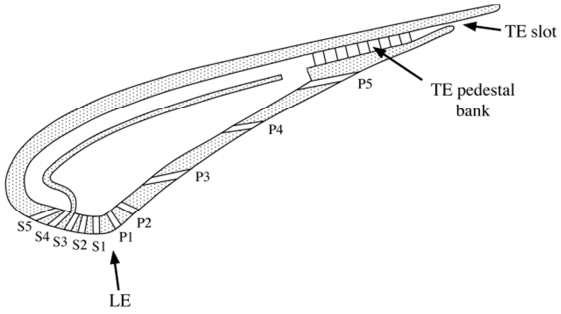


Figure 4.1. General SS reverse-pass concept.

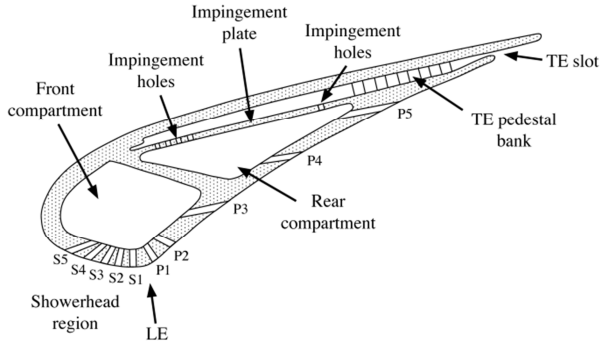


Figure 4.2. Typical HPNGV cooling system.

The reverse-pass layout in Fig. 4.1 is optimum for a given span, though it may not be optimum for the aerofoil as a whole, depending on the radial mainstream temperature distribution. The midspan of the aerofoil typically experiences the greatest external heat load and the maximum metal temperature. Consequently, a radially *uniform* reverse-pass cooling system operating in an environment with a radial mainstream temperature distribution effectively *over-cools* the vane everywhere but midspan. In this case, a radially *non-uniform* reverse-pass cooling system would use coolant more efficiently.

In Fig. 4.1, the last two SS film cooling rows (S4 and S5) are nominally fed by the reverse-pass system because they may maintain a safe pressure margin despite the additional pressure loss incurred by the reverse-pass system. For systems where the nominal coolant capacity of S4 and S5 is relatively small compared to the TE coolant capacity, or there is insufficient pressure margin across S4 and S5, it may be preferable to route all of the reverse-pass passages back out of the TE and feed the SS film cooling holes with a separate plenum.

The SS reverse-pass topologies considered for this study are shown schematically in Fig. 4.3. The optimum operating conditions (radial mainstream temperature distortion and S4/S5-TE coolant mass flow split) of each topology was assessed using the aerodynamic and thermal models described later. The results of this analysis are summarised in the decision matrix in Fig. 4.4.

For radially uniform mainstream temperature, the 1D reverse-pass topology RP 1D is preferable as reasoned from symmetry. For a modest radial mainstream temperature distortion, e.g., recent lean burn combustors such as EFE, the modified 1D reverse-pass topology RP 1D+ may improve metal temperature uniformity[1]. The reverse-pass flow in RP 1D+ is fastest at the point of entry into the system and progressively slows as the reverse-pass compartment expands towards S4 and S5. The internal heat transfer coefficient (HTC) in the reverse-pass passage is therefore greatest near the midspan TE, where the external heat load is greatest. Regions with lower mainstream gas temperature or greater film cooling effectiveness—i.e., near the leading-edge and at hub and case—require less internal convective cooling to maintain the wall at the same maximum metal temperature. The RP 1D+ TE system at hub and case is therefore longer than at midspan, and the Reynolds number (and hence internal HTC) of the reverse-pass flow decreases towards the LE.

The 2D reverse-pass topology RP 2DA is designed for more non-uniform radial mainstream temperature distributions than RP 1D+, e.g., Trent 500 temperature traverse. The midspan reverse-pass passage is narrower over a greater length than RP 1D+, increasing the average midspan internal HTC. Since the mainstream temperature drops off steeply at hub and case for more non-uniform radial mainstream temperature distributions, internal convective cooling can likewise reduce away

[1] The '+' in RP 1D+ symbolises that RP 1D+ is predominantly 1D but contains some 2D elements—though not as many 2D elements as RP 2DA and RP2DB. In all legacy files and documents, RP 1D is known as RP1DA1, RP 1D+ is known as RP1DB2, and RP 3D is known as RP3D2

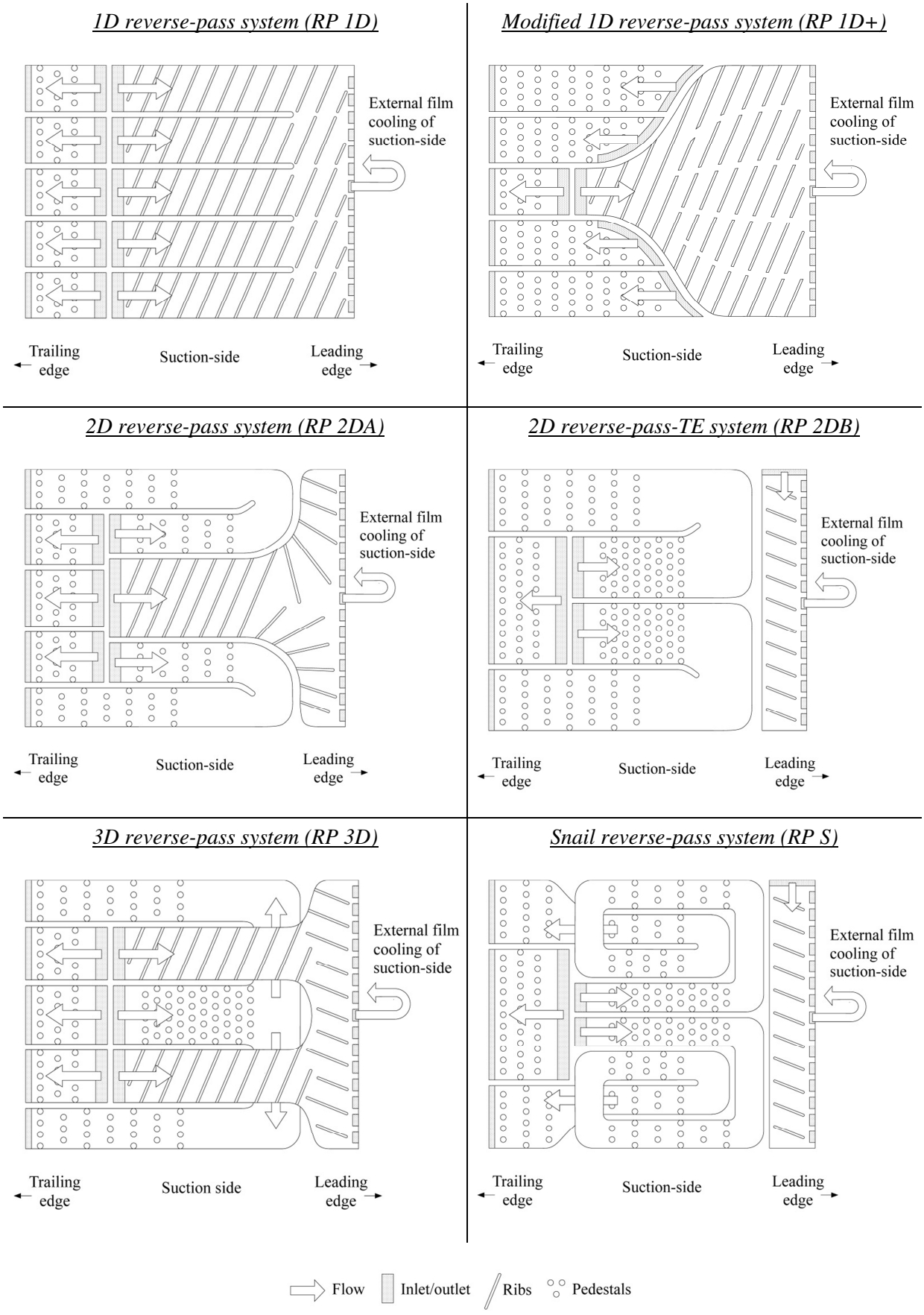


Figure 4.3. Suction-side reverse-pass topologies considered for optimisation.

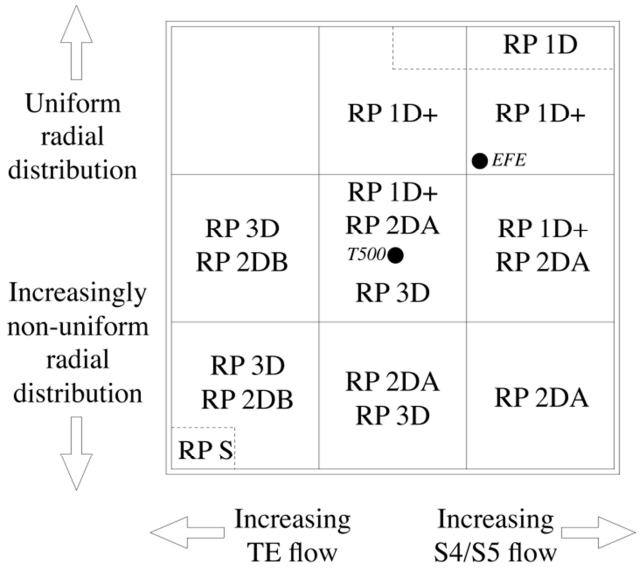


Figure 4.4. Preliminary reverse-pass topology decision matrix. Trent 500 overall temperature distribution factor (OTDF) = 36.5% (Rawlinson, 2011), EFE OTDF = 25.5% (Downes, 2014). Trent 500 TE/(S4+S5) coolant mass flow rate = 0.77; EFE TE/(S4+S5) coolant mass flow rate = 0.42.

from midspan. The hub and case portions of the TE are therefore cooled with the same air that cools the off-midspan regions in the reverse-pass passages.

The 3D reverse-pass topology RP 3D is also designed for a highly non-uniform temperature traverse, but for systems with a greater proportion of TE flow compared to S4/S5 flow—thus maintaining high midspan internal HTC. The RP 3D midspan reverse-pass passage splits in two and under-passes the off-midspan reverse-pass passages, exiting the vane at hub and case TE. A patent has been filed for this system.

For systems where the nominal coolant capacity of S4 and S5 is relatively low compared to the TE coolant capacity, or the pressure margin across S4 and S5 is insufficient, it may be beneficial to route all of the reverse-pass passages out of the TE and feed the SS film cooling holes with a separate plenum. Topologies RP 2DB and RP S in Fig. 4.3 are designed for this purpose. They aim to maximise the amount of reverse-pass in the system while simultaneously maximising internal convective heat transfer at midspan. For an extreme mainstream radial temperature distribution in which the external film temperature at hub or case is lower than the local internal coolant temperature, a snail-like topology (RP S) could be implemented. In RP S, coolant picks up heat at midspan, rejects heat back into the mainstream at hub and case (re-cooling the coolant), picks up heat in the off-midspan region, and is finally ejected through the trailing-edge.

It was decided to focus on topologies RP 1D, RP 1D+ and RP 3D in this work. These designs cover a good range of the decision matrix in Fig. 4.4 while being readily optimisable for both Trent 500

(T500) and EFE boundary conditions. Designs RP 2DA, RP 2DB and RP S were less flexible and could not be optimised as easily.

4.2 Aerothermal Optimisation

All reverse-pass geometries were designed using Trent 500 HPNGV engine boundary conditions. The external aerofoil shape and the location of the film cooling rows in the reverse-pass designs were the same as the baseline cast T500 HPNGV.

The reverse-pass systems were designed to satisfy the following aerodynamic objectives:

1. Per-row coolant capacity the same as the baseline cast T500 HPNGV;
2. Pressure ratio across the TE slot equal to 1.3;
3. Pressure ratio across row S4 greater than 1.03 to mitigate the risk of ingestion.

These objectives were achieved by iteratively adjusting the internal layout, dimensions and the location of pedestals and ribs (see optimisation flow chart, Fig. 4.5). The purpose of matching the external aerofoil shape, film cooling row locations and per-row coolant capacity is to match the hot-side (external) aerothermodynamics and thus isolate the effect of cold-side (internal) cooling geometry on thermal performance. The geometric area of the TE slot was fixed because of the relative complexity and time required to alter the TE system in the CAD drawings. As a consequence, the same pressure ratio across the TE was targeted for all designs (1.3) to match TE coolant capacity.

Based on industry advice, a minimum pressure ratio across S4 of 1.03 was targeted. Ingestion of hot core gas into the vane causes local hot spots and reduces component life. The risk of ingestion is reduced by imposing a minimum nominal pressure ratio across each film cooling row during design, which compensates for uncertainty in spatial pressure variation (e.g., radial pressure distribution) and temporal pressure variation (e.g., changes during flight cycle or engine life cycle). In the reverse-pass designs, S4 is at greater risk of ingestion than S5 because it exhausts into a region of greater static pressure. The S4 minimum pressure ratio constraint was therefore sufficient to mitigate the ingestion risk of both S4 and S5.

Further to the aerodynamic objectives, the reverse-pass systems were designed to best satisfy the following thermal objectives:

1. Maximise uniformity of SS metal temperature;
2. Minimise the maximum SS metal temperature.

These thermal objectives were chosen to maximise component life and minimise the coolant mass flow requirement (Kirollos and Povey, 2015b), and were achieved by iteratively adjusting the internal layout, dimensions and the location of pedestals and ribs. The judgement about whether the maximum

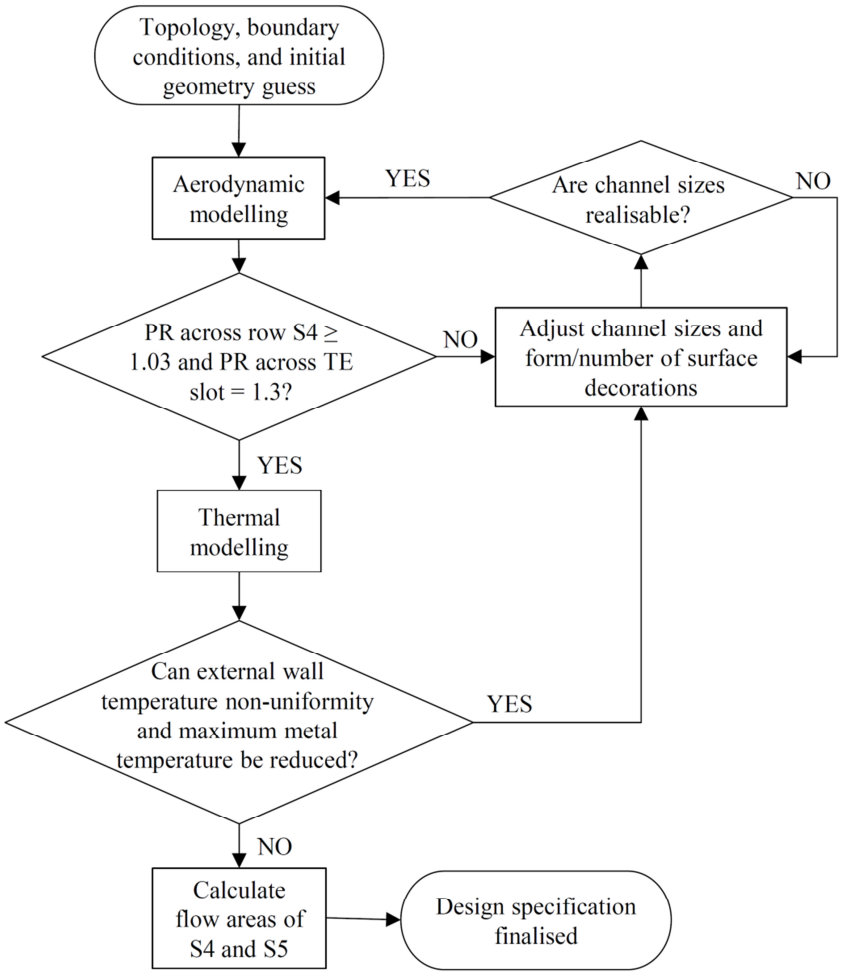


Figure 4.5. Design optimisation flow chart.

metal temperature had been minimised and the metal temperature made as uniform as possible was made by the author after comparison of multiple geometries with differing channel dimensions and surface decorations.

In order to achieve both aerodynamic and thermal objectives, a MATLAB numerical conjugate heat transfer and pressure loss model was developed to quickly predict pressures and temperatures, allowing for rapid design optimisation. This would not have been possible in the time available with high-fidelity RR codes (e.g., JB56 and SC03). The optimisation process is summarised in Fig. 4.5.

4.3 Aerodynamic Modelling

The internal aerodynamics of each reverse-pass system is predicted using zero-dimensional, incompressible (internal Mach number $M < 0.3$) pressure loss correlations from the literature. Systems are first approximated as a network of interconnecting channels, comprising five fundamental loss elements: channels with pedestal banks; channels with chevron turbulator ribs; smooth channels; impingement systems; and pipe fittings (specifically contractions, expansions or bends). Loss

elements are combined to best approximate the design geometry. The network flow models used in preliminary design are shown in Figs. 4.12-4.15.

The mass flow rate through each channel is known since it is a design objective (Table 4.1). Pressure loss within each network loss element is approximated using the local dynamic head and the loss characteristic of the element. The feed pressures of rows S4/S5 and the TE slot are subsequently estimated by subtracting the total pressure loss through the system (from vane inlet to mainstream ejection location) from the total pressure at vane inlet. Feed pressures are then compared to the design objectives. If the feed pressures do not meet the design objectives, the channel dimensions or the form/number of surface decorations are modified to alter total pressure loss. Upon satisfaction of the aerodynamic objectives, the thermal performance of the geometry is estimated using a thermal model (discussed later) and the film cooling flow areas sized.

The aerodynamic model is described in this section. The results of the aerodynamic model are described in a later section. The aerodynamic boundary conditions used to design the reverse-pass cooling systems are reported in Table 4.1.

4.3.1 Corrected Aerodynamic Boundary Conditions

The total pressure at vane-inlet used to design the reverse-pass systems was over-estimated because the total pressure loss around the combustor can was not accounted for—i.e., the combustor exit total pressure was used as the total pressure at vane-inlet. Additionally, the model did not account for the increase in internal surface roughness due to the laser-sintering process. The designs are optimised based on the surface roughness of cast components, which is approximately three times lower than the surface roughness of laser-sintered components (Rawlinson, 2001, and Stimpson, 2015).

The pressure ratio across rows S4 and S5 were therefore over-estimated in the design and consequently rows S4/S5 were initially under-sized in the laser-sintered vanes. S4/S5 row areas were modified after manufacture by drilling out the holes, in an attempt to achieve the design coolant mass flow rate but at the expense of the S4 pressure margin constraint. The modifications made to the laser-sintered designs are discussed later and are summarised in Table 4.8.

The internal coolant pressure distributions in the manufactured designs (i.e., the designs optimised for the original, partially inaccurate boundary conditions) were re-estimated using the correct aerodynamic boundary conditions which are reported in Table 4.2. The retrospective estimations compare well with the subsequent experimental measurements of pressure and coolant mass flow rate in Chapter 8. This lends confidence to the preliminary design tools described in this chapter, despite the unfortunate inaccuracy in the original boundary conditions. Both the initial results of the aerodynamic model (used for design), and the retrospective results, are summarised in Tables 4.4-4.7.

The thermal predictions are unaffected by the inaccuracy of the pressure boundary condition since the per-channel mass flow rates are matched after the hole areas have been corrected.

Table 4.1. Boundary conditions for aerodynamic model, used for design. Data from Rawlinson (2001), Howatson et al. (2009), Han and Zhang (1992), Park et al. (1992), Armstrong and Winstanley (1988) and Hippensteele (1974).

Parameter	Symbol	Units	Value
Topology			Fig. 4.3
Total coolant pressure at vane inlet, used for design	p_{30}	MPa	4.360
Static mainstream pressure at S4 exit	p_{S4}	MPa	4.056
Static mainstream pressure at S5 exit	p_{S5}	MPa	3.908
Static mainstream pressure at TE slot exit	p_{TE}	MPa	2.938
Mass flow rate through row S4	$\dot{m}_{S4}$	g/s/vane	31.1
Mass flow rate through row S5	$\dot{m}_{S5}$	g/s/vane	39.7
Mass flow rate through TE	$\dot{m}_{TE}$	g/s/vane	49.6
Discharge coefficient of row S4	$C_{D,S4}$		0.79
Discharge coefficient of row S5	$C_{D,S5}$		0.83
Discharge coefficient of TE slot	$C_{D,TE}$		0.69
Geometric area of TE slot	A_{TE}	mm^2	~ 18
Minimum pressure ratio across row S4			1.03
Density of air @ 950 K, 4.3 MPa	ρ		15.7
Dynamic viscosity of air @ 950 K	μ	Nsm^{-2}	$4.0x10^{-5}$
Specific gas constant of air	R	$Jkg^{-1}K^{-1}$	287
Ratio of specific heats of air @ 950 K	γ		1.33
Coolant temperature feedings row S4 and S5	$T_{0c,S4}/T_{0c,S5}$	K	950
Coolant temperature at TE slot	$T_{0c,TE}$	K	1100
Smooth channel friction factor (without ribs)	f_0		0.005
Friction factor with 45° chevron broken ribs	f		0.0375
Vane inlet contraction loss coefficient	$K_{L,inlet}$		0.5
Expansion loss coefficient	$K_{L,expansion}$		1
Impingement loss coefficient	$K_{L,impingement}$		1
180° bend loss coefficient	$K_{L,180° bend}$		2.2

Table 4.2. Boundary conditions for aerodynamic model, retrospective corrections. Data from Rawlinson (2001) and Stimpson et al. (2015).

Parameter	Symbol	Units	Value
Total coolant pressure at vane inlet	p_{30}	MPa	4.269
Discharge coefficient of TE slot	$C_{D,TE}$		0.72
Smooth channel friction factor (without ribs)	f_0		0.007
Friction factor with 45° chevron broken ribs	f		0.0525

4.3.2 Pedestal Bank Total Pressure Loss Correlation

The total pressure loss within each pedestal bank is estimated using the friction factor correlation of Metzger et al. (1982) in Armstrong and Winstanley (1988):

$$f = 1.76\,\mathrm{Re}_D^{-0.318}, \tag{4.1}$$

for Reynolds numbers $10^4 < \mathrm{Re}_D < 10^5$, pedestal height to diameter ratio $0.5 \leq H/D \leq 6.0$, pedestal spacing (perpendicular to flow direction) to diameter ratio $2.0 \leq S/D \leq 4.0$, and pedestal spacing (streamwise) to diameter ratio $1.5 \leq x/D \leq 5.0$. The dimensions of the pedestal banks used in design are shown in Fig. 4.6.

f is the friction factor, defined with respect to the total pressure loss Δp_0:

$$\Delta p_0 = 2f\rho v_{\max}{}^2 N, \tag{4.2}$$

where ρ is the coolant density, $v_{\max}$ is the maximum velocity within the pedestal bank, and N is the number of rows of pedestals in the streamwise direction. $v_{\max}$ is estimated using the local mass flow rate through *half* the area in Tables 4.4-4.7 in order to approximate the flow area reduction due to the pedestals:

$$v_{\max} = \frac{2\dot{m}}{\rho A}. \tag{4.3}$$

The Reynolds number in equation (4.1) is defined based on the maximum flow velocity and the diameter of the pedestal:

$$\mathrm{Re}_D = \frac{\rho v_{\max} D}{\mu}, \tag{4.4}$$

where μ is the dynamic viscosity of air at 1000 K.

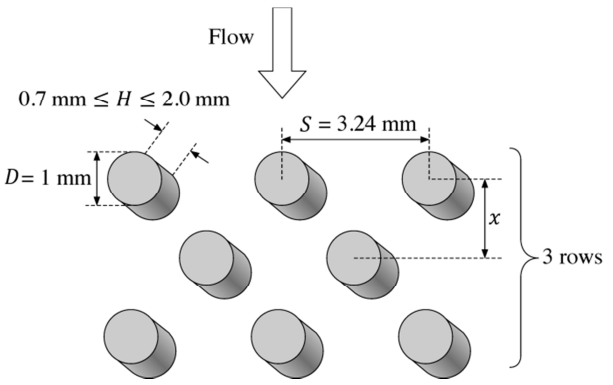


Figure 4.6. Specification of pedestals.

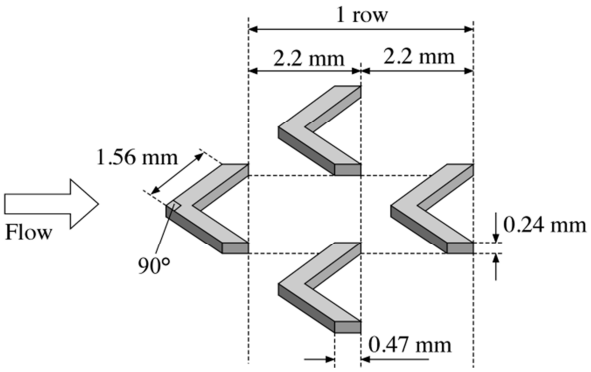


Figure 4.7. Specification of 45° chevron ribs.

Correlation (4.1) is used for pedestal systems N_2 in the baseline design (Fig. 4.12), N_2 in RP 1D (Fig. 4.13), N_2, N_4 and N_6 in RP 1D+ (Fig. 4.14), and N_2 and N_{10} in RP 3D (Fig. 4.15). It is assumed that the total pressure loss due to the pin fins N_3 is negligible because they span approximately 10% of the passage height.

4.3.3 Chevron Rib Total Pressure Loss Correlation

45° V-shaped broken chevron turbulator ribs, as reported in Han and Zhang (1992), were used to induce total pressure loss and increase local heat transfer rates in channels which were not able to afford the pressure losses incurred by pedestal arrays, i.e., the reverse-pass channels feeding S4 and S5. This type of rib was chosen because of its insensitivity of friction factor to Reynolds number.

The specification of the chevron ribs used in the reverse-pass designs is shown in Fig. 4.7. The mean friction factor f of a square channel containing 45° V-shaped broken chevron turbulator ribs on opposite sides with rib height to channel hydraulic diameter of 0.06 is approximately 7 times the smooth wall friction factor of the equivalent passage without ribs, f_0. Park et al. (1992) showed that the mean friction factor of a channel with aspect ratio 3-4 is approximately double the friction factor of the equivalent square channel reported in Han and Zhang (1992).

The friction factor measurements in Park et al. (1992) and Han and Zhang (1992) are for ribs on two opposite walls, while the ribs in the reverse-pass designs are located only on the hot-side wall. The approximation is made that the mean friction factor enhancement for chevron ribs located on a *single wall* (the case in all designs in this thesis) is the area-weighted mean of the smooth wall friction factor and the rib-roughened friction factor compensating for the difference in aspect ratio, i.e.,

$$f \sim \tfrac{1}{2}(f_0 + (2)(7)f_0) \sim 7.5f_0. \tag{4.5}$$

A smooth wall friction factor f_0 of 0.005 was used during the design process, based on a *cast* surface roughness of 3 μm (Rawlinson, 2001), a nominal hydraulic diameter of 3.5 mm, and the Moody diagram in Howatson et al., (2009). f_0 is approximately independent of Reynolds number above $1\text{x}10^5$, based on hydraulic diameter.

The total pressure loss Δp_0 incurred by the rib-roughened channel is thus calculated:

$$\Delta p_0 = \frac{1}{2}\rho v^2 \frac{4L}{d} f, \tag{4.6}$$

where ρ is the coolant density, L is the streamwise length of the rib-roughened channel, d is the hydraulic diameter of the channel and v is the local velocity in the channel calculated using the local areas and mass flow rates in Tables 4.4-4.7:

$$v = \frac{\dot{m}}{\rho A}. \tag{4.7}$$

The hydraulic diameter is calculating using

$$d = \frac{4A}{P}, \tag{4.8}$$

where P is the channel perimeter. Correlation (4.5) is used for rib-roughened systems N_5 and N_6 in RP 1D (Fig. 4.13), N_8 and N_9 in RP 1D+ (Fig. 4.14), and N_4 and N_5 in RP 3D (Fig. 4.15).

Recently, Stimpson et al. (2015) showed that the nominal surface roughness of *laser-sintered* components is of the order 10 μm, which equates to a smooth wall friction factor f_0 of 0.007. This value was used in the retrospective estimation of total pressure distribution in the reverse-pass designs, for the correct coolant total pressure at vane inlet.

4.3.4 Smooth Duct Total Pressure Loss Estimation

For channel sections without ribs, the total pressure loss Δp_0 is estimated using equation (4.6) with $f = f_0$:

$$\Delta p_0 = \frac{1}{2}\rho v^2 \frac{4L}{d} f_0, \tag{4.9}$$

where ρ is the coolant density, L is the streamwise length of the rib-free channel, d is the hydraulic diameter of the channel and v is the local velocity in the channel calculated using local area and mass flow rates (4.7). Equation (4.9) is used to estimate the total pressure loss between point 8 and 9 in RP 3D.

4.3.5 Impingement and Pipe Fitting Total Pressure Loss Estimation

Based on the work of Hippensteele (1974), the total pressure drop Δp_0 incurred by an impingement system is approximately equal to the local dynamic head $\frac{1}{2}\rho v^2$—i.e., the loss coefficient is constant and equal to unity:

$$\Delta p_0 = \frac{1}{2}\rho v^2. \tag{4.10}$$

v is calculated using equation (4.7). Equation (4.10) is used to model the total pressure loss created by A_1 in the baseline design, A_1 and A_4 in RP 1D (Fig. 4.13), A_1, A_3 and A_5 in RP 1D+ (Fig. 4.14), and A_3 and A_6 in RP 3D (Fig. 4.15).

The total pressure loss Δp_0 at bends, contractions and expansions is assumed to be directly proportional to the local dynamic head $\frac{1}{2}\rho v^2$, e.g., Howatson et al. (2009):

$$\Delta p_0 = K_L \frac{1}{2} \rho v^2, \tag{4.11}$$

where K_L is a dimensionless loss coefficient and v is calculated using equation (4.7). A loss coefficient K_L = 0.5 is used to model the total pressure loss due to the contraction at vane inlet, occurring at planes A_0 and A_3 in the baseline design and RP 1D and plane A_0 in RP 1D+ and RP 3D. A loss coefficient K_L = 2.2 is used to model the total pressure loss due to the close return 180° bend in RP 3D between points 7 and 8. The total pressure loss due to the expansion of the RP 3D off-midspan reverse-pass passages into a shared S4/S5 plenum is modelled using a loss coefficient K_L = 1.

4.3.6 S4 and S5 Preliminary Area Estimation and TE Mass Flow Rate Estimation

The nominal geometric areas of rows S4 and S5 are estimated using the 1D isentropic compressible mass flow relation:

$$A = \frac{\dot{m}}{C_d \frac{p_{0u}}{\sqrt{T_{0c}}} \left(\frac{p_{0u}}{p_d}\right)^{-\frac{\gamma+1}{2\gamma}} \sqrt{\frac{2\gamma}{R(\gamma-1)}\left[\left(\frac{p_{0u}}{p_d}\right)^{\frac{\gamma-1}{\gamma}} - 1\right]}}, \tag{4.12}$$

where A is the geometric flow area of the row, $\dot{m}$ is the total mass flow rate through the row; p_{0u} is the total pressure within the plenum feeding the row, p_d is the exit static pressure into which the film is ejected set by the pressure distribution around the vane ($p_{d,\mathrm{S4}}$ = 4.056 MPa, $p_{d,\mathrm{S5}}$ = 3.908 MPa), T_{0c} is the total coolant temperature within the feed plenum (950 K), C_d is the discharge coefficient of the row ($C_{d,\mathrm{S4}} \sim 0.79$, $C_{d,\mathrm{S5}} \sim 0.83$), R is the specific gas constant for air, and γ is the ratio of specific heats.

The geometric area of the TE slot is heavily constrained because of space limitations and so the geometric area of the TE slot is the same for all designs. The mass flow rate through the TE slot is controlled by the spacing and number of pedestals within the TE system which dictates total pressure drop. The mass flow rate through the TE is calculated using the inverse of equation (4.12):

$$\dot{m} = A C_d \frac{p_{0u}}{\sqrt{T_{0c}}} \left(\frac{p_{0u}}{p_d}\right)^{-\frac{\gamma+1}{2\gamma}} \sqrt{\frac{2\gamma}{R(\gamma-1)}\left[\left(\frac{p_{0u}}{p_d}\right)^{\frac{\gamma-1}{\gamma}} - 1\right]}, \tag{4.13}$$

where A is the TE slot geometric area (~ 18 mm^2), C_d is the discharge coefficient of the TE slot, p_{0u} is the total pressure after the TE pedestal system and immediately before the TE slot, p_d is the exit static pressure into which the TE film ejects (2.94 MPa), T_{0c} is the coolant total temperature after the TE pedestal system and immediately before the TE slot (1100 K), and γ and R are the ratio of specific heats and the specific gas constant, respectively.

The designs were optimised based on a slot discharge coefficient of 0.69 which was estimated using the incorrect coolant inlet total pressure. The retrospective estimation of total pressure distribution in the reverse-pass designs uses a more representative value of 0.72.

4.4 Thermal Modelling

Once the cooling geometry had been optimised to satisfy the aerodynamic constraints (i.e., pressure margin and per-row coolant mass flow rates), the thermal performance of the SS cooling system was estimated using the following numerical thermal model. Based on the resulting temperature prediction, the design was either modified further to improve temperature uniformity and reduce the maximum metal temperature, or the design was finalised for DMLS manufacture.

The thermal model comprises three steps:

(i) the geometric/aerodynamic conditions from the aerodynamic model and the thermodynamic boundary conditions in Table 4.3 are used to estimate the internal heat transfer coefficient within each SS coolant passage;

(ii) the internal HTC distribution, external HTC distribution, film effectiveness distribution and mainstream gas temperature distribution (Fig. 4.8) are used to estimate the external wall, internal wall, and internal coolant temperature distributions;

(iii) A locally weighted scatter plot smooth—*Lowess* smoothing—is applied to the resulting temperature distributions to partially compensate for spanwise discretisation coarseness and lateral conduction. Lowess smoothing is a type of non-parametric regression in which the regression function is estimated directly without specifying the form explicitly (e.g., Fox and Weisberg, 2010). Lowess smoothing is implemented in MATLAB.

The thermal model is described in this section, and the results described in a later section.

4.4.1 Thermal Boundary Conditions

The cooling systems are thermally modelled at engine boundary conditions, summarised in Table 4.3 and Fig. 4.8. To simplify analysis, it is assumed that the external heat transfer coefficient distribution and the film effectiveness distribution are uniform with span and are not affected by cooling geometry. Differences in external HTC and film effectiveness caused by unmatched blowing ratio and momentum flux ratio are not considered in the thermal model. The external HTC and film effectiveness distributions are taken from the Trent 500 Cooling Design Report by Rawlinson (2001).

To first order, the local internal HTC depends on the shape and size of the channel, the coolant mass flow rate, and the surface decorations, i.e., pedestals or chevron ribs. These are discussed in detail in the following sub-sections. The HTC enhancement due to impingement cooling was not modelled,

Table 4.3. Boundary conditions for thermal model.

Parameter	Symbol	Units	Value
Geometric properties			Tables 4.4-4.7
Coolant inlet temperature	T_{0c}	K	950
Specific heat capacity of air @ 950 K	c_p	$Jkg^{-1}K^{-1}$	1130
Thermal conductivity of air @ 950 K	k	$Wm^{-1}K^{-1}$	0.065
Dynamic viscosity of air @ 950 K	μ	Nsm^{-2}	$4.0x10^{-5}$
Density of air @ 950 K, 4.27 MPa	ρ	kgm^{-3}	15.7
Prandtl number of air @ 950 K	Pr		0.70
Wall thickness	t_w	mm	1
Wall thermal conductivity @ 1300 K	k_w	$Wm^{-1}K^{-1}$	28

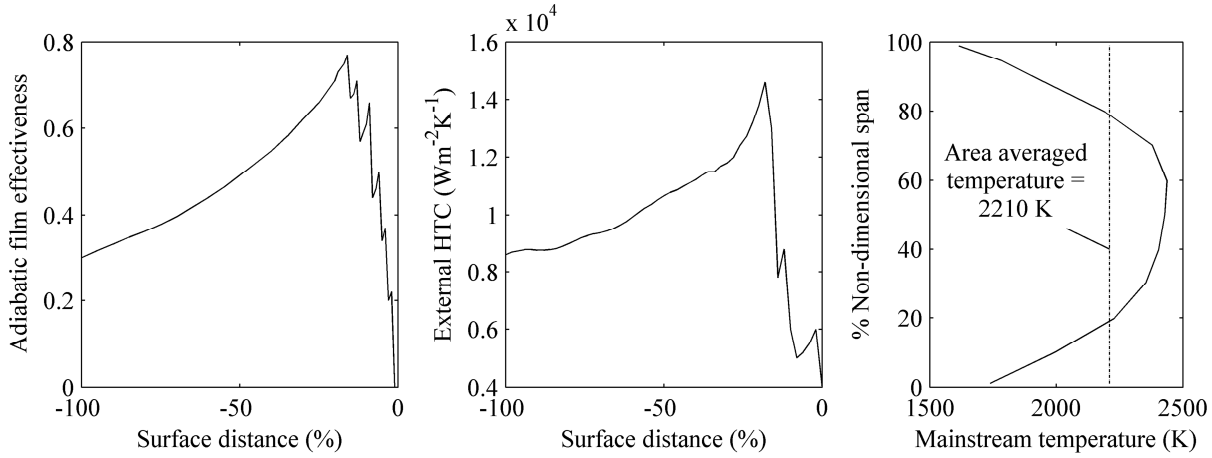


Figure 4.8. Boundary conditions for thermal model. Film effectiveness and external HTC from Rawlinson (2001). Mainstream gas temperature from Rawlinson (2014).

which was seen as reasonable because only a very small proportion of the suction-side is impingement cooled and the effect is spatially limited. The effect of mainstream recovery is neglected.

The designs are optimised for the engine-realistic radial mainstream gas temperature distribution in Fig. 4.8. The thermal performance of the finalised designs is then assessed in *uniform* radial mainstream gas temperature (2210 K) conditions. This is to aid interpretation of the experimental results obtained in the Annular Sector Heat Transfer Facility, where the mainstream temperature is approximately uniform.

4.4.2 Pedestal Bank Internal HTC Correlation

The average Nusselt number in a pedestal bank is estimated using the correlation of Metzger et al. (1986) in Armstrong and Winstanley (1988):

$$\mathrm{Nu}_D = 0.135\,\mathrm{Re}_D{}^{0.69}(x/D)^{-0.34}, \tag{4.14}$$

for Reynolds numbers $10^3 < \mathrm{Re}_D < 10^5$, pedestal height to diameter ratio $H/D = 1$, pedestal spacing to diameter ratio $S/D = 2.5$, and pedestal spacing to diameter ratio $1.5 \leq x/D \leq 5.0$. The Reynolds number is defined in equation (4.4) and (4.3). The area averaged internal heat transfer coefficient $\bar{h}_2$ is determined from the Nusselt number:

$$\bar{h}_2 = A' \frac{\mathrm{Nu}_D k}{D}, \tag{4.15}$$

where k is the thermal conductivity of air at the coolant temperature and A' is the increase in internal area (relative to the external area) created by the pedestals. A' is estimated from the geometry. Equations (4.14) and (4.15) are used to estimate internal HTCs for pedestal systems N_2 in the baseline design (Fig. 4.12), N_2 in RP 1D (Fig. 4.13), N_2, N_4 and N_6 in RP 1D+ (Fig. 4.14), and N_2 and N_{10} in RP 3D (Fig. 4.15).

4.4.3 Smooth Duct and Chevron Rib Internal HTC Correlation

In channels without ribs or pedestals—i.e., smooth channels—the Nusselt number Nu_d is estimated using the correlation of Dittus and Boelter (1930) for turbulent, heated flow:

$$\mathrm{Nu}_d = 0.023\, \mathrm{Re}_d{}^{0.8} \mathrm{Pr}^{0.4}, \tag{4.16}$$

where d is the hydraulic diameter of the channel (4.8) and Pr is the Prandtl number of the coolant. Re_d is the Reynolds number based on the channel hydraulic diameter:

$$\mathrm{Re}_d = \frac{\rho v d}{\mu}, \tag{4.17}$$

where the flow speed v is calculated using equation (4.7). The area-averaged internal HTC $\bar{h}_2$ is determined from the Nusselt number:

$$\bar{h}_2 = \frac{\mathrm{Nu}_d k}{d}. \tag{4.18}$$

Equations (4.16)-(4.18) are used to estimate the internal HTC within the RP 3D hub and case TE passages before the pedestals.

The heat transfer coefficient generated by 45° V-shaped broken chevron turbulator ribs is estimated to be three times greater than the heat transfer coefficient of the equivalent smooth duct (Han and Zhang, 1992).

4.4.4 Coolant and Wall Temperature Prediction

Each cooling system is discretised into a number of one-dimensional domains. The domains for RP 1D+ are shown in Fig. 4.9. Domains are oriented in the axial direction and coincide with each cooling

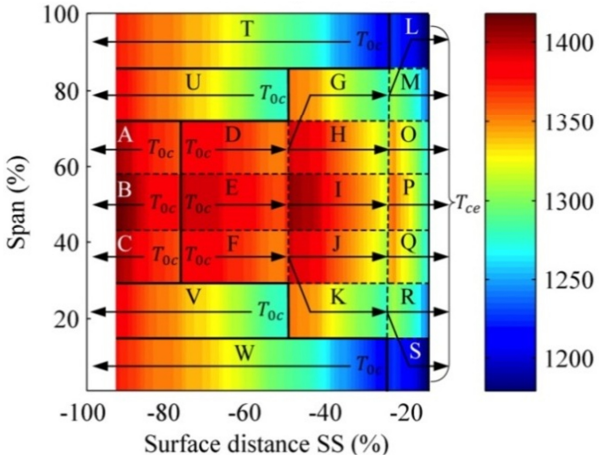


Figure 4.9. RP 1D+ numerical domains (letters) and external wall temperature (K). Solid lines are physical channel boundaries. Dashed lines are artificial domain boundaries.

channel. Coolant temperature, internal wall temperature and external wall temperature are estimated as a function of axial surface distance within each domain. Channels which cover a large span (e.g., the plenum feeding S4 and S5 in the reverse-pass designs) are split into multiple domains to compensate for span-wise variation in mainstream gas temperature. Coolant is assumed to be uniformly distributed across the span of each channel.

The coolant temperature distribution $T_c(x')$ within a domain is found by solving the equation

$$\frac{dT_c(x')}{dx'} = \frac{wU(x')}{\dot{m}_c c_p}(T_{aw}(x') - T_c(x')), \tag{4.19}$$

where x' is axial distance relative to the domain inlet and increases in the direction of coolant flow (i.e., direction of positive x' is contrary to the mainstream flow direction for reverse-pass passages and in the same direction as the mainstream flow for forward-pass passages); w is the span-wise width of the domain; $\dot{m}_c$ is the coolant mass flow rate within the domain; c_p is the specific heat capacity of the coolant; $U(x')$ is the local overall heat transfer coefficient (4.20); and $T_{aw}(x')$ is the local adiabatic external wall temperature (4.21). Equation (4.19) is derived by equating local heat flux across the wall to coolant enthalpy gain.

Implicit in equation (4.19) is that heat transfer only takes place across one wall of the channel, i.e., all other walls are adiabatic. This was seen as a reasonable approximation for channels which back onto the main coolant plenum, since the heat flux on the back wall is far smaller than the heat flux across the external wall. However, this was not assumed in the TE pedestal bank between -95% and -80% surface distance because heat is transferred into the coolant channel from both suction-side and pressure-side walls. The approximation was made that only half the coolant mass flow rate $\dot{m}_c$ within the TE pedestal bank cools the SS—equivalent to doubling the area over which heat transfer takes

place. This assumes that the PS and SS wall temperature are the same at a given point in the TE pedestal bank.

The initial condition is $T_c(0) = T_{0c}$ if the domain is fed directly from the main coolant plenum; for example, domains A-F and T-W in Fig. 4.9. If the domain is fed by another domain, the initial coolant temperature $T_c(0)$ is equal to the coolant exit temperature of the upstream domain, e.g., $T_{c,\text{domain H}}(0) = T_{c,\text{domain G}}(0) = T_{c,\text{domain D}}(\text{end})$ in Fig. 4.9. The domains are analysed in order of flow dependency.

The local overall heat transfer coefficient $U(x')$ is defined as

$$U(x') = \left(\frac{1}{h_1(x')} + \frac{1}{h_2(x')} + \frac{t_w}{k_w}\right)^{-1}, \tag{4.20}$$

where $h_1(x')$ is the external heat transfer coefficient given in Fig. 4.8, $h_2(x')$ is the internal heat transfer coefficient calculated using equations (4.14)-(4.18) and t_w/k_w is the ratio of wall thickness to wall thermal conductivity. The systems do not include thermal barrier coating.

The local adiabatic external wall temperature is defined as

$$T_{aw}(x') = T_{0m} - \eta(x')(T_{0m} - T_{ce}), \tag{4.21}$$

where T_{0m} is the mean mainstream gas temperature over the span of the domain (Fig. 4.8), $\eta(x')$ is the local adiabatic film cooling effectiveness (Fig. 4.8), and T_{ce} is the coolant exit temperature, i.e., the temperature of the coolant at the point of injection into the mainstream. The coolant exit temperature T_{ce} is found by averaging the final coolant temperature of the domains feeding the S4 and S5 films. In the example in Fig. 4.9, T_{ce} is the mean final coolant temperature of domains L-S. Since T_{ce} is a dependent variable, equations (4.19)-(4.21) are solved iteratively using the MATLAB ordinary differential equation solver *ode45.m* until a steady solution is obtained.

After the coolant temperature distribution $T_c(x')$ has been calculated, the internal wall temperature distribution $T_{w2}(x')$ and external wall temperature distribution $T_{w1}(x')$ are estimated using

$$T_{w2}(x') = T_c(x') + \frac{U(x')}{h_2(x')}(T_{aw}(x') - T_c(x')) \tag{4.22}$$

$$T_{w1}(x') = T_{aw}(x') - \frac{U(x')}{h_1(x')}(T_{aw}(x') - T_c(x')), \tag{4.23}$$

which are derived by equating local through wall conduction to local internal and external convection. The resulting 1D temperature distributions are assumed constant with span in the domain. The temperature distributions are then merged into a single suction-side temperature plot, e.g., Fig. 4.9.

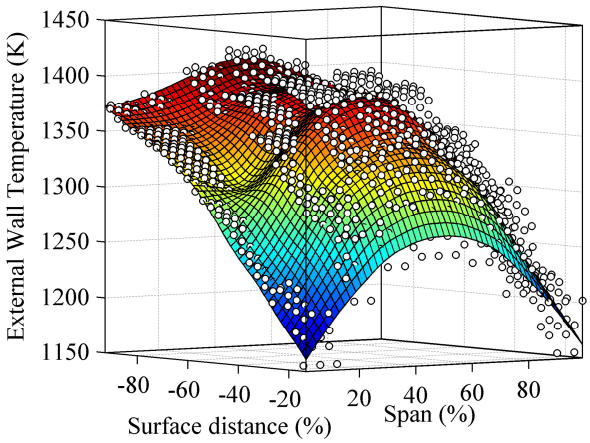


Figure 4.10. Example of Lowess (locally weighted scatter plot smooth, e.g., Fox and Weisberg, 2010) surface fit (0.1 span) to 50 x 50 sampling of coarse solution in Fig. 4.9. White points are raw data; coloured surface is Lowess surface fit.

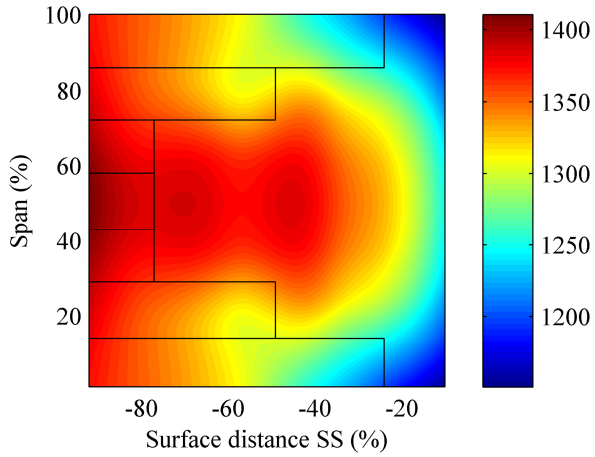


Figure 4.11. Example of final external wall temperature prediction after Lowess (locally weighted scatter plot smooth, e.g., Fox and Weisberg, 2010) surface fit.

The external wall temperature prediction in Fig. 4.9 is coarse in the span-wise direction and does not account for lateral thermal conduction. To partially compensate for span-wise coarseness and lateral conduction, a Lowess surface is fit to the raw, coarse data in Fig. 4.9 using the MATLAB function *fit.m*, which performs a locally weighted linear regression within a user-defined span (set to 0.1). The result of the Lowess smoothing is shown in Figs. 4.10 and 4.11.

4.5 Final Results of Aerothermal Modelling

The internal total pressure distributions of the reverse-pass designs are summarised in Tables 4.5-4.7, predicted using the aerodynamic model for T500 engine conditions. The aerodynamic model was also used to predict the pressures within the *baseline* T500 HPNGV cooling geometry for comparison, reported in Table 4.4. Both the predictions used for design and the retrospective predictions (based on the corrected inlet total coolant pressure) are tabulated.

Table 4.4. Design values and retrospective corrections for baseline SS at engine conditions, based on Rawlinson (2001).

Parameter	Used for Design	Corrected	Parameter	Used for Design	Corrected
p_{30} (total, MPa)	4.360	4.269			
p_{00} (total, MPa)	4.359	4.268	$\dot{m}_0$ (g/s/vane)	49.6	-
p_{01} (total, MPa)	4.343	4.252	$\dot{m}_1$ (g/s/vane)	7.1	-
p_{02} (total, MPa)	3.848	3.757	$\dot{m}_2$ (g/s/vane)	7.1	-
p_{03} (total, MPa)	4.359	4.268	$\dot{m}_3$ (g/s/vane)	70.8	-
p_{S4} (static, MPa)	4.056	-	$\dot{m}_{S4}$ (g/s/vane)	31.1	-
p_{S5} (static, MPa)	3.908	-	$\dot{m}_{S5}$ (g/s/vane)	39.7	-
p_{TE} (static, MPa)	2.938	-	$\dot{m}_{TE}$ (g/s/vane)	49.6	-
A_0 (mm^2)	233	-	N_2 (rows)	20	-
A_1 (mm^2)	10	-	D_2 (mm)	1	-
A_2 (mm^2)	1.2 x 6.5	-	$(x/D)_2$	1.5	-
A_3 (mm^2)	396	-	N_3 (rows)	4	-
C_d x A_{S4} (mm^2)	0.79 x 13.2	0.79 x 15.7	D_3 (mm)	1.5	-
C_d x A_{S5} (mm^2)	0.83 x 13.4	0.83 x 15.0	L_a (mm)	55	-
C_d x A_{TE} (mm^2)	0.69 x 0.4 x 44.8	0.72 x 0.4 x 44.8	L_b (mm)	17	-

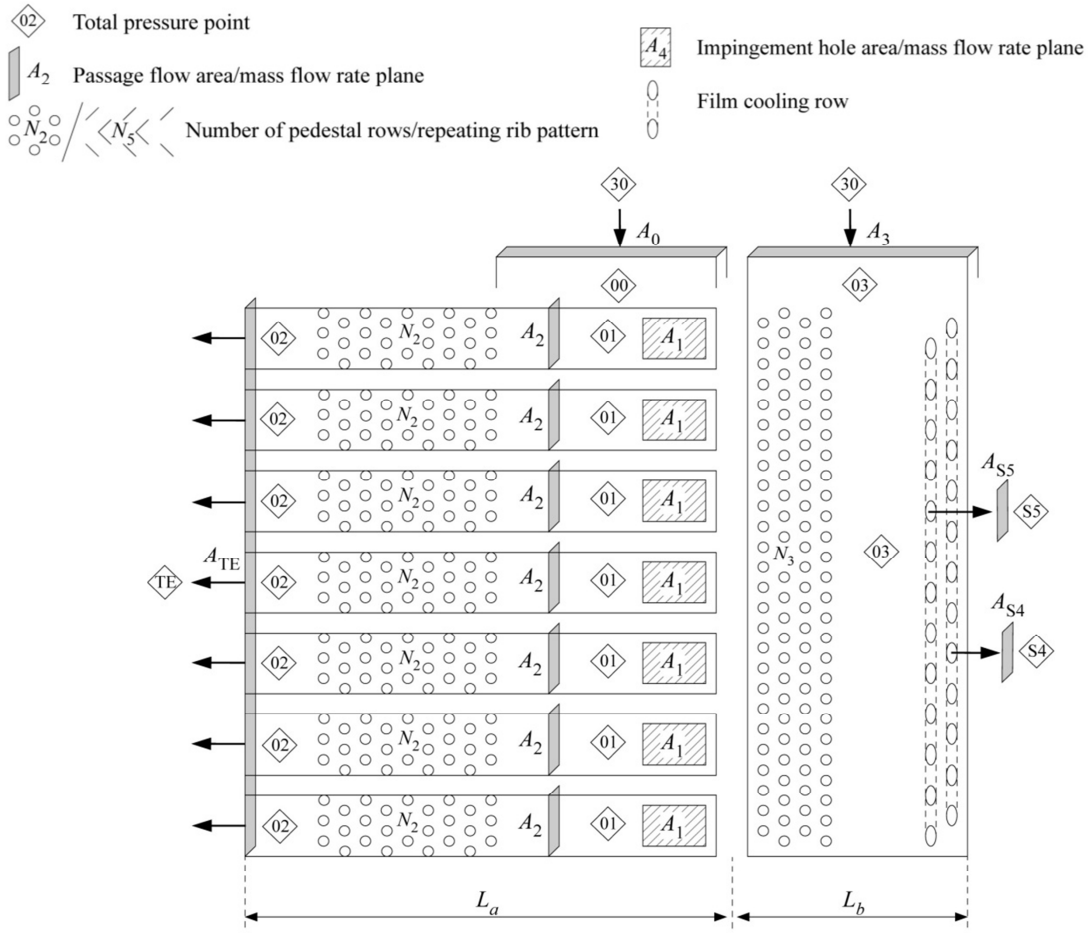


Figure 4.12. Reference schematic for baseline SS.

Table 4.5. Design values and retrospective corrections for SS of RP 1D at engine conditions.

Parameter	Used for design	Corrected	Parameter	Used for design	Corrected	Parameter	Used for design	Corrected
p_{30} (total, MPa)	4.360	4.269						
p_{00} (total, MPa)	4.355	4.264	A_0 (mm^2)	91.9	-	$\dot{m}_0$ (g/s/vane)	51.0	52.9
p_{01} (total, MPa)	4.223	4.132	A_1 (mm^2)	3.5	-	$\dot{m}_1$ (g/s/vane)	7.3	7.6
p_{02} (total, MPa)	3.877	3.785	A_2 (mm^2)	1.2 x 6.5	-	$\dot{m}_2$ (g/s/vane)	7.3	7.6
p_{03} (total, MPa)	4.353	4.262	A_3 (mm^2)	178.5	-	$\dot{m}_3$ (g/s/vane)	70.8	-
p_{04} (total, MPa)	4.349	4.258	A_4 (mm^2)	26.7	-	$\dot{m}_4$ (g/s/vane)	8.9	-
p_{05} (total, MPa)	4.328	4.228	A_5 (mm^2)	5.7 x 2.4	-	$\dot{m}_5$ (g/s/vane)	8.9	-
p_{06} (total, MPa)	4.328	4.228	A_6 (mm^2)	2.4 x 55	-	$\dot{m}_6$ (g/s/vane)	70.8	-
p_{S4} (static, MPa)	4.056	-	C_d x A_{S4} (mm^2)	0.79 x 13.9	0.79 x 17.5	$\dot{m}_{S4}$ (g/s/vane)	31.1	-
p_{S5} (static, MPa)	3.908	-	C_d x A_{S5} (mm^2)	0.83 x 13.9	0.83 x 15.9	$\dot{m}_{S5}$ (g/s/vane)	39.7	-
p_{TE} (static, MPa)	2.938	-	C_d x A_{TE} (mm^2)	0.69 x 0.4 x 44.8	0.72 x 0.4 x 44.8	$\dot{m}_{TE}$ (g/s/vane)	51.0	52.9
N_2 (rows)	14	-	N_5 (rows)	6	-	N_6 (rows)	1	-
D_2 (mm)	1	-	Rib height 5 (mm)	0.24	-	Rib height 6 (mm)	0.24	-
$(x/D)_2$	1.5	-	Rib width 5 (mm)	0.47	-	Rib width 6 (mm)	0.47	-
L_a (mm)	29.6	-	L_b (mm)	24	-	L_c (mm)	12	-

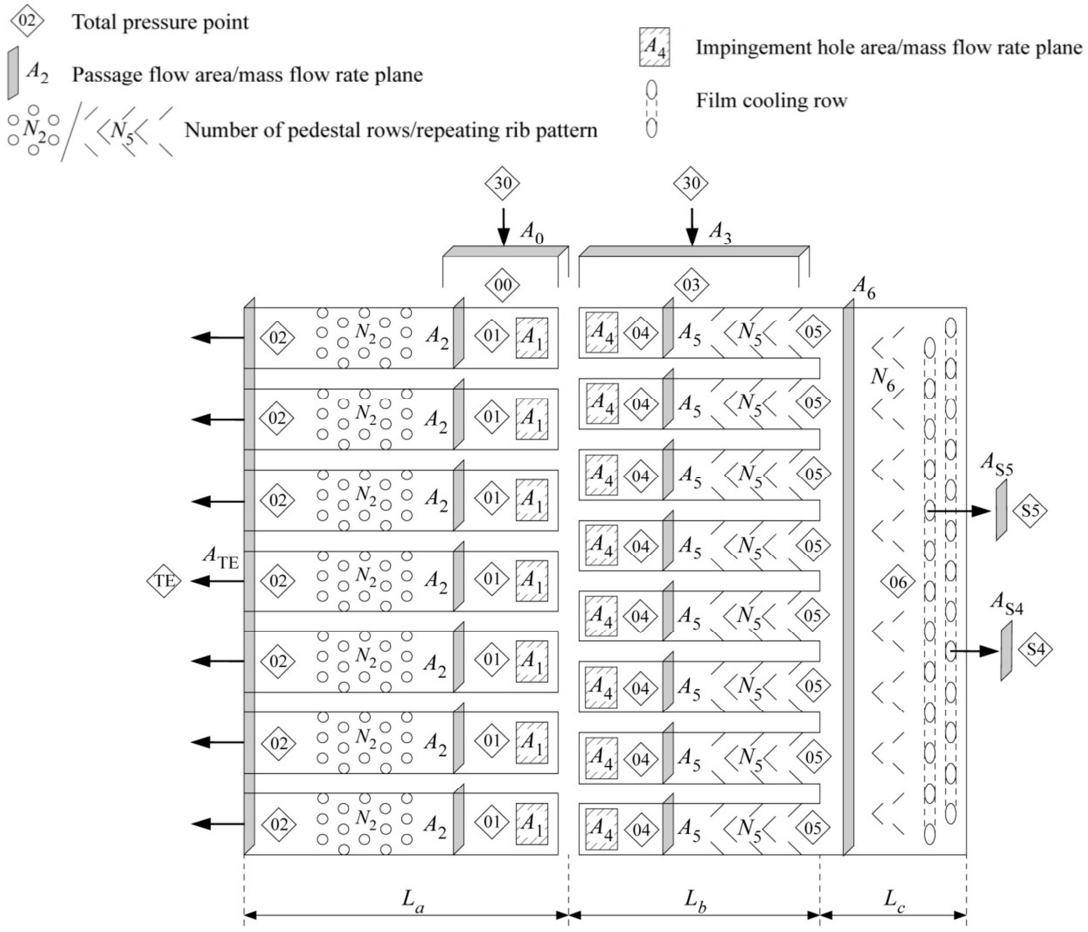


Figure 4.13. Reference schematic for RP 1D SS.

Table 4.6. Design values and retrospective corrections for SS of RP 1D+ at engine conditions.

Parameter	Used for Design	Corrected	Parameter	Used for Design	Corrected	Parameter	Used for Design	Corrected
p_{30} (total, MPa)	4.360	4.269						
p_{00} (total, MPa)	4.355	4.264	A_0 (mm^2)	220	-	$\dot{m}_0$ (g/s/vane)	120.1	119.5
p_{01} (total, MPa)	4.074	3.983	A_1 (mm^2)	2.4	-	$\dot{m}_1$ (g/s/vane)	7.0	7.0
p_{02} (total, MPa)	3.826	3.735	A_2 (mm^2)	1.2 x 6.5	-	$\dot{m}_2$ (g/s/vane)	7.0	7.0
p_{03} (total, MPa)	4.187	4.096	A_3 (mm^2)	3.1	-	$\dot{m}_3$ (g/s/vane)	7.0	7.0
p_{04} (total, MPa)	3.820	3.729	A_4 (mm^2)	1.2-2 x 6.5	-	$\dot{m}_4$ (g/s/vane)	7.0	7.0
p_{05} (total, MPa)	4.021	3.930	A_5 (mm^2)	2.2	-	$\dot{m}_5$ (g/s/vane)	7.0	7.0
p_{06} (total, MPa)	3.820	3.729	A_6 (mm^2)	1.2-2 x 6.5	-	$\dot{m}_6$ (g/s/vane)	7.0	7.0
p_{07} (total, MPa)	4.291	4.200	A_7 (mm^2)	50	-	$\dot{m}_7$ (g/s/vane)	70.8	-
p_{08} (total, MPa)	4.213	4.091	A_8 (mm^2)	2 x 19.5	-	$\dot{m}_8$ (g/s/vane)	70.8	-
p_{09} (total, MPa)	4.207	4.082	A_9 (mm^2)	2 x 60	-	$\dot{m}_9$ (g/s/vane)	70.8	-
p_{S4} (static, MPa)	4.056	-	C_d x A_{S4} (mm^2)	0.79 x 18.6	0.79 x 44.8	$\dot{m}_{S4}$ (g/s/vane)	31.1	-
p_{S5} (static, MPa)	3.908	-	C_d x A_{S5} (mm^2)	0.83 x 16.4	0.83 x 21.5	$\dot{m}_{S5}$ (g/s/vane)	39.7	-
p_{TE} (static, MPa)	2.938	-	C_d x A_{TE} (mm^2)	0.69 x 0.4 x 44.8	0.72 x 0.4 x 44.8	$\dot{m}_{TE}$ (g/s/vane)	49.3	48.7
N_2 (rows)	10	-	N_4 (rows)	24	-	N_6 (rows)	15	-
D_2 (mm)	1	-	D_4 (mm)	1	-	D_6 (mm)	1	-
$(x/D)_2$	1.5	-	$(x/D)_4$	1.5	-	$(x/D)_6$	4	-
L_a (mm)	13.6	-	N_8 (rows)	7	-	N_9 (rows)	3	-
L_b (mm)	21.5	-	Rib height 8 (mm)	0.24	-	Rib height 9 (mm)	0.24	-
L_c (mm)	20	-	Rib width 8 (mm)	0.47	-	Rib width 9 (mm)	0.47	-
L_d (mm)	10.5	-						

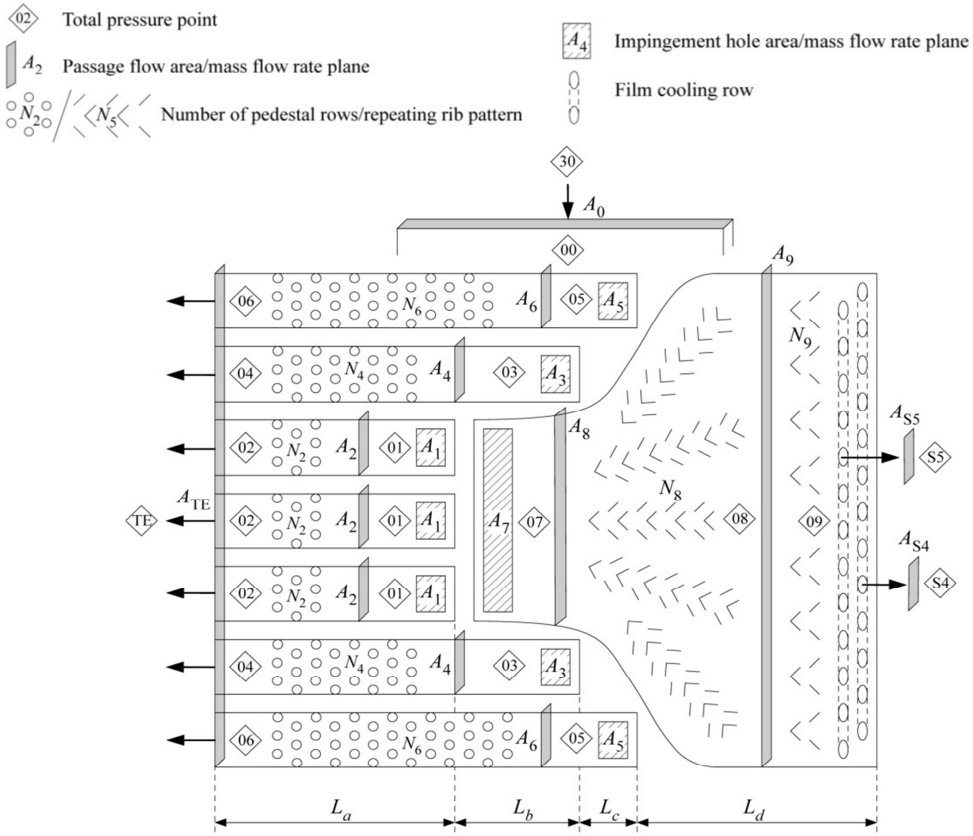


Figure 4.14. Reference schematic for RP 1D+ SS.

Table 4.7. Design values and retrospective corrections for SS of RP 3D at engine conditions.

Parameter	Used for Design	Corrected	Parameter	Used for Design	Corrected	Parameter	Used for Design	Corrected
p_{30} (total, MPa)	4.360	4.269						
p_{00} (total, MPa)	4.355	4.264	A_0 (mm^2)	220	-	$\dot{m}_0$ (g/s/vane)	121.6	121.1
p_{01} (total, MPa)	4.052	3.961	A_1 (mm^2)	11	-	$\dot{m}_1$ (g/s/vane)	34.6	34.2
p_{02} (total, MPa)	3.841	3.750	A_2 (mm^2)	40.8	-	$\dot{m}_2$ (g/s/vane)	34.6	34.2
p_{03} (total, MPa)	4.335	4.244	A_3 (mm^2)	45	-	$\dot{m}_3$ (g/s/vane)	35.4	35.4
p_{04} (total, MPa)	4.206	4.063	A_4 (mm^2)	2 x 11	-	$\dot{m}_4$ (g/s/vane)	35.4	35.4
p_{05} (total, MPa)	4.189	4.043	A_5 (mm^2)	2 x 60	-	$\dot{m}_5$ (g/s/vane)	70.8	70.8
p_{06} (total, MPa)	4.243	4.152	A_6 (mm^2)	8.5	-	$\dot{m}_6$ (g/s/vane)	16.2	15.9
p_{07} (total, MPa)	3.938	3.847	A_7 (mm^2)	2 x 12	-	$\dot{m}_7$ (g/s/vane)	16.2	15.9
p_{08} (total, MPa)	3.927	3.836	A_8 (mm^2)	2 x 10	-	$\dot{m}_8$ (g/s/vane)	8.1	8.0
p_{09} (total, MPa)	3.925	3.833	A_9 (mm^2)	2 x 8	-	$\dot{m}_9$ (g/s/vane)	8.1	8.0
p_{010} (total, MPa)	3.819	3.728	A_{10} (mm^2)	9.6	-	$\dot{m}_{10}$ (g/s/vane)	8.1	8.0
p_{S4} (static, MPa)	4.056	-	C_d x A_{S4} (mm^2)	0.79 x 19.8	0 (PR < 1)	$\dot{m}_{S4}$ (g/s/vane)	31.1	0
p_{S5} (static, MPa)	3.908	-	C_d x A_{S5} (mm^2)	0.83 x 16.9	0.83 x 43.5	$\dot{m}_{S5}$ (g/s/vane)	39.7	70.8
p_{TE} (static, MPa)	2.938	-	C_d x A_{TE} (mm^2)	0.69 x 18.4	0.72 x 18.4	$\dot{m}_{TE}$ (g/s/vane)	50.8	50.3
N_2 (rows)	10	-	N_4 (rows)	6	-	N_5 (rows)	3	-
D_2 (mm)	1	-	Rib height 4 (mm)	0.24	-	Rib height 5 (mm)	0.24	-
$(x/D)_2$	1.5	-	Rib width 4 (mm)	0.47	-	Rib width 5 (mm)	0.47	-
L_a (mm)	13.6	-	N_7 (rows)	21	-	N_{10} (rows)	5	-
L_b (mm)	32.3	-	D_7 (mm)	1	-	Rib height 10 (mm)	1	-
L_c (mm)	17	-	$(x/D)_7$	1.5	-	Rib width 10 (mm)	6	-

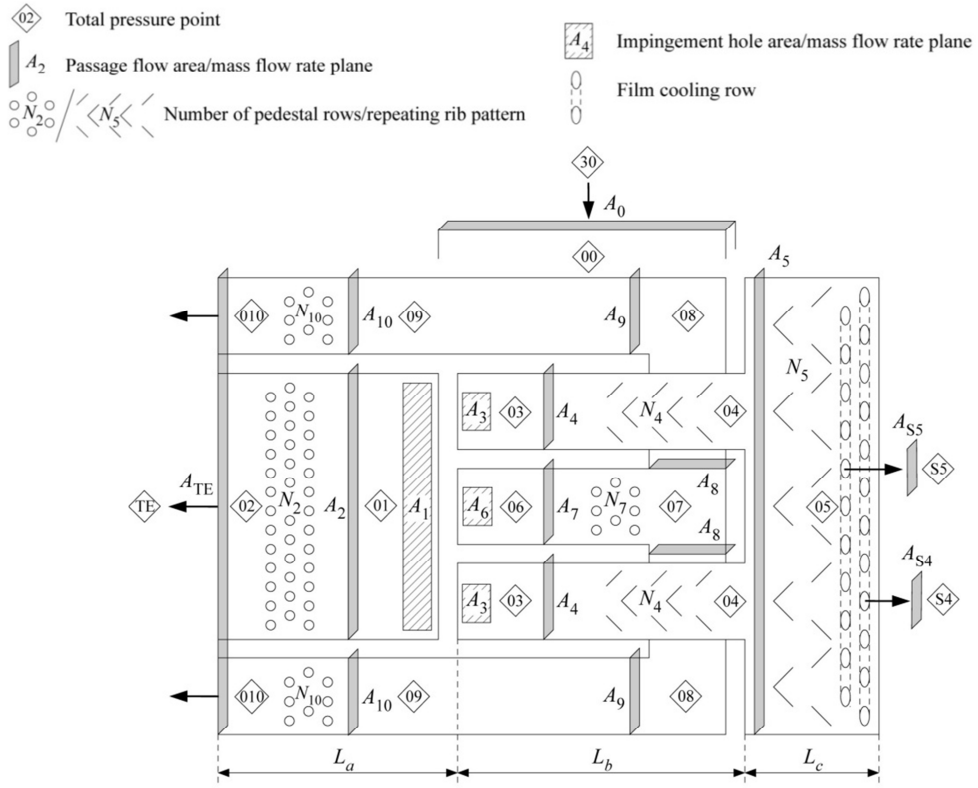


Figure 4.15. Reference schematic for RP 3D SS.

Of the reverse-pass designs, RP 1D was originally designed to maintain the greatest local pressure ratio across S4 (1.067), followed by RP 1D+ (1.037) and then RP 3D (1.033). The reverse-pass designs were manufactured based on these estimates. However, using the updated aerodynamic boundary conditions, the estimated pressure ratio across S4 is much lower: RP 1D = 1.042; RP 1D+ = 1.006; RP 3D = 0.997, i.e., the aerodynamic model predicts that RP 3D row S4 ingests at the correct pressure boundary condition. S4 ingestion is indeed observed in both the aerodynamic experiments in Chapter 8 and the experimental thermal assessment in Chapter 7. Row S4 in RP 1D+, though operating very close to the ingestion limit, is not observed to ingest in the aerothermal experiments at the design coolant-to-mainstream pressure ratio.

The holes were drilled out after manufacture in an attempt to match the design coolant mass flow rate. The modifications made to the laser-sintered vanes after manufacture are summarised in Table 4.8.

The design S4 and S5 row areas were re-calculated in retrospect using the correct inlet coolant total pressure. Corrected row areas are reported in Tables 4.4-4.7. In the updated prediction, row S4 RP 3D is blocked entirely because it operates under an adverse pressure gradient. To compensate, all S4 flow is ejected from S5.

Figure 4.16 shows the internal HTC predictions for the reverse-pass and baseline T500 designs. Figure 4.17 shows the external metal temperature predictions (no thermal barrier coating) in both an engine-representative radial mainstream temperature distribution environment, and also a uniform mainstream temperature environment. RP 1D+ and RP 3D were optimised for the radial mainstream temperature distribution.

In Fig. 4.18, the midspan temperature prediction of the baseline HPNGV (with radial temperature distribution) is compared to the numerical predictions of Rawlinson (2001). Rawlinson used a suite of RR numerical codes to predict HPNGV temperature at the same boundary conditions, but additionally modelled the effect of thermal barrier coating (TBC). Despite the fact that the thermal model described in this chapter did not model TBC, the predictions can to some extent be compared, since it is reasonable to assume that the external metal temperature of a vane without TBC is somewhere between the bond-coat temperature and the external TBC temperature of the equivalent vane with TBC. Bearing this in mind, the predictions compare well; the thermal model generally predicts a metal temperature between the bond-coat and TBC temperature predicted by Rawlinson. In both predictions, a hot-spot at -30% S.D. and maximum SS metal temperature at the TE are observed—caused by undirected coolant flow and low internal convective heat transfer, respectively.

RP 1D was designed before the numerical concept study and the implementation of the iterative aerothermal optimisation process, and so the design of RP 1D was less guided than RP 1D+ and RP 3D. The RP 1D TE pedestal system is longer than optimum and the reverse-pass system shorter than

optimum: the RP 1D TE system begins at -60% S.D. compared to -80% S.D. for RP 1D+ and RP 3D. The baseline TE system begins at -38% S.D.

Figure 4.17 demonstrates the advantage of locating the inlet to the TE pedestal bank as far back along the SS as possible. The maximum TE temperature of RP 1D+ and RP 3D is far lower than RP 1D (~1450 K, ~1440 K and ~1490 K, respectively, with radial mainstream temperature distribution), which is far lower than the baseline system (~ 1510 K), owing to a shorter TE system length. The 20 K difference in SS TE midspan temperature between the baseline and RP 1D design agrees with the numerical concept study. The hot spot in RP 1D around -50% surface distance is caused by relatively low internal HTCs in the reverse-pass passages due to reduced Reynolds numbers.

The predicted mean SS midspan metal temperatures of the baseline vane, RP 1D, RP 1D+ and RP 3D are ~1380 K, ~1390 K, ~1370 K and ~1350 K, respectively (radial mainstream temperature distribution). These trends are also observed in the experimental results in Chapter 7. The mean SS

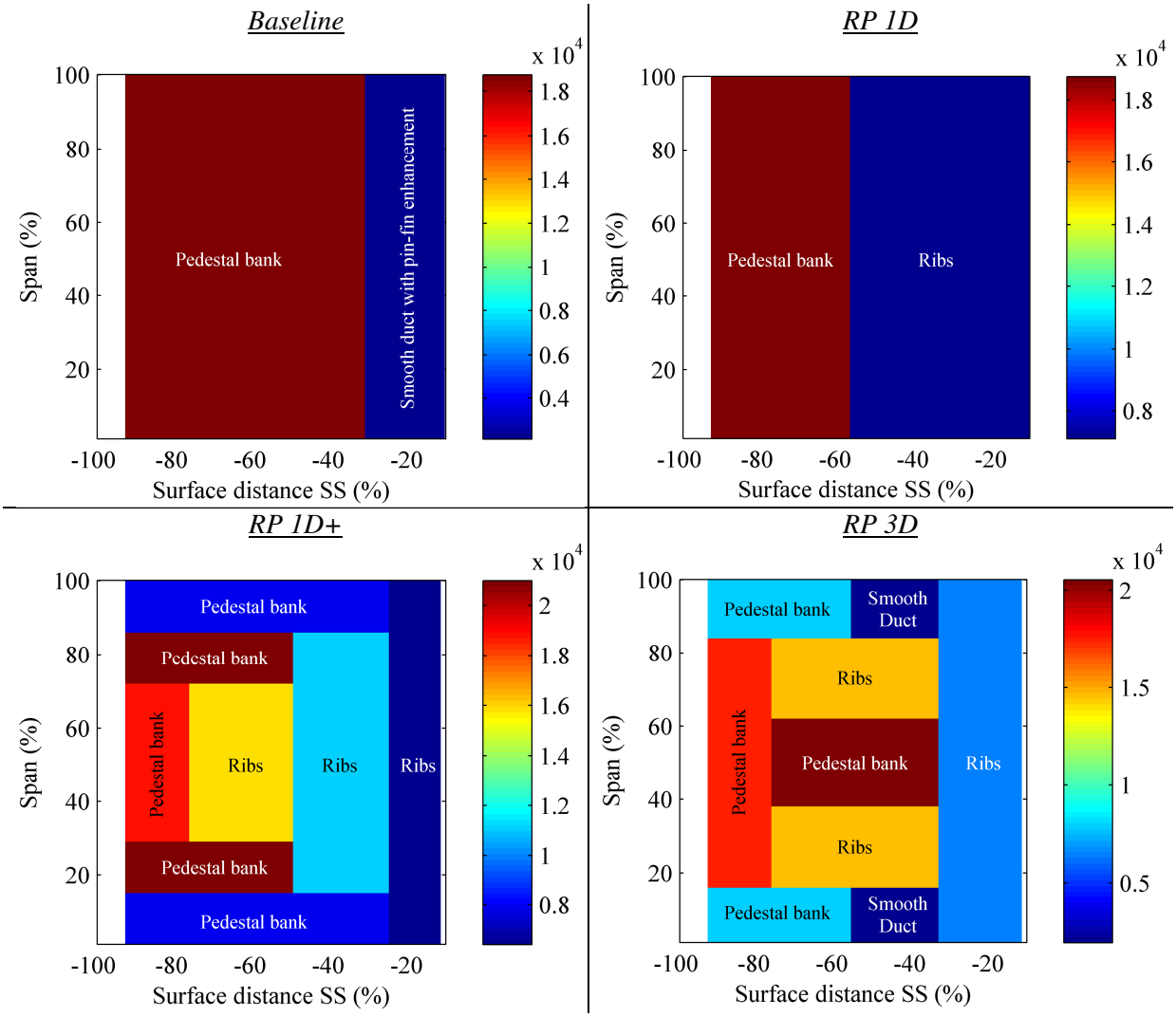


Figure 4.16. Internal heat transfer coefficient (HTC) distributions ($Wm^{-2}K^{-1}$)

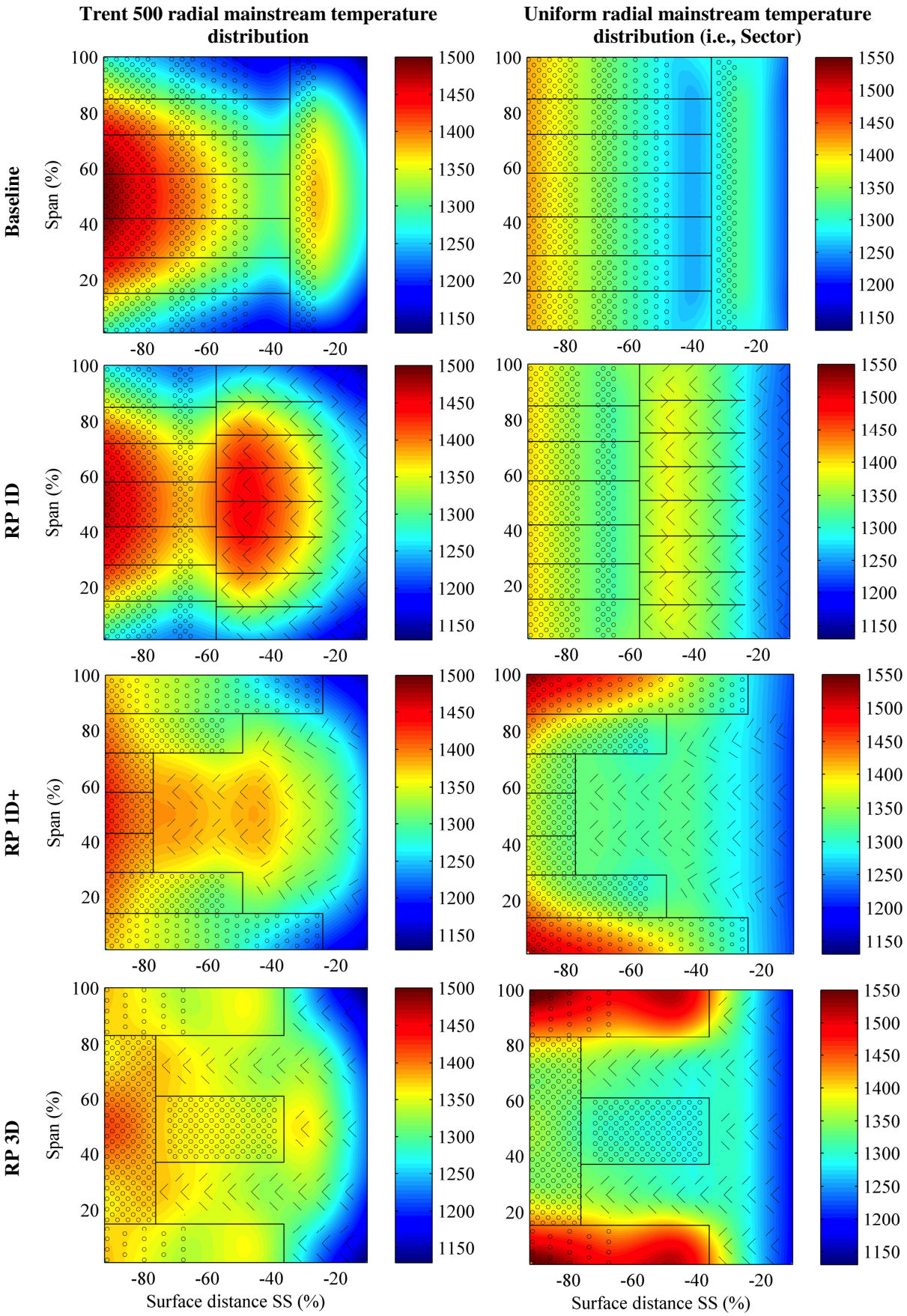


Figure 4.17. SS external wall temperature predictions (K) for both Trent 500 mainstream radial temperature distribution and uniform radial temperature distribution. RP 1D+ and RP 3D optimised for Trent 500 distribution.

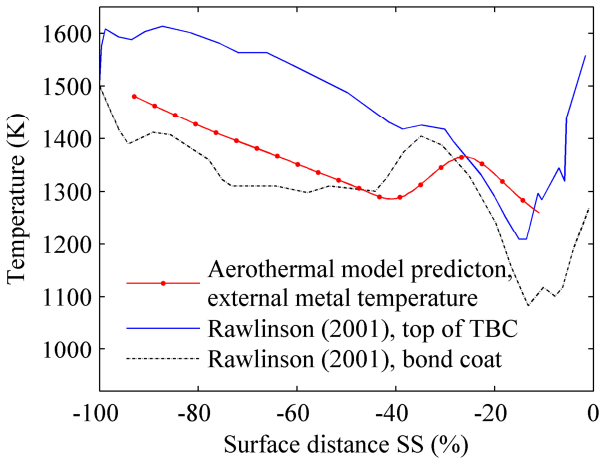


Figure 4.18. SS midspan external surface temperature (K) predictions for the baseline T500 HPNGV Rawlinson (2001) vs. aerothermal model.

midspan internal HTCs are 14600 $Wm^{-2}K^{-1}$, 12100 $Wm^{-2}K^{-1}$, 13500 $Wm^{-2}K^{-1}$ and 16200 $Wm^{-2}K^{-1}$, respectively. The mean SS metal temperature over the entire surface of the baseline vane is around 10-20 K lower than the reverse-pass designs, but is far less uniform, as also observed in the concept study.

Figure 4.17 demonstrates the impact of radial mainstream gas temperature distribution on the performance of a HPNGV cooling system. The predicted spanwise TE temperature of RP 1D+ and RP 3D is far more uniform than RP 1D and the baseline Trent 500 when operating with radial mainstream temperature distribution. RP 1D+ and RP 3D take advantage of the relatively cold mainstream temperatures around the hub and case due to platform and combustor liner film cooling flow. For uniform mainstream temperature, the trend is reversed: the TE spanwise temperature of the baseline and RP 1D is more uniform than RP 1D+ and RP 3D.

4.6 Final Specification

The final three-dimensional CAD drawings (made in SolidWorks) of RP 1D, RP 1D+, RP 3D and the laser-sintered baseline vane are shown in Figs. 4.19-4.22. The external aerofoil shape and the position of the film cooling rows is the same as the 3D, 10 row Trent 500 trailing-vane cast HPNGV (Fig. 4.23). A complete description of the Trent 500 HPNGV aerofoil is given by Luque Martinez (2011).

The final hole specifications are summarised in Table 4.8. The geometric areas of S4 and S5 are predicted using the aerothermal optimisation process and the boundary conditions in Table 4.1. The design of all other rows (S3 – P5) is nominally the same as the baseline cast Trent 500 HPNGV. The reverse-pass geometries were designed at different times using the best available data at that moment.

The film cooling rows in the CAD geometry were over-sized to compensate for the shrinkage of the holes due to imperfections in the laser-sintering process based on the work of Batstone (2011). The TE was not altered because of the relative complexity and time required to alter the CAD TE system.

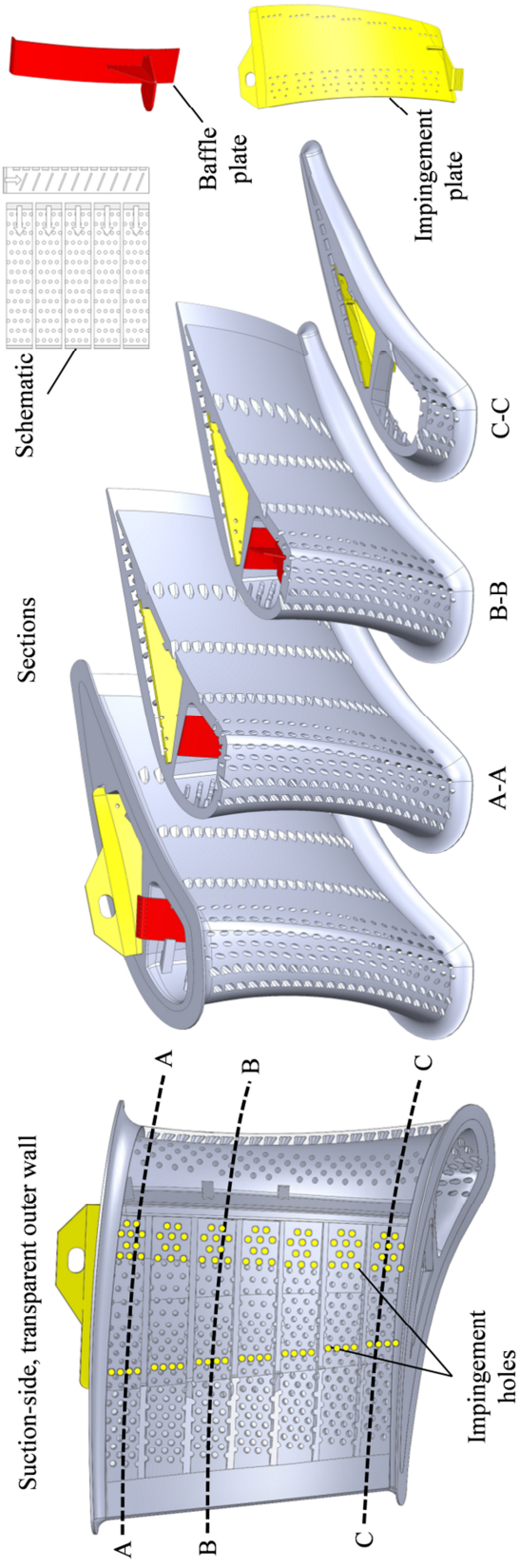


Figure 4.19. Baseline Trent 500 CAD model.

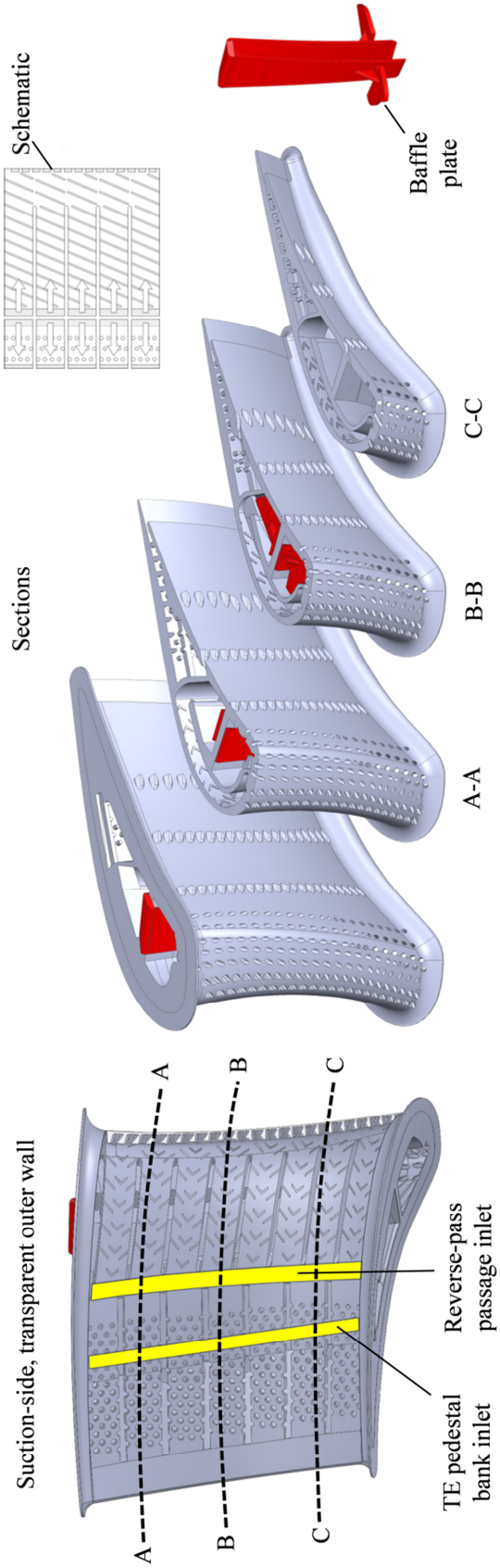


Figure 4.20. RP 1D CAD model.

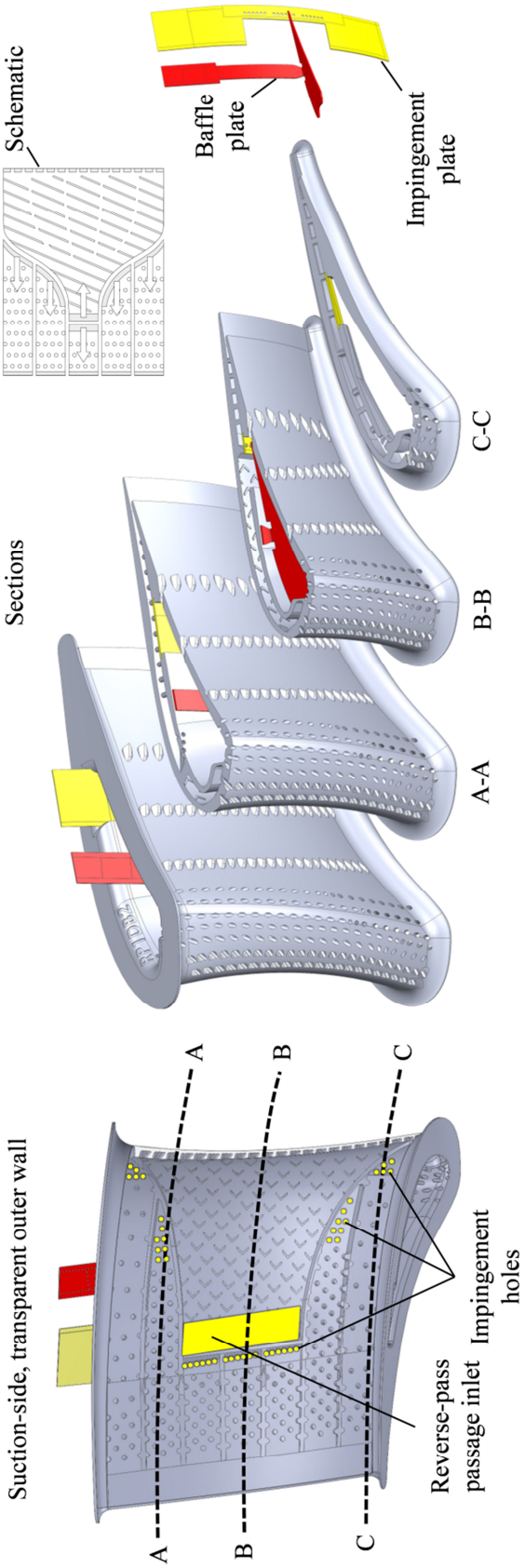


Figure 4.21. RP 1D+ CAD model.

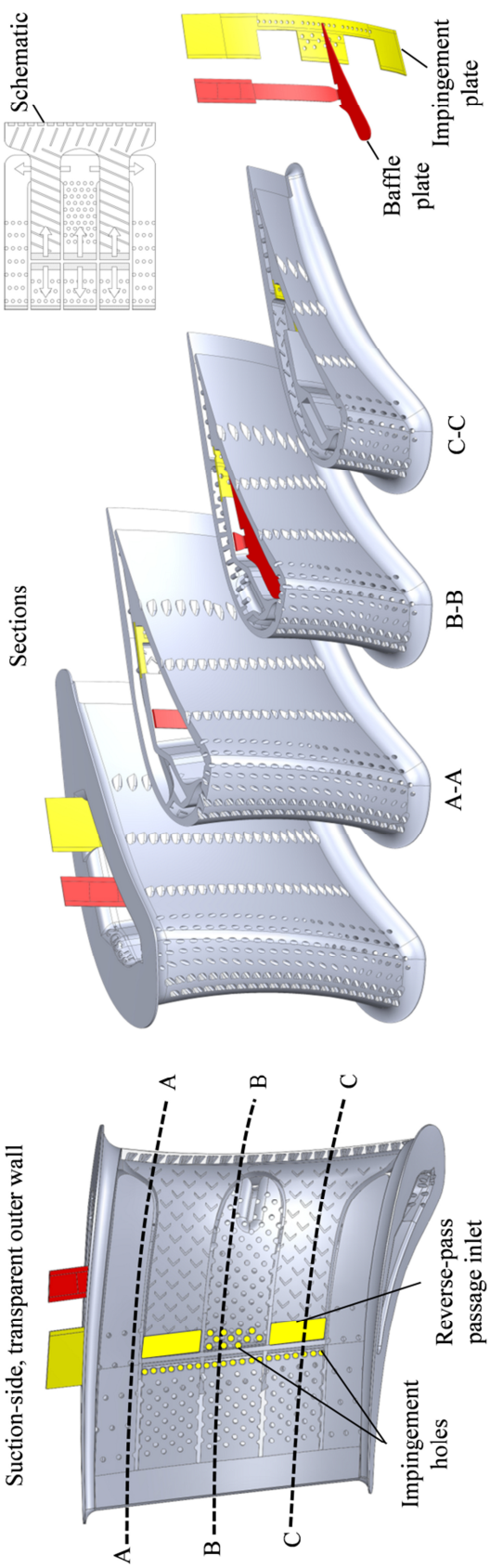


Figure 4.22. RP 3D CAD model.

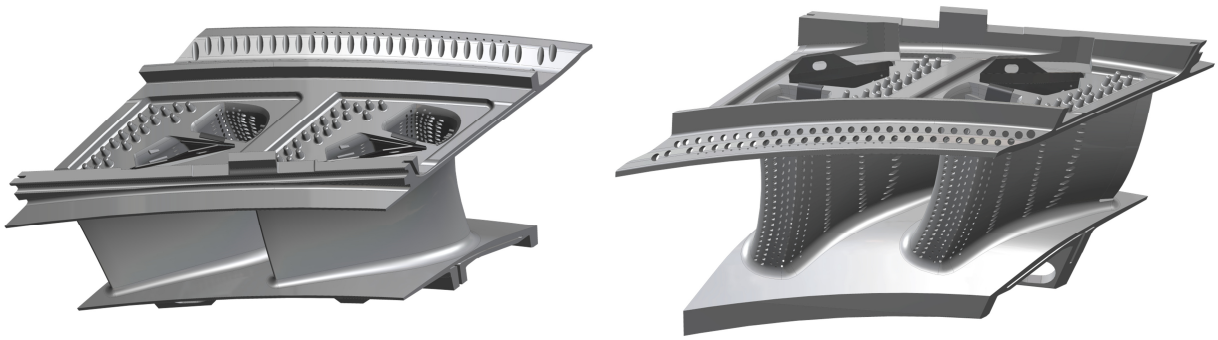


Figure 4.23. 10 row Trent 500 HPNGV baseline cast pair.

Coolant is fed into the baseline vane from hub and case into the leading-edge compartment which feeds film cooling rows S5-P3, and into the trailing-edge compartment which feeds P4, P5 and an impingement system that feeds the TE slot via a pedestal bank. The baseline vane incorporates a real engine impingement plate in the trailing-edge compartment and a real engine baffle plate in the leading-edge compartment, which are installed after manufacture. The impingement plate contains five rows of holes; from LE to TE: 14 x 0.57 mm diameter; 21 x 0.57 mm diameter; 14 x 0.75 mm diameter; 21 x 0.75 mm diameter; 28 x 0.72 mm diameter. The SS wall is between 1 and 2 mm thick, which is in the same range as all the reverse-pass designs.

Table 4.8. Final hole specifications of manufactured vanes. Based on original boundary conditions in Table 4.1. [a] Interpolated from Rawlinson (2001). [b] Hole type to mimic laser-manufactured 3-into-1 and 2-into-1 film cooling holes (S5-P2) and EDM manufactured 3-into-1 film cooling holes (P3-P5). [c] Multiple holes drilled at 30° intersection.

		S5	S4	S3	S2	S1	P1	P2	P3	P4	P5	TE slot
% of total coolant mass flow, design intent [a]		16.2	12.7	6.4	6.0	5.7	5.7	5.7	6.7	7.3	7.4	20.3
Number of holes		23	24	22	23	22	22	22	22	20	15	-
Hole Type [b]		3 in 1	3 in1	2 in1	2 in 1	2 in 1	2 in 1	2 in1	3 in1	3 in1	3 in 1	-
Surface length (%)		-15	-11	-7	-4	-2	2	7	20	41	59	95
Geometric area, original design intent (mm^2)	Baseline	13.4	13.2	9.5	9.9	9.5	9.5	9.5	9.5	9	6.8	17.9
	RP 1D	13.9	13.9	9.5	9.9	9.5	9.5	9.5	9.5	9	6.8	17.9
	RP 1D+	16.4	18.6	9.5	9.9	9.5	9.5	9.5	9.5	9	6.8	17.9
	RP 3D	16.9	19.8	9.5	9.9	9.5	9.5	9.5	9.5	9	6.8	18.4
Geometric area, CAD (mm^2)	Baseline	21.6	22.6	14.7	15.4	14.7	14.7	14.7	13.6	12.4	9.3	17.9
	RP 1D	20.4	22.8	15.4	16.1	15.4	15.4	15.4	13.4	12.2	9.5	17.9
	RP 1D+	25.3	22.1	13.9	14.5	13.9	13.9	13.9	13.9	12.6	9.5	17.9
	RP 3D	25.3	22.6	13.9	14.5	13.9	13.9	13.9	13.9	12.6	9.5	18.4
Drill ø (mm) of post-manufacture modifications	Baseline	-	-	-	-	-	-	-	-	-	-	-
	RP 1D	1	1.2	0.85	0.85	0.85	0.85	0.85	0.85	0.85	0.85	-
	RP 1D+	1.5	1.5	0.85	0.85	0.85	0.85	0.85	0.85	0.85	0.85	-
	RP 3D	1.2 x 1.5 [c]	1.5 x 1 x 1 [c]	0.85	0.85	0.85	0.85	0.85	0.85	0.85	0.85	-

RP 1D is fed from hub and case into a leading-edge compartment, trailing-edge compartment and reverse-pass compartment. The leading-edge compartment feeds rows S3-P3, the trailing-edge compartment feeds the TE pedestal bank and rows P4 and P5, and the reverse-pass compartment feeds the reverse-pass channels which deliver coolant to rows S4 and S5. RP 1D was run without an impingement plate in the trailing-edge compartment to better match the TE coolant capacity in RP 1D with the baseline TE capacity. A baffle plate is located at midspan in the leading-edge compartment and reverse-pass compartment to replicate the baffle plate in the baseline geometry. The reverse-pass channels are approximately 2.4 mm wide.

Coolant is fed into RP 1D+ from both hub and case into a single compartment, which feeds rows S3-P5 directly. The middle three TE passages are fed from the main compartment via a total of 18 x 0.72 mm diameter holes in the impingement plate. The other four TE passages are fed from the main compartment via holes created in the laser-sintering process: TE passages 1 and 7 are fed with five 0.75 mm diameter holes each and the TE passages 2 and 6 are fed with 8 x 0.70 mm diameter holes each. The reverse-pass passage is around 2 mm wide and is connected to the main compartment via a large opening in the impingement plate to minimise inlet loss. The impingement plate acts as the back wall for a portion of the off-midspan TE passages. A baffle plate is located at midspan in the main compartment.

Like RP 1D+, RP 3D is fed from hub and case into a single compartment, feeding rows S3-P5 directly. The middle three TE passages are fed from the main compartment via a total of 21 x 0.82 mm diameter holes in the impingement plate. The reverse-pass passages are approximately 2 mm wide. The midspan reverse-pass passage is fed from the main compartment via 11 x 1 mm diameter holes in the impingement plate. The off-midspan reverse-pass passages are connected to the main compartment through two large openings in the impingement plate. The impingement plate also acts as the back wall for a portion of the hub and case TE passages. A baffle plate is located at midspan in the main compartment.

4.7 Manufacture

4.7.1 Design Visualisation

Large scale plastic prototypes were manufactured for visualisation. These are shown in Figs. 4.24-4.26. Stereolithorgraphy (SLA) parts were made of both the positive space (i.e., walls, Fig. 4.24) and the negative space (i.e., coolant passages, Fig. 4.25) by CRDM (UK). The negatives were used to visualise and assess the viability of the core that would be necessary in the casting process. Fused deposition modelled (FDM) parts were made within the University, shown in Fig. 4.26.

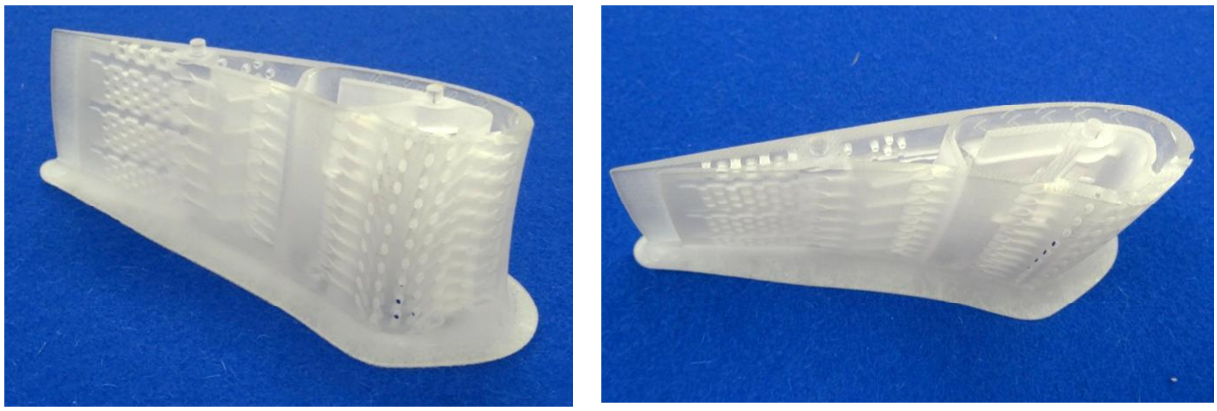


Figure 4.24. 2x scale SLA (7870) visualisation of RP 1D (Manufactured by CRDM, SL 7870 material, clear, C3 finish, natural colour).

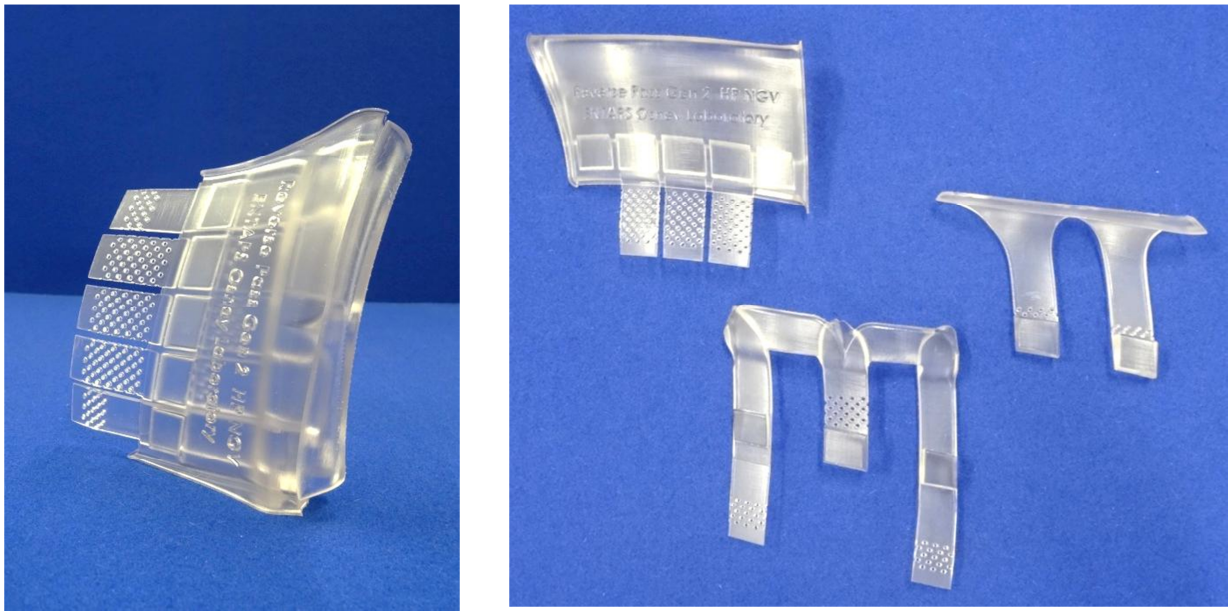


Figure 4.25. 2x scale SLA visualisation of cast cores: (L) assembled; (R) disassembled (Manufactured by CRDM, SL 7870 material, clear, no finish, natural colour).

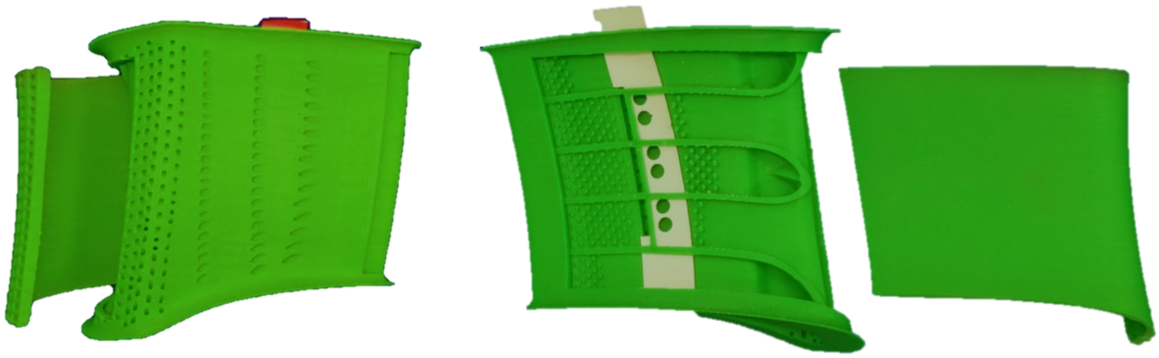


Figure 4.26. 2x scale FDM of an earlier design iteration of RP 3D: (L) pressure-side (R) suction-side (Manufactured by Bob Scott, Engineering Science, University of Oxford).

4.7.2 Material Selection

The laser-sintered parts were manufactured from a titanium alloy (Ti6Al4V) in order to match the Sector Facility metal Biot number to the engine metal Biot number (~ 0.8). The Biot number Bi is defined as

$$\mathrm{Bi} \equiv \frac{h_1 t_w}{k_w}, \tag{4.24}$$

where h_1 is the external heat transfer coefficient, t_w is the wall thickness, and k_w is the wall conductivity.

The external HTC at Sector Facility conditions is around one quarter than at engine conditions. This is primarily due to differences in the thermal conductivity of air, with an additional small effect due to differences in Reynolds number. The thermal conductivity of the titanium alloy at Sector Facility conditions is around one quarter than the thermal conductivity of cast Nickel super-alloy at engine conditions (Boyer et al., 1994, Zielińska et al., 2010). Thus, Biot number can be matched. The dimensional analysis is reported in Chapter 5.

The Biot number of the cast parts at Sector Facility conditions is ~ 0.53, around two thirds of the Biot number at engine conditions. This is due to the reduction of the material thermal conductivity with temperature. The mismatch in Biot number between cast parts and laser-sintered titanium alloy vanes at Sector Facility conditions causes the overall cooling effectiveness of the cast vane to be 0.01 greater than the laser-sintered vane (calculated to first order using Kirollos and Povey, 2015b). This difference is relatively small compared to differences in overall cooling effectiveness caused by internal surface roughness/film effects (discussed later) but should be kept in mind when comparing vanes.

A set of vanes was also laser-sintered from Nickel Alloy In718. However, these were not tested because they did not match the engine Biot number. The In718 laser-sintered parts were heavier and had a smaller deviation from the design intent than Ti6Al4V.

4.7.3 Laser-Sintered Parts and Impingement/Baffle Plates

The laser-sintered vanes were manufactured by 3TRPD Ltd. (UK). Only the aerofoils—not the platforms—were laser-sintered. Cast platforms were used in order to reduce cost and guarantee the fit of the vanes into the Sector Facility. Build orientation was aligned with the axial chord (i.e., TE at the bottom, LE at the top) in order to maximise build quality in the TE pedestal bank. The RP 1D (Ti6Al4V) design as-manufactured is shown in Figs. 4.27 and 4.28.

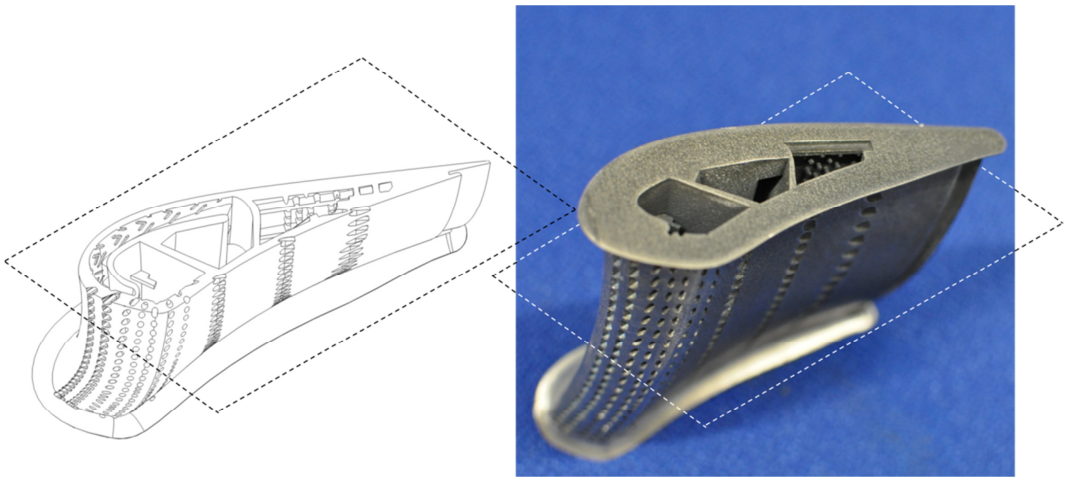


Figure 4.27. RP 1D as laser-sintered, with comparison to CAD model.

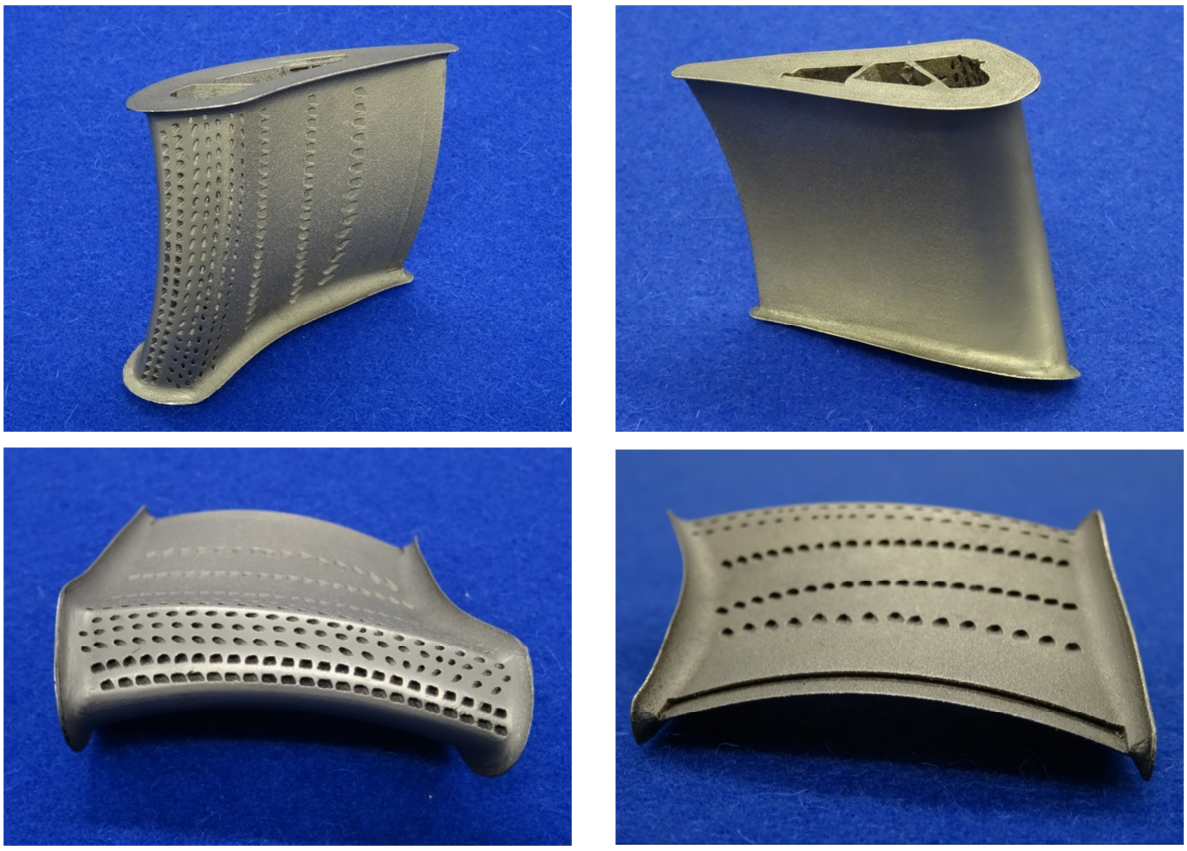


Figure 4.28. RP 1D as laser-sintered. Top-left: pressure-side. Top-right: suction-side. Bottom-left: leading-edge. Bottom-right: trailing-edge.

The laser-sintered vanes were 3D scanned at 3TRPD to measure deviation from the design intent, shown in Figs. 4.30 and 4.31. A good level of accuracy was observed (± 0.15 mm standard deviation from design intent, max. deviation ~0.5 mm). To analyse the build-quality of the internal structure, the vane was cut into with an angle grinder. However, the Ti6Al4V melted and fused upon

destruction, although this did not occur with the cast or In718 parts. A wire-cutter or EDM could be used in the future. The external surface of the Ti6Al4V parts was smoothed with a compact rotary surface grinder to obtain the same external surface roughness as the cast vane. A vane before and after smoothing is shown in Fig. 4.29.

Real engine impingement and baffle plates were used in the cast and laser-sintered baseline vanes. The plates in the reverse-pass designs were made by hand from stainless steel shim. These are shown in Fig. 4.32.

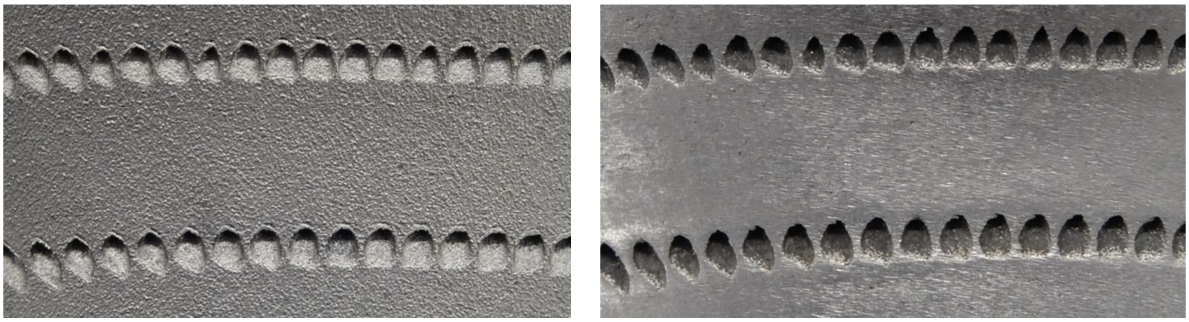


Figure 4.29. PS external surface of Ti6Al4V vanes as laser-sintered (L) and after smoothing with rotary surface grinder (R).

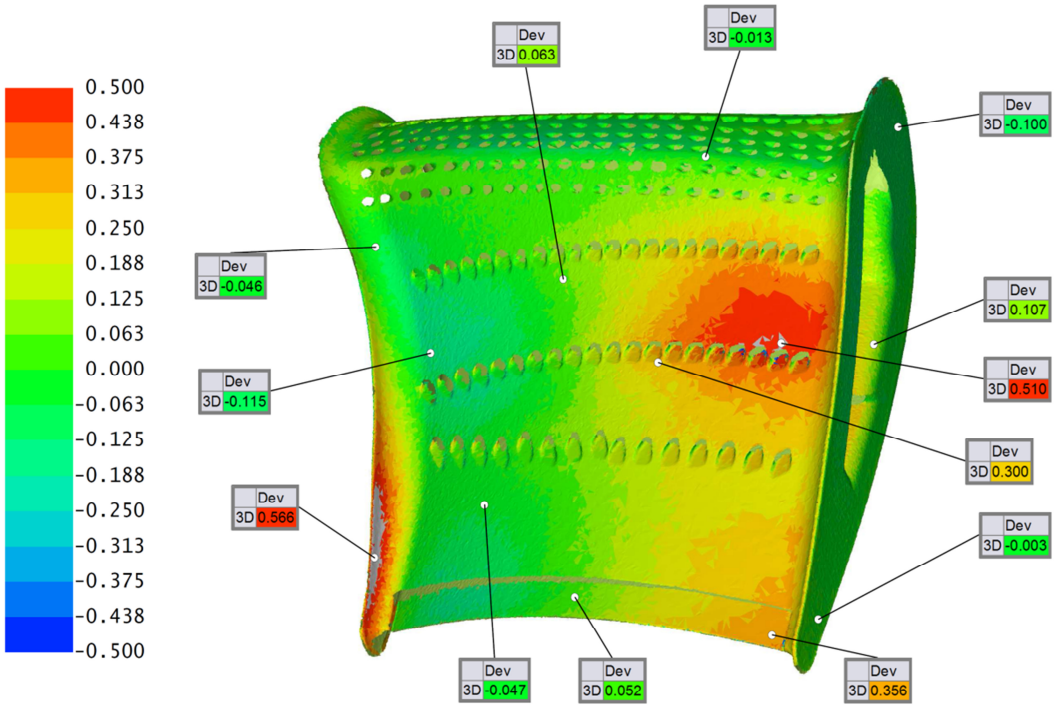


Figure 4.30. PS 3D scan, Ti6Al4V vane (deviation 'Dev' in mm).

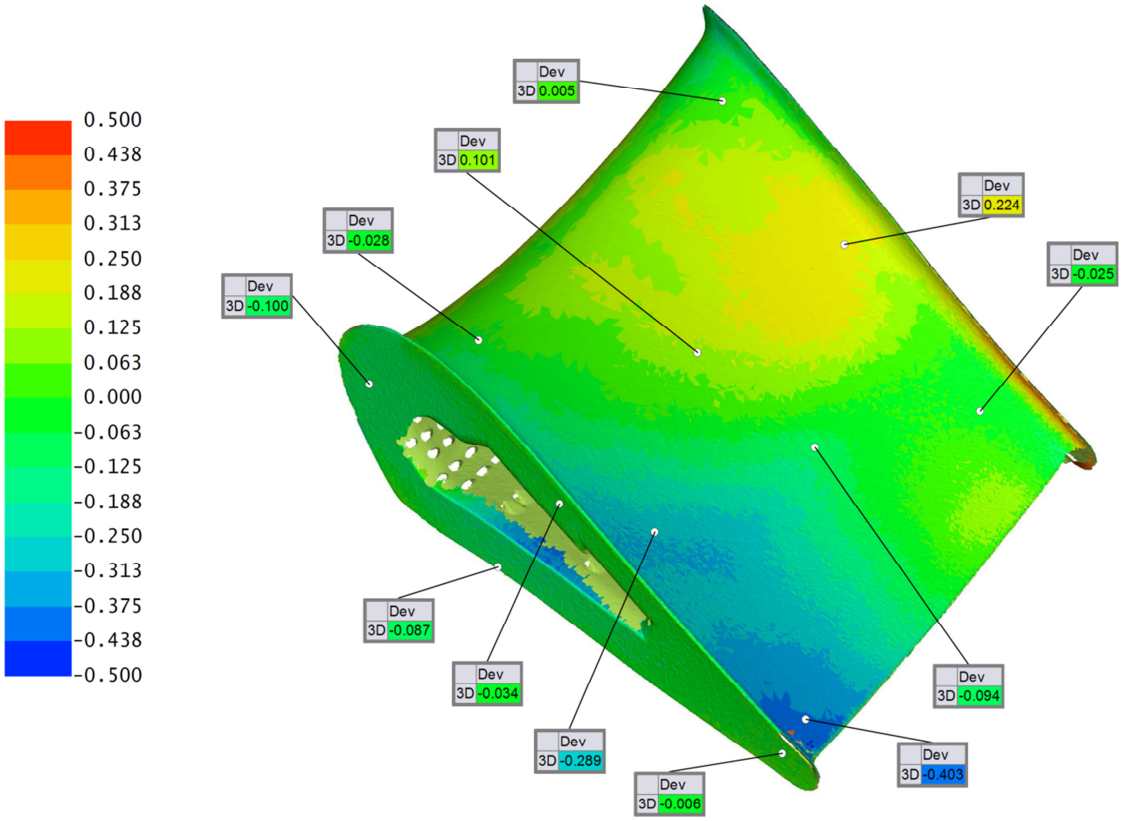


Figure 4.31. SS 3D scan, Ti6Al4V vane (deviation 'Dev' in mm).

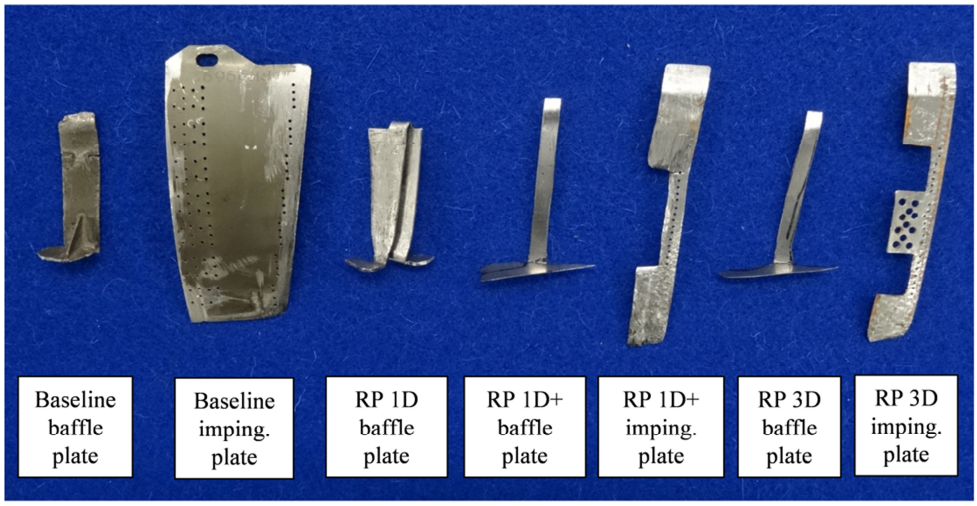


Figure 4.32. Baffle and impingement plates.

4.7.4 Platform Manufacture and Vane Pair Assembly

The platforms were manufactured by removing the vanes from an engine cast HPNGV vane pair (consisting of two vanes and hub/case platforms) and then electro-discharge machining 0.5 mm deep

footprints into the platforms using bespoke, contoured, copper tool-electrodes. The process is shown in Figs. 4.33-4.38.

The laser-sintered vanes were subsequently bonded and sealed into the footprints using a contoured assembly jig (Figs. 4.39 and 4.40) and Loctite 5940 Superflex Black Silicone Sealant. Araldite was also tested for this purpose but did not seal or bond as well as Loctite Superflex. A number of clamps were used as the sealant set to ensure that the vane pair had the correct dimensions to fit into the Sector Facility.

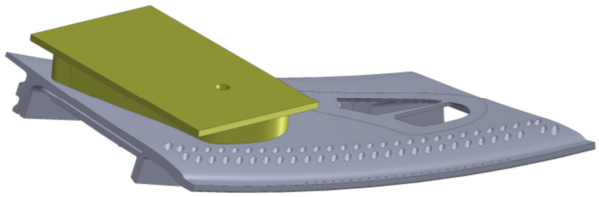


Figure 4.33. CAD model of EDM copper cutter and case platform.



Figure 4.34. Casing platform in EDM machine.



Figure 4.35. EDM copper cutters after use (Manufactured by Ashby Precision Engineering).

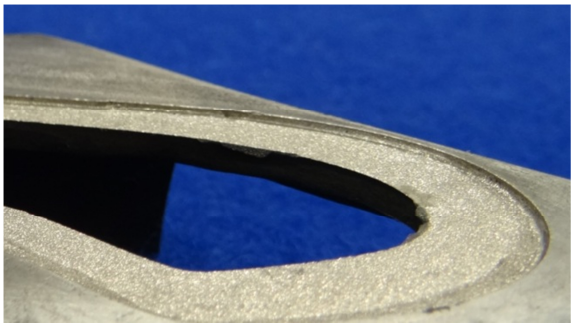


Figure 4.36. Close up of casing footprint after EDM.



Figure 4.37. Casing cast platforms after EDM.



Figure 4.38. Hub cast platforms after EDM.

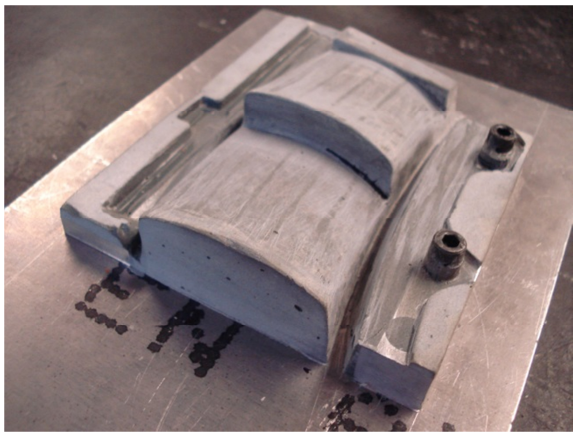


Figure 4.39. Contoured assembly jig.

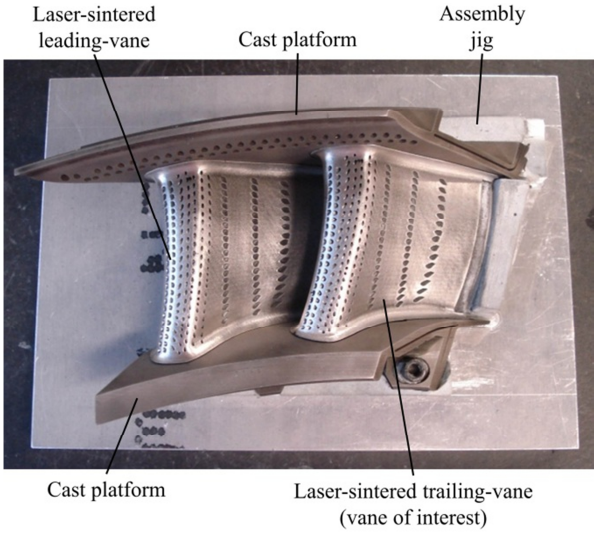


Figure 4.40. Laser-sintered vane pair, dry assembly.

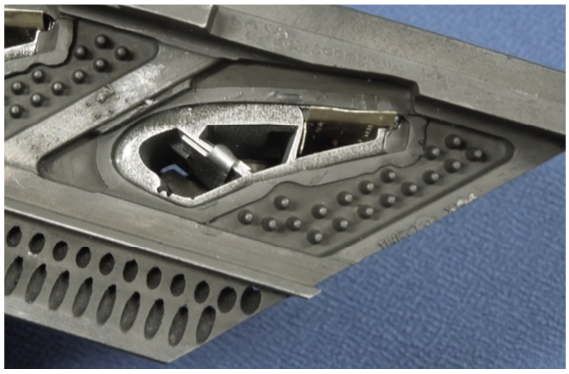


Figure 4.41. Casing view of RP 1D trailing-vane. Impingement plate removed for tests. Silicone sealant used to bond vanes to platforms, instead of Araldite shown here.



Figure 4.42. Laser-sintered vane pair assembly, glued and painted.

The final vane assembly (Figs. 4.41 and 4.42) was then sprayed with matt black paint for infra-red thermography (discussed in Chapter 6).

4.8 Proposed Improvements

Wire-cut or EDM sections. To assess internal build-quality of the laser-sintered parts.

Assess viability of entire laser-sintered cast pair. Cost and deviation estimates.

Boroscope. Utilise a boroscope to non-destructively examine the internal geometry of the laser-sintered parts.

Add compressibility to TE pedestal bank model in preliminary design. The flow within the TE pedestal is at M ~ 0.3, at the limit of the incompressibility assumption. A Fanno flow model may instead be used.

4.9 Conclusions

In this chapter, the optimum implementation of a fully 3D reverse-pass system to a high pressure nozzle guide vane has been investigated. A bespoke 3D numerical conjugate heat transfer and pressure loss model was developed to quickly predict mass flow rates and external wall temperatures of novel HPNGV cooling geometries, allowing for rapid design optimisation. Systems were optimised by adjusting the layout, dimensions and the location of pedestals and ribs. Three reverse-pass systems were subsequently designed to minimise peak vane temperature and decrease wall temperature gradients. The optimum cooling system depends on the radial mainstream temperature distribution and the coolant mass flow split between the TE and the reverse-pass-fed cooling rows.

Vanes were manufactured in their entirety, at engine-scale, using direct metal laser sintering (DMLS)—a first within the open literature. The subsequent post-manufacture modifications, such as the assembly into a vane pair with cast platforms, have been reported.

5. Annular Sector Heat Transfer Facility

In this chapter, the Annular Sector Heat Transfer Facility hardware and operating conditions are summarised, and the non-dimensional groups governing vane temperature estimated. From this analysis, the absolute accuracy of the Sector overall cooling effectiveness measurement is estimated (15%). The Sector Facility was developed by Vasco (2005) and subsequently Luque Martinez (2011). Updates to the Sector Facility since the work of Luque Martinez are recorded in detail in this chapter, including: the investigation of new heater mesh specifications; the control and measurement of coolant mass flow rate; the installation of a new pressure regulator; and the implementation of a new leak test procedure. Finally, a number of improvements are proposed in order to ease reconfiguration and operation of the Sector Facility.

5.1 Purpose of Annular Sector Heat Transfer Facility

Engine manufacturers validate cooling system designs for HPNGVs using a thermal paint engine-test. This is required for engine verification (pass-off) and occurs after the engine design process is complete. The thermal paint test is costly and complex to perform, and therefore is restricted to engine validation. A cast vane pair tested using thermal paint is shown in Fig. 5.1. The Annular Sector Heat Transfer Facility (Oxford) is used to re-create thermal paint test conditions at low-cost laboratory conditions. The relevant non-dimensional groups for heat transfer are approximately matched between the rig and the engine. Engine vane temperature is predicted to an absolute accuracy of 15% and to a precision (repeatability) of 2%. The Sector Facility is best used to compare the relative thermal performance for cooling design downselect. Luque Martinez (2011) used the Sector Facility to predict the engine temperature of a cast Trent 500 HPNGV, with and without leading-edge dendritic insert. The Sector-predicted vane temperature is compared to the thermal paint test result in Figs. 5.2. and 5.3.



Figure 5.1. Trent 500 HPNGVs after thermal paint test.

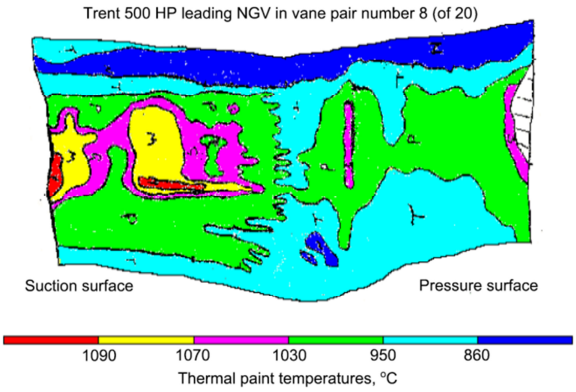


Figure 5.2. Trent 500 HPNGV thermal paint test butterfly plot—reproduced from Rawlinson and Falla (2000).

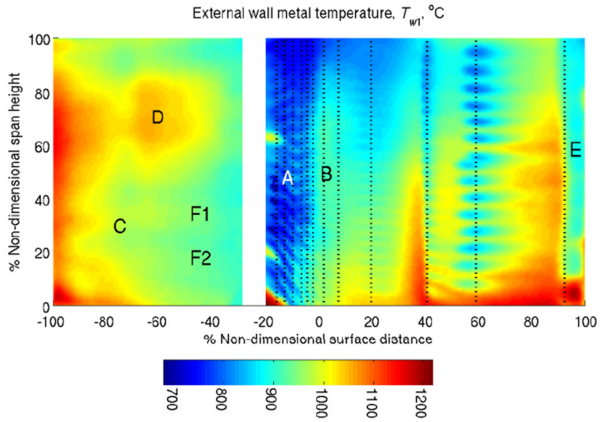


Figure 5.3. Trent 500 HPNGV temperature predictions from Sector overall cooling effectiveness measurements (Luque Martinez, 2011).

5.2 Overview of Sector Facility and Operating Conditions

The Annular Sector Heat Transfer Facility (Sector Facility) is a transonic, non-rotating blow-down type annular sector facility at the Osney Thermofluids Laboratory, Oxford. A photograph of the Facility is shown in Fig. 5.4. The test section comprises an annular sector of three pairs of 1-1 scale Trent 500 HPNGVs. Real three-dimensional HPNGV geometry is used, which automatically generates an engine-realistic radial pressure gradient; secondary flow features and coolant redistribution are thus engine-representative. A schematic of the working section is shown in Fig. 5.5.

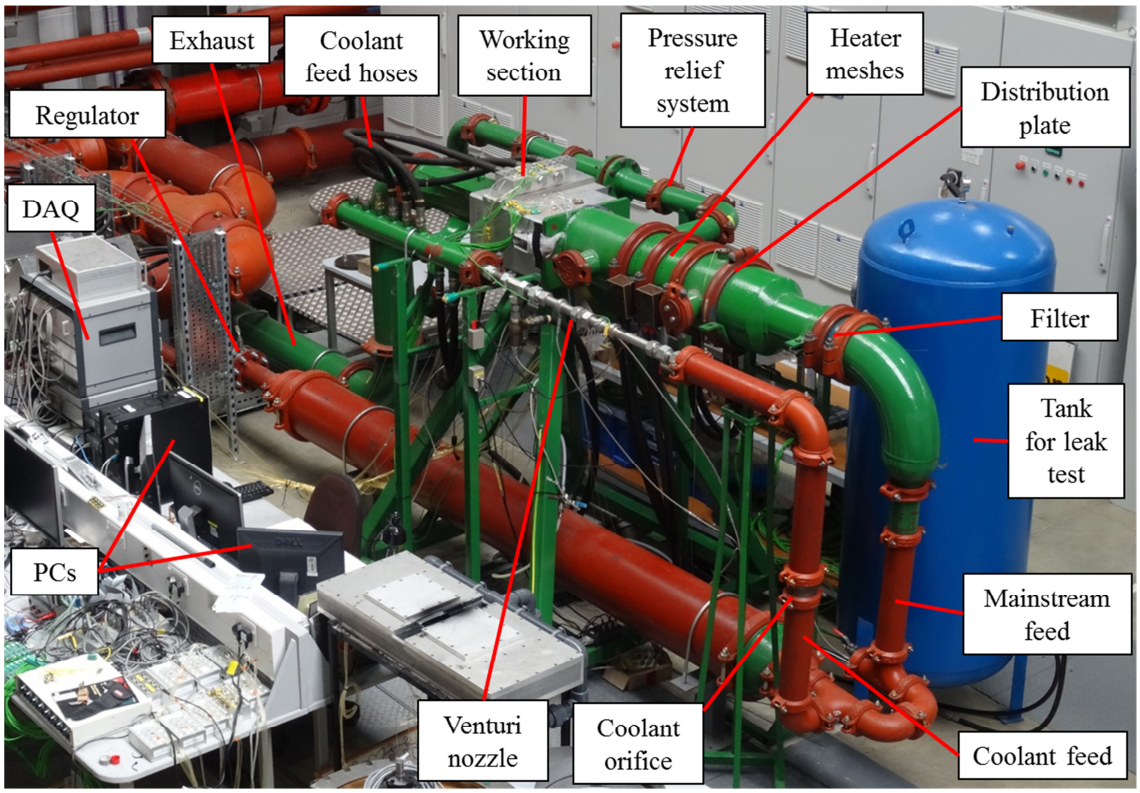


Figure 5.4. Annular Sector Heat Transfer Facility.

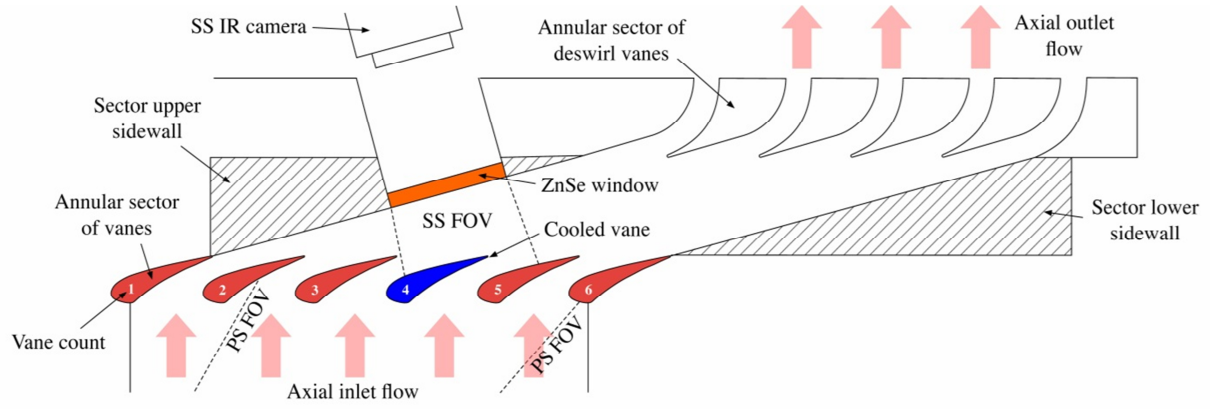


Figure 5.5. 2D unwrapped schematic of working section in the Sector (adapted from Luque et al., 2014).

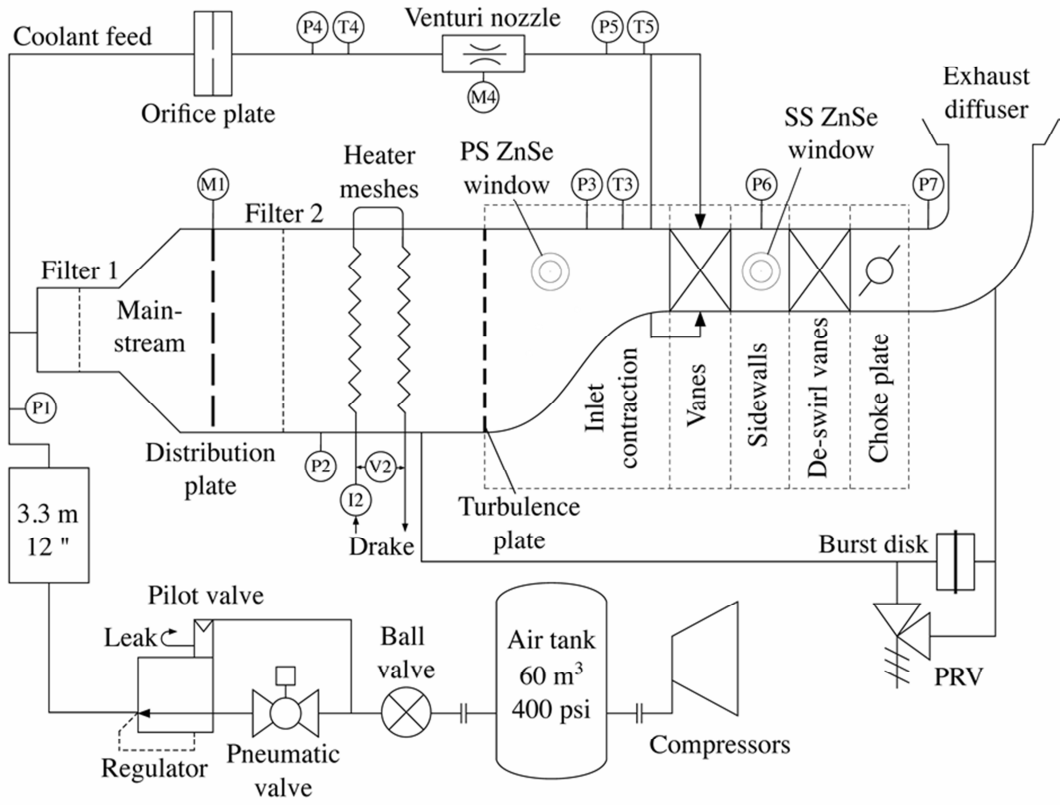


Figure 5.6. Schematic of the Annular Sector Heat Transfer Facility.

Referring to Fig. 5.5, the leading vane pair (vanes 1 and 2) and the trailing vane pair (5 and 6) are real, cast Trent 500 vane pairs with thermal barrier coating. The laser-sintered vane pair assembly (Chapter 4) is placed in positions 3 and 4, with the vane to be assessed at position 4. Only the vane of interest (4) is cooled in the Sector Facility. All other vanes and platform cooling holes are blocked.

Mainstream flow enters the working section after an engine-representative inlet contraction, shown schematically in Fig. 5.6. A turbulence plate upstream of the inlet contraction is designed to generate

an engine mainstream turbulence intensity of 11%, using the design rules of Roach (1987). The vane cassette, inlet contraction and turbulence plate are shown in Figs. 5.7, 5.8, 5.9 and 5.10.

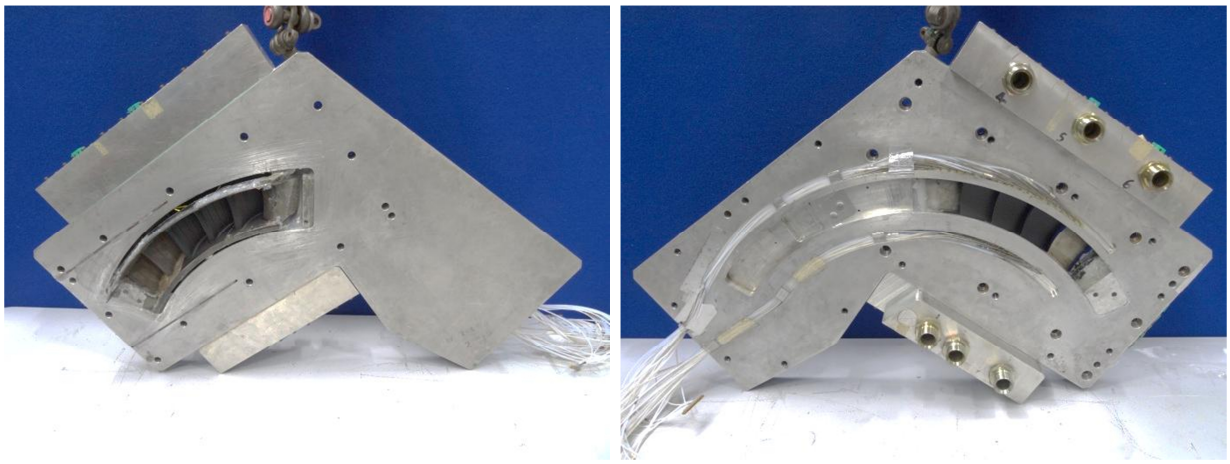


Figure 5.7. Vane cassette layer: (L) upstream face; (R) downstream face showing coolant manifold inlets.

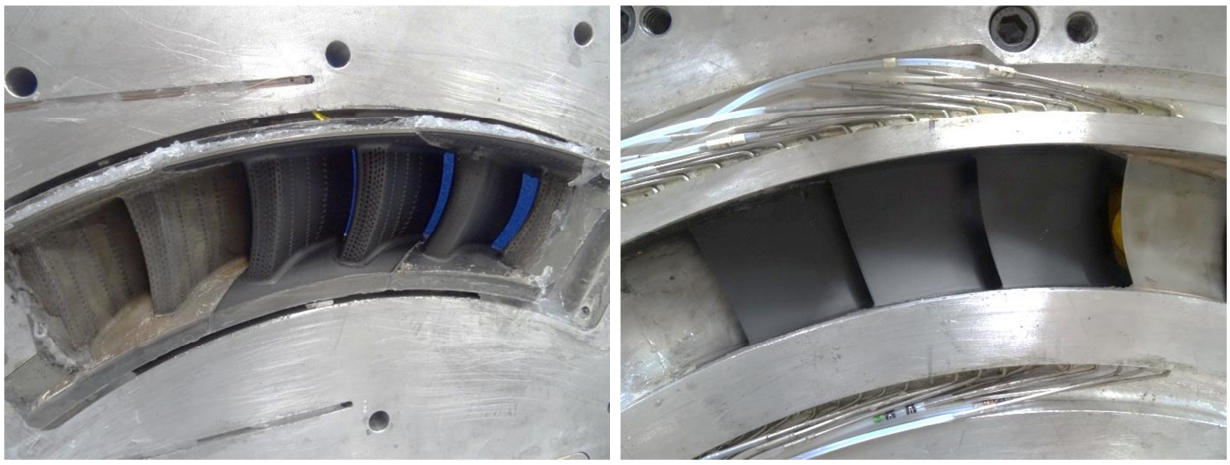


Figure 5.8. Zoomed in on vane cassette layer: (L) upstream face; (R) downstream face.



Figure 5.9. Upstream side of turbulence plate.

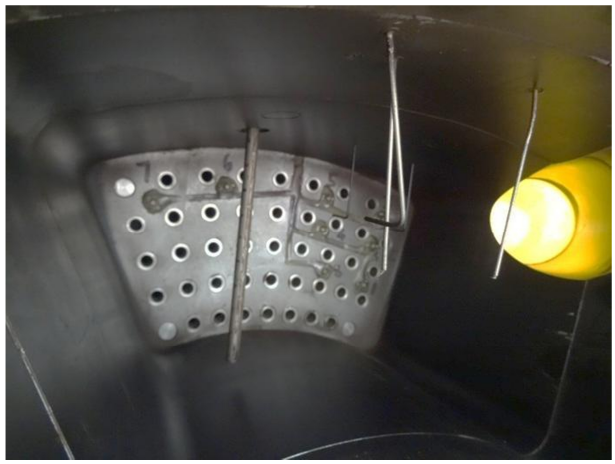


Figure 5.10. Inlet contraction, downstream side of turbulence plate, and PS ZnSe window.

Periodic boundaries are created using carefully designed sidewalls and deswirl vanes, developed for the Sector by Luque Martinez (2011). The sidewalls (Fig. 5.11) are highly three dimensional to account for high exit swirl, vane compound lean, and flow deviation from the vane metal angle. The deswirl vanes downstream of the sidewalls (Fig. 5.12) remove mainstream swirl to create an engine-representative pressure boundary condition at exit. A choke plate downstream of the deswirl vanes (Fig. 5.13) is used to control the Mach number within the Sector.

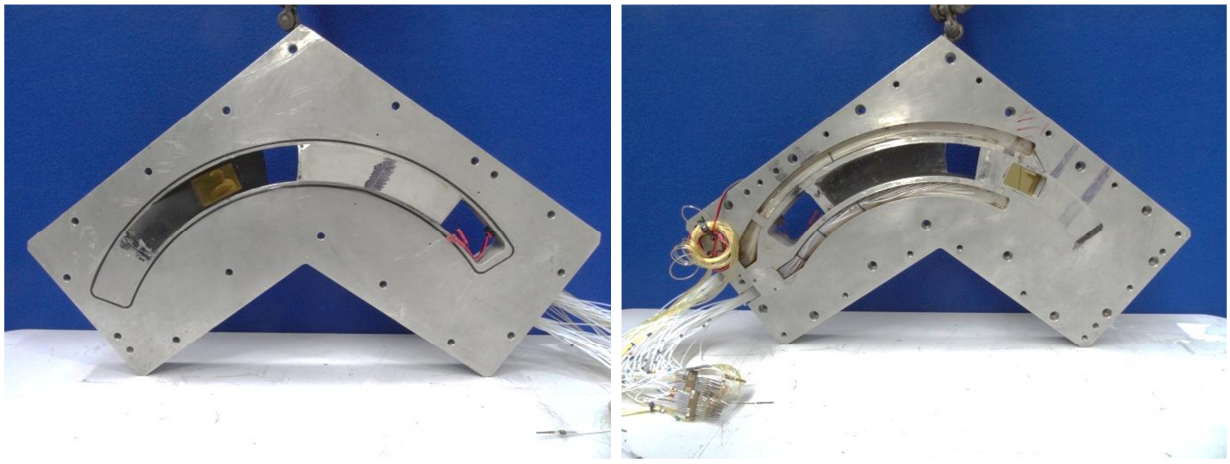


Figure 5.11. Sidewalls with SS ZnSe window: (L) upstream side; (R) downstream side.

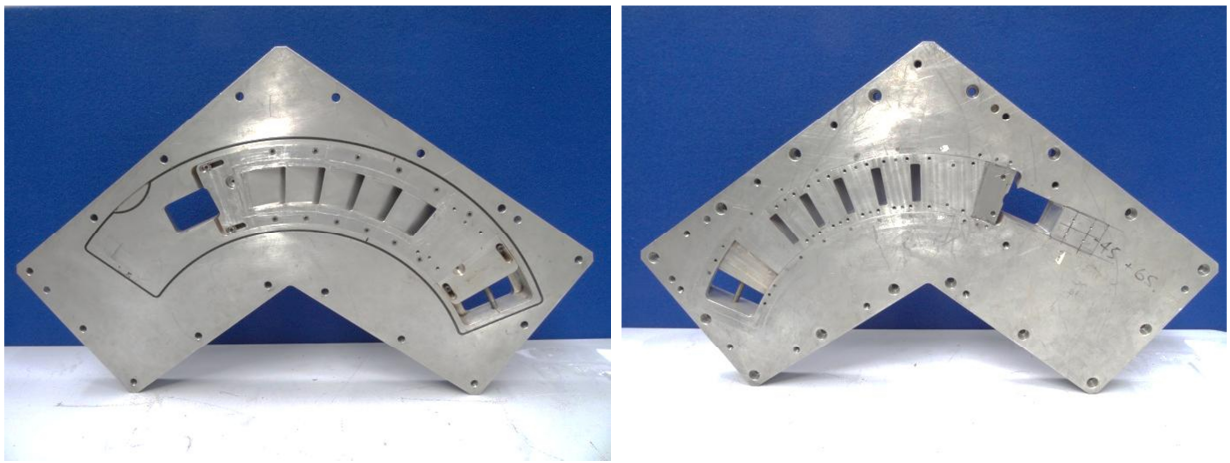


Figure 5.12. Deswirl vanes: (L) upstream side; (R) downstream side.

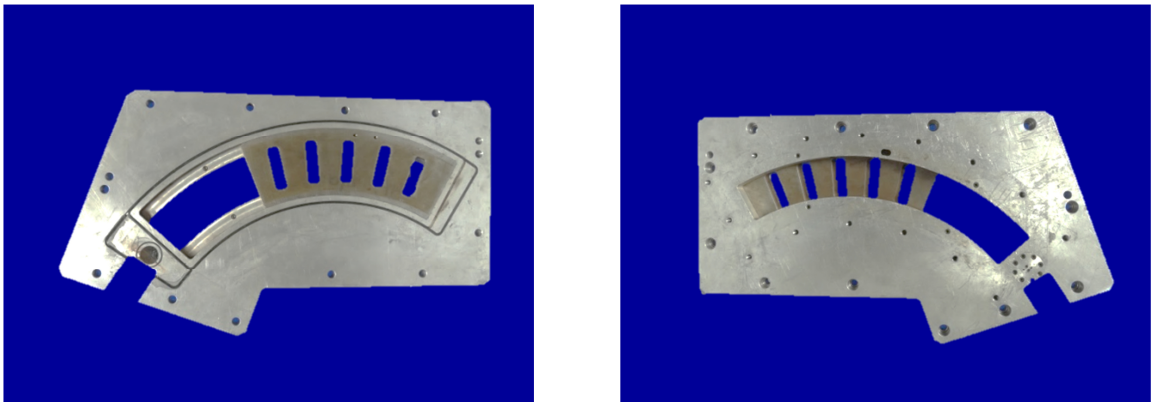


Figure 5.13. Choke plate: (L) upstream side; (R) downstream side.

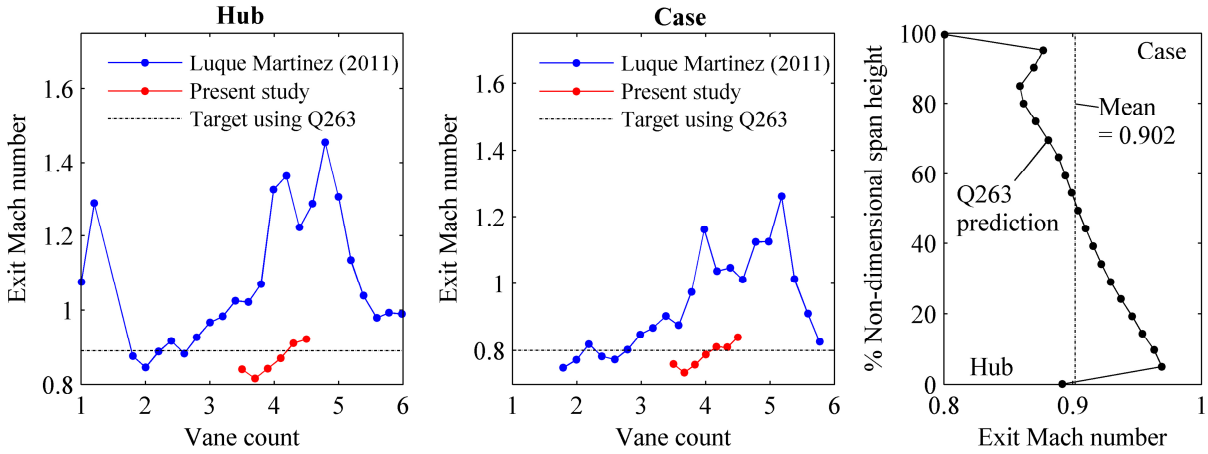


Figure 5.14. Circumferential Mach number distribution on hub and case at the vane exit; measurement vs. Q263 predictions from Luque Martinez (2011). Vane count with reference to Fig. 5.5.

The hub and case circumferential Mach number distributions at vane exit are plotted in Fig. 5.14 for both the present study and the experiments carried out by Luque Martinez. The exit Mach number in this study is smaller because only one vane is cooled, where all vanes were cooled in the experiments of Luque Martinez. The measurements are compared to the Q263 (Rolls-Royce software) prediction of exit Mach number at engine conditions. It was concluded that the radial exit Mach number distribution in the present study is matched to the engine, since hub and case Mach number measurements match the Q263 prediction. The exit Mach number for RP 1D was ~ 12% lower than the other designs, likely due to misalignment of the laser-sintered vanes in the platforms.

Pressurised air at ambient temperature is used as the coolant. The coolant is fed via a choked orifice plate and Venturi nozzle into hub and case coolant feed plena. The coolant to mainstream total pressure ratio is varied by adjusting the orifice diameter of the coolant orifice plate. Typically, a cooling design is tested across a range of 40 + pressure ratios. The details of this process are described later. Mainstream and coolant Reynolds number are of the same order as engine conditions, Table 5.1. Pressure traces during a nominal 90 second Sector run are shown in Fig. 5.15.

The mainstream is heated using two heater meshes upstream of the turbulence grid (Fig. 5.16). The specification of the heater meshes is given in Table 5.3. The heater meshes generate a step-change in mainstream temperature of up to 59 K, depending on the voltage applied across the meshes. The heater meshes are typically started 30 seconds after the beginning of the run, and are left on for 30 seconds or until the temperature of the vane of interest is steady. Flow is continued for a further 30 seconds after the heater meshes have been turned off to cool the rig down. Typical Sector temperature traces are shown in Fig. 5.17. The radial mainstream temperature distribution at the inlet contraction is approximately uniform, Fig. 5.18. Each vane design is tested at four mainstream temperatures at 10+ coolant-to-mainstream mass flow ratios, i.e., each design is tested up to 44 times. The mainstream temperature is varied to assess the validity of the overall cooling effectiveness scaling method.

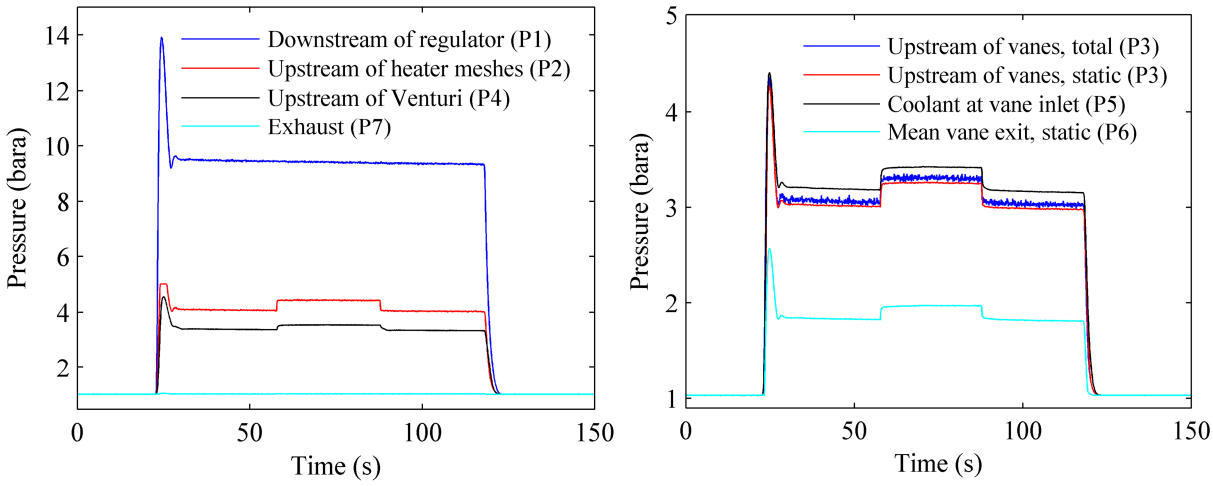


Figure 5.15. Typical pressure traces during nominal Sector operation. Model points in parentheses referenced to Fig. 5.6. Hump in middle when heater meshes are on.



Figure 5.16. Heater mesh assembly: (L) Upstream side of Filter 2; (M) Downstream side of upstream heater mesh (broken); (R) Power cables and Tufnol protection boxes.

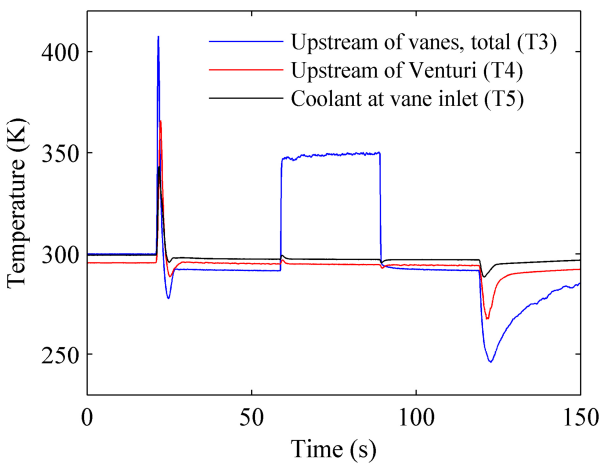


Figure 5.17. Typical temperature traces during nominal Sector operation. Model points in parentheses referenced to Fig. 5.6.

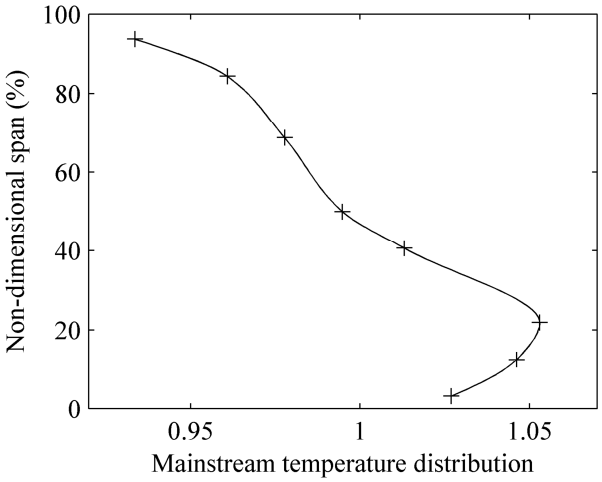


Figure 5.18. Mainstream radial temperature distribution at steady state. Normalised Mainstream temperature distribution = $(\boldsymbol{T_{0m}} - \overline{\boldsymbol{T}}_{\boldsymbol{0c}})/(\overline{\boldsymbol{T}}_{\boldsymbol{0m}} - \overline{\boldsymbol{T}}_{\boldsymbol{0c}})$.

The vane of interest is cooled by film and internal convection. Internal and external heat transfer is fully coupled via through-wall conduction. The vane of interest is manufactured from Ti6Al4V to match engine Biot number. The external wall temperature of the vane is measured using two infra-red cameras, recording both suction-side and pressure-side simultaneously. The cameras are situated outside of the rig and view the vanes through zinc-selenide (ZnSe) windows. The IR thermography methods developed for these experiments are discussed separately in Chapter 6. External wall temperature is non-dimensionalised in terms of an overall cooling effectiveness.

All thermocouples are connected to an National Instruments (NI) TC 2095 module. Pressure is measured using 5 bara or 910 mbarg Sensortechnic pressure transducers. All pressure transducer boxes and the NI TC 2095 module are connected to an NI PXI 1050 chassis (via an NI PXI-6031E Multifunction I/O card and NI SCXI-1102B card, respectively), and then to a PC using an NI PXI 8360 MXI-Express card. Data are acquired on the PC using a LabView script at 150 Hz. Total mainstream pressure upstream of the vanes is measured at model point number (205); static mainstream pressure at model point number (203); mainstream total temperature at model point number (12); and the coolant total temperature is the average of model points (15-18). A summary of nominal Sector operation temperatures, pressures, mass flow rates and other conditions is given in Table 5.1.

The exhaust duct downstream of the choke plate is shown in Fig. 5.19. Air is subsequently exhausted out of the building. A pressure relief system bypasses the working section in case of working section over-pressurisation, shown in Fig. 5.20. The system consists of a burst disk and pressure relief valve (PRV) in parallel for redundancy. Details on the burst disk are given later in the chapter.

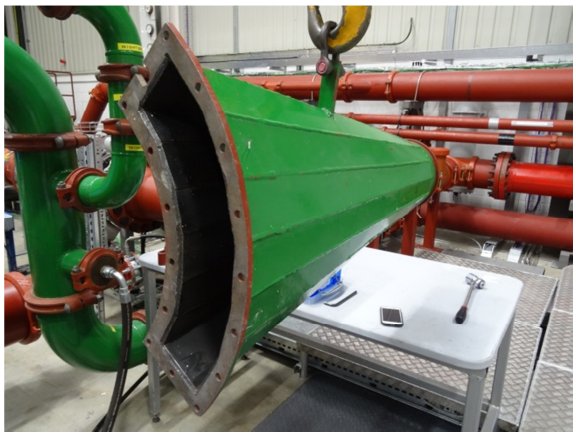


Figure 5.19. Exhaust duct.

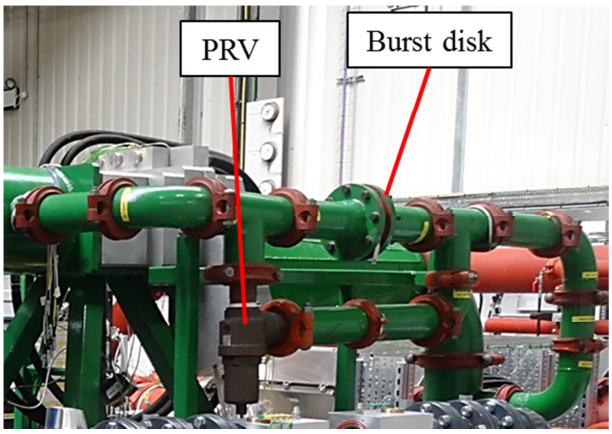


Figure 5.20. Pressure relief system.

Table 5.1. Nominal Sector operating conditions at 10% coolant-to-mainstream mass flow ratio and maximum heater mesh setting. † Further heater mesh data given in Table 5.3. Model points in parenthesis referenced to Fig. 5.6.

Location	Attributes	Evaluation method	Value
Tank	Pressure	Pressure gauge	400 – 180 psi
Regulator	Pilot valve set-point	Pressure gauge	9.4 bara
	Downstream pressure (P1)	Measured	9.4 bara
	Downstream Temperature	Estimated	297 K
Distribution plate	Flow area	Luque Martinez (2011)	1265 mm^2 (11x12.1 mmø)
	Discharge coefficient	Ward-Smith (1979)	0.83
	Choked capacity	Equation (5.32)	$4.24x10^{-5}$ $kgs^{-1}Pa^{-1}K^{0.5}$
	Mach number	From (P1) and (P2)	1
	Mass flow rate (M1)	Equation (5.32)	2.31 kgs^{-1}
Coolant orifice plate	Diameter	Nominal specification	5.4 mm
	Discharge coefficient	Estimated using (M4)	0.82
	Mach number	From (P1) and (P4)	1
Venturi nozzle	Upstream pressure (P4)	Measured	3.54 bara
	Upstream temperature (T4)	Measured	294 K
	Diameter	Calibration certificate	8.28 mm
	Discharge coefficient	Calibration certificate	1.00
	Choked capacity	Equation (5.34)	$2.18x10^{-7}$ $kgs^{-1}Pa^{-1}K^{0.5}$
	Mass flow rate (M4)	Equation (5.34)	45 gs^{-1}
	Mach number	From (P4) and (P5) and (5.34)	1
Heater meshes†	Voltage across pair (V2)	Readout Blowdown panel	91 V
	Current (I2)	Readout Drake panel	1520 A
	Upstream pressure (P2)	Measured	4.4 bara
Turbulence plate	Flow area	Luque Martinez (2011)	6958 mm^2 (41x14.7 mmø)
	Discharge coefficient	Ward-Smith (1979)	0.83
	Mach number	Compressible flow equation	0.34
	Upstream pressure	Compressible flow equation	3.52 bara
	Turbulence intensity	Luque Martinez (2011)	11%
	Length scale	Luque Martinez (2011)	15 mm
Inlet contraction	Total pressure (P3)	Measured	3.30 bara
	Static pressure (P3)	Measured	3.25 bara
	Total temperature (T3)	Measured	350 K
	Mach number	Compressible flow equation	0.15
Vanes	Coolant pressure (P5)	Measured	3.42 bara
	Coolant temperature (T5)	Measured	297 K
	Mean exit Mach number around vane of interest	Compressible flow equation and (P6), (P3)	0.90
Choke plate	Blockage	Physically set	0%
Exhaust	Pressure	Measured	1.03 bara

5.3 Non-Dimensional Groups

The Sector Facility is designed to operate at engine-representative conditions so that the vane temperature measured in the rig is scalable to engine conditions. In this section, the relevant non-dimensional groups are evaluated at rig and engine conditions, and their effect on overall cooling effectiveness—i.e., normalised wall temperature—is estimated using the approximations in Holland and Thake (1980) and Kirollos and Povey (2015b). The difference between the rig and engine overall cooling effectiveness is thus determined to be less than 15%.

The external vane temperature is non-dimensionalised in terms of an overall cooling effectiveness θ[1]:

$$\theta \equiv \frac{T_r - T_{w1}}{T_{0m} - T_{0c}}. \tag{5.1}$$

T_{w1} is the external wall temperature, T_{0m} is the mainstream temperature, T_{0c} is the coolant total temperature at entry to the vane, and T_r is the mainstream recovery temperature:

$$T_r/T_{0m} = f(\mathrm{M}_m, \mathrm{Pr}_m, \boldsymbol{x}, \text{geometry}). \tag{5.2}$$

The overall cooling effectiveness is a function of the following non-dimensional groups (adapted from Kirollos and Povey (2015b) to take into account mainstream recovery effects):

$$\theta = f(m^*, h^*, \eta, \mathrm{Bi}, \mathrm{M}_m, \mathrm{Pr}_m, \boldsymbol{x}, \text{geometry}), \tag{5.3}$$

where m^* is the non-dimensional coolant mass flow rate, h^* is the ratio of the external to internal heat transfer coefficient, η is the adiabatic film cooling effectiveness, Bi is the Biot number, M_m is the mainstream Mach number, Pr_m is the mainstream Prandtl number and $\boldsymbol{x}$ is normalised position on the vane. $\mathrm{M}_m, \mathrm{Pr}_m, \boldsymbol{x}$, geometry are matched between engine and rig conditions. The other dimensionless groups in equation (5.3) are now estimated.

5.3.1 Non-Dimensional Coolant Mass Flow Rate

The non-dimensional coolant mass flow rate m^* is the ratio of internal advection to external convection, defined as:

$$m^* \equiv \frac{\dot{m}_c c_{p,c}}{h_1 A_{m^*}}, \tag{5.4}$$

where $\dot{m}_c$ is coolant mass flow rate, $c_{p,c}$ is the specific heat capacity of the coolant, h_1 is the external heat transfer coefficient, and A_{m^*} is the surface area of the vane. Physically, the non-dimensional

[1] There is some debate over the best definition of overall cooling effectiveness. Luque Martinez (2011) proposed an alternative definition ϕ in which the recovery factor also appears in front of the mainstream temperature in the denominator.

mass flow rate is the ratio of the coolant temperature rise to the external driving temperature difference for heat transfer. m^* is also equivalent to:

$$m^* = \frac{\mathrm{Re}_c \mathrm{Pr}_c}{\mathrm{Nu}_m}\left(\frac{k_c}{k_m}\right)\left(\frac{x_{\mathrm{Nu}_m} s}{A_{m^*}}\right), \tag{5.5}$$

where Re_c is the coolant Reynolds number, Pr_c is the coolant Prandtl number, s is the span of the vane, x_{Nu_m} is the axial position along the surface of the vane, k_c is the thermal conductivity of the coolant, k_m is the thermal conductivity evaluated at the external wall temperature, and Nu_m is the Nusselt number of the mainstream:

$$\mathrm{Nu}_m \equiv \frac{h_1 x_{\mathrm{Nu}_m}}{k_m}. \tag{5.6}$$

Nusselt number depends on Reynolds number and Prandtl number (Sieder and Tate, 1936) and is also influenced by surface roughness Ra (Guo et al, 2000). Defining the normalised surface roughness $\widetilde{\mathrm{Ra}}_1$, and assuming Nusselt number of the form

$$\mathrm{Nu}_m \sim {\mathrm{Re}_m}^{n_1} {\mathrm{Pr}_m}^{n_2} {\widetilde{\mathrm{Ra}}_1}^{n_3} \left(\frac{\mu_m}{\mu_{m,w}}\right)^{n_4}, \tag{5.7}$$

the ratio of the rig to engine non-dimensional coolant mass flow rate is:

$$\frac{{m^*}_{\mathrm{rig}}}{{m^*}_{\mathrm{eng.}}} \sim \frac{\left(\frac{\mathrm{Re}_c \mathrm{Pr}_c}{{\mathrm{Re}_m}^{n_1} {\mathrm{Pr}_m}^{n_2} {\widetilde{\mathrm{Ra}}_1}^{n_3}}\left(\frac{k_c}{k_m}\right)\left(\frac{\mu_{m,w}}{\mu_m}\right)^{n_4}\right)_{\mathrm{rig}}}{\left(\frac{\mathrm{Re}_c \mathrm{Pr}_c}{{\mathrm{Re}_m}^{n_1} {\mathrm{Pr}_m}^{n_2} {\widetilde{\mathrm{Ra}}_1}^{n_3}}\left(\frac{k_c}{k_m}\right)\left(\frac{\mu_{m,w}}{\mu_m}\right)^{n_4}\right)_{\mathrm{eng.}}}. \tag{5.8}$$

μ_m is the dynamic viscosity evaluated at the mainstream temperature and $\mu_{m,w}$ is the dynamic viscosity evaluated at the external wall temperature. At rig conditions, $\mu_{m,w} \sim \mu_m$. Since the Prandtl number of air is approximately equal at both engine and rig conditions (for both coolant and mainstream) and the exponent n_2 is small, the effect of Prandtl number is neglected. The external surface roughness is assumed equal at engine and rig conditions because the laser-sintered vane is smoothed (Chapter 4). Since the rig coolant capacity is approximately equal to the engine coolant capacity (Chapter 9), and likewise for the mainstream capacity, equation (5.8) is simplified to:

$$\frac{{m^*}_{\mathrm{rig}}}{{m^*}_{\mathrm{eng.}}} \sim \sqrt{\frac{T_{0c,\mathrm{eng.}}}{T_{0c,\mathrm{rig}}}} \frac{p_{0c,\mathrm{rig}}}{p_{0c,\mathrm{eng.}}} \frac{\mu_{c,\mathrm{eng.}}}{\mu_{c,\mathrm{rig}}} \left(\sqrt{\frac{T_{0m,\mathrm{rig}}}{T_{0m,\mathrm{eng.}}}} \frac{p_{0m,\mathrm{eng.}}}{p_{0m,\mathrm{rig}}} \frac{\mu_{m,\mathrm{rig}}}{\mu_{m,\mathrm{eng.}}}\right)^{n_1} \left(\frac{\mu_{m,\mathrm{eng}}}{\mu_{m,w,\mathrm{eng.}}}\right)^{n_4} \frac{k_{c,\mathrm{rig}}}{k_{c,\mathrm{eng.}}} \frac{k_{m,\mathrm{eng.}}}{k_{m,\mathrm{rig}}}. \tag{5.9}$$

Assuming exponents $n_1 = 0.8$ and $n_4 = 0.14$ (Sieder and Tate, 1936) and the values in Table 5.2, the ratio of rig to engine non-dimensional coolant mass flow rate is 0.52. Assuming an engine value of

Table 5.2. Relevant non-dimensional groups.

†h^*, ε and θ given as a range at engine conditions due to uncertainty in the internal heat transfer coefficient of laser-sintered parts. Data amalgamated from Sector experimental measurements, Rawlinson (2001), Luque Martinez (2011), Telisinghe (2006), Zielińska et al. (2010), Boyer et al. (1994), and estimations from equations (5.4)-(5.30).

	Symbol	Sector Facility	Engine	Sector / Engine
Geometry		- Matched -		1
Location on vane	x	- Matched -		1
Mainstream total pressure (bara)	p_{0m}	3.30	41.47	
Coolant total pressure (bara)	p_{0c}	3.42	42.69	
Total pressure ratio	p_{0c}/p_{0m}	1.0295	1.0295	1
Mainstream total temperature (K)	T_{0m}	350	2200	
Coolant total temperature (K)	T_{0c}	300	950	
Total temperature ratio	T_{0c}/T_{0m}	0.86	0.43	2
Mainstream mass flow rate/passage (kgs^{-1})	$\dot{m}_m$	0.46	2.28	
Coolant mass flow rate / vane (kgs^{-1})	$\dot{m}_c$	0.040	0.26	
Mainstream capacity/passage (kgs^{-1}Pa^{-1}K$^{0.5}$)	Γ_m	~ 2.6x10^{-5}	~ 2.6x10^{-5}	~ 1
Coolant capacity / passage (kgs^{-1}Pa^{-1}K$^{0.5}$)	Γ_c	~ 2.0x10^{-6}	~ 1.9x10^{-6}	~ 1
Turbulence intensity (%)	Tu	11	11	1
Exit Mach number	M_m	0.90	0.90	1
Coolant Reynolds number at inlet to vane, based on nominal hole diameter (0.75 mm)	Re_c	~ 3000	~ 9000	~ 0.33
	$\dot{m}$ (kgs^{-1})	0.040	0.26	
	A (mm^2)	500	500	
	d (mm)	0.75	0.75	
	μ (Nsm^{-2})	1.85x10^{-5} (300K)	4.03x10^{-5} (950K)	
Mainstream Reynolds number at passage exit, based on axial chord (29.7 mm)	Re_m	1.0x10^5	1.4x10^5	~ 0.7
	$\dot{m}$ (kgs^{-1})	0.50	2.54	
	A (mm^2)	702	702	
	d (mm)	29.7	29.7	
	μ (Nsm^{-2})	2.08x10^{-5} (350K)	7.2x10^{-5} (2200K)	
Coolant Prandtl number	Pr_c	0.71 (300K)	0.70 (950K)	1.01
Mainstream Prandtl number	Pr_m	0.70 (350K)	0.68 (2200K)	1.03
Coolant dynamic viscosity (Nsm^{-2})	μ_c	1.85x10^{-5} (300K)	4.03x10^{-5} (950K)	
Mainstream dynamic viscosity (Nsm^{-2})	μ_m	2.08x10^{-5} (350K)	7.02x10^{-5} (2200K)	
Mainstream dynamic viscosity at wall (Nsm^{-2})	$\mu_{m,w}$	1.96x10^{-5} (325K)	5.11x10^{-5} (1300K)	
Coolant thermal conductivity (Wm^{-1}K^{-1})	k_c	0.026 (300K)	0.065 (950K)	
Mainstream thermal conductivity at wall (Wm^{-1}K^{-1})	k_m	0.028 (325K)	0.083 (1300K)	
Wall thermal conductivity (Wm^{-1}K^{-1})	k_w	6.6 (Ti6Al4V, 300K)	28 (Ni superalloy, 1300 K)	
Coolant specific heat capacity (Jkg^{-1}K^{-1})	$c_{p,c}$	1004.9 (300K)	1131.3 (950K)	
Mainstream specific heat capacity (Jkg^{-1}K^{-1})	$c_{p,m}$	1008.2 (350K)	1250 (2200K)	
Non-dimensional coolant mass flow rate	m^*	~ 0.94	~ 1.8	~ 0.52
External-internal HTC ratio†	h^*	~ 0.3-1.5	~ 1	~0.3-1.5
Momentum flux ratio	MR			~ 1
Blowing ratio	BR			~ 0.74
Mean adiabatic film cooling effectiveness	η	~ 0.43	~ 0.5	~ 0.86
Biot number	Bi	~ 0.8	~ 0.8	~ 1
Cooling efficiency†	ε	~ 0.56–0.37	0.26	~2.2-1.4
Overall cooling effectiveness†	θ	~ 0.55-0.52	0.63	~0.83-0.87

$m^*_{\text{eng.}}$ ~ 1.8 (Kirollos and Povey, 2015b), the rig non-dimensional coolant mass flow rate is m^*_{rig} ~ 0.94. The impact of this difference is estimated later.

5.3.2 Ratio of External to Internal Heat Transfer Coefficient

The ratio of the external to internal heat transfer coefficients h^* is defined as:

$$h^* \equiv \frac{h_1}{h_2}. \tag{5.10}$$

where h_1 is the external heat transfer coefficient and h_2 is the internal heat transfer coefficient. This is equivalent to

$$h^* = \frac{\text{Nu}_m}{\text{Nu}_c}\frac{k_m}{k_c}\frac{x_{\text{Nu}_c}}{x_{\text{Nu}_m}}. \tag{5.11}$$

Using assumption (5.7), the ratio of h^* between rig and engine conditions is approximated by:

$$\frac{h^*_{\text{rig}}}{h^*_{\text{eng.}}} \sim \frac{\left(\left(\frac{\text{Re}_m}{\text{Re}_c}\right)^{n_1}\left(\frac{\text{Pr}_m}{\text{Pr}_c}\right)^{n_2}\left(\frac{\widetilde{\text{Ra}}_1}{\widetilde{\text{Ra}}_2}\right)^{n_3}\left(\frac{\mu_m}{\mu_c}\frac{\mu_{c,w}}{\mu_{m,w}}\right)^{n_4}\frac{k_m}{k_c}\right)_{\text{rig}}}{\left(\left(\frac{\text{Re}_m}{\text{Re}_c}\right)^{n_1}\left(\frac{\text{Pr}_m}{\text{Pr}_c}\right)^{n_2}\left(\frac{\widetilde{\text{Ra}}_1}{\widetilde{\text{Ra}}_2}\right)^{n_3}\left(\frac{\mu_m}{\mu_c}\frac{\mu_{c,w}}{\mu_{m,w}}\right)^{n_4}\frac{k_m}{k_c}\right)_{\text{eng.}}}. \tag{5.12}$$

The Prandtl number of air is approximately equal at both engine and rig conditions (for both coolant and mainstream) and the exponent n_2 is small, and therefore the effect of Prandtl number is neglected. At rig and engine conditions, $\mu_c \sim \mu_{c,w}$. At rig conditions, $\mu_m \sim \mu_{m,w}$. The external surface roughness is assumed equal at engine and rig conditions.

In Chapter 8, it will be shown that the coolant capacity Γ_c, defined as

$$\Gamma_c \equiv \frac{\dot{m}_c\sqrt{T_{0c}}}{p_{0c}}, \tag{5.13}$$

is approximately matched between between rig and engine conditions. The coolant capacity Γ_c is defined with respect to the coolant total pressure p_{0c} and coolant total temperature T_{0c} at the vane coolant inlet, and the coolant mass flow rate $\dot{m}_c$. Similarly, the mainstream capacity Γ_m, defined as

$$\Gamma_m \equiv \frac{\dot{m}_m\sqrt{T_{0m}}}{p_{0m}}, \tag{5.14}$$

is approximately matched between between rig and engine conditions. The mainstream capacity Γ_m is defined with respect to the mainstream total pressure p_{0m} and mainstream total temperature T_{0m} at the mainstream inlet contraction, and the total mainstream mass flow rate per passage $\dot{m}_m$.

Since mainstream and coolant capacity are approximately matched, equation (5.12) is simplified to:

$$\frac{h^*_{\text{rig}}}{h^*_{\text{eng.}}} \sim \left(\frac{\mu_{m,\text{eng.}}}{\mu_{c,\text{eng.}}} \frac{\mu_{c,\text{rig}}}{\mu_{m,\text{rig}}} \sqrt{\frac{T_{0m,\text{eng.}}}{T_{0c,\text{eng.}}} \frac{T_{0c,\text{rig}}}{T_{0m,\text{rig}}}} \right)^{n_1} \left(\frac{\widetilde{\text{Ra}}_{2,\text{eng.}}}{\widetilde{\text{Ra}}_{2,\text{rig}}} \right)^{n_3} \left(\frac{\mu_{m,w,\text{eng}}}{\mu_{m,\text{eng.}}} \right)^{n_4} \frac{k_{m,\text{rig}}}{k_{m,\text{eng.}}} \frac{k_{c,\text{eng.}}}{k_{c,\text{rig}}}. \quad (5.15)$$

The internal surface roughness of the laser-sintered vanes is much greater than the engine cast parts (concluded from visual examination—roughness measurements were not taken). Guo et al. (2000) showed that rough thermochromic liquid crystals (Ra ~ 25 μm) doubled the external heat transfer coefficient of a HPNGV compared to the equivalent un-coated, hydraulically smooth vane. Since very little additional literature exists on the effect of surface roughness on HTC, a range of $\left(\widetilde{\text{Ra}}_{2,\text{eng.}}/\widetilde{\text{Ra}}_{2,\text{rig}}\right)^{n_3}$ factors were tested: $0.2 < \left(\widetilde{\text{Ra}}_{2,\text{eng.}}/\widetilde{\text{Ra}}_{2,\text{rig}}\right)^{n_3} < 1$, with the limits corresponding to a 5-fold and 1-fold increase in internal HTC due to increased surface roughness. Using this approximation, $n_1 = 0.8$, $n_4 = 0.14$, the values in Table 5.2, and equation (5.15), the ratio of rig to engine external-internal HTC was estimated to be between $0.3 < h^*_{\text{rig}}/h^*_{\text{eng.}} < 1.5$. The impact of this difference on overall cooling effectiveness is estimated later.

5.3.3 Adiabatic Film Cooling Effectiveness

The adiabatic film cooling effectiveness is defined as

$$\eta \equiv \frac{T_r - T_{ad}}{T_r - T_{ce}}, \quad (5.16)$$

where T_{ad} is the adiabatic wall temperature, T_r is the mainstream recovery temperature, and T_{ce} is the coolant exit temperature—i.e., the temperature of the coolant at the point it is injected into the mainstream (Eckert, 1983). From Han et al. (2001) and Goldstein (1971), the adiabatic film cooling effectiveness is a function of:

$$\eta = f\left(\frac{\dot{m}_c c_{p,c}}{\dot{m}_m c_{p,m}}, \text{Tu, BR, MR}, \widetilde{\text{Ra}}_1, \text{M}_m, \text{Pr}_m, \boldsymbol{x}, \text{geometry} \right). \quad (5.17)$$

where $\dot{m}_c c_{p,c}/\dot{m}_m c_{p,m}$ is the energy flux ratio—derived from a control volume analysis of the film—Tu is turbulent intensity, BR is blowing ratio, and MR is momentum flux ratio. MR, Tu, $\widetilde{\text{Ra}}_1$,M_m, $\boldsymbol{x}$ and the geometry are matched between rig and engine conditions. The mainstream Prandtl number Pr_m is approximately matched. The momentum flux ratio is equivalent to:

$$\text{MR} \equiv \frac{\rho_c {u_c}^2}{\rho_m {u_m}^2} = \frac{p_m}{p_c} \frac{T_c}{T_m} \left(\frac{\dot{m}_c}{\dot{m}_m} \frac{A_{\dot{m}_m}}{A_{\dot{m}_c}} \right)^2. \quad (5.18)$$

Assuming coolant static conditions approximately equal to total conditions, and that coolant capacity (5.13), mainstream capacity (5.14) and total coolant-to-mainstream pressure ratio are matched between rig and engine, the MR is also matched:

$$\mathrm{MR_{rig}} \sim \mathrm{MR_{eng.}}. \tag{5.19}$$

The blowing ratio is equivalent to:

$$\mathrm{BR} \equiv \frac{\rho_c u_c}{\rho_m u_m} = \frac{\dot{m}_c}{\dot{m}_m} \frac{A_{\dot{m}_m}}{A_{\dot{m}_c}}. \tag{5.20}$$

Since the coolant and mainstream capacity and coolant-to-mainstream pressure ratio is matched between the rig and the engine, the ratio of the rig BR to engine BR is:

$$\frac{\mathrm{BR_{rig}}}{\mathrm{BR_{eng.}}} \sim \sqrt{\frac{T_{0c,\mathrm{eng.}}}{T_{0m,\mathrm{eng.}}} \frac{T_{0m,\mathrm{rig}}}{T_{0c,\mathrm{rig}}}}. \tag{5.21}$$

$\mathrm{BR_{rig}}/\mathrm{BR_{eng.}}$ is around 0.74. The ratio of $\dot{m}_c c_{p,c}/\dot{m}_m c_{p,m}$ between rig and engine conditions can be found in a similar way:

$$\frac{\left(\dot{m}_c c_{p,c}/\dot{m}_m c_{p,m}\right)_{\mathrm{rig}}}{\left(\dot{m}_c c_{p,c}/\dot{m}_m c_{p,m}\right)_{\mathrm{eng.}}} \sim \frac{c_{p,c,\mathrm{rig}}}{c_{p,c,\mathrm{eng.}}} \frac{c_{p,m,\mathrm{eng.}}}{c_{p,m,\mathrm{rig}}} \sqrt{\frac{T_{0c,\mathrm{eng.}}}{T_{0m,\mathrm{eng.}}} \frac{T_{0m,\mathrm{rig}}}{T_{0c,\mathrm{rig}}}} \tag{5.22}$$

which is approximately equal to 0.82. BR and energy flux ratio differ only by the ratio of specific heat capacity. Since $\mathrm{BR_{rig}}/\mathrm{BR_{eng.}} \sim \left(\dot{m}_c c_{p,c}/\dot{m}_m c_{p,m}\right)_{\mathrm{rig}}/\left(\dot{m}_c c_{p,c}/\dot{m}_m c_{p,m}\right)_{\mathrm{eng.}}$, and both affect film cooling effectiveness via the same physical mechanism of mainstream mixing, only the influence of BR on film effectiveness is considered; the effect of energy flux ratio is mostly accounted for by investigating BR.

The effect of BR on film effectiveness can be estimated based on the control volume method of Goldstein (1971), and assuming a constant mainstream entrainment capacity:

$$\frac{\dot{m}_{e,\mathrm{rig}}\sqrt{T_{0m,\mathrm{rig}}}}{p_{0m,\mathrm{rig}}} \sim \frac{\dot{m}_{e,\mathrm{eng.}}\sqrt{T_{0m,\mathrm{eng.}}}}{p_{0m,\mathrm{eng.}}} \sim \frac{\dot{m}_{c,\mathrm{rig}}\sqrt{T_{0m,\mathrm{rig}}}}{p_{0m,\mathrm{rig}}}\left(\frac{1}{\eta_{,\mathrm{rig}}} - 1\right) \sim \frac{\dot{m}_{c,\mathrm{eng.}}\sqrt{T_{0m,\mathrm{eng.}}}}{p_{0m,\mathrm{eng.}}}\left(\frac{1}{\eta_{,\mathrm{eng.}}} - 1\right) \tag{5.23}$$

where $\dot{m}_e$ is the mainstream entrainment rate into the film. Using the equation for BR (5.21) and assuming that the coolant capacity and coolant-mainstream pressure ratio are matched between rig and engine, the rig film cooling effectiveness can be approximated as a function of BR ratio and the engine film cooling effectiveness:

$$\eta_{,\mathrm{rig}} \sim \left(\frac{\mathrm{BR}_{\mathrm{eng.}}}{\mathrm{BR}_{\mathrm{rig}}} \left(\frac{1}{\eta_{,\mathrm{eng.}}} - 1 \right) + 1 \right)^{-1}. \tag{5.24}$$

Assuming an average engine film effectiveness of 0.5 (e.g., Rawlinson, 2011) and using the BR ratio of 0.74 calculated from equation (5.21), the film effectiveness in the rig is approximately 0.43.

5.3.4 Biot Number

The Biot number is defined as

$$\mathrm{Bi} \equiv \frac{h_1 t_w}{k_w}, \tag{5.25}$$

where t_w and k_w are the wall thickness and wall conductivity, respectively. Since the rig and engine geometries are identical, the ratio of the rig Biot number to the engine Biot number is:

$$\frac{\mathrm{Bi}_{\mathrm{rig}}}{\mathrm{Bi}_{\mathrm{eng.}}} = \frac{(\mathrm{Nu}_m k_m / k_w)_{\mathrm{rig}}}{(\mathrm{Nu}_m k_m / k_w)_{\mathrm{eng.}}}. \tag{5.26}$$

Assuming the Nusselt functional form in equation (5.7), cancelling the effects of Prandtl number and external surface roughness (assumed matched between rig and engine conditions), and applying matched mainstream capacity (5.14), equation (5.26) reduces to:

$$\frac{\mathrm{Bi}_{\mathrm{rig}}}{\mathrm{Bi}_{\mathrm{eng.}}} \sim \left(\frac{p_{0m,\mathrm{rig}}}{p_{0m,\mathrm{eng.}}} \frac{\mu_{m,\mathrm{eng.}}}{\mu_{m,\mathrm{rig}}} \sqrt{\frac{T_{0m,\mathrm{eng.}}}{T_{0m,\mathrm{rig}}}} \right)^{n_1} \left(\frac{\mu_{m,w,\mathrm{eng}}}{\mu_{m,\mathrm{eng.}}} \right)^{n_4} \frac{k_{m,\mathrm{rig}}}{k_{m,\mathrm{eng.}}} \frac{k_{w,\mathrm{eng.}}}{k_{w,\mathrm{rig}}}. \tag{5.27}$$

Using the approximation that n_1 = 0.8, n_4 = 0.14, and the values in Table 5.2, the Biot number ratio between rig and engine is $\mathrm{Bi}_{\mathrm{rig}}/\mathrm{Bi}_{\mathrm{eng.}}$ = 1.02. It should be noted that this is without TBC at both engine and rig conditions. The Biot number at engine conditions is approximately 0.8 (Luque Martinez, 2011) and therefore the rig Biot number is around 0.8.

5.3.5 Accuracy of Sector Overall Cooling Effectiveness Prediction

The mean overall cooling effectiveness of the vane can be estimated to first order using the one-dimensional analysis of Holland and Thake (1980), assuming r = 1:

$$\theta = \frac{m^* \varepsilon + \eta(1 - \varepsilon)}{1 + \varepsilon(m^* - \eta)}, \tag{5.28}$$

where ε is the cooling efficiency, defined as:

$$\varepsilon = \frac{T_{ce} - T_{0c}}{T_{w1} - T_{0c}}. \tag{5.29}$$

The cooling efficiency can be approximated using the Biot number, non-dimensional coolant mass flow rate and HTC ratio (Kirollos and Povey, 2015b):

$$\varepsilon = \frac{1 - \exp\left(-\frac{1}{m^* h^*}\right)}{1 + m^* \mathrm{Bi}\left(1 - \exp\left(-\frac{1}{m^* h^*}\right)\right)}. \tag{5.30}$$

The cooling efficiency is estimated to be between 0.37 and 0.56 at rig conditions—0.56 corresponding to a five-fold increase in internal HTC due to laser-sintering-induced surface roughness, and 0.37 corresponding to no increase in internal HTC due to the laser-sintering process. The cooling efficiency at engine conditions is estimated to be 0.26.

The overall cooling effectiveness at rig conditions is estimated to be between 0.52 (no increase in internal HTC due to surface roughness) and 0.55 (x5 increase in internal HTC due to surface rougheness). Therefore, the uncertainty in internal HTC due to surface roughness has a small effect on the overall cooling effectiveness prediction. This is because the film contribution to overall cooling outweighs the internal convective cooling contribution. The overall cooling effectiveness in the engine is estimated to be 0.63—approximately 15% greater than the overall cooling effectiveness measured in the rig. This difference is primarily due to reduced blowing ratio in the rig, and secondly due to reduced non-dimensional coolant mass flow rate in the rig. A summary of these results is shown in Table 5.2.

5.4 Summary of Sector Updates since Luque Martinez (2011)

A summary of all updates to the Sector Facility since the work of Luque Martinez (2011) is included below. Most are Sector specific, but some are lab-wide or area-wide upgrades that have influenced Sector testing (e.g., the Drake upgrade and the use of a Blowdown operating procedure and safety checklist). The upgrades marked with asterisks (*) are discussed further, either after the summary or in different chapters.

*Infra-red camera hardware and software**

Previously a single FLIR A325sc IR camera (320x240 pixels) was used to measure pressure-side and suction-side radiation intensity—each side measured in separate runs by relocating the camera. Videos were recorded in LabView using the NI Vision acquisition software NI-IMAQ. The Sector Facility now uses two FLIR A655sc IR cameras (640x480 pixels) to measure the pressure-side and suction-side simultaneously. A new physically-based temperature calibration procedure is utilised. An additional PC, Intel Pro/1000 PT network adaptor card, serial communication system (including com0com software) and IR lenses were acquired for this purpose. Videos are now recorded using the FLIR ResearchIR program, triggered via an updated LabView script that also records thermocouple and pressure transducer signals.

*Laser-sintered middle vane pair**

Luque Martinez (2011) used the Sector Facility to assess the thermal performance of a real, cast RR T500 HPNGV, and a variant in which the leading-edge region of the cast RR T500 HPNGV was replaced with a metal laser-sintered dendritic cooling system. The Sector Facility is now used to perform thermal assessments on fully laser-sintered HPNGV geometries. The vanes are manufactured from Ti6Al4V by 3TRPD. Two DMLS vanes are bonded to real, cast hub and case platforms; the laser sintered pair then replaces the central vane pair in the Sector Facility.

*Heater mesh**

The original supplier of heater mesh (G. Bopp) ceased production of 180 mm aperture, 125 mm diameter, 83 mesh count, 34.8% open area, SS 304 woven mesh. A new supplier of the same specification mesh (Plastok) was eventually found. In the interim, a more easily sourced and power-dissipative specification of mesh was tested (178 mm aperture, 140 mm diameter, 80 mesh count, 31.3% open area, SS 304 woven mesh from the Mesh Company). The interim mesh increased the maximum change in mainstream temperature by 10% as compared to the original material, but lasted for only 16 high-powered 30 second runs. The original specification of mesh survived up to 160 runs.

*Coolant mass flow rate measurement nozzle and orifice plate**

The coolant mass flow rate is now measured using a Flow Systems CEESI-calibrated 8.28 mm diameter sonic nozzle located in the coolant feed. An interchangeable orifice plate has been added upstream of the nozzle which sets the coolant-to-mainstream mass flow ratio. 78 laser-cut orifice plates have been manufactured to allow for a wide range of coolant mass flow rates: orifice diameters every 0.2 mm from 3.0 mm to 10 mm, and every 0.5 mm from 10 mm to 30 mm.

*Capability to perform in-situ coolant capacity tests**

A 100 psi air feed line and a 0.875 m^3 air storage tank have been installed next to the Sector Facility. By removing the back-end of the Sector Facility (deswirl vane layer, choke plate layer and exhaust duct) and discharging the tank at 50 psi through the Sector coolant feed, the coolant capacity of the test vane is measured. This result is compared to the equivalent ex-situ results from the Coolant Capacity Rig, to identify any leaks in the Sector coolant manifolds.

*Regulator**

The Sector Facility previously shared a regulator with other test facilities. Two new Sector-dedicated regulators were tested: an off-the-shelf regulator from Auld Valves (100 mm Standfast Pressure Reducing Valve), and a prototype regulator from Oxford Flow (OX-0402). The Oxford Flow regulator out-performed the Auld Valves regulator in all key areas and is currently installed in the Sector Facility. A 3.3 m length of 12” pipework was installed downstream of the regulator to improve regulator performance.

Data acquisition hardware

The former NI PXI 8196 Embedded Controller expired unexpectedly. It was replaced with an up-to-date NI PXI 1050 chassis containing an NI PXI 8360 MXI-Express card for PC connection, an NI PXI-6031E Multifunction I/O card to link to the pressure transducer boxes and x2 NI SCXI-1102B cards for thermocouple acquisition and conditioning.

Drake power supply system

As part of the lab-wide upgrade to the Drake power supply system, the previous bus-bar based distribution panel was replaced with a switch-and-key interlock system. All distribution power cables were increased in size—the diameter of the copper wires has been approximately doubled to a new cross-sectional area of 185 mm^2. A new trench between the Blowdown control room and the Sector Facility was commissioned to house the new larger cables. The previous Perspex protection boxes around the heater mesh terminals were replaced with Tufnol equivalents.

Burst disk

The Sector Facility used to operate with a Zook PB-R 4" 9 barg 316 SS concave forward-acting metal burst disk to prevent working-section over-pressurisation. However, this type of disk was found to rupture off-design because of the back-pressure generated by other facilities using the same vent line. It was subsequently replaced with a Zook PB-V burst disk—a similar forward-acting metal concave disk but with an additional 'vacuum' support that can withstand a nominal back-pressure of 1 bar. It was later observed in another facility that exposure to back-pressure reduces the integrity of the PB-V disk in the forward direction, meaning the disk will rupture when exposed to the working forward pressure after a substantial back-pressurisation event. The Sector Facility now operates with a Zook Inverted-A Graphite 4" 9 barg burst disk, which has yet to rupture due to back-pressurisation.

Deswirl vanes

The deswirl vanes were remanufactured from Dural. The previous stereolithographed deswirl vanes had distorted from prolonged thermal exposure and had caused flow blockage.

Relocations

The Sector Facility has been relocated and re-commissioned three times to allow for the excavation of two service-system trenches and the installation of the ECAT power units.

Zinc Selenide (ZnSe) window

The downstream ZnSe window fell into the working section and shattered during a period of Sector down-time, likely caused by a loss of integrity of the Araldite holding the window in place. A replacement window and spare were manufactured by II-VI Incorporated. Now, the window is additionally held captive by two small, removable, metal overhangs on the flow-side, preventing a similar mode of failure.

Coolant feeds test vane only

Previously, coolant was distributed to all six vanes as well as the rear outer discharge nozzle (RODN) platform cooling rows. In order to isolate the coolant mass flow rate through the vane of interest, the other five vanes have been filled with Tecbond 7718 polyamide based adhesive; the RODN cooling holes sealed using silicone sealant; and the RODN feed plenum disconnected from the coolant feed hoses. The polyamide based adhesive was chosen because of its rigidity and heat resistance at temperatures below 135°C—i.e., at temperatures seen during Sector operation—but has a very low viscosity in its molten state. The adhesive was administered using a hot glue gun. The vanes were pre-heated before applying the adhesive, so that the adhesive ran fluidly through all vane internal cooling passages before the vane cooled and the adhesive set. It was demonstrated that the adhesive can be removed by re-heating the vane with a blow-torch. The adhesive liquefies and runs out of the vane without residue.

Operating procedure

The Sector Facility now operates according to the general run procedure and safety checklist recently written for the Profile Generator Rig and the Regulator Rig, also operating in the Blowdown area. This has allowed for a greater number of trained running partners while maintaining high levels of safety. Tests are now carried out with greater frequency and greater continuity.

5.5 Heater Mesh

Step changes in mainstream air temperature (Fig. 5.17) are achieved with two heater meshes, connected electrically and fluidly in series. A maximum mainstream temperature rise of 59 K can be achieved at a time constant of 0.22 s. A detailed review of heater mesh theory and developments for Sector Facility application is given by Luque Martinez (2011). Except for the change in power cable diameter (now 185mm^2 cross-sectional area), corresponding adjustment to heater mesh terminals, and new Tufnol terminal isolation boxes, the specification of the current heater mesh assembly is unchanged from the experiments of Luque Martinez.

The current heater mesh material is 180 mm aperture, 125 mm diameter, 83 mesh count, 34.8% open area, SS 304 woven mesh, and is supplied by Plastok. The mesh supplier used by Luque Martinez—G. Bopp—no longer produces mesh in this specification. Microscopic comparison of the Plastok and G. Bopp mesh show no visible dissimilarities (Fig. 5.21). When operating at maximum voltage, the meshes dissipate around 138 kW at 1520 A—approximately 2.7 A through every 0.125 mm diameter wire. A summary of the electrical and physical characteristics of the mesh currently in use in the Sector Facility is given in Table 5.3.

This type of mesh typically survives more than 100 high-powered (95 – 115 V set-point at Drake) 30 second runs when assembled according to best practise. Figure 5.22 shows a mesh that failed after 97

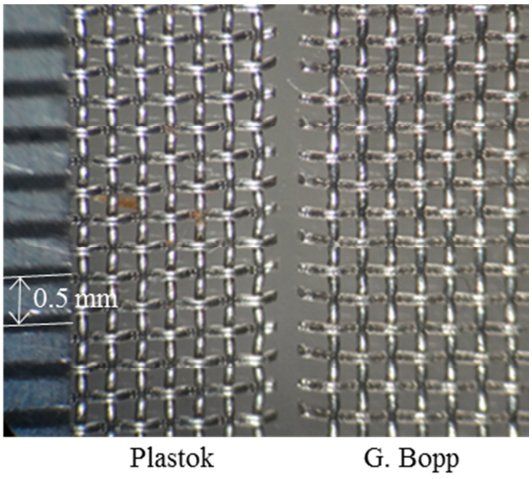


Figure 5.21. Plastok and G. Bopp mesh.

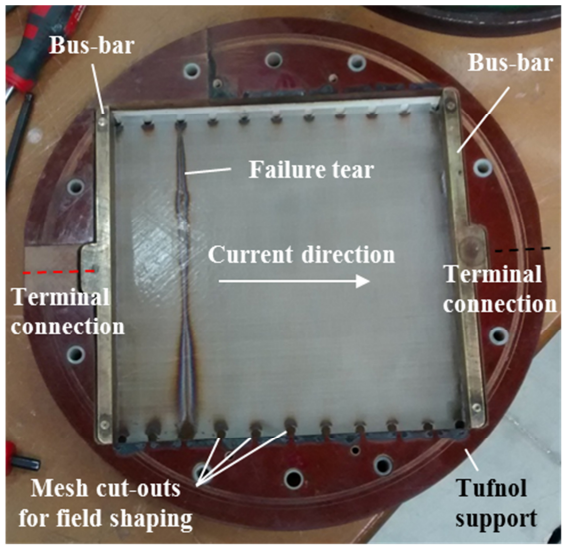


Figure 5.22. Failed heater mesh after 97 runs.

runs. Failure generally occurs when a localised burn or weakness (cause unknown) initiates a tear that propagates almost instantaneously across the mesh perpendicular to the current direction. Tears always start and end at a cut-out (marked in Fig. 5.22). Cut-outs prevent current flow in the parts of the mesh clamped between the Tufnol surrounds, which would otherwise burn out.

The 180 mm aperture, 125 mm diameter mesh proved difficult to source. In the interim of finding a supplier, a more easily sourced and power-dissipative specification of mesh was tested: 178 mm aperture, 140 mm diameter, 80 mesh count, 31.3% open area, SS 304 woven mesh from the Mesh Company. The resistance of the interim mesh was 17% lower than the current mesh, and dissipated 151 kW at 1740 A when operated at the maximum voltage setting. The maximum mainstream

Table 5.3. Electrical/physical characteristics of Plastok SS304 180 mm aperture, 125 mm Ø mesh.

	Symbol	Method	Value
Drake (power supply) set-point	-	Set	114 V
Voltage generated by Drake	V	Measured	96 V
Total voltage across meshes	V_{mesh}	Measured	91 V
Current	I	Measured	1520 A
Total resistance of meshes	R_{mesh}	V_{mesh}/I	60 mΩ
Total resistance of cabling between Drake and meshes	$R_{cabling}$	$(V - V_{mesh})/I$	3.3 mΩ
Total power dissipated by meshes	P	IV_{mesh}	138 kW
Mainstream mass flow rate	$\dot{m}$	Measured	2.31 kg/s
Specific heat capacity of air at constant pressure	c_p	Look-up table	1006.3 $Jkg^{-1}K^{-1}$
Change in mainstream temperature across meshes	ΔT	$P/(\dot{m}c_p)$	59 K
		Measured	59 K
Wire diameter	d	Specification	0.125 mm
Wire aperture	a	Specification	0.180 mm
Cross-sectional area per unit width	A'	$(\pi d^2)/(4(a+d))$	0.040 mm
Life (no. of 30 second runs at > 95 V Drake set-point)	-	-	Average 100 +

Table 5.4. Electrical/physical characteristics of The Mesh Company SS304 178 mm ap., 140 mm Ø mesh.

	Symbol	Method	Value
Drake (power supply) set-point	-	Set	114 V
Total voltage across meshes	V_{mesh}	Measured	87 V
Change in mainstream temperature across meshes	ΔT	Measured	65 K
Mainstream mass flow rate	$\dot{m}$	Measured	2.31 kg/s
Specific heat capacity of air at constant pressure	c_p	Look-up table	1006.3 $Jkg^{-1}K^{-1}$
Total power dissipated by meshes	P	$\dot{m}c_p\Delta T$	151 kW
Current	I	P/V_{mesh}	1740 A
Wire diameter	d	Specification	0.14 mm
Wire aperture	a	Specification	0.178 mm
Cross-sectional area per unit width	A'	$(\pi d^2)/(4(a+d))$	0.048 mm
Total resistance of meshes	R_{mesh}	V_{mesh}/I	50 mΩ
		$\frac{((RA')_{0.125\,\emptyset\,mesh})}{(A'_{0.14\,\emptyset\,mesh})}$	50 mΩ
Life (no. of 30 second runs at > 95 V Drake set-point)	-	-	16

temperature rise increased by 10% as compared to the current material, but lasted for only 16 high-powered 30 second runs. Despite the increase in mainstream temperature, the life was deemed unacceptably short, and so this specification of mesh was discontinued in the Sector Facility. A summary of the electrical and physical characteristics of the interim mesh are given in Table 5.4.

5.6 Regulator

A high pressure reservoir of 10^3 kg, 400 psi air at room temperature supplies the Sector Facility. The facility is run with steady mass flow rate and pressure during a run using a high mass flow rate regulator. The regulator generates a constant outlet pressure of 9.4 bara despite decaying reservoir pressure by dynamically self-adjusting flow area. Luque Martinez (2011) used the Oldfield (MLGO) high mass flow rate regulator (Fig. 5.24) with a limiter, which maintains constant inlet pressure to within ±0.5%. This regulator is also used by the Capacity Rig and the supersonic nozzle calibration tunnel. A new Sector-dedicated regulator was sought to increase running autonomy. Two regulators were tested for this purpose: an off-the-shelf 100 mm Standfast Pressure Reducing Valve from Auld Valves (Fig. 5.23), and a prototype OX-0402 regulator from Oxford Flow (Fig. 5.25).

The Auld regulator uses a spring-pressure force balance method, in which the desired downstream pressure is set by mechanically adjusting spring tension. During commission, the regulator would often stick open, causing the rig to over-pressurise and the burst disk to rupture. It was eventually found that one of the supplied PTFE O-rings within the regulator did not seal adequately at low ambient temperatures. The problem was solved by replacing the PTFE O-ring with a spring energised seal supplied by OmniSeal. The regulator also displayed significant under-damping, which was reduced slightly by increasing the downstream volume with a 3.3 m length of 12” pipe and decreasing the speed of the pneumatic valve by restricting the 100 psi marton-air feed. Regulation was stable for

inlet pressures 330 – 350 psi and 230 – 260 psi. For all other inlet pressures, regulation was unstable, causing the outlet pressure to oscillate.

The regulated pressure using the Auld regulator during a singular Sector run is plotted in Fig. 5.26. It is important to note that the reliability of the regulator was poor; Figure 5.26 was the very best regulated run using the Auld regulator, and most Auld runs were substantially worse. For the run in Fig. 5.26, the initial underdamped oscillations decay after 15 seconds. During steady operation, the regulated pressure oscillates within ±1% of target pressure.



Figure 5.24. MLGO regulator



Figure 5.23. 100mm Standfast Auld regulator

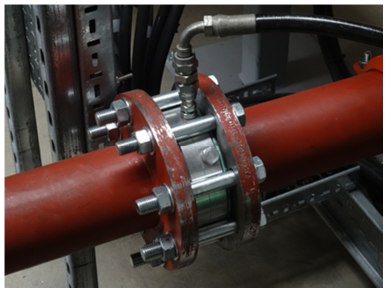


Figure 5.25. OX-0402 Oxford Flow regulator

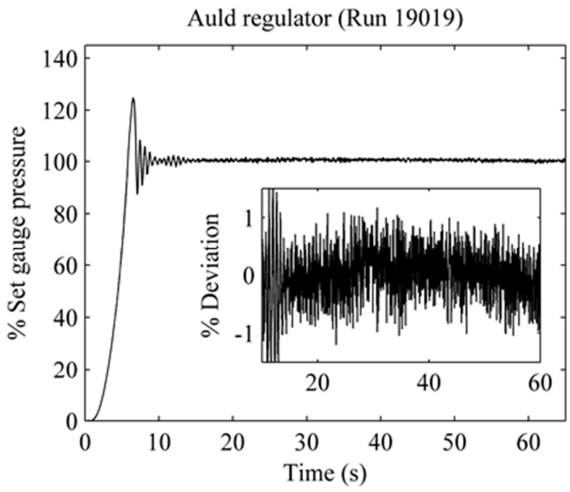


Figure 5.26. Regulated pressure of very best run using Auld regulator.

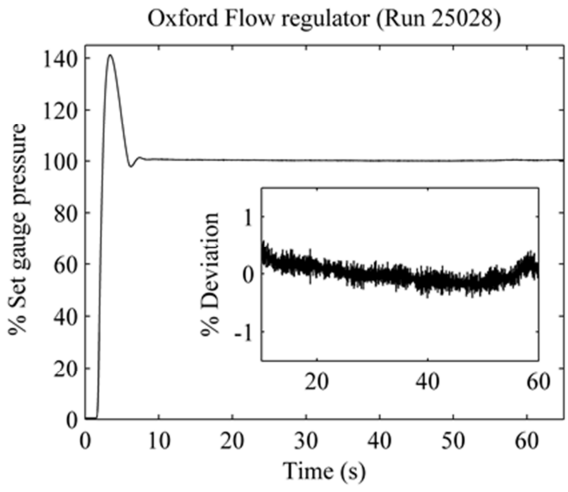


Figure 5.27. Regulated pressure of standard run using Oxford Flow regulator.

A prototype regulator from Oxford Flow was also tested, which operates using a pressure-pressure force balance method. The desired downstream pressure is fed into a sealed manifold inside the regulator and the flow area then self-adjusts until the manifold pressure equals the downstream pressure. For Sector application, the desired pressure within the sealed manifold was set by a small pilot regulator fed from the 400 psi line. The operation of the pilot regulator was improved by introducing a small leak to atmosphere between the pilot regulator and Oxford Flow regulator. No pneumatic valve restriction was necessary. Regulation is stable for inlet pressures between 180 – 400 psi, below which the regulated pressure begins to droop. The Oxford Flow regulator is considerably lighter than the Auld regulator.

The regulated pressure during a typical Sector run using the Oxford Flow regulator is plotted in Fig. 5.27. Steady conditions are reached in 8 seconds; after this point, the regulated pressure is always within ±0.4% of target pressure. The Oxford Flow regulator outperformed the Auld regulator in all areas: increased range of allowable inlet pressures; improved regulation stability and reduced oscillations; reliability; ease of pressure adjustment; weight; risk associated with malfunction (Auld regulator locks open). The Oxford Flow regulator was therefore used for all experiments reported in this thesis.

5.7 Sector Mass Flow Variation and Measurement

The thermal performance of each design was measured over a range of coolant mass flow rates $\dot{m}_c$ and at a constant mainstream mass flow rate $\dot{m}_m$. All overall cooling effectiveness measurements are reported as a function of the ratio $\left(\dot{m}_c\sqrt{T_{0c}}\right)/\left(\dot{m}_m\sqrt{T_{0m}}\right)$. This ratio was chosen as the most appropriate method of baselining each design because (a) it is matched between rig and engine; (b) with knowledge of the temperature ratio T_{0c}/T_{0m}, the mass flow ratio $\dot{m}_c/\dot{m}_m$ can be determined which can be used to estimate cycle-efficiency (Horlock et al., 2001).

The coolant mass flow rate during standard Sector operation was controlled using a choked orifice plate in the coolant feed, shown in Fig. 5.28. The orifice plate is a laser cut, 2mm thick, 2" OD stainless steel disk which is clamped against a nozzle holder and face O-ring using a brass clamp ring. A large number of orifice plates were manufactured with various orifice diameters (every 0.2 mm from 3.0 mm to 10 mm and every 0.5 mm from 10 mm to 30 mm) to allow for a range of coolant mass flow rates to be tested. The overall cooling effectiveness of each cooling design was typically measured at 11 coolant mass flow rates in the Sector Facility by using orifice diameters every 0.2 mm from 4.4 mm to 6.4 mm—corresponding to coolant-to-mainstream (per passage) mass flow ratios between 5.7 – 12.4%.

The coolant orifice was used to control, but not to measure, coolant mass flow rate. Coolant mass flow was measured using a CEESI-calibrated Flow Systems Venturi nozzle downstream of the

orifice—discussed later. However, for set-up and indication purposes, the coolant mass flow rate through the orifice was estimated using the 1D, isentropic, compressible mass flow relation. Since the orifice plate was choked, the capacity of the orifice was estimated from:

$$\Gamma_{orifice} \equiv \frac{\dot{m}_c\sqrt{T_{01}}}{p_{01}} = C_{d,orifice}A_{orifice}\sqrt{\frac{\gamma}{R}}\left(\frac{\gamma+1}{2}\right)^{-\frac{\gamma+1}{2(\gamma-1)}}, \tag{5.31}$$

where $\Gamma_{orifice}$ is the capacity of the orifice, $\dot{m}_c$ is the mass flow rate through the coolant feed; T_{01} is the total temperature upstream of the orifice (~ 297 K); p_{01} is the total pressure upstream of the orifice (~ 9.4 bara); $A_{orifice}$ is the geometric area of the orifice; $C_{d,orifice}$ is the discharge coefficient of the orifice (~ 0.82); R is the specific gas constant of air (287 $Jkg^{-1}K^{-1}$); and γ is the ratio of specific heats (~ 1.4). The discharge coefficient was estimated using the mass flow rate measured at the Venturi nozzle and equation (5.31). A value of 0.82 agrees well with Ward-Smith (1979), who showed that for sharp-edged, choked orifices with thickness-to-diameter $0.28 < t/d < 5.13$, the discharge coefficient is in the range $0.82 < C_{d,orifice} < 0.845$.

The mainstream mass flow rate was nominally constant for all runs and was measured using a choked distribution plate upstream of the heater meshes (Fig. 5.29). The mainstream distribution plate consists of 11, 12.1 mm diameter holes. The mass flow rate through the plate is calculated according to the equation:

$$\Gamma_{distr.} \equiv \frac{5\dot{m}_m\sqrt{T_{01}}}{p_{01}} = C_{d,distr.}A_{distr.}\sqrt{\frac{\gamma}{R}}\left(\frac{\gamma+1}{2}\right)^{-\frac{\gamma+1}{2(\gamma-1)}}. \tag{5.32}$$

where $\Gamma_{distr.}$ is the capacity of the mainstream distribution plate ($4.24\text{x}10^{-5}$ $kgs^{-1}Pa^{-1}K^{0.5}$) and is constant; $C_{d,distr.}$ is the discharge coefficient of the distribution plate (0.83) which is estimated from Ward-Smith (1979); $A_{distr.}$ is the total geometric area of the orifices (1265 mm^2); $\dot{m}_m$ is the mainstream mass flow rate *per passage* (total mainstream mass flow rate $5\dot{m}_m$ ~ 2.31 kgs^{-1}); T_{01} is the total temperature upstream of the distribution plate (~ 297 K); p_{01} is the total pressure upstream of the distribution plate (~ 9.4 bara); and R and γ are the same as equation (5.31). The total mainstream mass flow rate is assumed constant at 2.31 kgs^{-1} for all experimental runs.

Since both coolant orifice and mainstream distribution plate are choked and fed at the same total pressure and temperature, the ratio of the coolant mass flow rate to the mainstream mass flow rate per passage is therefore the ratio of their respective effective areas:

$$\frac{\dot{m}_c}{\dot{m}_m} \sim 5\frac{C_{d,orifice}A_{orifice}}{C_{d,dist.}A_{distr.}}. \tag{5.33}$$

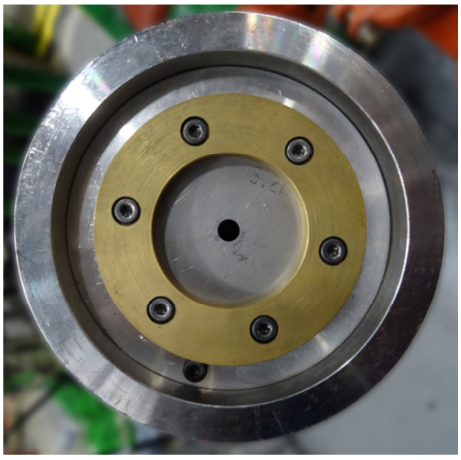


Figure 5.28. Upstream face of coolant orifice plate and assembly, shown with 6.2 mm diameter orifice. Fits in 4" Victaulic (new spec.) pipework.

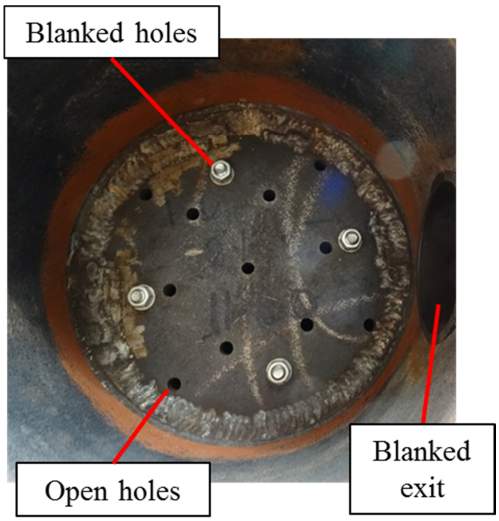


Figure 5.29. Downstream face of mainstream distribution plate. Fits in 12" Victaulic (old spec.) pipework.

The factor of 5 converts the total mainstream mass flow measurement into a per-passage measurement.

Equation (5.33) was used for indication purposes. The coolant mass flow rate $\dot{m}_c$ was actually measured using the CEESI-calibrated Flow Systems Venturi nozzle downstream of the orifice, which was also used to calibrate the CCR orifice in Chapter 8. The Venturi nozzle calibration is based on the equation for compressible, choked flow through a 1D isentropic nozzle:

$$\dot{m}_c = C_{d,\text{Venturi}} C_* \frac{\pi d_{\text{Venturi}}^2}{4} \frac{p_{0u,\text{Venturi}}}{\sqrt{R T_{0u,\text{Venturi}}}}, \qquad \frac{p_{0u,\text{Venturi}}}{p_{0d,\text{Venturi}}} > 1.03, \tag{5.34}$$

where $p_{0u,\text{Venturi}}$ and $T_{0u,\text{Venturi}}$ are the total pressure and temperature upstream of the Venturi nozzle, $p_{0d,\text{Venturi}}$ is the total pressure downstream of the nozzle, d_{Venturi} is the nominal diameter of the nozzle (8.28 mm), R is the specific gas constant of air, $C_{d,\text{Venturi}}$ is the discharge coefficient of the nozzle, and C_* is the critical flow function of air. The nozzle remains choked even at low pressure ratios ($p_{0u,\text{Venturi}}/p_{0d,\text{Venturi}} > 1.03$) because of a well-formed downstream divergent section for pressure recovery. The discharge coefficient $C_{d,\text{Venturi}}$ is a factory-supplied function of Reynolds number $\text{Re}_{d,\text{Venturi}} = 4\dot{m}_c/\mu\pi d_{\text{Venturi}}$, described by a fourth-order polynomial best-fit:

$$C_{d,\text{Venturi}} = \sum_{i=1}^{i=5} a_i \left(\text{Re}_{d,\text{Venturi}}\right)^{i-1}, \; 1.381\text{x}10^5 < \text{Re}_{d,\text{Venturi}} < 14.852\text{ x}10^5 \tag{5.35}$$

$a_1 = 0.9923$, $a_2 = 4.3248\text{x}10^{-8}$, $a_3 = -6.6111\text{x}10^{-14}$, $a_4 = 4.1869\text{x}10^{-20}$, $a_5 = -9.4241\text{x}10^{-27}$.

Dynamic viscosity is a function of temperature $T_{0u,\text{Venturi}}$, plotted in Chapter 8. The critical flow function is taken from BS EN ISO 9300 (2005) and is a function of temperature and pressure:

$$C_* = \sum_i a_i \pi^{b_i} \tau^{c_i}, \tag{5.36}$$

where $\pi = p_{0u,\text{Venturi}}/p_{crit}$ and $\tau = T_{0u,\text{Venturi}}/T_{crit}$, T_{crit} = 132.53 K, p_{crit} = 3.786x10^6 Pa, and the coefficients a_i, b_i and c_i are given in BS EN ISO 9300 (2005).

The temperature measurement $T_{0u,\text{Venturi}}$, pressure measurement $p_{0u,\text{Venturi}}$, equations (5.34)-(5.36) and the dynamic viscosity as a function of temperature, uniquely determined the mass flow rate $\dot{m}_c$ through the Venturi nozzle, when the nozzle was choked ($p_{0u,\text{Venturi}}/p_{0d,\text{Venturi}}$ > 1.03). Unfortunately, the Venturi nozzle was only choked at the upper end of the range of coolant mass flow rates tested in the Sector Facility. At the lower end, the Venturi nozzle was unchoked and could not be used to measure coolant mass flow rate directly. The following procedure was subsequently used to calculate coolant mass flow rate:

1. For runs in which the Venturi nozzle was choked, the coolant mass flow rate was measured using the Venturi nozzle.
2. Using the coolant capacity measurements from step (1), the capacity characteristic of the vane was determined. The capacity characteristic of a vane operating at engine conditions is well described by the equation

$$\frac{\dot{m}_c\sqrt{T_{0c}}}{p_{0c}} = A^* \sqrt{\frac{2\gamma}{R(\gamma-1)}\left[\left(\frac{p_{0c}}{p_{0m}}+p^*\right)^{-\frac{2}{\gamma}} - \left(\frac{p_{0c}}{p_{0m}}+p^*\right)^{-\frac{\gamma+1}{\gamma}}\right]}, \tag{5.37}$$

   in the range 1.013 < p_{0c}/p_{0m}< 1.1, where A^* and p^* are constants. Justification for the form of this characteristic is given later. p_{0c} and T_{0c} are the total coolant pressure and temperature immediately upstream of the vane; p_{0m} is the total mainstream pressure at the inlet contraction. The constants A^* and p^* are found for a given vane by least squares regression of equation (5.37) with the experimental data found in step (1).

3. For runs in which the Venturi nozzle was unchoked, the coolant mass flow rate was estimated using (5.37) and the measurements p_{0c}, p_{0m} and T_{0c}.

The results of this process are plotted in Fig. 5.30. Also plotted is the maximum possible error in vane capacity due to leaks—leaks are discussed in the following section.

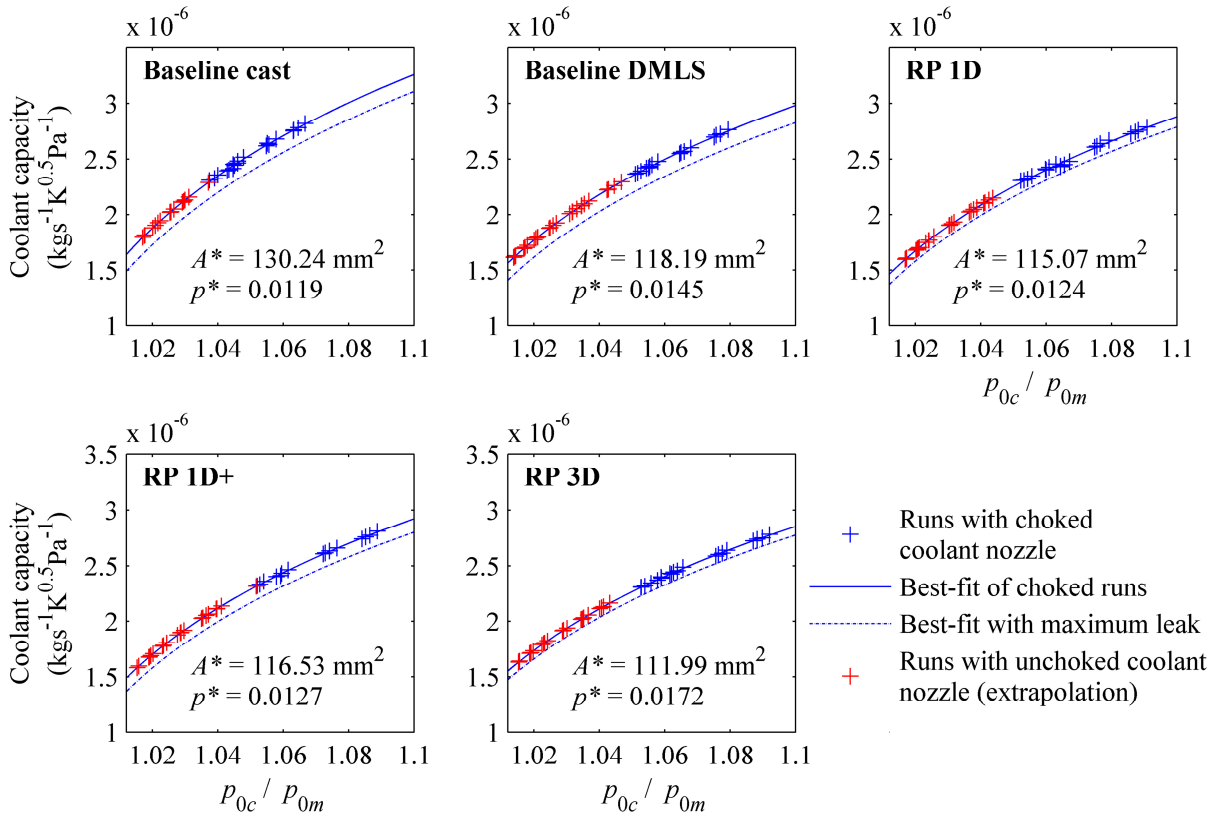


Figure 5.30. Total vane coolant capacity during Sector runs; measured (blue +) and extrapolated using vane capacity characteristic (red +).

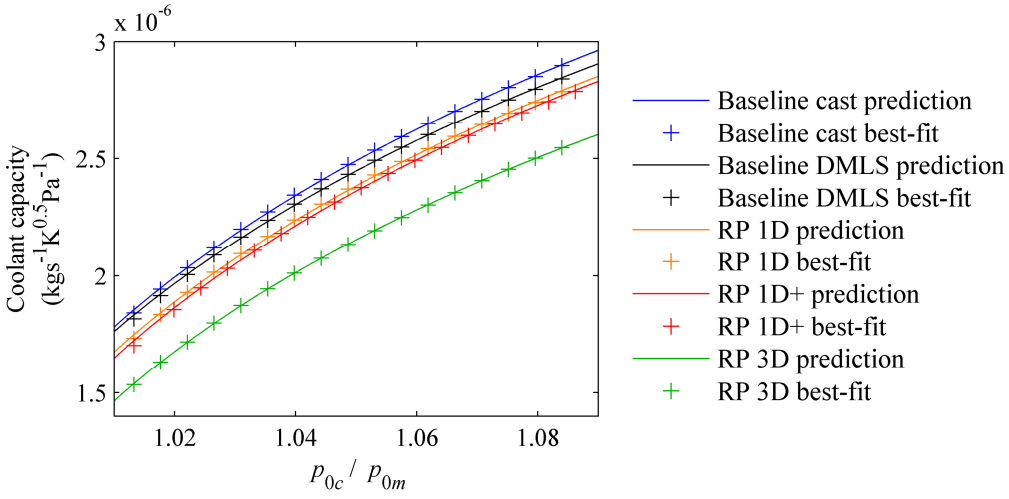


Figure 5.31. Justification for the form of best-fit equation (5.45); comparison of network flow model predictions of total vane coolant capacity to best-fit equation (5.37) .

The vane capacity characteristic in equation (5.37) is semi-physical, based on the 1D isentropic, compressible mass flow equation but adapted to describe systems where the outlet pressure varies around the vane using the first order approximation of an overall pressure ratio offset p^*. The form of the characteristic is validated in Fig. 5.31, in which the capacity characteristic is best-fit (with respect to a single value of A^* and p^* for each design) to the network flow model coolant capacity predictions

taken from Chapter 9. The equation fits the network flow model predictions to within 1% in the range $1.013 < p_{0c}/p_{0m} < 1.1$, which is sufficiently accurate to describe experimental coolant capacity data over the low coolant mass flow rate range in the Sector Facility.

The coolant to mainstream mass flow ratio $\dot{m}_c/\dot{m}_m$ is set *solely* by the coolant orifice plate and mainstream distribution plate, equation (5.33). The pressure ratio across the vane p_{0c}/p_{0m} is then a function of the mass flow ratio $\dot{m}_c/\dot{m}_m$ and the ratio of coolant to mainstream total temperature, for a given vane geometry. This is shown rigorously in the following analysis.

As described in Chapter 8, the coolant capacity Γ_c of the vane (5.13) is a function of the pressure ratio across the vane p_{0c}/p_{0m}, the vane geometry, and the ratio of specific heats γ:

$$\Gamma_c = f_2\left(\frac{p_{0c}}{p_{0m}}, \gamma, \text{vane geometry}\right). \tag{5.38}$$

Mainstream capacity Γ_m (5.14) is a function of the mainstream Mach number M_m and ratio of specific heats γ:

$$\Gamma_m = f_1(\mathrm{M}_m, \gamma). \tag{5.39}$$

The ratio of the coolant capacity to the mainstream capacity is therefore

$$\frac{\Gamma_c}{\Gamma_m} \equiv \frac{\dot{m}_c}{\dot{m}_m}\frac{p_{0m}}{p_{0c}}\sqrt{\frac{T_{0c}}{T_{0m}}} = f_2\left(\frac{p_{0c}}{p_{0m}}, \gamma, \text{vane geometry}\right)\Big/ f_1(\mathrm{M}_m, \gamma). \tag{5.40}$$

The ratio of specific heats γ and mainstream Mach number M_m are constant for a test campaign, and so for a specific vane design:

$$\frac{\dot{m}_c}{\dot{m}_m}\sqrt{\frac{T_{0c}}{T_{0m}}} = F\left(\frac{p_{0c}}{p_{0m}}\right). \tag{5.41}$$

The ratio $\left(\dot{m}_c\sqrt{T_{0c}}\right)/\left(\dot{m}_m\sqrt{T_{0m}}\right)$ for all five designs and for all Sector experiments is plotted as a function of pressure ratio p_{0c}/p_{0m} in Fig. 5.32, for both experimentally measured $\dot{m}_c$ and extrapolated $\dot{m}_c$ (using equation (5.37)). Also shown is the maximum possible error that could be present due to leaks. Both the non-extrapolated data (blue) and extrapolated data (red) collapse onto a single line, as predicted by equation (5.41).

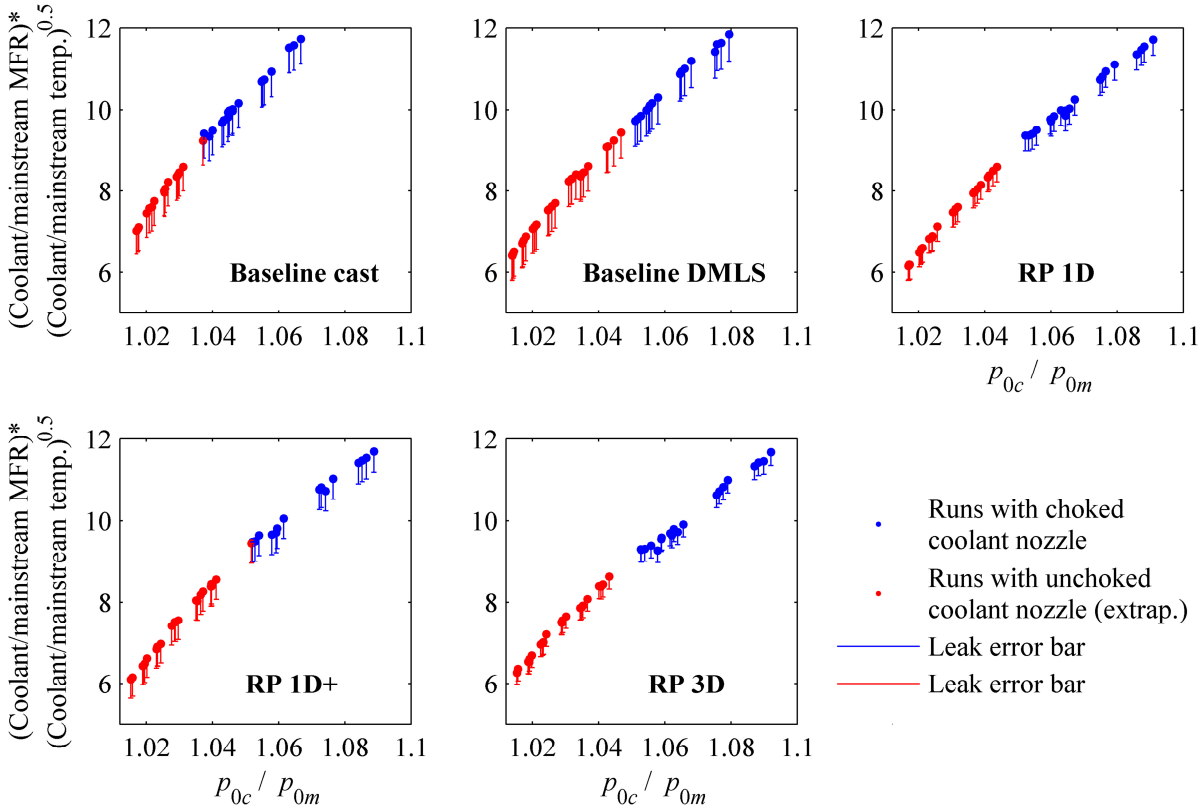


Figure 5.32. $(\dot{m}_c\sqrt{T_{0c}})/(\dot{m}_m\sqrt{T_{0m}})$ for all designs with error bars for maximum possible leak error.

5.8 In-Situ Leak Test

All coolant from the Venturi nozzle should ideally enter the coolant manifold and exit into the mainstream via the vane of interest. Consequently, the vane cassette was silicone-sealed into the Sector Facility to prevent any extraneous flow paths between coolant manifolds and the mainstream, all other vanes were blocked internally using polyamide based adhesive, and the RODN platform cooling holes were blocked on the coolant side using silicone sealant. Despite best practise, coolant leakage still occurred and meant that the mass flow rate measured by the Venturi nozzle was greater than the coolant mass flow rate passing through the vane of interest. This leakage error had to be taken into account when baselining the thermal performance of the designs with respect to the $(\dot{m}_c\sqrt{T_{0c}})/(\dot{m}_m\sqrt{T_{0m}})$ ratio.

Leakage flow can generally be characterised by an effective area A_{leak}, a driving pressure ratio $p_{0u,\text{leak}}/p_{d,\text{leak}}$, ratio of specific heats γ and specific gas constant R:

$$\frac{\dot{m}_{\text{leak}}\sqrt{T_{0u,\text{leak}}}}{p_{0u,\text{leak}}} = \begin{cases} A_{\text{leak}}\sqrt{\dfrac{2\gamma}{R(\gamma-1)}\left[\left(\dfrac{p_{0u,\text{leak}}}{p_{d,\text{leak}}}\right)^{-\frac{2}{\gamma}} - \left(\dfrac{p_{0u,\text{leak}}}{p_{d,\text{leak}}}\right)^{-\frac{\gamma+1}{\gamma}}\right]}, & \dfrac{p_{0u,\text{leak}}}{p_{d,\text{leak}}} < 1.89 \\ A_{\text{leak}}\sqrt{\dfrac{\gamma}{R}}\left(\dfrac{\gamma+1}{2}\right)^{-\frac{\gamma+1}{2(\gamma-1)}}, & \dfrac{p_{0u,\text{leak}}}{p_{d,\text{leak}}} > 1.89 \end{cases} \quad (5.42)$$

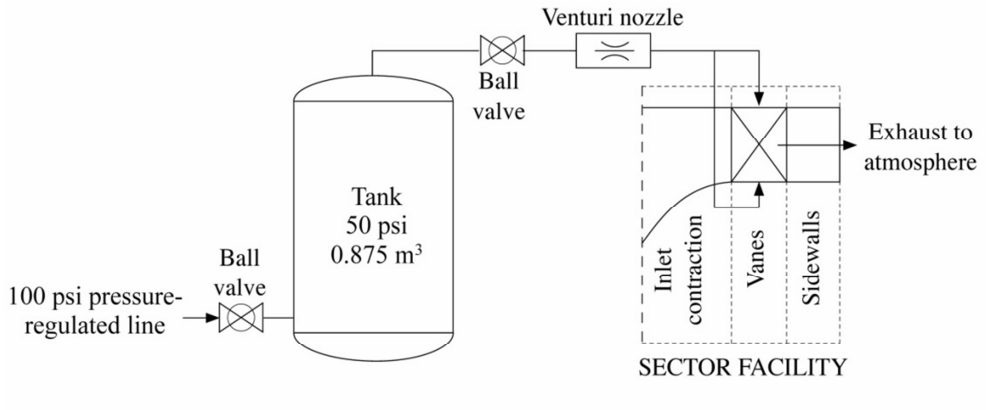


Figure 5.33. Schematic of in-situ Sector leak test.

If the leakage area A_{leak}, driving pressure ratio $p_{0u,\text{leak}}/p_{d,\text{leak}}$, upstream total temperature $T_{0u,\text{leak}}$ and pressure $p_{0u,\text{leak}}$ are known, then the leakage mass flow rate $\dot{m}_{\text{leak}}$ can be estimated, and hence the coolant mass flow rate through the vane can be calculated:

$$\dot{m}_{c,\text{vane}} = \dot{m}_{c,\text{Venturi}} - \dot{m}_{\text{leak}}. \tag{5.43}$$

The effective area of the leak A_{leak} was measured experimentally using an in-situ leak test. After the vanes were installed into the Sector Facility, the coolant feed was connected to a 0.875 m^3 air storage tank. The back-end of the Sector Facility (deswirl vane layer, choke plate layer and exhaust duct) were removed, so that the pressure within the mainstream duct equalled atmospheric. A schematic of this setup is shown in Fig. 5.33.

The tank was charged to 50 psi, and then discharged through the coolant feed. The coolant mass flow rate through the system was measured during discharge using the Venturi nozzle. The total vane coolant capacity when all rows exhaust to atmosphere $\Gamma_{\text{CCR}}\left|\frac{p_{0c}}{p_{\text{atm}}}\right.$ was known from tests carried out in the Coolant Capacity Rig (CCR), and compared to the coolant capacity measured in the Sector leak test $\dot{m}_{c,\text{Venturi}}\sqrt{T_{0c}}/p_{0c}$. It was assumed that the driving pressure ratio and upstream total temperature and pressure were the same for both vane and leaks during the leak test, and therefore the leak area was estimated using:

$$A_{\text{leak}} = \frac{\dfrac{\dot{m}_{c,\text{Venturi}}\sqrt{T_{0c}}}{p_{0c}} - \Gamma_{\text{CCR}}\left|\dfrac{p_{0c}}{p_{\text{atm}}}\right.}{\sqrt{\dfrac{2\gamma}{R(\gamma-1)}\left[\left(\dfrac{p_{0c}}{p_{\text{atm}}}\right)^{-\frac{2}{\gamma}} - \left(\dfrac{p_{0c}}{p_{\text{atm}}}\right)^{-\frac{\gamma+1}{\gamma}}\right]}}, \tag{5.44}$$

where p_{0c} is the total coolant pressure in the manifold, p_{atm} is atmospheric pressure and T_{0c} is the coolant total temperature. The total coolant capacity measured in the CCR is compared to that

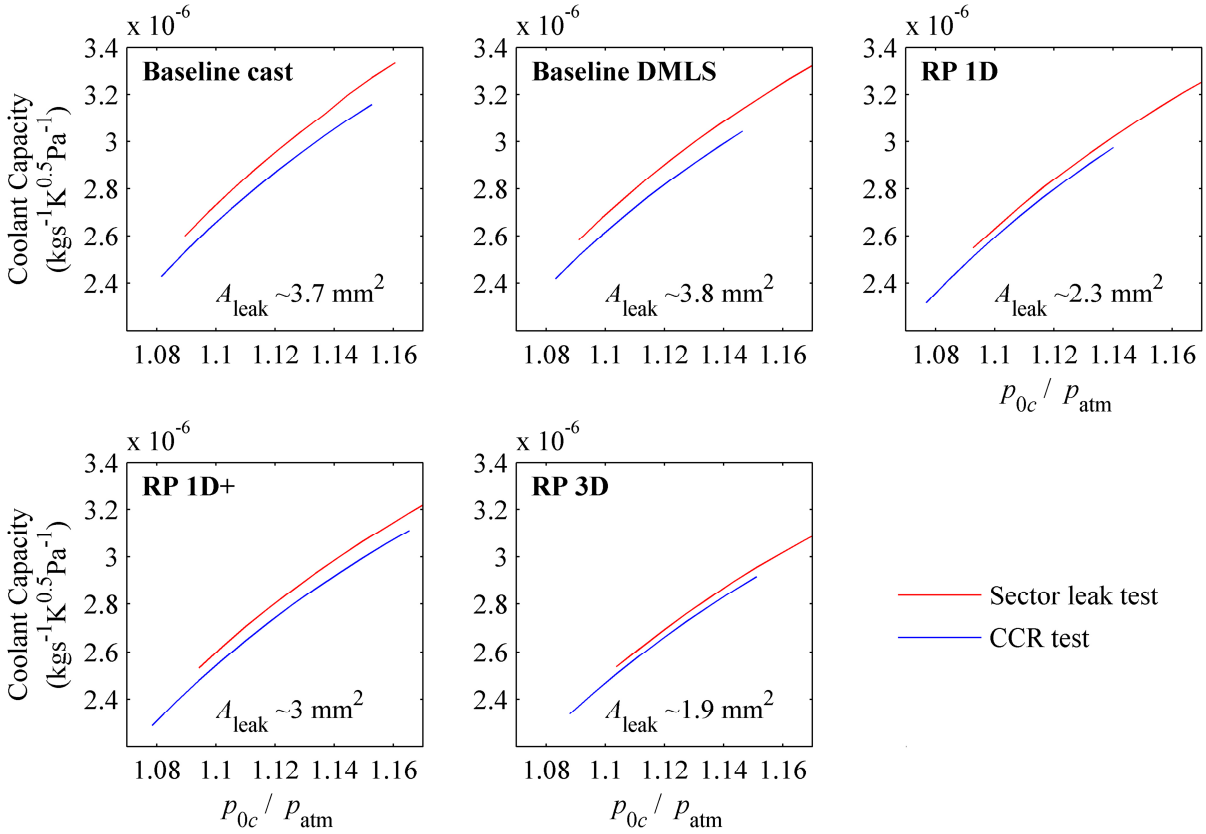


Figure 5.34. Coolant capacity measured in CCR and Sector Facility. Difference due to leaks in Sector.

measured in the Sector Facility leak test in Fig. 5.34, for each design. It can be seen that the coolant capacity measured in the Sector is greater than the CCR measurement due to leaks. The difference between the capacity curves is proportional to the leak area, according to equation (5.42). The effective leak area for each design is recorded in Fig. 5.34.

The in-situ leak test estimates the total effective area of the leak, but gives no indication of the number or location of the leaks. Without this information, it is impossible to calculate the leakage mass flow rate when the Sector Facility is operating at nominal conditions because the driving pressure ratio in equation (5.42) is unknown. The leakage may be between the coolant feed and atmosphere, and/or between the coolant manifolds and the mainstream. The driving pressure ratio was known in the in-situ leak test because the vane and leaks all exhausted to atmosphere and the coolant feed operated at a single pressure.

As a compromise, the *maximum possible leakage mass flow rate* during nominal Sector operation was estimated by assuming the greatest possible driving pressure ratio across the leak. This occurs between the coolant feed and atmosphere at approximately $p_{0c}/p_{\text{atm}} \sim 3.5$, in which case the leak is choked. The error in the coolant-to-mainstream mass flow ratio due to the maximum possible leak was then estimated using:

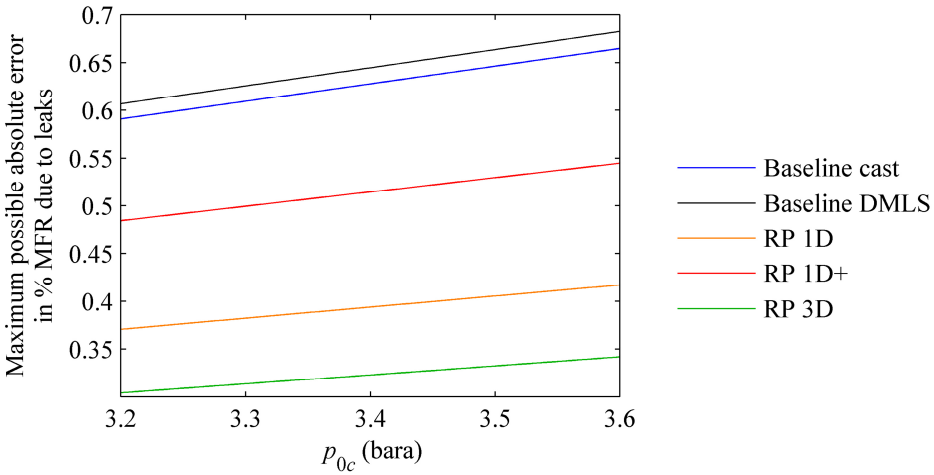


Figure 5.35. Maximum possible leakage mass flow rate / mainstream mass flow rate per passage.

$$\Delta\left(\frac{\dot{m}_{\text{leak}}}{\dot{m}_m}\right) = A_{\text{leak}} \frac{p_{0c}}{\dot{m}_m\sqrt{T_{0c}}}\sqrt{\frac{\gamma}{R}}\left(\frac{\gamma+1}{2}\right)^{-\frac{\gamma+1}{2(\gamma-1)}}. \tag{5.45}$$

The absolute error in coolant-to-mainstream mass flow ratio caused by the *worst possible* leak is plotted in Fig. 5.35 for each design, as a function of the coolant total pressure. These data define the magnitude of the *leakage error bars* in the $\left(\dot{m}_c\sqrt{T_{0c}}\right)/\left(\dot{m}_m\sqrt{T_{0m}}\right)$ vs. overall cooling effectiveness plots in the following chapter. It must be noted that the worst case is very unlikely since leaks between the coolant feed system and atmosphere are relatively easy to detect and fix. It is more likely that the leak occurs between the coolant manifold and the mainstream.

5.9 Proposed Improvements to Ease Reconfiguration and Operation

Ex-situ assembly of vane cassette layer, upstream layer and sidewall layer. The bolt arrangement for the vane cassette layer, the layer immediately upstream of the vane cassette layer, and the sidewall layer could be re-designed so they can be bolted together outside of the Sector Facility and then installed onto the back of the Sector as a single, triple-layer assembly. This would mean that both upstream and downstream sides of the triple-layer assembly are accessible when silicone-sealing the vanes into the coolant manifold—presently only the downstream side is accessible. This would result in a more reliable and less flow-intrusive seal. The coolant capacity leak test could then be performed out of the Sector Facility, with the advantage that leaks could be identified and rectified more easily.

Intermediate thermocouple station within coolant manifold. Presently, the vane cassette thermocouples exit the layer through two small open-top channels which are potted with silicone sealant to prevent leaks. The channels must be cleared of sealant and re-potted when changing the vane geometry. This process poses a number of risks: the wires may escape the channel during assembly (if the sealant has not set), becoming trapped between metal layers; the wires may break when sealant is removed from the channel; the channel may still leak, even after potting. These risks

could be reduced by introducing an intermediate thermocouple plug station within the coolant manifold. The leads between the intermediate station and the outside of the facility could then be sealed permanently through a drilled hole rather than temporarily-sealed in an open-top channel.

CNC manufacture of extreme vane pairs and sidewalls. Real, cast RR Trent 500 HPNGVs pairs (filled with polyamide adhesive) are used for the two extreme vane pairs. Three main difficulties arise from using real geometries in these positions: sealing into the coolant manifold; transitioning smoothly between the trailing-edges of the extreme vanes and the downstream contoured sidewalls; transitioning between the leading-edges of the extreme vanes and the upstream sidewalls. Since neither extreme vane pair is cooled in the current configuration, it may be possible to remanufacture uncooled versions with CNC which replicate the important features (i.e., aerodynamic shape) while simplifying and consolidating the internal sealing faces and the transition to the upstream/downstream sidewalls. This would also give greater flexibility to design a trailing-edge/contoured sidewall transition that further improved periodicity.

Heater mesh health monitoring system. It may be useful to record the temperature of the heater mesh bus-bars and terminals during service, as this may reveal patterns that indicate heater mesh life-expectancy. This information could then be used to decide when to prepare mesh replacements or to modify the run procedure (e.g., time between runs or power) to eke out further runs. Currently, the temperature of the heater mesh terminals is measured between runs with embedded, mineral insulated, K-type thermocouples and a handheld temperature indicator. The thermocouples were not connected to the data acquisition system for fear of mineral insulation failure and unwanted electrical surges. An optically-isolated thermocouple would remove this risk.

Spare heater mesh assembly. A spare heater mesh assembly would reduce the delay caused by mesh failure.

Pilot regulator. The Sector Facility currently shares a pilot regulator with the Profile Generator Rig. A Sector-dedicated pilot regulator would give the Sector Facility greater running autonomy.

Variable orifice diameter assembly. Currently, orifice plates have to be changed in order to control coolant mass flow rate, involving the removal of certain sections of pipework. Installing some kind of assembly in which the orifice diameter can be altered in-situ (i.e., without having to remove any pipework) would improve turn-around time.

New Venturi nozzle. The 8.28 mm diameter Venturi nozzle is unchoked at certain coolant mass flow rates. A new Venturi nozzle with a smaller diameter could be purchased so that the nozzle is always choked.

Increase number of trained operators. Run frequency can be increased by increasing the number of trained running partners.

Simplify instrumentation. During reconfiguration, the pressure tubing must be disconnected from the Sector Facility. A new assembly that simplifies connection/reconnection of tubing would decrease turnaround time.

Testing new heater mesh materials. The heater mesh is currently manufactured from stainless steel. There may be a way to treat the heater mesh beforehand (e.g., oxidising with a blowtorch) that may increase heater mesh life; or alternatively, there may be other materials that are better suited to the purpose.

5.10 Conclusions

The Annular Sector Heat Transfer Facility is used to perform the equivalent of the thermal paint test at laboratory conditions. In this chapter, an overview of the hardware and operating conditions of the facility has been given. Modifications since the experiments of Luque Martinez (2011) have been reported, summarised as:

- Laser-sintered middle vane pair
- New infra-red hardware, software, and calibration techniques
- Different heater mesh specification tested
- Overall cooling effectiveness over a range of coolant mass flow rates and temperatures
- Coolant mass flow rate controlled and measured using orifice/Venturi combination
- In-situ leak test performed before each test campaign
- New regulator
- New data acquisition hardware
- Lab-wide upgrade to Drake power supply system
- New burst disk specification
- Deswirl vanes remanufactured from aluminium
- New suction side zinc-selenide window
- All vanes other than the vane of interest blocked

Additionally, the non-dimensional groups governing vane temperature have been estimated. From this analysis, the absolute accuracy of the Sector overall cooling effectiveness measurement is estimated at 15%. The precision of the measurements is approximately 2% (Luque Martinez, 2011).

6. Infra-Red Thermography

In this chapter, the IR thermography techniques used in this thesis are described. A novel, physically based infra-red thermography method is used to measure and compensate for time-varying surrounding radiation, increasing the accuracy of the wall temperature measurement (eliminating a possible absolute error in overall cooling effectiveness of 0.05). Updates to the IR hardware and software in the Sector Facility are discussed.

6.1 Introduction

The use of infra-red thermography for turbomachinery heat transfer experiments has become widespread in recent years. IR hardware and software are increasingly affordable, and the spatial/temporal resolution of IR is now on a par with other full-coverage thermographic techniques (e.g., thermo-chromic liquid crystals, temperature sensitive paint). IR thermography is attractive because it is non-intrusive, full-coverage, reliable, versatile, fast-response and because relatively few calibrations are required for reasonably accurate temperature measurement. Increased PC processing power has now simplified data acquisition—gigabytes of IR video can be recorded from a single test without incident. For these reasons, IR thermography is used to measure the vane wall temperature distribution in the Annular Sector Heat Transfer Facility.

Although IR thermography avoids many of the complications associated with other full-coverage thermographic techniques, there are several complexities unique to radiometric measurement. The main factors affecting IR temperature predictions are summarised as: (a) conversion of the radiometric measurement to an equivalent black-body temperature; (b) the transmittance of IR wavelengths through any external optics between the camera and the object of interest; (c) the surface emissivity of the object of interest and its surroundings as a function of viewing angle and position; (d) the temperature of the surroundings.

The Planck-like correlation of Martiny et al. (1996) and the linearised approximation of Wang et al. (2003) are two commonly used methods to correlate radiance measurements with black-body temperature. Astarita et al. (1995) deduced the emissivity of the test section by placing an additional, small black-body inside the test facility. The temperature of the black-body and grey-body were recorded with embedded thermocouples, and then compared to the IR camera measurements to deduce surface emissivity. The transmittance of the windows is usually considered to be accounted for by the calibration techniques described above (e.g., Sweeney and Rhodes, 2000).

Ambient reflections are normally ignored, or assumed to be accounted for by other calibrations. Notable exceptions are Ding (1985), Luque Martinez (2011) and Lawson et al. (2013). Ding (1985)

used a ray-tracing program to calculate the reflections within a linear cascade. Luque Martinez (2011) estimated the ambient reflections by running experiments at different mainstream temperatures and calculating the per-run surrounding radiance that minimised standard deviation in overall cooling effectiveness. Lawson et al. (2013) used a combination of physically based in-situ and ex-situ calibration methods to estimate the emissivity, reflectivity and surrounding radiance. Novelly, surrounding radiance is measured for each run and takes into consideration variation in mainstream temperature.

6.2 Infra-Red Hardware and Data Acquisition Software

Suction-side and pressure-side thermographic data are now acquired simultaneously using two FLIR A655sc infra-red cameras, purchased from Thermal Vision Research Ltd. The pressure-side IR camera is fitted with a 13 mm, 45° lens and the suction-side IR camera with a 24.5 mm 24° lens to take into account the variation in object distance and size between the SS and PS field of view. Two spare lenses (13 mm and 24.5 mm) were also acquired for flexibility. The attachment positions of each camera are shown in Figs. 6.1 and 6.2.

Each camera is connected to its own dedicated PC with a GigE connection and an Intel Pro/1000 GT desktop adapter card for high data transfer rates. FLIR ResearchIR 3.4 software is used to configure each camera (e.g., focus position, ambient drift compensation, trigger settings, sample rate etc.), to acquire and save thermographic video, and to export frames/points of interest. Data acquisition within FLIR ResearchIR 3.4 is triggered by a LabView script operating on the master PC. When initiated, the LabView script uses VISA protocol to activate two serial communication ports: a virtual serial communications port within the master PC (created using the com0com null modem emulator freeware) and a physical serial communications port connected to the slave PC via an RS 232 cable and null-modem adapter. Each FLIR ResearchIR instance is then configured to activate/deactivate on instruction from the virtual (master) or physical (slave) serial com port.



Figure 6.1. PS IR camera in-situ.



Figure 6.2. SS IR camera in-situ.

The LabView script simultaneously acquires pressure and temperature data from the National Instruments PXI 1050 chassis. The chassis uses an NI PXI 8360 MXI-Express card to link to the master PC, an NI PXI-6031E Multifunction I/O card to link to the Sensortechnic pressure transducers, and an NI SCXI-1102B card to condition temperature signals from an NI TC 2095 module.

The IR cameras are configured to record the entire run duration (180 seconds) at 12.5 Hz. FLIR ResearchIR software is used to extract and export (in .mat format) the equivalent black-body temperature maps $T_{bb}(\boldsymbol{x})$ of the last 6 frames of the heated period. MATLAB is used to average these frames and to apply the black-body calibration and emissivity/reflection corrections (grey-body parameters) in order to estimate the vane temperature $T_w(\boldsymbol{x})$. The grey-body correction is discussed later. Typical black-body temperature maps acquired at the end of the heated period are shown in Figs. 6.3 and 6.4.

6.3 Surface Thermocouples

In addition to the IR thermographs, wall temperature is also measured by two Omega K-type 0.013 mm Cement-On (style 2) foil thermocouples, located on the external SS and PS surfaces of vane 5 (positions shown in Figs. 6.3 and 6.4). The thermocouple measurements are used for black-body and grey-body calibrations, discussed later. Vane 5 was chosen as the location of the surface thermocouples for the following reasons.

Vane 5 is uncooled, and therefore surface temperature variation around the thermocouple is low, which is beneficial for comparison to thermographic data. Vane 5 also has a layer of thermal barrier coating (TBC). TBC is an electrical insulator, so that the foil thermocouples are floating (i.e., not connected to ground). This eliminates any cross-talk between thermocouples that would be present if connected to a common ground. The NI TC-2095 is thus configured for floating signals.

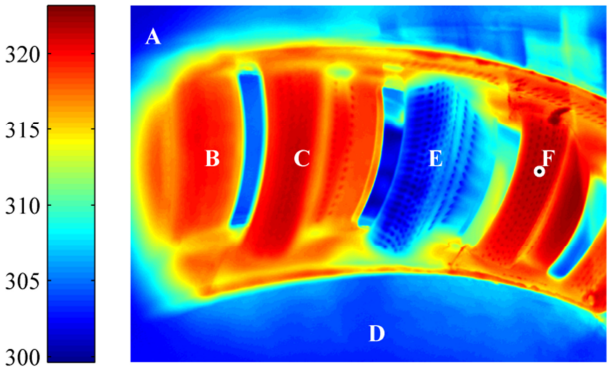


Figure 6.3. Typical PS black-body temperature (K) recorded during Sector run.

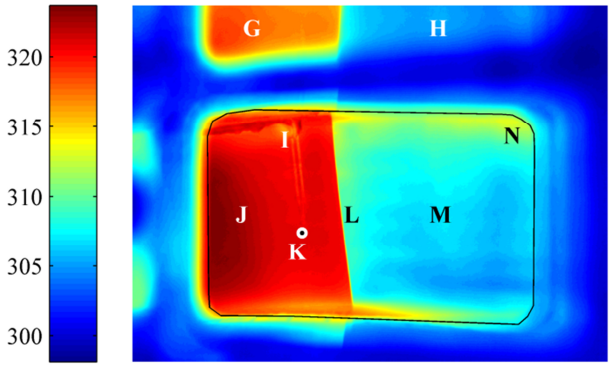


Figure 6.4. Typical SS black-body temperature (K) recorded during Sector run.

A = outside of circular ZnSe window FOV; B = vane 2, uncooled, trailing-vane in leading pair; C = vane 3, uncooled, leading-vane in middle pair; D = combustor annulus profile; E = vane 4, vane of interest, cooled, trailing-vane in middle pair; F = thermocouple location; G = reflection of vane 5 (uncooled) in unpainted Al window housing; H = reflection of vane 4 (cooled) in unpainted Al window housing; I = thermocouple leads; J = vane 5, uncooled; K = thermocouple location; L = trailing-edge of vane 4, vane of interest; M = vane 4, cooled vane; N = ZnSe window.

Whereas the middle vane pair must be removed, cleaned and reconfigured between test campaigns, the trailing vane pair (vane 5 and 6) is relatively untouched during reconfiguration. Vane 5 is in view of both IR cameras, and is located at a viewing angle similar to the vane of interest to reduce discrepancies in grey-body parameters between vane 5 and vane 4. Furthermore, locating the thermocouples on the vane of interest would reduce the amount of useful data that could be extracted due to spoiling around the thermocouple.

Vane 4 and vane 5 are painted identically and are angled similarly to the camera, reducing differences in effective emissivity. It was seen as reasonable to apply the results of the grey-body calibrations—which are calculated using the thermocouples on vane 5—to the vane of interest. The grey-body calibrations are described in detail later.

6.4 Selection of High Emissivity Paint

The vanes are coated with high emissivity paint in order to reduce the impact of ambient reflections on the camera radiometric measurement. Two paints were tested: RS Acrylic Matt Black aerosol spray paint, nominal emissivity = 0.92 - 0.97 (FLIR, 2012a); and NEXTEL Velvet Coating 811-21, nominal emissivity > 0.97 (Kwor and Mattei, 2001). Coated vanes are shown in Fig. 6.5. The RS Matt Black spray offered a number of key advantages over the NEXTEL Velvet Coating, and was subsequently used for all tests. An evaluation of the two paints tested now follows.

The RS Matt Black paint was applied as a single coat using a continuous mist of 10 or more passes at a distance of 0.5 m. A heat gun was used to dry the paint. The roughness of the painted surface was visually and tactilely similar to smooth SS thermal barrier coating (Fig. 6.6). In contrast, the application of the NEXTEL paint was far more complex and time consuming. The NEXTEL coating had to be applied in multiple stages with NEXTEL Primer 5523 and NEXTEL Thinner 8061. The result was visually and tactilely similar to rough PS thermal barrier coating (Fig. 6.6).

It was found that the NEXTEL paint tended to block the film cooling holes more than the RS Matt Black spray, since the resultant NEXTEL coating was much thicker that the RS coating. No apparatus was available to blow through the vane while painting, and so the holes were manually cleaned out using a drill bit. The effectiveness of this cleaning was doubtful.

Additionally, it was difficult to apply the NEXTEL coating uniformly to the vane of interest, especially on the early SS where access was difficult due to the proximity of the leading vane in the middle vane pair (vane 3). This resulted in exaggerated surface roughness on the early SS compared to the rest of the vane. This problem did not occur with the RS Matt Black spray. Figure 6.7 shows the IR black-body temperature measurements of two similar (but not identical) laser sintered vanes that were tested in the Sector Facility, painted with RS Matt Black and NEXTEL velvet paint, respectively. The colour scale is chosen to enhance contrast of the roughness effects. A bobble effect

is evident on the early SS of the NEXTEL coated vane, where surface roughness is greater. On average, the measured black-body temperature is grainier across the NEXTEL coated vane than the RS spray painted vane due to increased surface roughness.

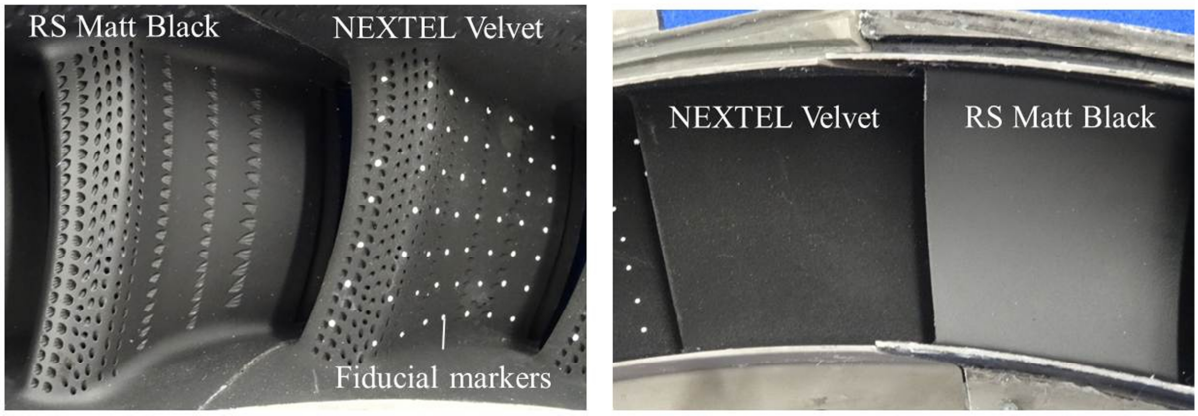


Figure 6.5. PS and SS of NEXTELVelvet and RS Matt Black coated vanes.

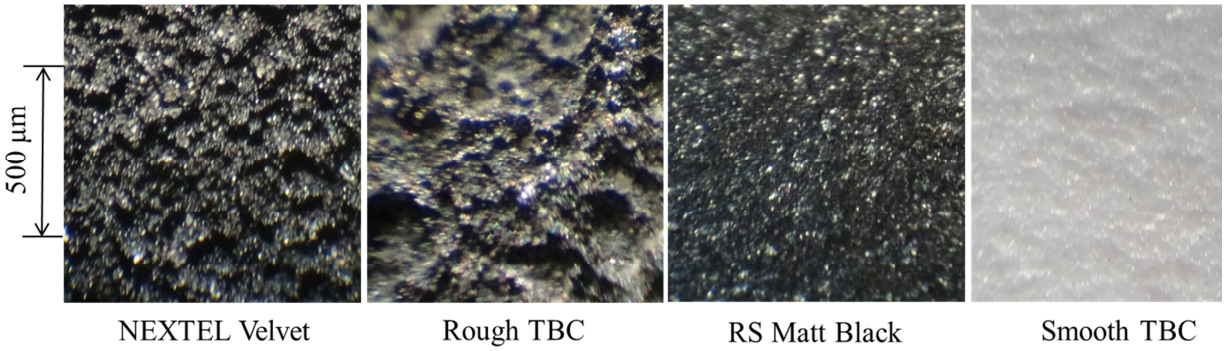


Figure 6.6. Microscopic comparisons of high emissivity paints with rough/smooth TBC.

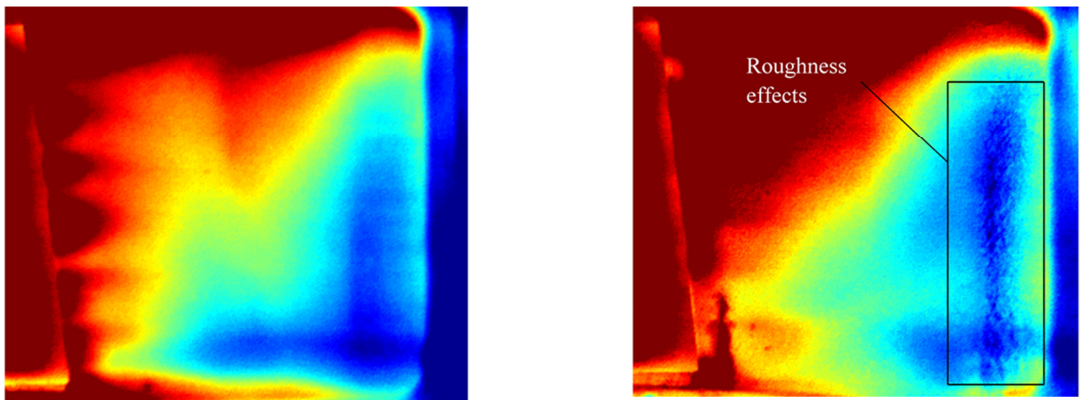


Figure 6.7. Black-body temperature of SS during standard Sector test.
(L) Vane painted with RS Matt black paint. (R) Vane painted with NEXTEL velvet paint. Different geometries tested, colour scale chosen to increase contrast of roughness effects.

The influence of paint-induced surface roughness on the overall cooling effectiveness of the vane was not assessed. It may be that increased surface roughness is associated with increased external heat transfer coefficient (HTC), in which case the rig Biot number, as designed, would deviate from the engine Biot number. On the other hand, increased external HTC may help to match the rig and engine internal/external HTC ratio—since the laser-sintering process creates rougher internal passages and possibly greater internal HTC. Moreover, surface roughness in the engine depends on age and position around the vane. The paints could be used to predict overall cooling effectiveness at different points in engine life.

Without further study of the complex scaling space, RS Matt black paint was chosen because it was easier to apply. This was seen as acceptable given the comparative nature of the tests. The lower emissivity of the RS Matt black paint was compensated for by a comprehensive grey-body correction, discussed in detail later.

6.5 Infra-Red Thermography Theory Overview

Converting the fundamentally radiometric measurement made by an IR camera into a value of surface wall temperature is non-trivial. It requires knowledge of both the camera hardware (black-body calibration) and the object and its surroundings (grey-body calibration). Both must be accounted for accurate wall temperature measurement. Before discussion of the black- and grey-body calibrations, the general theoretical basis of infra-red thermography is outlined.

The FLIR A655sc 13 mm/45° infra-red camera uses a focal plane array (FPA) of 640 x 480 microbolometers to infer the incident infra-red radiation (7.5-14 μm) from the voltage across the detectors. The electrical resistance of the microbolometers is a function of temperature, which is a function of the incident electromagnetic (EM) radiation. The camera software applies offset compensation, 16 bit A/D conversion, gain compensation and a non-uniformity correction factor to normalise the voltage readings across the FPA to compensate for variation in pixel electronic characteristics, FLIR (2012b). The radiation emitted from the camera is also detected by the microbolometers—the camera continually monitors the internal temperature and sends feedback to the camera processor which then corrects for these *parasitic* radiation influences. This process is often referred to as ambient drift compensation (ADC).

The resultant pixel raw digital count $R(\boldsymbol{x})$ ($\boldsymbol{x}$ is the pixel location in the FPA and is used interchangeably with the position on the object of interest in the FOV) is between 0 – 65,535 (16 bit) and is approximately linear with incident infra-red radiance $q_{\mathrm{cam}}(\boldsymbol{x})$ in the spectral band 7.5-14 μm and for radiances of 450-650 $\mathrm{Wm^{-2}sr^{-1}}$:

$$q_{\mathrm{cam}}(\boldsymbol{x}) = \sigma {T_{bb}}^4(\boldsymbol{x}) = aR(\boldsymbol{x}) + b, \tag{6.1}$$

where a and b are constant for a given camera across the entire FPA, and $T_{bb}(\boldsymbol{x})$ is the equivalent black-body temperature, i.e., the temperature of an ideal black-body required to generate the same level of incident infra-red radiation. In this thesis, $T_{bb}(\boldsymbol{x})$ is used rather than the incident infra-red radiance $q_{\mathrm{cam}}(\boldsymbol{x})$ to simplify checks.

The equivalent black-body temperature $T_{bb}(\boldsymbol{x})$ can be used to estimate the temperature $T_w(\boldsymbol{x})$ of the object in the field of view (FOV). It is common to assume that the emissivity of the object is independent of wavelength and direction, and no radiation is transmitted through the object, i.e., a grey, opaque body with a diffuse surface. For this kind of object the absorptivity α is equal to the emissivity ε of the surface (Kirchhoff's Law). The assumption of an opaque, grey surface is reasonable in the spectral band (7.5-14 μm) and for painted metallic test objects. The assumption that the surface is diffuse (emissivity the same in all directions) breaks down at large viewing angles. Kirchhoff's Law, the definitions for emissivity and transmittance, and the Stefan-Boltzmann Law for the total radiated energy from a black-body, are commonly related by equation (6.2) to estimate the temperature of the object $T_w(\boldsymbol{x})$ from the black-body temperature measurement $T_{bb}(\boldsymbol{x})$.

$$T_{bb}{}^4(\boldsymbol{x}) = \varepsilon\tau T_w{}^4(\boldsymbol{x}) + (1-\varepsilon)\tau T_R{}^4 + (1-\tau)T_{\mathrm{atm}}{}^4. \tag{6.2}$$

where τ is the atmospheric transmittance, T_{atm} is the atmospheric temperature, and T_R is the effective temperature of the object's surroundings (not to be confused with the recovery temperature T_r), assuming a surrounding emissivity of 1 (reflected ambient background temperature).

The parameters that must be known or calibrated for accurate infra-red thermographic measurements can be split into two types:

(1) Black-body parameters a and b. Functions of the camera hardware, which affect the equivalent black-body temperature. Can be calibrated in-situ or ex-situ. May or may not need grey-body parameters to calculate black-body parameters.
(2) Grey-body parameters ε, τ, T_R and T_{atm}. Functions of the objects and temperatures within the camera environment, affecting the estimation of the object temperature. T_R and T_{atm} can be measured directly or found through calibration; values of ε and τ can be taken from literature or found through calibration. Values must be calibrated in a similar environment to the test section (ideally in-situ); black-body parameters must be known.

While an isothermal calibration is ideal for estimating black-body parameters, it cannot be used to evaluate grey-body parameters—since equation (6.2) is independent of grey-body parameters when $T_w = T_R = T_{\mathrm{atm}}$. On the other hand, non-isothermal test conditions (i.e., the object temperature, reflected temperature and atmospheric temperature are sufficiently different) are ideal for grey-body calibration.

The following sections detail the methods/results of the black-body and grey-body calibrations of the Sector Facility cameras. In summary, an isothermal, black-body calibration is performed in the Sector Facility and compared to the factory calibration. The factory-calibrated black-body temperature agrees with the laboratory-calibrated black-body temperature to within 0.3 K. The laboratory black-body calibration is used in this study. A *bi-thermal* calibration is used to estimate the product of transmittance and emissivity, and the surrounding radiance is measured instantaneously using the thermographic/thermocouple data from a surrogate surrounding radiance correction vane. Accounting for reflections in this way can change the overall cooling effectiveness prediction by as much as 0.05—approximately 50 K difference in the predicted engine wall temperature.

6.6 Black-Body Calibration Theory

The aim of a black-body calibration is to determine the camera hardware coefficients a and b in equation (6.1). There are two common black-body calibration methods.

(1) *Cavity-type black-body calibration*. The IR camera observes the inside of an isothermal cavity, usually cylindrical, conical or spherical in shape. The temperature of the isothermal enclosure T_w and the IR raw count R are recorded. Equations (6.1) and (6.2) reduce to:

$$\sigma {T_{bb}}^4(\boldsymbol{x}) = \sigma {T_w}^4(\boldsymbol{x}) = aR(\boldsymbol{x}) + b, \tag{6.3}$$

which is independent of grey-body parameters for a perfect isothermal enclosure. The temperature of the isothermal cavity is varied and the coefficients a and b found by regression. This method of calibration is especially useful for in-situ calibrations where the emissivity of the surfaces is unknown.

(2) *Hot-plate black-body calibration*. The IR camera observes a flat, temperature-controlled hot-plate. The hot-plate has a very high emissivity (e.g., two layers NEXTEL Velvet Coating). The calibration usually takes place in an environment without hot external radiation sources, so that the reflected radiation T_R is approximately equal to the ambient temperature T_{amb}. The flat-plate temperature T_w, ambient room temperature T_{amb} and IR raw count R are measured over a range of hot-plate temperatures. Equations (6.1) and (6.2) reduce to:

$$\sigma {T_{bb}}^4(\boldsymbol{x}) = \sigma\varepsilon\tau {T_w}^4(\boldsymbol{x}) + (1-\varepsilon\tau)\sigma {\mathrm{T}_{\mathrm{amb}}}^4(\boldsymbol{x}) = aR(\boldsymbol{x}) + b, \tag{6.4}$$

The coefficients a and b are then found by regression. Hot-plate calibrators are generally cheaper and less cumbersome, but require knowledge of the surface emissivity, atmospheric transmittance and the ambient temperature.

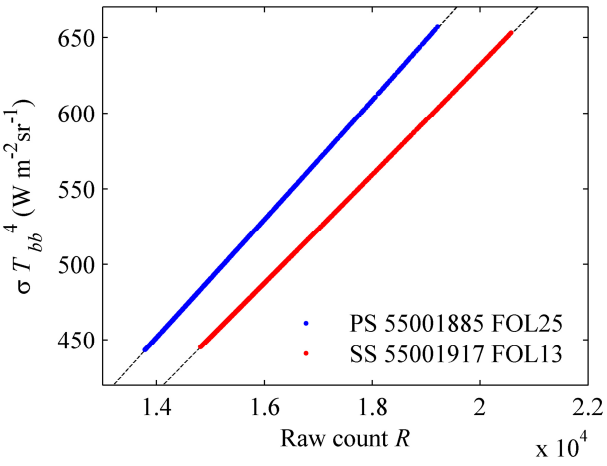


Figure 6.8. Raw count R vs factory-calibrated incident radiance $\sigma T_{bb}{}^4$. Every pixel plotted.

The FLIR A655sc IR cameras are calibrated in-factory using a combination of methods to a quoted accuracy of ±2°C or ±2% in black-body temperature, over the range -20 – 650 °C (FLIR, 2014). The black-body calibration is then stored within the camera hardware. The factory calibration was inferred by exporting both the equivalent black-body temperature $T_{bb}(\boldsymbol{x})$ and the raw count $R(\boldsymbol{x})$ from each camera during the in-Sector isothermal black-body calibration (discussed in detail later). The black-body calibrations for every pixel on the pressure-side (PS) A655sc IR camera (serial number 55001885, 25 mm lens) and suction-side (SS) A655 sc IR camera (serial number 55001917, 13 mm lens) are plotted in Fig. 6.8.

It can be seen that there is negligible variation in the factory black-body calibration across the FPA within a given camera, but there is a large difference in calibration between cameras. This may be due to the difference in lens and focal position. The incident radiation $\sigma T_{bb}{}^4$ is almost perfectly linear with raw count R. The factory black-body calibration regressions are given below.

PS 55001885 FOL 25: $$\sigma T_{bb}^4 = 0.0394\ R - 100.8 \tag{6.5}$$

SS 55001917 FOL 13: $$\sigma T_{bb}^4 = 0.0361\ R - 89.6 \tag{6.6}$$

The factory black-body calibration is now compared to the black-body calibration performed in the Sector Facility.

6.7 In-Situ Black-Body Calibration

To test the validity of the factory black-body calibration, a cavity-type black-body calibration was performed in the Sector Facility. The Sector Facility lends itself to a cavity-type calibration as it is completely enclosed but contains many surfaces of differing and unknown emissivity. The rig was heated to 65 °C (limited by the maximum operating temperature of Araldite) over the course of 8 hours. Heating was achieved by bleeding pressurised air from a 100 psi line through a small heater

mesh into the coolant manifolds. The heater mesh was powered by the Drake power supply system, set to 20 V. One positive 185 mm^2 lead and one negative 185 mm^2 lead were connected to the heater mesh. The unused leads (normally used when powering the Sector heater mesh) were isolated. The Sector mainstream feed was blanked.

The rig was then allowed to cool naturally over 18 hours. The facility was covered in bubble-wrap to slow down the rate of cooling and to improve facility temperature uniformity. Surface temperature was measured by two Omega K-type 0.013 mm Cement-On (style 2) foil thermocouples, located on the PS and SS. The thermocouple temperatures during the cooling leg are shown in Fig. 6.9. The factory-calibrated black-body temperature of a point next to each thermocouple is plotted during the cooling leg in Fig. 6.10. The IR cameras, placed in their nominal operating positions (SS and PS), recorded factory-calibrated black-body temperatures—shown at 5 hours in Figs. 6.11 and 6.12. All data were acquired at 0.02 Hz.

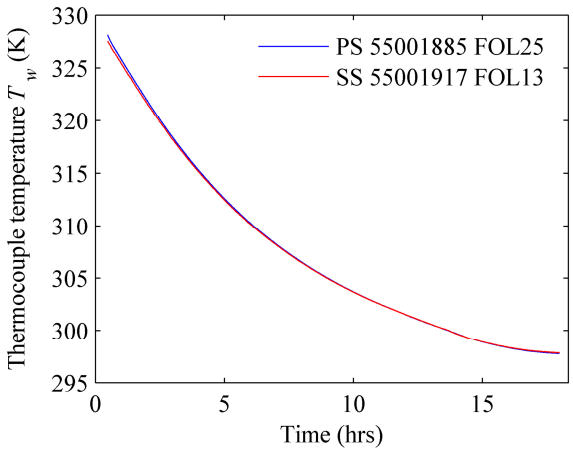


Figure 6.9. PS and SS thermocouple temperatures T_w (K) during Sector black-body calibration.

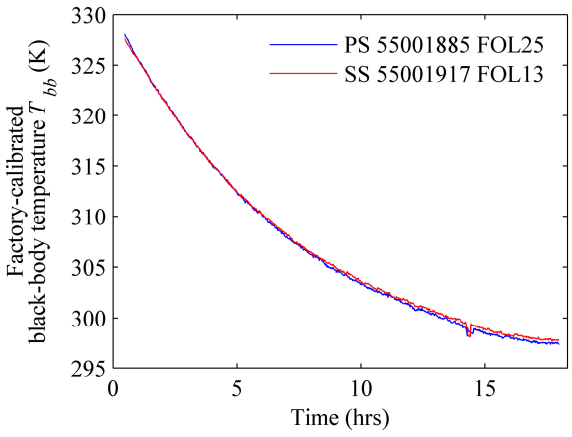


Figure 6.10. Factory-calibrated black-body temperature T_{bb} beside thermocouples during Sector black-body calibration.

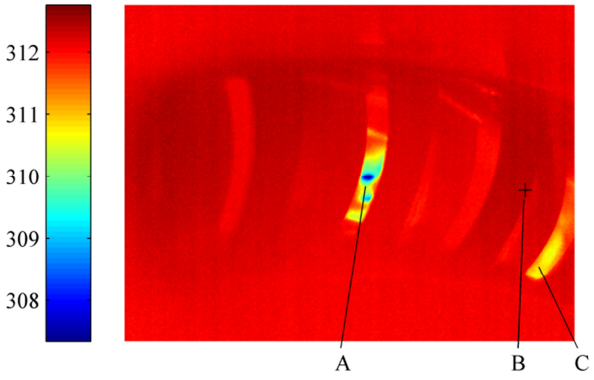


Figure 6.11. Black-body temperature (K) of PS at 5 hrs, viewed with A655 sc 55001885 FOL 25.
A & C = non-isothermal deswirl vanes. B = thermocouple location.

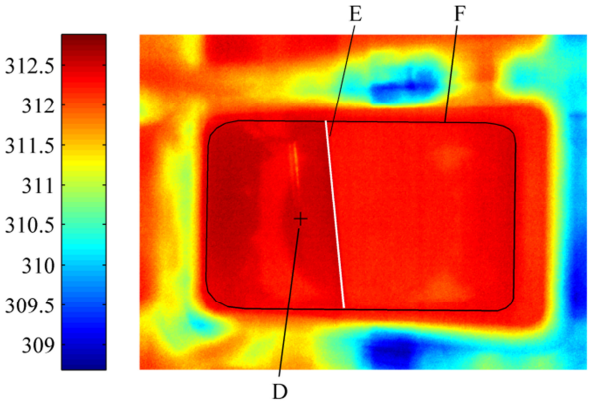


Figure 6.12. Black-body temperature (K) of SS at 5 hrs, viewed with A655 sc 55001917 FOL 13.
D = thermocouple location. E= trailing-edge of vane of interest. F = boundary of region of interest.

Quasi-isothermal conditions—and therefore black-body conditions—were achieved between 55 °C and 25 °C during the cooling leg, within the region of interest (ROI). The PS ROI is defined as the entire FOV except the regions marked A and C in Fig. 6.11. Downstream de-swirl vanes are located in areas A and C and are apparently colder, but are far enough away from the ROI as to have negligible effect on the black-body temperature in the ROI. The SS ROI is defined as everything within boundary F (Fig. 6.12). F marks the outline of the ZnSe window. Surrounding F are the walls of the unpainted window port within the aluminium housing. The apparent temperature of the region outside F is a function of: the through-wall temperature drop; the geometry of the aluminium housing around the window port; reflections originating from inside the test-section; reflections originating from the camera. It is assumed that the area outside of F had little impact on the black-body temperature within the ROI, given that the PS and SS black-body temperatures matched up closely (Fig. 6.9). The standard deviation in black-body temperature within the ROI is plotted in Fig. 6.13 as a function of time during the cooling leg. It can be seen that the standard deviation in black-body temperature across the ROI at any given time is never more than 0.25 K.

The accuracy of the factory calibration can be assessed by comparing the thermocouple temperature measurements T_w (Fig. 6.9) to the IR black-body temperature measurements T_{bb} (Fig. 6.10)—since they should be equal in an ideal cavity-based black-body calibration, equation (6.3). This comparison is shown in Fig. 6.14. The wall temperature T_w matches the factory-calibrated black-body temperature T_{bb} to within 0.3 K, lending confidence to the accuracy of the factory calibration. However, the black-body calibration drifts over time and so the laboratory in-situ calibration was preferred. Rather than correlate black-body temperature with raw count, it proved more convenient—and algebraically identical—to apply a linear correction to the factory-calibrated black-body temperature to the fourth power.

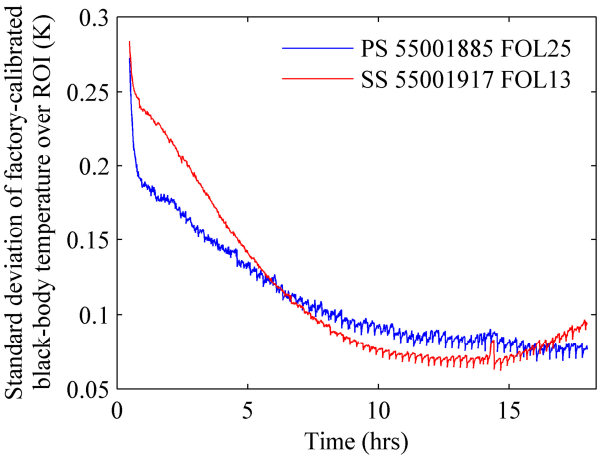


Figure 6.13. Standard deviation in factory-calibrated black-body temperature across the ROI during the cooling leg.

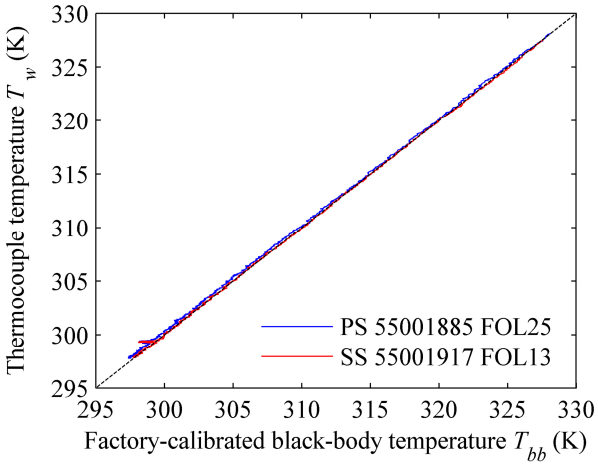


Figure 6.14. Thermocouple temperature vs factory-calibrated black-body temperatures. Black solid line is $\boldsymbol{T_w = T_{bb}}$.

PS 55001885 FOL 25: $$T^4_{bb,\text{laboratory}} = 0.9938\, T^4_{bb,\text{factory}} + 4.8829\ /\sigma. \quad (6.7)$$

SS 55001917 FOL 13: $$T^4_{bb,\text{laboratory}} = 0.9953\, T^4_{bb,\text{factory}} + 2.4276\ /\sigma. \quad (6.8)$$

The factory black-body temperature is output directly from FLIR ResearchIR 3.4 by setting the in-software emissivity and transmittance to 1, and is then corrected in post-processing according to the in-situ black-body calibration. This avoided the need to process raw count directly. Grey-body parameters are then applied in post-processing, and the wall temperature estimated. This is discussed in the following section.

6.8 Grey-Body vs Black-Body Predictions

The black-body calibration makes it possible to estimate the temperature of a black-body from the camera radiance measurement. However, the vane of interest cannot be modelled as a black-body during a standard Sector run because (a) the vane emissivity was not unity *and* the temperature of the surroundings was not equal to the vane temperature; (b) the transmittance of the ZnSe window was not unity *and* the temperature of the window was not equal to the temperature of the vane. (During the black-body calibration, the temperatures of the window, vane and surroundings were the same and so a black-body system could be assumed even though transmittance and emissivity were not unity). In order to estimate the vane temperature during a standard, non-isothermal run, the grey-body parameters—transmittance, emissivity and effective surrounding temperature—must be known in addition to the black-body calibration. The method used to estimate the grey-body parameters is discussed later.

The error of assuming a black-body as opposed to a grey-body is highlighted in Figs. 6.15 and 6.16. The 1st order best-fit in Fig. 6.15 and the 2nd order best-fit in Fig. 6.16 are to aid visualisation only and are not used in any analyses. The IR-predicted overall cooling effectiveness is shown at a representative point on the PS and SS of the vane of interest, for 37 runs at different coolant-to-mainstream mass flow ratios, using both black-body and grey-body approximations. The greatest difference between black- and grey-body predictions is around 0.05 on the PS at high mass flow rates, corresponding to an error in the predicted engine wall temperature of around 50 K, highlighting the need to take into account grey-body effects.

The grey-body approximation used in this thesis is now outlined. The theoretical basis of the approximation and its application to Sector-testing is discussed.

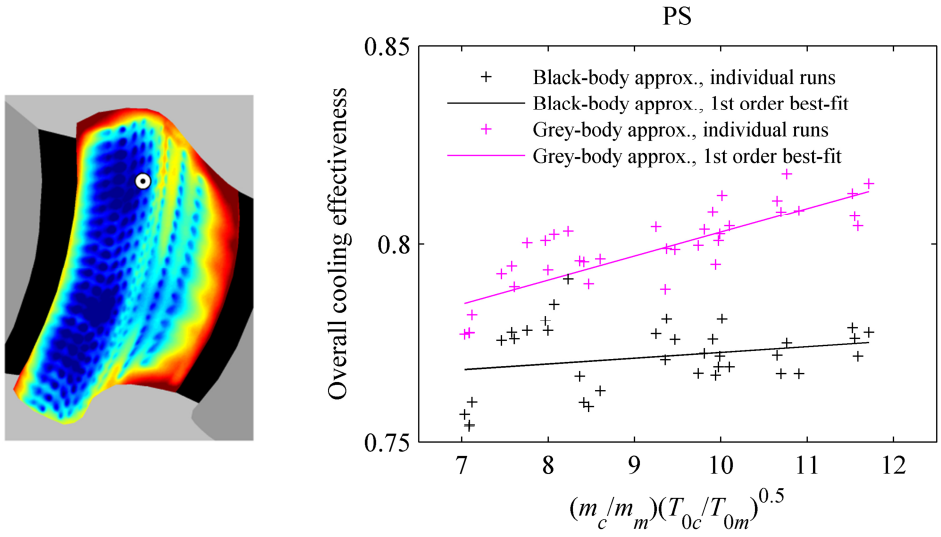


Figure 6.15. Representative point on PS of vane of interest, IR overall cooling effectiveness predictions using black-body and grey-body approximations.

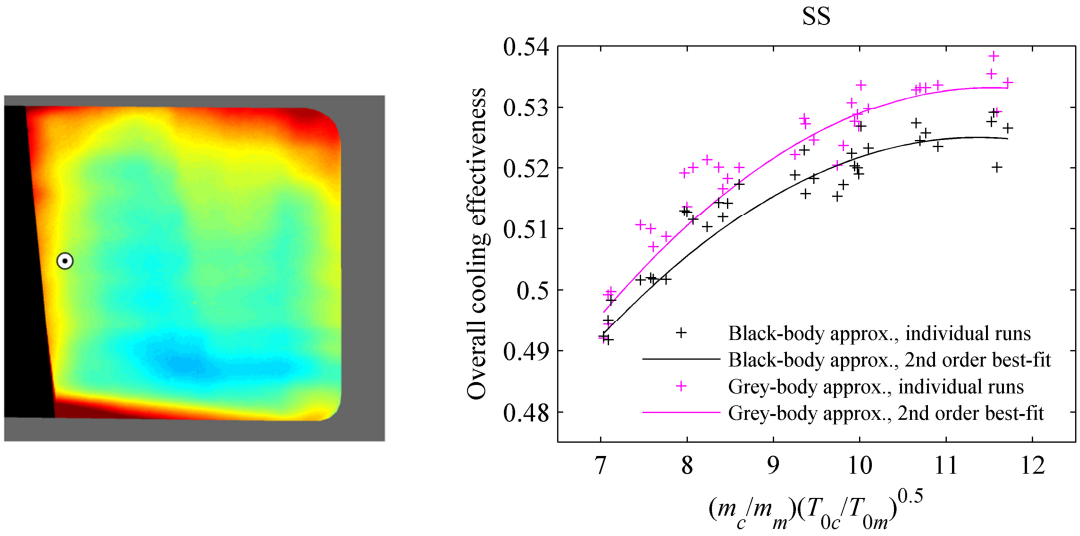


Figure 6.16. Representative point on SS of vane of interest, IR overall cooling effectiveness predictions using black-body and grey-body approximations.

6.9 Grey-Body Calibration Theory

During nominal operation in the Sector Facility, the camera-incident radiance $q_{\text{cam}}(\boldsymbol{x}, t)$ is the sum of the radiance due to the temperature of the vane of interest $q'_w(\boldsymbol{x}, t)$, the radiance due to the temperature of the surroundings $q''_R(\boldsymbol{x}, t)$ reflecting off the vane surface, and the radiance due to the temperature of the external optics (ZnSe window) $q_{\text{opt}}(t)$:

$$q_{\text{cam}}(\boldsymbol{x}, t) = q'_w(\boldsymbol{x}, t) + q''_R(\boldsymbol{x}, t) + q_{\text{opt}}(t). \tag{6.9}$$

Absorption and emission from the test gas are ignored since the transmittance of air at nominal humidity over small distances (< 0.5 m) is approximately unity (FLIR, 2012a). Stylised ray traces of

the camera-incident IR from one cooled vane (A) and one uncooled vane (B) within the Sector Facility during a typical run are shown schematically in Fig. 6.17.

From the camera radiometric measurement $q_{\mathrm{cam}}(\boldsymbol{x},t)$, we wish to estimate the wall temperature of the vane of interest $T_w(\boldsymbol{x},t)$. The individual terms in the equation above will now be analysed, which will set the physical basis for the grey-body calibration used in this thesis.

As previously discussed, the radiance measured by the camera can be redefined in terms of an equivalent black-body temperature $T_{bb}(\boldsymbol{x},t)$:

$$q_{\mathrm{cam}}(\boldsymbol{x},t) \equiv \sigma T_{bb}^4(\boldsymbol{x},t). \tag{6.10}$$

The camera hardware performs this conversion using the factory calibration. The current in-situ black-body calibration differs from the historic factory calibration (Fig. 6.14), and so a correction to the camera recorded black-body temperature is performed in post-processing using equations (6.7) and (6.8) .

The camera-incident radiance due to the temperature of the vane of interest $q'_w(\boldsymbol{x},t)$ is related to the vane temperature $T_w(\boldsymbol{x},t)$ using the transmittance of the window τ and the emissivity of the vane surface $\varepsilon(\boldsymbol{x},\theta_{\mathrm{cam}})$:

$$q'_w(\boldsymbol{x},t) \equiv \tau q_w(\boldsymbol{x},t) \equiv \sigma\tau\varepsilon(\boldsymbol{x},\theta)T_w^4(\boldsymbol{x},t). \tag{6.11}$$

The emissivity is a function of the viewing angle θ and the position on the vane $\boldsymbol{x}$. σ is the Stefan-Boltzmann constant, and $q_w(\boldsymbol{x},t)$ is the radiance before the ZnSe window due to the temperature of the vane. $T_w(\boldsymbol{x},t)$ is the temperature of interest and is used for overall cooling effectiveness scaling in the following chapter. It is assumed that the transmittance is constant over the area of the window and does not change over the range of ray angles from the FOV. It is shown later that the transmittance is relatively independent of input black-body temperature over the temperature range of interest (Fig. 6.20).

The camera-incident radiance due to the temperature of the surrounding walls $q''_R(\boldsymbol{x},t)$ reflecting off the vane surface is related to an equivalent surrounding temperature $T_R(\boldsymbol{x},t)$ using the vane emissivity and window transmittance:

$$q''_R(\boldsymbol{x},t) \equiv \tau q'_R(\boldsymbol{x},t) \equiv \tau\big(1-\varepsilon(\boldsymbol{x},\theta)\big)q_R(\boldsymbol{x},t) \equiv \sigma\tau\big(1-\varepsilon(\boldsymbol{x},\theta)\big)T_R^4(\boldsymbol{x},t), \tag{6.12}$$

where $q'_R(\boldsymbol{x},t)$ is the radiance before the window and $q_R(\boldsymbol{x},t)$ is the radiance before reflection from the vane of interest. $T_R(\boldsymbol{x},t)$ is effectively an integral over all the surroundings; it takes into account any variation in surrounding emissivity and temperature. This makes it very difficult to calculate $T_R(\boldsymbol{x},t)$ directly.

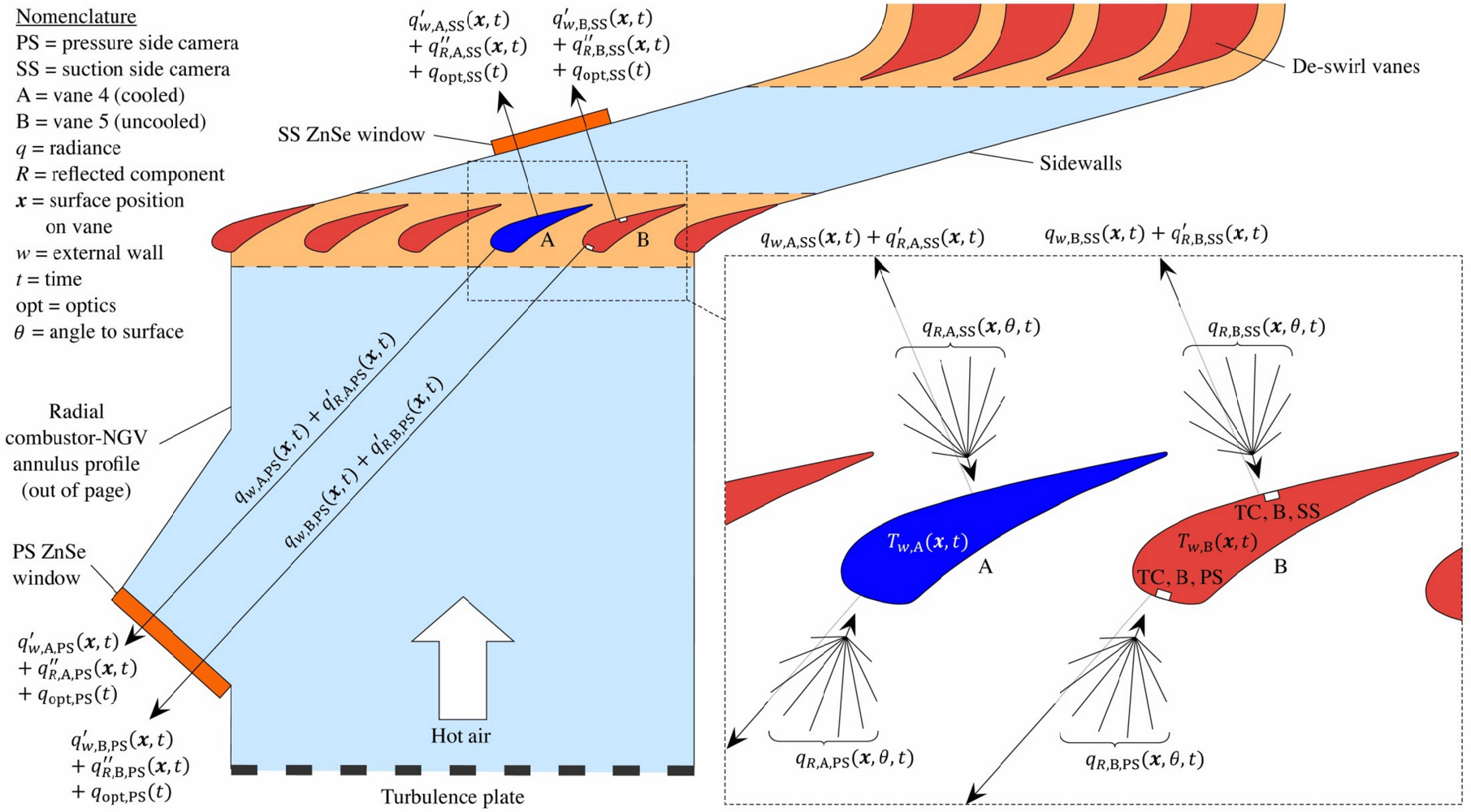


Figure 6.17. Stylised IR ray traces in the Sector Facility during nominal operation.

The camera-incident radiation due to the window $q_{\text{opt}}(t)$ is related to the window temperature $T_{\text{opt}}(t)$ and the transmittance of the window τ:

$$q_{\text{opt}}(t) \equiv \sigma(1-\tau)T_{\text{opt}}^4(t). \tag{6.13}$$

Substituting definitions (6.10) - (6.13) into equation (6.9):

$$T_{bb}^4(\boldsymbol{x},t) = \tau\varepsilon(\boldsymbol{x},\theta)T_w^4(\boldsymbol{x},t) + \tau\big(1-\varepsilon(\boldsymbol{x},\theta)\big)T_R^4(\boldsymbol{x},t) + (1-\tau)T_{\text{opt}}^4(t). \tag{6.14}$$

Of these terms, $T_{bb}(\boldsymbol{x},t)$ is measured by the camera, $T_w(\boldsymbol{x},t)$ is the temperature of interest, and all other parameters are unknown. The last two terms in the summation can be grouped together into a *surrounding radiance* term that is dependent on surface position, viewing angle and time:

$$q^*(\boldsymbol{x},\theta,t) \equiv \frac{\sigma\left(\tau\big(1-\varepsilon(\boldsymbol{x},\theta)\big)T_R^4(\boldsymbol{x},t) + (1-\tau)T_{\text{opt}}^4(t)\right)}{1-\tau\varepsilon(\boldsymbol{x},\theta)}. \tag{6.15}$$

The additional $1-\tau\varepsilon$ on the denominator normalises the function so that the surrounding radiance is independent of grey-body parameters when the system is isothermal. The surrounding radiance $q^*(\boldsymbol{x},\theta,t)$ is a physical function that incorporates all extraneous radiation sources. The *surrounding radiance correction* is defined as $q^*(\boldsymbol{x},\theta,t)(1-\tau\varepsilon(\boldsymbol{x},\theta))$.

The wall temperature of interest $T_w(\boldsymbol{x},t)$ then becomes:

$$T_w(\boldsymbol{x},t) = \sqrt[4]{\frac{\sigma T_{bb}^4(\boldsymbol{x},t) - (1-\tau\varepsilon(\boldsymbol{x},\theta))q^*(\boldsymbol{x},\theta,t)}{\sigma\tau\varepsilon(\boldsymbol{x},\theta)}}. \tag{6.16}$$

Knowledge of the surrounding radiance correction and the transmittance-emissivity product $\tau\varepsilon(\boldsymbol{x},\theta)$ make it possible to estimate the vane temperature.

The assumptions and methods for calculating these quantities are now discussed. In summary, variation with surface position and viewing angle is ignored; the transmittance-emissivity product is found through an in-situ bi-thermal calibration; the surrounding radiance is found per run using a surrogate surrounding radiance correction vane.

6.10 Grey-Body Calibration Assumptions

A complete grey-body calibration, in which the surrounding radiance and transmittance-emissivity product are functions of surface position and camera viewing angle, is very complex. Due to time and resource constraints, a number of assumptions—in addition to the implicit assumption of wavelength-independence—were made to simplify the grey-body calibration. A methodology for an improved grey-body calibration method with fewer assumptions is suggested at the end of this chapter.

Firstly, the surface emissivity is assumed constant over the vane surface and independent of camera viewing angle, though different for the PS and SS:

$$\varepsilon(\boldsymbol{x}, \theta) \sim \varepsilon. \tag{6.17}$$

Since the vane is uniformly spray-painted, $\varepsilon(\boldsymbol{x}, \theta) \sim \varepsilon(\theta)$ was seen as reasonable for both PS and SS. The surface viewing angle on the SS is approximately normal across the entire ROI, leading to the assumption that $\varepsilon(\theta) \sim \varepsilon$. This assumption is less valid on the PS, however, as viewing angles range between 0° and 70°. Experiments performed in the Infra-Red Research Facility (IRRF) showed that the viewing angle had a large effect on the effective emissivity of RS Matt black spray paint for viewing angles above 30°. Despite the non-ideal nature of this assumption, it was seen as acceptable for the purposes of this study—i.e., to compare the overall cooling effectiveness of multiple HPNGV cooling geometries, painted identically and viewed at the same angle.

The surrounding radiance is assumed to be constant over the vane surface and independent of camera viewing angle, though different for the PS and SS:

$$q^*(\boldsymbol{x}, \theta, t) \sim q^*(t). \tag{6.18}$$

The validity of this assumption is unknown. On the one hand, SS viewing angles are more uniform than the PS. On the other hand, some surfaces are in view of a cooled vane, while others are in view of an uncooled vane. This assumption becomes important later in the radiance correction measurement method— specifically, the radiance correction is calculated on a vane that is adjacent to a cooled vane on the SS and an uncooled vane on the PS, and then applied to the vane of interest which was adjacent to uncooled vanes on both SS and PS. Further tests are required to gain more insight, and a method for eliminating this discrepancy is included at the end of the chapter. However, this assumption was seen as acceptable for the comparative purposes of this study.

Assumptions (6.17) and (6.18) are substituted into (6.16) to find:

$$T_w(\boldsymbol{x}, t) = \sqrt[4]{\frac{\sigma T_{bb}^4(\boldsymbol{x}, t) - (1 - \tau\varepsilon) q^*(t)}{\sigma\tau\varepsilon}} \tag{6.19}$$

This is the form of the grey-body correction that is used for all proceeding work in this thesis.

6.11 Determining $\tau\varepsilon$

Calibrating the transmittance-emissivity product in-situ has a number of advantages over using tabulated values of emissivity, or using the transmission spectrum issued by the window supplier. Emissivity is a strong function of paint type, surface type, and application method. The transmission spectrum issued by the supplier of the PS window is more than 5 years old and the anti-reflective

(AR) coating may have since deteriorated. The transmission of the window relies heavily upon the AR coating, being around 70% uncoated and 98.5% coated. The maximum operating temperature of AR coated ZnSe is around 200°C (Sweeney, 2000).

An in-situ calibration may also go some way to account for more complex phenomena, such as lens diffraction and point spreading, reflection of the camera itself in the ZnSe window, re-reflection of the test article in the ZnSe window, and wavelength-dependent transmission. Furthermore, grouping the transmittance and emissivity together into a single term reduces the amount of uncertainty that would otherwise occur if both were calibrated or assumed separately.

The transmittance-emissivity product $\tau\varepsilon$ is found from a *bi-thermal* calibration using the surrogate radiance correction vane, marked B in Fig. 6.16. Vane B is uncooled, instrumented with two thin foil thermocouples, and is beside the cooled vane of interest A. Bi-thermal references the assumption that the system can be described by two temperatures at any point in time during the calibration—the temperature of vane B, and the ambient temperature. Emissivity and transmittance are assumed to be constant across each camera view and therefore the transmittance-emissivity of vane A is assumed equal to that calculated using vane B:

$$(\tau\varepsilon)_{\mathrm{A}} \sim (\tau\varepsilon)_{\mathrm{B}}. \tag{6.20}$$

The transmittance-emissivity product of vane B was estimated as follows.

Vane B was removed from the Sector Facility and was heated to 65°C using a water bath and IV bag. Once at temperature, vane B was quickly re-installed into the Sector Facility. Vane B was then allowed to cool down naturally. The facility remained open during the calibration to improve ambient air flow. The wall temperature at a point on vane B $T_w(\boldsymbol{x}_{\mathrm{TC,B}}, t)$ was recorded over time by the surface thermocouples, and the equivalent black-body temperature at a position next to the thermocouples $T_{bb}(\boldsymbol{x}_{\mathrm{TC,B}}, t)$ was recorded by the IR cameras. Importantly, the camera view and optics were identical to a nominal Sector blowdown run. The middle vane pair was absent during calibration to reduce heat conduction to the surrounding walls, in order to improve the bi-thermal assumption. IR black-body measurements during a typical bi-thermal calibration run are shown in Figs. 6.18 and 6.19.

Ambient temperature $T_{\mathrm{amb}}(t)$ was recorded over time using a mineral insulated thermocouple. By assuming that everything but vane B remained at ambient temperature during the calibration, that vane B did not reflect back or emit onto itself, and that emissivity and transmittance were independent of position/viewing angle, equation (6.14) becomes:

$$T_{bb}^4(\boldsymbol{x}_{\mathrm{TC,B}}, t) = \tau\varepsilon T_w^4(\boldsymbol{x}_{\mathrm{TC,B}}, t) + \tau(1-\varepsilon)T_{\mathrm{amb}}^4(t) + (1-\tau)T_{\mathrm{amb}}^4(t). \tag{6.21}$$

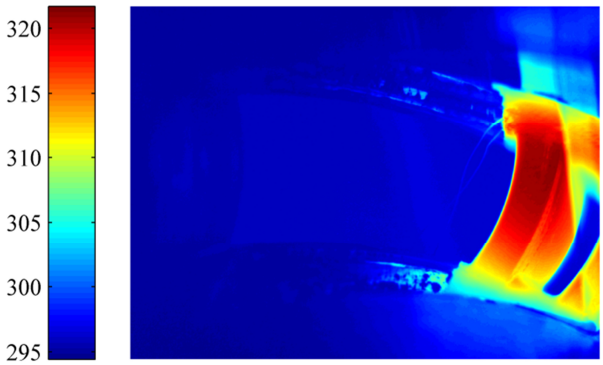


Figure 6.18. Black-body temperature (K) of PS vane B during $\tau\varepsilon$ calibration.

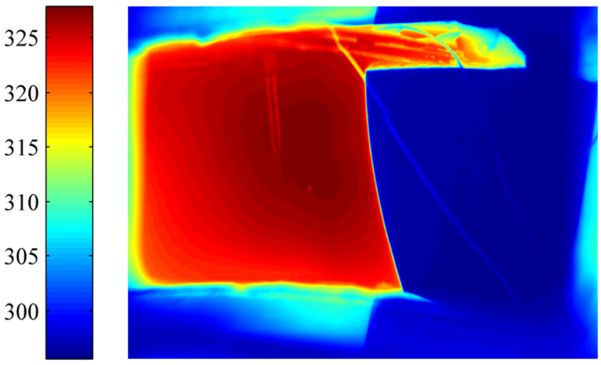


Figure 6.19. Black-body temperature (K) of SS vane B during $\tau\varepsilon$ calibration.

Therefore $\tau\varepsilon$ was determined as the only unknown in equation (6.21):

$$\tau\varepsilon = \frac{T_{bb}^4(\boldsymbol{x}_{\mathrm{TC,B}}, t) - T_{\mathrm{amb}}^4(t)}{T_w^4(\boldsymbol{x}_{\mathrm{TC,B}}, t) - T_{\mathrm{amb}}^4(t)}. \tag{6.22}$$

The transmittance-emissivity product calculated from the bi-thermal calibration is plotted against thermocouple temperature for both PS and SS in Fig. 6.20. The mean transmittance-emissivity for the PS and SS are given below. The mean values were used for all subsequent IR analyses.

PS: $$\overline{\tau\varepsilon} = 0.848. \tag{6.23}$$

SS: $$\overline{\tau\varepsilon} = 0.956. \tag{6.24}$$

The product is approximately independent of wall temperature for both PS and SS, a good indication that a geometric/material property has been found. The precision of the calibration deteriorates as the wall temperature approaches the ambient temperature and the denominator in equation (6.22) approaches zero. The difference between the PS and SS calibrations may be due to the reasons discussed previously, and demonstrates the necessity of an in-situ calibration since these could not have been predicted a-priori.

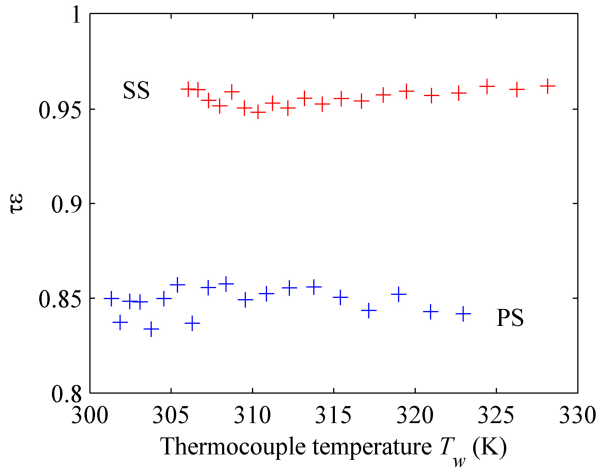


Figure 6.20. Transmittance-emissivity product calculated in the bi-thermal calibration for PS and SS.

6.12 Run to run $q^*(t)$

The surrounding radiance $q^*(t)$ must also be known in order to estimate the vane temperature from the equivalent black-body temperature measurement, equation (6.19). $q^*(t)$ depends on the temperature of the surroundings, the window temperature, the transmittance of the window, and the emissivity of all surrounding surfaces, equation (6.15). $q^*(t)$ varies during a run, especially during mesh-on when the facility heats up. Each run has a unique temperature history, based on ambient conditions, initial conditions, heater mesh power setting, coolant mass flow rate and run initiation/cessation times. It is therefore necessary to determine the surrounding radiance at all times during a run, and for each run.

Like the transmittance-emissivity product, surrounding radiance is measured using the surrogate surrounding radiance correction vane B. Unlike the transmittance-emissivity product, however, the surrounding radiance is measured during each run.

The surface temperature at a point on the SS and PS of the surrogate vane $T_w(\boldsymbol{x}_{\mathrm{TC,B}}, t)$ is measured using two thin foil thermocouples. The equivalent black-body temperature at a point next to each thermocouple $T_{bb}(\boldsymbol{x}_{\mathrm{TC,B}}, t)$ is measured using the IR cameras. The choice of pixel is important and is discussed later. The thermocouple and IR temperature histories and the transmittance-emissivity product are then used to estimate the surrounding radiance, given the assumption of spatial independence:

$$q^*(t) = \frac{\sigma T_{bb}^4(\boldsymbol{x}_{\mathrm{TC,B}}, t) - \sigma\tau\varepsilon T_w^4(\boldsymbol{x}_{\mathrm{TC,B}}, t)}{1 - \tau\varepsilon}. \tag{6.25}$$

The radiance correction function is shown in Fig. 6.21 for a low powered run and in Fig. 6.22 for a high powered run.

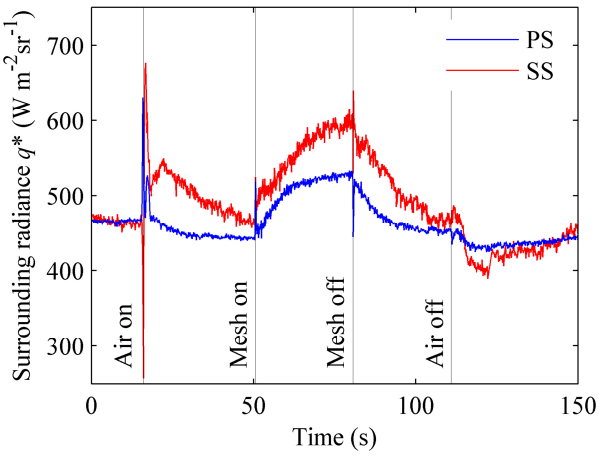


Figure 6.21. Surrounding radiance during run 30033, 95 V Drake set-point.

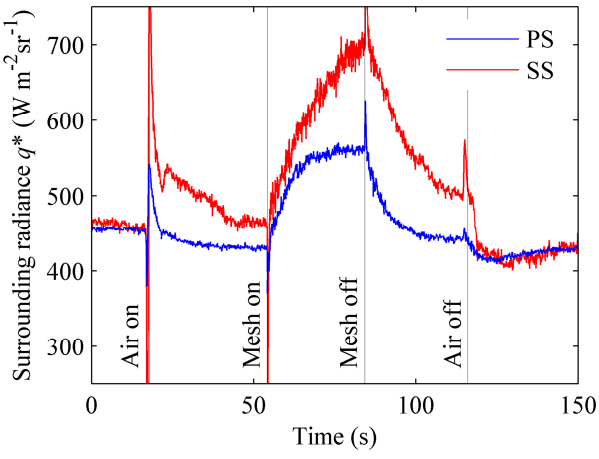


Figure 6.22. Surrounding radiance during run 30017, 114 V Drake set-point.

Surrounding radiance follows a rig-temperature-like trend during the course of a run—partly by design; see section on choosing pixel location. The method is sensitive enough to pick up the initial shock-heating due to the compression wave at air-on, the temperature rise of the facility during mesh-on, the cooling of the rig after mesh-off, and expansion cooling at air-off. No smoothing has been performed on the results in Figs. 6.21 and 6.22. The thermocouple and IR data are manually aligned in time by applying a constant time shift to one set of data. The δ spikes at air-on, mesh-on and mesh-off are caused by the residual differences in the time stamp between the two data sets.

The SS surrounding radiance is greater than the PS surrounding radiance correction. This may be because the SS surroundings are best characterised by the region downstream of the vanes where Mach numbers and HTC are greater, and the PS surroundings best characterised by the upstream inlet contraction where HTC is relatively low. Without knowledge of the emissivity, transmittance and the temperature of the window, the effective temperature of the SS and PS surroundings cannot be deduced from the surrounding radiance measurement, equation (6.15). The PS results are better conditioned than the SS results because there is a larger temperature difference between the thermocouple and the black-body measurements on the PS. A corollary of this observation is that the precision of the surrounding radiance measurement increases with reflectivity of the surrogate surrounding radiance correction vane.

Before air-on, the surrounding radiance is predominantly a function of the initial rig temperature and the transmittance-emissivity product, because the facility is approximately isothermal. This can be seen in Fig. 6.23, where the surrounding radiance at $t = 0$ is plotted against the thermocouple temperature at $t = 0$ for all 250 runs. Also shown in Fig. 6.23 is the theoretical surrounding radiance for an isothermal rig at the thermocouple temperature. This is predicted from equation (6.15) by recognising that the equivalent black-body temperature is equal to the rig temperature for isothermal conditions—for the same reasons as the cavity-type black-body discussed previously. The isothermal surrounding radiance is therefore

$$q^*_{\mathrm{iso}}(t) = \sigma T_w^4\big(\boldsymbol{x}_{\mathrm{TC,B}}, t\big). \tag{6.26}$$

Some runs were initially non-isothermal because the facility had been run not long before. These runs deviate from the theoretical isothermal correction in Fig. 6.23.

Surrounding radiance increases with power input during the heated phase. It was found that the surrounding radiance just before mesh-off ($t = t_h$) is well correlated with mainstream temperature. The maximum surrounding radiance during the heated period $q^*(t_h)$ is plotted against the mainstream temperature $T_{0m}(t_h)$ for all 250 runs in Fig. 6.24. Surrounding radiance is plotted relative to the surrounding radiance at $t = 0$ and mainstream temperature relative to the facility temperature at $t = 0$.

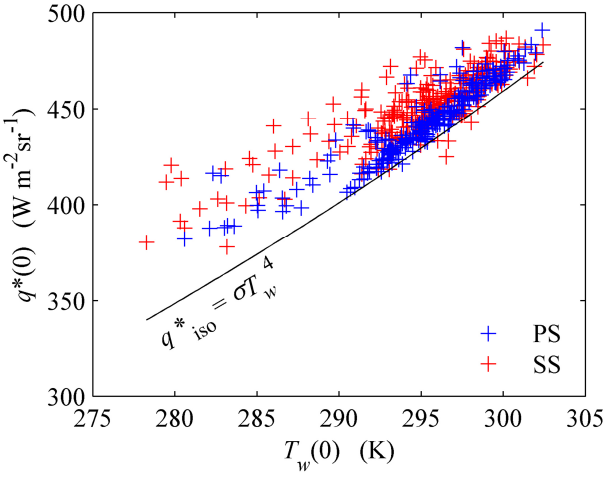


Figure 6.23. Initial surrounding radiance as a function of initial thermocouple temperature, 250 runs.

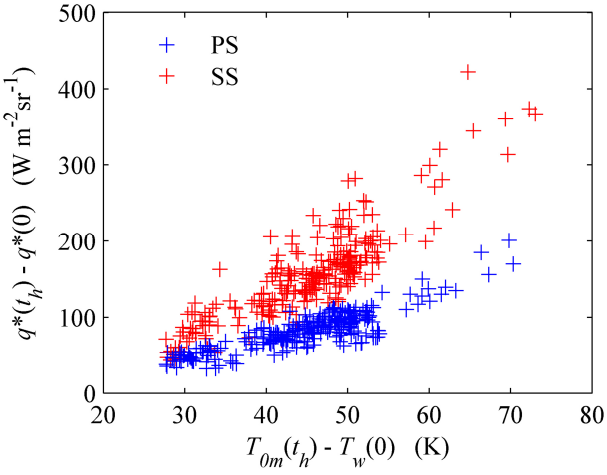


Figure 6.24. Maximum surrounding radiance during heated period as a function of mainstream temperature, 250 runs.

The surrounding radiance is approximately linearly dependent on mainstream temperature just before mesh-off. The SS surrounding radiance is larger than the PS, for the reasons conjectured previously. The scatter of the SS data compared to the PS data may be due in part to the SS surrounding radiance not being fully steady-state by the end of the heated period (Figs. 6.21 and 6.22). The 15 runs situated away from the main group used the more power-dissipative 178 mm aperture, 140 mm diameter heater mesh. The physically intuitive results lend confidence to the grey-body calibration procedure used in this thesis. If desired, the results could be used to estimate the steady state surrounding radiance correction a-priori.

In order to quantify the amount of background radiance that the camera receives, the PS and SS surrounding radiance q^* is multiplied by $1-\tau\varepsilon$ to generate the surrounding radiance correction, and compared to the total radiance measured by the camera, $\sigma T_{bb}^4(\boldsymbol{x}_{\mathrm{TC,B}}, t)$. Ideally, $q^*(1-\tau\varepsilon)$ should be as low as possible in order to reduce uncertainty carried forward from the grey-body calibration, and to increase measurement sensitivity. This can be achieved by maximising the transmittance-emissivity product.

$q^*(1-\tau\varepsilon)$ accounts for 13-15% of the total radiance received by the camera on the PS (Fig. 6.25), and 5% on the SS (Fig. 6.26). The PS surrounding radiance correction changes the apparent PS wall temperature of vane B (hot vane) by up to 0.2 K, and vane A (cold vane) by up to 3 K which is an overall cooling effectiveness of 0.05 (Fig. 6.15). The SS surrounding radiance correction changes the apparent SS wall temperature of vane B (hot vane) by up to 0.2 K, and of vane A (cold vane) by up to 0.8 K, which is an overall cooling effectiveness of 0.013 (Fig. 6.16).

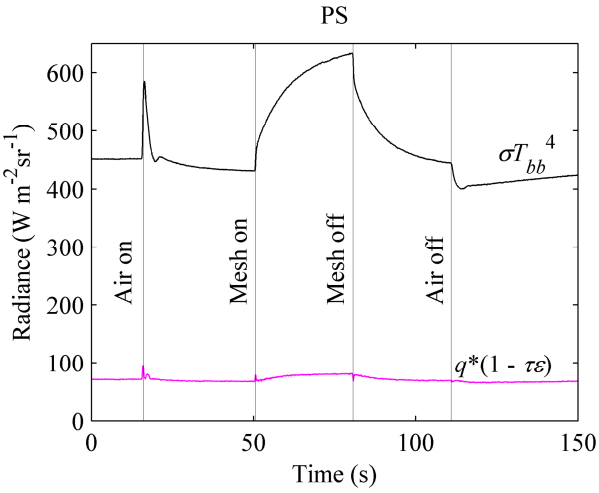


Figure 6.25. PS radiation correction $q^*(1-\tau\varepsilon)$ compared to total radiance measured by the camera σT_{bb}^4, run 30033.

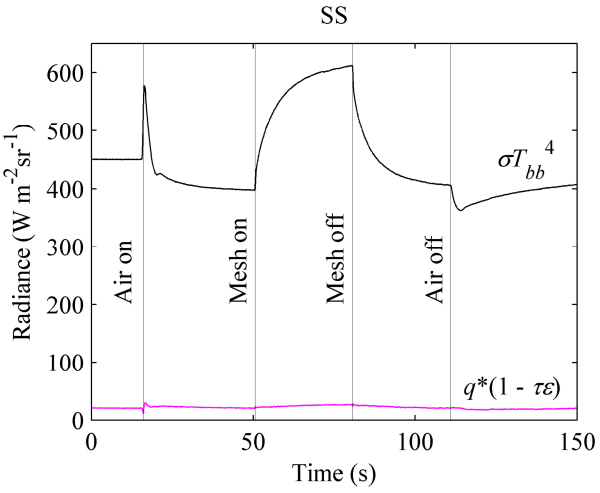


Figure 6.26. SS radiation correction $q^*(1-\tau\varepsilon)$ compared to total radiance measured by the camera σT_{bb}^4, run 30033.

6.13 Pixel location for $q^*(t)$ evaluation

The grey-body calibration developed in this chapter implicitly assumes that the thermocouples measure point wall temperature non-intrusively, and that the cameras measure the black-body temperature of the wall at the same point. In reality, the thin foil thermocouples have finite size—both in the plane of the wall and normal to the wall. The thermocouple measurement therefore depends on the temperature distribution over the contact patch and, to a much lesser extent, the thermal boundary layer. The thermocouple surface is also bumpy and at a different camera viewing angle to the surrounding vane surface, creating a different effective emissivity.

The problem of thermal gradients across the contact patch is acute on the PS. The film cooling holes are filled with polyamide that has different thermal properties to the surrounding metal. During thermal transients, the temperature of the metal and the polyamide differ, as can be seen in the IR measurements in Fig. 6.27. The PS thermocouple is located on top of both metal and polyamide in a position that is most normal to the IR camera. The PS thermocouple consequently measures somewhere between the polyamide temperature and metal temperature. The SS thermocouple also experiences transient thermal gradients because of variation in underlying vane metal wall thickness, Fig. 6.29.

It is reasonable to assume that there exists a single point near the thermocouple on the vane surface which has the same temperature history as that measured by the thermocouple. The IR measurement at this single point can then be compared to the thermocouple measurement to calculate the surrounding radiance. The pixel location of this single point on the PS is marked D in Fig. 6.27, and

on the SS is marked H in Fig. 6.29. Black-body temperature images are taken just after the compression wave at air-on when wall thermal gradients are greatest.

The points were not known a-priori. They were found by exporting the IR measurements from a number of locations around the thermocouple and examining the physicality of the resultant surrounding radiance predictions. Nine locations around the SS and PS thermocouple were tested, shown in Figs. 6.27 and 6.29. Locations are spaced 8 pixels apart. The surrounding radiance predictions based on the IR measurement from each test location are plotted in Figs. 6.28 and 6.30. Results are for a single run, but are representative of every Sector run. The surrounding radiance histories were median-filtered to remove the downsample-sync induced spikes seen in Figs. 6.21 and 6.22.

On the PS, locations A, C and E are discounted because the corresponding surrounding radiance appears to decrease during the heated phase—an unphysical result. Locations F, G and H are discounted because the surrounding radiance appears to step down at mesh-on, and step up at mesh-off. I is discounted because the surrounding radiance increases at air-off, when in reality the expansion wave at air-off should cause the surrounding radiance to go down. Since the thermal time constant of the surroundings is in the tens of seconds, we do not expect step changes in surrounding temperature or surrounding radiance. For this reason, location B is discounted. Location D is chosen by virtue of it predicting the most physical surrounding radiance history.

On the SS, locations A-E are discounted because the surrounding radiance appears to decrease during the heated phase. Locations F and I are discounted because of the step change in surrounding radiance. Location G is discounted because of the dips at mesh-on and mesh-off. Location H is chosen by virtue of it predicting the most physical surrounding radiance history.

Sensitivity to pixel location can be reduced by increasing vane temperature uniformity and by decreasing thermocouple size and thickness. Suggestions to achieve this are included in the following section.

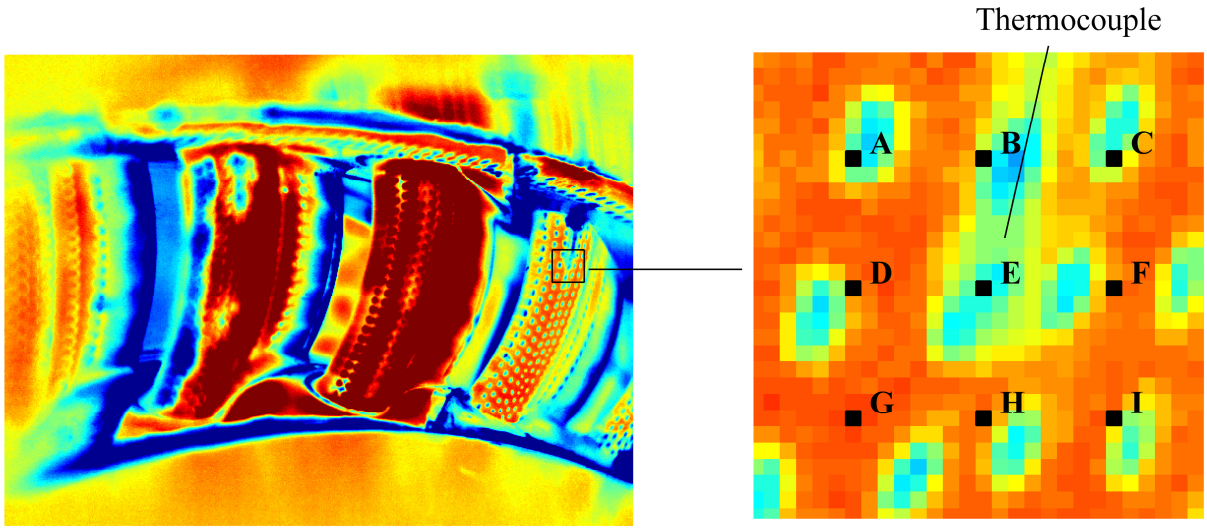


Figure 6.27. PS image just after compression wave, zoomed in around thermocouple.
Pixel locations A – I tested. Pixel location D chosen.

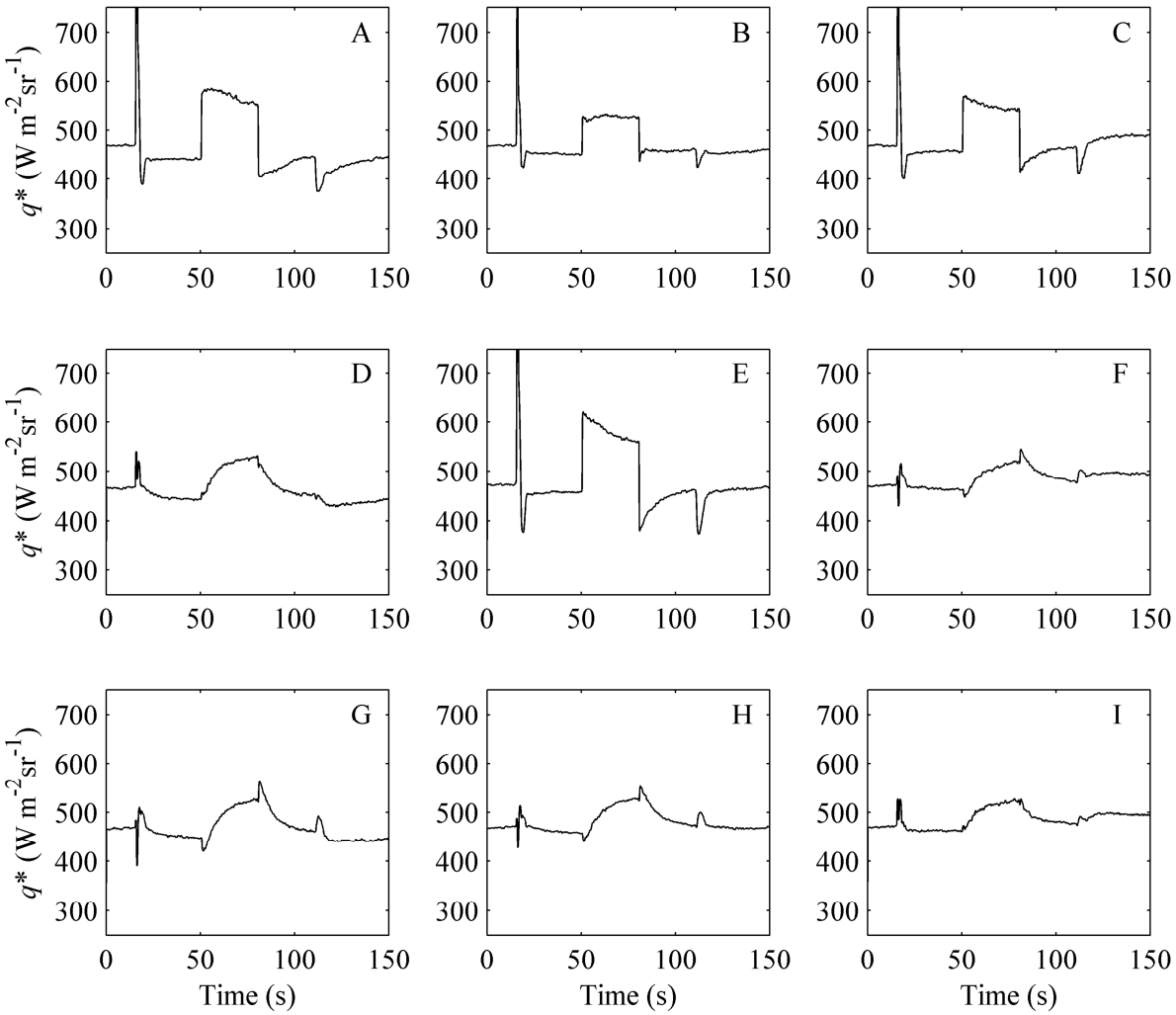


Figure 6.28. PS surrounding radiation q^* calculated from pixel locations A - I, run 30033.
Pixel location D chosen.

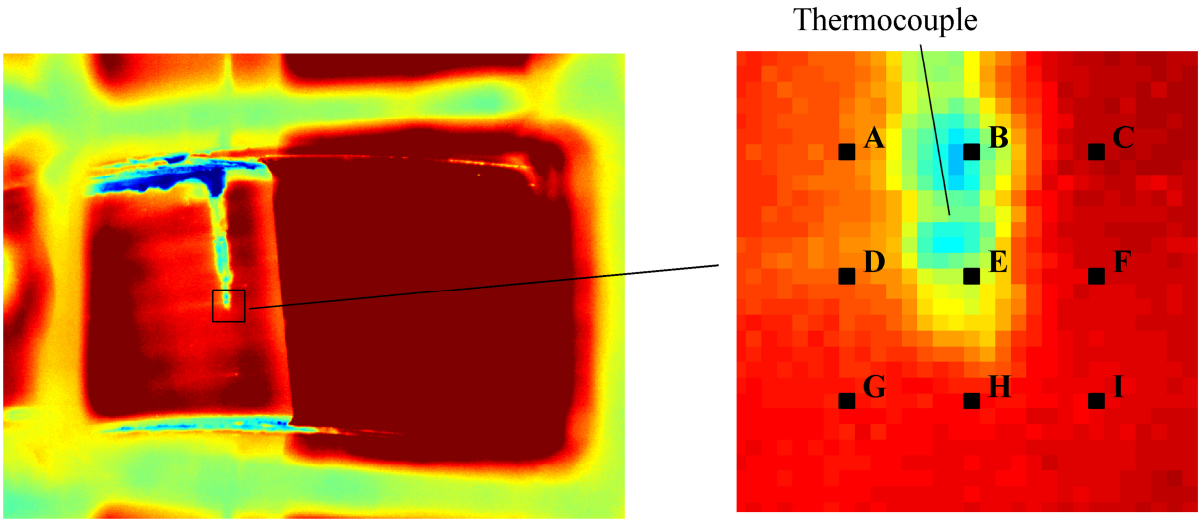


Figure 6.29. SS image just after compression wave, zoomed in around thermocouple.
Pixel locations A – I tested. Pixel location H chosen.

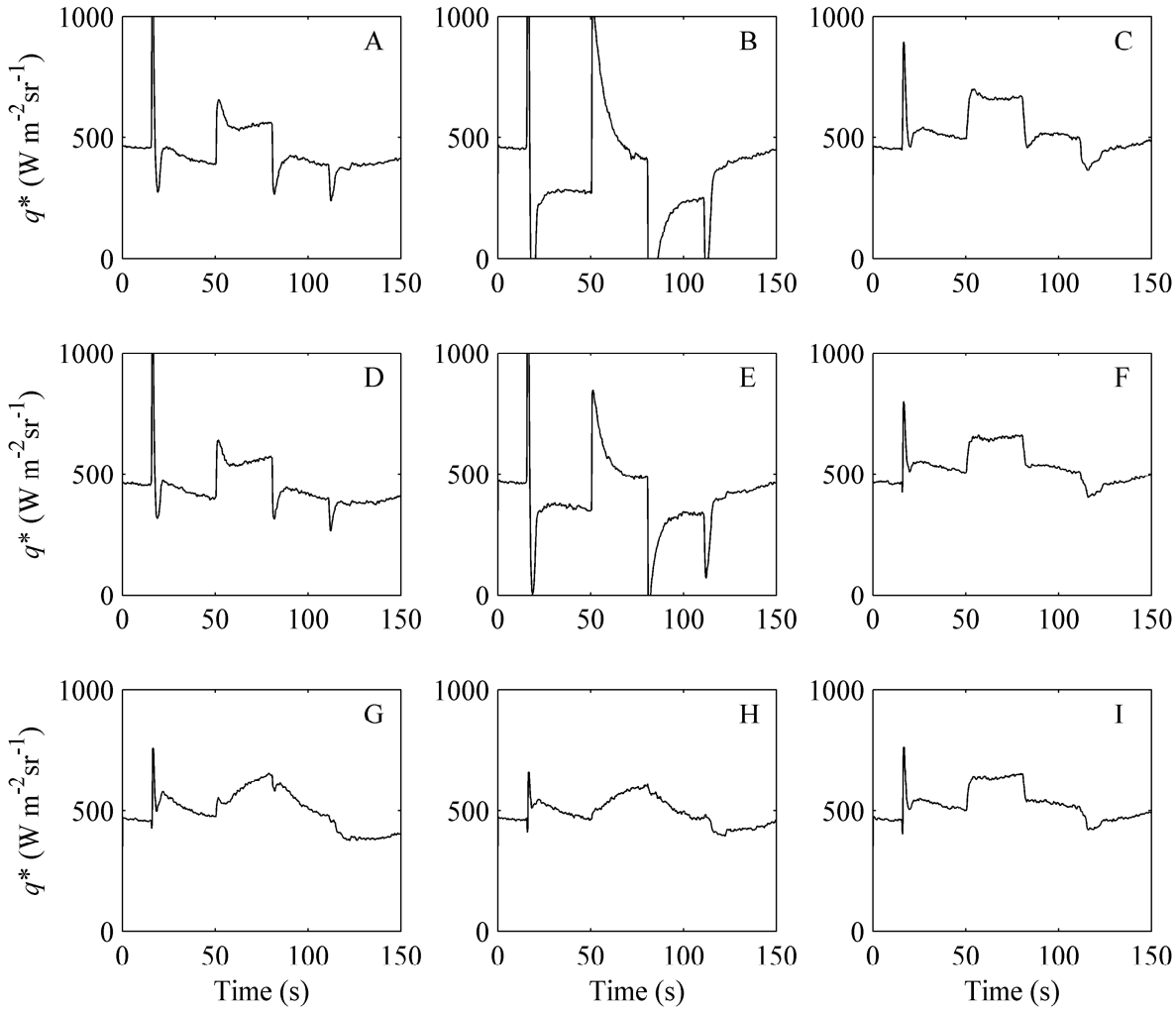


Figure 6.30. SS surrounding radiance q^* calculated from pixel locations A - I, run 30033.
Pixel location H chosen.

6.14 Proposed Improvements

A number of suggestions for improving the accuracy, precision and coverage of the IR measurements now follow.

Run heater mesh for extra 15-20 seconds. To increase temperature uniformity of the surroundings and improve the assumption of thermal steady-state at the end of the heated period.

Replace surrogate surrounding radiance correction vane with solid CNCed equivalent. Improves temperature uniformity and reduces sensitivity to pixel location. Also aids sealing (see previous chapter).

Instrument the surrogate surrounding radiance correction vane with as many thin film gauges as possible. Improves accuracy of vane temperature measurement, and means surrounding radiance correction can be estimated over the entire surface, $q^*(\boldsymbol{x}, \theta, t)$.

Purchase an off-the-shelf cavity-type black-body calibrator. The IR cameras could then be calibrated more easily and frequently, important since the black-body calibration changes with time. The results from the calibrator can be compared to the in-situ black-body calibration for validation.

Use focal stacking on the PS. Currently, not all the PS can be focussed simultaneously. By automating a high frequency sinusoidal variation in focus position during the run the images could be focally stacked and interpolated to generate sharp video of the entire PS for the duration of the run.

Relocate surrogate surrounding radiance correction vane. In the current configuration, the surrogate vane is flanked by a cooled vane (vane of interest) and an uncooled vane, while the vane of interest is flanked on both sides by uncooled vanes. To better represent the surrounding radiance conditions on the vane of interest, the surrogate vane could be two removed from the vane of interest to be surrounded by uncooled vanes on both sides. This may require the repositioning of ZnSe windows or the vane of interest in the cassette.

Increase reflectivity of surrogate surrounding radiance correction vane. Increasing reflectivity will reduce the uncertainty of the surrounding radiance measurement.

More IR cameras. The PS viewing angle could be improved by placing a camera on the trailing side of the upstream inlet contraction. Currently, a portion of the early-mid SS is not covered by either camera. The vane leading the vane of interest could be remanufactured to incorporate a small IR camera (e.g., FLIR ONE) that observes the SS of the vane of interest through a small ZnSe window on its PS.

Create a transmittance-emissivity map. The bi-thermal calibration could be improved by performing the calibration in the Coolant Capacity Rig, modified to include a heater mesh. Performing the

calibration ex-situ and running the heater mesh in steady-state would improve the bi-thermal assumption of temperature uniformity of the surroundings and the vane. If the surrogate vane were instrumented with as many thin-film gauges as possible, a transmittance-emissivity map $\tau\varepsilon(\boldsymbol{x}, \theta)$ could be generated. The relative camera and ZnSe window positions must be replicated exactly.

6.15 Conclusions

In this chapter, the methodology for full-surface infra-red temperature measurement in the Sector Facility has been described. A flow diagram summarising this methodology is shown in Fig. 6.31. A number of innovations have been incorporated into the methodology, such as the introduction of two cameras which record PS and SS simultaneously and the associated hardware/software updates. A comprehensive physically based grey-body correction procedure is now utilised, which measures and corrects for surrounding radiance errors at every point in time, takes into account the transmittance of the external optics and the surface emissivity of the object, and compensates for the black-body temperature-radiometric characteristics of the camera. Failure to correct for the surrounding radiance can result in an absolute error in overall cooling effectiveness of 0.05.

It is hoped that this methodology provides a rigorous approach to IR thermography in situations where the emissivity of the object is not equal to one, the external optics have finite transmittance, and the surrounding radiance cannot be ignored. Improvements to the method have been proposed to further increase accuracy.

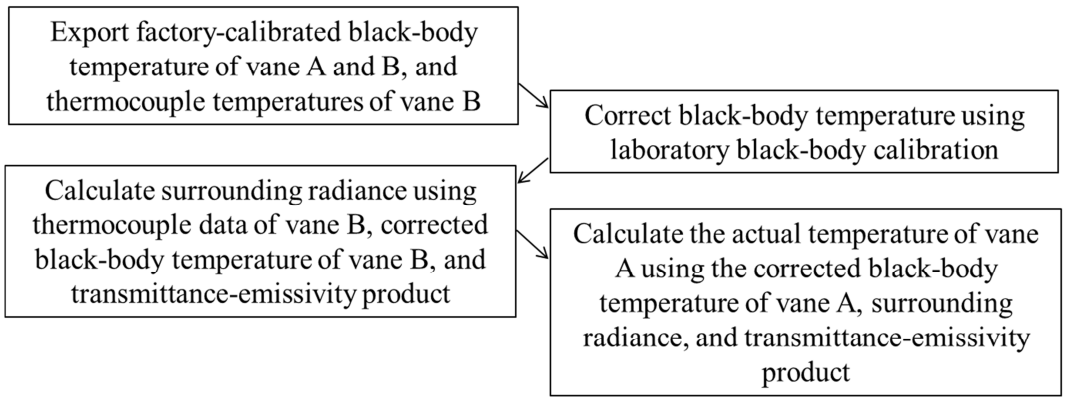


Figure 6.31. Flow diagram of black-body and grey-body corrections.

7. Cooling Effectiveness Measurements

In this chapter, the overall cooling effectiveness measurements of the cast T500, laser-sintered T500 and reverse-pass HPNGVs are reported. Results are shown over a range of coolant-to-mainstream mass flow and pressure ratios. A regression method for measuring both overall cooling effectiveness and mainstream recovery temperature from a series of experiments is detailed.

7.1 Overall Cooling Effectiveness and Mainstream Recovery Ratio

Wall temperature measured in the Sector Facility is non-dimensionalised in terms of overall cooling effectiveness θ because it is independent of temperature for constant fluid properties[1]. This allows the wall temperature measured in the Sector Facility to be scaled to engine conditions as long as the other non-dimensional groups are matched—discussed in Chapter 5. The overall cooling effectiveness θ is defined as:

$$\theta \equiv \frac{T_r - T_{w1}}{T_{0m} - T_{0c}}, \tag{7.1}$$

where T_{w1} is the external wall temperature, T_{0m} is the mainstream temperature, T_{0c} is the coolant total temperature at vane inlet, and T_r is the mainstream recovery temperature. The points at which the mainstream and coolant temperatures are measured are reported in Chapter 5. The wall temperature is measured using infra-red thermography.

The recovery temperature T_r is lower than the mainstream total temperature when $\mathrm{Pr} < 1$ because wall-normal heat conduction in high Mach number thermal boundary layers outweighs viscous heating. The recovery temperature is commonly related to the mainstream Mach number M and a recovery factor r (e.g., Eckert and Drake, 1972) by:

$$T_r = T_{0m} \frac{1 + r\frac{\gamma - 1}{2}\mathrm{M}^2}{1 + \frac{\gamma - 1}{2}\mathrm{M}^2}. \tag{7.2}$$

The recovery factor is typically related to the Prandtl number:

$$r = \begin{cases} \mathrm{Pr}^{1/2} & \text{laminar} \\ \mathrm{Pr}^{1/3} & \text{turbulent.} \end{cases} \tag{7.3}$$

[1] This can be demonstrated using a similar linear superposition argument to Luque Martinez (2011), by changing the boundary condition of the first homogenous solution in equation (6.9) in Luque Martinez (2011) from $T_{02} - T_r$ to $T_{02} - T_{01}$. This is arguably more physical as it allows for internal heat transfer up to the point of interest.

The mainstream temperature recovery ratio T_r/T_{0m} is matched between engine and rig because the external Mach number distribution, recovery factor and ratio of specific heats are approximately matched at engine and rig conditions. The mainstream temperature recovery ratio, defined as

$$c = T_r/T_{0m} \tag{7.4}$$

is approximately independent of temperature, depending mainly on the state of the aerodynamic external boundary layer. The recovery ratio is therefore affected by film injection and is a function of pressure ratio p_{0c}/p_{0m}.

7.2 $\theta - c$ Regression

Each vane was tested at 44 pressure ratios p_{0c}/p_{0m} (i.e., 44 $\dot{m}_c\sqrt{T_{0c}}/\dot{m}_m\sqrt{T_{0m}}$) : 11 mass flow ratios $\dot{m}_c/\dot{m}_m$ and four mainstream temperatures. It is assumed that the overall cooling effectiveness θ and the mainstream recovery ratio c only depend on the coolant to mainstream pressure ratio and position on the vane. Consequently for test i:

$$c_i\left(\frac{T_{0m,i}}{T_{w,i}}\right) + \theta_i\left(\frac{T_{0c,i} - T_{0m,i}}{T_{w,i}}\right) = 1. \tag{7.5}$$

There is not enough information from a single run to calculate c_i and θ_i directly—instead, c_i and θ_i are estimated regressively. A zeroth order regression was considered but not utilised, where runs with the closest pressure ratio are paired and c_i and θ_i are assumed equal for both runs. This effectively gives two equations and two unknowns, allowing c_i and θ_i to be determined. The effectiveness of the zeroth order regression increases with the density of runs and decreases with gradients $dc_i/d(p_{0c}/p_{0m})$ and $d\theta_i/d(p_{0c}/p_{0m})$. However, any error in an individual measurement directly affects the output of the zeroth order regression.

The regression used in this study reduces error propagation by utilising information on the *local spread* of data, i.e., uses data from multiple runs with similar pressure ratios. The overall cooling effectiveness θ_i and mainstream recovery ratio c_i of run i are found by least squares minimisation of the weighted sum of residuals (7.5) of all runs j = 1:N:

$$\underset{\theta_i,c_i}{\operatorname{argmin}} \sum_{j=1}^{N} \left[\mathrm{G}\left(\frac{p_{0c,j}}{p_{0m,j}} - \frac{p_{0c,i}}{p_{0m,i}}\right)\right]^{\frac{1}{2}} \left[c_i\left(\frac{T_{0m,i}}{T_{w,i}}\right) + \theta_i\left(\frac{T_{0c,i} - T_{0m,i}}{T_{w,i}}\right) - 1\right]^2. \tag{7.6}$$

G is a Gaussian weighting function:

$$\mathrm{G}(x) = e^{-\frac{x^2}{2\sigma^2}}. \tag{7.7}$$

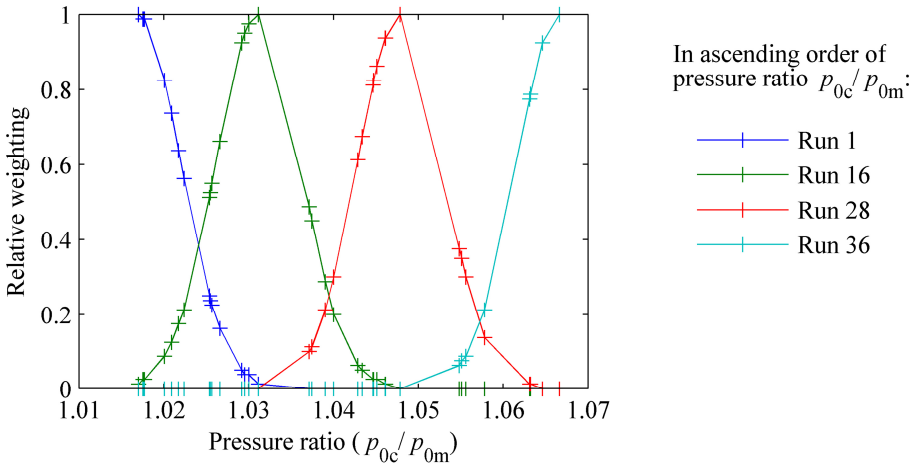


Figure 7.1. Gaussian weighting function for $\boldsymbol{\theta - c}$ regression.

σ is the standard deviation set to 0.005. The relative weightings of each run j when calculating the overall cooling effectiveness and mainstream recovery ratio of run i are shown in Fig. 7.1. It is assumed that the overall cooling effectiveness and mainstream recovery ratio are constant within the local area $p_{0c,i}/p_{0m,i} \pm \sim 2\sigma$.

The minimisation is performed by solving the weighted normal equation

$$(\boldsymbol{X}^T \boldsymbol{W_i} \boldsymbol{X})\boldsymbol{\beta}_i = \boldsymbol{X}^T \boldsymbol{W_i} \boldsymbol{y}, \tag{7.8}$$

where for N runs in a data set:

$$\boldsymbol{\beta}_i = \begin{bmatrix} c_i \\ \theta_i \end{bmatrix}, \boldsymbol{X} = \begin{bmatrix} \left(\frac{T_{0m}}{T_w}\right)_1 & \left(\frac{T_{0c}-T_{0m}}{T_w}\right)_1 \\ \vdots & \vdots \\ \left(\frac{T_{0m}}{T_w}\right)_N & \left(\frac{T_{0c}-T_{0m}}{T_w}\right)_N \end{bmatrix}, \boldsymbol{W_i} = \text{diag}\left\{ \text{G}\left(\frac{p_{0c,1}}{p_{0m,1}} - \frac{p_{0c,i}}{p_{0m,i}}\right) \ldots \text{G}\left(\frac{p_{0c,N}}{p_{0m,N}} - \frac{p_{0c,i}}{p_{0m,i}}\right) \right\} \tag{7.9}$$

and $\boldsymbol{y}$ is a column vector of N ones. Equation (7.8) is solved for $\boldsymbol{\beta}_i$ using Gaussian elimination (backslash operator in MATLAB).

The resulting mainstream recovery ratio c_i is shown in Fig. 7.2 at three representative vane locations. For most locations, the mainstream recovery factor is approximately constant over the range of pressure ratios tested. This is reasonable, since the recovery ratio is primarily governed by the external aerodynamic field, which is constant. The film also affects the recovery temperature, though to a much smaller extent than the mainstream aerodynamic field. In order to account for any variation in recovery ratio due to film changes while simultaneously eliminating the noise introduced by the Gaussian weighting function (e.g., point H in Fig. 7.2), a first order best-fit is applied to the mainstream recovery ratio as a function of pressure ratio at each point on the vane. This is shown by the solid lines in Fig. 7.2. The first order best-fit is described by:

$$c_i = a\frac{p_{0c,i}}{p_{0m,i}} + b, \tag{7.10}$$

where a and b are constant for a given location. The order of the best-fit is justified since $dc_i/d(p_{0c}/p_{0m})$ is small compared to $d\theta_i/d(p_{0c}/p_{0m})$. The overall cooling effectiveness θ_i of run i is then found using:

$$\theta_i = \frac{T_{0m,i}c_i|\frac{p_{0c,i}}{p_{0m,i}} - T_{w1,i}}{T_{0m,i} - T_{0c,i}}, \tag{7.11}$$

where $c|(p_{0c,i}/p_{0m,i})$ is the mainstream recovery ratio evaluated using the best-fit equation (7.10) at the coolant to mainstream pressure ratio.

In summary, the overall cooling effectiveness θ_i and mainstream recovery ratio c_i are found for each run as follows:

1. θ_i and c_i are first estimated using data from the entire test sequence (~ 44 runs) and a Gaussian-weighted linear regression, using equations (7.8) and (7.9).
2. A 1st order best-fit of c_i as a function of coolant-to-mainstream pressure ratio is determined for each pixel. The mainstream recovery ratio c_i is subsequently evaluated according to the best-fit equation (7.10).
3. The overall cooling effectiveness θ_i is re-evaluated at the best-fit value of c_i, equation (7.11).

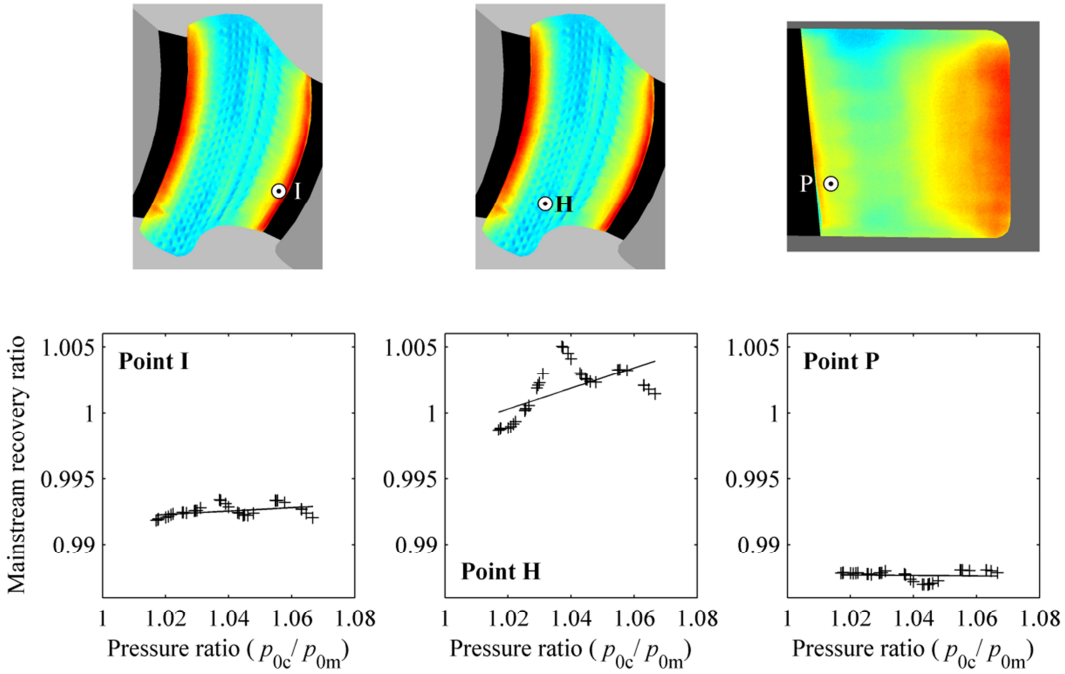


Figure 7.2. Typical mainstream recovery ratios c_i using local Gaussian weighted regression.

7.3 Justification for Overall Cooling Effectiveness vs $\dot{m}_c\sqrt{T_{0c}}/\dot{m}_m\sqrt{T_{0m}}$

In this section, the choice of plotting overall cooling effectiveness against $\dot{m}_c\sqrt{T_{0c}}/\dot{m}_m\sqrt{T_{0m}}$ is justified.

The ratio $\dot{m}_c\sqrt{T_{0c}}/\dot{m}_m\sqrt{T_{0m}}$ is matched between rig and engine since Mach number and coolant-to-mainstream total pressure ratio are matched. It can be shown that the ratio $\dot{m}_c\sqrt{T_{0c}}/\dot{m}_m\sqrt{T_{0m}}$ depends only upon the pressure ratio p_{0c}/p_{0m} (shown in Chapter 5), being independent of temperature:

$$\frac{\dot{m}_c}{\dot{m}_m}\sqrt{\frac{T_{0c}}{T_{0m}}} = F\left(\frac{p_{0c}}{p_{0m}}\right). \tag{7.12}$$

Mass flow ratio $\dot{m}_c/\dot{m}_m$ is *not* matched between rig and engine since it depends upon temperature. The function F depends on the vane coolant capacity. The vanes were designed to utilise the same amount of coolant, i.e., have the same function F. However, deviation in coolant capacity between designs meant that $\dot{m}_c\sqrt{T_{0c}}/\dot{m}_m\sqrt{T_{0m}}$ and p_{0c}/p_{0m} could not be matched simultaneously.

In this chapter, all overall cooling effectiveness measurements are reported as a function of $\dot{m}_c\sqrt{T_{0c}}/\dot{m}_m\sqrt{T_{0m}}$. This ratio was chosen instead of p_{0c}/p_{0m} as the most appropriate method of baselining each design since the mass flow ratio $\dot{m}_c/\dot{m}_m$—easily determined from $\dot{m}_c\sqrt{T_{0c}}/\dot{m}_m\sqrt{T_{0m}}$—can be used to estimate cycle-efficiency. The total pressure ratio p_{0c}/p_{0m}, while important from a hardware perspective and for matching several non-dimensional groups affecting film effectiveness, does not indicate the relative cycle efficiency cost of each vane design.

Overall cooling effectiveness is shown at $\dot{m}_c\sqrt{T_{0c}}/\dot{m}_m\sqrt{T_{0m}}$ ratios of 7%, 8.9% and 10.9% for data reduction. The equivalent pressure ratios p_{0c}/p_{0m} and mass flow ratios $\dot{m}_c/\dot{m}_m$ (for known temperatures) at rig and engine conditions are summarised in Table 7.1.

Table 7.1. $\dot{m}_c\sqrt{T_{0c}}/\dot{m}_m\sqrt{T_{0m}}$, p_{0c}/p_{0m} and $\dot{m}_c/\dot{m}_m$ assuming temperatures in Table 5.2.

	Baseline cast			Baseline DMLS			RP 1D			RP 1D+			RP 3D		
$\frac{\dot{m}_c\sqrt{T_{0c}}}{\dot{m}_m\sqrt{T_{0m}}}$ (%)	7	8.9	10.9	7	8.9	10.9	7	8.9	10.9	7	8.9	10.9	7	8.9	10.9
$\frac{p_{0c}}{p_{0m}} - 1$	.017	.035	.058	.021	.042	.071	.025	.047	.077	.023	.046	.075	.022	.046	.078
$\left(\frac{\dot{m}_c}{\dot{m}_m}\right)_{\text{rig}}$ (%)	7.6	9.6	11.8	7.6	9.6	11.8	7.6	9.6	11.8	7.6	9.6	11.8	7.6	9.6	11.8
$\left(\frac{\dot{m}_c}{\dot{m}_m}\right)_{\text{eng}}$ (%)	10.7	13.5	16.6	10.7	13.5	16.6	10.7	13.5	16.6	10.7	13.5	16.6	10.7	13.5	16.6

The maximum possible error in $\dot{m}_c\sqrt{T_{0c}}/\dot{m}_m\sqrt{T_{0m}}$ caused by leaks within the Sector Facility is estimated using the method in Chapter 5. The practical effect of the leak error on the results reported in this chapter is to non-uniformly translate the overall cooling effectiveness against $\dot{m}_c\sqrt{T_{0c}}/\dot{m}_m\sqrt{T_{0m}}$ plots in the *x*-direction. This can be seen most clearly in Fig. 7.10. The overall cooling effectiveness at a given $\dot{m}_c\sqrt{T_{0c}}/\dot{m}_m\sqrt{T_{0m}}$ is then given as the *y*-range between the shifted overall cooling effectiveness curve (which assumes the worst possible leak error) and the non-shifted overall cooling effectiveness curve (which assumes no leak).

7.4 Image Registration

Due to the movement of the IR cameras between runs, the infra-red images were not exactly aligned. To compensate, the images were automatically re-aligned against a reference image using the MATLAB image registration functions. A flow diagram of the method is given in Fig. 7.3. After the IR black and grey-body calibrations were applied to the raw image, the entire 640x480 image was registered to a 640x480 reference image using *imregister.m* and multimodal similarity, which consists of translation, rotation and scale. The image was then cropped to remove padding—seen at the bottom of *Registered image 1* in Fig. 7.3. A second multimodal translational registration was performed for fine-tuning, and was subsequently cropped to remove padding.

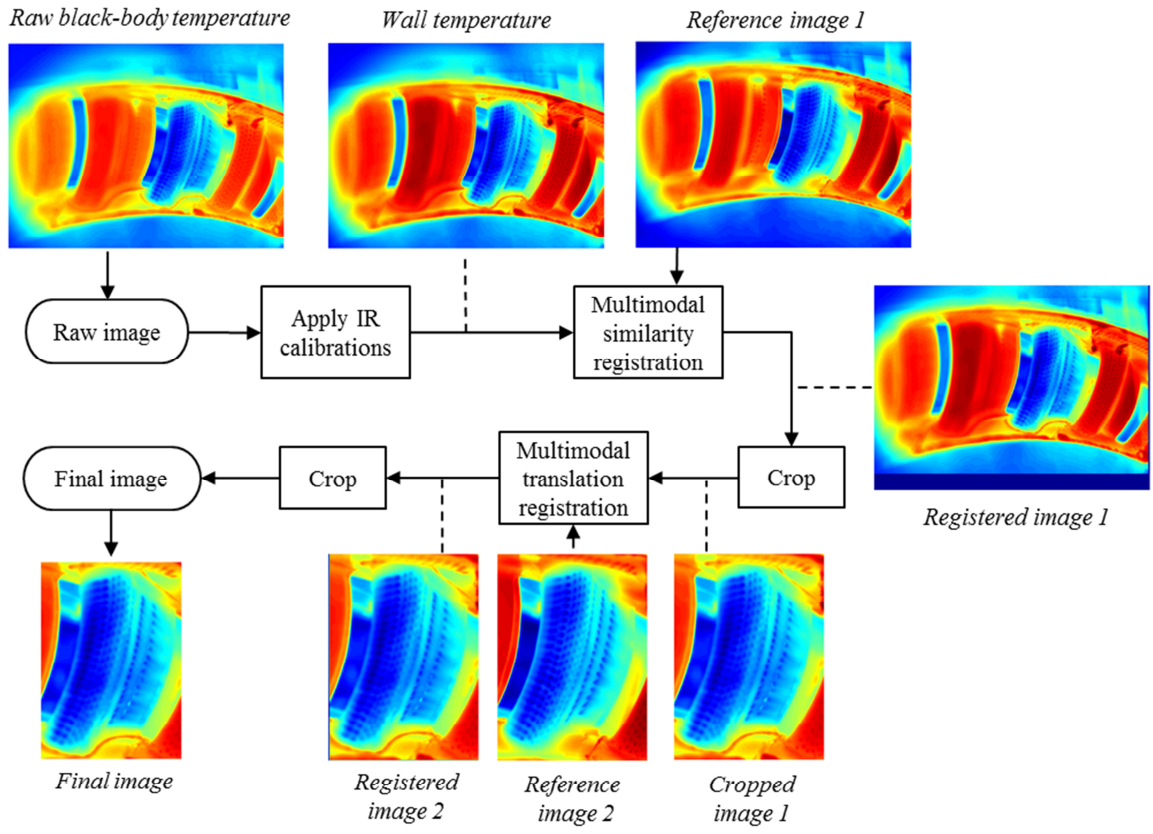


Figure 7.3. Image registration process.

7.5 Mainstream Recovery Ratio *c*: Results

The mainstream recovery ratio distributions c are shown in Figs. 7.4 and 7.5 at $\dot{m}_c\sqrt{T_{0c}}/\dot{m}_m\sqrt{T_{0m}}$ ratios 7%, 8.9% and 10.9% for the PS and SS of all designs. The recovery ratio distributions at 25% span, 50% span, and 75% span, are shown in Fig. 7.6 for $\dot{m}_c\sqrt{T_{0c}}/\dot{m}_m\sqrt{T_{0m}}$ = 8.9%.

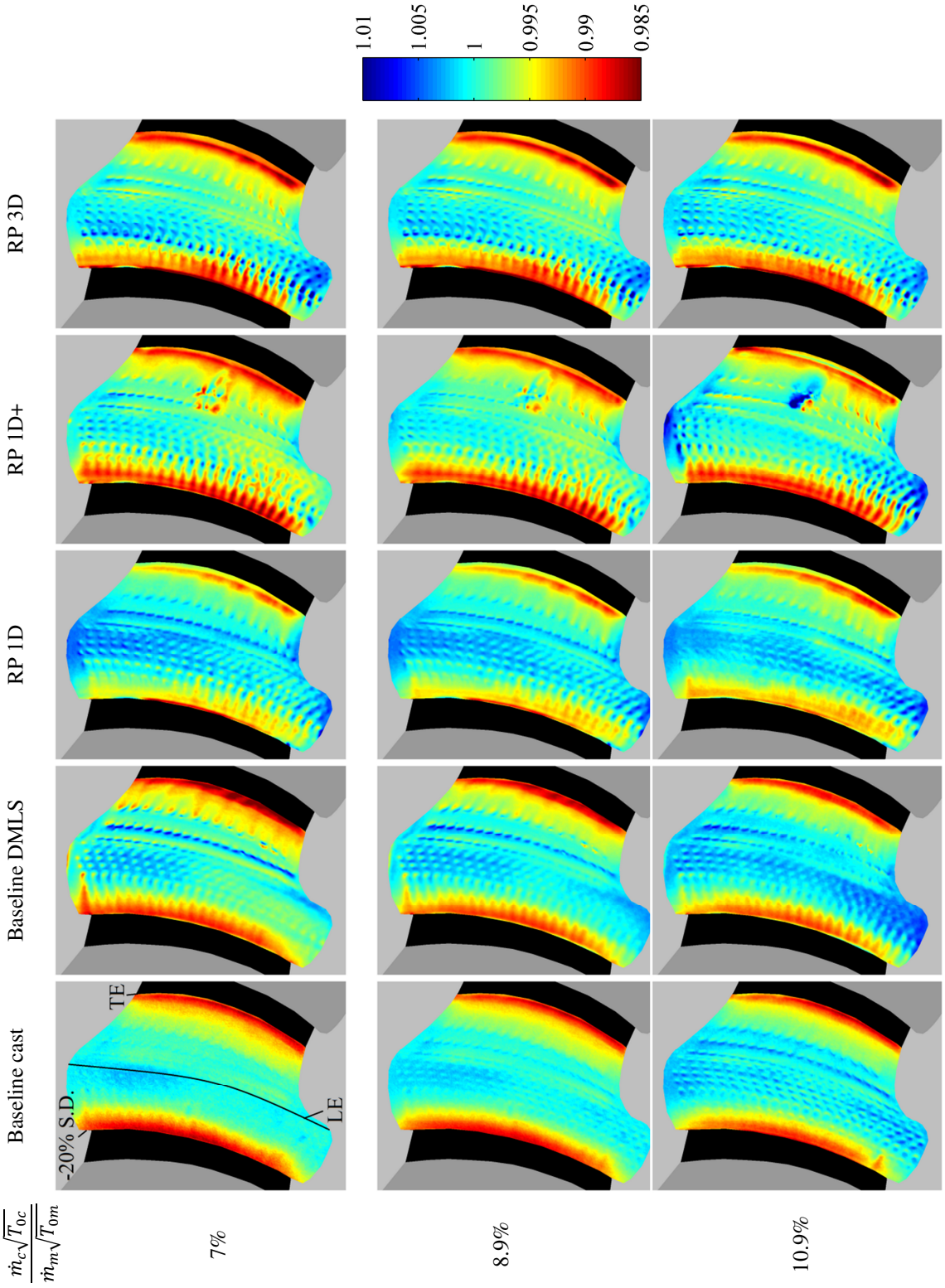


Figure 7.4. Pressure-side mainstream recovery ratio.

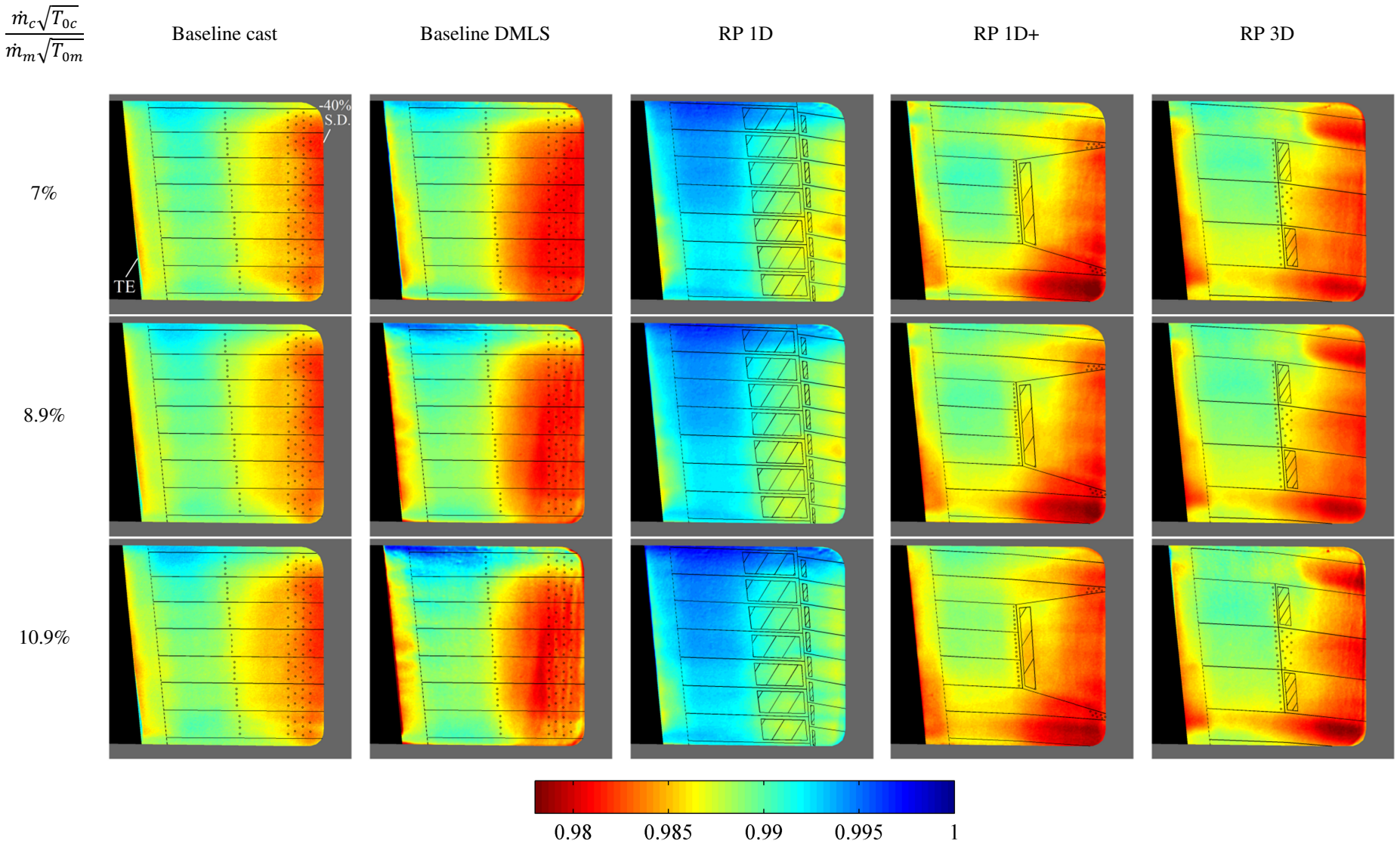


Figure 7.5. Suction-side mainstream recovery ratio.

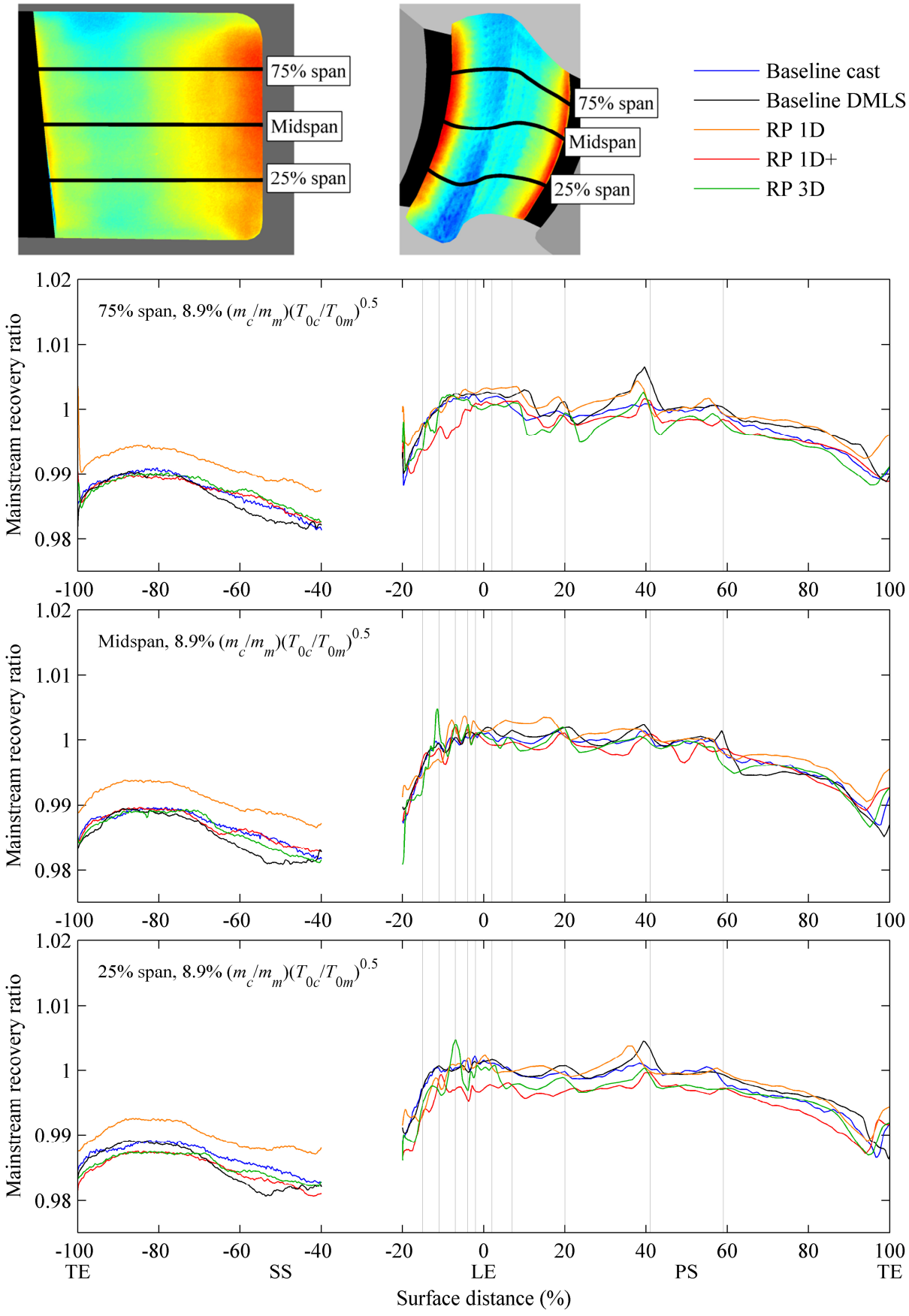


Figure 7.6. Mainstream recovery ratio at 25%, 50% and 75% span at 8.9% $\dot{m}_c\sqrt{T_{0c}}/\dot{m}_m\sqrt{T_{0m}}$.

7.6 Mainstream Recovery Ratio *c*: Discussion

General Magnitude and Distribution

The recovery ratio is between 0.98 and 1, which is in the same range and has the same trend as the recovery ratio predicted by Luque Martinez (2011)—shown in Fig. 7.7. Luque Martinez estimated the recovery ratio using the external Mach number distribution from a CFD simulation of an uncooled T500 HPNGV and equations (7.1) and (7.2). The origin and quality of this prediction is unknown and therefore caution is recommended when comparing the distributions.

The mean SS recovery ratio is lower than the mean PS recovery ratio, likely because the mean SS Mach number is greater than the mean PS Mach number. The acceleration of the mainstream around the SS shoulder creates a substantial drop in the recovery ratio—seen at -20% surface distance in Fig. 7.6. The PS recovery ratio decreases with surface distance, which corresponds to the increase in mainstream Mach number. The PS recovery ratio is minimum at the TE where the PS Mach number is greatest. The recovery ratio is approximately constant with span for all designs.

Variation with $\left(\dot{m}_c\sqrt{T_{0c}}\right)/\left(\dot{m}_m\sqrt{T_{0m}}\right)$

There is little variation in recovery ratio with $\dot{m}_c\sqrt{T_{0c}}/\dot{m}_m\sqrt{T_{0m}}$ (Figs. 7.4 and 7.5). However, it is observed that the PS recovery ratio reduces around the showerhead film cooling holes as $\dot{m}_c\sqrt{T_{0c}}/\dot{m}_m\sqrt{T_{0m}}$ increases, which is seen most clearly around the hub for rows S1-S3 in the baseline cast/DMLS designs in Fig. 7.4. This may be because the film energises the boundary layer and therefore increases local Mach number, i.e., the introduction of the film increases the local total pressure for the same static pressure, resulting in increased local Mach number. The SS recovery ratio distribution for baseline cast/DMLS appears to narrow towards midspan as $\dot{m}_c\sqrt{T_{0c}}/\dot{m}_m\sqrt{T_{0m}}$ increases (Fig. 7.5). This could be a result of secondary flow redistribution due to increased coolant mass flow.

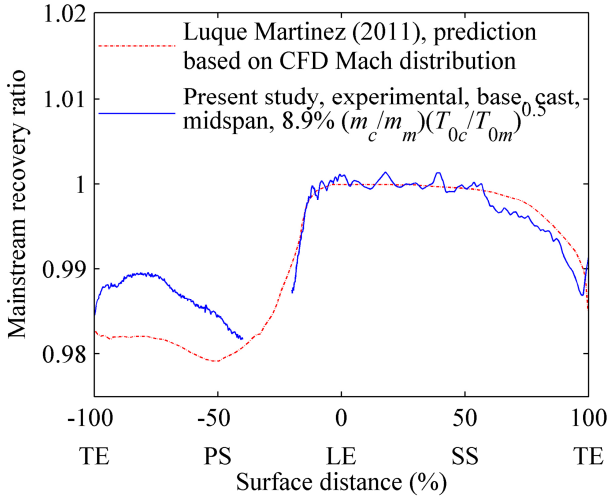


Figure 7.7. Mainstream recovery ratio compared to the prediction of Luque Martinez (2011).

RP 1D+ and RP 3D Recovery Ratio Distributions

The hump in RP 1D+ recovery ratio at midspan around rows P4 and P5 on the PS (Fig. 7.4) is caused by an Araldite leak from row P4. RP 1D+ SS recovery ratio is lowest at the hub. This corresponds to an area of high overall cooling effectiveness (shown later) and suggests that the SS area of low recovery ratio around the hub may be due to high film effectiveness generating high local total pressure and subsequently high local Mach number. Alternatively, the recovery ratio may be low here because of variation in aerofoil shape, or may be affected by the local internal cooling system as theorised by Luque Martinez (2011). The RP 3D SS recovery ratio distribution appears to follow the reverse-pass passages, possibly due to the same reasons.

Comparison Between Recovery Ratio Distributions

The SS recovery ratio distributions are similar for all designs apart from RP 1D, for reasons discussed shortly. Compared to the SS distributions, the PS recovery ratio distributions are noisier and less matched, though still to within 0.005. This is probably because the SS wall temperature measurement is more accurate than the PS wall temperature measurement, since the PS IR camera is further away and views the surface over a large range of angles.

The RP 1D SS recovery ratio is 0.004 greater than the other designs (Fig. 7.6) because the mainstream Mach number is ~12% lower in the RP 1D experiments. This was only discovered after all experiments were performed. The probable cause of the RP 1D Mach number disparity was the misalignment of the leading laser-sintered vane in the RP 1D vane pair, resulting in greater passage area between vane 4 and 5. However, the vane pair was disassembled before this theory could be validated. Though the reduced RP 1D mainstream Mach number reduces confidence in the effectiveness comparisons between RP 1D and the other designs, it nevertheless verifies that the mainstream Mach number influences recovery ratio distribution predictably. The overall cooling effectiveness results of RP 1D are still included in this chapter though comparisons between the SS of RP 1D and the SS of the other designs should be made with caution.

7.7 Overall Cooling Effectiveness θ: Results and Discussion

Overall cooling effectiveness θ is plotted in Figs. 7.8-7.18 for each vane. Figures 7.8 and 7.9 show the PS and SS overall cooling effectiveness distributions of each vane at three $\dot{m}_c\sqrt{T_{0c}}/\dot{m}_m\sqrt{T_{0m}}$ ratios. Figures 7.10 and 7.11 show the overall cooling effectiveness as a function of $\dot{m}_c\sqrt{T_{0c}}/\dot{m}_m\sqrt{T_{0m}}$ at 9 points on the PS and 9 points on the SS. Each curve consists of 40 + experimental data points, a best-fit curve, and the maximum possible error in the measurement due to leaks. Figures 7.12 to 7.18 show chordwise and spanwise overall cooling effectiveness distributions at 25, 50, 75% span, and -95, -78, -62, -45, - 18, -3, 50, 95% surface distance. Each distribution is plotted at $\dot{m}_c\sqrt{T_{0c}}/\dot{m}_m\sqrt{T_{0m}}$ ratios 7%, 8.9% and 10.9%. Each distribution is shown as a range to indicate the possible error due to leaks.

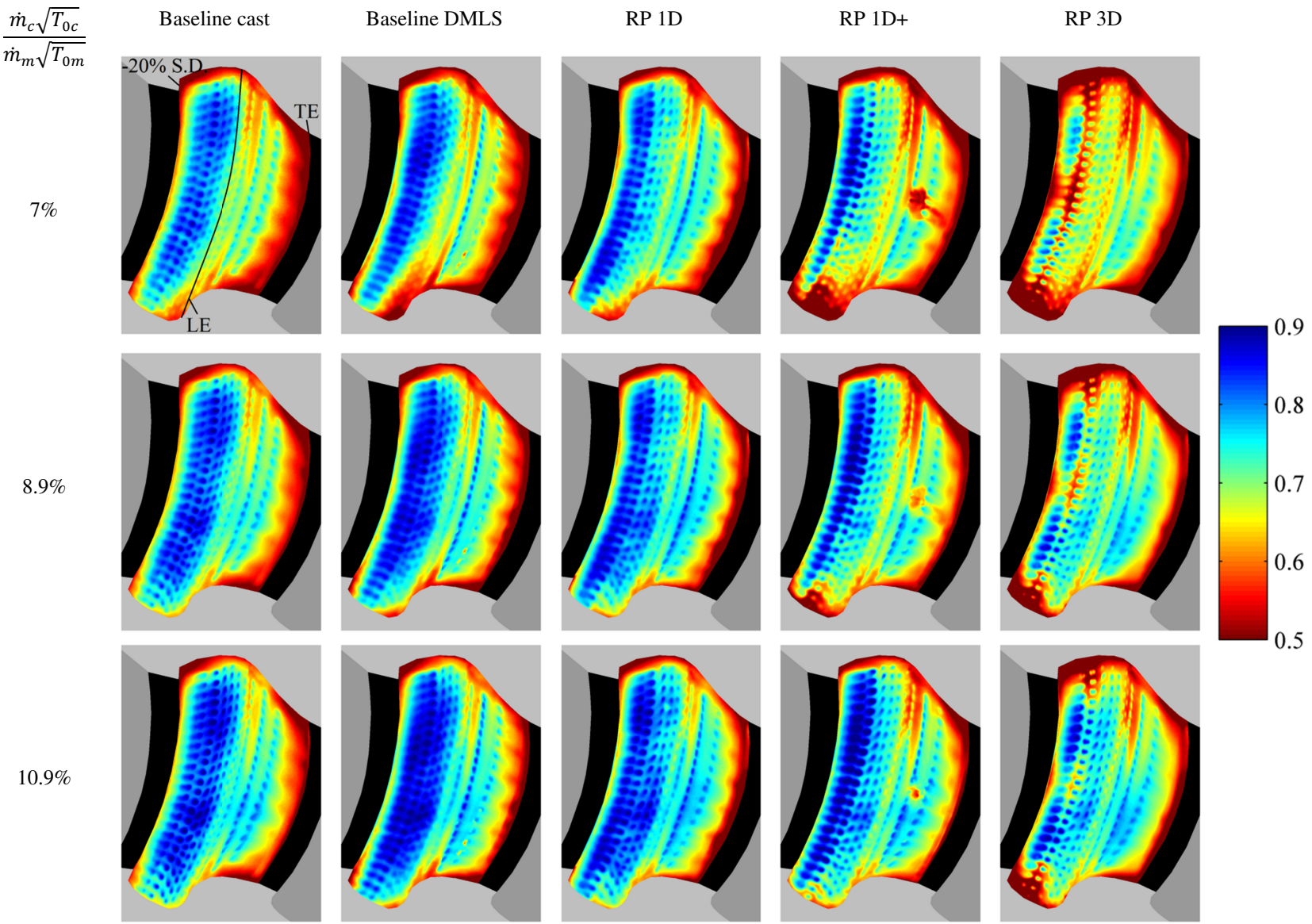


Figure 7.8. Pressure-side overall cooling effectiveness.

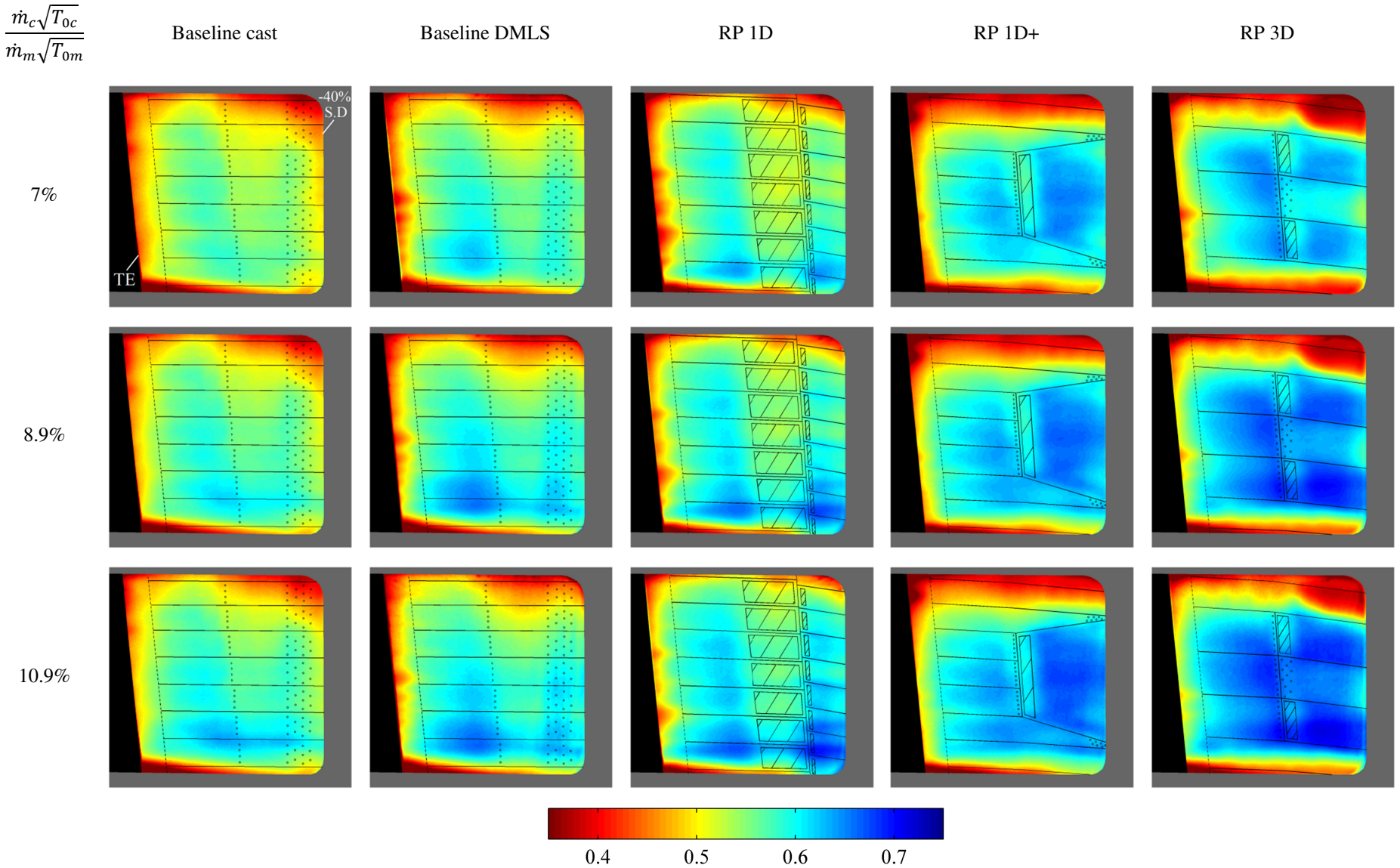


Figure 7.9. Suction-side overall cooling effectiveness.

7.7.1 Discussion of Figure 7.8

On the pressure side, the vanes are coldest near the leading-edge and hottest at the trailing-edge. The PS is cooler at midspan than at hub and case. In the Sector Facility, the mainstream radial temperature profile is approximately uniform. In the engine, the mainstream temperature is generally greater at midspan than at hub/case, and platform film cooling flow washes up onto the vane (e.g., Thomas et al, 2013). The radial *vane* temperature distribution at engine conditions will therefore be more uniform than the Sector experiments.

The apparent trough in overall cooling effectiveness at midspan around P4 and P5 on RP 1D+ is due to an Araldite leak through one of the P4 cooling holes. The radial striations in overall cooling effectiveness around rows P2 and P3 for all designs are likely to be artefacts of obtuse viewing angles because the effective surface emissivity in these regions is lower than the rest of the vane.

The PS overall cooling effectiveness distribution is similar across all designs apart from RP 3D (values given later). The cast and laser-sintered baseline vanes are marginally cooler around rows S1 and S3 than the other vanes. RP 3D has a hot-spot around the midspan S4/S5 cooling holes, which are likely starved of coolant due to the abrupt expansion of the RP passages into a shared S4/S5 plenum.

Reducing $\dot{m}_c\sqrt{T_{0c}}/\dot{m}_m\sqrt{T_{0m}}$ causes starvation and ingestion of the film cooling holes around the hub LE (P2–S3) for all designs. Row S4 in RP 3D ingests for $\dot{m}_c\sqrt{T_{0c}}/\dot{m}_m\sqrt{T_{0m}} < 10\%$, clearly shown by the hot region between S3 and S5 in the overall cooling distribution at $\dot{m}_c\sqrt{T_{0c}}/\dot{m}_m\sqrt{T_{0m}} = 7\%$.

7.7.2 Discussion of Figure 7.9

Suction side overall cooling effectiveness decreases towards the TE. The midspan SS is cooler than the hub SS, which is cooler than the case SS. The cast and laser-sintered baseline SS overall cooling effectiveness distributions are broadly similar, both exhibiting cold regions around the impingement points and a cold chordwise streak around the hub which are likely due to the re-distribution of film cooling via secondary flow. The SS of the laser-sintered baseline vane are generally cooler than the SS of the cast baseline. The difference in overall cooling effectiveness between the cast and laser-sintered baseline is likely due to additional internal surface roughness in the laser-sintered designs. In both designs, increasing $\dot{m}_c\sqrt{T_{0c}}/\dot{m}_m\sqrt{T_{0m}}$ predominantly increases the overall cooling effectiveness in existing cold regions.

The SS overall cooling effectiveness of RP 1D is similar in magnitude and distribution to the laser-sintered baseline, though the early RP 1D SS is cooler around the hub. This may be because of enhanced internal convective cooling in this area, or differences in the radial distribution of the film. The hatched boxes in RP 1D indicate the intended location of an impingement plate. However, the impingement plate was not included during Sector and CCR experiments to better match the TE

coolant mass flow rate to the other designs. The overall cooling effectiveness of RP 1D within the hatched region is lower than in the equivalent regions of all other designs. This is probably because the flow is undirected within the RP 1D TE compartment, creating areas of low internal HTC. This highlights the benefit of locally controlled, directed flow. These comparisons are made hesitantly, since the mainstream Mach number distribution for RP 1D was 12.5% lower than the other designs.

The SS of RP 1D+ is cooler than the SS of the cast and laser-sintered baseline everywhere except near the case—exact values reported shortly. Significantly, the trailing-edge temperature is lower in the RP 1D+ design than both baseline vanes. RP 1D+ is also particularly effective at cooling the early SS, which is convectively cooled by the reverse-pass passage. It is likely that the case (upper) trailing-edge passage in RP 1D+ did not flow coolant—either by manufacturing limitations within the TE pedestal bank or high exit static pressure at the TE slot at the case—causing the relatively hot region near the case.

The SS of RP 3D is cooler than the SS of all other designs, especially the mid-to-late SS. This may be because: (i) the entrance to the TE pedestal bank in RP 3D is much closer to the TE than the cast/DMLS baseline and RP 1D, and therefore coolant within the TE pedestal bank is colder in RP 3D; (ii) the trailing-edge pedestal bank in RP 3D consists of five chordal passages, compared to 7 in all other designs, which may be beneficial for TE pedestal convective heat transfer. The RP 3D design is particularly strong in the areas that are convectively cooled by the off-midspan reverse-pass passages which feed S4 and S5. The cooling capability of the off-midspan reverse-pass (RP) passages appears similar to that of the RP passage in RP 1D+.

The RP 3D midspan RP passage—which feeds the hub and case portions of the TE via a flow split and 180 degree turn—appears less effective than the RP 3D off-midspan passages, though still more effective than baseline and RP 1D designs. This is probably caused by lower coolant flow and external film effectiveness than designed. Reduced flow in the midspan RP passage is indicated by low overall cooling effectiveness near the case, which is convectively cooled using coolant fed via the midspan RP passage. It appears that all the coolant that flows through the midspan RP passage in RP 3D travels preferentially to the hub TE passage. This may be because the TE exit static pressure is lower at the hub than at the case, or due to blockage within the case TE passage. Midspan RP 3D overall cooling effectiveness increases with $\dot{m}_c\sqrt{T_{0c}}/\dot{m}_m\sqrt{T_{0m}}$ because the midspan film effectiveness increases—as shown by the removal of the RP 3D midspan hotspot around S4 and S5 in Fig. 7.8.

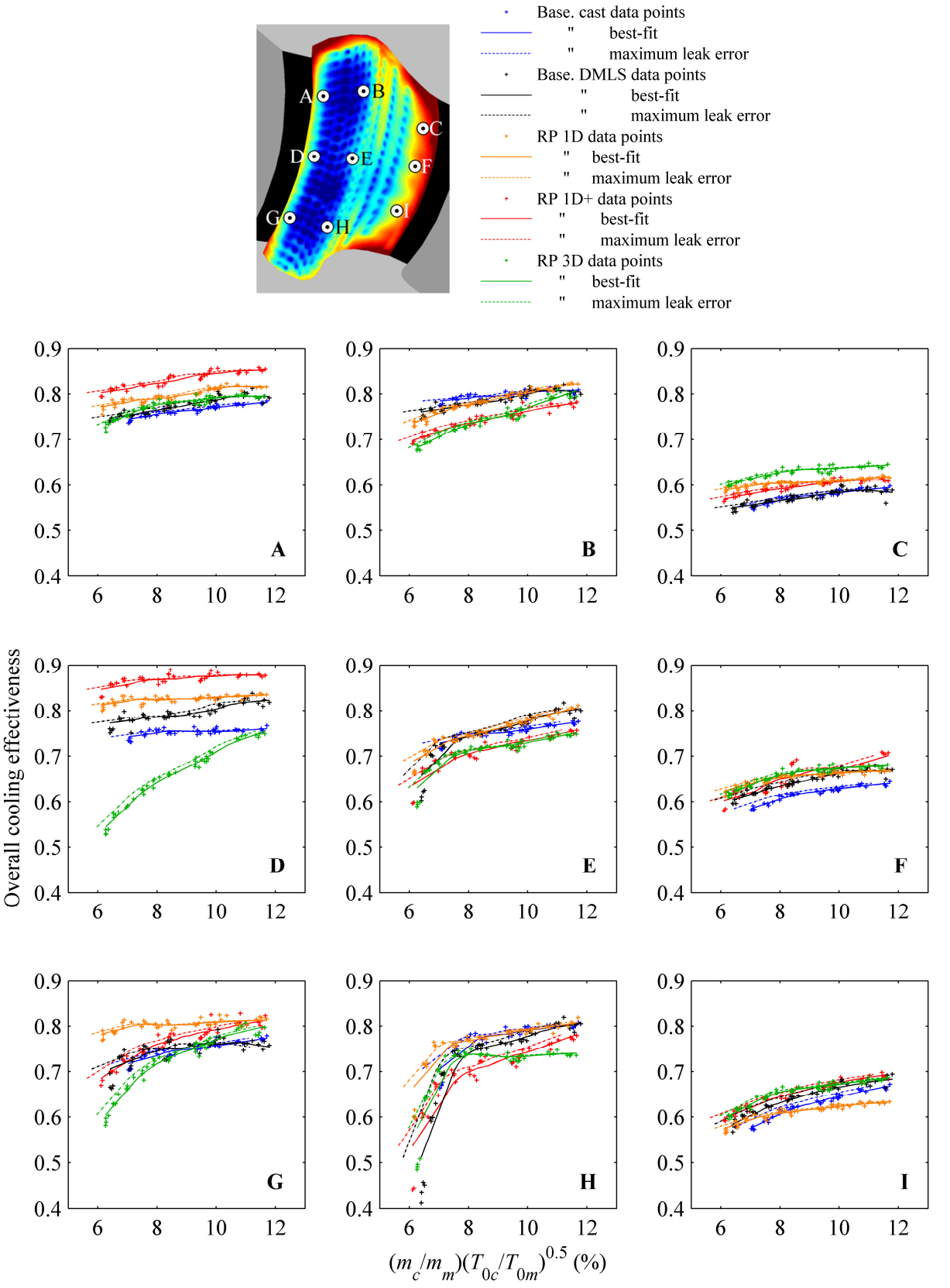


Figure 7.10. Pressure-side overall cooling effectiveness at 9 points, as a function of $\dot{m}_c\sqrt{T_{0c}}/\dot{m}_m\sqrt{T_{0m}}$.

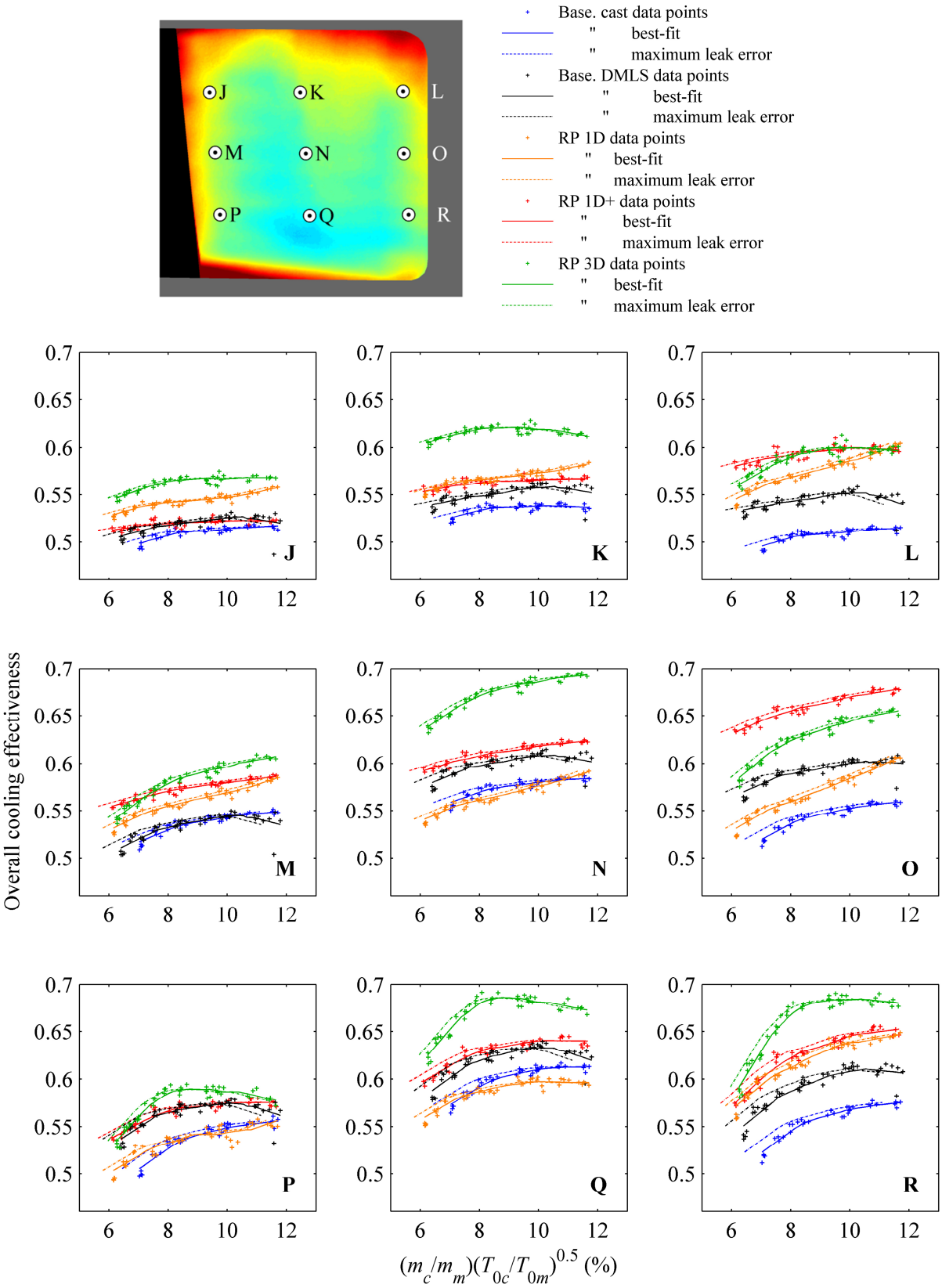


Figure 7.11. Suction-side overall cooling effectiveness at 9 points, as a function of $\dot{m}_c\sqrt{T_{0c}}/\dot{m}_m\sqrt{T_{0m}}$.

7.7.3 Discussion of Figure 7.10

The raw experimental data lie within 0.01 θ of the best-fit line. The collapse gives confidence that the scaling techniques and IR thermography methods are adequate. Experimental leak errors, shown by the dashed lines, do not affect the ranking of design performance. The absolute error caused by a leak at a given $\dot{m}_c\sqrt{T_{0c}}/\dot{m}_m\sqrt{T_{0m}}$ increases with the rate of change of overall cooling effectiveness with respect to $\dot{m}_c\sqrt{T_{0c}}/\dot{m}_m\sqrt{T_{0m}}$. The largest overall cooling effectiveness gradient occurs at point H on the PS, where leaks cause a maximum error in overall cooling effectiveness of 0.1 at a given $\dot{m}_c\sqrt{T_{0c}}/\dot{m}_m\sqrt{T_{0m}}$. In contrast, the effect of leaks is negligible where the overall cooling effectiveness has plateaued, e.g., on the SS for $\dot{m}_c\sqrt{T_{0c}}/\dot{m}_m\sqrt{T_{0m}} > 10\%$.

The overall cooling effectiveness at points E and H (LE midspan and LE hub, respectively) is approximately constant for $\dot{m}_c\sqrt{T_{0c}}/\dot{m}_m\sqrt{T_{0m}} > 8\%$. Below 8%, the overall cooling effectiveness reduces significantly due to the ingestion of the hub-to-midspan showerhead rows. Overall cooling effectiveness increases linearly with $\dot{m}_c\sqrt{T_{0c}}/\dot{m}_m\sqrt{T_{0m}}$ around the PS case (points A, B and C), and around the PS trailing-edge (points C, F and I). Just downstream of S5 at midspan (point D), the overall cooling effectiveness is approximately constant with $\dot{m}_c\sqrt{T_{0c}}/\dot{m}_m\sqrt{T_{0m}}$ for all designs apart from RP 3D. The RP 3D S5 cooling holes around midspan ingest at lower PRs (as seen in Fig. 7.8) because of the relatively abrupt expansion of the two RP passages into the shared S4/S5 plenum.

The overall cooling effectiveness behaviour immediately downstream of the S5 cooling holes at the hub (point G) depends on the geometry. RP 1D+ and RP 3D both see a sharp drop in overall cooling effectiveness for $\dot{m}_c\sqrt{T_{0c}}/\dot{m}_m\sqrt{T_{0m}} < 8\%$, indicative of ingestion at some point in the showerhead region. Overall cooling effectiveness at point G in the baseline cast and RP 1D designs is maximum at $\dot{m}_c\sqrt{T_{0c}}/\dot{m}_m\sqrt{T_{0m}} = 8\%$. This is likely due to a local optimum in film effectiveness due to optimal momentum flux or blowing ratio. The baseline DMLS overall cooling effectiveness at point G increases linearly with $\dot{m}_c\sqrt{T_{0c}}/\dot{m}_m\sqrt{T_{0m}}$.

7.7.4 Discussion of Figure 7.11

On the SS, the overall cooling effectiveness tends to plateau at $\dot{m}_c\sqrt{T_{0c}}/\dot{m}_m\sqrt{T_{0m}} > 10\%$, apart from RP 1D. The overall cooling effectiveness of RP 1D increases at a higher rate than the other designs, possibly because the mainstream Mach number is unmatched for the RP 1D experiments. RP 3D had a peak overall cooling effectiveness around the hub and case (points J, K, P, Q and R) at $\dot{m}_c\sqrt{T_{0c}}/\dot{m}_m\sqrt{T_{0m}} = 8\%$. This may be due to a local optimum in film effectiveness.

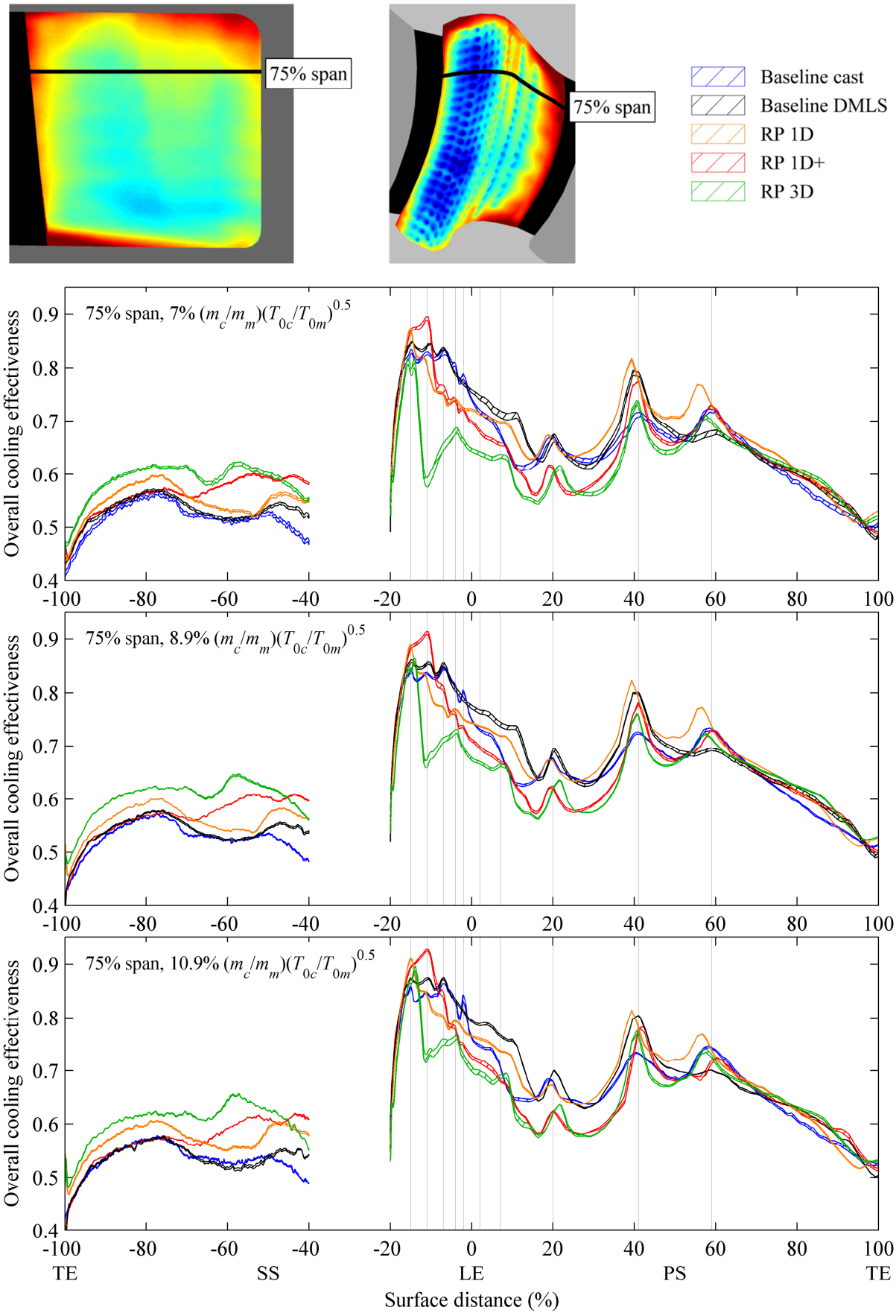


Figure 7.12. 75% span overall cooling effectiveness for 7%, 8.9% and 10.9% $\dot{m}_c\sqrt{T_{0c}}/\dot{m}_m\sqrt{T_{0m}}$.

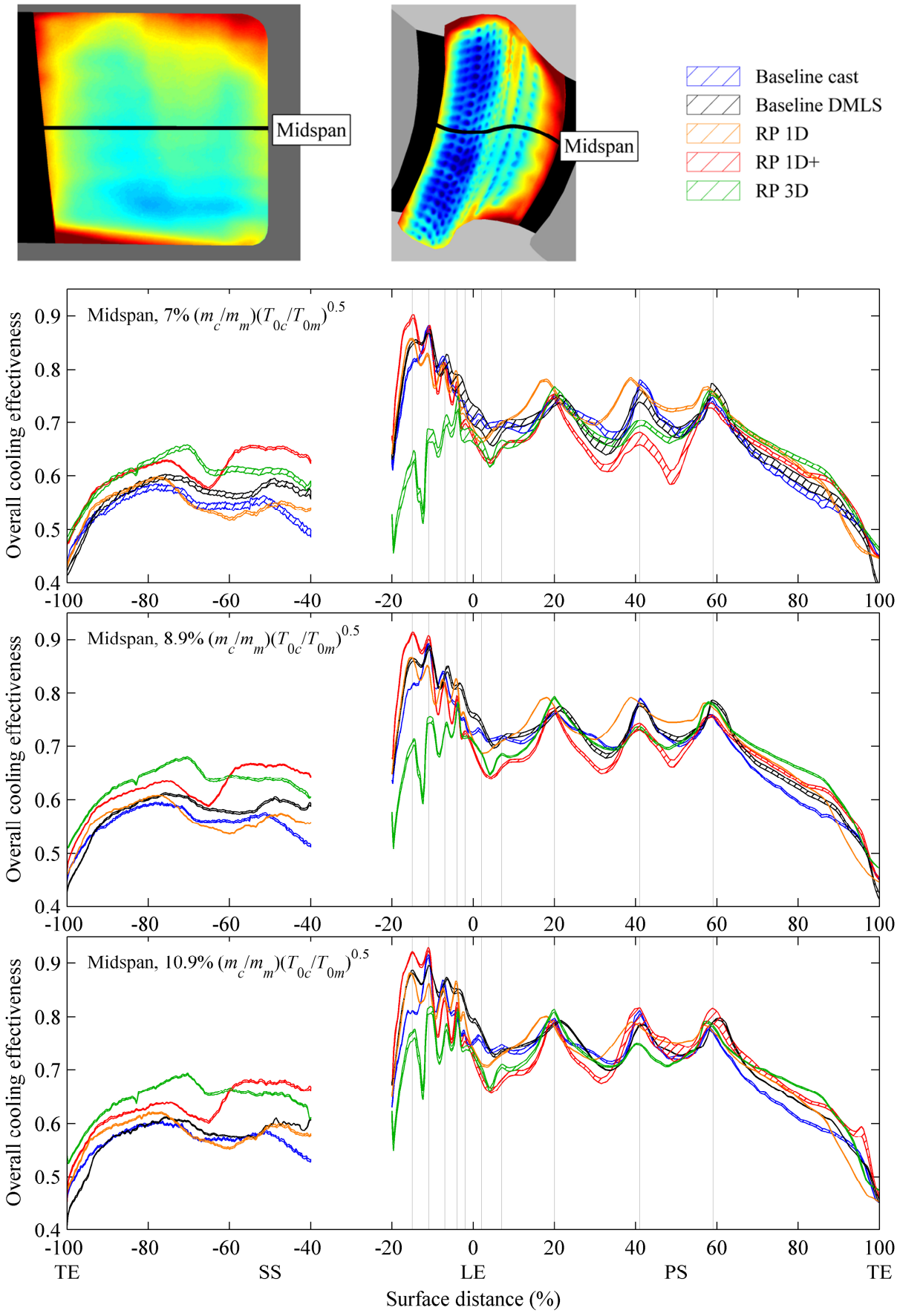


Figure 7.13. Midspan overall cooling effectiveness for 7%, 8.9% and 10.9% $\dot{m}_c\sqrt{T_{0c}}/\dot{m}_m\sqrt{T_{0m}}$.

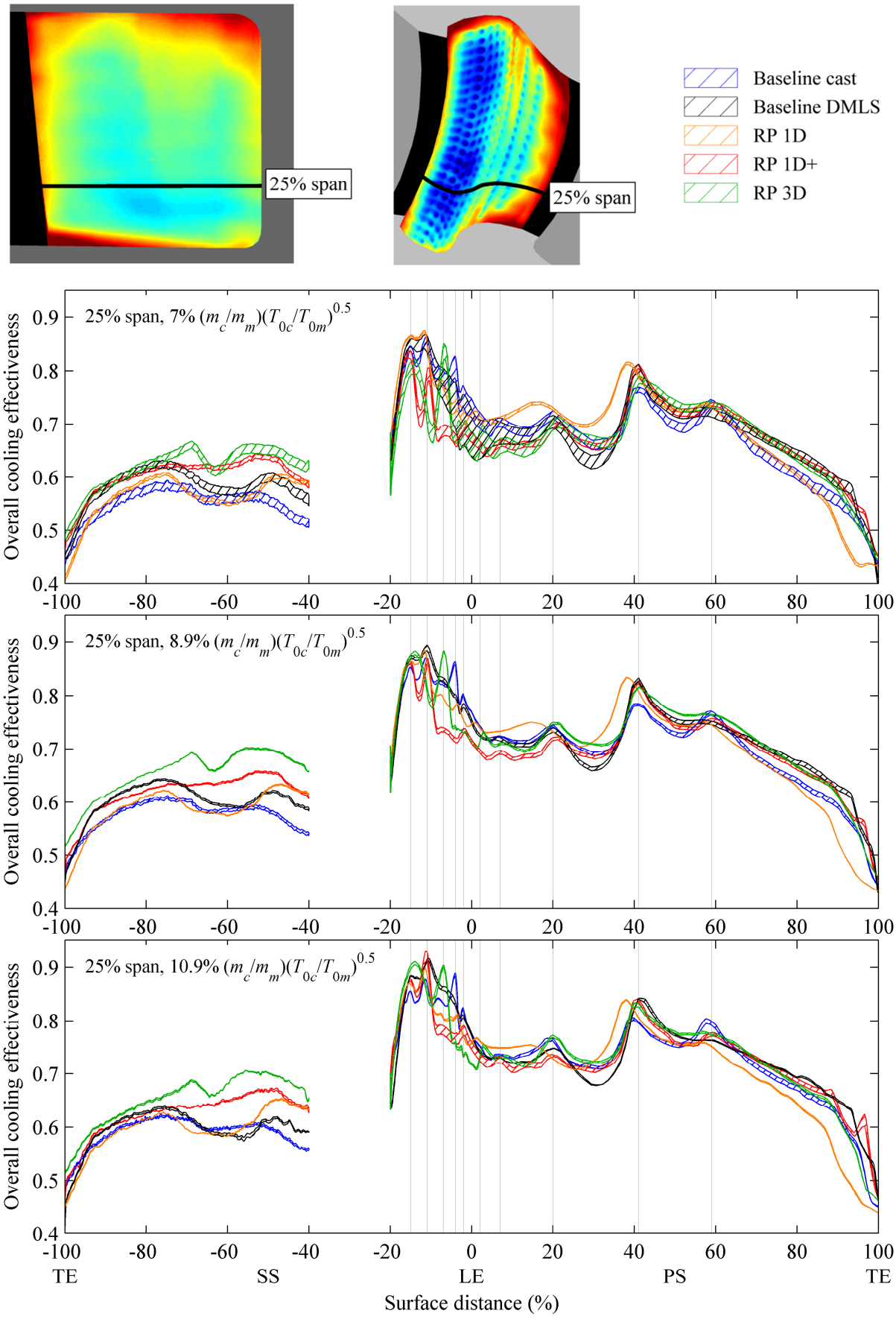


Figure 7.14. 25% span overall cooling effectiveness for 7%, 8.9% and 10.9% $\dot{m}_c\sqrt{T_{0c}}/\dot{m}_m\sqrt{T_{0m}}$.

7.7.5 Discussion of Figures 7.12–7.14

Suction-side

Overall cooling effectiveness is shown as a hatched range to indicate the maximum error due to leaks.

The overall cooling effectiveness on the SS is lower on average and more uniform than on the PS for all designs, because the film effectiveness is lower and more uniform on the SS. The mean SS overall cooling effectiveness of the cast baseline is 0.02-0.04 lower (i.e., 20-40 K hotter) than the laser-sintered baseline at all $\dot{m}_c\sqrt{T_{0c}}/\dot{m}_m\sqrt{T_{0m}}$. This difference is likely due to differences in internal surface roughness.

The SS RP 1D+ effectiveness distribution between -70% and -40% surface distance (i.e., the section convectively cooled by the RP passage) is 0.06 more effective (60 K cooler) than the laser-sintered baseline at all spans and at all $\dot{m}_c\sqrt{T_{0c}}/\dot{m}_m\sqrt{T_{0m}}$. The RP 1D+ SS TE effectiveness at 25% and 75% span is approximately the same as the baseline designs, since the TE pedestal system at these spans is of a similar length and form. At midspan, the RP 1D+ TE system is shorter than the baseline TE systems and therefore the internal coolant temperature is lower, resulting in an overall cooling effectiveness enhancement of 0.03 at SS TE (30 K cooler) compared to the baseline/RP 1D designs.

The dip in RP 1D+ overall cooling effectiveness around -65% surface distance at 50% and 75% span coincides with the slot entrance to the RP passage. The slot is fairly wide (~ 6 mm), resulting in an area of undirected flow and low convective heat transfer. This can be seen within the hatched region in Fig. 7.9. The effectiveness in this area could be improved by reducing the slot width, though this would incur greater coolant pressure loss.

RP 3D SS overall cooling effectiveness is approximately 0.06 greater (60 K cooler) than the laser-sintered baseline at all spans and at all $\dot{m}_c\sqrt{T_{0c}}/\dot{m}_m\sqrt{T_{0m}}$. RP 3D is the most effective design around the SS TE, with an effectiveness improvement compared to the baseline designs of around 0.03 (30 K cooler). RP 3D cools the entire TE span very uniformly (apart from very near the hub and case), because the RP 3D TE system is as short as possible. It may also be because the RP 3D TE is fed by 5 chordal passages rather than 7 as in the other designs.

The dip in RP 3D effectiveness at -65% surface distance at 25% and 75% span coincides with the slot entrances to the off-midspan RP passages. Like RP 1D+, the slot entrance is fairly wide, and the undirected flow causes reduction in internal heat transfer. At midspan, the overall cooling effectiveness of RP 3D decreases between -70% and -40% surface distance as compared to the effectiveness later on the SS because the midspan RP passage flows less coolant than designed. However, RP 3D is still more effective (~ 0.05 greater) than the baseline designs in this area.

Pressure-side

The overall cooling effectiveness distributions are less uniform on the PS than the SS. Generally, the PS is coolest around the leading edge and hottest around the TE. The locations of the film cooling rows are shown by the vertical grey lines; each film cooling row corresponds to a local peak in overall cooling effectiveness.

The effectiveness of the cast and laser-sintered baseline are approximately the same in the showerhead region, at all spans and all $\dot{m}_c\sqrt{T_{0c}}/\dot{m}_m\sqrt{T_{0m}}$. There is some disparity between cast/laser-sintered baseline designs at 75% span around 0% to 20% surface distance, which may be due to obtuse IR camera viewing angles. The peak in effectiveness due to the injection of coolant at P4 is greater in the laser-sintered baseline than the cast baseline. Contrastingly, the effectiveness peak at P5 is greater in the cast baseline than in the laser-sintered baseline. Between P5 and the TE, the effectiveness of the laser-sintered baseline is consistently 0.03 greater (30 K cooler) than the cast baseline—likely due to greater internal surface roughness within the laser-sintered pedestal bank.

The PS RP 1D overall cooling effectiveness distribution is broadly similar to the laser-sintered baseline. The PS effectiveness distributions of RP 1D+ and RP 3D are similar, except for near the LE at 50% and 75% span. The PS overall cooling effectiveness between 0% and 40% surface distance for RP 1D+/RP 3D is approximately 0.04 lower (40 K greater) than the baseline/RP 1D designs. Between 60% and 100%, the overall cooling effectiveness of RP 1D+/RP 3D is equal to or greater than the other designs.

RP 3D has a much lower effectiveness than the other designs between -20% to 0% surface distance at midspan—a reduction in effectiveness of around 0.25, or increase in temperature of 250 K. This is because of the starvation of the midspan S4/S5 holes due to the abrupt expansion of the two off-midspan RP passages into a shared plenum. RP 3D also experiences low effectiveness around S4, especially at 75% span at low $\dot{m}_c\sqrt{T_{0c}}/\dot{m}_m\sqrt{T_{0m}}$, because of high pressure losses in the off-midspan passages and the starvation and ingestion of S4.

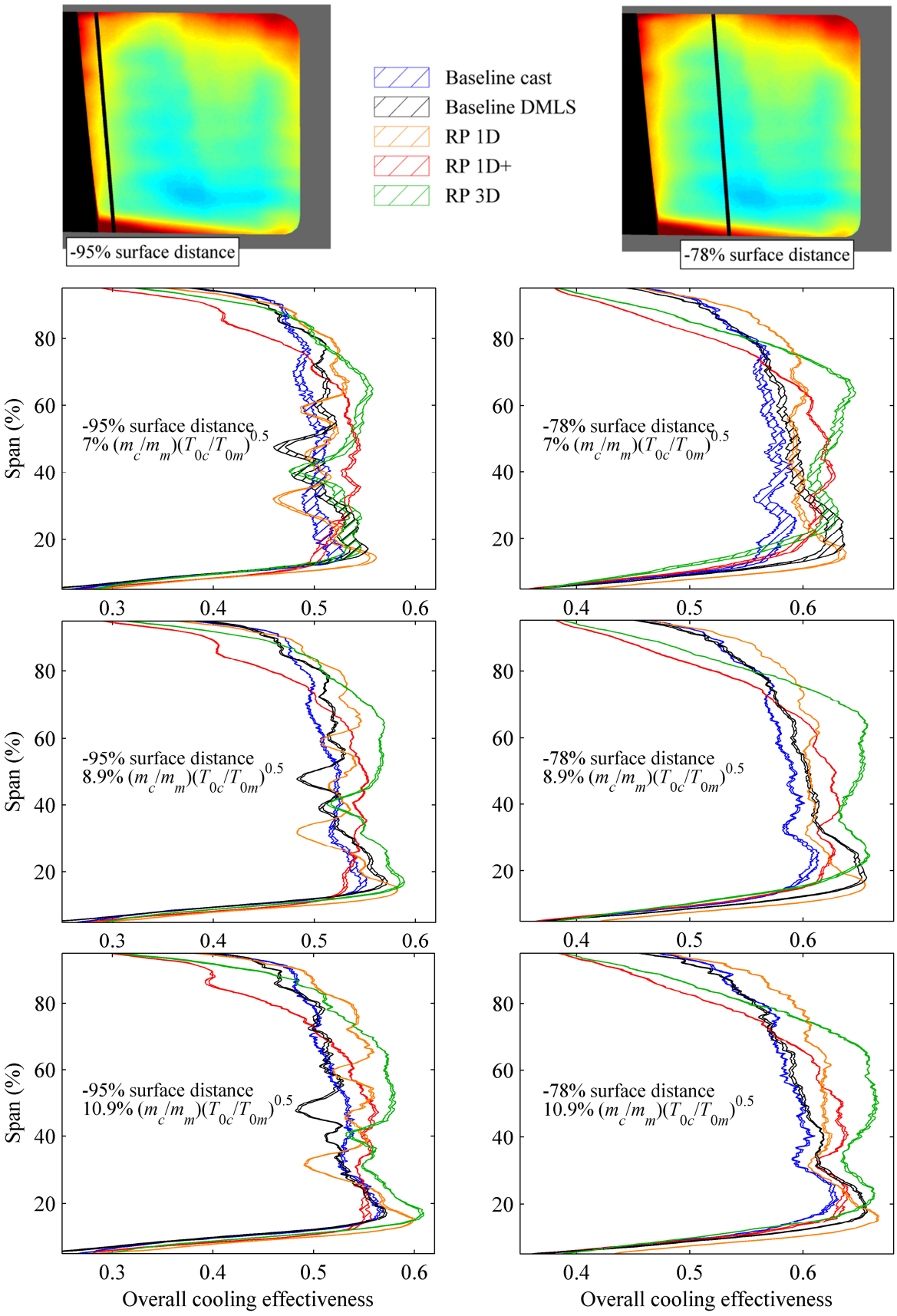


Figure 7.15. Radial overall cooling effectiveness distributions for 7%, 8.9% and 10.9% $\dot{m}_c\sqrt{T_{0c}}/\dot{m}_m\sqrt{T_{0m}}$ at -95% and – 78% surface distance.

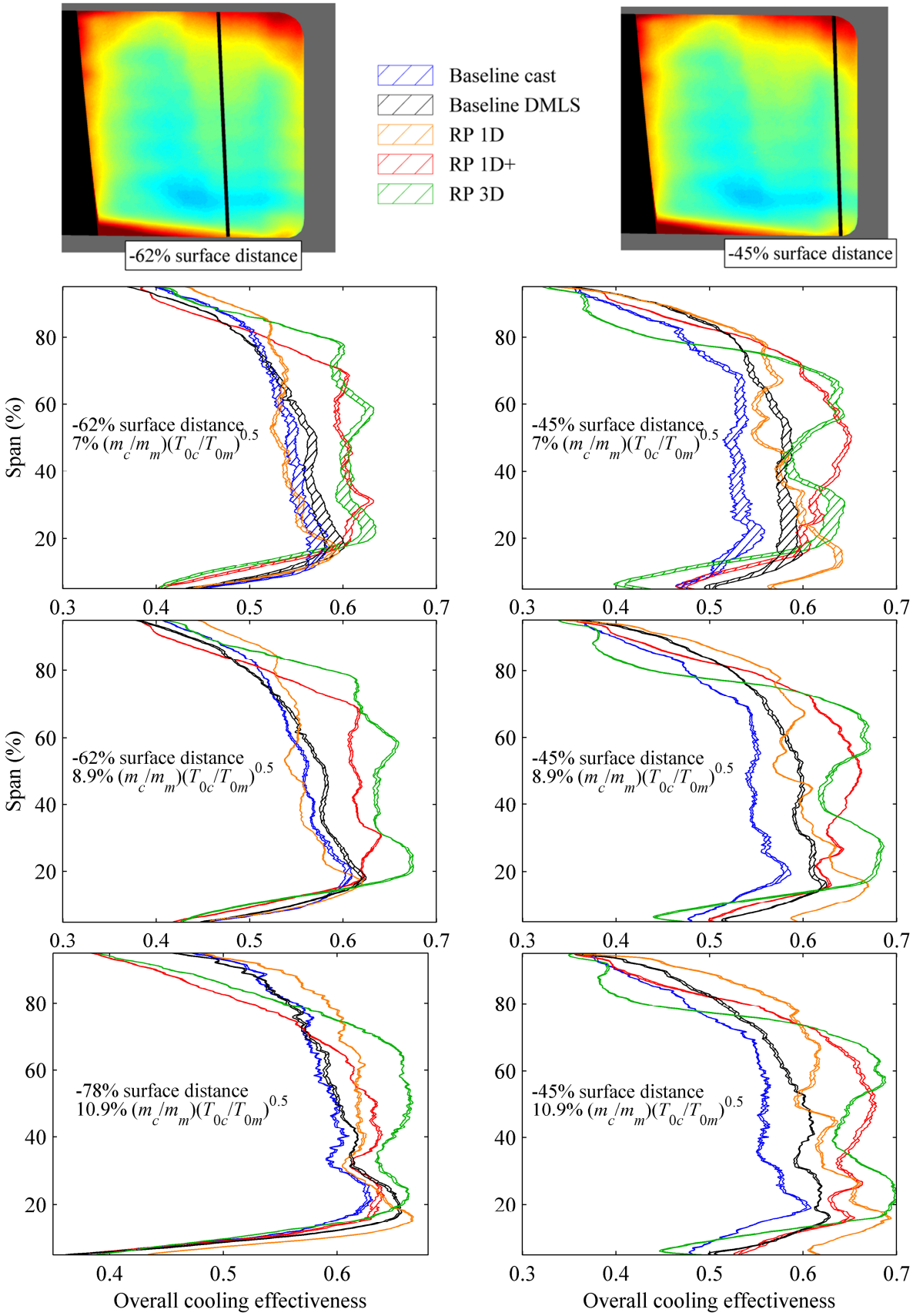


Figure 7.16. Radial overall cooling effectiveness distributions for 7%, 8.9% and 10.9% $\dot{m}_c\sqrt{T_{0c}}/\dot{m}_m\sqrt{T_{0m}}$ at -62% and – 45% surface distance.

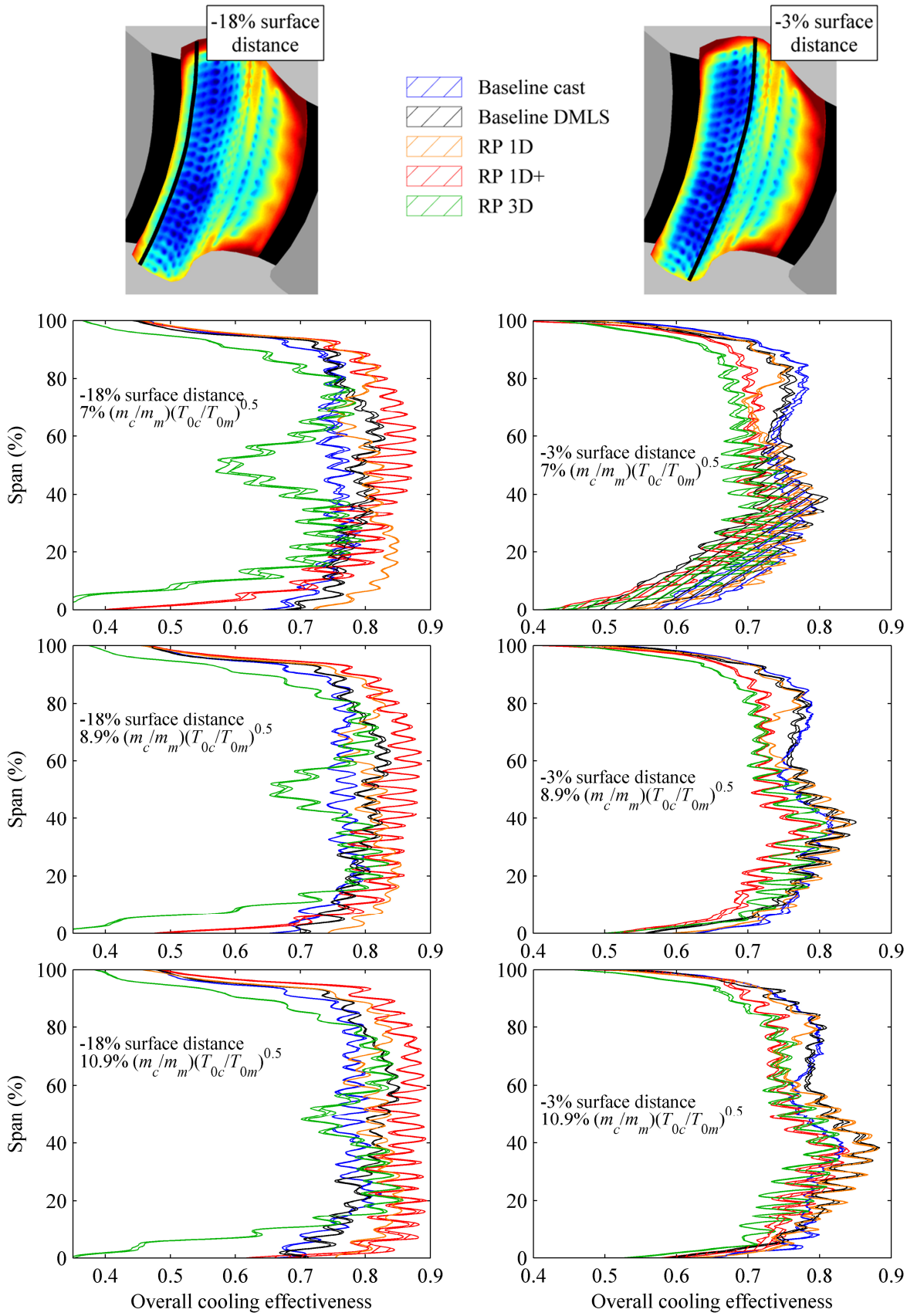


Figure 7.17. Radial overall cooling effectiveness distributions for 7%, 8.9% and 10.9% $\dot{m}_c\sqrt{T_{0c}}/\dot{m}_m\sqrt{T_{0m}}$ at -18% and – 3% surface distance.

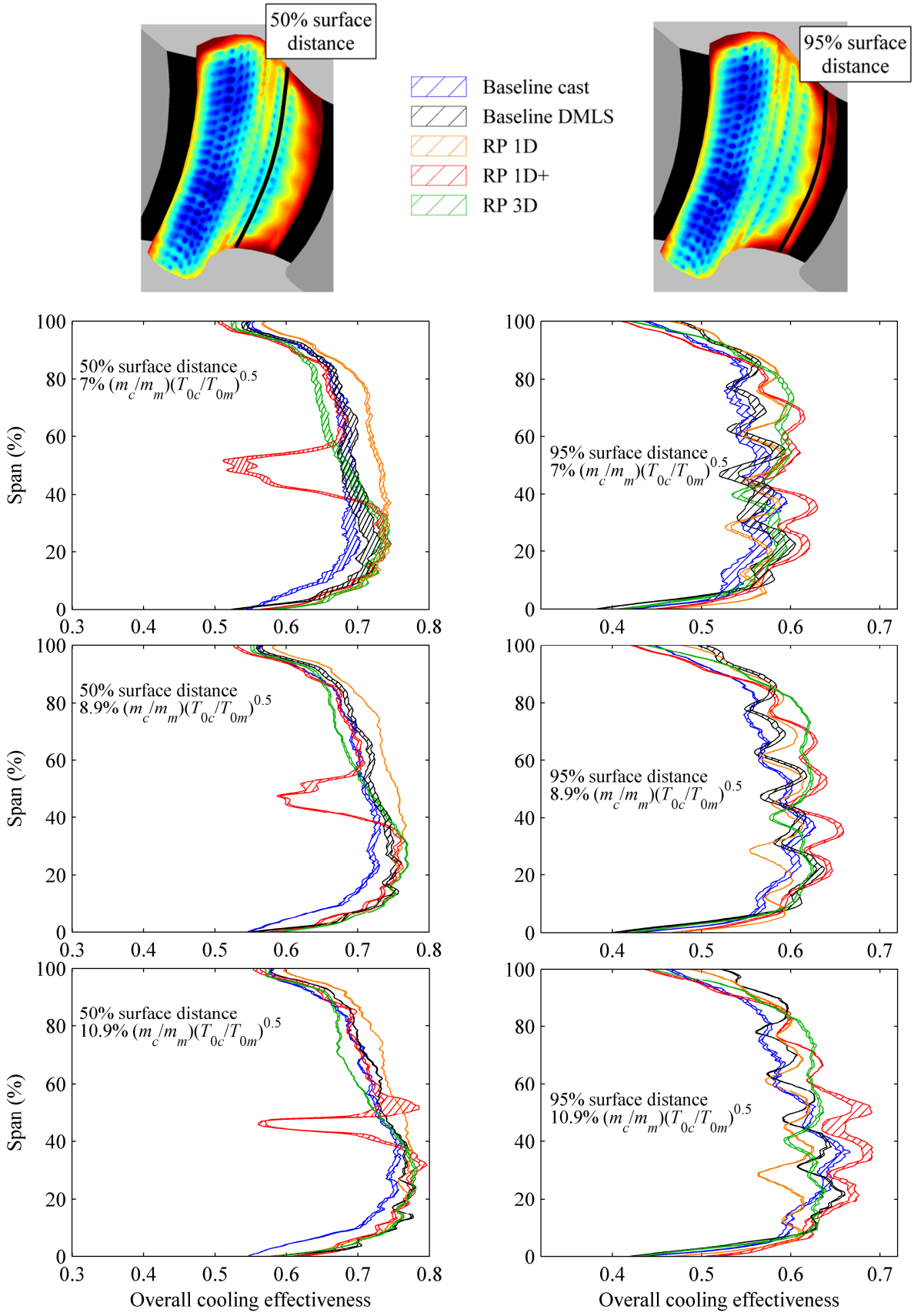


Figure 7.18. Radial overall cooling effectiveness distributions for 7%, 8.9% and 10.9% $\dot{m}_c\sqrt{T_{0c}}/\dot{m}_m\sqrt{T_{0m}}$ at 50% and 95% surface distance.

7.7.6 Discussion of Figures 7.15-7.18

The worst possible leak error occurs at -3% surface distance from 0% to 50% at $\dot{m}_c\sqrt{T_{0c}}/\dot{m}_m\sqrt{T_{0m}}$ = 7% because the rate of change of overall cooling effectiveness with respect to $\dot{m}_c\sqrt{T_{0c}}/\dot{m}_m\sqrt{T_{0m}}$ is very high since the showerhead rows are at the limit of starvation.

The fluctuations in overall cooling effectiveness at -18% and -3% surface distance are due to individual cooling holes. The fluctuations in overall cooling effectiveness at 95% surface distance correspond to the locations of the chordal ribs within the TE pedestal bank—peaks coinciding with the TE passages, and troughs with the chordal ribs. Overall cooling effectiveness is reduced around the chordal ribs because there is no local internal convection. Seven peaks in effectiveness at 95% surface distance are observed for all designs but RP 3D, corresponding to seven TE passages. The split between passages is less obvious in RP 3D which contains 5 TE passages.

For all designs, all surface distances and all $\dot{m}_c\sqrt{T_{0c}}/\dot{m}_m\sqrt{T_{0m}}$ ratios, the overall cooling effectiveness drops off at the hub (0% span) and case (100% span). In the engine, it is likely that this drop off is less severe than in the Sector Facility due to up-wash of platform film cooling flow and reduced mainstream temperature near the hub and case.

All designs appear to have a localised peak in overall cooling effectiveness at 20% span on the SS, seen most clearly at -78% and -62% surface distance. This is likely caused by the redistribution and concentration of the upstream film into a localised cold streak. All designs also appear to have a double-hump radial overall cooling effectiveness distribution at -3% surface distance (LE). The trough in effectiveness at midspan is probably due to the loss in total pressure as the coolant travels through the radial leading-edge compartment and the blockage caused by the midspan baffle plate.

Figures 7.15-7.18 show that the cast and laser-sintered baseline have similarly shaped radial distributions of overall cooling effectiveness at all surface distance locations. The effectiveness of the cast baseline is generally lower than that of the laser-sintered baseline. The difference in overall cooling effectiveness between the cast and laser-sintered baseline depends on the position, and is between 0.02 and 0.04. The overall cooling effectiveness of RP 1D at 50% span is very similar to the laser-sintered baseline at all surface distances.

The dip in RP 1D+ overall cooling effectiveness at 50% span and 50% surface distance is caused by the Araldite leak from the midspan P4 hole. RP 1D+ overall cooling effectiveness between 10% and 75% span on the SS (-95%, -78%, -62%, -45% and -18% surface distance) is consistently greater than the baseline/RP 1D designs. RP 1D+ overall cooling effectiveness at -95% and -78% surface distance around the case (above 75% span) is lower than the other designs, likely due to the blockage of the upper (case) TE passage. RP 1D+ is one of the least effective designs around the LE (-3% span).

However, on the PS, the effectiveness of RP 1D+ compared to other designs increases towards the PS TE, until RP 1D+ is the most effective design at the PS TE.

RP 3D is consistently the most effective design on the SS, followed closely by RP 1D+. The midspan trough in RP 3D overall cooling effectiveness at -45% and -18% surface distance is caused by low midspan film effectiveness due to the starvation of S4/S5 around midspan, and is also likely due to reduced internal coolant flow through the midspan RP passage than designed. RP 3D has the lowest overall cooling effectiveness of all designs around the LE (-3%), but its effectiveness relative to the other designs increases around the PS until it is one of the most effective designs at the PS TE (95% surface distance).

7.8 Proposed Improvements to Methodology

Check mainstream Mach number before each test campaign. Avoids unmatched mainstream Mach number (see RP 1D). Improvement to the vane pair assembly jig may reduce the risk of altered mainstream blockage.

7.9 Conclusions

Contributions to Methodology

- A regression method has been developed for estimating both the overall cooling effectiveness and recovery distribution from the experimental series of 40+ runs. The method estimates overall cooling effectiveness and recovery distribution as a function of $\dot{m}_c\sqrt{T_{0c}}/\dot{m}_m\sqrt{T_{0m}}$ over the entire vane, and uses the local spread of data to improve regressive conditioning.
- The decision to baseline overall cooling effectiveness against $\dot{m}_c\sqrt{T_{0c}}/\dot{m}_m\sqrt{T_{0m}}$ is justified.
- Leaks in the Sector Facility have been indicated by plotting overall cooling effectiveness as a range.
- An automatic image registration method for aligning infra-red images has been implemented.

Mainstream Recovery Distribution

- The recovery distributions of the baseline cast, baseline laser-sintered, RP 1D+ and RP 3D vanes are very similar, and are close to those predicted by Luque Martinez (2011).
- The recovery distribution is predictably affected by the mainstream Mach number. This is seen on the SS of RP 1D which was tested at a lower mainstream Mach number than the other designs, and has a greater mainstream recovery ratio than the other designs.
- It is shown that mainstream recovery is slightly affected by $\dot{m}_c\sqrt{T_{0c}}/\dot{m}_m\sqrt{T_{0m}}$ (i.e., pressure ratio), likely due to the redistribution of film cooling and subsequent alteration of local Mach number.

- The recovery distribution may be affected by the internal system because the mainstream recovery distribution appears to align with the RP 3D internal passages. This may, however, be due to differences in film cooling distribution or deviation in aerofoil shape.

Overall Cooling Effectiveness: General Conclusions

- The reverse-pass systems RP 1D+ and RP 3D outperform the baseline cast/DMLS systems on the SS by an overall cooling effectiveness of around 0.06—i.e., 60 K cooler. The cooler areas in RP 1D+ and RP 3D coincide with the reverse-pass passages and the short TE systems.
- The SS midspan TE overall cooling effectiveness is 0.03 greater (30 K cooler) in RP 1D+ and RP 3D designs compared to the baseline designs.
- The overall cooling effectiveness at the TE is strongly correlated to the length of the TE system. Shorter TE systems improve the overall cooling effectiveness at the TE because the internal coolant temperature at the TE is reduced for shorter systems.
- The effectiveness of reverse-pass systems increases with length, concluded from comparisons between RP 1D and RP 1D+/RP 3D.
- PS wall temperatures are approximately the same for all designs.
- The cast and laser-sintered baseline have similarly shaped overall cooling effectiveness distributions. The effectiveness of the laser-sintered baseline is generally greater than the cast baseline (by ~0.02) despite the Biot number of the cast baseline being greater. This is probably because the laser-sintered baseline has greater internal surface roughness and therefore greater internal HTC.
- A cold, chordwise streak is observed in all designs on the SS at around 20% span. This may be due to the concentration of the SS film by secondary flows. Internal cooling around the area of the cold streak could be reduced to take advantage of locally enhanced film effectiveness.
- For all designs, the overall cooling effectiveness at the LE was greatest at 75% and 25% span and is lower at midspan. This is likely the result of progressive internal pressure loss within the leading edge compartment and blockage caused by the midspan baffle plate.
- The first vane location to ingest at low $\dot{m}_c\sqrt{T_{0c}}/\dot{m}_m\sqrt{T_{0m}}$ is the hub portion of the LE.
- Overall cooling effectiveness increases linearly with $\dot{m}_c\sqrt{T_{0c}}/\dot{m}_m\sqrt{T_{0m}}$ on the PS, apart from the hub portion of the LE which is first to starve.
- In some positions on the SS a peak in overall cooling effectiveness is observed at intermediate values of $\dot{m}_c\sqrt{T_{0c}}/\dot{m}_m\sqrt{T_{0m}}$, probably caused by a local optimum in film blowing ratio or momentum flux ratio.
- Undirected internal flow reduces local overall cooling effectiveness because of low internal HTC. This is observed both in RP 1D in the trailing-edge compartment, and in RP 1D+/RP 3D next to the slots which feed the reverse-pass passages.

- Unfortunately, the mainstream Mach number during the RP 1D experiments was lower than the experiments for all other designs, and so conclusions about the overall cooling effectiveness of RP 1D are made with caution. However, it appears that RP 1D suffers from undirected flow in the TE compartment (no impingement plate), a TE system that is too long, and a reverse-pass that is too short; though it does show improvement compared to the baseline designs in the vicinity of the reverse-pass passages. RP 1D could be improved by maximising RP length, minimising TE length, incorporating an impingement plate, and increasing the loss within the RP passage by reducing the RP passage width.

Overall Cooling Effectiveness: Suggested Improvements to RP 3D and RP 1D+

- Row S4 in RP 3D ingests at low $\dot{m}_c\sqrt{T_{0c}}/\dot{m}_m\sqrt{T_{0m}}$, resulting in a radial hot section around S4. The pressure loss within the RP 3D off-midspan reverse-pass passages is too high to feed S4, and it is suggested that RP 3D S4 be fed instead from the leading-edge compartment.
- The abrupt expansion and merge of the RP 3D off-midspan reverse-pass passages into a shared S4/S5 plenum starves the S4/S5 film cooling holes at midspan. This starvation could be eliminated by decreasing the rate of expansion of the off-midspan passages.
- The RP 3D midspan reverse-pass passage appears to flow less coolant than desired, and it is likely that this passage did not feed the case TE passage at all. It is suggested that the midspan RP passage not split in two but instead feed only the hub TE passage. The case TE passage could be cooled with a separate passage similar to those in the RP 1D+ design.
- The width of the slot feeding the reverse-pass passages in RP 1D+ and RP 3D could be reduced to remove the associated local hot spot caused by undirected internal flow.

It is the author's opinion that the SS improvement in effectiveness afforded by the reverse-pass systems is sufficient to warrant their further optimisation for use in HPNGVs. Specifically, it is concluded that RP 1D+ shows greatest potential for HPNGV engine implementation for current radial mainstream temperature distributions. RP 1D+ incorporates the cooling advantages of long, high HTC reverse-pass systems and short TE systems, while not suffering from the ingestion and manufacturing issues of RP 3D. As radial mainstream temperature distributions become flatter, designs such as RP 1D may become viable.

8. Raw Coolant Capacity Measurements

In this chapter, the experimental method used to measure the coolant mass flow distribution (per row and per compartment) is discussed. The Coolant Capacity Rig (CCR) was devised, developed, manufactured and commissioned specifically for this study, and is described in this chapter. The raw experimental results are also presented in this chapter, assuming no interaction between rows. This sets the basis for the following chapter, in which the raw results are processed to account for interaction induced loss in order to estimate the effective area of each row of cooling holes, the internal loss, and the coolant mass flow distribution at engine conditions.

8.1 Introduction

In order to isolate the effect of cooling geometry on thermal performance—and, importantly, to remove dependence on coolant mass flow rate—all the cooling systems in this thesis were designed to flow the same amount of coolant per row as the baseline cast Trent 500 HPNGV. In reality, manufacturing limitations and the approximations used in preliminary design meant that variation in coolant mass flow rate between geometries was unavoidable. It was necessary, therefore, to measure the coolant mass flow rate, to modify the geometries where possible, and to account for mass flow variation when performing aero-thermal comparisons.

The coolant mass flow rate per row, per compartment, and per vane, was measured both before and after thermal assessment in the Sector Facility for each design. The relatively crude pre-Sector coolant mass flow measurements were used to modify the designs in order to best match the coolant mass flow per row of the Trent 500 HPNGV; film cooling holes were enlarged, and impingement areas adjusted. This trial-and-error modification process is discussed in Chapter 4.

Any remaining flow disparity between designs was accounted for by measuring the thermal performance over a *range* of total coolant mass flow rates in the Sector Facility. The effect of total coolant mass flow rate on thermal performance was automatically captured, and designs could be compared back-to-back at the same total coolant mass flow rate. This method captures the influence of *total* coolant mass flow rate on thermal performance, which is arguably the highest level of dependence as the information feeds directly into the estimation of cycle-efficiency.

The post-Sector coolant mass flow measurements—the subject of this and the following chapter—were performed to a high degree of accuracy in order to baseline the thermal assessments made in the Sector Facility. There are many difficulties associated with the accurate measurement of HPNGV coolant mass flow rates, not least of which is the relatively small size of the vanes, their complex shape, the large range in mass flow rates that must be measured (from row-scale mass flow rate to

vane-scale mass flow rate), and the interaction between rows within the vane. Much effort went in to solving the practical problems associated with performing these intricate measurements and developing a method to turn the raw measurements into meaningful quantities, such as the effective area of each row of cooling holes, the losses and pressure drops within certain internal passages, and the scaling of the measurements to engine conditions.

8.2 Capacity Theory

Fundamentally, coolant mass flow rate measured in the laboratory must be scalable to engine conditions. The primary, relevant, non-dimensional groups are the non-dimensional mass flow rate $\dot{m}\sqrt{RT_0}/p_0 d^2$, total-to-static pressure ratio p_0/p, ratio of specific heats γ and the coolant Reynolds number Re_d:

$$\frac{\dot{m}\sqrt{RT_0}}{p_0 d^2} = f\left(\frac{p_0}{p}, \gamma, \mathrm{Re}_d\right). \tag{8.1}$$

where $\dot{m}$ is mass flow rate, T_0 is total temperature, p_0 is total pressure, p is static pressure, d is the diameter of the flow area, and R is the specific gas constant[1]. These dependencies are observed in the compressible mass flow relation:

$$\frac{\dot{m}\sqrt{RT_0}}{p_0 d^2} = C_d \frac{\pi}{4}\left(\frac{p_0}{p}\right)^{-\frac{\gamma+1}{2\gamma}} \sqrt{\frac{2\gamma}{(\gamma-1)}\left[\left(\frac{p_0}{p}\right)^{\frac{\gamma-1}{\gamma}} - 1\right]}, \tag{8.2}$$

where the discharge coefficient C_d is a function of coolant Reynolds number Re_d (e.g., Rowbury, 1998). Consequently, if p_0/p, γ and Re_d are matched to engine conditions, then the non-dimensional mass flow rate measured in the laboratory is equal to the non-dimensional mass flow rate in the engine. Since R is identical at laboratory and engine conditions and d is approximately equal at engine and laboratory conditions, R and d are commonly dropped from the non-dimensional mass flow rate, to form a new group *capacity* Γ:

$$\Gamma = \frac{\dot{m}\sqrt{T_0}}{p_0}, \tag{8.3}$$

As long as R and d are constant, capacity can be thought of as a non-dimensional group, albeit with units of $\mathrm{kgs^{-1}K^{0.5}Pa^{-1}}$.

[1] The specific gas constant R only depends upon the molecular composition of the test gas, and *not* temperature. This is useful for cold-rig coolant capacity tests, since the coolant molecular composition is the same for rig and engine (consisting of air only—though altitude may cause a small difference) and hence R is matched. However, care should be taken when scaling mainstream capacity (not the subject of this thesis), since additional combustion products in the engine situation will cause unmatched specific gas constant between rig and engine.

Assuming a system in which the cooling rows do not interact, a total pressure at vane inlet p_{0c}, and assuming the total temperature of the coolant remains constant within the vane, equation (8.1) is applied to an individual cooling row in a non-interacting system:

$$\Gamma_i^r = \frac{\dot{m}_i^r \sqrt{T_{0c}}}{p_{0c}} = f\left(\frac{p_{0c}}{p_{ext,i}}, \gamma_i, \mathrm{Re}_{d,i}\right), \tag{8.4}$$

where $p_{ext,i}$ is the exit static pressure into which the film is ejected. In a non-interacting system, the capacity of each row can be measured in isolation without the need to consider the effect of other cooling rows.

For a system in which rows interact, the total pressure at the entrance to a cooling row is lower than the total pressure at the vane inlet by an amount dictated by a number of unitless loss coefficients related to the local geometry and the dynamic head distribution within the vane, which is a function of the coolant flow through *all* rows. The coolant capacity of an individual row becomes dependent on the capacity of all the other rows and loss coefficients:

$$\Gamma_i^r = f\left(\frac{p_{0c}}{p_{ext,i}}, \gamma_i, \mathrm{Re}_{d,i}, \Gamma_1^r, \Gamma_2^r, \Gamma_3^r, \ldots, K_A^c, K_B^c, K_C^c, \ldots\right), \tag{8.5}$$

Where K_A^c, K_B^c, K_C^c, ... are a number of loss coefficients that describe the geometry within the vane and $\Gamma_1^r, \Gamma_2^r, \Gamma_3^r$, ... are the capacities of all the other rows in the vane.

In the CCR experiments, $p_{0c}/p_{ext,i}$ is matched to engine conditions. K_A^c, K_B^c, K_C^c, ... at engine conditions is assumed equal to laboratory conditions, based on the work of Hippensteele (1974). The ratio of specific heats for air at laboratory conditions is γ = 1.4, compared to γ = 1.3 at engine conditions (Fig. 8.11). The effect of the ratio of specific heats on capacity can be accounted for using equation (8.2)—this is performed in the following chapter.

The coolant Reynolds number cannot be matched to engine conditions since the cooling rows in the CCR exhaust directly to atmosphere. The experimental coolant Reynolds number is approximately 4 times smaller than the engine coolant Reynolds number. This was seen as an acceptable compromise given the comparative nature of the tests (i.e., to compare the relative mass flow rates of a number of different cooling geometries), the fact that the coolant Reynolds number is of secondary influence after matching the pressure ratio $p_{0c}/p_{ext,i}$, and the massive reduction in rig complexity afforded by exhausting to atmosphere as compared to the alternative of running at elevated pressures and exhausting into a pressurised vessel. The absolute error caused by unmatched Reynolds number is around 6%, as concluded from Fig. 8.1.

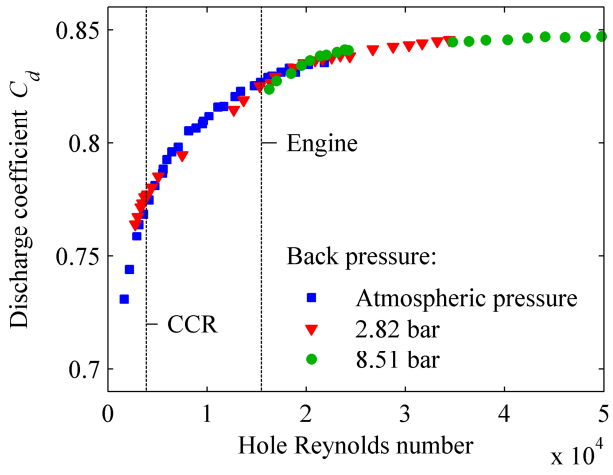


Figure 8.1. Typical discharge coefficient through cylindrical film hole, as a function of hole Reynolds number based on nominal hole diameter, Rowbury (1998). Back pressure used to control Re range.

Similarly, the capacity of all other rows $\Gamma_1^r, \Gamma_2^r, \Gamma_3^r, \ldots$ cannot be matched simultaneously with Γ_i^r, since all rows exhaust to the same pressure in the experiment, as compared to the engine where each row operates at a different exit static pressure. The experimental method of measuring mass flow rate per row in the CCR—blocking the row of interest and measuring a mass flow delta—also does not allow row capacities to be matched simultaneously to engine conditions. However, by estimating the function f in (8.5) with a simple loss model, the dependence of row capacity on loss and the coolant capacity of all other rows can be accounted for. This is discussed in the following chapter.

In this chapter, all experimental results are processed assuming the non-interacting definition of capacity (8.4). The validity of the non-interacting capacity definition is tested using continuity. It will be shown that the applicability of the assumption depends on the geometry. In the following chapter, all experimental data are processed in terms of the interacting definition of capacity (8.5). The capacity of all other rows $\Gamma_1^r, \Gamma_2^r, \Gamma_3^r, \ldots$ is taken into account. In the process, the loss coefficients $K_A^c, K_B^c, K_C^c, \ldots$ are determined. Capacity is scaled to engine conditions by taking into account the change in γ using equation (8.2).

8.3 Coolant Capacity Rig

The Coolant Capacity Rig (CCR) was designed and built specifically to measure row, compartmental and total coolant capacity of the HPNGV cooling designs in this thesis. Photographs of the rig are shown in Fig. 8.2 and a schematic shown in Fig. 8.3. The CCR is an evolution of the Flow Testing Facility (FTF), a rig developed and utilised by Luque Martinez (2011) to measure the total and compartmental coolant capacity of a pair of standard cast Trent 500 HPNGVs, and a pair of cast Trent 500 HPNGVs with a laser-sintered leading-edge dendritic insert. However, the aim and scope of this study is different to that of Luque Martinez—i.e., new aims of per-row measurements, and testing individual laser-sintered vanes rather than a cast pair—and so it was decided to commission a new rig.

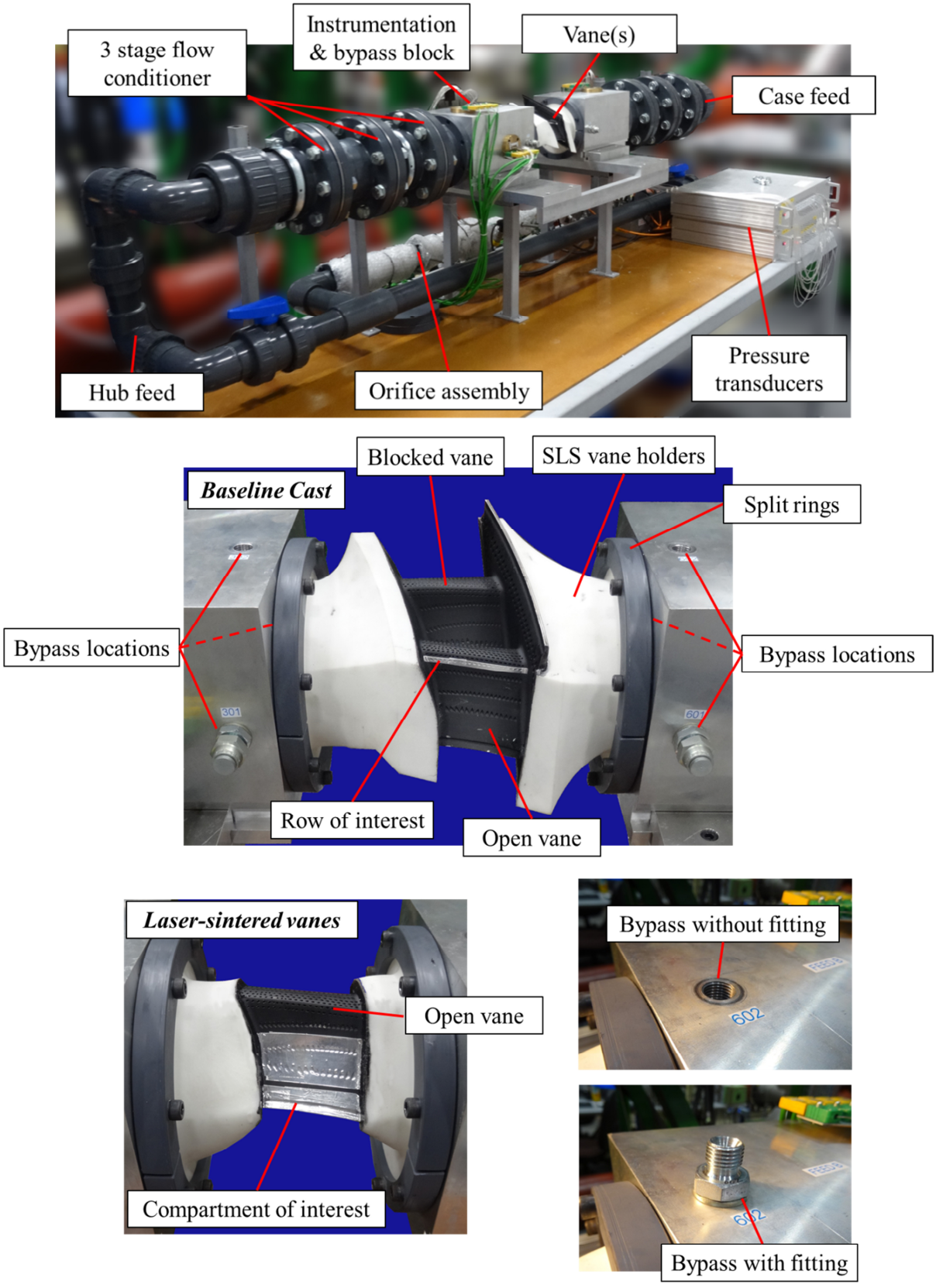


Figure 8.2. Photographs of CCR. Entire rig (top); vane assembly for cast pair, surrounded by instrumentation blocks (middle); vane assembly for single laser-sintered vane (left bottom); bypass locations (right bottom).

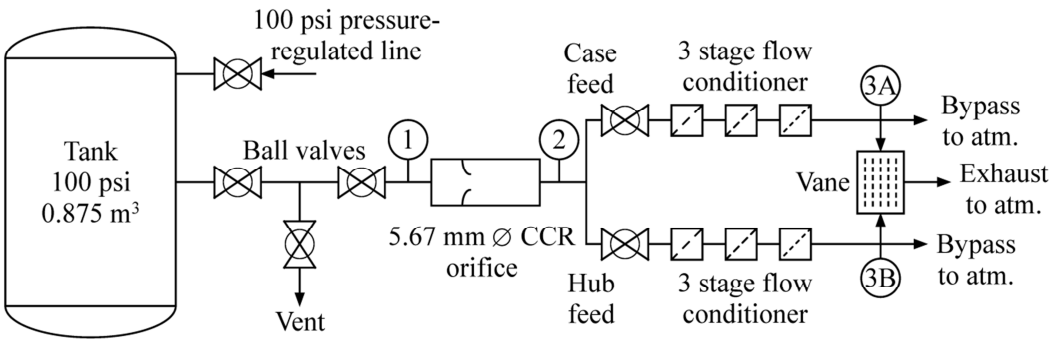


Figure 8.3. Schematic of CCR.

The rig consists of a 0.875 m^3 air tank connected via a sonic mass flow measurement orifice to the hub and case feeds of the vane of interest (either single laser-sintered vane or cast pair), through a number of flow-conditioning and measurement devices. Compressed air from the tank discharges through the system, exhausting to atmosphere through the film cooling holes and trailing-edge slot until the tank is empty. By calculating the instantaneous mass flow rate using the total pressure and temperature upstream of the orifice, and recording atmospheric pressure and instantaneous total pressure and temperature upstream of the vanes, the coolant capacity of the HPNGV is measured over a range of pressure ratios in a single run. Typical pressure, temperature and mass flow traces during a 600 second blow-through run are shown in Fig. 8.4.

The details of the CCR are now discussed. The mass flow measurement method and the calibration of the CCR orifice are discussed in separate sections.

PVC pipework is used to minimise heat transfer and to simplify manufacture. The pipe diameter is 2" until the flow-conditioning section to minimise stored volume and hence unsteady mass flow. The remainder of the rig (flow conditioning section, sleeve within the instrumentation/bypass blocks) comprises 4" PVC pipework to reduce the dynamic head at the measurement points upstream of the vanes to improve measurement accuracy and to reduce total pressure loss between the measurement points and the vane inlet.

The CCR contains a number of detachable PVC union joints, which, in conjunction with the sliding hub/case instrumentation blocks, allows the hub and case feeds to move relative to one another, thus accommodating varying vane sizes. Ball valves in both hub and case feeds allow for hub-fed-only and case-fed-only measurements (not conducted in this thesis) and localised leak testing. A static leak test of the feed supply was conducted by blanking the instrumentation/bypass blocks, charging the system to 1.7 bara, closing all ball valves, then monitoring the pressure decay within the compartments. The leakage mass flow rate was estimated using (8.16) and the effective leakage area from (8.2). The error in coolant capacity due to leaks in the feed pipework was thus estimated as 0.005%.

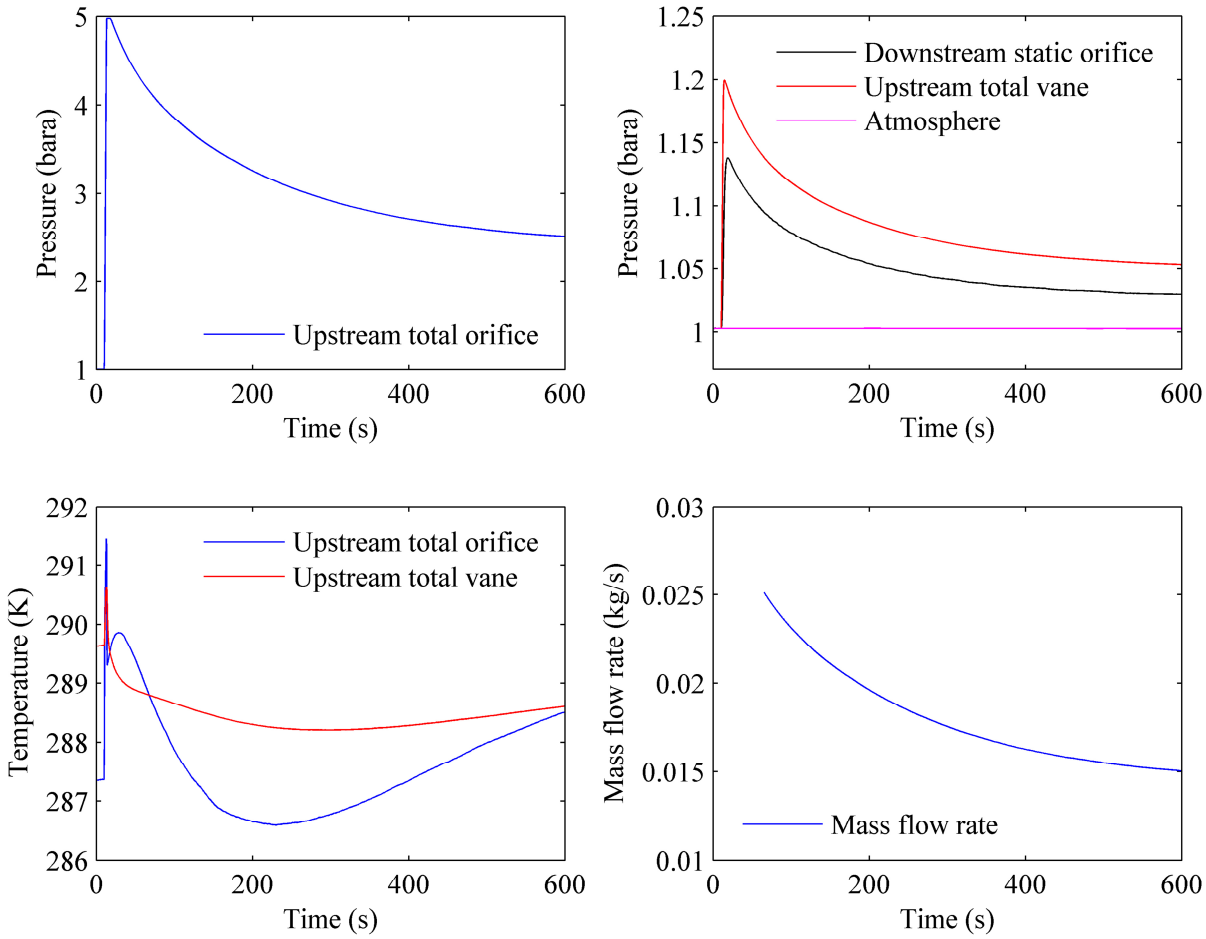


Figure 8.4. Typical pressure and temperature measurements during CCR blow-through experiment.

A three stage flow conditioner is fitted into the hub and case feeds to remove flow non-uniformity at the measurement points upstream of the vane(s). Each flow conditioner consists of a 2 mm thick perforated laser cut stainless steel plate, sandwiched between two PN16 flanges with gaskets. The first stage conditioner contains a hexagonal array of 5 mm diameter holes, with a total open area of 30%. A 25 mm thick section of honeycomb packing is attached to the upstream face of the first conditioner to remove flow swirl. The second conditioner is located 140 mm downstream of the first conditioner and consists of a more densely packed hexagonal array of 5 mm diameter holes, with a total open area of 60%. The final flow conditioner is 140 mm downstream of the second conditioner and consists of a grid pattern of 4.8 x 4.8 mm squares, with a total open area of 75%. The conditioning system is designed so that the effective-hole-diameter to length-between-conditioner ratio is greater than 25. The open area fraction of the first flow conditioner is chosen so that the local dynamic head is at least four times the maximum local dynamic head non-uniformity.

The instrumentation/bypass blocks are manufactured from solid aluminium, with a 4" hole bored through the middle and sleeved with PVC pipe to reduce ambient heat transfer. The hub and case blocks are clamped down to a common support frame to rigidify the vane assembly. This prevents the

weight of the feed pipework from stressing the plastic selective laser sintered (SLS) vane holders and silicone joints. Each block contains two instrumentation rakes, perpendicular to each other and offset by 40 mm in the streamwise direction. Each rake crosses the width of the passage, and contains four total temperature K-type beaded thermocouples and four total pressure probes in an alternating pattern. Each instrumentation block also contains three bypass ports. The bypass ports can be used for instrumentation, to feed other test articles, or to increase the total mass flow rate through the system by enlarging the total exit area, discussed later.

The laser-sintered vanes and cast pairs are interfaced with the instrumentation/bypass blocks using custom-made vacuum impregnated SLS holders, Fig. 8.2. The walls of the SLS holders are approximately 4 mm thick. A 10 mm thick, flat lip protrudes around the block-end of the vane holders, which is pressed against a groove-located silicone BS 427 face O-ring on the instrumentation block using two split rings, to form an air tight seal. The vanes are seated in a recessed footprint at the other end of the vane holders. The vanes are potted into the footprint with externally applied Loctite SI 5940 black silicone. The silicone sealant is applied *after* the entire assembly has been made rigid (the instrumentation/bypass blocks tightened onto the shared frame), so that the sealant and the vane do not move during curing. Row(s) of interest are blocked using externally applied 3M aluminium foil tape (the purpose of this is discussed in detail later).

All thermocouples are connected to a National Instruments (NI) TC 2095 module. The total pressure rakes within the instrumentation block are connected via Scanivalve vinyl tubing to two 8 channel 910 mbarg Sensortechnic differential pressure transducer boxes. Pressure in the instrumentation blocks is also measured at bypass locations #603 and #303 using 2 bara Sensortechnic transducers. Pressure downstream of the mass flow measurement orifice (model points #007, #009 and #011, Fig. 8.6) is measured with 2 bara Sensortechnic transducers; and upstream of the mass flow measurement orifice (model points #001, #002 and #005) using 5 bara Sensortechnic transducers. All pressure transducer boxes and the NI TC 2095 module are connected to an NI PXI 1050 chassis (via an NI PXI-6031E Multifunction I/O card and NI SCXI-1102B card, respectively), and then to a PC using an NI PXI 8360 MXI-Express card. Data are acquired on the PC using a LabView script at 150 Hz and filtered to remove 50 Hz noise using *sgolayfilt* in MATLAB.

The 2 bara and 5 bara pressure transducers were calibrated according to the equation

$$p = \frac{V}{k_1} + k_2, \tag{8.6}$$

where p = absolute pressure (bara), V= voltage (volts), k_1= constant (volts/bara), k_2= offset (bara). k_1 was found for the absolute pressure transducers using a GE PACE 7000 Ruska 7250xi Digital

Pressure Controller and the LabView VI *DPC_2.vi*. It was assumed that k_1 did not change between runs. k_2 was calculated for every run from atmospheric pressure:

$$k_2 = p_{\mathrm{atm}} - \frac{V_{\mathrm{atm}}}{k_1}, \tag{8.7}$$

where p_{atm} is measured using a barometer and V_{atm} is the transducer voltage measurement at atmospheric conditions. The differential transducers were cross-calibrated against the 2 bara transducers during the static leak test.

8.4 Mass Flow Measurement

Mass flow rate in the CCR is measured using a choked orifice, Fig. 8.5. The CCR orifice is modified from the FTF hub nozzle (Luque Martinez, 2011). The 5.67 mm nominal diameter hub nozzle was originally designed in accordance with BS EN ISO 9300 (2005) for a cylindrical throat, but without the downstream divergent section – more similar to an orifice plate with filleted entry and sharp exit. In the present embodiment, a small chamfer was added to the hole exit of the original hub orifice to reduce the effect of exit geometry variation on discharge coefficient during operational life. The orifice was recalibrated to take into account the modifications.

The CCR orifice assembly is shown in Fig. 8.6 and consists of a 450 mm 1" diameter upstream pipe length for flow conditioning and a 450 mm 2" diameter downstream pipe length. The temperature and pressure measurement locations are shown in Fig. 8.6. Pressure is measured at points #001, #002, #005, #007, #009 and #011. Temperature is measured at #003, #004, #006, #008 and #010. The CCR orifice is calibrated using model point #002 as the upstream orifice total pressure p_{01}, model point #007 as the downstream orifice static pressure p_2 and model point #003 as the upstream orifice total temperature T_{01}. The mass flow rate though the CCR orifice is calculated according to the relation

$$\dot{m} = C_{D_1} \frac{\pi {d_1}^2}{4} \frac{p_{01}}{\sqrt{T_{01}}} \sqrt{\frac{\gamma}{R}\left(\frac{\gamma+1}{2}\right)^{-\frac{\gamma+1}{\gamma-1}}}, \qquad \frac{p_{01}}{p_2} > 1.89. \tag{8.8}$$

where d_1 is the nominal throat diameter (5.67 mm), $\dot{m}$ is the mass flow rate through the orifice, and R is the specific gas constant of air and γ is the ratio of specific heats of air.



Figure 8.5. CCR measurement orifice. Upstream face (left); downstream face with chamfer (right).

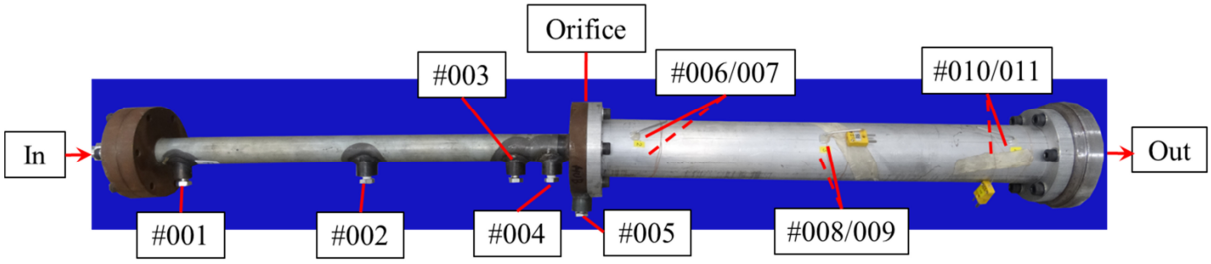


Figure 8.6. CCR orifice assembly. #002: upstream total pressure measurement; #003 used for upstream total temperature measurement; #007 used for downstream static pressure measurement.

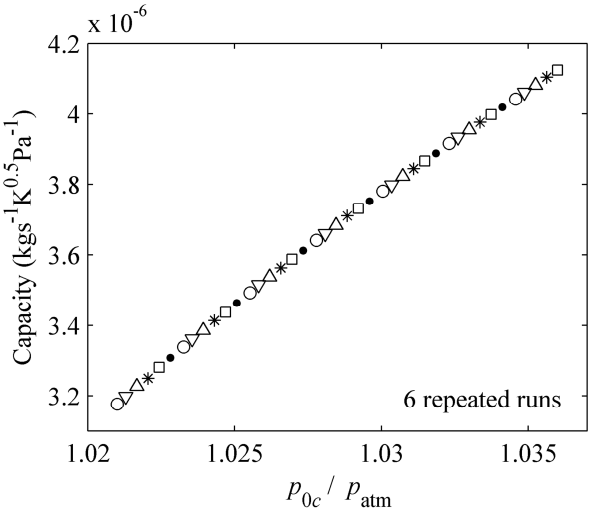


Figure 8.7. Repeatability of CCR capacity measurements. 6 runs, precision of 0.03%.

The definition (8.8) is based on choked flow through an isentropic, 1D nozzle, as reported in many standards (e.g., BS EN ISO 9300, 2005). The discharge coefficient subscript D_1 references that the discharge coefficient is correlated with the Reynolds number based on the upstream pipe diameter D_1, equation (8.9). The discharge coefficient is determined experimentally in the following section.

$$C_{D_1} = f\left(\mathrm{Re}_{D_1}\right) = f\left(\frac{4\dot{m}}{\mu\pi D_1}\right). \tag{8.9}$$

Because the runs are unsteady (i.e., decaying pressure), the instantaneous mass flow rate measured at the CCR orifice is different to the instantaneous mass flow rate at the vane. Using the unsteady mass flow correction of Povey et al. (2011), the difference between the two mass flow rates is estimated to be at most 0.05%. Consequently, this unsteadiness was neglected, and the coolant capacity was evaluated using the mass flow rate at the orifice $\dot{m}$ and the total temperature and pressure upstream of the vane p_{03} and T_{03}:

$$\Gamma = \frac{\dot{m}\sqrt{T_{03}}}{p_{03}}. \tag{8.10}$$

The capacity curves from six identical runs are plotted in Fig. 8.7, agreeing to a precision of 0.03%.

8.5 Calibration of CCR Orifice

The CCR orifice was calibrated using a discharge coefficient for choked flow according to:

$$C_{D_1} = \frac{4}{\pi {d_1}^2} \frac{\dot{m}\sqrt{T_0}}{p_0} \sqrt{\frac{R}{\gamma}\left(\frac{\gamma+1}{2}\right)^{\frac{\gamma+1}{\gamma-1}}}, \tag{8.11}$$

which is the inverse of (8.8). C_{D_1} was determined experimentally. The CCR orifice assembly (Fig. 8.6) was connected to a reference nozzle of known discharge coefficient via an intermediate restriction. A schematic and photo of the arrangement are shown in Figs. 8.8 and 8.9. Air from a 0.875 m^3 tank initially at 100 psi was discharged into the system until the tank pressure reached atmospheric. Three repeat runs with a 20 mm restriction and three repeat runs with a 30 mm restriction were performed.

The pressure and temperature at points 1, 2 and 3 (defined in Fig. 8.8) were measured throughout blow-through. This allowed a range of mass flow rates and therefore Reynolds numbers to be tested during a single run. The mass flow rate at the reference nozzle was calculated using total pressure and temperature measurements at point 3 and the factory-issued reference nozzle calibration. The mass flow rate through the CCR orifice was determined using the mass flow rate at the reference nozzle and an unsteady mass flow rate correction term. The mass flow rate through the CCR orifice and the total temperature and pressure measurements at point 1 were then used to determine the discharge coefficient of the CCR orifice C_{D_1} for a range of Reynolds numbers.

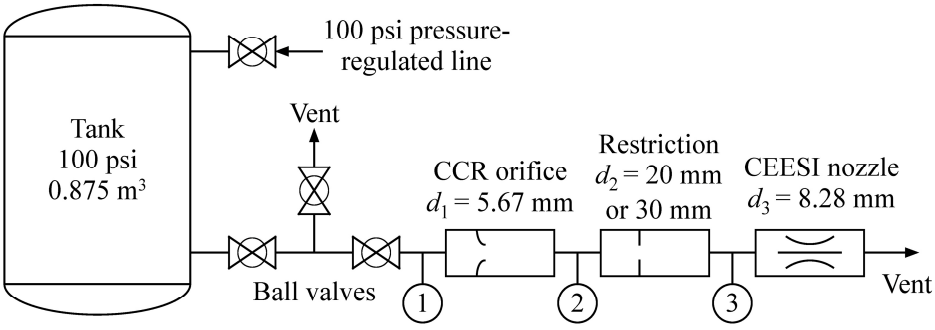


Figure 8.8. Schematic of CCR orifice calibration setup.

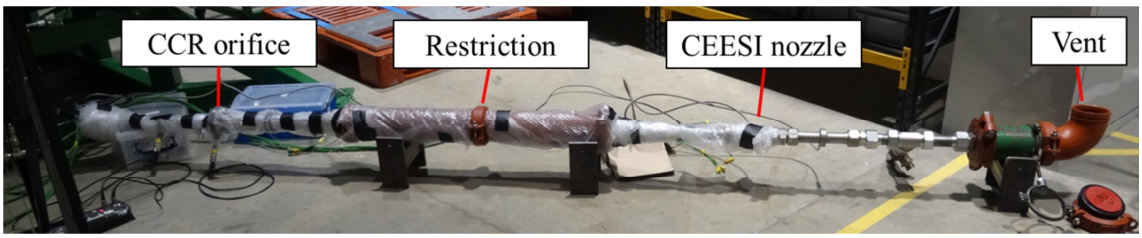


Figure 8.9. Photograph of CCR orifice calibration setup.

A Flow Systems, CEESI-calibrated choked Venturi nozzle with nominal diameter d_3 = 8.28 mm was used as the reference nozzle. The CEESI reference nozzle remains choked even at low pressure ratios (p_{03}/p_{atm} = 1.03) because of a well-formed downstream divergent section for pressure recovery. In the calibration setup, the reference nozzle was placed downstream of the CCR orifice in order to choke both the CCR orifice and the reference nozzle simultaneously, since the throat area of the reference nozzle is larger than the CCR orifice. In this arrangement, the pressure ratio p_{01}/p_{03} remained constant during blow-through so long as the reference nozzle remained choked:

$$\frac{p_{01}}{p_{03}} \sim \frac{{d_3}^2}{{d_1}^2} = 2.13. \tag{8.12}$$

The pressure ratio across the CCR orifice p_{01}/p_{02} was adjusted by altering the diameter of a restriction between the CCR orifice and the reference nozzle, thus changing the total pressure drop $p_{02} - p_{03}$. A 30 mm and a 20 mm restriction were both tested. The 30 mm restriction incurred minimal pressure loss, so that p_{01}/p_{02} = 2.13. The 20 mm restriction dropped some pressure, so that p_{01}/p_{02} = 2.11 during the run. This can be seen in the capacity curves shown in Fig 8.12.

The mass flow rate through the reference nozzle was calculated using the equation

$$\dot{m}_3 = C_{d_3} C_* \frac{\pi {d_3}^2}{4} \frac{p_{03}}{\sqrt{R T_{03}}}, \tag{8.13}$$

where $\dot{m}_3$ is the mass flow rate through the reference nozzle (at point 3, defined in Fig. 8.8), p_{03} and T_{03} are the total pressure and temperature upstream of the reference nozzle, d_3 is the nominal diameter of the reference nozzle (8.28 mm), R is the specific gas constant of air, C_{d_3} is the discharge coefficient of the reference nozzle, and C_* is the critical flow function of air. The discharge coefficient C_{d_3} is a factory-supplied function of Reynolds number $\mathrm{Re}_{d_3} = 4\dot{m}_3/\mu\pi d_3$, described by a fourth-order polynomial best-fit to a number of discrete experimental data points (plotted in Fig. 8.10):

$$C_{d_3} = a_1 + a_2 \mathrm{Re}_{d_3} + a_3 {\mathrm{Re}_{d_3}}^2 + a_4 {\mathrm{Re}_{d_3}}^3 + a_5 {\mathrm{Re}_{d_3}}^4, \quad 1.381\text{x}10^5 < \mathrm{Re}_{d_3} < 14.852\ \text{x}10^5 \tag{8.14}$$

a_1 = 0.9923, a_2 = 4.3248x10^{-8}, a_3 = -6.6111x10^{-14}, a_4 = 4.1869x10^{-20}, a_5 = -9.4241x10^{-27}.

Dynamic viscosity is a function of temperature T_{03}, plotted in Fig. 8.11. The critical flow function is taken from BS EN ISO 9300 (2005) and is a function of temperature and pressure:

$$C_* = \sum_i a_i \pi^{b_i} \tau^{c_i}, \tag{8.15}$$

where $\pi = p_{03}/p_{crit}$ and $\tau = T_{03}/T_{crit}$, T_{crit} = 132.53 K, p_{crit} = 3.786x10^6 Pa, and the coefficients a_i, b_i and c_i are given in BS EN ISO 9300 (2005).

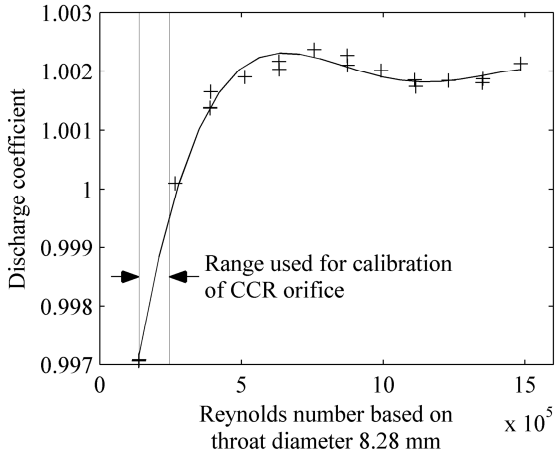


Figure 8.10. Discharge coefficient of CEESI nozzle, nominal diameter d_3 = 8.28 mm. Reynolds number based on CEESI throat diameter d_3. Discrete experimental data points (crosses) and 4th order best-fit (solid line).

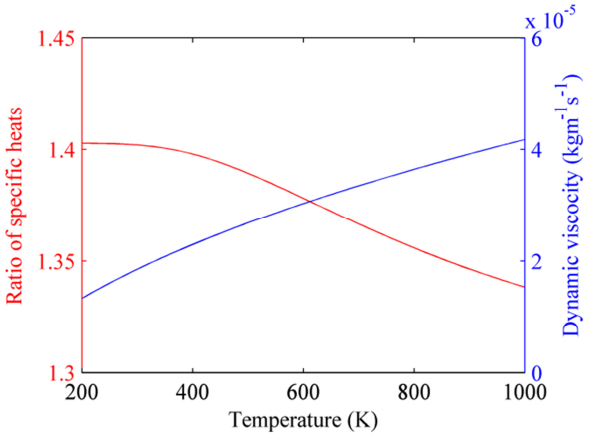


Figure 8.11. Ratio of specific heats and dynamic viscosity of air from Oldfield and Guo (1997).

The temperature measurement T_{03}, pressure measurement p_{03}, equations (8.13-8.15), and Figs. 8.10 and 8.11 uniquely determined the mass flow rate through the measurement nozzle $\dot{m}_3$.

The unsteady mass flow correction of Povey et al. (2011) was used to estimate the instantaneous CCR orifice mass flow rate from the reference nozzle measurement:

$$\dot{m}_1(t) = \dot{m}_3(t) + \frac{V}{RT_{03}(t)}\left(\frac{dp_{03}(t)}{dt} - \frac{p_{03}(t)}{T_{03}(t)}\frac{dT_{03}(t)}{dt}\right), \tag{8.16}$$

where $\dot{m}_1(t)$ is the instantaneous mass flow rate at the CCR orifice and V is the volume between the CCR orifice and the reference nozzle (0.0093 m^3). The unsteady mass flow rate correction alters the inferred CCR orifice discharge coefficient by up to 0.7% at high Reynolds numbers. Below $\mathrm{Re}_{D_1} = 7\mathrm{x}10^4$, the unsteady correction changes the inferred discharge coefficient by less than 0.3%. Capping the calibration at $\mathrm{Re}_{D_1} = 7\mathrm{x}10^4$ was thus seen as a reasonable balance between maximising the calibrated range while minimising the dependence of the calibration on the unsteady mass flow correction.

The mass flow rate $\dot{m}_1$, total temperature measurement T_{01}, and total pressure measurement p_{01} are plotted in Fig. 8.12 in terms of CCR orifice capacity $\dot{m}_1\sqrt{T_{01}}/p_{01}$, as a function of p_{02}/p_{01} for all six calibration runs and for all times during the choked run duration. The pressure ratio (PR) across the CCR orifice remains approximately constant during blow-down while the reference nozzle is choked. The 20 mm diameter restriction decreases the PR across the CCR orifice. The scatter within each restriction group is due to the variation in CCR orifice discharge coefficient with Reynolds number.

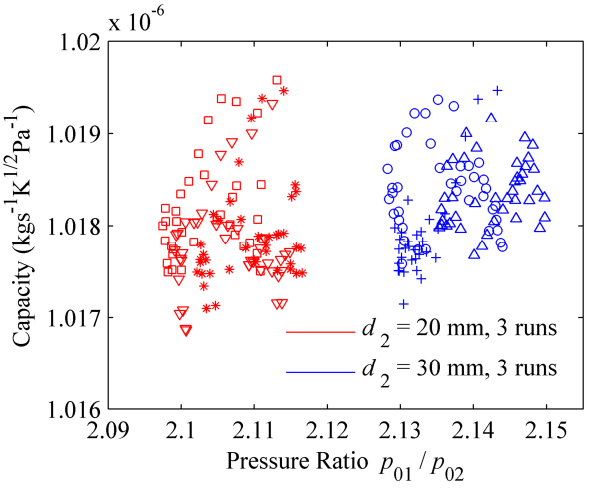


Figure 8.12. Capacity of CCR orifice during blow-through calibration. 3 runs with 20 mm restriction and 3 runs with 30 mm restriction.

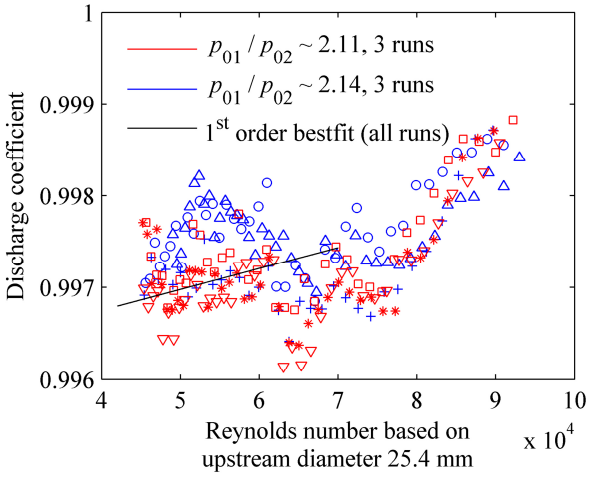


Figure 8.13. Discharge coefficient of CCR orifice, nominal diameter d_1 = 5.67 mm. Re number based on CCR upstream pipe diameter D_1 = 25.4 mm.

The discharge coefficient was calculated using the orifice capacity measurement and (8.11). The result is plotted against Reynolds number in Fig. 8.13. The repeatability is very good, with all repeat runs within each restriction group agreeing to within 0.03%. There is around 0.1% variation in discharge coefficient with PR at low Reynolds numbers, suggesting that the choked orifice has some dependence on PR. Due to time constraints this effect was not explored further. A first order polynomial was best-fit to the entire data for use in all subsequent mass flow measurements using the CCR orifice:

$$C_{D_1} = a_1 + a_2 \mathrm{Re}_{D_1},\ 4.2\mathrm{x}10^4 < \mathrm{Re}_{D_1} < 7\mathrm{x}10^4 \qquad (8.17)$$

where a_1= 0.9958 and a_2 = 2.2690x10^{-8}.

The use of the best-fit was restricted to $4.2\mathrm{x}10^4 < \mathrm{Re}_{D_1} < 7\mathrm{x}10^4$.

A leak test was performed before every calibration run by blanking the exhaust, pressurising the system to 25 psi, and monitoring the pressure and temperature decay of the system. These measurements and the unsteady mass flow approximation (8.16) were used to estimate that leakage caused a 0.01% change in inferred discharge coefficient. This was seen as negligible and was therefore discounted in the analysis. The system was wrapped in bubble-wrap to make the setup as adiabatic as possible to reduce thermal boundary layer effects. The walls of the system were pre-cooled using a purge run before every calibration run, in order to reduce in-run heat transfer as much as possible.

8.6 Differential Mass Flow Measurement and Bypass Flow

The CCR orifice is calibrated to measure between 14.8 – 24.9 g/s at standard laboratory conditions. In contrast, an entire vane blows between 9 g/s – 20 g/s (1.025 < PR < 1.15) at laboratory conditions, while a single row of cooling holes may flow as little as 0.2 g/s (PR = 1.025). Consequently, the mass flow rate through a single row, or the whole vane at low pressure ratios, cannot be measured using a single, absolute measurement in the CCR.

For these cases, a *differential* mass flow measurement technique is used: in addition to the row(s) to be measured, the exit flow area is increased so that the mass flow rate through the CCR orifice remains in the calibrated range. The capacity of the additional exit area is measured from a second experiment and subtracted from the initial measurement to estimate the capacity of the row(s) of interest. The total exit area of the *high-differential* run consists of the effective area of the row(s) of interest, the effective area of all other rows on the vane, and the effective area of the bypass exhaust. The capacity of the high-differential run Γ_H can be described as a function of these areas and the driving pressure ratio p_{0c}/p_{atm}, based on the 1D isentropic mass flow relation (8.2):

$$\Gamma_H = \left[A_{row(s)\ of\ interest}\left(\frac{p_{0c}}{p_{\mathrm{atm}}}\right) + A_{all\ other\ rows}\left(\frac{p_{0c}}{p_{\mathrm{atm}}}\right) + A_{bypass}\left(\frac{p_{0c}}{p_{\mathrm{atm}}}\right)\right] f\left(\frac{p_{0c}}{p_{\mathrm{atm}}}\right). \tag{8.18}$$

The areas are functions of pressure ratio to take into account variation in discharge coefficient.

The row(s) of interest are blocked using 3M Aluminium Tape (Fig. 8.2), so that for the *low-differential* run:

$$\Gamma_L = \left[A_{all\ other\ rows}\left(\frac{p_{0c}}{p_{\mathrm{atm}}}\right) + A_{bypass}\left(\frac{p_{0c}}{p_{\mathrm{atm}}}\right)\right] f\left(\frac{p_{0c}}{p_{\mathrm{atm}}}\right). \tag{8.19}$$

The capacity of the row(s) of interest is defined as:

$$\Gamma_{row(s)} = A_{row(s)\ of\ interest}\left(\frac{p_{0c}}{p_{\mathrm{atm}}}\right) . f\left(\frac{p_{0c}}{p_{\mathrm{atm}}}\right). \tag{8.20}$$

Assuming no interaction between rows,

$$\begin{aligned} A_{row(s)\ of\ interest}&\left(\frac{p_{0c}}{p_{\mathrm{atm}}}\right) \\ &= \left[A_{row(s)\ of\ interest}\left(\frac{p_{0c}}{p_{\mathrm{atm}}}\right) + A_{all\ other\ rows}\left(\frac{p_{0c}}{p_{\mathrm{atm}}}\right) + A_{bypass}\left(\frac{p_{0c}}{p_{\mathrm{atm}}}\right)\right] \\ &- \left[A_{all\ other\ rows}\left(\frac{p_{0c}}{p_{\mathrm{atm}}}\right) + A_{bypass}\left(\frac{p_{0c}}{p_{\mathrm{atm}}}\right)\right], \end{aligned} \tag{8.21}$$

and substituting in equations (8.18)-(8.20), the capacity of a row can be estimated from the high- and low-differential runs:

$$\Gamma_{row(s)} = \Gamma_H - \Gamma_L. \tag{8.22}$$

This result is derived for a system in which the film cooling rows do not internally interact with each other. The analogous result for an interacting system cannot be written explicitly, depending on the capacities of all the other rows. This is investigated in the following chapter.

The differential mass flow measurement process used in this chapter is shown diagrammatically in Fig. 8.14. The low-differential capacity measurement is subtracted from the high-differential capacity measurement at each pressure ratio to estimate the capacity of the row(s) of interest. A key benefit of differential mass flow measurement is that a constant area leak does not affect the result. The leak area is accounted by the bypass area in (8.21), and therefore the resultant differential capacity measurement is also independent of leaks. Leaks can form at any time during a test campaign, and so this independence is very useful. In contrast, absolute measurements are affected by leaks. The techniques employed to reduce leak-induced errors on absolute measurements are discussed in the following section.

By keeping all rows other than the row(s) of interest open for both high- and low- differential runs, the amount of foil tape that must be applied to the vane is minimised. This is advantageous as it minimises the handling of the vanes, reduces turnaround time, and reduces the risk of a leak forming underneath the foil tape. Compare to the situation where all rows other than the row(s) of interest are covered with tape for both high-differential and low-differential runs: a differential measurement can still be performed by covering/uncovering the row(s) of interest, but the chance of a leak forming underneath the tape is greater because the taped area is larger. This is not a problem if the leak area is constant for both high-differential and low-differential runs, though this cannot be guaranteed. A further advantage of blocking one row is that pressure losses within the vane are much better matched to conditions when all rows are blowing. This is beneficial if the raw capacity results are used to predict engine capacity, but is inconsequential for the network flow analysis in the following chapter.

The CCR contains six dedicated bypass exhaust ports, three on the hub instrumentation/bypass block (#301-303) and three on the case instrumentation/bypass block (#601-603). The bypass ports are positioned as close to the vane as possible, to minimise the difference in feed pressure between the bypass ports and the vane. The bypass exit area is controlled by the addition or removal of ¼” male-male BSP fittings or caps (Fig. 8.2).

A key advantage of the variable bypass system is that the PR across the vane can be varied while the mass flow rate through measurement orifice remains within the calibrated range. This allows the capacity of the row(s) of interest to be measured over a broad range of pressure ratios. A high bypass area, e.g., #302 and #602 open without fittings, allows the capacity of a row(s) to be measured at low PRs (approximately 1.02 – 1.04). No bypass area, i.e., all bypass ports capped, allows the capacity of

a row(s) to be measured at high PRs. This principle is demonstrated in Fig. 8.15 for P5 of the baseline laser-sintered vane. The resultant capacity curve comprises five data sets. Each data set is the result of a high-differential and low-differential run at a given bypass area (i.e., 10 runs are required in total for this curve). The bypass areas are defined in Fig. 8.16. All data sets collapse onto a single curve. This lends confidence to the experimental techniques, CCR orifice calibration, and assumptions.

The capacity and PR range that can be measured within the CCR are determined by the calibrated range of the CCR orifice, the bypass exit area, the total vane exit area, and the area of the row(s) of interest. This information is summarised in Fig. 8.16. The figure is based on a typical vane exit area, and assumes that the entire calibration range of the orifice ($4.2\text{x}10^4 < \text{Re}_{D_1} < 7\text{x}10^4$) is utilised. Typical capacity characteristics for the whole vane and for a single row are also shown. For a single row, the capacity curve is contained within the differential measurement regime. The bypass area required to measure single row capacity over a specific PR range is shown by the different coloured areas—demonstrated in practise in Fig. 8.15. In order to make the number of experiments manageable, only the high bypass and the very low bypass ranges were generally measured. This was seen as a reasonable compromise since the high and very low bypass areas cover most of the PR range of interest.

The whole vane capacity crosses both absolute and differential measurement regimes. Both techniques were therefore employed to measure the capacity of the whole vane. There are large regions in which the capacity of the whole vane cannot be measured using the CCR, notably at very low pressure ratios, and approximately over $1.03 < \text{PR} < 1.09$. These regions could be measured in future by increasing the calibrated range of the CCR orifice.

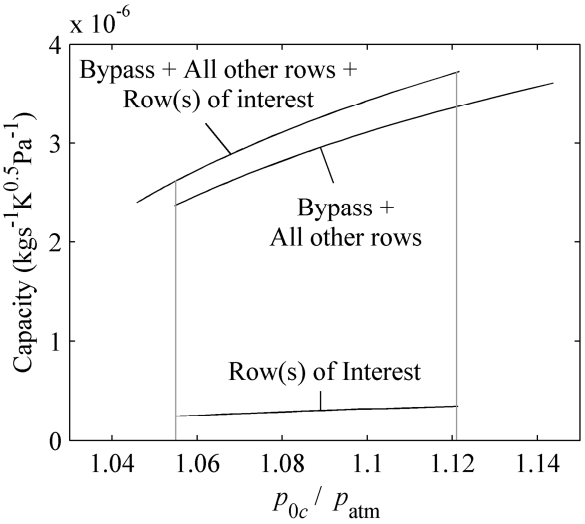


Figure 8.14. Differential mass flow measurement technique.

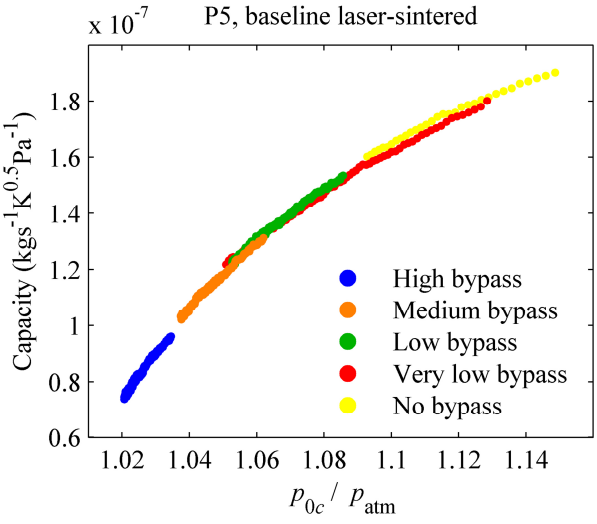
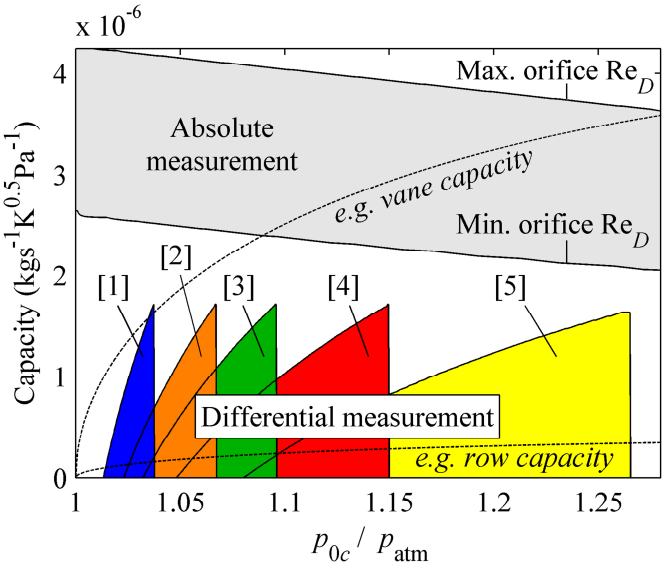


Figure 8.15. Raw capacity of a cooling row. Result of 10 experimental runs at 5 bypass flow rates.



[1] = High bypass, 162 mm^2 (302, 602 w/o fittings)

[2] = Medium bypass, 96 mm^2 (301-303, 601-603 w. fittings)

[3] = Low bypass, 64 mm^2 (301, 302, 601, 602 w. fittings)

[4] = Very low bypass, 32 mm^2 (302, 602 w. fittings)

[5] = No bypass

Figure 8.16. CCR capacity measurement ranges.

The capacities of the bypass ports alone were also measured by removing the vane assembly, blanking the hub and case feeds, and measuring absolute mass flow. The results are shown in Fig. 8.17 for the high, medium and low bypass arrangements (the capacity of the very low bypass system was too low to measure absolutely). The high bypass measurement in Fig. 8.17 was used both for the low-differential measurement for the whole vane at low PR, and also for comparison to the dynamic leak test (discussed in the following section). Notably, the experimental capacity curves matches the theoretical capacity curve for a 1D isentropic nozzle of constant area (8.2) to within 0.15%, as shown in Fig. 8.18. This is reassuring since the bypass ports are close in shape to an ideal nozzle.

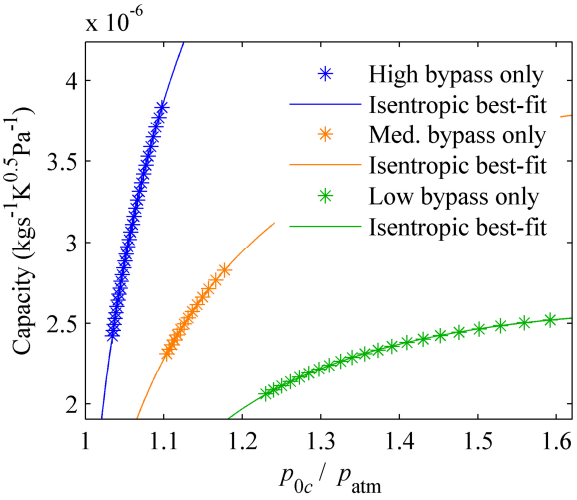


Figure 8.17. Capacity of bypass ports only.

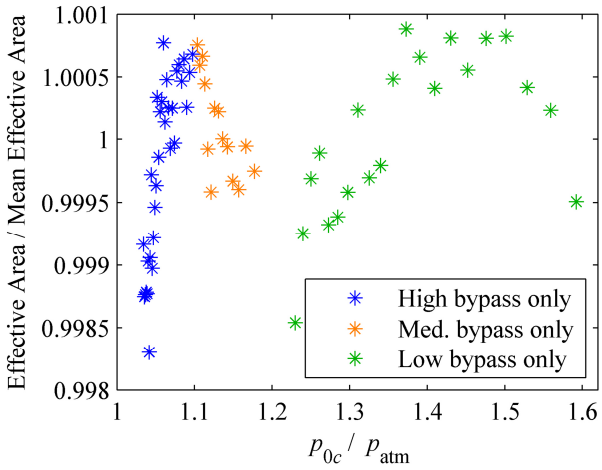


Figure 8.18. Deviation of bypass port capacity from 1D isentropic mass flow equation (8.2).

8.7 Experimental Procedure – Practical Details

A test procedure was designed to minimise the risk and impact of leak errors and to maximise repeatability. The techniques practically eliminated the effect of leaks on the differential mass flow measurements, and substantially reduced the risk and impact of leaks on the absolute mass flow measurements. Implementation of the procedure generated the repeatability illustrated in Fig. 8.7.

As previously discussed, differential mass flow measurement is independent of leaks if the leakage area is the same for both the high-differential run and the low-differential run. The impact of leak formation during a test campaign was therefore isolated to a pair of runs by repeating the high-differential mass flow experiment after every low-differential mass flow experiment, i.e., all differential measurements were carried out in high-low differential run pairs. This did not remove the risk of a leak forming between runs within the pair, but when this occurred the high bypass and very low bypass capacity curves generally failed to align—unlike in Fig. 8.15. In the case of misalignment, all four runs for a single row or compartment (2x high bypass, 2x very low bypass) were repeated.

The mass flow rate through the whole vane and the leading edge compartment had to be measured using the absolute method (Fig. 8.16), which is affected by leaks. Leaks were reduced by performing a dynamic leak test before each test campaign. The entire vane was covered with foil tape, the high bypass ports were opened, and the rig was run steadily in blow-through mode (tank pressure 25 psi). Leaks were located with leak test spray and were sealed with silicone sealant. As a quantitative check, the capacity measured during the dynamic leak test was compared to the high bypass only capacity (Fig. 8.17), as they should be equal for a sealed system. All absolute mass flow experiments were undertaken immediately after the dynamic leak test, when leaks were likely to be at their lowest during the test campaign. The linear analysis of the experimental data (discussed in this chapter) lends confidence to the technique, since the sum of the compartmental mass flow rates equals the total vane mass flow rate for most geometries (Fig. 8.24)—an outcome that would be very unlikely unless the absolute measurements were accurate.

To maximise the effectiveness of the seal formed by the foil tape on top of the row of interest, skin contact with the tape and the vane was minimised to avoid grease marks. The tape was applied with razor blade and tweezers, pressed down firmly by (gloved) hand and then smoothed using a rounded applicator. The tape can withstand a pressure ratio of 1.3, above which the seal weakens and ultimately blows off. During operation, the ball valves that supply the CCR with compressed air were opened slowly to eliminate pressure spikes and reduce the strain on the foil tape.

The CCR is designed to be as adiabatic as possible in order to reduce thermal boundary layer induced errors: all pipework is PVC except the CCR orifice assembly (manufactured from aluminium) which is covered in multiple layers of bubble-wrap. In order to minimise heat transfer between the walls and

Table 8.1. Typical run parameters in the CCR.

Open area	*Tank starting pressure (psi)*	*Position of valve filling tank from 100 psi line during run*	*Run duration (s)*
e.g., Whole vane	50	Fully open	300
e.g., Leading-edge compartment	40	Fully open	300
e.g., Whole vane + high bypass – 1 row	90	Fully open	600
e.g., Whole vane + very low bypass – 1 row	75	Half open	600
e.g., High bypass only	75	Half open	600

the test gas during operation, a purge run was performed at the beginning of each sequence of testing. The purge run is identical to a nominal CCR run and cools down the rig (especially the CCR orifice assembly) so that the wall temperature is close to the flow temperature. Purge runs were re-performed if the rig had not been run for 30 minutes.

Run length, starting tank pressure, and the rate at which the tank was filled from the 100 psi line during the run (controlled by a feed valve) differed depending on open flow area. These are tabulated in Table 8.1. The choice was a compromise between: attempting to reduce unsteady effects by reducing pressure decay; measuring coolant capacity over as wide a range of pressure ratios as possible in a single run; ensuring that the maximum pressure in the CCR did not far exceed 1.3 bara to prevent the foil tape from blowing off; ensuring that the pressure upstream of the orifice did not far exceed 5 bara because of the upper measurement limit of the transducers; maintaining manageable run lengths for realistic turn-around times.

8.8 Best-Fit Curves

Best-fit lines are added to the figures to aid interpretation only, and are not used to process the data. The general best-fit curve $\Gamma(p_{0c}/p_{\mathrm{atm}})$ is defined in equation (8.23). This semi-physical polynomial approximation has four constants b_1 to b_4 and is well conditioned as $p_{0c}/p_{\mathrm{atm}} \to 1$ ($\Gamma \to 0$). The best-fit curve is only used between a pressure ratio of unity and the maximum experimental pressure ratio, i.e., is not used to extrapolate upwards.

$$\Gamma^2 = b_1\left(\frac{p_{0c}}{p_{\mathrm{atm}}}-1\right) + b_2\left(\frac{p_{0c}}{p_{\mathrm{atm}}}-1\right)^2 + b_3\left(\frac{p_{0c}}{p_{\mathrm{atm}}}-1\right)^3 + b_4\left(\frac{p_{0c}}{p_{\mathrm{atm}}}-1\right)^4. \qquad (8.23)$$

The constants in (8.23) are calculated from the least squares solution

$$\begin{bmatrix} b_1 \\ b_2 \\ b_3 \\ b_4 \end{bmatrix} = (\boldsymbol{V}^T\boldsymbol{V})^{-1}\boldsymbol{V}^T \begin{bmatrix} {\Gamma_1}^2 \\ {\Gamma_2}^2 \\ \vdots \\ {\Gamma_n}^2 \end{bmatrix}, \qquad (8.24)$$

where $\boldsymbol{V}$ is a fourth order Vandermonde matrix without unity column for n data points:

$$\boldsymbol{V} = \begin{bmatrix} \left.\frac{p_{0c}}{p_{\text{atm}}}\right|_1 - 1 & \left(\left.\frac{p_{0c}}{p_{\text{atm}}}\right|_1 - 1\right)^2 & \left(\left.\frac{p_{0c}}{p_{\text{atm}}}\right|_1 - 1\right)^3 & \left(\left.\frac{p_{0c}}{p_{\text{atm}}}\right|_1 - 1\right)^4 \\ \left.\frac{p_{0c}}{p_{\text{atm}}}\right|_2 - 1 & \left(\left.\frac{p_{0c}}{p_{\text{atm}}}\right|_2 - 1\right)^2 & \left(\left.\frac{p_{0c}}{p_{\text{atm}}}\right|_2 - 1\right)^3 & \left(\left.\frac{p_{0c}}{p_{\text{atm}}}\right|_2 - 1\right)^4 \\ \vdots & \vdots & \vdots & \vdots \\ \left.\frac{p_{0c}}{p_{\text{atm}}}\right|_n - 1 & \left(\left.\frac{p_{0c}}{p_{\text{atm}}}\right|_n - 1\right)^2 & \left(\left.\frac{p_{0c}}{p_{\text{atm}}}\right|_n - 1\right)^3 & \left(\left.\frac{p_{0c}}{p_{\text{atm}}}\right|_n - 1\right)^4 \end{bmatrix}. \tag{8.25}$$

Equation (8.23) is flexible enough to accurately describe all experimental data, while requiring a minimal number of constants. Figures 8.19 and 8.2 show the best-fit curves applied to the raw experimental capacity data of the whole vane and the trailing-edge slot, respectively. Also shown in Figs. 8.19 and 8.2 are the 1D, isentropic capacity curves for a constant area subsonic nozzle, best-fit to the data.

The equation of this curve is

$$\Gamma = A_{bestfit,isentropic}\left(\frac{p_{0c}}{p_{\text{atm}}}\right)^{-\frac{\gamma+1}{2\gamma}}\sqrt{\frac{2\gamma}{R(\gamma-1)}\left[\left(\frac{p_{0c}}{p_{\text{atm}}}\right)^{\frac{\gamma-1}{\gamma}} - 1\right]}, \tag{8.26}$$

where $A_{bestfit,isentropic}$ is found through least squares regression. The isentropic, constant area equation is unable to describe precisely the raw measurements in full with only one constant, due to the effects of variable discharge coefficient and pressure loss through the vane, though it is reasonably close.

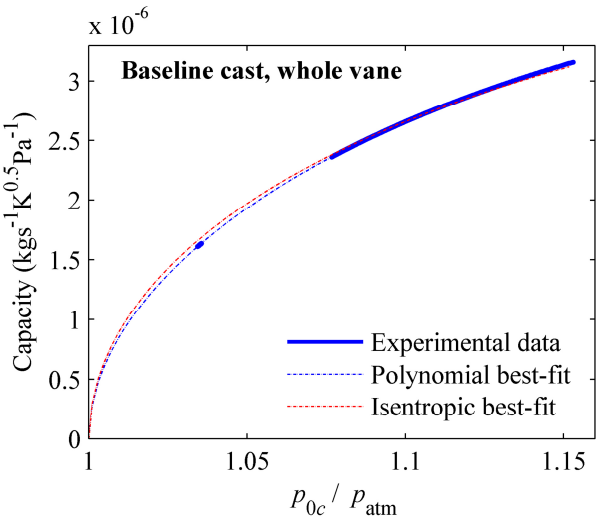


Figure 8.19. Comparison of best-fit definitions to experimental data of baseline cast, whole vane.

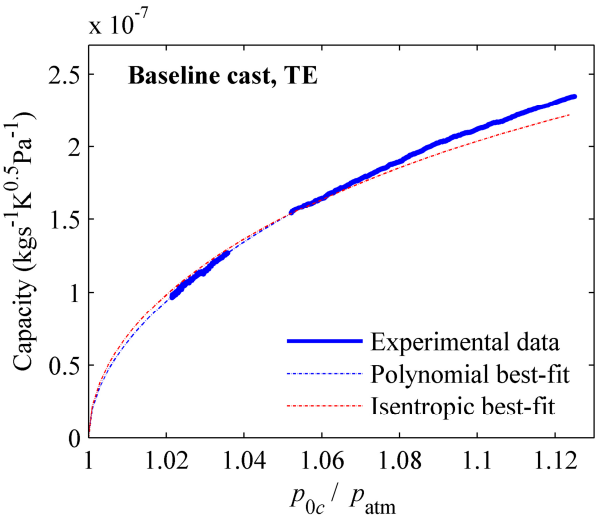


Figure 8.20. Comparison of best-fit definitions to experimental data of baseline cast, trailing-edge.

8.9 Raw Coolant Capacity Results

The raw coolant capacity measurements (assuming no interaction) are now plotted for all the HPNGV designs: cast baseline Trent 500 (trailing-vane), laser-sintered baseline Trent 500, RP 1D, RP 1D+ and RP 3D. Individual rows are measured using the differential mass flow measurement method at a high PR range and a low PR range. These results are plotted in Fig. 8.21. The coolant capacity of the compartments is measured using both absolute and differential methods. For the differential measurements, the rows within the compartment of interest are blocked using foil tape; in the absolute measurements, all other rows are blocked. The capacity of the whole vane is measured using the absolute measurement method at high PRs and using the differential measurement method at low PRs. Compartmental and whole vane data are plotted in Fig. 8.22. Results are re-plotted in Fig. 8.23 separately for each design in terms of a cumulative row capacity sum.

The equation of the best-fit lines is defined in (8.23). The capacity of a 1D isentropic nozzle (8.26) over a range of areas is plotted in the background of each figure for comparison. All rows exhaust to atmosphere.

The high PR and low PR data sets for each row collapse well onto a single best-fit curve. The shape of the raw row and compartmental capacity curves is similar for all designs over the range of measured PRs, lending confidence to the experimental method. Most of the raw capacity curves follow a 1D isentropic capacity trend, which suggests that the discharge coefficient does not vary significantly within the measurement range. On the other hand, the raw TE capacity deviates noticeably from 1D isentropic, with the discharge coefficient increasing with PR. This may be because the friction factor within the TE pedestal system decreases with Reynolds number as reported in a number of papers, e.g., Armstrong and Winstanley (1988). The effective area of each row is estimated in the next chapter after interaction effects are taken into account.

The raw total vane capacity of the laser-sintered vanes is within 7% of the raw baseline cast total capacity, which has a total effective area (when all rows are blowing to atmosphere) of approximately 112 mm^2. The compartmental data is, at this stage, shown for completeness, but is important later for interaction testing (performed in the following section). With the exception of the TE, S4 and S5, the raw per-row capacity of the laser-sintered designs is within 20% of the baseline cast raw per-row capacity. The raw TE capacity of the laser-sintered vanes is up to 40% smaller than the baseline cast vane, due to the additional blockage and roughness created by the laser-sintering process.

The raw capacity of S4 and S5 vary significantly between designs. This difference is due to the significant interaction between rows S4 and S5 in the reverse-pass geometries. The differential mass flow measurement technique is inherently *intrusive*. When a row is blocked for the low-differential measurement, the total mass flow rate through the vane decreases compared to the high-differential

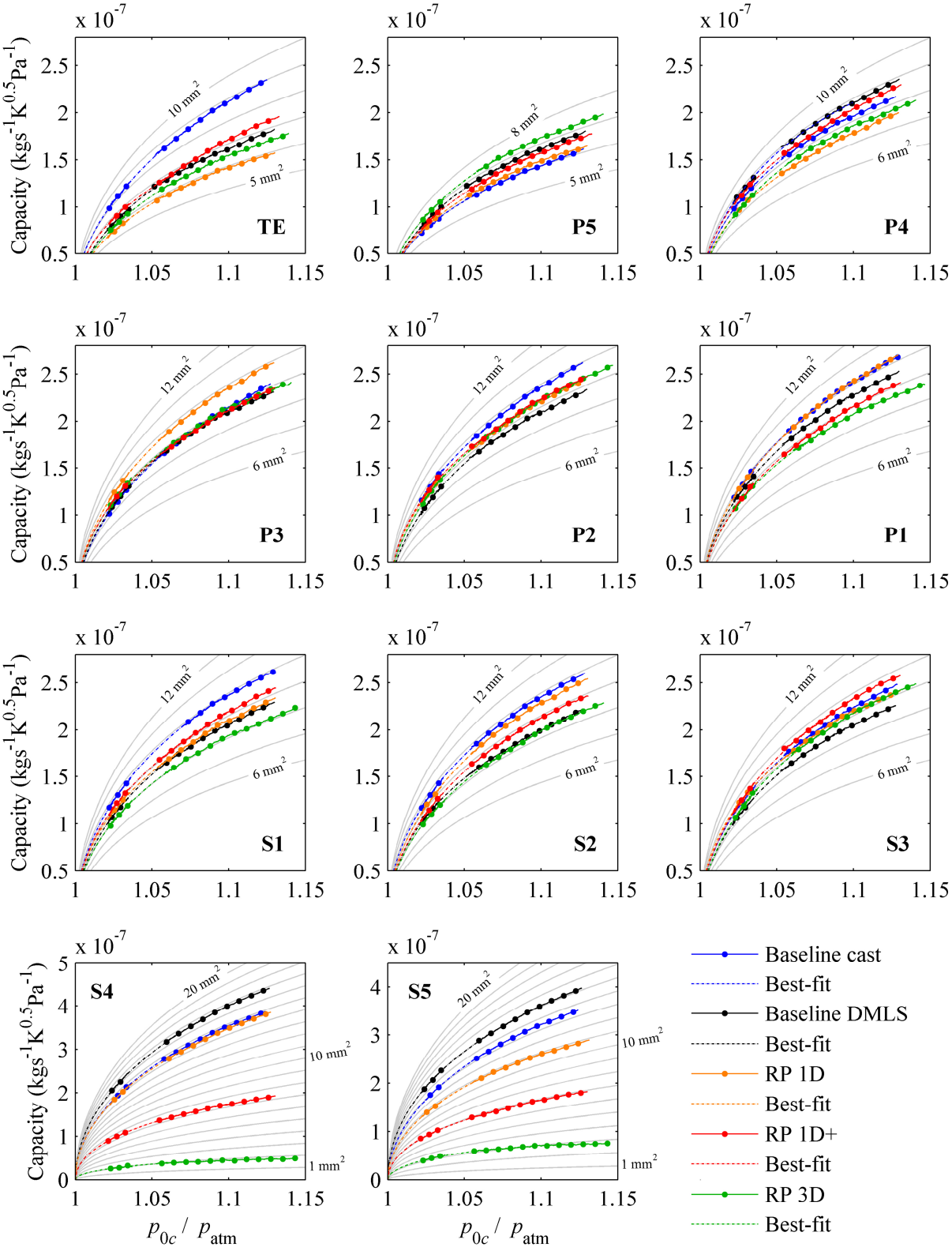


Figure 8.21. Row-by-row raw coolant capacity.
Five designs tested; 1D isentropic capacity for constant area shown in background of each subplot.

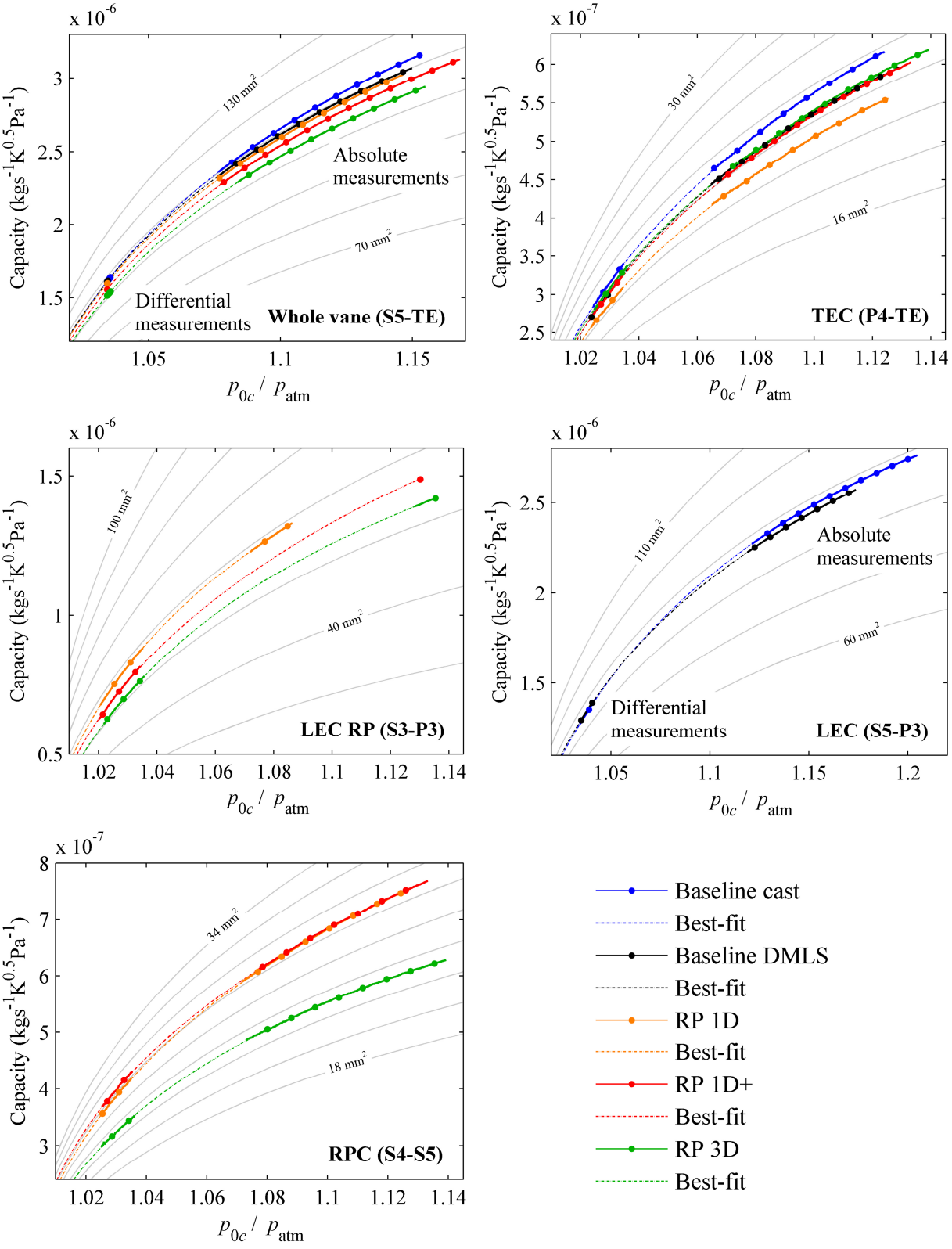


Figure 8.22. Compartmental and total raw coolant capacity.
Five designs tested; 1D isentropic capacity for constant area shown in background of each subplot. RPC = rows within reverse-pass compartment (S4-S5); LEC RP = group of rows in the leading-edge of reverse-pass systems (S3-P3); LEC = group of rows in the leading-edge compartment of baseline vanes (S5-P3); TEC = group of rows around the trailing-edge (P4-TE). All differential measurements unless indicated.

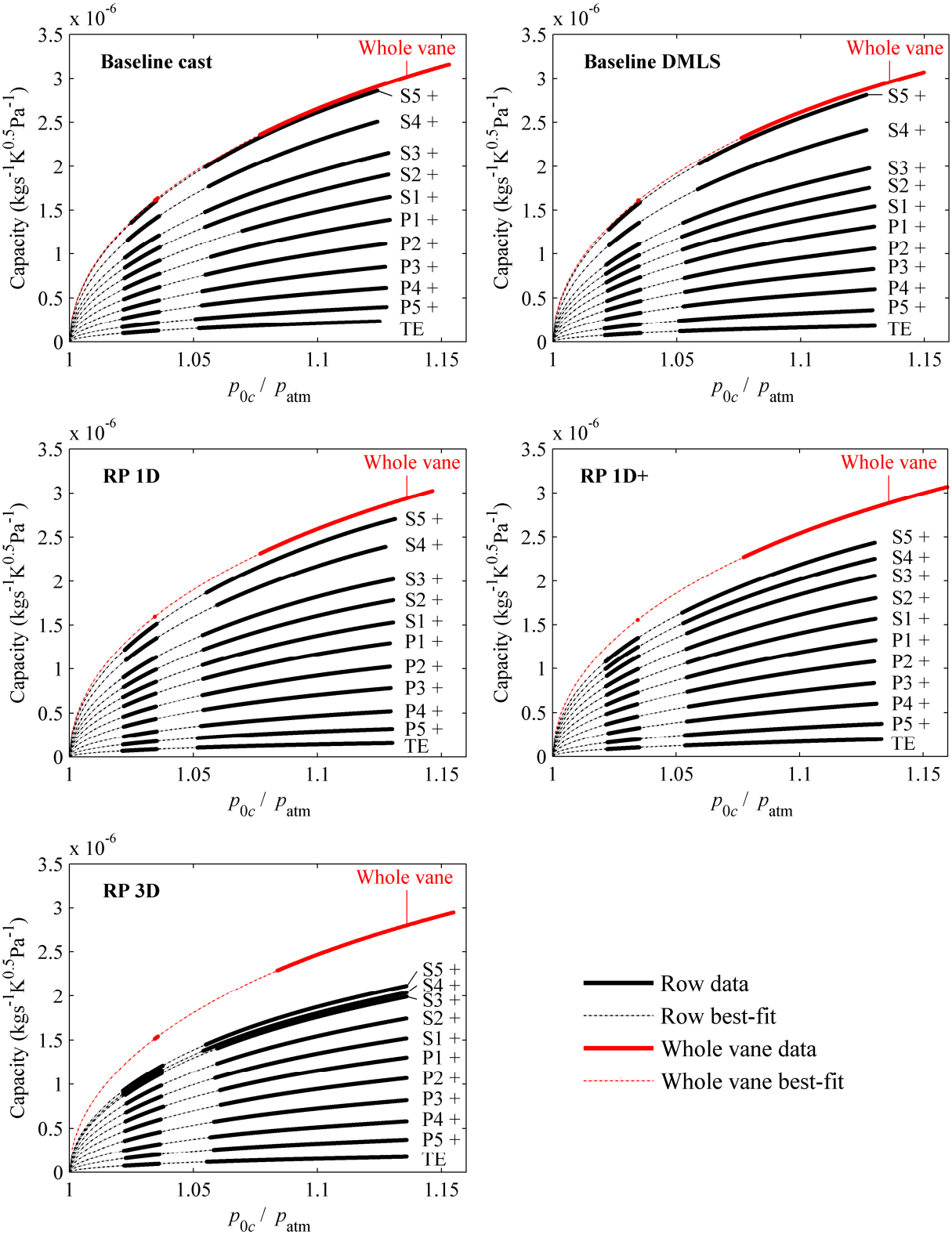


Figure 8.23. Raw row-by-row coolant capacity plotted cumulatively.
Each design plotted separately. The total capacity of the whole vane shown in red.

measurement, and therefore the total pressure loss decreases. Subsequently, the mass flow rate in the low-differential measurement is *higher* than it would have been if all rows were blowing, and therefore the row mass flow rate measured by the experiment is *lower* than the row mass flow rate when all rows are blowing. The amount by which it is lower is dictated by the amount of interaction. The capacity of S4 and S5 when all rows are blowing is much higher than the raw capacity plotted in Fig. 8.22.

From continuity, the sum of the row capacities *when all rows are blowing* equals the total capacity. Since the row capacity measured in the CCR is less than the row capacity when all rows are blowing, the sum of the row capacities measured in the CCR is lower than the total vane capacity. This can be seen clearly in Fig. 8.23 for all geometries. Interaction is discussed further in the following section.

While additional processing of the experimental data is required to predict the row capacity when all rows are blowing, it also presents the opportunity to experimentally measure the interaction loss coefficients K_A^c, K_B^c, K_C^c, ... etc. This forms the basis of the following chapter.

8.10 Interaction Testing

The interaction between rows within the vane is now investigated in greater detail.

The raw row capacity Γ_i^r is defined in terms of the total pressure p_{0c} and total temperature T_{0c} at vane inlet and raw row mass flow rate through row i, $\dot{m}_i^r$, which is determined from the CCR experiments described in this chapter:

$$\Gamma_i^r = \dot{m}_i^r \sqrt{T_{0c}}/p_{0c}\,, \qquad i \in \text{ROW}, \tag{8.27}$$

where ROW is the set of rows defined as:

$$\text{ROW} = \{\text{TE,P5,P4,P3,P2,P1,S1,S2,S3,S4,S5}\}. \tag{8.28}$$

Similarly, the total coolant capacity Γ is defined using the total coolant mass flow rate $\dot{m}$:

$$\Gamma = \dot{m}\sqrt{T_{0c}}/p_{0c}, \tag{8.29}$$

A compartment is used to refer to a general group of rows that are either contained within a physical compartment, or are close enough together and far enough away from other rows that they may be considered ‘compartment-like’. The raw compartmental capacity Γ_j^c is determined from the CCR experiments and is defined using the total pressure p_{0c} and total temperature T_{0c} at vane inlet and the raw mass flow rate through compartment j, $\dot{m}_j^c$:

$$\Gamma_j^c = \dot{m}_j^c \sqrt{T_{0c}}/p_{0c}\,, \qquad j \in \text{CMP}, \tag{8.30}$$

where CMP is the set of compartments within a design. For the baseline cast and baseline laser-sintered designs,

$$\text{CMP} = \{\text{LEC,TEC}\}, \tag{8.31}$$

where each compartment contains the following rows:

$$\text{LEC} = \{\text{P3,P2,P1,S1,S2,S3,S4,S5}\},\ \text{TEC} = \{\text{TE,P5,P4}\}. \tag{8.32}$$

For the reverse-pass designs,

$$\text{CMP} = \{\text{LEC,TEC,RPC}\}, \tag{8.33}$$

where

$$\text{LEC} = \{\text{P3,P2,P1,S1,S2,S3}\},\ \text{TEC} = \{\text{TE,P5,P4}\},\ \text{RPC} = \{\text{S4,S5}\}. \tag{8.34}$$

If the rows within a compartment interact, then the raw row capacity measured in the CCR Γ_i^r will be less than the row capacity when all rows are blowing, by an amount dictated by the interaction. The reasons for this are discussed in the previous section. Interaction between rows within a compartment is therefore present when:

$$\Gamma_j^c > \sum_{\mu \in j} \Gamma_\mu^r, \tag{8.35}$$

where j is a compartment set containing a number of rows, as defined in equations (8.30)-(8.34). μ is the summation index. Interaction between compartments is present when:

$$\Gamma > \sum_{\mu \in \text{CMP}} \Gamma_\mu^c, \tag{8.36}$$

where CMP is defined in equation (8.31) or (8.33) (depending on the geometry) and μ is the summation index.

The size of the inequality increases with the local loss coefficient and local dynamic head. The summation and inequality for the compartments is shown in Fig. 8.24, and similarly for the rows within compartments in Fig. 8.25. For all designs but RP 3D, the sum of the compartment capacities measured in the CCR is equal to the total coolant capacity. The compartments in these designs can therefore be considered non-interacting. RP 3D, however, has some interaction between compartments. This compartmental interaction is likely to be between the reverse-pass passage compartment feeding S4 and S5 (RPC) and the trailing-edge rows TE-P4, since the entrances to the two systems are extremely close together at the rear of the vane. The layout of the compartments is shown in Figs. 4.19-4.22.

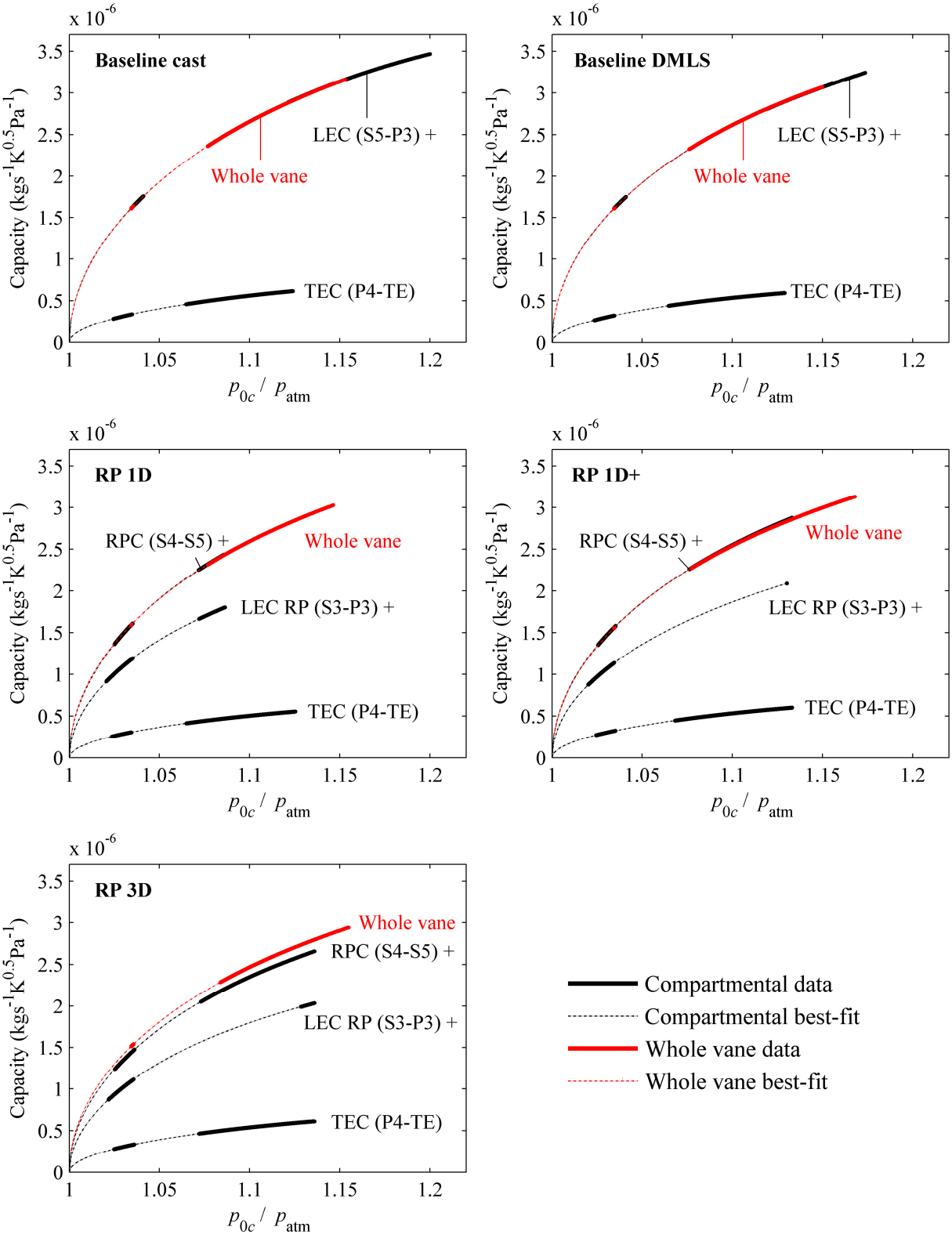


Figure 8.24. Results of inter-compartmental interaction testing.
Cumulative sum of compartments for each design. The laser-sintered designs are baseline DMLS, RP 1D, RP 1D+ and RP 3D.

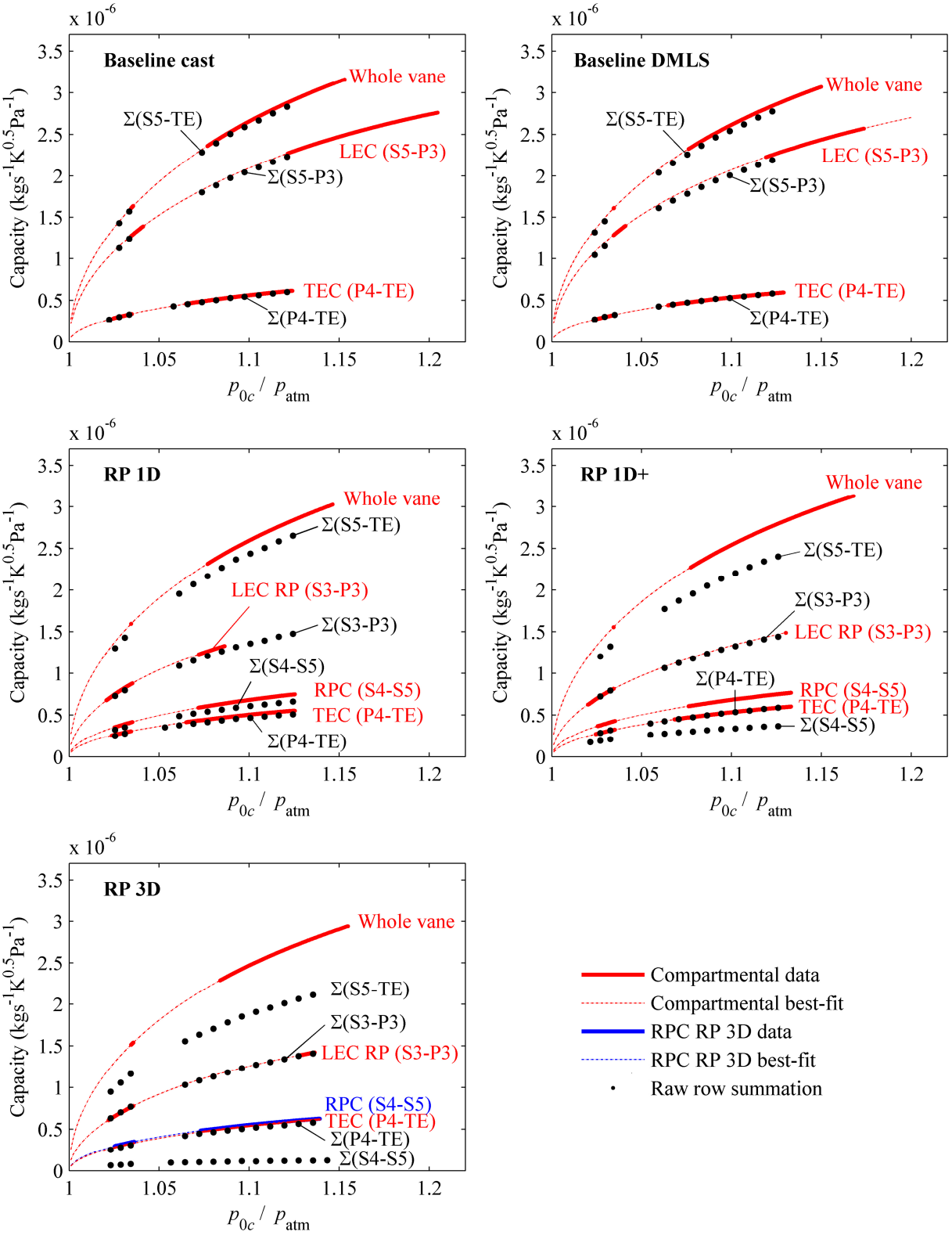


Figure 8.25. Results of inter-row interaction testing.
Cumulative sum of rows within each compartment, for each design.

The results plotted in Fig. 8.25 indicate the interaction losses within each compartment. For all designs, the interaction loss within the trailing-edge group of rows (TEC) is shown to be minimal, as the sum of the raw capacities TE-P4 is approximately equal to the raw capacity of the entire group. The capacity sum of the rows within the leading-edge compartment (LEC) is slightly lower than total LEC capacity for both the cast baseline and the laser-sintered baseline vanes, indicating there is a small amount of interaction between cooling rows in the LEC. The same is seen for the LEC RP in RP 1D. The capacity sum of rows S3-P3 in the RP 1D+ and RP 3D designs is almost exactly equal to the total S3-P3 capacity, suggesting minimal interaction loss within this group. This seems physical since the RP 1D+ and RP 3D both feature a single, large plenum for all cooling rows, while all other designs have smaller, multiple plena.

The reverse-pass compartments (RPC), consisting rows S4 and S5, show the largest difference between the summation and the total RPC capacity. RP 3D has most interaction between S4 and S5, then RP 1D+, then RP 1D. This suggests that the RP 3D geometry has the largest total pressure drop through the RP passage, while RP 1D has the lowest pressure drop through the RP passage. This is reassuring, since RP 3D was designed to incur the largest pressure drop of the RP designs, and RP 1D the smallest.

The data plotted in Figs. 8.24 and 8.25 are used to estimate the loss coefficients within each system in the following chapter. In the process, row capacity *when all rows are blowing* is estimated—as opposed to the raw row capacity results presented here in which total pressure loss is unmatched. From these predictions the effective row area is also determined, and the capacity scaled to engine conditions.

8.11 Proposed Improvements

Increase range of CCR orifice calibration. Increasing the calibrated range of the CCR orifice increases the range of PRs and capacity that could be measured in a single run. Dead-zones where capacity cannot currently be measured (Fig. 8.16) would be eliminated. The orifice could be calibrated at lower Reynolds numbers by cross-calibrating with a smaller reference nozzle, and at higher Reynolds numbers and lower unsteadiness by supplying the calibration setup with 400 psi air instead of 100 psi. It would also be useful to calibrate the orifice as a function of PR, and perhaps calibrate the nozzle for subsonic operation. This process was started but not completed.

Increase 100 psi supply rate. The rate of blow-down could be decreased by increasing the supply rate of air from the 100 psi line. This would further reduce unsteady effects. This could be achieved by shortening, or widening, the current 100 psi supply hose. The system may even be operated steadily by connecting directly to a high mass flow 100 psi feed though a variable restriction. Capacity points, rather than curves, would be recorded. This may prove too time-consuming, however.

Increase maximum range of transducer upstream of CCR orifice. A 5 bara transducer was used upstream of the CCR orifice to measure total pressure. This meant that some data at high pressure could not be recorded. A 7 bara transducer would cover the entire range (max. 100 psi).

Install PRVs on instrumentation blocks. The 2.2 barg PRVs from the FTF could be attached to the instrumentation/bypass blocks.

8.12 Conclusions

Knowledge of the coolant flow distribution within each cooling design is necessary to assess aero-thermal performance. In this chapter, the experimental technique used to measure row-by-row, compartmental and total coolant capacity of each design is reported. A number of advances have allowed for accurate and repeatable coolant capacity measurement, including: the design, development and manufacture of a new rig specifically for measuring per-row coolant capacity at high accuracy and minimal turnaround time; high accuracy calibration of the mass flow measurement orifice; the implementation of a differential mass flow measurement technique and bypass system which allows for calibrated mass flow measurement from 0 g/s to 24.9 g/s over a large range of pressure ratios.

The raw coolant capacity measurements have been reported. The total vane capacities of the laser-sintered designs agree with the total vane capacity of the cast baseline to 7%. This disparity is compensated in the Sector Facility by performing the thermal assessment over a range of coolant mass flow rates. The maximum deviation in per-row raw capacity of S3-P5 between designs is around 20%, except the laser-sintered TEs which flow around 40% less than the cast equivalent due to the difficulty in laser-sintering the trailing-edge pedestal bank and slot. Values included here should be taken as indications only; the next chapter post-processes the raw capacity data in this chapter to take into account internal interaction.

The raw row capacity measured in the CCR is less than the row capacity when all rows are blowing, by an amount dictated by the internal interaction of the rows. This is because the differential mass flow measurement technique changes the flow distribution within the vane. The size of this difference depends on the total pressure loss within the internal system; it is negligible in the cast and laser-sintered baseline designs but significant for the reverse-pass fed cooling rows (S4 and S5). While additional post-processing of the experimental data is therefore required to predict the row capacity when all rows are blowing, it also presents the unique opportunity to experimentally measure the interaction loss coefficients. This is performed in the following chapter.

9. Effective Row Area, Loss Coefficients, and Engine Coolant Capacity Prediction

In this chapter, network flow models used to describe each design are defined and justified. The method of populating each model with effective row areas and loss coefficients is described, and the results presented. The population process is fairly complex, requiring the simultaneous analysis of all CCR experimental data. The network models are then used to predict the actual row-by-row coolant capacity at CCR, Sector and engine boundary conditions. The network flow model is validated using the total vane capacity measured in the Sector Facility, giving confidence in the ability of the model to predict row-by-row capacity at engine conditions.

9.1 Introduction

In the previous chapter, the experimental method used to determine raw row-by-row coolant capacity is discussed, and the results of the raw analysis are reported. It is shown that the differential mass flow technique utilised in the CCR alters the internal flow distribution because it is an intrusive measurement technique; by blocking the row of interest, the internal pressure loss in the CCR experiments is lower than when all rows are blowing. The raw row-by-row coolant capacity is therefore lower than the actual row coolant capacity.

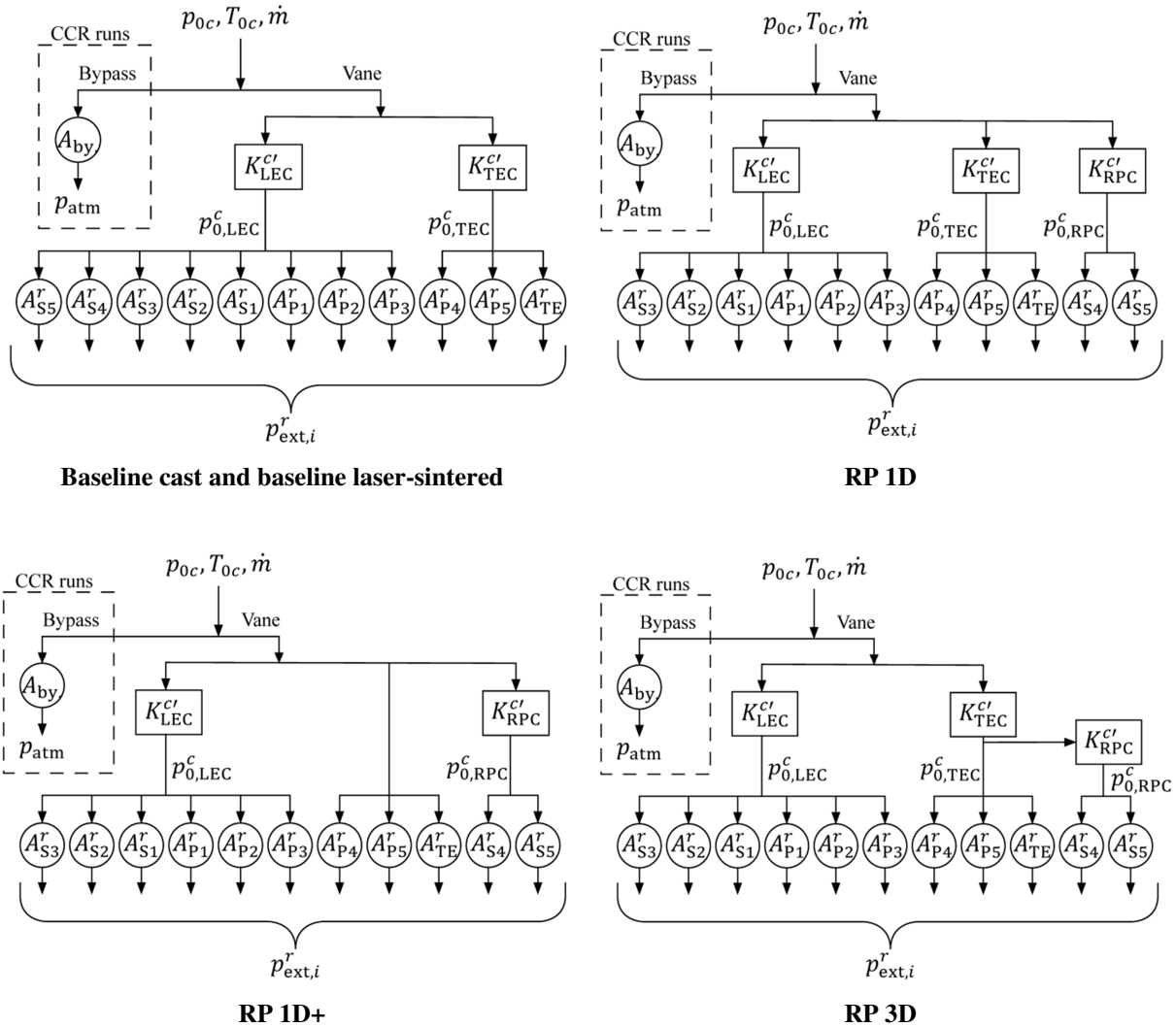
The difference between the raw capacity and the actual capacity depends on the amount of internal interaction between cooling rows. For non-interacting cooling rows, the flow to each row is unaffected by blocking the row of interest, and therefore the raw row capacity equals the actual row capacity. This is more or less the case for the baseline geometry, because the design consists of large feed plena and is relatively lossless. In contrast, row interaction is significant in the reverse-pass designs—especially between rows S4 and S5 because they are fed by a small, shared plenum via a high-loss reverse-pass passage. The raw row capacity of S4 and S5 in the reverse-pass designs is hence far smaller than their capacity when all rows are blowing.

This discrepancy may seem less than ideal, but actually presents a unique opportunity to quantify the losses within each system from the raw CCR measurements. By comparing the *sum* of the raw row-by-row coolant capacities to the *compartmental* coolant capacity measurements, the amount of internal loss due to the interaction between rows can be predicted, and non-dimensionalised in terms of a loss coefficient. This is fortuitous because the internal loss coefficients must be known in order to scale the CCR results to engine conditions. It is also a much simpler method of estimating internal pressure loss than the alternative of inserting multiple pressure probes within the vane.

In order to calculate loss coefficients from the CCR measurements, it necessary to build and utilise an internal network flow model that captures interaction induced loss. The *form* of the network flow model depends on how the rows interact ('interaction testing', described in the previous chapter), defining the pertinent loss coefficients required to describe the internal flow system. Flow through each row is defined in terms of an effective area, based on the 1D, isentropic, compressible mass flow relation. The network flow model is populated using the experimental data from the CCR, and is then used to predict the *actual* row-by-row capacity (not raw) for any external pressure distribution, any combination of blocked or unblocked rows, and at any ratio of specific heats—e.g., at CCR, Sector and engine conditions.

9.2 Network Flow Models

The network flow models for each design are shown in Fig. 9.1. The form of each network flow models is justified separately for each network model.



Baseline cast and baseline laser-sintered

RP 1D

RP 1D+

RP 3D

Figure 9.1. Network flow models, based on results of interaction testing in previous chapter.

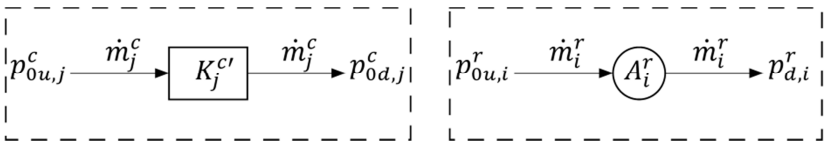


Figure 9.2. Loss element (L) and nozzle element (R)

The mass flow rate measured in the CCR is the sum of the bypass flow (shown in the dashed box) and the vane flow. The bypass segment is shown for completeness, but drops out of the proceeding analysis because the CCR mass flow rate always appears as the difference between a high run where all rows are blowing (subscript i, H) and a low run where row i is blocked (subscript i, L):

$$\frac{\dot{m}_{i,H}\sqrt{T_{0c}}}{p_{0c}} - \frac{\dot{m}_{i,L}\sqrt{T_{0c}}}{p_{0c}} = \left(\frac{\dot{m}_{i,bypass}\sqrt{T_{0c}}}{p_{0c}} + \frac{\dot{m}_{vane,i,H}\sqrt{T_{0c}}}{p_{0c}}\right) - \left(\frac{\dot{m}_{i,bypass}\sqrt{T_{0c}}}{p_{0c}} + \frac{\dot{m}_{vane,i,L}\sqrt{T_{0c}}}{p_{0c}}\right). \tag{9.1}$$

Since $\dot{m}_{i,bypass}$ is the same for both high- and low-differential runs in the pair, and using the definition that $\Gamma_{i,H} = \dot{m}_{i,H}\sqrt{T_{0c}}/p_{0c}$ and $\Gamma_{i,L} = \dot{m}_{i,L}\sqrt{T_{0c}}/p_{0c}$, the bypass flow drops out:

$$\Gamma^r_i = \Gamma_{i,H} - \Gamma_{i,L} = \frac{\dot{m}_{vane,i,H}\sqrt{T_{0c}}}{p_{0c}} - \frac{\dot{m}_{vane,i,L}\sqrt{T_{0c}}}{p_{0c}}. \tag{9.2}$$

Γ^r_i is the raw row coolant capacity (superscript r referring to *row*) , discussed in the previous chapter. Equation (9.2) assumes that there is no pressure loss between the bypass and the entrance to the vane. The bypass segment is removed when the model is used to predict coolant capacity at other conditions.

Each loss model comprises loss elements (shown in the boxes), and nozzle elements (shown in the circles). A general loss element and nozzle element are shown in Fig. 9.2, to define the nomenclature that follows. Loss elements are used to model total pressure loss and nozzle elements are used to model mass flow rate through each film cooling row. Flow travels along the routes defined by the arrowed lines. Continuity is satisfied at all flow splits. Flow through the nozzle elements is modelled as compressible; flow everywhere else is modelled as incompressible. This is justified since the maximum Mach number within the internal passages is approximately 0.3 (found inside the TE pedestal bank).

The total pressure loss $p^c_{0u,j} - p^c_{0d,j}$ induced by a loss element is assumed to be a constant proportion K^c_j of the local dynamic head $\frac{1}{2}\rho\left(v^c_j\right)^2$:

$$K^c_j = \frac{p^c_{0u,j} - p^c_{0d,j}}{\frac{1}{2}\rho\left(v^c_j\right)^2}. \tag{9.3}$$

K_j^c is the loss coefficient of loss element j, and is assumed to be constant for all pressure ratios and dynamic heads (superscript c referring to *compartment*). This assumption is briefly examined later. Subscript j is used to describe a location within the vane where loss occurs, typically a compartment. j is defined in equation (8.28). Subscript u and subscript d are used generally to describe 'upstream' and 'downstream', respectively.

The local velocity v_j^c can be related to the local mass flow rate $\dot{m}_j^c$ and local area A_j^c:

$$v_j^c = \frac{\dot{m}_j^c}{\rho A_j^c}. \tag{9.4}$$

The density at the loss element ρ is approximately equal to the ratio of the upstream total pressure $p_{0u,j}^c$ and the inlet coolant temperature T_{0c} multiplied by the specific gas constant (equation of state):

$$\rho = \frac{p_u}{RT_u} \approx \frac{p_{0u,j}^c}{RT_{0c}}. \tag{9.5}$$

Since the loss coefficient K_j^c, the local area A_j^c and the specific gas constant R are assumed constant, it proves convenient to define a new, 'dimensional loss coefficient' $K_j^{c\prime}$ that incorporates all of these elements:

$$K_j^{c\prime} = \sqrt{\frac{K_j^c R}{2\left(A_j^c\right)^2}}. \tag{9.6}$$

The dimensional loss coefficient is similar to capacity in that it can effectively be considered as a non-dimensional quantity since K_j^c, A_j^c and R are constant to first order. Combining equations (9.3)-(9.6):

$$\dot{m}_j^c = \frac{p_{0u,j}^c}{K_j^{c\prime}\sqrt{T_{0c}}}\sqrt{1 - \frac{p_{0d,j}^c}{p_{0u,j}^c}}. \tag{9.7}$$

The mass flow rate $\dot{m}_j^c$ is normalised with respect to the total pressure at vane inlet p_{0c} and the root of total temperature at vane inlet T_{0c} to estimate the capacity of the loss element:

$$\frac{\dot{m}_j^c\sqrt{T_{0c}}}{p_{0c}} = \frac{1}{K_j^{c\prime}}\frac{p_{0u,j}^c}{p_{0c}}\sqrt{1 - \frac{p_{0d,j}^c}{p_{0c}}\frac{p_{0c}}{p_{0u,j}^c}}. \tag{9.8}$$

Defining the capacity of a loss element in terms of the inlet total pressure p_{0c} (rather than the upstream total pressure $p_{0u,j}^c$) is useful as it simplifies applying continuity at flow splits.

Mass flow through a nozzle element (row) is approximated using the 1D, isentropic, compressible mass flow relation. The mass flow rate through a row i, $\dot{m}_i^r$, is defined using the total upstream pressure $p_{0u,i}^r$, the downstream static pressure $p_{d,i}^r$, an effective area A_i^r, ratio of specific heats γ, inlet total temperature T_{0c}, and the specific gas constant R:

$$\dot{m}_i^r = A_i^r \frac{p_{0u,i}^r}{\sqrt{T_{0c}}} \left(\frac{p_{0u,i}^r}{p_{d,i}^r}\right)^{-\frac{\gamma+1}{2\gamma}} \sqrt{\frac{2\gamma}{R(\gamma-1)}\left[\left(\frac{p_{0u,i}^r}{p_{d,i}^r}\right)^{\frac{\gamma-1}{\gamma}} - 1\right]}. \tag{9.9}$$

i is defined in equation equation (8.25). The effective area A_i^r is a function of the geometric area of the film cooling rows, the discharge coefficient, and—to first order—the loss across the nozzle element. Like the loss element, the mass flow rate through the nozzle element is normalised with respect to the total pressure and total temperature at the vane inlet to simplify the application of continuity; the capacity of a nozzle element is therefore:

$$\frac{\dot{m}_i^r \sqrt{T_{0c}}}{p_{0c}} = A_i^r \frac{p_{0u,i}^r}{p_{0c}} \left(\frac{p_{0u,i}^r}{p_{0c}} \frac{p_{0c}}{p_{d,i}^r}\right)^{-\frac{\gamma+1}{2\gamma}} \sqrt{\frac{2\gamma}{R(\gamma-1)}\left[\left(\frac{p_{0u,i}^r}{p_{0c}} \frac{p_{0c}}{p_{d,i}^r}\right)^{\frac{\gamma-1}{\gamma}} - 1\right]}, \tag{9.10}$$

where $p_{0u,i}^r/p_{d,i}^r$ has been replaced with the product of $p_{0u,i}^r/p_{0c}$ and $p_{0c}/p_{d,i}^r$ to simplify the network analysis. To avoid repetition of the above equation, a function ζ is defined

$$\zeta(x, y, \gamma) = x(xy)^{-\frac{\gamma+1}{2\gamma}} \sqrt{\frac{2\gamma}{R(\gamma-1)}\left[(xy)^{\frac{\gamma-1}{\gamma}} - 1\right]}, \tag{9.11}$$

which reduces equation (9.10) to:

$$\frac{\dot{m}_i^r \sqrt{T_{0c}}}{p_{0c}} = A_i^r \zeta\left(\frac{p_{0u,i}^r}{p_{0c}}, \frac{p_{0c}}{p_{d,i}^r}, \gamma\right). \tag{9.12}$$

ζ is referred to here as 'specific capacity', since it is capacity $\dot{m}_i^r \sqrt{T_{0c}}/p_{0c}$ that is specific to a given area A_i^r. ζ is the non-dimensional mass flow rate multiplied by $\sqrt{R}$. The use of specific capacity ζ is justified by its ubiquity in the subsequent analysis.

The capacity of row i when all rows are blowing is given the symbol $\tilde{\Gamma}_i^r$ to differentiate it from the raw row capacity Γ_i^r measured in the CCR. The actual capacity $\tilde{\Gamma}_i^r$ is found from (9.13) and is a function of the total pressure ratio between the feed plena j and the vane inlet $p_{0,j}^c/p_{0c}$, the total pressure ratio between the vane inlet and the static exit pressure $p_{0c}/p_{\mathrm{ext},i}^r$, the ratio of specific heats γ, and the effective row area A_i^r:

$$\tilde{\Gamma}_i^r = \frac{\dot{m}_i^r \sqrt{T_{0c}}}{p_{0c}} = A_i^r \zeta\left(\frac{p_{0,j}^c}{p_{0c}}, \frac{p_{0c}}{p_{\text{ext},i}^r}, \gamma\right). \tag{9.13}$$

If the row does not interact with other rows, then the actual capacity and the raw capacity are equal:

$$\tilde{\Gamma}_i^r = \Gamma_i^r; \tag{9.14}$$

otherwise for interacting rows,

$$\tilde{\Gamma}_i^r > \Gamma_i^r. \tag{9.15}$$

9.3 Population and Use of Network Flow Models

There are 13/14 unknowns within the network flow model: 11 effective areas A_i^r and either two or three loss coefficients K_j^c. The workflow for calculating these unknowns from the CCR measurements is summarised in Fig. 9.3. Also summarised in the workflow are the inputs and outputs required to use the network flow model to predict coolant capacity at different boundary conditions.

Loss coefficients are defined by the network flow model and are calculated using the raw CCR differential measurements of row capacity (x11 capacity curves) and the raw compartmental capacity curves (x2 or x3). 'Compartment' is used to refer to a general group of rows that are either contained within a physical compartment (e.g., leading-edge compartment), or are close enough together and far enough away from other rows that they may be considered 'compartment-like'.

Because the calibrated range of the CCR mass flow measurement orifice is limited, only two portions of the compartmental capacity curves are measured: at low PRs in the range 1.02-1.03, and at high PRs in the range 1.12-1.2 (the exact PR range depends on the exit area of the compartment). Loss coefficients are determined using the high PR capacity data, over a PR range where capacity data exist for all rows and all compartments—given by the red dashed box in Fig. 9.3. Only high PR capacity data are used to determine loss coefficients because the effect of loss is much greater at larger PR; the accuracy of the loss coefficient measurement is therefore maximised for the available data. Loss coefficients are determined as a function of PR over a small range of high PRs. The effective area of each row is simultaneously calculated over this narrow PR range. These effective area data are not used, however; instead, the mean loss coefficient (mean over PR) is calculated, and used in all subsequent analysis to determine effective area—justified by the minimal variation in loss coefficient with PR, and the agreement between the network flow model prediction and the CCR/Sector whole vane capacity over a broad PR range.

Effective areas are defined in the network flow model, and are calculated using the raw CCR differential capacity measurements of each row (x11 curJves) and the mean loss coefficients. The

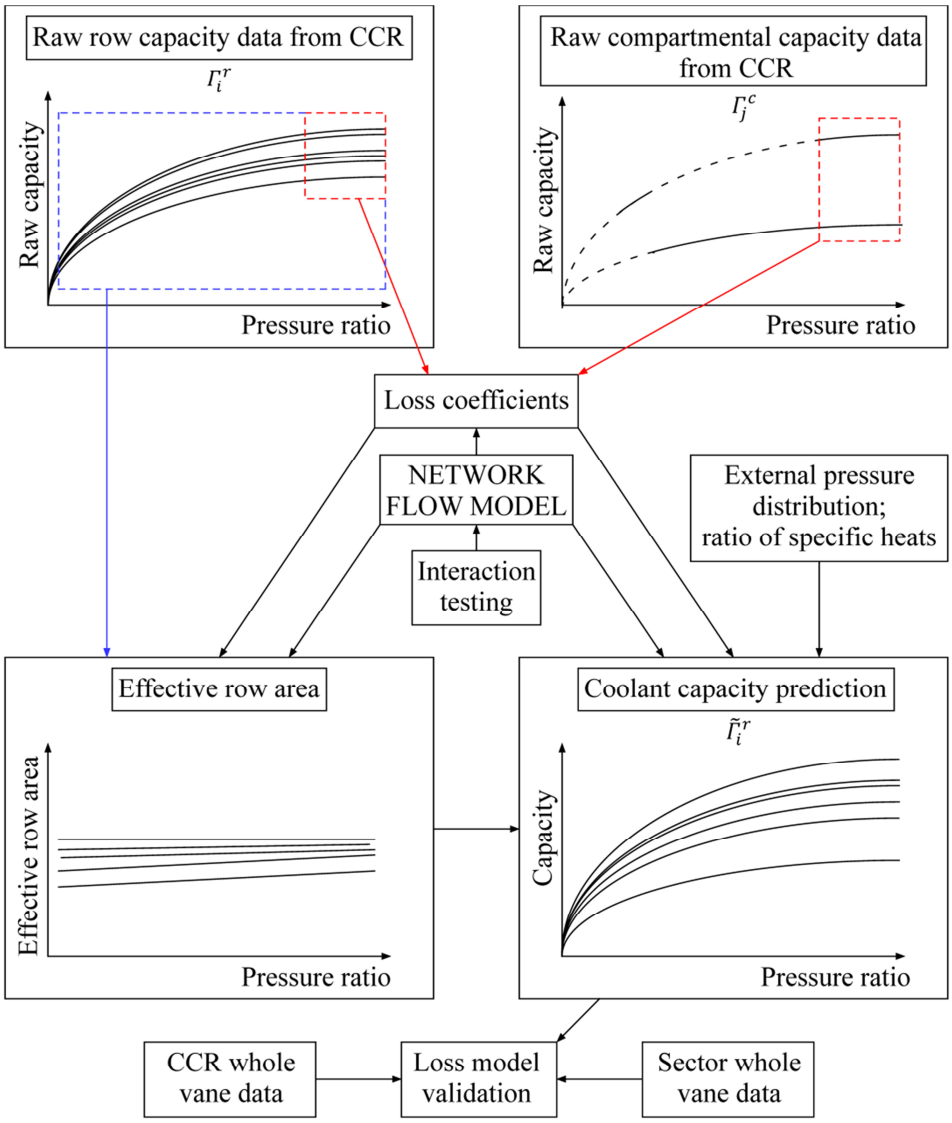


Figure 9.3. Workflow for the population and use of the network flow models.

entire PR range of the raw capacity curves is used—given by the blue dashed box in Fig. 9.3. The effective area is determined as a function of the local total-to-static pressure ratio across the row. Ideally, the effective area would be characterised using coolant Reynolds number (Rowbury, 1998), but the coolant Reynolds number in the CCR is approximately four times smaller than at engine conditions. It was deemed that any error in effective area caused by matching PR but not Reynolds number would be lower than extrapolating Reynolds-number-characterised results to engine conditions.

Actual row-by-row coolant capacity $\tilde{\Gamma}_i^r$ is then estimated using the network flow model, the mean loss coefficients, effective row areas (as a function of PR), the external distribution of static pressure around the aerofoil, and the ratio of specific heats. These predictions are then validated against the

total vane capacity measurements made in the Sector Facility (where each row exhausts to a different static pressure). The row-by-row coolant capacity at engine conditions is also predicted.

Each network flow model is now discussed in detail.

9.4 Baseline Cast and Baseline Laser-Sintered Network Flow Model

The baseline network flow model is repeated in Fig. 9.4. The model consists of two loss elements: one to account for losses within the leading-edge compartment (LEC) due to interaction between rows S5-P3, and the other to account for losses within the trailing-edge compartment (TEC) due to interaction between rows P4-TE.

Interaction testing demonstrated that there is no interaction between the LEC and TEC, but there is interaction between rows within each compartment. LEC and TEC loss elements are therefore placed in parallel, so that the TEC and LEC operate independently but induce local loss within each compartment.

9.4.1 Calculating Baseline Loss Coefficients and Effective Row Areas

The method used to calculate the loss coefficients and effective areas within the baseline network flow model is now described. A system of equations is generated from the experimental CCR results, which are solved simultaneously to determine the unknowns (loss coefficients, effective areas and pressure ratios).

For the rows contained within the LEC, $i = \{\text{S5,S4,S3,S2,S1,P1,P2,P3}\}$ (8 equations), the raw row capacity Γ_i^r measured in the CCR (i.e., the difference in capacity between the high-differential H run and low-differential L run where row i is blocked) is equated to the difference in capacity through the LEC between high and low runs, since the TEC and the bypass flow are the same for H and L. Using the capacity through the LEC loss element (9.8), it can be shown that:

$$\Gamma_i^r = \frac{1}{K_{\text{LEC}}^{c\prime}}\left(\sqrt{1-\left.\frac{p_{0,\text{LEC}}^c}{p_{0c}}\right|_H} - \sqrt{1-\left.\frac{p_{0,\text{LEC}}^c}{p_{0c}}\right|_{i,L}}\right), \tag{9.16}$$

where $p_{0,\text{LEC}}^c\big|_H$ is the total pressure within the LEC during the high-differential run (constant for all i), and $p_{0,\text{LEC}}^c\big|_{i,L}$ is the total pressure within the LEC during the low-differential run (changes with i).

Similarly, for the rows contained within the TEC, $i = \{\text{P4,P5,TE}\}$ (3 equations), only the TEC flow is affected in the low differential measurements, and hence:

$$\Gamma_i^r = \frac{1}{K_{\text{TEC}}^{c\prime}}\left(\sqrt{1-\left.\frac{p_{0,\text{TEC}}^c}{p_{0c}}\right|_H} - \sqrt{1-\left.\frac{p_{0,\text{TEC}}^c}{p_{0c}}\right|_{i,L}}\right), \tag{9.17}$$

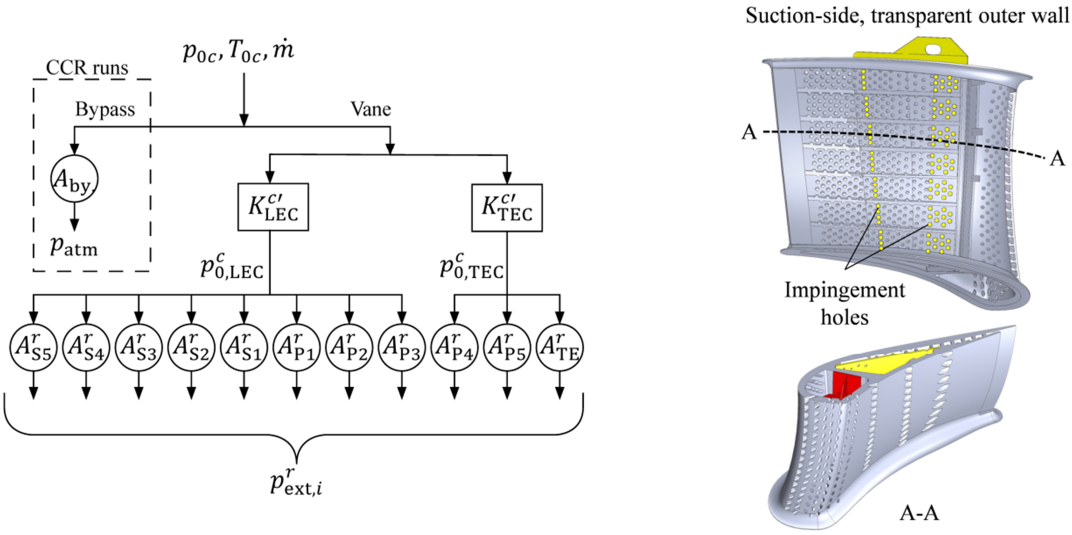


Figure 9.4. Baseline cast and baseline laser-sintered network flow model, with CAD of passage layouts. (modified from § 4.6).

where $p^{c}_{0,\mathrm{TEC}}\big|_{H}$ is the total pressure within the TEC during the high-differential run (constant for all i), and $p^{c}_{0,\mathrm{TEC}}\big|_{i,L}$ is the total pressure within the TEC during the low-differential run (changes with i).

The LEC raw capacity $\Gamma^{c}_{\mathrm{LEC}}$ is measured absolutely. The bypass and TEC are blocked, and so the capacity through the system is equal to the capacity through the LEC loss element:

$$\Gamma^{c}_{\mathrm{LEC}} = \frac{1}{K^{c\prime}_{\mathrm{LEC}}}\sqrt{1-\frac{p^{c}_{0,\mathrm{LEC}}}{p_{0c}}\bigg|_{H}}\,. \tag{9.18}$$

The TEC raw capacity $\Gamma^{c}_{\mathrm{TEC}}$ is measured differentially by blocking the TEC between high and low runs. The difference in capacity between H and L is due only to the blockage of the TEC:

$$\Gamma^{c}_{\mathrm{TEC}} = \frac{1}{K^{c\prime}_{\mathrm{TEC}}}\sqrt{1-\frac{p^{c}_{0,\mathrm{TEC}}}{p_{0c}}\bigg|_{H}}\,. \tag{9.19}$$

When all rows are blowing (high run H), the sum of the capacity through the LEC rows (nozzle elements) is equal to the capacity through the LEC loss element (continuity). Similarly, the capacity sum through the TEC cooling rows is equal to the capacity through the TEC loss element. Therefore:

$$\zeta\left(\frac{p^{c}_{0,\mathrm{LEC}}}{p_{0c}}\bigg|_{H}, \frac{p_{0c}}{p_{\mathrm{atm}}}, \gamma\right)\sum_{\mu\in\mathrm{LEC}} A^{r}_{\mu} = \frac{1}{K^{c\prime}_{\mathrm{LEC}}}\sqrt{1-\frac{p^{c}_{0,\mathrm{LEC}}}{p_{0c}}\bigg|_{H}}\,, \tag{9.20}$$

$$\zeta\left(\left.\frac{p_{0,\mathrm{TEC}}^{c}}{p_{0c}}\right|_{H},\frac{p_{0c}}{p_{\mathrm{atm}}},\gamma\right)\sum_{\mu\in\mathrm{TEC}}A_{\mu}^{r}=\frac{1}{K_{\mathrm{TEC}}^{c\prime}}\sqrt{1-\left.\frac{p_{0,\mathrm{TEC}}^{c}}{p_{0c}}\right|_{H}},\tag{9.21}$$

where $\mu \in$ LEC means all cooling contained within the LEC and $\mu \in$ TEC means all cooling rows contained within the TEC.

For runs in which a row within the LEC is blocked ($i = \{$S5,S4,S3,S2,S1,P1,P2,P3$\}$, 8 equations), the capacity through the LEC loss element is equal to the capacity sum through all open rows within the LEC:

$$\zeta\left(\left.\frac{p_{0,\mathrm{LEC}}^{c}}{p_{0c}}\right|_{i,L},\frac{p_{0c}}{p_{\mathrm{atm}}},\gamma\right)\left(-A_{i}^{r}+\sum_{\mu\in\mathrm{LEC}}A_{\mu}^{r}\right)=\frac{1}{K_{\mathrm{LEC}}^{c\prime}}\sqrt{1-\left.\frac{p_{0,\mathrm{LEC}}^{c}}{p_{0c}}\right|_{i,L}}.\tag{9.22}$$

Similarly, for runs in which a row within the TEC is blocked ($i = \{$P4,P5,TE$\}$, 3 equations):

$$\zeta\left(\left.\frac{p_{0,\mathrm{TEC}}^{c}}{p_{0c}}\right|_{i,L},\frac{p_{0c}}{p_{\mathrm{atm}}},\gamma\right)\left(-A_{i}^{r}+\sum_{\mu\in\mathrm{TEC}}A_{\mu}^{r}\right)=\frac{1}{K_{\mathrm{TEC}}^{c\prime}}\sqrt{1-\left.\frac{p_{0,\mathrm{TEC}}^{c}}{p_{0c}}\right|_{i,L}}.\tag{9.23}$$

In total, there are 26 equations and 26 unknowns. The unknowns are:

$$A_{i}^{r}\ (\mathrm{x11}),\ K_{\mathrm{TEC}}^{c\prime},\ K_{\mathrm{LEC}}^{c\prime},\ \left.\frac{p_{0,\mathrm{LEC}}^{c}}{p_{0c}}\right|_{H},\ \left.\frac{p_{0,\mathrm{TEC}}^{c}}{p_{0c}}\right|_{H},\ \left.\frac{p_{0,\mathrm{LEC}}^{c}}{p_{0c}}\right|_{i,L}(\mathrm{x8}),\ \left.\frac{p_{0,\mathrm{TEC}}^{c}}{p_{0c}}\right|_{i,L}(\mathrm{x3}).\tag{9.24}$$

Equations (9.16)-(9.24) are solved simultaneously using the CCR raw row and compartmental capacity data at high PRs and *fsolve* in MATLAB (either using the Levenberg-Marquardt or Trust-Region-Dogleg algorithm). The equations are solved at multiple pressure ratios p_{0c}/p_{atm}. The solution was deemed to have converged when the solution variables in (9.24) changed by less than $1\mathrm{x}10^{-30}$ per iteration. Convergence on the correct solution was verified by checking that the sum of the row capacities within a compartment when all rows are blowing $\tilde{\Gamma}_{i}^{r}$—calculated using the solution variables and several equations discussed in detail later—was equal to the raw compartmental capacity Γ_{j}^{c}, since $\sum_{i\in j}\tilde{\Gamma}_{i}^{r}=\Gamma_{j}^{c}$ by definition for all designs but RP 3D (since the compartments in RP 3D are deemed to interact).

Mean loss coefficients ($\overline{K}_{j}^{c\prime}=\frac{1}{PR_{2}-PR_{1}}\int_{PR_{1}}^{PR_{2}}K_{j}^{c\prime}d(PR)$) are calculated from the above analysis, and assumed to be valid across all PRs. The variation in loss coefficient with pressure ratio is shown in Fig. 9.9.

In the second stage, the effective areas are calculated across a much broader PR range: $1.025 > p_{0c}/p_{\mathrm{atm}} > 1.12$. The raw compartmental CCR capacity is no longer necessary in the

analysis because the loss coefficients are known. Consequently, equations (9.18) and (9.19) are removed, and the number of equations/unknowns reduces to 24. Equations (9.16)-(9.17) and (9.20)-(9.24) are solved simultaneously at multiple pressure ratios p_{0c}/p_{atm}. The effective area is then found as a function of the local total-to-static pressure ratio across each row:

$$A^r_{i\in\mathrm{LEC}}\left|\frac{p^c_{0,\mathrm{LEC}}}{p^r_{\mathrm{ext},i}}, A^r_{i\in\mathrm{TEC}}\right|\frac{p^c_{0,\mathrm{TEC}}}{p^r_{\mathrm{ext},i}}, \tag{9.25}$$

where $A^r_{i\in\mathrm{LEC}}\left|\left(p^c_{0,\mathrm{LEC}}/p^r_{\mathrm{ext},i}\right)\right.$ means the effective area of row i within the LEC, evaluated at the local pressure ratio across the cooling row $p^c_{0,\mathrm{LEC}}/p^r_{\mathrm{ext},i}$.

9.4.2 Calculating Baseline Row Capacities at Scaled Conditions

The network flow model is fully populated from the preceding analysis and is then used to estimate the actual row-by-row capacity at different boundary conditions. At CCR conditions, all rows exhaust to atmospheric pressure p_{atm}. The capacity sum of all the rows within the LEC equals the capacity through the LEC loss element, and the capacity sum of the rows within the TEC equals the capacity through the TEC loss element:

$$\zeta\left(\frac{p^c_{0,\mathrm{LEC}}}{p_{0c}}, \frac{p_{0c}}{p_{\mathrm{atm}}}, \gamma\right)\sum_{\mu\in\mathrm{LEC}} A^r_\mu\left|\frac{p^c_{0,\mathrm{LEC}}}{p_{\mathrm{atm}}} = \frac{1}{K^{c\prime}_{\mathrm{LEC}}}\sqrt{1-\frac{p^c_{0,\mathrm{LEC}}}{p_{0c}}}\right., \tag{9.26}$$

$$\zeta\left(\frac{p^c_{0,\mathrm{TEC}}}{p_{0c}}, \frac{p_{0c}}{p_{\mathrm{atm}}}, \gamma\right)\sum_{\mu\in\mathrm{TEC}} A^r_\mu\left|\frac{p^c_{0,\mathrm{TEC}}}{p_{\mathrm{atm}}} = \frac{1}{K^{c\prime}_{\mathrm{TEC}}}\sqrt{1-\frac{p^c_{0,\mathrm{TEC}}}{p_{0c}}}\right.. \tag{9.27}$$

Equations (9.26) and (9.27) can be solved separately to calculate $p^c_{0,\mathrm{LEC}}/p_{0c}$ and $p^c_{0,\mathrm{TEC}}/p_{0c}$ as a function of p_{0c}/p_{atm}. This can then be used to estimate the actual capacity through each cooling row:

$$\tilde{\Gamma}^r_{i\in\mathrm{LEC}} = A^r_i\left|\frac{p^c_{0,\mathrm{LEC}}}{p_{\mathrm{atm}}}\zeta\left(\frac{p^c_{0,\mathrm{LEC}}}{p_{0c}}, \frac{p_{0c}}{p_{\mathrm{atm}}}, \gamma\right)\right., \tag{9.28}$$

$$\tilde{\Gamma}^r_{i\in\mathrm{TEC}} = A^r_i\left|\frac{p^c_{0,\mathrm{TEC}}}{p_{\mathrm{atm}}}\zeta\left(\frac{p^c_{0,\mathrm{TEC}}}{p_{0c}}, \frac{p_{0c}}{p_{\mathrm{atm}}}, \gamma\right)\right.. \tag{9.29}$$

Compartmental and total vane capacity can be found from summing the relevant rows.

At Sector and engine conditions, the exit static pressure of a cooling row $p^r_{\mathrm{ext},i}$ depends on the Mach number distribution around the vane. The specific capacity ζ is therefore different for each row. The capacity sum of the cooling rows within the LEC still equals the capacity through the LEC loss element (and likewise for the TEC) but the specific capacity ζ must be included within the row summation as it is no longer constant within a compartment:

$$\sum_{\mu\in\mathrm{LEC}} A_\mu^r \left|\frac{p_{0,\mathrm{LEC}}^c}{p_{\mathrm{ext},i}^r}\right| \zeta\left(\frac{p_{0,\mathrm{LEC}}^c}{p_{0c}}, \frac{p_{0c}}{p_{\mathrm{ext},i}^r}, \gamma\right) = \frac{1}{K_{\mathrm{LEC}}^{c\prime}} \sqrt{1-\frac{p_{0,\mathrm{LEC}}^c}{p_{0c}}}, \tag{9.30}$$

$$\sum_{\mu\in\mathrm{TEC}} A_\mu^r \left|\frac{p_{0,\mathrm{TEC}}^c}{p_{\mathrm{ext},i}^r}\right| \zeta\left(\frac{p_{0,\mathrm{TEC}}^c}{p_{0c}}, \frac{p_{0c}}{p_{\mathrm{ext},i}^r}, \gamma\right) = \frac{1}{K_{\mathrm{TEC}}^{c\prime}} \sqrt{1-\frac{p_{0,\mathrm{TEC}}^c}{p_{0c}}}. \tag{9.31}$$

It is important to note that the ratio of specific heats γ at engine conditions will be different to that at CCR conditions. The pressure ratios $p_{0,\mathrm{LEC}}^c/p_{0c}$ and $p_{0,\mathrm{TEC}}^c/p_{0c}$ are determined by solving the above equations. Row capacity is then found by evaluating the specific capacity ζ at the correct pressure ratio and multiplying by the effective row area:

$$\tilde{\Gamma}_{i\in\mathrm{LEC}}^r = A_i^r \left|\frac{p_{0,\mathrm{LEC}}^c}{p_{\mathrm{ext},i}^r}\right| \zeta\left(\frac{p_{0,\mathrm{LEC}}^c}{p_{0c}}, \frac{p_{0c}}{p_{\mathrm{ext},i}^r}, \gamma\right) \tag{9.32}$$

$$\tilde{\Gamma}_{i\in\mathrm{TEC}}^r = A_i^r \left|\frac{p_{0,\mathrm{TEC}}^c}{p_{\mathrm{ext},i}^r}\right| \zeta\left(\frac{p_{0,\mathrm{TEC}}^c}{p_{0c}}, \frac{p_{0c}}{p_{\mathrm{ext},i}^r}, \gamma\right) \tag{9.33}$$

Compartmental and total vane capacity are found by summing row capacity.

9.5 RP 1D Network Flow Model

The network flow model for design RP 1D is shown in Fig. 9.5. The design consists of three physical compartments: the leading-edge compartment (LEC) containing rows S3 to P3; the trailing-edge compartment (TEC) containing rows P4 to TE; and the reverse-pass compartment (RPC) containing rows S4 and S5.

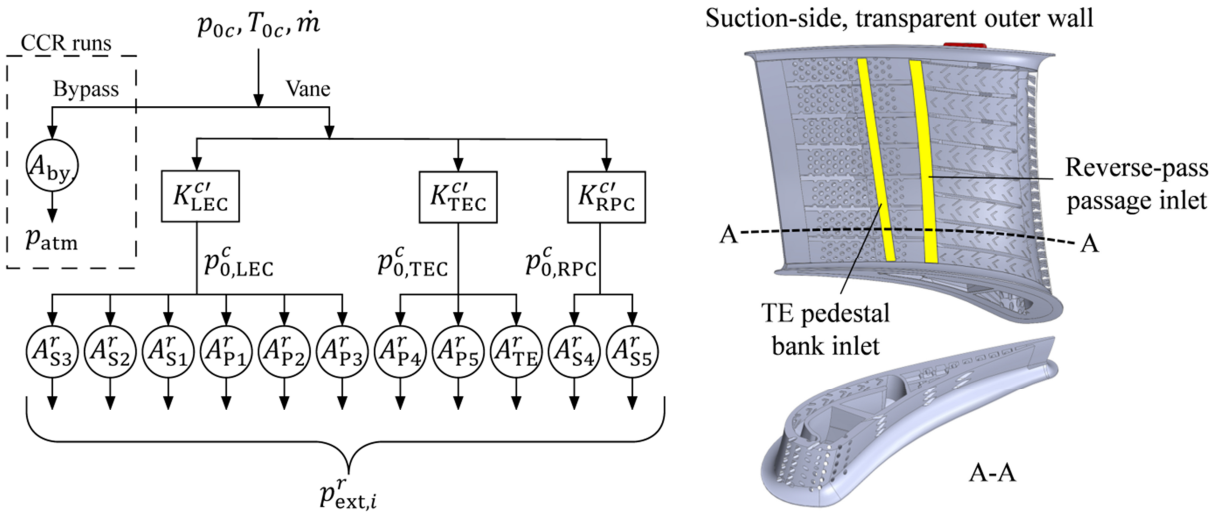


Figure 9.5. RP 1D network flow model and CAD schematic (modified from § 4.6).

Interaction testing (in the previous chapter) demonstrated that there is no interaction between compartments in the RP 1D design, but there is interaction between rows within each compartment. The network flow model is therefore composed of three parallel loss elements, representing the loss within each plenum.

The equations derived for the baseline network flow model also apply to RP 1D, but with LEC referencing rows S3-P3, and not S5-P3 as in the baseline model. The raw LEC capacity is measured differentially in RP 1D, and not absolutely as in the baseline experiments.

A number of further equations are required to describe the flow within the RPC. For rows S4 and S5, the raw coolant capacity measurement Γ_i^r is equal to the difference in capacity through the RPC loss element caused by blocking a cooling row. For $i = \{\text{S4,S5}\}$ (two equations):

$$\Gamma_i^r = \frac{1}{K_{\text{RPC}}^{c\prime}}\left(\sqrt{1-\left.\frac{p_{0,\text{RPC}}^c}{p_{0c}}\right|_H} - \sqrt{1-\left.\frac{p_{0,\text{RPC}}^c}{p_{0c}}\right|_{i,L}}\right). \tag{9.34}$$

The raw coolant capacity measurement of the RPC (blocking both S4 and S5) equals the capacity through the RPC loss element:

$$\Gamma_{\text{RPC}}^c = \frac{1}{K_{\text{RPC}}^{c\prime}}\sqrt{1-\left.\frac{p_{0,\text{RPC}}^c}{p_{0c}}\right|_H}. \tag{9.35}$$

When all rows are blowing, the sum of the capacity of S4 and S5 equals the capacity through the RPC loss element:

$$\zeta\left(\left.\frac{p_{0,\text{RPC}}^c}{p_{0c}}\right|_H, \frac{p_{0c}}{p_{\text{atm}}}, \gamma\right)\sum_{\mu\in\text{RPC}} A_\mu^r = \frac{1}{K_{\text{RPC}}^{c\prime}}\sqrt{1-\left.\frac{p_{0,\text{RPC}}^c}{p_{0c}}\right|_H} \tag{9.36}$$

For runs in which a row within the RPC is blocked ($i = \{\text{S4,S5}\}$, 2 equations), the capacity through the RPC loss element is equal to the capacity sum through all open rows within the RPC:

$$\zeta\left(\left.\frac{p_{0,\text{RPC}}^c}{p_{0c}}\right|_{i,L}, \frac{p_{0c}}{p_{\text{atm}}}, \gamma\right)\left(-A_i^r + \sum_{\mu\in\text{RPC}} A_\mu^r\right) = \frac{1}{K_{\text{RPC}}^{c\prime}}\sqrt{1-\left.\frac{p_{0,\text{RPC}}^c}{p_{0c}}\right|_{i,L}} \tag{9.37}$$

In total, 28 equations and 28 unknowns describe the RP 1D flow network. Compared to the baseline model, 2 extra equations/unknowns are necessary to determine the RPC loss coefficient. The RP 1D unknowns are:

$$A_i^r \text{ (x11)}, K_{\text{TEC}}^{c\prime}, K_{\text{LEC}}^{c\prime}, K_{\text{RPC}}^{c\prime}, \left.\frac{p_{0,\text{LEC}}^c}{p_{0c}}\right|_H, \left.\frac{p_{0,\text{TEC}}^c}{p_{0c}}\right|_H, \left.\frac{p_{0,\text{RPC}}^c}{p_{0c}}\right|_H, \left.\frac{p_{0,\text{LEC}}^c}{p_{0c}}\right|_{i,L} \text{(x6)}, \left.\frac{p_{0,\text{TEC}}^c}{p_{0c}}\right|_{i,L} \text{(x3)}, \left.\frac{p_{0,\text{RPC}}^c}{p_{0c}}\right|_{i,L} \text{(x2)}. \tag{9.38}$$

The loss coefficients are determined by simultaneously solving the RP 1D flow equations (x28). The equations are then reduced and re-solved to calculate effective row areas: equations (9.18), (9.19) and (9.35) are removed; pressure ratios between $1.025 > p_{0c}/p_{\text{atm}} > 1.12$ are tested; the compartmental raw capacity data are no longer required. The number of equations/unknowns reduces to 25 since $K_{\text{TEC}}^{c\prime}$, $K_{\text{LEC}}^{c\prime}$ and $K_{\text{RPC}}^{c\prime}$ are known. The effective row areas are hence determined as a function of local pressure ratio:

$$A_{i\in\text{LEC}}^{r}\left|\frac{p_{0,\text{LEC}}^{c}}{p_{\text{ext},i}^{r}}, A_{i\in\text{TEC}}^{r}\right|\frac{p_{0,\text{TEC}}^{c}}{p_{\text{ext},i}^{r}}, A_{i\in\text{RPC}}^{r}\left|\frac{p_{0,\text{RPC}}^{c}}{p_{\text{ext},i}^{r}}\right.. \tag{9.39}$$

When exhausting to a uniform exit pressure (e.g., CCR conditions), the capacity of each row within the LEC (S3-P3) and TEC (P4-TE) is calculated from equations (9.26)-(9.29). To calculate the capacity of rows S4 and S5, the pressure within the RPC $p_{0,\text{RPC}}^{c}/p_{0c}$ is calculated by solving:

$$\zeta\left(\frac{p_{0,\text{RPC}}^{c}}{p_{0c}}, \frac{p_{0c}}{p_{\text{atm}}}, \gamma\right)\sum_{\mu\in\text{RPC}} A_{\mu}^{r}\left|\frac{p_{0,\text{RPC}}^{c}}{p_{\text{atm}}} = \frac{1}{K_{\text{RPC}}^{c\prime}}\sqrt{1-\frac{p_{0,\text{RPC}}^{c}}{p_{0c}}}\right.. \tag{9.40}$$

Once $p_{0,\text{RPC}}^{c}/p_{0c}$ is known, the capacity of S4 and S5 is calculated from

$$\tilde{\Gamma}_{i\in\text{RPC}}^{r} = A_{i}^{r}\left|\frac{p_{0,\text{RPC}}^{c}}{p_{\text{atm}}}\zeta\left(\frac{p_{0,\text{RPC}}^{c}}{p_{0c}}, \frac{p_{0c}}{p_{\text{atm}}}, \gamma\right)\right.. \tag{9.41}$$

When each row exhausts to a different pressure (e.g., Sector Facility, engine), the capacity of the rows in the LEC (S3-P3) and TEC (P4-TE) are determined using equations (9.30)-(9.33). The total pressure in the RPC $p_{0,\text{RPC}}^{c}/p_{0c}$ is calculated by solving

$$\sum_{\mu\in\text{RPC}} A_{\mu}^{r}\left|\frac{p_{0,\text{RPC}}^{c}}{p_{\text{ext},i}^{r}}\zeta\left(\frac{p_{0,\text{RPC}}^{c}}{p_{0c}}, \frac{p_{0c}}{p_{\text{ext},i}^{r}}, \gamma\right) = \frac{1}{K_{\text{RPC}}^{c\prime}}\sqrt{1-\frac{p_{0,\text{RPC}}^{c}}{p_{0c}}}\right.. \tag{9.42}$$

The capacity of rows S4 and S5 are then determined using:

$$\tilde{\Gamma}_{i\in\text{RPC}}^{r} = A_{i}^{r}\left|\frac{p_{0,\text{RPC}}^{c}}{p_{\text{ext},i}^{r}}\zeta\left(\frac{p_{0,\text{RPC}}^{c}}{p_{0c}}, \frac{p_{0c}}{p_{\text{ext},i}^{r}}, \gamma\right)\right.. \tag{9.43}$$

9.6 RP 1D+ Network Flow Model

The network flow model for design RP 1D+ is shown in Fig. 9.6. The design consists of two physical compartments: a shared plenum which feeds all rows except S4 and S5, and the reverse-pass plenum which feeds S4 and S5. The interaction testing demonstrated that rows P4, P5 and the TE did not

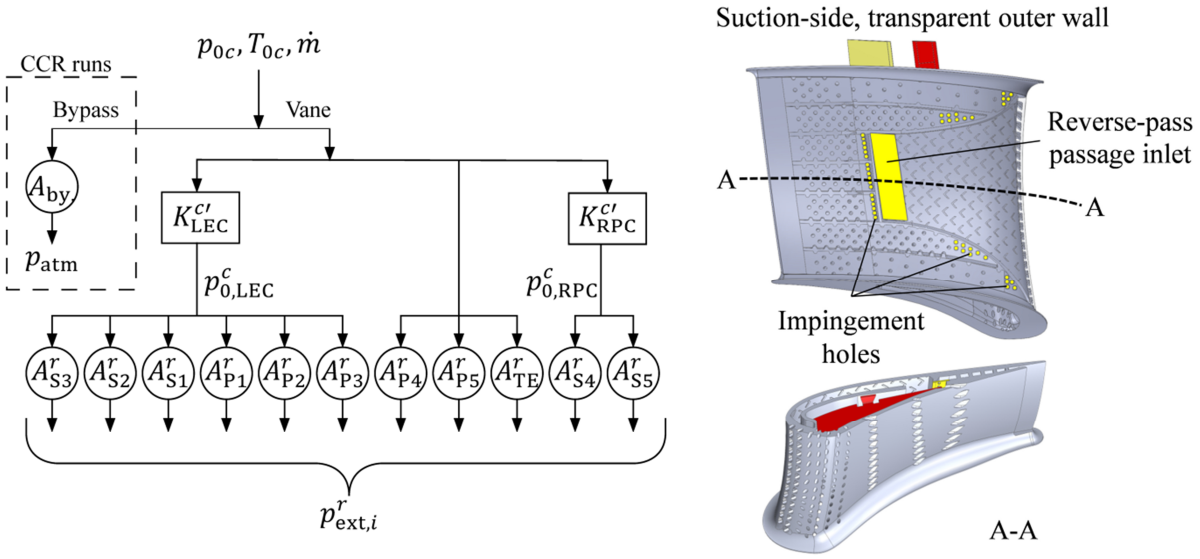


Figure 9.6. RP 1D+ network flow model and CAD schematic (modified from § 4.6).

interact with any other rows, and are therefore fed directly from the vane inlet in the network flow model. There is no interaction between the S3-P3 group (referred to here as the LEC) and S4-S5 group (RPC), but there is interaction *within* each group. The network flow model therefore consists of two parallel loss elements—the LEC loss element that feeds rows S3-P3, and the RPC loss element that feeds S4 and S5.

The network flow model is described by the same equations as RP 1D, but without equations (9.17) (3 equations), (9.19), (9.21) and (9.23) (3 equations) because there is no TEC loss element. The effective row areas of P4, P5 and the TE are found directly from the raw capacity measurements:

$$A_i^r \left| \frac{p_{0c}}{p^r_{\text{ext},i}} = \frac{\Gamma_i^r}{\zeta\left(1, \frac{p_{0c}}{p_{\text{atm}}}, \gamma\right)} \right. \tag{9.44}$$

For RP 1D+, there are 23 equations and 23 unknowns:

$$A_i^r \text{ (x11)}, K^{c\prime}_{\text{LEC}}, K^{c\prime}_{\text{RPC}}, \left.\frac{p^c_{0,\text{LEC}}}{p_{0c}}\right|_H, \left.\frac{p^c_{0,\text{RPC}}}{p_{0c}}\right|_H, \left.\frac{p^c_{0,\text{LEC}}}{p_{0c}}\right|_{i,L} \text{ (x6)}, \left.\frac{p^c_{0,\text{RPC}}}{p_{0c}}\right|_{i,L} \text{ (x2)}. \tag{9.45}$$

The loss coefficients $K^{c\prime}_{\text{LEC}}$, $K^{c\prime}_{\text{RPC}}$ are found by solving the 23 simultaneous equations. To calculate the effective row areas, equations (9.18) and (9.35) are removed, leaving 21 equations in 21 unknowns. The effective area of each row is then calculated over a broad range of driving pressure ratios.

When exhausting to a common pressure, the capacities of rows S4-P3 are calculated in the same way as RP 1D. The capacities of rows P4, P5 and the TE when exhausting to atmosphere are given by:

$$\tilde{\Gamma}^r_{i\in\mathrm{TEC}} = A^r_i \left|\frac{p_{0c}}{p_{\mathrm{atm}}}\right| \zeta\left(1, \frac{p_{0c}}{p_{\mathrm{atm}}}, \gamma\right). \tag{9.46}$$

When the rows exhaust to different static pressures, the capacities of S4-P3 are calculated in the same way as RP 1D+, but the capacities of rows P4, P5 and the TE are calculated using

$$\tilde{\Gamma}^r_{i\in\mathrm{TEC}} = A^r_i \left|\frac{p_{0c}}{p^r_{\mathrm{ext},i}}\right| \zeta\left(1, \frac{p_{0c}}{p^r_{\mathrm{ext},i}}, \gamma\right). \tag{9.47}$$

9.6.1 RP 1D+ S4 Ingestion

For some combinations of $p_{0c}/p^r_{\mathrm{ext},i}$, row S4 ingests because the pressure loss within the reverse-pass passage creates a local pressure ratio across S4 that is lower than 1, i.e., S4 ingests when $p^c_{0,\mathrm{RPC}}/p^r_{\mathrm{ext,S4}} < 1$. Ingestion is only possible when there is variation in exhaust pressure around the aerofoil (e.g., Sector and engine), and does not occur when all rows exhaust to the same pressure (e.g., CCR experiments) when S4 and S5 both operate at the same local pressure ratio $p^c_{0,\mathrm{RPC}}/p_{\mathrm{atm}}$. Consequently, ingestion need not be considered when populating the network flow model using the CCR data, but must be accounted for when using the model to predict coolant capacity at Sector and engine conditions.

S4 backflow is modelled using the 1D, isentropic, compressible mass flow relation at a driving pressure ratio $p^r_{\mathrm{ext,S4}}/p^c_{0,\mathrm{RPC}}$ (compared to $p^c_{0,\mathrm{RPC}}/p^r_{\mathrm{ext,S4}}$ for ejecting flow). The effective area is evaluated at the pressure ratio $p^r_{\mathrm{ext,S4}}/p^c_{0,\mathrm{RPC}}$. Therefore for $p^c_{0,\mathrm{RPC}}/p^r_{\mathrm{ext,S4}} < 1$:

$$\dot{m}^r_{\mathrm{S4}} = -\left(A^r_{\mathrm{S4}}\left|\frac{p^r_{\mathrm{ext,S4}}}{p^c_{0,\mathrm{RPC}}}\right|\frac{p^r_{\mathrm{ext,S4}}}{\sqrt{T_{0c}}}\left(\frac{p^r_{\mathrm{ext,S4}}}{p^c_{0,\mathrm{RPC}}}\right)^{-\frac{\gamma+1}{2\gamma}}\sqrt{\frac{2\gamma}{R(\gamma-1)}\left[\left(\frac{p^r_{\mathrm{ext,S4}}}{p^c_{0,\mathrm{RPC}}}\right)^{\frac{\gamma-1}{\gamma}}-1\right]}\right). \tag{9.48}$$

In terms of specific capacity ζ, the capacity through S4 when ingesting is given by:

$$\tilde{\Gamma}^r_{\mathrm{S4}} = \frac{\dot{m}^r_{\mathrm{S4}}\sqrt{T_{0c}}}{p_{0c}} = -A^r_{\mathrm{S4}}\left|\frac{p^r_{\mathrm{ext,S4}}}{p^c_{0,\mathrm{RPC}}}\right|\zeta\left(\frac{p^r_{\mathrm{ext,S4}}}{p_{0c}}, \frac{p_{0c}}{p^c_{0,\mathrm{RPC}}}, \gamma\right). \tag{9.49}$$

This approximation ensures that the capacity of S4 is a continuous function of PR as $p^c_{0,\mathrm{RPC}}/p^r_{\mathrm{ext,S4}}$ drops below unity. The continuity equation (9.42) must be modified for S4 ingesting:

$$A^r_{\mathrm{S5}}\left|\frac{p^c_{0,\mathrm{RPC}}}{p^r_{\mathrm{ext,S5}}}\right|\zeta\left(\frac{p^c_{0,\mathrm{RPC}}}{p_{0c}}, \frac{p_{0c}}{p^r_{\mathrm{ext,S5}}}, \gamma\right) - A^r_{\mathrm{S4}}\left|\frac{p^r_{\mathrm{ext,S4}}}{p^c_{0,\mathrm{RPC}}}\right|\zeta\left(\frac{p^r_{\mathrm{ext,S4}}}{p_{0c}}, \frac{p_{0c}}{p^c_{0,\mathrm{RPC}}}, \gamma\right) = \frac{1}{K^{cr}_{\mathrm{RPC}}}\sqrt{1-\frac{p^c_{0,\mathrm{RPC}}}{p_{0c}}}. \tag{9.50}$$

This equation is solved to estimate $p^c_{0,\mathrm{RPC}}/p_{0c}$ when S4 ingests; the capacities of S4 and S5 are then evaluated from (9.49) and (9.43), respectively.

9.7 RP 3D Network Flow Model

The RP 3D network flow model is shown in Fig. 9.7. This model is more complex than the other network models because the reverse-pass flow loses a significant amount of total pressure both within the main feed plena and within the reverse-pass compartment. This does not happen in the RP 1D+ design because the reverse-pass offtakes in the main feed plena are situated further away from rows P4-TE, minimising interaction between groups P4-TE and S4-S5.

Initially, three groups of interacting rows (or 'compartments') were assumed: rows S3-P3, referred to as the LEC; rows P4-TE, referred to as the TEC; and rows S4 and S5, referred to as the RPC. However, interaction testing demonstrated that there was in fact some interaction between these compartments, since the sum of the compartment capacities did not equal the total vane capacity. It was assumed that this interaction occurred between the TEC and RPC groups because of the proximity of the RPC offtake to the TEC group. The network model in Fig. 9.7 was chosen as the most physical network model that captured the interaction between the RPC and TEC, while minimising the number of loss coefficients.

The population of the RP 3D network model requires more equations than the other network models because the TEC and RPC loss elements are linked. These equations are now reported.

9.7.1 Calculating RP 3D Loss Coefficients and Effective Row Areas

For the rows contained within the LEC group ($i = \{\text{S3,S2,S1,P1,P2,P3}\}$, 6 equations), the raw coolant capacity measurement Γ_i^r equals the capacity difference through the LEC loss element because the row is blocked:

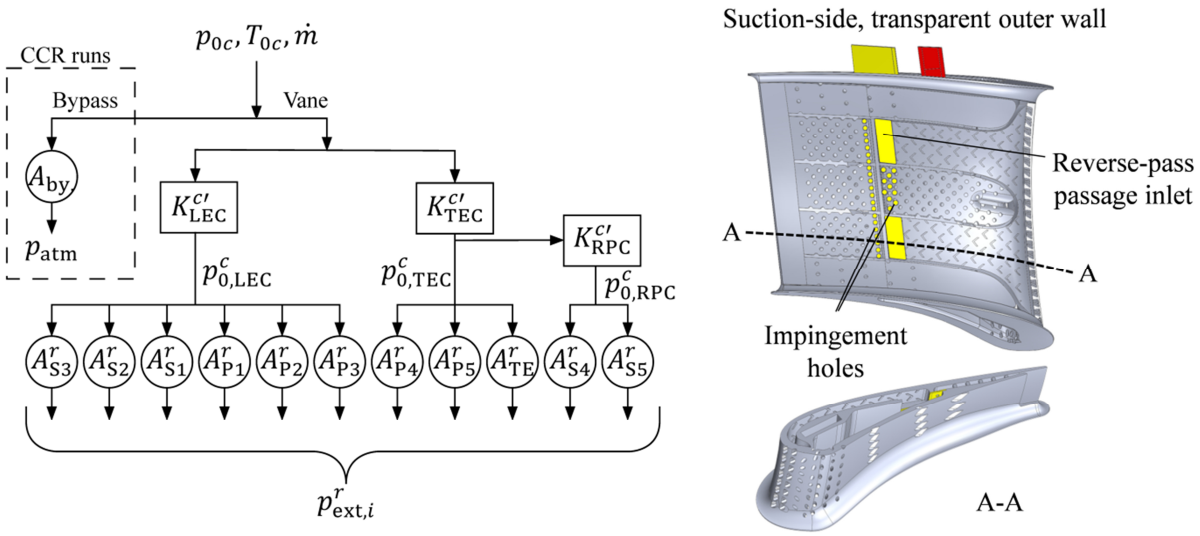


Figure 9.7. RP 3D network flow model and CAD schematic (modified from § 4.6).

$$\Gamma_i^r = \frac{1}{K_{\mathrm{LEC}}^{c\prime}}\left(\sqrt{1-\left.\frac{p_{0,\mathrm{LEC}}^c}{p_{0c}}\right|_H} - \sqrt{1-\left.\frac{p_{0,\mathrm{LEC}}^c}{p_{0c}}\right|_{i,L}}\right). \tag{9.51}$$

The raw capacity of the LEC compartment is measured differentially by blocking the LEC between high and low differential runs, and equals the capacity difference through the LEC loss element. Since the total pressure within the LEC equals the inlet total pressure when the LEC is blocked (low run):

$$\Gamma_{\mathrm{LEC}}^c = \frac{1}{K_{\mathrm{LEC}}^{c\prime}}\sqrt{1-\left.\frac{p_{0,\mathrm{LEC}}^c}{p_{0c}}\right|_H}. \tag{9.52}$$

For the rows contained within the TEC and the RPC ($i = \{\mathrm{P4,P5,S4,S5,TE}\}$, 5 equations), the differential raw capacity measurement equals the capacity difference through the TEC loss element because the row is blocked:

$$\Gamma_i^r = \frac{1}{K_{\mathrm{TEC}}^{c\prime}}\left(\sqrt{1-\left.\frac{p_{0,\mathrm{TEC}}^c}{p_{0c}}\right|_H} - \sqrt{1-\left.\frac{p_{0,\mathrm{TEC}}^c}{p_{0c}}\right|_{i,L}}\right). \tag{9.53}$$

The raw capacity of the TEC compartment is measured differentially by blocking the TEC between high and low differential runs, and equals the capacity difference through the TEC loss element:

$$\Gamma_{\mathrm{TEC}}^c = \frac{1}{K_{\mathrm{TEC}}^{c\prime}}\left(\sqrt{1-\left.\frac{p_{0,\mathrm{TEC}}^c}{p_{0c}}\right|_H} - \sqrt{1-\left.\frac{p_{0,\mathrm{TEC}}^c}{p_{0c}}\right|_{\mathrm{TEC},L}}\right). \tag{9.54}$$

Similarly, the raw capacity of the RPC compartment is measured by blocking the RPC rows and measuring differential capacity. This is equated to the difference in capacity through the TEC loss element:

$$\Gamma_{\mathrm{RPC}}^c = \frac{1}{K_{\mathrm{TEC}}^{c\prime}}\left(\sqrt{1-\left.\frac{p_{0,\mathrm{TEC}}^c}{p_{0c}}\right|_H} - \sqrt{1-\left.\frac{p_{0,\mathrm{TEC}}^c}{p_{0c}}\right|_{\mathrm{RPC},L}}\right). \tag{9.55}$$

When all rows are blowing, the sum of the capacity through the LEC rows is equal to the capacity through the LEC loss element. Similarly, the capacity sum through the RPC cooling rows is equal to the capacity through the RPC loss element. The capacity sum of the RPC and TEC cooling rows equals the capacity through the TEC loss element. Therefore:

$$\zeta\left(\left.\frac{p_{0,\mathrm{RPC}}^c}{p_{0c}}\right|_H, \frac{p_{0c}}{p_{\mathrm{atm}}}, \gamma\right)\sum_{\mu\in\mathrm{RPC}} A_\mu^r + \zeta\left(\left.\frac{p_{0,\mathrm{TEC}}^c}{p_{0c}}\right|_H, \frac{p_{0c}}{p_{\mathrm{atm}}}\right)\sum_{\mu\in\mathrm{TEC}} A_\mu^r = \frac{1}{K_{\mathrm{TEC}}^{c\prime}}\sqrt{1-\left.\frac{p_{0,\mathrm{TEC}}^c}{p_{0c}}\right|_H} \tag{9.56}$$

$$\zeta\left(\left.\frac{p_{0,\mathrm{RPC}}^{c}}{p_{0c}}\right|_{H},\frac{p_{0c}}{p_{\mathrm{atm}}},\gamma\right)\sum_{\mu\in\mathrm{RPC}}A_{\mu}^{r}=\frac{1}{K_{\mathrm{RPC}}^{c\prime}}\left.\frac{p_{0,\mathrm{TEC}}^{c}}{p_{0c}}\right|_{H}\sqrt{1-\left.\frac{p_{0,\mathrm{RPC}}^{c}}{p_{0c}}\right|_{H}\left.\frac{p_{0c}}{p_{0,\mathrm{TEC}}^{c}}\right|_{H}} \tag{9.57}$$

$$\zeta\left(\left.\frac{p_{0,\mathrm{LEC}}^{c}}{p_{0c}}\right|_{H},\frac{p_{0c}}{p_{\mathrm{atm}}},\gamma\right)\sum_{\mu\in\mathrm{LEC}}A_{\mu}^{r}=\frac{1}{K_{\mathrm{LEC}}^{c\prime}}\sqrt{1-\left.\frac{p_{0,\mathrm{LEC}}^{c}}{p_{0c}}\right|_{H}} \tag{9.58}$$

Notably, (9.57) contains the additional $p_{0,\mathrm{TEC}}^{c}/p_{0c}\big|_{H}$ term, derived in equation (9.8). For runs in which a row within the LEC is blocked ($i=\{\mathrm{S3,S2,S1,P1,P2,P3}\}$, 6 equations), the capacity through the LEC loss element is equal to the capacity sum of all open rows within the LEC:

$$\zeta\left(\left.\frac{p_{0,\mathrm{LEC}}^{c}}{p_{0c}}\right|_{i,L},\frac{p_{0c}}{p_{\mathrm{atm}}},\gamma\right)\left(-A_{i}^{r}+\sum_{\mu\in\mathrm{LEC}}A_{\mu}^{r}\right)=\frac{1}{K_{\mathrm{LEC}}^{c\prime}}\sqrt{1-\left.\frac{p_{0,\mathrm{LEC}}^{c}}{p_{0c}}\right|_{i,L}}. \tag{9.59}$$

For runs in which a row within the TEC is blocked ($i=\{\mathrm{P4,P5,TE}\}$, 3 equations), the capacity through the RPC loss element is equal to the capacity sum of all rows within the RPC:

$$\zeta\left(\left.\frac{p_{0,\mathrm{RPC}}^{c}}{p_{0c}}\right|_{i,L},\frac{p_{0c}}{p_{\mathrm{atm}}},\gamma\right)\sum_{\mu\in\mathrm{RPC}}A_{\mu}^{r}=\frac{1}{K_{\mathrm{RPC}}^{c\prime}}\left.\frac{p_{0,\mathrm{TEC}}^{c}}{p_{0c}}\right|_{i,L}\sqrt{1-\left.\frac{p_{0,\mathrm{RPC}}^{c}}{p_{0c}}\right|_{i,L}\left.\frac{p_{0c}}{p_{0,\mathrm{TEC}}^{c}}\right|_{i,L}}. \tag{9.60}$$

When the entire TEC is blocked, the capacity through the RPC loss element is equal to the capacity sum of all rows within the RPC:

$$\zeta\left(\left.\frac{p_{0,\mathrm{RPC}}^{c}}{p_{0c}}\right|_{\mathrm{TEC},L},\frac{p_{0c}}{p_{\mathrm{atm}}},\gamma\right)\sum_{\mu\in\mathrm{RPC}}A_{\mu}^{r}=\frac{1}{K_{\mathrm{RPC}}^{c\prime}}\left.\frac{p_{0,\mathrm{TEC}}^{c}}{p_{0c}}\right|_{\mathrm{TEC},L}\sqrt{1-\left.\frac{p_{0,\mathrm{RPC}}^{c}}{p_{0c}}\right|_{\mathrm{TEC},L}\left.\frac{p_{0c}}{p_{0,\mathrm{TEC}}^{c}}\right|_{\mathrm{TEC},L}}. \tag{9.61}$$

For runs in which a row within the TEC is blocked ($i=\{\mathrm{P4,P5,TE}\}$, 3 equations), the capacity through the TEC loss element is equal to the capacity sum of all rows within the RPC and the open rows in the TEC:

$$\zeta\left(\left.\frac{p_{0,\mathrm{RPC}}^{c}}{p_{0c}}\right|_{i,L},\frac{p_{0c}}{p_{\mathrm{atm}}},\gamma\right)\sum_{\mu\in\mathrm{RPC}}A_{\mu}^{r}+\zeta\left(\left.\frac{p_{0,\mathrm{TEC}}^{c}}{p_{0c}}\right|_{i,L},\frac{p_{0c}}{p_{\mathrm{atm}}},\gamma\right)\left(-A_{i}^{r}+\sum_{\mu\in\mathrm{TEC}}A_{\mu}^{r}\right)=\frac{1}{K_{\mathrm{TEC}}^{c\prime}}\sqrt{1-\left.\frac{p_{0,\mathrm{RPC}}^{c}}{p_{0c}}\right|_{i,L}} \tag{9.62}$$

For runs in which a row within the RPC is blocked ($i=\{\mathrm{S4,S5}\}$, 2 equations), the capacity through the TEC loss element is equal to the capacity sum of the open rows within the RPC and all rows in the TEC:

$$\zeta\left(\left.\frac{p_{0,\mathrm{RPC}}^{c}}{p_{0c}}\right|_{i,L},\frac{p_{0c}}{p_{\mathrm{atm}}},\gamma\right)\left(-A_{i}^{r}+\sum_{\mu\in\mathrm{RPC}}A_{\mu}^{r}\right)+\zeta\left(\left.\frac{p_{0,\mathrm{TEC}}^{c}}{p_{0c}}\right|_{i,L},\frac{p_{0c}}{p_{\mathrm{atm}}},\gamma\right)\sum_{\mu\in\mathrm{TEC}}A_{\mu}^{r}=\frac{1}{K_{\mathrm{TEC}}^{c\prime}}\sqrt{1-\left.\frac{p_{0,\mathrm{TEC}}^{c}}{p_{0c}}\right|_{i,L}}. \tag{9.63}$$

Table 9.1 Unknowns for RP 3D network flow model equations

i	TE	P5	P4	P3	P2	P1	S1	S2	S3	S4	S5
$\left.\frac{p_{0,\mathrm{LEC}}^c}{p_{0c}}\right\|_{i,L}$				✓	✓	✓	✓	✓	✓		
$\left.\frac{p_{0,\mathrm{TEC}}^c}{p_{0c}}\right\|_{i,L}$	✓	✓	✓							✓	✓
$\left.\frac{p_{0,\mathrm{RPC}}^c}{p_{0c}}\right\|_{i,L}$	✓	✓	✓							✓	✓

and A_i^r (x11), $K_{\mathrm{TEC}}^{c\prime}$, $K_{\mathrm{RPC}}^{c\prime}$, $K_{\mathrm{LEC}}^{c\prime}$, $\left.\frac{p_{0,\mathrm{LEC}}^c}{p_{0c}}\right|_H$, $\left.\frac{p_{0,\mathrm{TEC}}^c}{p_{0c}}\right|_H$, $\left.\frac{p_{0,\mathrm{RPC}}^c}{p_{0c}}\right|_H$, $\left.\frac{p_{0,\mathrm{TEC}}^c}{p_{0c}}\right|_{\mathrm{TEC},L}$, $\left.\frac{p_{0,\mathrm{RPC}}^c}{p_{0c}}\right|_{\mathrm{TEC},L}$, $\left.\frac{p_{0,\mathrm{TEC}}^c}{p_{0c}}\right|_{\mathrm{RPC},L}$.

For runs in which a row within the RPC is blocked ($i = \{\mathrm{S4,S5}\}$, 2 equations), the capacity through the RPC loss element is equal to the capacity sum of the open rows within the RPC:

$$\zeta\left(\left.\frac{p_{0,\mathrm{RPC}}^c}{p_{0c}}\right|_{i,L}, \frac{p_{0c}}{p_{\mathrm{atm}}}, \gamma\right)\left(-A_i^r + \sum_{\mu\in\mathrm{RPC}} A_\mu^r\right) = \frac{1}{K_{\mathrm{RPC}}^{c\prime}}\left.\frac{p_{0,\mathrm{TEC}}^c}{p_{0c}}\right|_{i,L}\sqrt{1 - \left.\frac{p_{0,\mathrm{RPC}}^c}{p_{0c}}\right|_{i,L}\left.\frac{p_{0c}}{p_{0,\mathrm{TEC}}^c}\right|_{i,L}}. \tag{9.64}$$

When the entire RPC is blocked, the capacity through the TEC loss element is equal to the capacity sum of all rows within the TEC:

$$\zeta\left(\left.\frac{p_{0,\mathrm{TEC}}^c}{p_{0c}}\right|_{\mathrm{RPC},L}, \frac{p_{0c}}{p_{\mathrm{atm}}}, \gamma\right)\sum_{\mu\in\mathrm{TEC}} A_\mu^r = \frac{1}{K_{\mathrm{TEC}}^{c\prime}}\sqrt{1 - \left.\frac{p_{0,\mathrm{TEC}}^c}{p_{0c}}\right|_{\mathrm{RPC},L}}, \tag{9.65}$$

and when the TEC is blocked, the capacity through the TEC loss element is equal to the capacity sum of all rows within the RPC:

$$\zeta\left(\left.\frac{p_{0,\mathrm{RPC}}^c}{p_{0c}}\right|_{\mathrm{TEC},L}, \frac{p_{0c}}{p_{\mathrm{atm}}}, \gamma\right)\sum_{\mu\in\mathrm{RPC}} A_\mu^r = \frac{1}{K_{\mathrm{TEC}}^{c\prime}}\sqrt{1 - \left.\frac{p_{0,\mathrm{TEC}}^c}{p_{0c}}\right|_{\mathrm{TEC},L}}. \tag{9.66}$$

In total, 36 equations and 36 unknowns describe the RP 3D network flow model. The unknowns are summarised in Table 9.1.

Equations (9.51)-(9.66) are solved simultaneously using the CCR raw row and compartmental capacity data at high PRs and *fsolve* in MATLAB. Mean loss coefficients are calculated and assumed to be valid across all PRs. The effective areas are then calculated across a much broader PR range: $1.025 < p_{0c}/p_{\mathrm{atm}} < 1.12$. The raw compartmental CCR capacity is no longer necessary in the analysis because the loss coefficients are known. Consequently, equations (9.52), (9.54), (9.55), (9.61), (9.65) and (9.66) are removed, and the number of equations/unknowns reduces to 30 (no

longer need to solve for $p^c_{0,\mathrm{TEC}}/p_{0c}\big|_{\mathrm{TEC},L}$, $p^c_{0,\mathrm{RPC}}/p_{0c}\big|_{\mathrm{TEC},L}$, $p^c_{0,\mathrm{TEC}}/p_{0c}\big|_{\mathrm{RPC},L}$ and $K^{c\prime}_{\mathrm{TEC}}$, $K^{c\prime}_{\mathrm{RP}}$, $K^{c\prime}_{\mathrm{LEC}}$). The remaining equations are solved simultaneously at multiple pressure ratios p_{0c}/p_{atm}. The effective area is found as a function of the local total-to-static pressure ratio across each row:

$$A^r_{i\in\mathrm{LEC}}\left|\frac{p^c_{0,\mathrm{LEC}}}{p^r_{\mathrm{ext},i}}, A^r_{i\in\mathrm{TEC}}\right|\frac{p^c_{0,\mathrm{TEC}}}{p^r_{\mathrm{ext},i}}, A^r_{i\in\mathrm{RPC}}\left|\frac{p^c_{0,\mathrm{RPC}}}{p^r_{\mathrm{ext},i}}\right.. \tag{9.67}$$

9.7.2 Calculating RP 3D Row Capacities at Scaled Conditions

When all rows exhaust to atmospheric pressure p_{atm}, the total pressure within the RPC $p^c_{0,\mathrm{RPC}}/p_{0c}$, TEC $p^c_{0,\mathrm{TEC}}/p_{0c}$, and LEC $p^c_{0,\mathrm{LEC}}/p_{0c}$ are calculated by solving the following continuity equations:

$$\zeta\left(\frac{p^c_{0,\mathrm{RPC}}}{p_{0c}}, \frac{p_{0c}}{p_{\mathrm{atm}}}, \gamma\right)\sum_{\mu\in\mathrm{RPC}} A^r_\mu\left|\frac{p^c_{0,\mathrm{RPC}}}{p_{\mathrm{atm}}} + \zeta\left(\frac{p^c_{0,\mathrm{TEC}}}{p_{0c}}, \frac{p_{0c}}{p_{\mathrm{atm}}}, \gamma\right)\sum_{\mu\in\mathrm{TEC}} A^r_\mu\right|\frac{p^c_{0,\mathrm{TEC}}}{p_{\mathrm{atm}}} = \frac{1}{K^{c\prime}_{\mathrm{TEC}}}\sqrt{1-\frac{p^c_{0,\mathrm{TEC}}}{p_{0c}}}, \tag{9.68}$$

$$\zeta\left(\frac{p^c_{0,\mathrm{RPC}}}{p_{0c}}, \frac{p_{0c}}{p_{\mathrm{atm}}}, \gamma\right)\sum_{\mu\in\mathrm{RPC}} A^r_\mu\left|\frac{p^c_{0,\mathrm{RPC}}}{p_{\mathrm{atm}}} = \frac{1}{K^{c\prime}_{\mathrm{RPC}}}\frac{p^c_{0,\mathrm{TEC}}}{p_{0c}}\sqrt{1-\frac{p^c_{0,\mathrm{RPC}}}{p_{0c}}\frac{p_{0c}}{p^c_{0,\mathrm{TEC}}}}, \tag{9.69}$$

$$\zeta\left(\frac{p^c_{0,\mathrm{LEC}}}{p_{0c}}, \frac{p_{0c}}{p_{\mathrm{atm}}}, \gamma\right)\sum_{\mu\in\mathrm{LEC}} A^r_\mu\left|\frac{p^c_{0,\mathrm{LEC}}}{p_{\mathrm{atm}}} = \frac{1}{K^{c\prime}_{\mathrm{LEC}}}\sqrt{1-\frac{p^c_{0,\mathrm{LEC}}}{p_{0c}}}. \tag{9.70}$$

The capacity of each row can then be calculated from:

$$\tilde{\Gamma}^r_{i\in\mathrm{LEC}} = A^r_i\left|\frac{p^c_{0,\mathrm{LEC}}}{p_{\mathrm{atm}}}\zeta\left(\frac{p^c_{0,\mathrm{LEC}}}{p_{0c}}, \frac{p_{0c}}{p_{\mathrm{atm}}}, \gamma\right)\right., \tag{9.71}$$

$$\tilde{\Gamma}^r_{i\in\mathrm{TEC}} = A^r_i\left|\frac{p^c_{0,\mathrm{TEC}}}{p_{\mathrm{atm}}}\zeta\left(\frac{p^c_{0,\mathrm{TEC}}}{p_{0c}}, \frac{p_{0c}}{p_{\mathrm{atm}}}, \gamma\right)\right., \tag{9.72}$$

$$\tilde{\Gamma}^r_{i\in\mathrm{RPC}} = A^r_i\left|\frac{p^c_{0,\mathrm{RPC}}}{p_{\mathrm{atm}}}\zeta\left(\frac{p^c_{0,\mathrm{RPC}}}{p_{0c}}, \frac{p_{0c}}{p_{\mathrm{atm}}}, \gamma\right)\right.. \tag{9.73}$$

Total and compartmental values can be found from summation of the relevant row capacities.

When the row exhausts to different pressures, S4 ingests. The total pressure within the RPC $p^c_{0,\mathrm{RPC}}/p_{0c}$, TEC $p^c_{0,\mathrm{TEC}}/p_{0c}$, and LEC $p^c_{0,\mathrm{LEC}}/p_{0c}$ are therefore calculated by solving the following:

$$\begin{aligned} &A^r_{\mathrm{S5}}\left|\frac{p^r_{\mathrm{ext,S5}}}{p^c_{0,\mathrm{RPC}}}\zeta\left(\frac{p^c_{0,\mathrm{RPC}}}{p_{0c}}, \frac{p_{0c}}{p^r_{\mathrm{ext,S5}}}, \gamma\right) - A^r_{\mathrm{S4}}\right|\frac{p^r_{\mathrm{ext,S4}}}{p^c_{0,\mathrm{RPC}}}\zeta\left(\frac{p^c_{0,\mathrm{RPC}}}{p_{0c}}, \frac{p_{0c}}{p^r_{\mathrm{ext,S4}}}, \gamma\right) \\ &\quad + \sum_{\mu\in\mathrm{TEC}} A^r_\mu\left|\frac{p^c_{0,\mathrm{TEC}}}{p^r_{\mathrm{ext},i}}\zeta\left(\frac{p^c_{0,\mathrm{TEC}}}{p_{0c}}, \frac{p_{0c}}{p^r_{\mathrm{ext},i}}, \gamma\right) = \frac{1}{K^{c\prime}_{\mathrm{TEC}}}\sqrt{1-\frac{p^c_{0,\mathrm{TEC}}}{p_{0c}}}\right. \end{aligned} \tag{9.74}$$

$$A_{\mathrm{S5}}^{r}\left|\frac{p_{\mathrm{ext,S5}}^{r}}{p_{0,\mathrm{RPC}}}\right|\zeta\left(\frac{p_{0,\mathrm{RPC}}^{c}}{p_{0c}},\frac{p_{0c}}{p_{\mathrm{ext,S5}}^{r}},\gamma\right)-A_{\mathrm{S4}}^{r}\left|\frac{p_{\mathrm{ext,S4}}^{r}}{p_{0,\mathrm{RPC}}^{c}}\right|\zeta\left(\frac{p_{0,\mathrm{RPC}}^{c}}{p_{0c}},\frac{p_{0c}}{p_{\mathrm{ext,S4}}^{r}},\gamma\right)$$
$$=\frac{1}{K_{\mathrm{RPC}}^{c\prime}}\frac{p_{0,\mathrm{TEC}}^{c}}{p_{0c}}\sqrt{1-\frac{p_{0,\mathrm{RPC}}^{c}}{p_{0c}}\frac{p_{0c}}{p_{0,\mathrm{TEC}}^{c}}} \tag{9.75}$$

$$\sum_{\mu\in\mathrm{LEC}}A_{\mu}^{r}\left|\frac{p_{0,\mathrm{LEC}}^{c}}{p_{\mathrm{ext},i}^{r}}\right|\zeta\left(\frac{p_{0,\mathrm{LEC}}^{c}}{p_{0c}},\frac{p_{0c}}{p_{\mathrm{ext},i}^{r}},\gamma\right)=\frac{1}{K_{\mathrm{LEC}}^{c\prime}}\sqrt{1-\frac{p_{0,\mathrm{LEC}}^{c}}{p_{0c}}} \tag{9.76}$$

The capacity of each row can then be calculated from:

$$\tilde{\Gamma}_{i\in\mathrm{LEC}}^{r}=A_{i}^{r}\left|\frac{p_{0,\mathrm{LEC}}^{c}}{p_{\mathrm{ext},i}^{r}}\right|\zeta\left(\frac{p_{0,\mathrm{LEC}}^{c}}{p_{0c}},\frac{p_{0c}}{p_{\mathrm{ext},i}^{r}},\gamma\right) \tag{9.77}$$

$$\tilde{\Gamma}_{i\in\mathrm{TEC}}^{r}=A_{i}^{r}\left|\frac{p_{0,\mathrm{TEC}}^{c}}{p_{\mathrm{ext},i}^{r}}\right|\zeta\left(\frac{p_{0,\mathrm{TEC}}^{c}}{p_{0c}},\frac{p_{0c}}{p_{\mathrm{ext},i}^{r}},\gamma\right) \tag{9.78}$$

$$\tilde{\Gamma}_{\mathrm{S5}}^{r}=A_{\mathrm{S5}}^{r}\left|\frac{p_{\mathrm{ext,S5}}^{r}}{p_{0,\mathrm{RPC}}^{c}}\right|\zeta\left(\frac{p_{\mathrm{ext,S5}}^{r}}{p_{0c}},\frac{p_{0\mathrm{c}}}{p_{0,\mathrm{RPC}}^{c}},\gamma\right). \tag{9.79}$$

$$\tilde{\Gamma}_{\mathrm{S4}}^{r}=-A_{\mathrm{S4}}^{r}\left|\frac{p_{\mathrm{ext,S4}}^{r}}{p_{0,\mathrm{RPC}}^{c}}\right|\zeta\left(\frac{p_{\mathrm{ext,S4}}^{r}}{p_{0c}},\frac{p_{0\mathrm{c}}}{p_{0,\mathrm{RPC}}^{c}},\gamma\right). \tag{9.80}$$

Total and compartmental values can be found from summation of the relevant row capacities.

9.8 Results: Effective Row Area and Loss Coefficients

Effective row areas calculated using the preceding method are shown in Fig. 9.8 for all cooling rows and each design, plotted as a function of the local inlet total-exit static pressure ratio. Each effective area distribution is the result of four CCR runs: a differential pair of runs at low PR, and a differential pair of runs at high PR. First order best-fits are calculated for all effective area distributions (given by the dashed lines), which are subsequently used when predicting coolant capacity at scaled conditions using the network flow models.

For cooling rows TE-S3, the effective area is relatively constant with driving pressure ratio, decreasing slightly as driving pressure ratio decreases. This discharge coefficient effect is also observed in the work of Rowbury (1998).

The effective areas of S4 and S5 are much higher in RP 1D+ and RP 3D than the other designs. They were designed in this way so that S4 and S5 flow the same coolant as the other designs while operating at a lower driving pressure ratio. Also, S4 and S5 of RP 1D+ and RP 3D have much greater variation in discharge coefficient than the other rows, most likely because they operate at extremely low PRs.

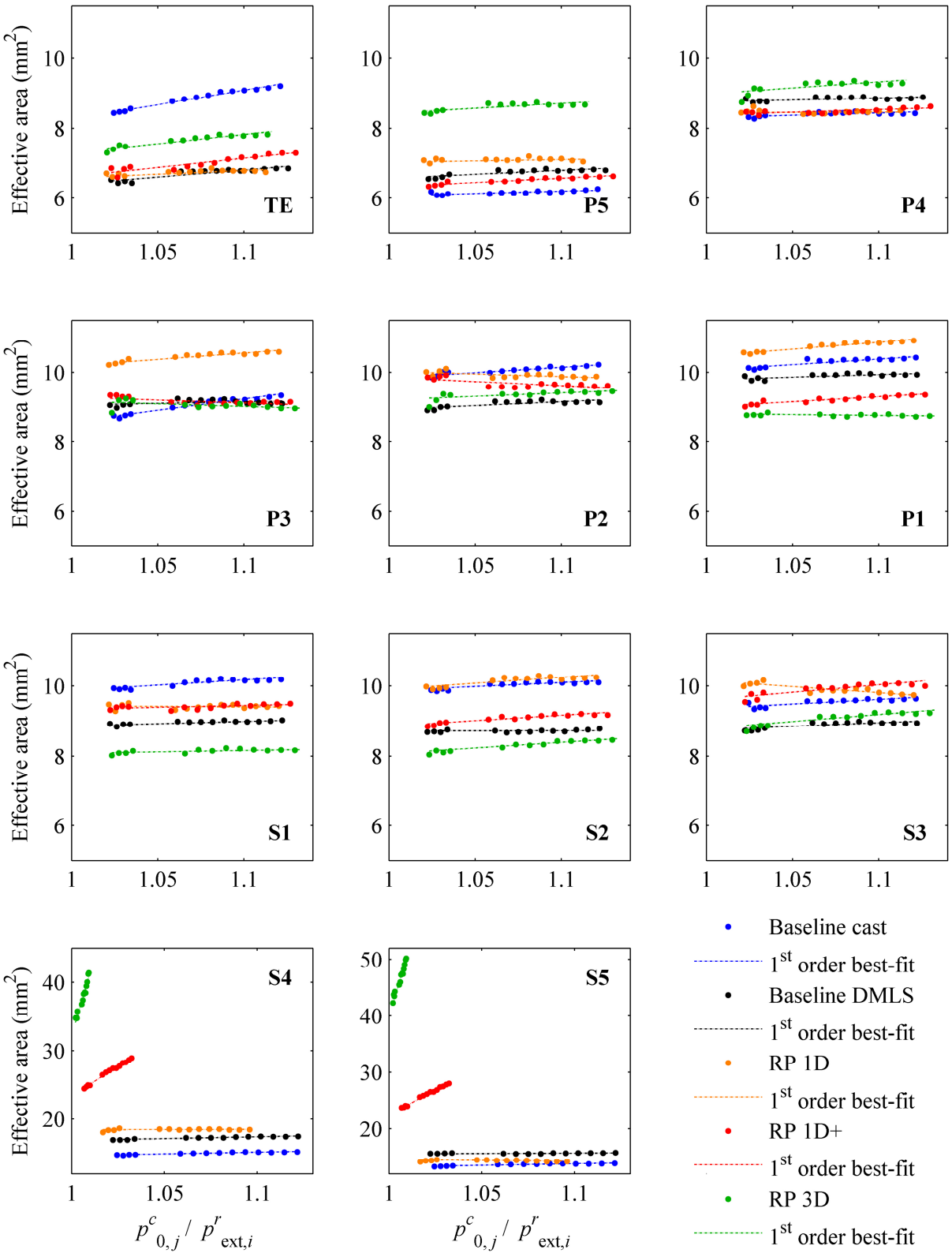
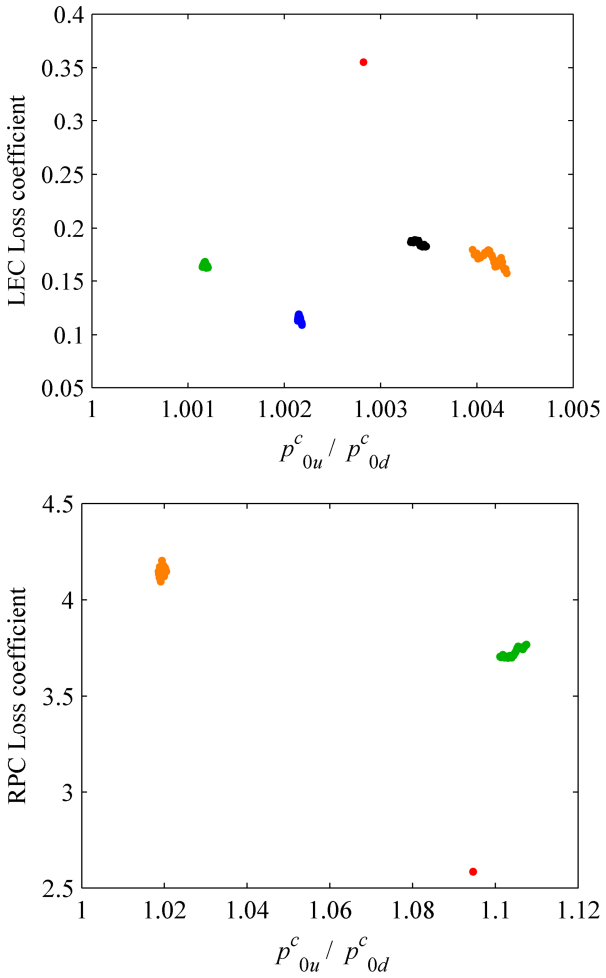
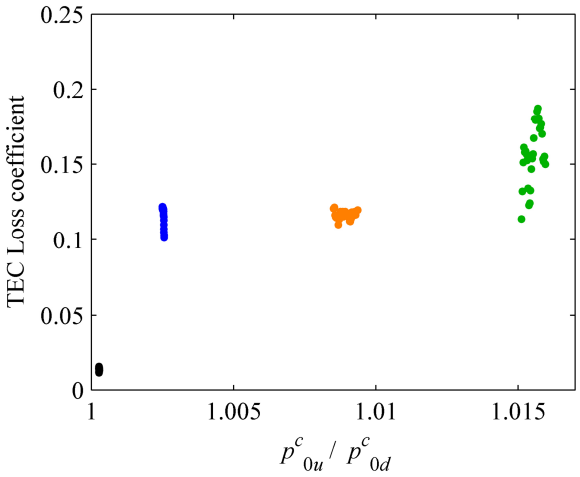


Figure 9.8. Effective row areas, as a function of the local total feed pressure to local exit static pressure ratio.

Dimensionless loss coefficients are shown in Fig. 9.9. The nominal area to which each loss coefficient is referenced is also tabulated in Fig. 9.9. Loss coefficients are plotted as a function of the upstream total to downstream total PR across the loss element. The data are sparse given that the loss coefficient can only be calculated at a given PR if raw capacity data exist for all rows and all compartments at that PR. This only occurs within two narrow PR ranges: at low PRs in the range 1.02-1.03, and at high PRs somewhere around 1.13. Only the high PR capacity data are used to determine loss coefficients in order to maximise the accuracy of the loss coefficient measurement for the available data.

It is unclear whether loss coefficient is constant with PR, given the limited data. Of the loss coefficients, the LEC RP 1D, TEC RP 1D and RPC RP 3D loss coefficients are evaluated across the broadest range of PRs and appear relatively constant. The assumption that the loss coefficient is constant with PR (assumed in the analytical method) is tested and validated against the total vane capacity measured in the Sector over a broad range of PRs.





	mm^2	A^c_{LEC}	A^c_{TEC}	A^c_{RPC}
Baseline cast	●	200	50	
Baseline DMLS	●	200	50	
RP 1D	●	100	20	110
RP 1D+	●	200		50
RP 3D	●	200	50	50

Figure 9.9. Dimensionless loss coefficient (K^c_j) calculated using CCR experimental data and network flow models.

The LEC/TEC loss coefficients are between 0.02 and 0.35, which agrees well with the loss coefficients for pipe contraction in Howatson et al. (2009). The loss coefficients within the RPC are between 2.5 and 4. High losses in the RPC are generated by the rough laser-sintered walls, the chevron ribs, and the impingement from the main feed plena into the reverse-pass passage. It is difficult to make informed comparisons of the relative sizes of the loss coefficients between designs, since the magnitude of the loss coefficients depends on the uncertain area to which it is referenced. It is far clearer to compare the actual pressure losses within the passages during operation, which is performed in the following section.

9.9 Loss Model Predictions at CCR Conditions

The network flow models are now used to predict the capacity of each cooling row at CCR conditions when all rows exhaust to atmosphere. These predictions are shown in Fig. 9.10. Row capacity is plotted cumulatively, given by the black lines. The total vane capacity prediction using the network flow models is given by the uppermost black line, marked S5 +. The total vane capacity measured in the CCR is shown in red. Also shown in cyan is the total vane capacity that would be predicted by summing the raw row-by-row capacity measurements, i.e., assuming no interaction between rows and no network flow model.

The total vane capacity prediction matches the experimentally measured total vane capacity exactly, for all designs except RP 3D. This partially validates the assumption that the loss coefficient is constant with PR. For RP 3D, the prediction matches the experiment to within 2%, suggesting that the form of the RP 3D network flow model could be improved. The raw coolant capacity sum always under-predicts the total vane capacity, depending on the amount of interaction between rows. For the cast and laser-sintered baseline designs, the rows do not interact significantly, and so the raw sum only under-predicts the total vane capacity by 2%. In contrast, interaction is significant in the reverse-pass designs: the raw sum under-predicts total vane capacity by 5%, 14% and 27% for designs RP 1D, RP 1D+ and RP 3D, respectively. This demonstrates the necessity of the network flow model to accurately predict row-by-row coolant capacity from the CCR experiments.

The network flow model predictions of compartmental capacity and the experimental CCR measurements match by definition at high PRs for all designs (apart from RP 3D). This is because the loss coefficients are calculated based on the compartmental capacity CCR measurements, and the solution is exact (before averaging). At low PRs, the compartmental capacity prediction and measurement match to high accuracy, further validating the assumption that the loss coefficient is constant with PR. The raw RP 3D compartmental capacity measurements do not match the network flow predictions by definition because the RP 3D compartments interact.

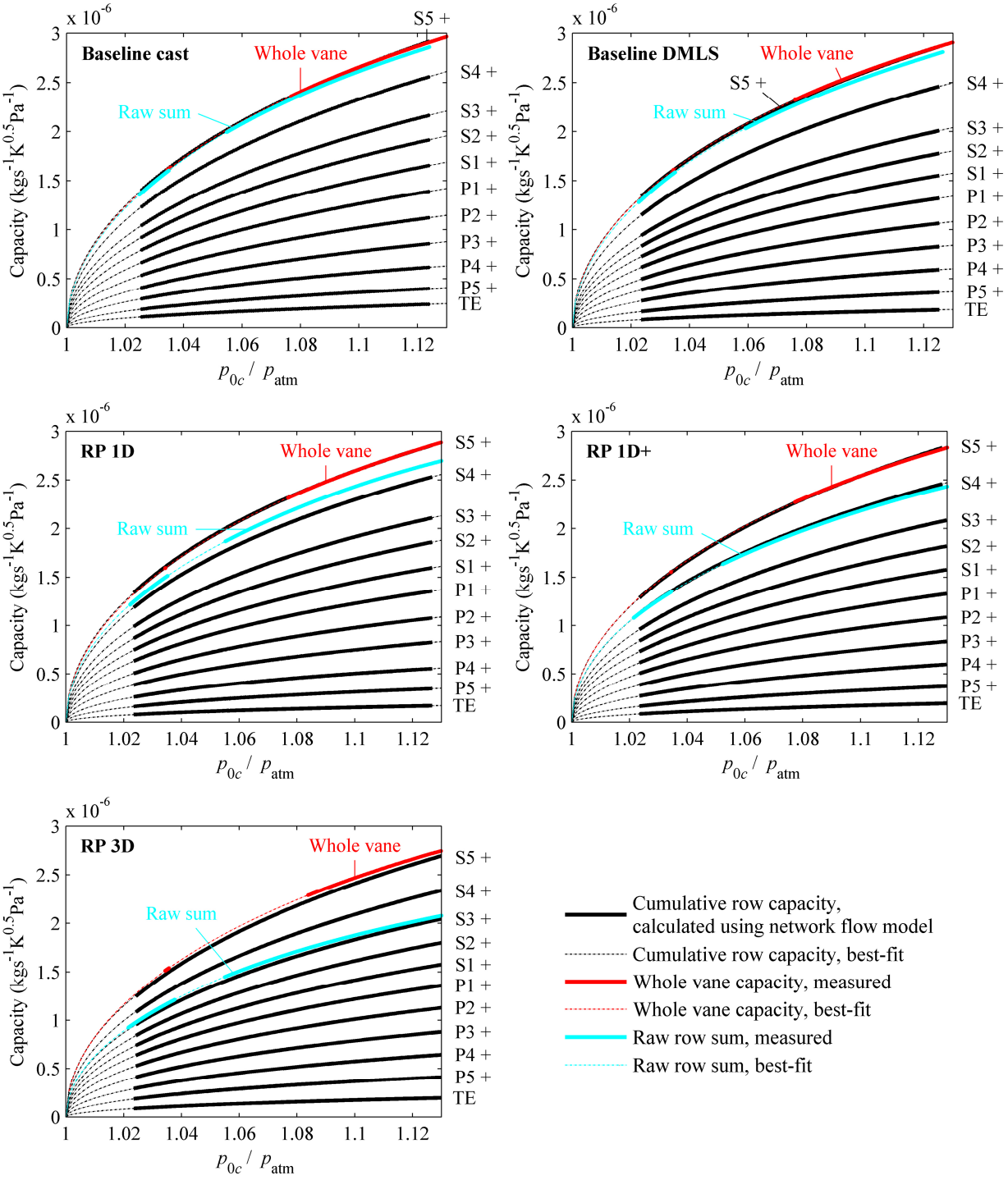


Figure 9.10. Row-by-row coolant capacity predicted for constant exhaust pressure, using network flow models, plotted cumulatively.

The local driving pressure ratios across each film cooling row $p_{0,j}^{c}/p_{\mathrm{atm}}$ (where j = LEC, TEC or RPC) are plotted as a function of total driving pressure ratio p_{0c}/p_{atm} in Fig. 9.11. For a lossless system, the total driving pressure equals the local driving pressure ratio. This is shown by the dotted line of unity gradient. For interacting, loss-inducing systems, the local driving pressure ratio is lower

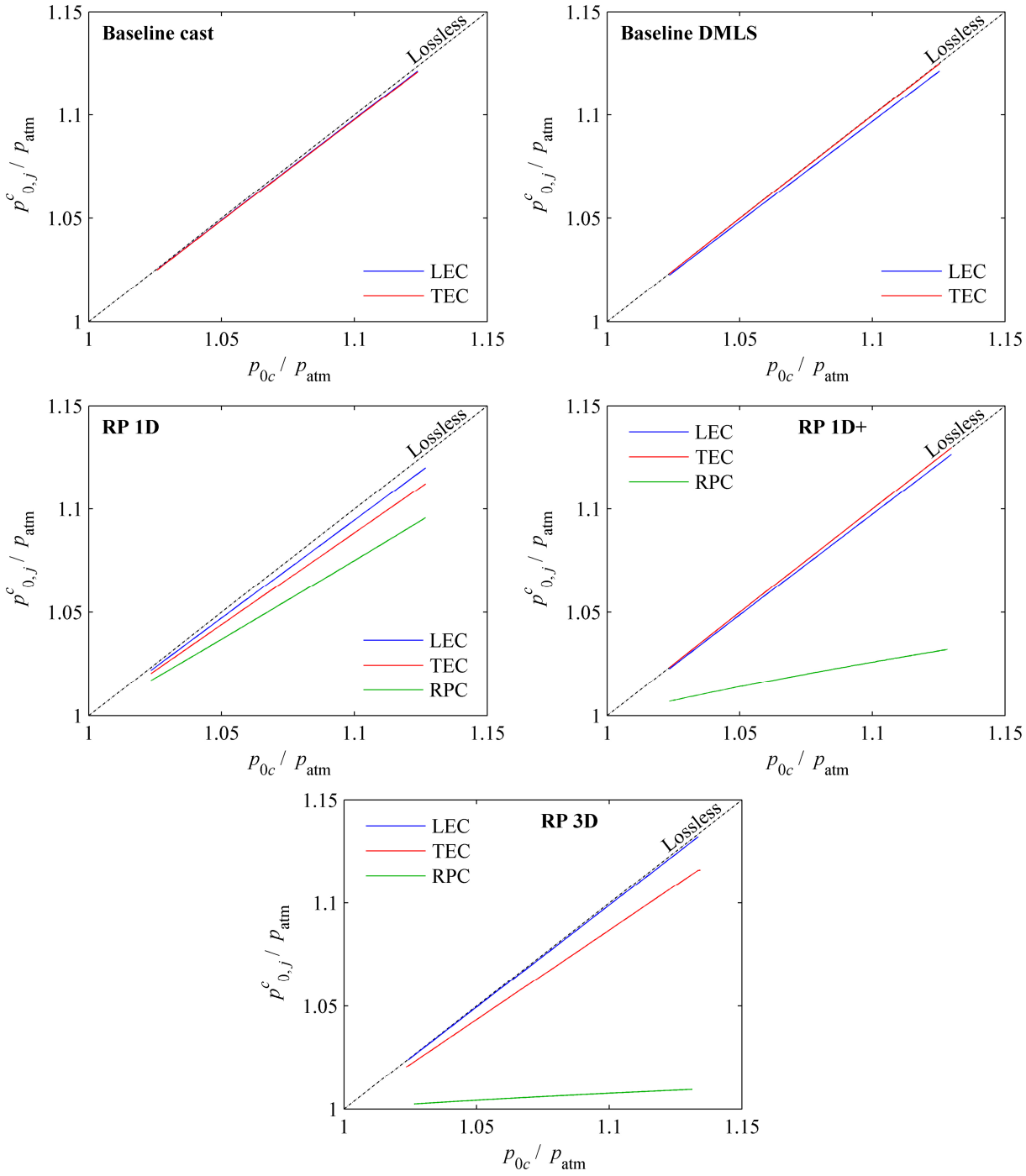


Figure 9.11. Pressure ratios within each compartment for constant exhaust pressure, predicted using network flow models.

than the total driving pressure ratio. The ratio $p^c_{0,j}/p_{0c}$ for a given compartment is approximately constant over all PRs.

The LEC and TEC local driving pressure ratios are approximately equal to the total driving pressure ratio for both baseline designs, since the rows within these compartments hardly interact. Similarly, the LEC and TEC local driving pressure ratio in RP 1D+ are approximately equal to the total driving

pressure ratio, and the LEC local driving pressure ratio for RP 3D is approximately equal to the total driving pressure ratio. The LEC and the TEC in RP 1D experience higher pressure losses than the baseline systems because the RP 1D LEC and TEC plena have smaller cross-section, and therefore have higher wetted area per unit flow and greater inlet contraction loss. The driving total pressure within the RP 1D LEC is 95% of the total pressure at vane inlet, while the driving total pressure within the RP 1D TEC is 88% of the total pressure at vane inlet. The TEC group in RP 3D (P4-TE) interacts strongly with the reverse-pass flow, and consequently the total pressure feeding the TEC group is 12% lower than the total pressure at vane inlet.

The total driving pressure within the RPC is notably 78% of the total pressure at vane inlet in RP 1D, 24% in RP2DB2, and only 7% in RP 3D. This is partially by design to sequentially push the reverse-pass concept. To compensate for the reduction in total driving pressure driving coolant through S4 and S5, the effective area of S4 and S5 is larger in the reverse-pass designs than the baseline designs (Fig. 9.8). It will be shown later that ingestion of S4 is a problem (especially for RP 3D) when the rows exhaust to different pressures (e.g., Sector or engine conditions).

The row-by-row coolant capacities for constant exhaust pressure—at a nominal pressure ratio of p_{0c}/p_{atm} = 1.0295 and predicted by the network flow models—are summarised in Fig. 9.12. The agreement between designs is reasonable. The total vane capacity at CCR conditions for each design is shown in the previous chapter, with the maximum total capacity difference at CCR conditions between designs being 7% (between RP 3D and cast baseline).

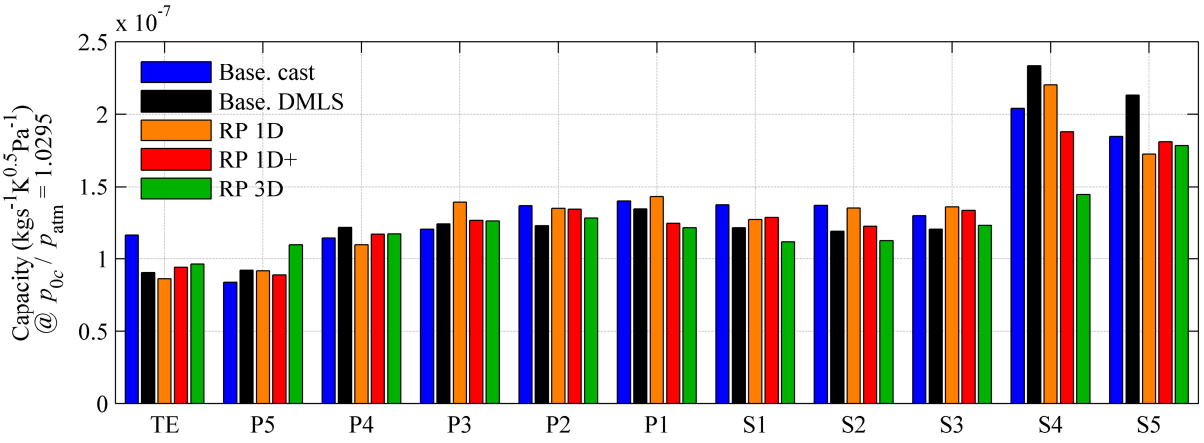


Figure 9.12. Row-by-row coolant capacity for constant exhaust pressure at an overall pressure ratio p_{0c}/p_{atm} = 1.0295, predicted using network flow models.

9.10 Coolant Capacity Prediction and Validation at Sector Conditions

In this section, the network flow models are used to estimate row-by-row coolant capacity at Sector conditions. The situation is complicated from CCR conditions because the exhaust pressure varies around the vane surface. The static pressure distribution around the vane during Sector operation is estimated from the isentropic Mach number distribution M adapted from Rawlinson (2001)—summarised in Table 9.2—and the equation:

$$\frac{p^r_{\text{ext},i}}{p_{0m}} = \left(1 + \frac{\gamma - 1}{2}\text{M}^2\right)^{-\frac{\gamma}{\gamma-1}}. \tag{9.81}$$

At Sector conditions γ = 1.4 and at engine conditions (mainstream ~ 2000 K) γ = 1.3. The row-by-row capacity is evaluated as a function of the ratio of the total coolant pressure at vane inlet to the total mainstream pressure, p_{0c}/p_{0m}, from 1 to 1.088. This was deemed the most appropriate global parameter to characterise coolant capacity at engine-realistic conditions.

The Sector row-by-row capacity predictions are plotted cumulatively in Fig. 9.13 for all designs. Also plotted in Fig. 9.13 is the total capacity prediction assuming no interaction between rows (raw sum, cyan line), and the experimental total capacity measured in the Sector Facility (blue crosses). Ingesting rows are shown in red.

The shape of the Sector capacity curves in Fig. 9.13 is different to the CCR capacity curves because the results are characterised with respect to the pressure ratio p_{0c}/p_{0m}. Even when p_{0c}/p_{0m} = 1, most of the cooling rows still exhaust into the mainstream because the local pressure ratio across the row is greater than 1, due to the dynamic head of the external flow. For rows where $p^r_{\text{ext},i}/p_{0m}$ is low—i.e., S5 and the TE—the capacity of the row is relatively insensitive to p_{0c}/p_{0m} in the range 1 – 1.088. This is demonstrated in Fig. 9.13, where the TE capacity is almost flat across p_{0c}/p_{0m} for all geometries, and the difference between lines S5 + and S4 + is approximately constant. This is because the local driving pressure across the row $p^c_{0,j}/p^r_{\text{ext},i}$ is so high that variation in p_{0c}/p_{0m} has a limited effect on the local driving pressure ratio. This is shown in Fig. 9.14, where the local driving pressure ratio across each row is plotted against p_{0c}/p_{0m}.

Table 9.2 Sector and engine exhaust pressure distributions, adapted from Rawlinson (2001)

Row	S5	S4	S3	S2	S1	P1	P2	P3	P4	P5	TE
External Mach number	0.407	0.230	0.116	0.079	0.047	0.022	0.053	0.088	0.159	0.287	0.743
Sector $p^r_{\text{ext},i}/p_{0m}$	0.892	0.964	0.991	0.996	0.999	1.000	0.998	0.995	0.983	0.945	0.693
Engine $p^r_{\text{ext},i}/p_{0m}$	0.899	0.966	0.991	0.996	0.999	1.000	0.998	0.995	0.984	0.948	0.709

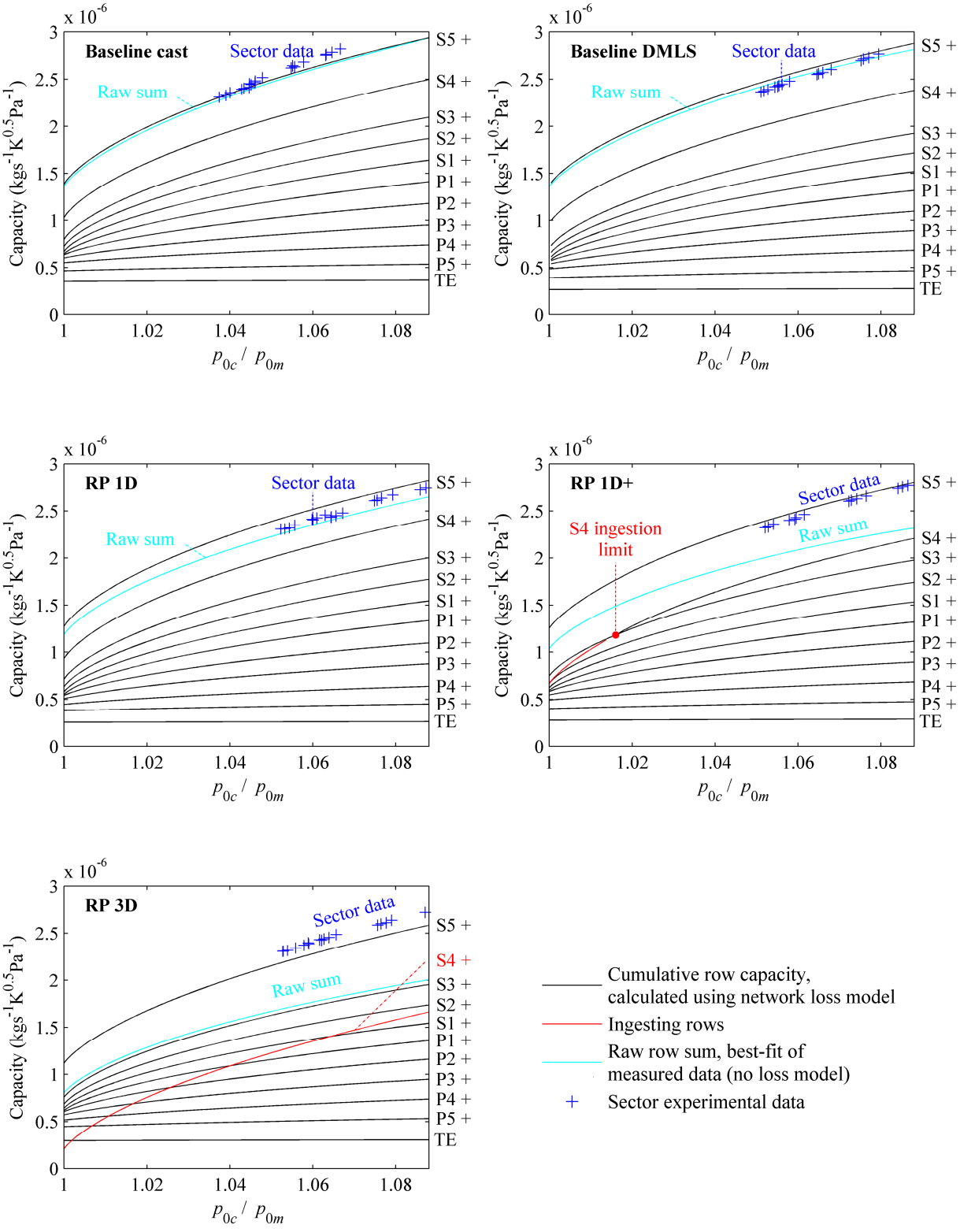


Figure 9.13. Row-by-row coolant capacity at Sector conditions, predicted using network flow models.

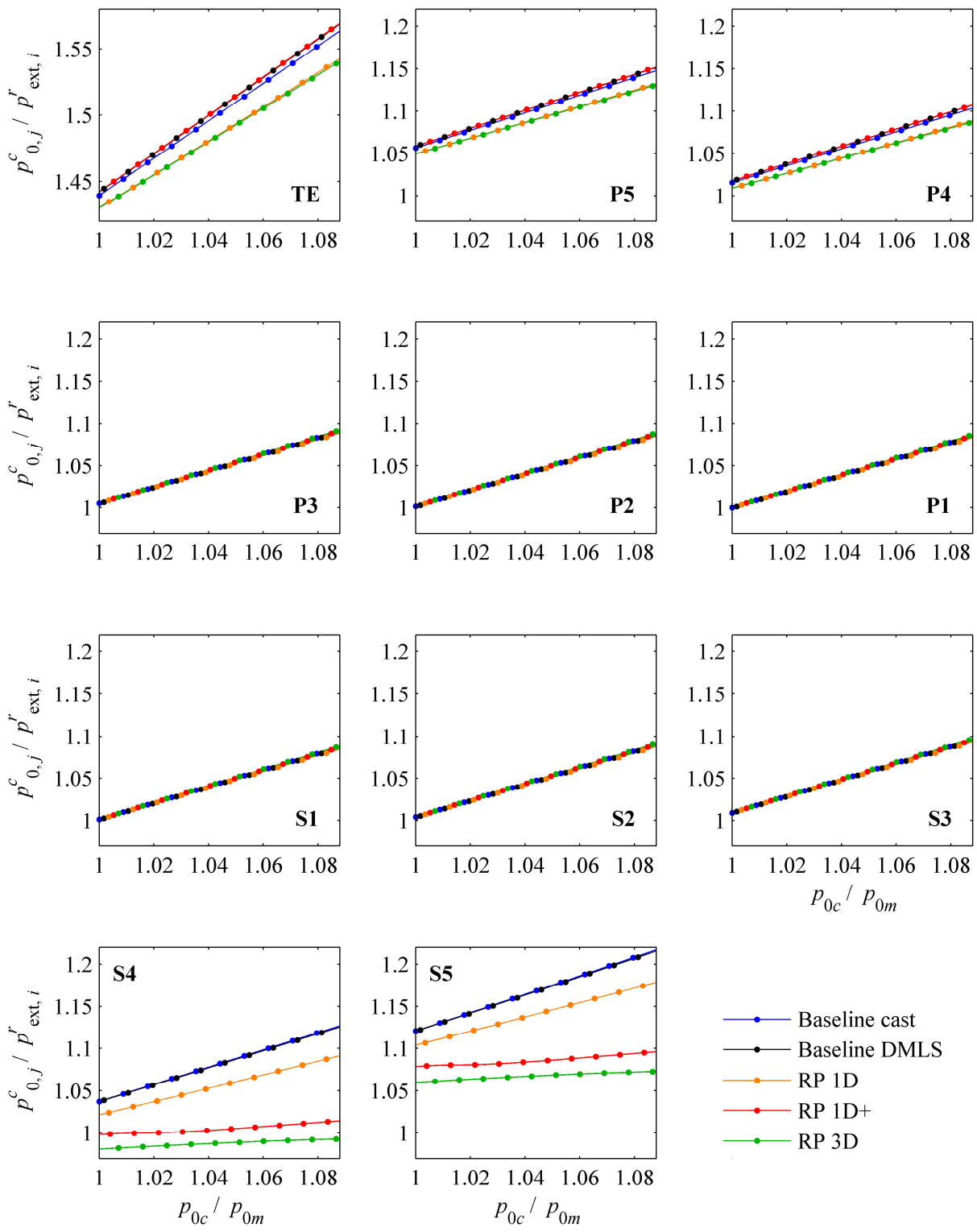


Figure 9.14. Local driving pressure ratio across each row at Sector conditions, predicted using network flow models.

The network flow model predictions compare well with the Sector measurements (Fig. 9.13), despite the uncertainty in the network flow model boundary conditions and the Sector experimental capacity measurements. Uncertainties include: the exit static pressures used in the network flow model, which are adapted from Rawlinson (2001); hole discharge coefficients, since the coolant Reynolds number is four times higher in the Sector Facility than the CCR; the assumption that loss coefficients are constant in the network flow model; the extrapolation of the model to S4 ingestion (§ 9.6.1); leaks within the Sector; and uncertainties in pressure and temperature Sector measurements. Furthermore, the TE effective area is calculated up to a local PR of 1.13 from the CCR data (Fig. 9.8), but the TE operates at a local PR of 1.44 in the Sector facility (Table 9.2); these predictions assume that the TE effective area at a local PR of 1.13 is equal to the TE effective area at a local PR of 1.44. Considering these uncertainties, the agreement is good, especially when compared to the raw sum prediction (cyan lines).

The raw sum prediction of total RP 3D capacity is 25% lower than the experimental measurement, compared to the network flow model prediction which is 5% lower than the experimental measurement. The raw sum prediction of total RP 1D+ capacity is 16% lower than the experimental measurement, while the network flow model prediction is 1% lower than the experimental measurement. This highlights the necessity of a network flow model to be able to accurately determine row-by-row coolant capacity at engine-realistic conditions. The raw sum and network flow model predictions for the baseline designs and RP 1D both compare well to the experimental measurements, because there is far less interaction between rows in these designs than in RP 1D+ and RP 3D.

The capacities of rows S3-TE at Sector conditions are similar for all designs, shown in Fig. 9.15 for a nominal pressure ratio of p_{0c}/p_{0m} = 1.0295. Strikingly, the flow split between S4 and S5 in RP 1D+ and RP 3D is very different to the S4-S5 flow split in the baseline and RP 1D designs. For the baseline and RP 1D designs, the flow split between S4 and S5 remains approximately constant across all PRs at 1:1.3 and the S4-S5 capacity sum is broadly similar. In the RP 1D+ design, the capacity of S4 is 20% the S4 baseline/RP 1D capacity, ingesting at a global PR of 1.018. S4 ingestion occurs when the local driving PR across S4 drops below unity (Fig. 9.14). In contrast, the capacity of RP 1D+ S5 is 50% larger than the S5 baseline/RP 1D capacity (Fig. 9.15). In fact, the RP 1D+ S5 capacity excess (compared to the baseline/RP 1D designs) almost exactly matches the S4 capacity deficit, with the result that the sum of S4 and S5 capacities in RP 1D+ is approximately equal to the sum of S4 and S5 capacities in the baseline/RP 1D designs (Fig. 9.15).

In the RP 3D design, S4 ingests over the entire PR range. The cause of this is clear in Fig. 9.14, where the local driving pressure ratio across S4 is always below unity for RP 3D because the losses within the reverse-pass passage are extremely high. The capacity of RP 3D S5 is approximately 2.5 times

larger than the S5 capacity in the baseline/RP 1D designs, while the S4 capacity is equal in magnitude to the other designs but is ingesting rather than egesting. Like RP 1D+, the sum of the RP 3D S4-S5 capacity is approximately equal to the S4-S5 capacity sum in the baseline/RP 1D designs.

Ingestion significantly reduces component life and must be avoided. This means operating RP 1D+, above a global pressure ratio p_{0c}/p_{0m} of 1.018, which is readily achieved as the nominal Trent 500 engine pressure ratio is p_{0c}/p_{0m} = 1.0295. RP 3D must be modified to avoid ingestion. S4 may be removed from the reverse-pass passage, and instead fed from the leading-edge passage. The effective areas of S4 and S5 would need to be modified accordingly.

Network model predictions of total vane capacity at a nominal global pressure ratio of p_{0c}/p_{0m} = 1.0295 are shown in Fig. 9.15. The models predict that the RP 1D+ design uses 5% less coolant than the cast baseline at Sector conditions, compared to 4% less at CCR conditions. The RP 3D design uses 14% less coolant than the cast baseline at Sector conditions, compared to 7% less at CCR conditions. This demonstrates how the exit conditions and loss characteristics significantly affect coolant capacity prediction and the necessity of a network flow model.

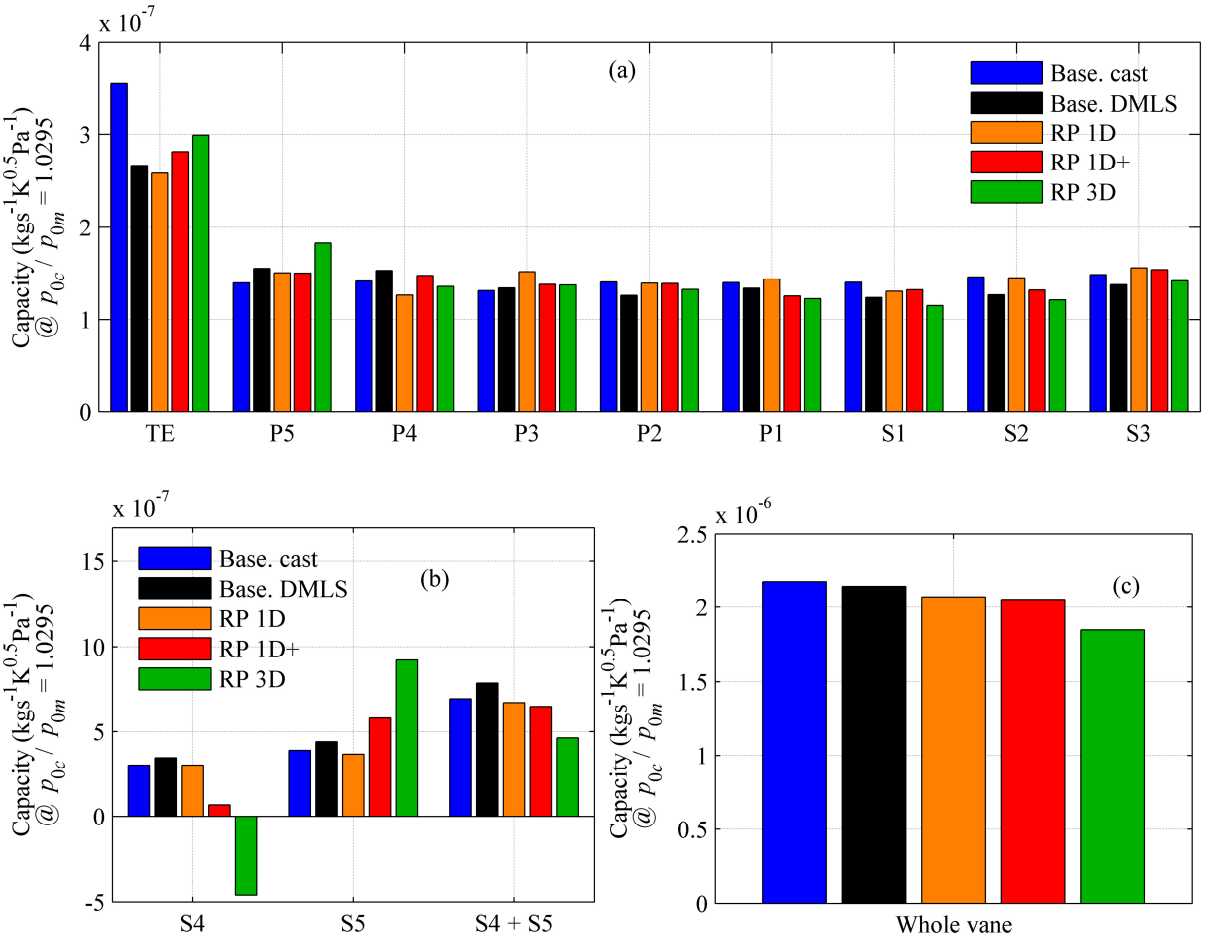


Figure 9.15. Row-by-row coolant capacity for engine-realistic exhaust pressures (Sector conditions) at an overall pressure ratio p_{0c}/p_{atm} = 1.0295, predicted using network flow models; (a) rows TE-S3; (b) rows S4, S5 and S4+S5; (c) whole vane.

9.11 Coolant Capacity Prediction at Engine Conditions

The network flow models are now used to predict the row-by-row coolant capacity at engine conditions by setting the ratio of specific γ to 1.33 for the coolant and 1.30 for the mainstream. The pressure boundary conditions are tabulated in Table 9.2. The results are plotted in the form of cumulative row capacity in Fig. 9.16. It can be seen that the effect of γ is negligible, since coolant capacity predicted at Sector conditions is almost identical to the engine predictions.

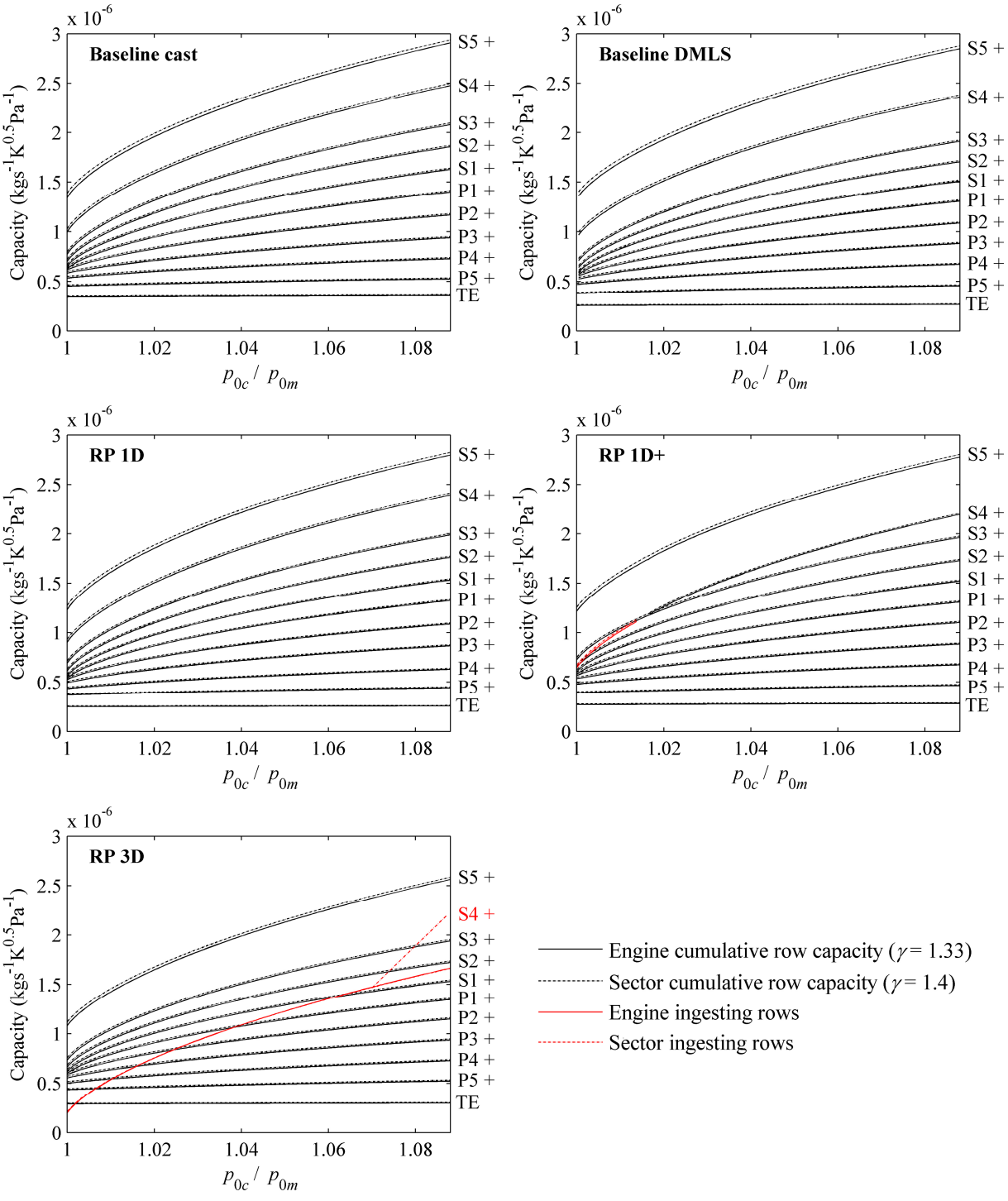


Figure 9.16. Row-by-row coolant capacity at engine conditions, predicted using network flow models.

9.12 Proposed Improvements

Feed S4 in RP 3D from the leading-edge compartment. S4 ingests in RP 3D (and at some PRs in RP 1D+). Feeding S4 from the leading-edge compartment would eliminate ingestion. The effective area of S4 and S5 would be reduced.

Characterise effective area using coolant Reynolds number. The effective area of film cooling holes is much better characterised by the coolant Reynolds number (Rowbury, 1998). This may be too difficult in practice, however, since the CCR would need to be significantly redesigned to operate at elevated pressures to achieve the desired coolant Reynolds numbers.

9.13 Conclusions

In this chapter, the effective row areas and loss coefficients that define each design have been calculated by post-processing the raw experimental data from the Coolant Capacity Rig. Network flow models have been designed to capture the interaction and losses specific to each vane, and are used to predict the row-by-row coolant capacity of each design at multiple conditions: at CCR conditions, where all rows exhaust to atmosphere; at Sector conditions, where each row exhausts to a different pressure; and at engine conditions, similar to Sector conditions but at a lower ratio of specific heats. The network models have been validated against experimental data from the Sector Facility. It is shown that the coolant capacity predictions at Sector conditions are almost identical to the predictions at engine conditions.

The flow split between rows at CCR conditions is approximately the same for all designs. The flow split at Sector conditions for the baseline and RP 1D designs are similar. The S4-S5 flow split in RP 1D+ and RP 3D is very different to the S4-S5 flow split in the baseline and RP 1D designs. In the RP 1D+ design, the capacity of S4 is 20% of the S4 baseline/RP 1D capacity, ingesting at a global PR of 1.018. The capacity of RP 1D+ S5 is 50% larger than the S5 baseline/RP 1D capacity. The total flow through S4 and S5 in RP 1D+ is approximately the same as the total flow through S4 and S5 in the baseline/RP 1D designs.

Row S4 in RP 3D ingests at all tested PRs—the loss through the reverse-pass compartment is too high for row S4. The capacity of RP 3D S5 is approximately 2.5 times larger than the S5 capacity in the baseline/RP 1D designs, while the S4 capacity is equal in magnitude but opposite in direction to the baseline/RP 1D designs. Like RP 1D+, the sum of the RP 3D S4-S5 capacity is approximately equal to the S4-S5 capacity sum in the baseline/RP 1D designs.

It is suggested that S4 in RP 3D be removed from the reverse-pass compartment and instead be fed from the leading-edge compartment, in order to eliminate ingestion. The effective areas of S4 and S5 should be reduced accordingly.

10. Conclusions

The three major conclusions of this thesis are now summarised. Proposals for future work are also included. More specific findings and contributions are included at the end of the relevant chapter.

10.1 Laboratory Thermal Assessment of Laser-Sintered HPNGVs

This thesis has demonstrated that the thermal performance of a cast HPNGV operating at engine conditions can be predicted using an equivalent laser-sintered vane operating at laboratory conditions. An entire HPNGV with complex internal cooling system has been laser-sintered to a good level of accuracy (±0.15 mm standard deviation from design intent). The effect of Biot number and the shrinkage of laser-sintered film cooling holes have been analysed and accounted for.

The overall cooling effectiveness (θ) distributions of a cast vane and the equivalent laser-sintered vane are shown to be very similar. The mainstream recovery ratio (c) distributions are also very similar. The laser-sintered overall cooling effectiveness is always greater than the cast overall cooling effectiveness, most likely because the internal convective heat transfer in the laser-sintered vane is greater than the cast vane due to increased internal surface roughness. The offset depends on surface location, but is ~0.02–0.04.

A number of innovations to the experimental methodology have been implemented, including: a new physically-based infra-red thermography calibration method; testing of HPNGVs over a range of pressure ratios and baselining effectiveness against $\dot{m}_c\sqrt{T_{0c}}/\dot{m}_m\sqrt{T_{0m}}$; use of regression to measure both overall cooling effectiveness and recovery ratio from a series of runs; a leak test to quantify leak errors.

10.2 Reverse-Pass Cooling Systems

Reverse-pass cooling systems are shown to improve the balance between internal convective cooling and external film cooling. Reverse-pass systems lower peak temperatures and significantly reduce lateral component surface temperature variation. The benefits of reverse-pass cooling can be fully realised in systems where there is long undisturbed surface length, such as the SS of HPNGVs, afterburner liners, and combustor liners. Every millimetre reduction in HPNGV TE system length reduces the maximum metal temperature at the TE extremity by ~1 K.

The optimum reverse-pass cooling system is three-dimensional, depending on the radial mainstream temperature distribution and the coolant mass flow split between the TE and the reverse-pass-fed cooling rows. Three reverse-pass systems (RP 1D, RP 1D+ and RP 3D) were designed with varying internal passage layouts, using bespoke 2D and 3D numerical conjugate heat transfer models. Systems

RP 1D+ and RP 3D outperform the baseline cast/laser-sintered systems on the SS by an overall cooling effectiveness of around 0.06—i.e., 60 K cooler. The cooler areas in RP 1D+ and RP 3D coincide with the reverse-pass passages and the short TE systems. The SS midspan TE overall cooling effectiveness is 0.03 greater (30 K cooler) in RP 1D+ and RP 3D designs compared to the baseline designs. There is further room for optimisation of the reverse-pass designs, e.g., the flow-split between S4 and S5.

10.3 Coolant Capacity and Loss Measurements

A new experimental facility—the Coolant Capacity Rig—has been devised, developed, manufactured and commissioned in order to measure row-by-row, compartmental and total coolant capacity to a high degree of accuracy and repeatability. The facility allows accurate mass flow rate measurement over a large range of pressure ratios and mass flows using a novel differential mass flow measurement technique, bypass system, and calibrated mass flow orifice.

A method for estimating the loss coefficients within the vane from the coolant capacity measurements has been formulated and implemented. Compared to the standard method of measuring loss coefficients using pressure probes within the vane, the new method is powerful in that no internal pressure probes are required. Network flow models are used to estimate row-by-row coolant capacity at engine conditions.

10.4 Future Study

In addition to the proposed improvements reported in each chapter, a number of additional ideas to continue the research are now detailed.

The possibility of applying reverse-pass cooling systems to HPNGV platforms, combustor liners, and similar systems could be examined. In contrast to HPNGVs in which internal space is limited, platforms and combustor liners have greater streamwise length, allowing longer reverse-pass systems. This may mean that platform and combustor liner reverse-pass systems would perform even better than HPNGV reverse-pass systems.

Foreign gases can be used to match the coolant-to-mainstream density ratio in laboratory tests. Sulphur hexafluoride is typically used for this purpose. Foreign gas was not used in the experiments undertaken for this thesis due to time constraints and a lack of certainty about emission regulations. It may prove worthwhile reinvestigating the use of foreign gas to assess the impact of density ratio on thermal performance.

In this thesis, only the *steady-state* vane temperature is analysed from the Sector experiments. It may be possible to estimate heat transfer coefficients and film effectiveness by analysing the *transient* vane temperature history. This analysis may prove ill-conditioned, however.

The mainstream recovery ratio is a function of Mach number, Prandtl number and flow regime, e.g., equations (7.2) and (7.3). It may be worthwhile investigating the feasibility of using the mainstream recovery ratio to estimate Mach number, assuming Prandtl number and flow regime. It would be a boon to measure full-coverage Mach number without the need of pressure tappings, pressure sensitive paint, or the like. However, it may turn out that the accuracy of the recovery ratio measurements and the many assumptions that would have to be made are inadequate to make the lucrative step from thermal measurement to aerodynamic measurement.

During the short initial compression spike at the start of a Sector run, the internal features and passages could be observed *through* the external wall. This extremely short duration 'X-ray' effect is caused by a number of transients, and could possibly be used to estimate the thermal and geometric properties of the vane. It would, however, be very challenging given the complex 3D design of the vane, the number of transients occurring simultaneously, and the short time duration of the compression spike.

11. References

Anderson, M. R., and Baughn, J. W., 2004, "Hysteresis in liquid crystal thermography," Journal of Heat Transfer, 126(3), 339-346.

Armstrong, J., and Winstanley, D., 1988, "A Review of Staggered Array Pin Fin Heat Transfer for Turbine Cooling Applications," Journal of Turbomachinery, Vol. 110, pp. 94-103.

Arora, S. C., and Abdel-Messeh, W., 1989, "Characteristics of partial length circular pin fins at heat transfer augmentors for airfoil internal cooling passages," ASME paper 89-GT-87.

Astarita, T., Cardone, G. and Carlomagno, G., 1995, "Heat Transfer and Flow Visualisation Around a 180 deg Turn in a Rectangular Channel," Proceedings HTD-Vol. 318, San Francisco, USA, 1995.

Baldauf, S., Scheurlen, M., Schulz, A., and Wittig, S., 2002, "Correlation of film-cooling effectiveness from thermographic measurements at enginelike conditions," Journal of Turbomachinery, 124, 686-698.

Batstone, J., 2011, *Dendritic cooling for nozzle guide vanes*, D.Phil. thesis, University of Oxford, Department of Engineering Science.

Battisti, L., Fedrizzi, R., and Cerri, G., 2006, "Novel technology for gas turbine blade effusion cooling," ASME Paper GT2006-90516.

Bettner, J. L., 1968, "Experimental investigation in an annular cascade sector of highly loaded turbine stator blading - volume I," Analysis and design. Technical Report CR-1219, NASA.

Bogard, D. G., 2006, "Airfoil film cooling," In *The Gas Turbine Handbook* (pp. 309-320). U.S. Department of Energy, Office of Fossil Energy, National Energy Technology Laboratory.

Bons, J. P., MacArthur, C. D., and Rivir, R. B., 1996, "The effect of high free-stream turbulence on film cooling effectiveness," Journal of Turbomachinery, 118, 814-825.

Boyer, R., Welsch, G., and Collings, E.W., 1994, *Materials Properties Handbook: Titanium Alloys*, ASM International.

Brevet, P., Dejeu, C., Dorignac, E., Jolly, M., and Vullierme, J. J., 2002, "Heat transfer to a row of impinging jets in consideration of optimization," Int. J. Heat Mass Transfer, 45, 4191-4200.

Bunker, R. S., 2005, "A review of shaped-hole turbine film cooling technology," Journal of Turbomachinery, 129(2), 441-453.

BS EN ISO 9300, 2005, *Measurement of gas flows by means of critical Venturi nozzles*, BSI, 389 Chiswick High Road, London, W4 4AL.

Calvert, H. F., Cochran, R. P., Dengler, R. P., Hickel, R. O., and Norris, J. W., 1970, "Turbine cooling research facility," Technical Report TM X-1927, NASA.

Childs, P. R., 2001, *Practical Temperature Measurement*. Butterworth-Heinemann.

Chyu, M. K., 1990, "Heat transfer and pressure drop for short pin-fin arrays with pin-endwall fillet," Journal of Heat Transfer, 112, 926-932.

Chyu, M. K., Hsing, Y. C., and Natarajan, V., 1998, "Convective heat transfer of cubic fin arrays in a narrow channel," Journal of Turbomachinery, 120, 362-367.

Chyu, M. K., Natarajan, V., and Metzger, D. E., 1992, "Heat/mass transfer from pin-fin arays with perpendicular flow entry," ASME HTD-Vol. 226, Fundamentals and Applied Heat Transfer Research for Gas Turbine Engines.

Colban, W., Gratton, A., and Thole, K. A., 2006, "Heat transfer and film-cooling measurements on a stator vane with fan-shaped cooling holes," Journal of Turbomachinery, 128(1), 53-61.

Crook, G., and Horlor, M., eds., 2005, *The Jet Engine*, 5th ed., Rolls-Royce Technical Publications, London, England, UK.

Cumpsty, N. (2003). Jet Propulsion - A simple guide to the aerodynamic and thermodynamic design and performance of jet engines. University Press, Cambridge.

Cunha, F. J., 2006, "Heat transfer analysis," In *The Gas Turbine Handbook* (pp. 389-410). U.S. Department of Energy, Office of Fossil Energy, National Energy Technology Laboratory.

Devore, M.A., Gleiner, M.S.V., and Jenne, D.C., 2010, Patent No. EP 2 325 440 A2.

Ding, K., 1985, "Test of jet engine turbine blades by thermography," Optical Engineering 24(6), pp. 1055-1059.

Dittus, F.W., and Boelter, L.M.K., 1930, "Heat Transfer in Automobile Radiators of the Tubular Type," Publications in Engineering, Vol. 2, pp. 443, University of California, Berkeley.

Downes, A., 2014, "RE: radial temperature traverse," e-mail correspondence, 6th August 2014.

Eastop, T.D., and McConkey, A., 1986, *Applied Thermodynamics*, 4th edition, Longman Group Ltd., England.

Eckert, E.R.G., 1983, "Analysis of Film Cooling and Full Coverage Film Cooling of Gas Turbine Blades," in Proceedings of the 1983 International Gas Turbines Congress, Tokyo, Japan, p. 109.

Eckert, E.R.G., and Drake, R.M., 1972, *Analysis of Heat and Mass Transfer*, McGraw-Hill, New York.

Eckert, E. R., and Livingood, J. N., 1953, "Comparison of effectiveness of convection-, transpiration- and film-cooling methods with air as coolant," National Advisory Committee for Aeronautics, Cleveland, Ohio.

Fletcher, D. A., 1997, *Internal cooling of turbine blades: the matrix cooling method*, D.Phil. Thesis, University of Oxford, Department of Engineering Science.

FLIR, 2012a, *User's manual, FLIR R&D Software 3.3*. Flir System, Inc., Wilsonville, USA, Publ. No. T559132.

FLIR, 2012b, *The Ultimate Infrared Handbook for R&D Professionals*, Flir System, Inc., Wilsonville, USA, Publ. No. T559243.

FLIR, 2014, FLIR Systems Thermography Product Catalog 2014, Flir System, Inc., Wilsonville, USA, Publ. No. T559480.

Florschuetz, L., Truman, C., and Metzger, D., 1981, "Streamwise flow and heat transfer distributions for jet array impingement with crossflow," Journal of Heat Transfer, 103, 337-342.

Fox, J., and Weisberg, S., 2010, "Nonparametric Regression in R,' an *Appendix to An R Companion to Applied Regression*, 2nd edition.

Friedrichs, S., Hodson, H. P., and Dawes, W. N., 1997, "Aerodynamic aspects of endwall film cooling," Journal of Turbomachinery, 119, 786-793.

Fujimoto, S., Okita, Y., and Nakamata, C., 2009, "Experimental study on the cooling performance of a turbine nozzle with an innovative internal cooling structure," ASME Paper GT2009-59597.

Ganzert, W., Hildebrandt, T., and Fottner, L., 2000, "Systematic experimental and numerical investigations on the aerothermodynamics of a film cooled turbine cascade with variation of the cooling hole shape, part 1, experimental approach," ASME Paper 2000-GT-295.

Gilboy, M. T., and Gan, X. P., 2003, "Validation of a new correlation parameter against film cooling data from a detailed literature survey," QINETIQ/FST/TR031284, QinetiQ ltd. Cody Technology Park, Farnborough, Hampshire GU14 0LX .

Gillespie, D. R., 1996, *Intricate internal cooling systems for gas turbine blading,* D.Phil. Thesis, University of Oxford, Department of Engineering Science.

Glezer, B., 2003, "Selection of a Gas Turbine Cooling System," in *Handbook of Turbomachinery*, 2nd edition.

Goldstein, R.J., 1971, "Film Cooling," in *Advances in Heat Transfer*, 7, pp. 280-284.

Goldstein, R. J., Eckert, E. R., Chiang, H. D., and Elovic, E., 1985, "Effect of surface roughness on film cooling performance," Journal of Engineering for Gas Turbines and Power, 107, 111-116.

Goldstein, R. J., Eckert, E. R., and Burggraf, F., 1974, "Effects of hole geometry and density on three-dimensional film cooling," Int. J. Heat Mass Transfer, 17, 595-607.

Goldstein, R. J., and Spores, R. A., 1988, "Turbulent transport on the endwall in the region between adjacent turbine blades," Journal of Heat Transfer, 110(4a), 862-869.

Gomes, R.A., and Neihuis, R., 2013, "The Concept of Adiabatic Heat Transfer Coefficient and Its Application to Turbomachinery," ASME Paper No. GT2013-94715.

Guo, S.M., Lai, C.C., Jones, T.V., Oldfield, M.L.G., Lock, G.D., and Rawlinson, A.J., 2000, "Influence of Surface Roughness on Heat Transfer and Effectiveness for a Fully Film Cooled Nozzles Guide Vane Measured by Wide Band Liquid Crystals and Direct Heat Flux Gages," Journal of Turbomachinery, Vol. 122, pp. 709-716.

Haas, W., Rodi, W., and Schönung, B., 1991, "The influence of density difference between hot and coolant gas on film cooling by a row of holes: predictions and experiments," ASME Paper 91-GT-255.

Hale, C.A., Plesniak, M.W., and Ramadhyani, S., 2000, "Film Cooling Effectiveness for Short Film Cooling Holes Fed by a Narrow Plenum," J. Turbomach., **122**, pp. 553-557.

Han, J. C., and Dutta, S., 1995, "Internal convection heat transfer and cooling: an experimental approach," In von Karman Institute for Fluid Dynamics, Lecture Series 1995-05 on Heat Transfer and Cooling in Gas Turbines, Belgium.

Han, J.-C., Dutta, S., and Ekkad, S., 2001, *Gas Turbine Heat Transfer and Cooling Technology*, CRC Press.

Han, J.C., and Zhang, Y.M., 1992, "High performance heat transfer ducts with parallel broken and V-shaped broken ribs," Int. J. Heat Mass Transfer, Vol. 35, No. 2, pp. 513-523.

Han, J. C., and Wright, L. M., 2006, "Enhanced internal cooling of turbine blades and vanes," In *The Gas Turbine Handbook* (pp. 321-352), U.S. Department of Energy, Office of Fossil Energy, National Energy Technology Laboratory.

Harstel, J. E., 1972, "Prediction of the effects of mass transfer cooling on the blade row efficiency of turbine aerofoils," AIAA Paper 72-11.

Herzig, H. Z., Hansen, A. G., and Costello, G. R., 1954, "A visualization study of secondary flows in cascades,", Technical Report TN 1163, NASA.

Hippensteele, S.A., 1974, "Pressure-Loss and Flow Coefficients inside a Chordwise-Finned, Impingement, Convection, and Film Air-Cooled Turbine Vane," NASA Technical Memorandum NASA TM X-3028.

Holland, M.J., and Thake, T.F., 1980, "Rotor Blade Cooling in High Pressure Turbines," J.Aircraft, 17(6), pp. 412-418.

Horlock, J.H., Watson, D.T., and Jones, T.V., 2001, "Limitations on Gas Turbine Performance Imposed by Large Turbine Cooling Flows," ," Journal of Turbomachinery, 123, pp. 487-494.

Howatson, A.M., Lund, P.G. and Todd, J.D., 2009, *Engineering Tables and Data*, University of Oxford, Department of Engineering Science.

Immarigeon, A., and Hassan, I., 2006, "An advanced impingement/film cooling scheme for gas turbines - numerical study," International Journal of Numerical Methods for Heat & Fluid Flow, 16(4), 470-493.

Ireland, P. T., and Jones, T. V., 2000, "Liquid crystal measurements of heat transfer and surface shear stress. Measurement Science and Technology," 11(7), 969-986.

Jambunatha, K., Lai, E., Moss, M. A., and Button, B. L., 1992, "A review of heat transfer data for single circular jet impingement," Int. J. Heat and Fluid Flow, 13(2), 106-115.

Jones, T. V., 1991, "Definition of heat transfer coefficients in the turbine situation,". In *Turbomachinery: Latest Developments in a Changing Scene*. C423/06: Proceedings of the Institution of Mechanical Engineers, London, UK.

Kays, W., Crawford, M., and Weigand, B., 2004, *Convective heat and mass transfer* (4th ed.). New York, NY, USA: McGraw-Hill Higher Education.

Kercher, D., and Tabakoff, W., 1970, "Heat transfer by a square array of round air jets impinging perpendicular to a flat surface including the effect of spent air," Journal of Engineering for Power, 92, 73-72.

Kingston, R., Bradley, C., and Bryant, D., 2011, *JB56 Training Course 2011,* 4th edition, Rolls-Royce plc., UK.

Kirollos, B., and Povey, T., 2014, "Reverse-Pass Cooling Systems for Improved Performance," Journal of Turbomachinery, 136.

Kirollos, B., and Povey, T., 2015a, "An Energy-Based Method for Predicting the Additive Effect of Multiple Film Cooling Rows," Journal of Engineering for Gas Turbines and Power, 137(12).

Kirollos, B., and Povey, T., 2015b, "Cooling Optimisation Theory, Part 1: Optimum Wall Temperature, Coolant Exit Temperature and The Effect of Wall/Film Properties on Performance," ASME Paper No. GT2015-43668, Turbo Expo, Montreal, Canada.

Kirollos, B., and Povey, T., 2015c, "Cooling Optimisation Theory, Part 2: Optimum Internal Heat Transfer Coefficient Distribution," ASME Paper No. GT2015-43674, Turbo Expo, Montreal, Canada.

Kollen, O., and Koschel, W., 1985, "Effect of film cooling on the aerodynamic performance of a turbine cascade," AGARD CP 390.

Kopmels, M., 2009, Patent No. GB2452327A/2009. G.B.

Kwor, E.T. and Simone, M., 2001, "Emissivity measurements for Nextel Velvet Coating 811-21 between -36°C and 82°C," High Temperatures – High pressures, 2001, volume 33, pp 551-556, 15 ECTP Proceedings pp. 1087 – 1092.

Kusterer, K., Bohn, D., Sugimoto, T., and Tanaka, R., 2006, "Double-jet ejection of cooling air for improved film-cooling," ASME Paper GT2006-90854.

Lakshminarayana, B., 1996, *Fluid Dynamics and Heat Transfer of Turbomachinery*. John Wiley & Sons, Inc.

Langston, L. S., 1980, "Crossflows in a turbine cascade passage," Journal of Engineering for Power, 102(4), 866-874.

Lawson, S.A., Straub, D.L., Beer, S., Casleton, K.H. and Sidwell T., 2013, "Direct Measurements of Overall Effectiveness and Heat Flux on a Film Cooled Test Article at High Temperatures and Pressures," ASME Turbo Expo Paper No. GT2013-94685.

LeGrives, E., and Nicolas, J. J., 1977, "Method nouvelle de calcul de l'efficacitede refroidissement des aubes de turbine par film d'air." AGARD CP 229.

Leylek, J. H., and Zerkle, R. D., 1993, "Discrete-jet film cooling: a comparison of computational results with experiments," ASME Paper 93-GT-207.

Liang, G., 2009, Patent No. US752747B1/2009. U.S.

Liang, G., 2010, Patent No. US2010183428A1/2010. U.S.

Liou, T. M., Chen, C. C., Tzeng, Y. Y., and Tsai, T. W., 2000, "Non-intrusive measurements of near-wall fluid flow and surface heat transfer in a serpentine passage," Int. J. Heat Mass Transfer, 43, 3233-3244.

Liu, C. L., Zhu, H. R., Bai, J. T., and Xu, D. C., 2010, "Film cooling performance of converging slot-hole rows on a gas turbine blade," Int. J. Heat Mass Transfer, 53, 5232-5241.

Luque, S., Aubry, J., and Povey, T., 2009, "A New Engine-Parts Annular Sector Cascade to Prove NGV Cooling Systems," 8th European Conference on Turbomachinery, Fluid Dynamics and Thermodynamics, Verlag der Technischen Universtat Graz, Graz, Austrai, March 23-27, pp.865-878.

Luque, S., and Povey, T., 2011, "A Novel Technique for Assessing Turbine Cooling System Performance," Journal of Turbomachinery, 133.

Luque, S., Batstone, J., Gillespie, D.R.H., Povey, T., and Romero, E., 2013, "Full Thermal Experimental Assessment of a Dendritic Turbine Vane Cooling Scheme," Journal of Turbomachinery, 136(2), pp. (021011-1)-(021011-9).

Luque Martinez, S.G., 2011, *A Fully Integrated Approach to Gas Turbine Cooling System Research*, PhD thesis, University of Oxford.

Martin, H., 1977, "Heat and mass transfer between impinging gas jets and solid surfaces," Advances in Heat Transfer, 13, 1-60.

Martiny, M., Schiele, R., Gritsch, M., Schulz, A. and Wittig, S., 1996, "In Situ Calibration for Quantitative Infrared Thermography," QIRT 96 – Eurotherm Series 50 – Edizioni ETS, Pisa 1997.

Mazur, Z., Luna-Ramirez, A., Juarez-Islas, J.A., Campos-Amezcua, A., 2005, "Failure analysis of a gas turbine blade made of Inconel 738LC alloy," Engineering Failure Analysis, **12**, pp. 474-486.

Metzger, D. E., Berry, R. A., and Bronson, J. P., 1982, "Developing heat transfer in rectangular ducts with staggered arrays of short pin fins,". Journal of Heat Transfer, 104, 700-706.

Metzger, D.E., Fan, Z.X., and Shepard, W.B., 1982, "Pressure Loss and Heat Transfer Through Multiple Rows of Short Pin Fins," *Heat Transfer 1982*, Vol. 3, U. Grigull et al., eds., Hemisphere, Washington, pp.137-142.

Metzger, D.E., Shepard, W.B., and Haley, S.W., 1986, "Row Resolved Heat Transfer Variations in Pin Fin Arrays Including Effects of Non-Uniform Arrays and Flow Convergence," ASME Paper No. 86-GT-132.

Neely, A. J., and Tracy, P. J., 2006, "Transient response of thermal paints for hypersonic flight test," 14th AIAA/AHI Space Planes and Hypersonic Systems and Technologies Conference.

Nowlin, S. R., 2009, *The use of intersecting film cooling passages for nozzle guide vane cooling*, D.Phil. Thesis, University of Oxford, Department of Engineering Science.

Okita, Y., and Nishihura, M., 2007, "Film-cooling effectiveness performance of an arrowhead-shaped film-cooling hole geometry," Journal of Turbomachinery, 129, 331-339.

Oldfield, M.L.G. and Guo, S.M., 1997, "Aero-thermal properties of foreign gas (SF_6/Ar) and air: recommended formulae from 160-1000 K," OUEL report 2141/97, University of Oxford, Department of Engineering Science.

Park, J.S., Han, J.C., Huang, Y., Ou, S., and Boyle, R.J., 1992, "Heat transfer performance comparisons of five different rectangular channels with parallel angled ribs," Int. J. Heat Mass Transfer, Vol. 25, No. 11, pp. 2891-2903.

Persico, G., Gaetani, P., and Dossena, V., 2009, "On the Definition of Secondary Flows in Annular Cascades," *Proceedings of the ETC 8.*

Povey, T., Jones, T. V., and Oldfield, M. L., 2007, "On a novel annular sector cascade technique," Journal of Turbomachinery, 129(1), 175-183.

Povey, T., Sharpe, M. and Rawlinson, A.J., 2011, "Experimental measurements of gas turbine flow capacity using a novel transient technique," Journal of Turbomachinery, Vol. 133(1), pp. 40-54.

Rådeklint, U. R., and Hjalmarsson, C. S., 1998, "Experimental and numerical investigation of heat transfer on a cooled turbine vane," ASME Paper 98-GT-212.

Rawlinson, A.J., 2001, "Trent 500 HP NGV aerofoil and platform cooling design report," Technical Report DKC168393, Rolls-Royce plc.

Rawlinson, A.J., 2014, "RE: radial temperature traverse," e-mail correspondence, 24th July 2014.

Rawlinson, A.J, and Falla, S.R., 2000, "Trent 500 HP nozzle guide vane in thermal paint test 70003/1—Summary of aerofoil and platform results," Technical Report DKC152898, Rolls-Royce plc.

Roach, P.E., 1987, "The generation of nearly isotropic turbulence by means of grids," International Journal of Heat and Fluid Flow, 8(2), pp. 82-92.

Rowbury, D., 1998, *Discharge Coefficients of Nozzle Guide Vane Film Cooling Holes*, DPhil thesis, University of Oxford.

Sabatino, D. R., Praisner, T. J., and Smith, C. R., 2000, "A high-accuracy calibration technique for thermochromic liquid crystal temperature measurements," Experiments in Fluids, 28(6), 497-505.

Saravanamuttoo, H.I.H., Rogers, G.F.C. and Cohen, H., 2001. *Gas turbine theory*. Pearson Education, Harlow, England, UK, 5th edition.

Sargison, J. E., Oldfield, M. L., Guo, S. M., Lock, G. D., and Rawlinson, A. J., 2005, "Flow visualisation of the external flow from a converging slot-hole film-cooling geometry," Experiments in Fluids, 38, 304-318.

Schultz, D. L., and Jones, T. V., 1973, "Heat transfer measurements in short duration hypersonic facilities," AGARD 165.

Schwarz, S., Goldstein, R., and Eckert, E., 1990, "The influence of curvature on film cooling performance," Journal of Turbomachinery, 112, 472-478.

Sellers, J. P., 1963, "Gaseous film cooling with multiple injection stations," AIAA Journal, 1(9), 2154-2156.

Sieder, E.N., and Tate, G.E., 1936, "Heat Transfer and Pressure Drops of Liquids in Tubes," Ind. Eng. Chem., 28(12), pp. 1429-1435.

Sieverding, C. H., Van Hove, W., and Boletis, E., 1984, "Experimental study of the three-dimensional flow field in an annular turbine nozzle guidevane," Journal for Gas Turbines and Power, 106(2), 437-444.

Sharma, O. P., and Butler, T. L., 1987, "Predictions of endwall losses and secondary flows in axial flow turbine cascades," Journal of Turbomachinery, 102(2), 229-236.

Sinha, A., Bogard, D. G., and Crawford, M. E., 1991, "Gas turbine cooling flow field due to a second row of holes," Journal of Turbomachinery, 113, 450.

Sinha, A., Bogard, D. G., and Crawford, M. E., 1991, "Gas turbine cooling flow field due to a second row of holes," Journal of Turbomachinery, 113, 450.

Snyder, J.C., Stimpson, C.K., and Thole, K.A., 2015, "Build Direction Effects on Additively Manufactured Channels," ASME Paper No. GT2015-43935, Turbo Expo Montreal.

Stimpson, C.K., Snyder, J.C., and Thole, K.A., 2015, "Roughness Effects on Flow and Heat Transfer for Additively Manufactured Channels," ASME Paper No. GT2015-43940, ASME Turbo Expo 2015, Montreal, Canada.

Sweeney, P.C. and Rhodes, J.F., 2000, "An Infrared Technique for Evaluating Turbine Airfoil Cooling Designs," Journal of Turbomachinery, Vol. 122, Jan. 2000, pp. 170-177.

Telisinghe, J., 2006, "AirProperties.jou," Fluent journal file, University of Oxford.

Thole, K. A., Sinha, A., Bogard, D. G., and Crawford, M. E., 1992, "Mean temperature measurements of jets with a crossflow for gas turbine film cooling application," In J. H. Kim, & W. J. Yang, *Rotating Machinery - Transport Phenomena*. Hemisphere Publishing Corporation, New York.

Thomas, M., 2014, *Optimization of Endwall Film-Cooling in Axial Turbines*, PhD thesis, University of Oxford.

Thomas, M., Kirollos, B., Jackson, D., and Povey, T., 2013, "Experimental studies of NGV Endwall Cooling," ASME Paper No. GT2013-95639, Proceeding of ASME Turbo Expo 2013, San Antonio, USA.

Tibbott, I., 2010, Patent No. US2010254801A1/2010. U.S.

Vasco, S., 2005, *Reduced pressure and temperature testing of film cooled nozzle guide vane at simulated engine conditions*. M.Sc. thesis, University of Oxford.

Van Fossen, G. J., 1982, "Heat transfer coefficients for staggered arrays of short pin fins," Journal of Engineering for Power, 104, 268-274.

Vogt, D. M., 2005, *Experimental investigation of three-dimensional mechanisms in low-pressure turbine flutter*, Ph.D. Thesis, KTH Royal Institute of Technology, Department of Energy Technology.

Wang, J.H., Messner, J. and Stetter, H., 2003, "An Experimental Investigation of Transpiration Cooling. Part I: Application of an Infrared Measurement Technique," Internal Journal of Rotating Machinery, 9(3): pp. 153-161.

Ward-Smith, A.J., 1979, "Critical flowmetering: The characteristics of cylindrical nozzles with sharp upstream edges," International Journal of Heat and Fluid Flow, Vol.1, Issue 3, pp. 123-132.

Wiberg, R., and Lior, N., 2004, "Errors in thermochromic liquid crystal thermometry," Review of Scientific Instruments, 75(9), 2985-2994.

Wilfert, G., and Fottner, L., 1996, "The aerodynamic mixing effect of discrete cooling jets with mainstream flow on a highly loaded turbine blade," Journal of Turbomachinery, 118, 468-478.

Wright, L. M., Gao, Z., Varvel, T. A., and Han, J. C., 2005, "Assessment of steady state PSP, TSP and IR measurement techniques for flat plate film cooling," ASME Paper HT2005-72363.

Zhu, H., Guo, T., and Xu, D., 2008, "Investigation of film cooling and superposition method for double row dustpan-shaped holes," Heat Transfer-Asian Research, 37(4), 208-217.

Zielińska, M., Yavorska, M., Poręba, M., amd Sieniawski, J., 2010, "Thermal properties of cast nickel based superalloys," Archives of Materials Science and Engineering, Vol. 44, Issue 1, pp. 35-38.